NASA Conference Publication 2475

Space Photovoltaic Research and Technology 1986

High Efficiency, Space Environment, and Array Technology

Proceedings of a conference
held at NASA Lewis Research Center
Cleveland, Ohio
October 7–9, 1986

NASA
National Aeronautics
and Space Administration

Scientific and Technical
Information Branch

1986

FOREWORD

The decade of the eighties has seen a rapid acceleration in the demand for more sophisticated technology in all aspects of the space program. Nowhere is this trend more evident than in the field of space power system technology, where projected power requirements range from a few kilowatts to megawatts and where increased emphasis is placed on high performance, reliability, and extended lifetime. At the same time, there has been an increased awareness of the effect of life cycle costs on total space mission costs. All of these factors, when coupled together, have spawned an intense interest in power generation using technologies that compete with photovoltaics, namely nuclear and solar thermal systems. The challenge to the space photovoltaic community is both harsh and clear. It is imperative that we fully understand the nature of future mission requirements and drivers, and that we meet them with new and enabling photovoltaic technology. The Space Photovoltaic Research and Technology (SPRAT) Conference provides a forum for the presentation of new ideas, issues, and challenges. Its purpose is to help direct the national space photovoltaic effort by providing the latest information available not only to members of the technical community, but to program planners in government and industry as well.

The structure of the conference was altered this year to include five workshops. Two of these because of the complexity of their topics and potential widespread interest, were convened for two sessions rather than one, as would be normal. The remaining three were more narrowly focused and were concluded in a single session. The workshop topics were as follows:

High Power/Large Area Systems (2 days)
Opportunities for PV Applications (2 days)
GaAs High Efficiency Limits
Device Modeling
InP Materials/Cell Fabrication

The workshops (in the order listed) were chaired by the following persons:

Joseph Wise, AFWAL, and Cosmo Baraona, NASA Lewis
John Scott-Monck, JPL, and Patrick Rahilly, Aerospace Corp.
Mark Spitzer, Spire Corp.
Richard Schwartz, Purdue University
Timothy Coutts, SERI

Workshop summaries were presented in oral session during the conference, and notes from those summaries have been included in this volume.

Key recommendations were made from the workshop deliberations:

- Photovoltaics must address system cost-reducing approaches to be viable for high power applications.

- It is crucial to have a PV option available for space station initial operational capability (IOC) add-on power in case a solar dynamic system is not ready.

- The dot junction geometry in III-V compounds should be investigated. (Radiation damage may be a key issue.)

- An improved fundamental understanding and more sophisticated modeling techniques (two-dimensional and Monte Carlo) are needed to further improve PV cell technology.

- The potential for 20 percent InP cells looks real.

This meeting may well be considered a landmark in the series, not only for the relevance of its output, but also for the opportunity it provided to introduce the potential of InP as a space solar cell material. The space PV community's growing interest in that material is illustrated by the very comprehensive report given by that working group. Although InP cell research and technology is at a relatively early stage compared with silicon and GaAs devices, AMO efficiency gains in the past 2 years have been impressive. There are, in addition, the intriguing preliminary results on the response of InP cells to electron and proton irradiations in the laboratory which suggest a vastly superior radiation resistance. The implications for future space PV systems are enormous.

The conference was organized by Michael Piszczor of the Lewis Research Center. He was ably assisted by Brian Good, Carrie Clapper, Pat Nicewander, and many other members of the Photovoltaic Branch.

Dennis J. Flood
Chief, Photovoltaic Branch
NASA Lewis Research Center Cleveland, Ohio 44135

CONTENTS

AN OVERVIEW OF PHOTOVOLTAIC APPLICATIONS IN SPACE

Robert A. Wasel
NASA Headquarters
Washington, D.C.

Power is certainly the backbone, the vital force of our program in space. As on earth, there is little we can do without it. Of all our space power sources, by far the most important is photovoltaic (PV) power (Fig. 1). Radioactive thermoelectric generators (RTG's) are also necessary for outer planetary missions where solar power is less effective. Not shown here but potentially an important power source of the future is the small nuclear reactor. Significant DOE and DOD funds are being utilized to develop a system capable of producing over 100 KW of power (SP-100) in the early 1990's. But little will occur in the near future to change this predominance of PV power, in fact there are environmental concerns that could lead to limitations on the use of RTG's, adding to the requirements for PV systems.

Fortunately for the satellite managers, PV system technology is improving at an impressive rate. Considering all the advanced spacecraft technologies, it is certainly among the leaders in performance improvements. NASA is a major participant in supporting PV technology and we are a primary user. The NASA PV effort is carried out in three parts: cell research at our Lewis Research Center (LeRC); concentrator research at our Marshall Space Flight Center (MSFC); and the lightweight array program at the Jet Propulsion Laboratory (JPL). LeRC acts as our Lead Center for overall coordination. Significant improvements have been made in all three areas and more are on the horizon.

PV systems contribute at all levels of NASA mission requirements (Fig. 2). Low to intermediate power levels are required for unmanned low earth orbit and inner planetary missions. Intermediate to high power levels are necessary for geostationary, lunar, outer planet, space station and electric propulsion thrusters. Incidentally, electric propulsion offers an interesting symbiosis with PV if they are selected for an outer planet mission. The PV system must be sized to produce a given power level in the low-solar intensity at the operating area. This array would be dramatically oversized in the early phase of the mission, near earth. The surplus could be used to power an electric thruster, shortening the trip time or increasing the payload. For example, if 500 watts are required at the end of a year of orbiting in the radiation environment of Jupiter, the required array could produce over 20 KW in the earth orbit for high efficiency electric thrusters.

NASA PV technology has developed along two paths (Fig. 3), one toward high power, the other high efficiency. High power will be attained through concentrator cells and reflecting arrays. Our goal here is to produce 200 watts/m^2, twice the level demonstrated in the collapsible array flown on the Space Shuttle in the SEPS experiment. For applications where weight is at a premium, we will use our most efficient, radiation tolerant cells with advanced deployment systems to attain our goal of 300 watts/Kg. JPL currently has designs in hand that are capable of 130 watts/Kg, almost twice the level of the SEPS flight test.

For high power requirements in earth orbit, like the Space Station, drag area becomes a consideration. Figure 4 shows the size advantage that the advanced con-

centrator cells offer. By using these 5mm square GaAs cells and efficient concentrator lenses, the required cell area is reduced, not only to less than half that required for current planar silicon arrays, but to even less area than that projected for the large focusing dish liquid organic rankine cycle power generators which are candidates for the Space Station.

In addition to the development of the lightest and highest efficiency arrays, lifetime characteristics are increasing in importance. Current arrays, if exposed to radiation, are certain to lose performance capability. Missions in the Van Allen belts or near Jupiter may see 50% degradation during a year, meaning that the initial array must be twice the normal size and weight. In this case an improvement in cell radiation resistance is a direct payload increase. In Figure 5, note that current silicon cells are almost destroyed by seven years in the radiation belts. GaAs offers a significant improvement, and Indium Phosphide (InP) is probably the best material tried to date. Of course the ultimate objective is a cell that is completely unaffected by radiation, or one that anneals or heals itself at ambient temperature.

The attendees at this meeting have made great strides in PV technology. Some of these are shown on Figure 6, and a number of additional ones are in store, perhaps to be reported at this meeting. What are the next mission opportunities? Several are illustrated in Fig. 7. The Space Station and its "satellites," the polar and co-orbiting platforms. These could be opportunities for advanced concepts, but may be restrained by conservatism or modularity for interchangeability. RTG's have the spectre of radioactive-during-launch to contend with, but are so remarkably efficient for outer-solar system missions that it would be a real challenge to replace them. SDI applications are not yet defined, but are sure to be interesting.

In addition to these, NASA has been getting a great deal of encouragement from advisory committees to expand its programs and research efforts. The prestigious National Commission on Space (NCOS Chairman Dr. Thomas Paine) after noting that the funding of Space R&T at NASA had dropped from over $800M in 1965 to less than $200M in 1986, stated that "NASA'S space research and technology program should be tripled, moving from its current 2% of NASA's budget to 6%." In terms of our 1987 budget this would be an increase from $170M to over $500M. Other advisory committees showed a remarkable concensus - that there should be a 2-3 times increase in NASA Space R&T to correct technology deficiencies. This advise was received from the Aeronautics and Space Engineering Board of the National Academy of Sciences, NASA's Space Systems Technology Advisory Committee, the American Institute of Aeronautics and Astronautics and the National Security Study Directive Team.

The NCOS also recommended an ambitious series of projects to be added to the NASA mission plan. Fig. 8 shows the NASA future mission blueprint with the NCOS additional proposed missions in boxes. NASA has already responded to this NCOS challenge and a proposal for a significant R&D program increase is being considered for FY 1988. Photovoltaic systems will obviously be an important part of any acceleration of space technology effort. The Initial Operational Configuration (IOC) Space Station will depend on PV systems for one half of its 75 Kw power. The system design is extremely conservative (about 25 w/kg), so a great deal of improvement is possible, ideally in time to contend for the "Growth" Station in the late 1990's which will require several hundred kilowatts. The next major NASA undertaking may be a Lunar base, potentially in 2010. Next to life support, power may be the most important issue. Power not only for the occupants and their exper-

iments but possibly for on-site operations such as propellant manufacturing. PV systems would be a reasonable contender for generating some of this power, probably in the hundreds of kilowatts, particularly if there is an efficient lightweight, low cost, transportable concept by that time. It might be shipped in a roll like a window shade and simply layed on the surface.

Meanwhile, the United States is not alone in space or in the development of PV systems for space. Fig. 9 shows the USSR Salyut 7 manned space craft with an appended module, currently in orbit as part of their manned station program. Salyut 7 was launched in 1982 with silicon cell solar arrays capable of generating 4KW. Within the next two years, this solar array was supplemented by the small extendable arrays shown beside the central array. These were reported to be gallium arsenide (GaAs) cells, the first to be used operationally in space. The GaAs arrays produced about 4 KW. This USSR capability should be a very sobering challenge to the attendees of this meeting, the technologists, researchers and managers of PV programs in this country.

In summary, PV has made possible much of our scientific accomplishments in space and with proper support and progress in the R&D community it will continue its contributions.

POWER IS THE BACKBONE/VITAL FORCE BEHIND THE SPACE PROGRAM

- **PV IS THE PRIMARY POWER SOURCE**

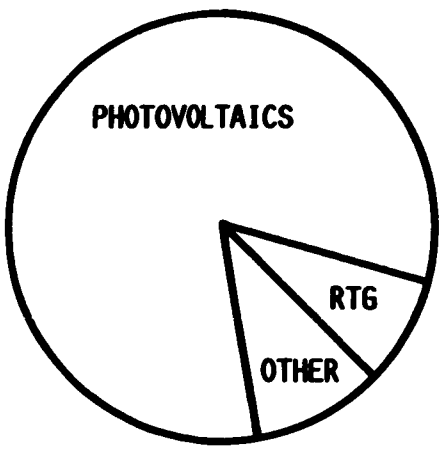

POWER PRODUCED FOR NASA MISSIONS (DOES NOT INCLUDE SPACE SHUTTLE)

Figure 1.

PHOTOVOLTAIC POWER GENERATION IS APPLICABLE ACROSS THE NASA MISSION MODEL

MISSION SUBSET	POWER LEVEL	SYSTEM ATTRIBUTES
UNMANNED NEAR EARTH (LEO, HEO, GEO) AND PLANETARY	LOW TO INTERMEDIATE	LOW MASS, LONG LIFE
SPACE STATION	HIGH	MINIMUM AREA, LOW MASS, LOW COST
GEO PLATFORM	INTERMEDIATE	LONG LIFE, LOW MASS
LUNAR BASE, MANNED PLANETARY	INTERMEDIATE TO HIGH	LOW MASS, LONG LIFE, PORTABILITY
ELECTRIC PROPULSION ORBIT TRANSFER (OTV)	HIGH	REUSABILITY, MINIMUM AREA, LOW MASS

Figure 2.

DUAL TECHNOLOGY PATHS SPAN THE NASA MISSION MODEL

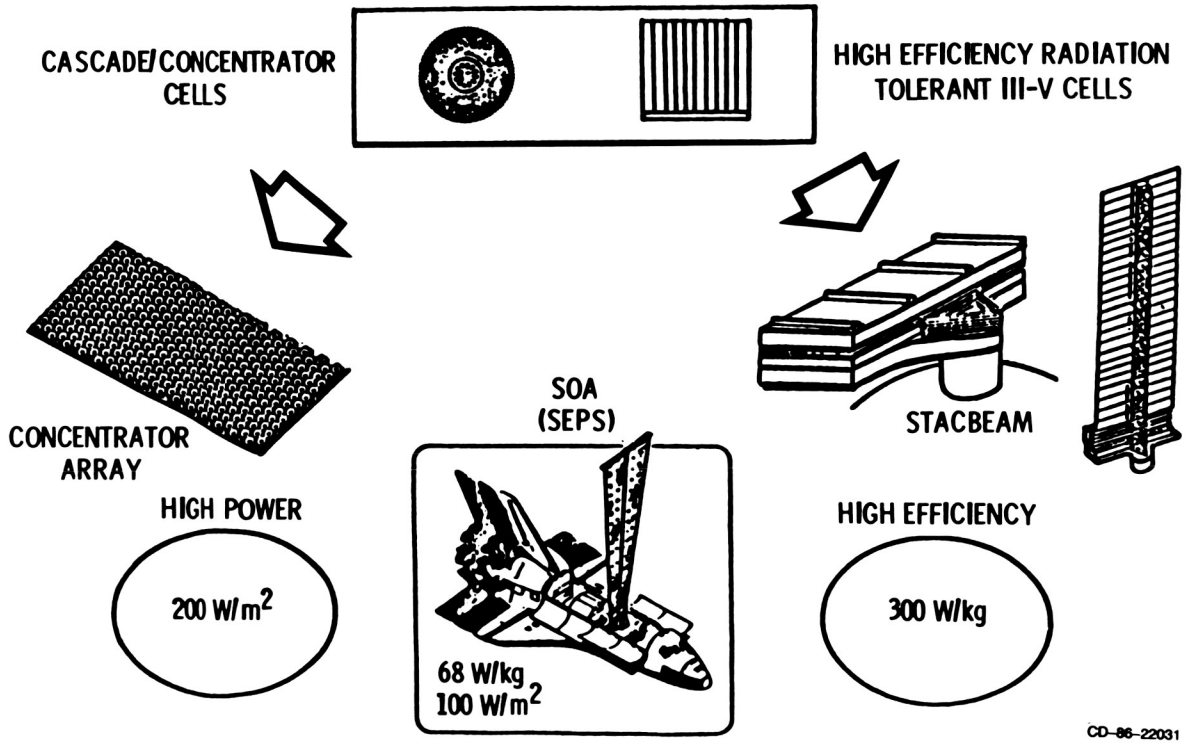

Figure 3.

THRUSTS

- o HIGH EFFICIENCY, SMALL AREA CELLS
- o LIGHTWEIGHT, EFFICIENT OPTICS
- o RIGID; DEPLOYABLE, LIGHTWEIGHT ARRAYS
- o REDUCED POINTING REQUIREMENTS

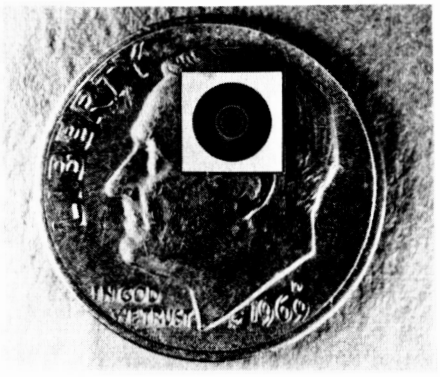

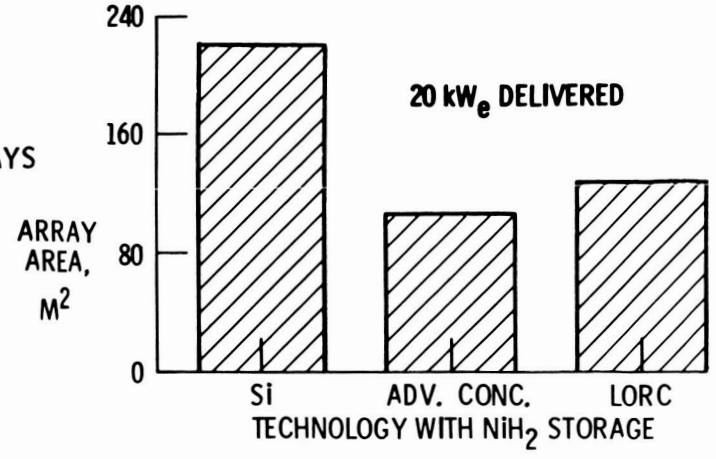

PLANAR Si:

14 % CELL

ADVANCED CONCENTRATORS:

> 30 % CELL

> 94 % OPTICAL EFFICIENCY

Figure 4.

COMPARISON OF SOLAR ARRAY CALCULATED OUTPUT AS FUNCTION OF ORBIT ALTITUDE BASED ON 1 MeV ELECTRON EQUIVALENT FLUENCES

TIME IN ORBIT = 7 YEARS, CIRCULAR ORBIT, 30^0 INCLINATION, T = $60\,^0C$

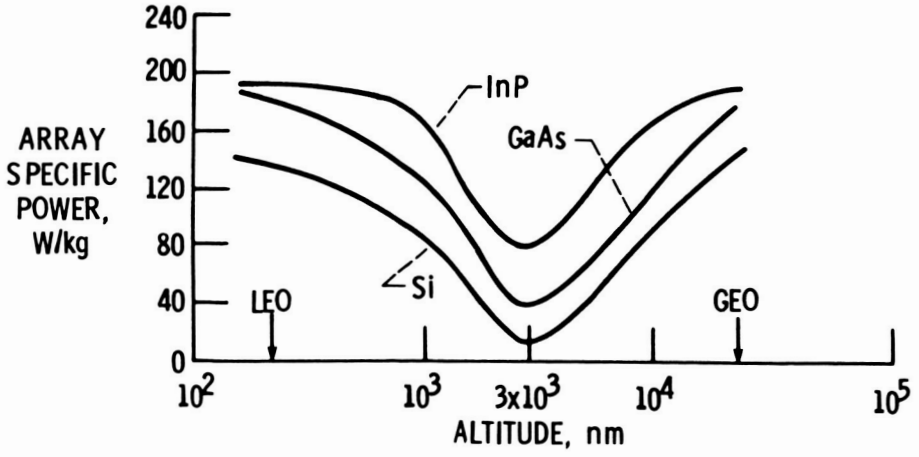

Figure 5.

SIGNIFICANT IMPROVEMENTS MADE AND MORE ARE COMING

	IMPROVEMENT	SIGNIFICANCE
DONE:	2 MIL SILICON CELL	RADIATION RESISTANCE, LIGHTWEIGHT ARRAYS
	GaAs CONCENTRATOR CELL	>20% EFFICIENCY, LOW COST/WATT
	SEP/OAST-1 ARRAY	>60% W/KG FLEXIBLE ARRAY TECHNOLOGY
	LARGE AREA Si CELL	LOW ARRAY COST
COMING:	>20% InP CELLS	RADIATION BELT SURVIVABLE ARRAYS
	CONCENTRATOR ARRAY	HIGH EFFICIENCY, HIGH POWER, RADIATION TOLERANCE
	STACBEAM, APSA	ULTRALIGHTWEIGHT ARRAYS

Figure 6.

WHAT'S NEXT

- SPACE STATION - LARGE SYSTEM, BUT POOR PERFORMANCE (5 W/KG 10C)
- CO-ORBITING AND POLAR FREE-FLYERS (CONSTRAINED BY MODULARITY?)
- RTG REPLACEMENT?
- ELECTRIC PROPULSION ORBIT TRANSFER?
- SDI APPLICATIONS (HOUSEKEEPING, RADIATION/BLAST RESISTANCE)

Figure 7.

BLUEPRINTS TO THE FUTURE

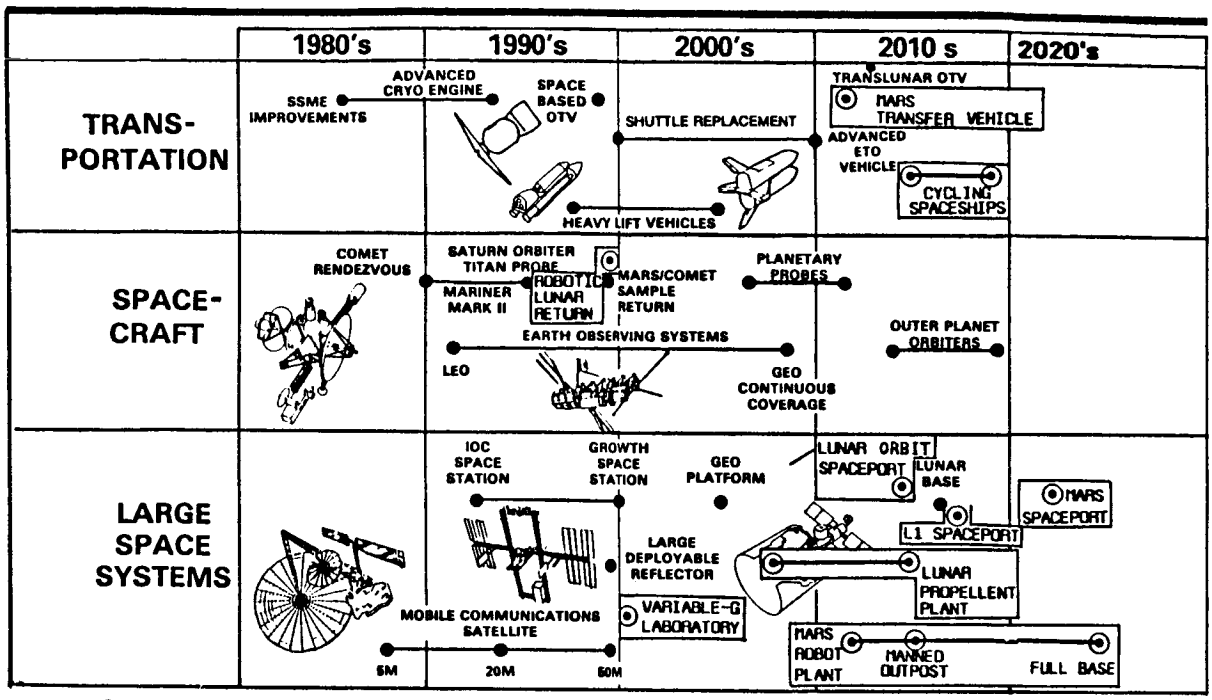

NASA

Figure 8.

CONCEPTUAL DRAWING OF INTERIOR OF KOSMOS 1443-TYPE MODULE, SALYUT 7, AND A SOYUZ T FERRY CRAFT

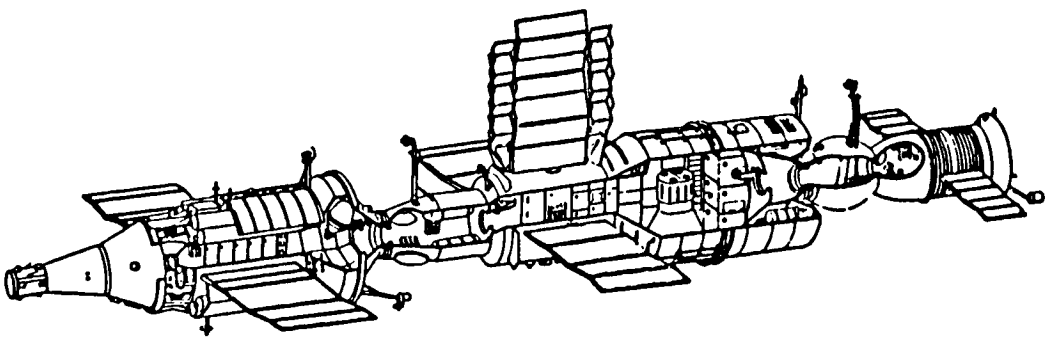

Figure 9.

AIR FORCE AND DOD SOLAR POWER REQUIREMENTS

Joseph F. Wise
AF Wright Aeronautical Laboratories
Wright-Patterson AFB, Ohio

The Air Force and other members of the Department of Defense have been operating in space since our space program began in 1957. Power requirements have grown to meet the needs of critical missions and in concert with launch vehicle capabilities. The performance parameters which have made photovoltaic solar cell arrays the principal power supplier for these satellite missions are long life, reliability, minimum vehicle disturbance, low weight and reasonable cost. These parameters will continue to make photovoltaics the primary choice for space power systems provided we develop the component and system technology needed for future, higher power, survivable systems.

Two major activities are guiding and determing future space missions and their power requirements - the Strategic Defense Initiative (SDI) and Project Forecast 2 (PF2). The SDI power requirements range from 10's to 100's of kilowatts steady-state power to many megawatts of burst or pulse power. (1) In addition, these systems are to be survivable, long life, affordable, and able to function under a variety of launch, operation and emergency conditions. The missions outlined under PF2 project new requirements for the traditional missions as well as new missions. These new requirements include survivability from not only direct attack, but also such electronic threats requiring antijamming, secure data and communication links, and operation without ground station support. These emerging requirements are driving the power needs up to the 50 to 100 kilowatt range for certain critical missions, but the bulk of the satellite power needs will be below 25 kW in the next 15 years.

There are several critical technologies that need to be developed to enable these new or expanded missions to be accomplished. These include survivability which includes weapon threats, environmental interactions, hardening and autonomy, longer life, higher power density and efficiency, and minimum vehicle disturbance. The specific technologies needed are shown in Table I.

Future system power requirements beyond 1995 will grow to the hundreds of kilowatts. This in turn requires on-orbit assembly and servicing, modularity, and standardization of interfaces. With a well supported photovoltaics program, I feel we can meet the needs of future systems with the most versatile, light weight, long life, and economical technology.

FUTURE SPACE POWER REQUIREMENTS

Studies relative to Air Force and Department of Defense missions for the future indicate requirements for increased capabilities and survivability of the standard missions as well as new missions in the areas of transportation and defense. Mission expansion requirements include improved surveillance both

infrared detection and radar, more secure data links to resist the effects of scrambling or signal upset, jamming, and functioning with fewer ground stations should some Earth geological areas be denied to us. These expanded capabilities push near-term requirements to the 50 kW power level for survivable system technology although many vehicle power requirements will still be below 25 kW. Figure 1 shows the trend in future power requirements. New missions such as Orbital Transfer Vehicle and Strategic Defense systems project not only higher power levels but newer requirements for radiation resistance and annealability, maneuverability and possibly on-orbit assembly, servicing and maintenance. These new missions may also require very large pulse or burst power as shown in Figure 2. The photovoltaic/battery supply would not supply all the power needed - specifically the burst power may utilize a chemical source - but the technology to handle the base load and the alert mode should be developed. These vehicle missions represent a large investment and need to operate 10 years or more.

TECHNOLOGY REQUIRED

The primary future power need is for survivable systems up to 50 KW. The concentrator concept being developed under the Air Force Survivable Concentrator Photovoltaic Array (SCOPA) program is our first attempt to meet this need from a hardening to laser and nuclear weapons standpoint. This concentrator is also a prime candidate for operation in high radiation environments because of the inherent shielding afforded to the solar cells by the metallic reflector optics. This is thus enabling technology for "Belt Fliers" in mid altitude orbits which traverse the Van Allen belts. Other aspects of survivability are being investigated in the Aero Propulsion Laboratory's program, Enhanced Survivability Array. This includes both increased hardening of array components as well as developing the technology for autonomous operation and control of solar cell arrays. Table II (2) presents a summary of what controls are needed to provide autonomy. Similar functions are needed for the other power subsystems such as Energy Storage, Power Conditioning and Switching, and Electrical Power System Management. One possible approach to achieving this is the use of artificial intelligence in the power system subsystem microprocessor controllers and to develop the algorithms for all operational, malfunction, or damage conditions. The third technology needed to be developed is thin light weight solar cell arrays. A paper by John Scott-Monck in 1984 (3) demonstrated that the potential for better than 200 watts/kg of the solar array was achievable utilizing thin silicon solar cells of 16% efficiency. This kind of technology is under development by the Jet Propulsion Laboratory except for the 16% efficient thin silicon cell. A new thin GaAs solar cell technology is emerging and will be reported on in this conference consisting of GaAs on thin germanium substrates with a potential efficiency of 18 to 20% with a solar array performance potential of 100 watts/lb or better. The fourth capability needed for future growth is development of solar cell concepts up to 30% efficiency. These cells also need to withstand high radiation doses and relatively high temperatures (600C) to be utilized in planar and contractor solar arrays. A 30% efficient solar cell will permit us to achieve 300 to 350 watts/kg (150 watts/lb) in a solar array and with improvements in power conditioning and battery technology up to 25 watts/lb can be achieved in a complete power system (4). The fifth technology development needed is how to design, develop, deploy, and operate high power survivable solar power systems. Several workshops and studies have been conducted to define the problems and the technologies needed in this area including the High Voltage High

Power Solar Power System Study for the Air Force by LMSC, the High Voltage Design Guide for the Air Force by Boeing (5), the Study of Multimegawatt Technology Needs for Photovoltaic Space Power Systems by General Dynamics (6) and the Space Power Workshop held by NASA LeRC in 1984 (7). These all identify new problems as shown in Table III from environmental interactions with high voltage solar arrays from the space plasma arcing and/or leakage, effects of natural and vehicle generated debris, radiation effects, and the synergistic effects of several of these species interacting simultaneously. Problems with high voltage will exist with all high power systems-terrestrial, aircraft, or space - and we need to develop the analytical and experimental tools to solve them. Flight experiments such as the Voltage Operating Limit Test (VOLT) series planned by NASA and the Interactions Measurement Payload for Shuttle (IMPS) series planned and under construction by the Air Force are needed to acquire quantitative data in space to validate the models and the plasma chamber experiments being conducted by NASA and the Air Force. The Photovoltaic Array Space Power (PASP) flight experiment, shown in Figure 4, is part of the IMPS/SPAS mission experiment and is to determine the performance and environmental interactions of the polar and equitorial environments with oriented, illuminated, voltage biased, advanced solar array modules. Both concentrator and planar arrays and silicon and gallium arsenide solar cell modules will be tested with bias voltages to +- 500 volts applied to simulate high voltage high power solar cell arrays. Other technology needed besides understanding environmental interactions is how to fabricate, launch, deploy or construct large power systems in space. On-orbit construction and servicing will make new demands on ruggedness, modularity and standardization of interfaces so that solar array modules can be exchanged or replaced to improve system performance.

SUMMARY

Future power requirements are increasing for some expanded and new missions within the Air Force and Department of Defense. New requirements are needed in terms of lifetime, survivability, power level, and performance. The photovoltaic arrays have a demonstrated record of reliable performance, life, affordable cost, and utility; and they can be a prime contender for these future high power missions. We need to push for the R & D resources needed to develop the technology base for these future power system needs.

List of References

1. L. D. Massie, et. al., Military Space Power Systems Technology for the Twenty-First Century. 21st IECEC San Diego, CA. August 1986

2. J. F. Wise, et. al., Autonomy Requirements for Satellite Power Systems. 19th IECEC, San Francisco, CA. August 1984, Vol 1

3. John Scott-Monck, et. al., Recent Developments in High Performance Planar Solar Array Technology. 19th IECEC, San Francisco, CA. 1984 Vol 1

4. J. F. Wise, Comparison of High Power Solar Power System Concepts to Other Options, 18th IEEE Photovoltaic Specialists Conference. Las Vegas, NV. October 1984

5. W. G. Dunbar, High Voltage Design Guide: Spacecraft. AFWAL TR 82-2057 January 1983

6. D. M. Peterson, et. al., Study of Multimegawatt Technology Needed for Photovoltaic Space Power Systems. Contract NAS3-21951 Final Report Vol I II, May 1981

7. J. F. Wise, L. D. Chidester, Space Power Workshop, Photovoltaic Working Group Report, NASA Conference Publication 2352, Cleveland, OH. April 1984

Table I Needed Technology For Future Space Power Systems

Concentrator Solar Arrays

Autonomous Operation

Lightweight Thin Array Technology

High Efficiency Solar Cells for Planar and Concentrator Application

High Power System Capability, High Voltage, Min. Environ. Interaction

Table II Solar Cell Array Autonomy Needs

Maintain Sun Orientation

Provide Power Management - On-Array Switching

Sense Malfunction and Damage - Reconfigure

Provide for Survivability and Graceful Degradation

Minimize Thermal Management Load - On-Array Switching

Annealing Radiation Damage to Array Segments

Monitor and Report Solar Array Status

Table III High Power System Concerns and Interactions

Survivability:	Direct Threats
	Loss of Ground Station Links
High Voltage:	Arcing, Leakage
	Corona
	Beads of Pearls
Structure/Array:	Stowage
	Deployment
	Vehicle Interfaces
Environmental Effects:	Plasma
	Debris
	Radiation
	Thermal
	Electrostatic
	Solar Storms

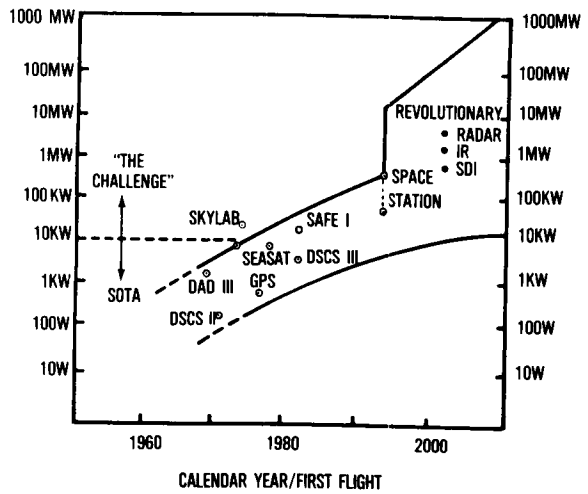

FIGURE 1. SPACECRAFT ELECTRICAL POWER TRENDS

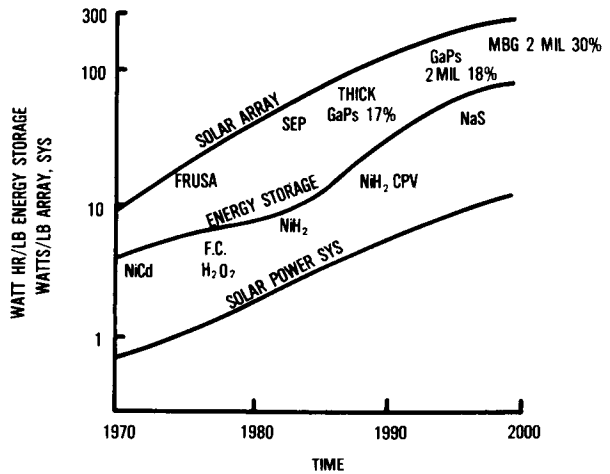

FIGURE 3. SOLAR CELL ARRAY CAPABILITIES

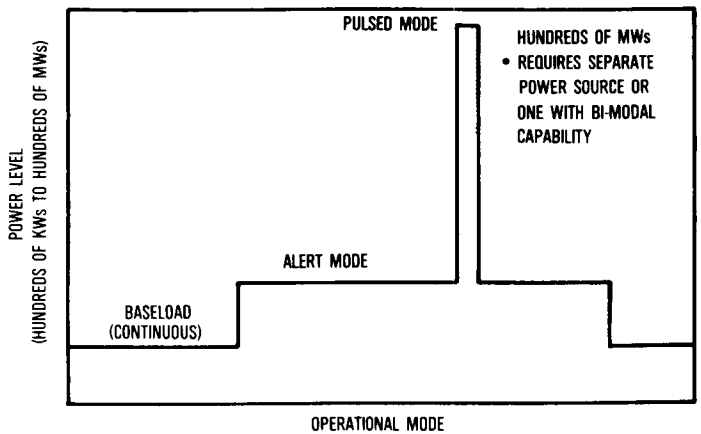

FIGURE 2. HYPOTHETICAL MISSION LOAD PROFILE

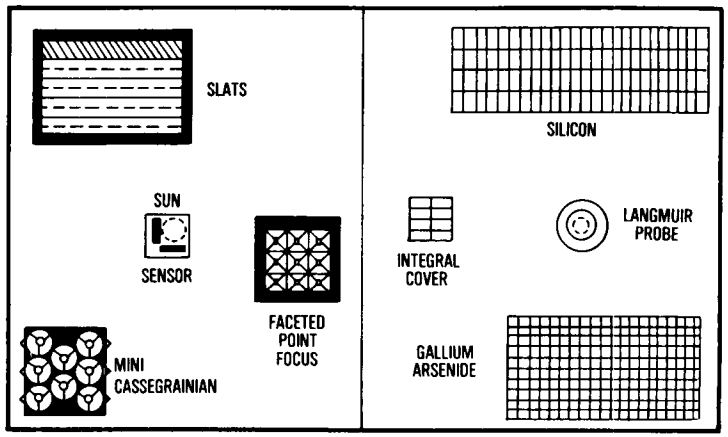

FIGURE 4. IMPS/PASP PANEL

POINT CONTACT SILICON SOLAR CELLS

Richard M. Swanson
Stanford University
Stanford, California

A new type of silicon concentrator solar cell has been developed. It is called the point-contact cell because the metal semiconductor contacts are restricted to an array of small points on the back of the cell. The point contact cell has recently demonstrated 22 percent conversion efficiency at one sun and 27.5 percent at 100 suns under an AM1.5 spectrum.

Text

The point-contact cell derives its high efficiency from a synergistic combination of:

- Light trapping between a texturized top surface and a reflective bottom,
- Thin, high resistivity, high lifetime base,
- Small point contact diffusions, alternating between n-type and p-type in a polka-dot pattern on the bottom, and
- Surface passivation on all surfaces between contact regions.

The operation and performance of experimental point contact cell is described in the following figures.

This work supported in part by the Electric Power Research Institute and the Department of Energy through Sandia National Laboratories.

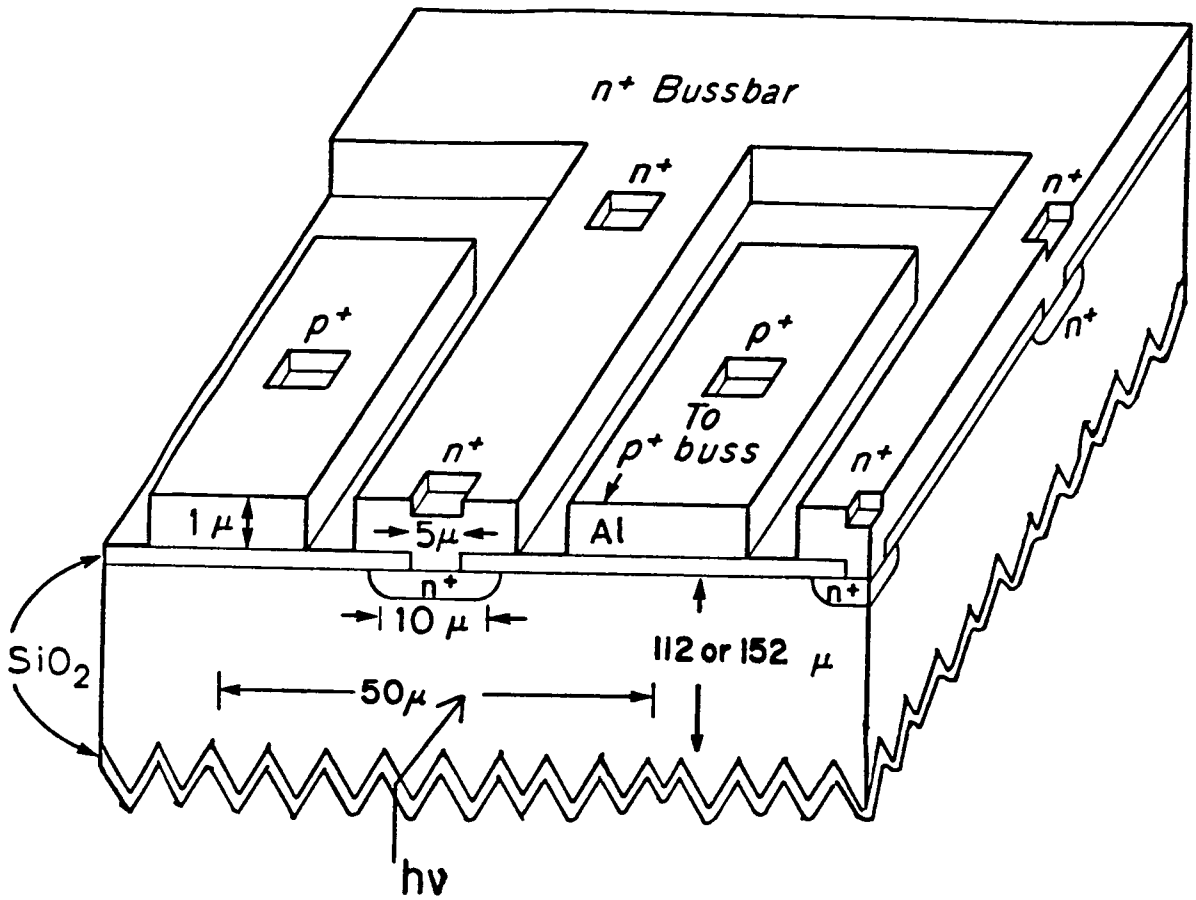

Figure 1: Structure of the test cells currently being made. Both electrical leads are on the back surface in an inter-digitated pattern. The metal touches the silicon only in an array of points, alternating between n and p-type in a checkerboard pattern. The cell is thin, around 100 μm, and fabricated of high lifetime, high resistivity float-zone silicon. The regions between contacts are passivated with SiO_2 and the front surface is texturized.

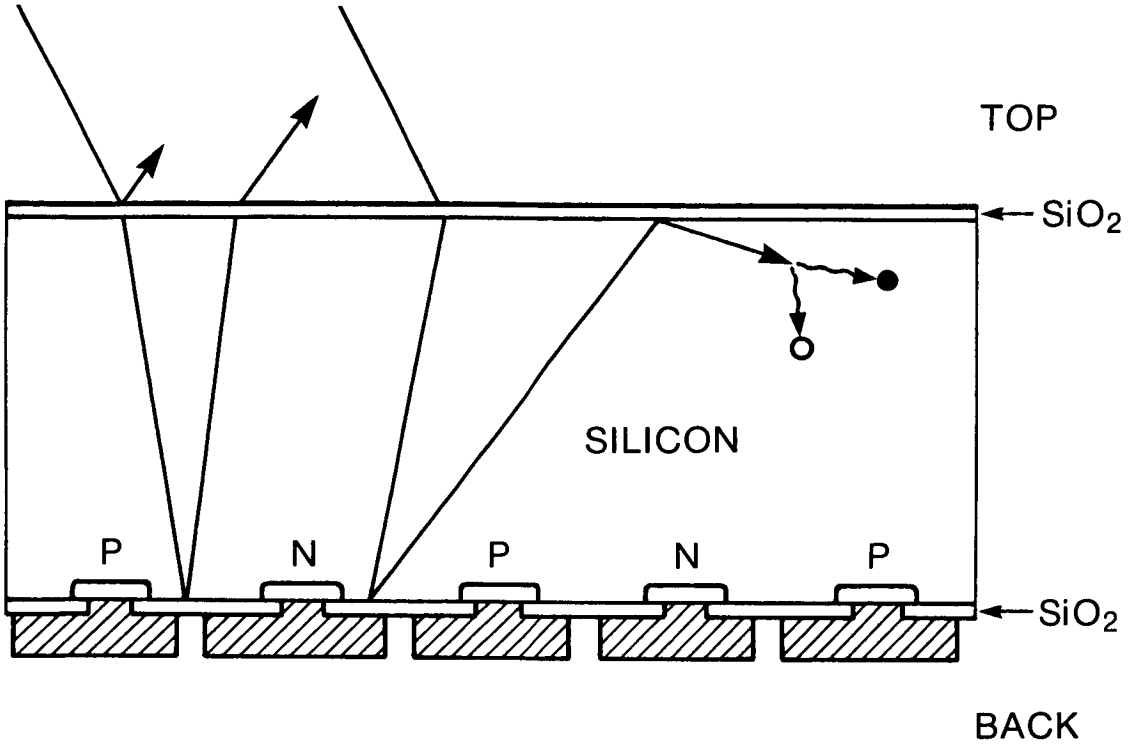

Figure 2: Light trapping is caused by the diffuse nature of scattering from a texturized surface. If a photon is not absorbed upon reaching the back surface it is reflected off the back surface reflector. If it is still not absorbed by time it reaches the top there is a very high probability (about 88 percent) that it will be beyond the angle for total internal reflection and hence will be reflected back into the cell. Much of the weakly absorbed near bandgap light is thus trapped within the cell.

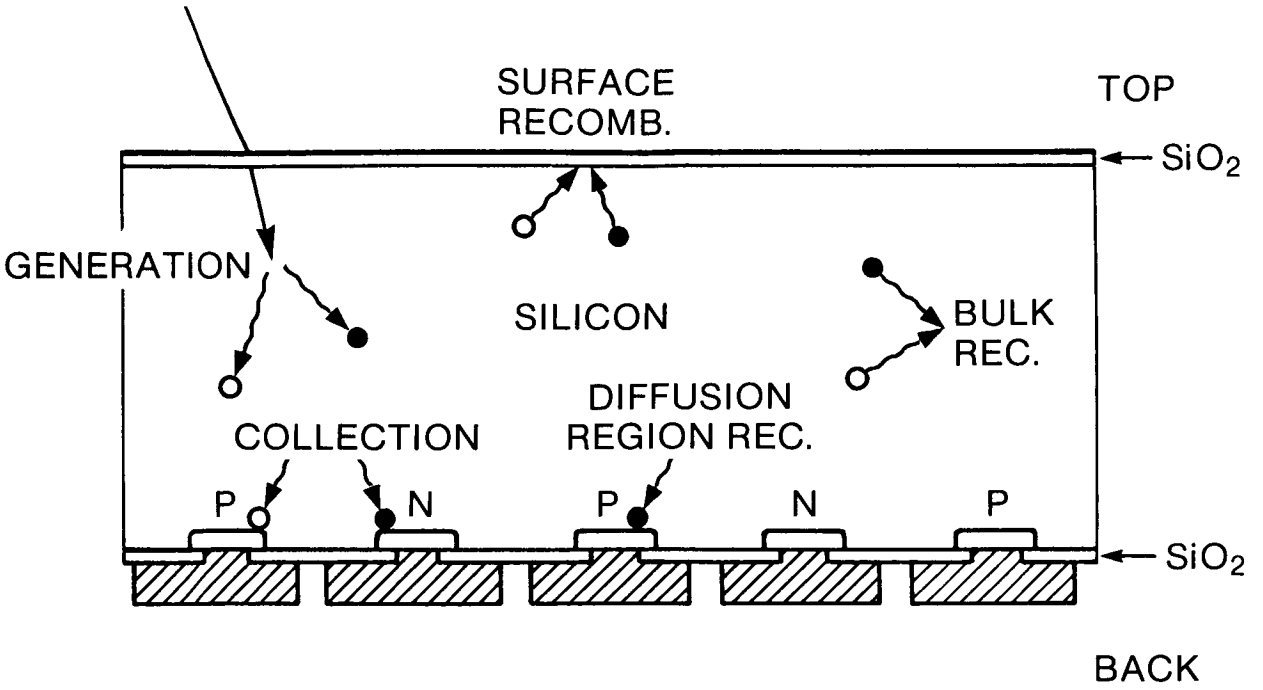

Figure 3: For high efficiency it is necessary to reduce carrier recombination as much as possible. This is to provide for:

- Collecting as large a fraction of the photo-generated carriers as possible,
- Generating as large a voltage (which goes exponentially in the p-n product) as possible, and
- Producing as much conductivity modulation in the base, and hence reducing base voltage drop, as much as possible.

The point contact cell reduces recombination by passivating the surfaces with SiO_2, using high lifetime float-zone silicon, and reducing the metal-semiconductor contact fraction through the point contact scheme.

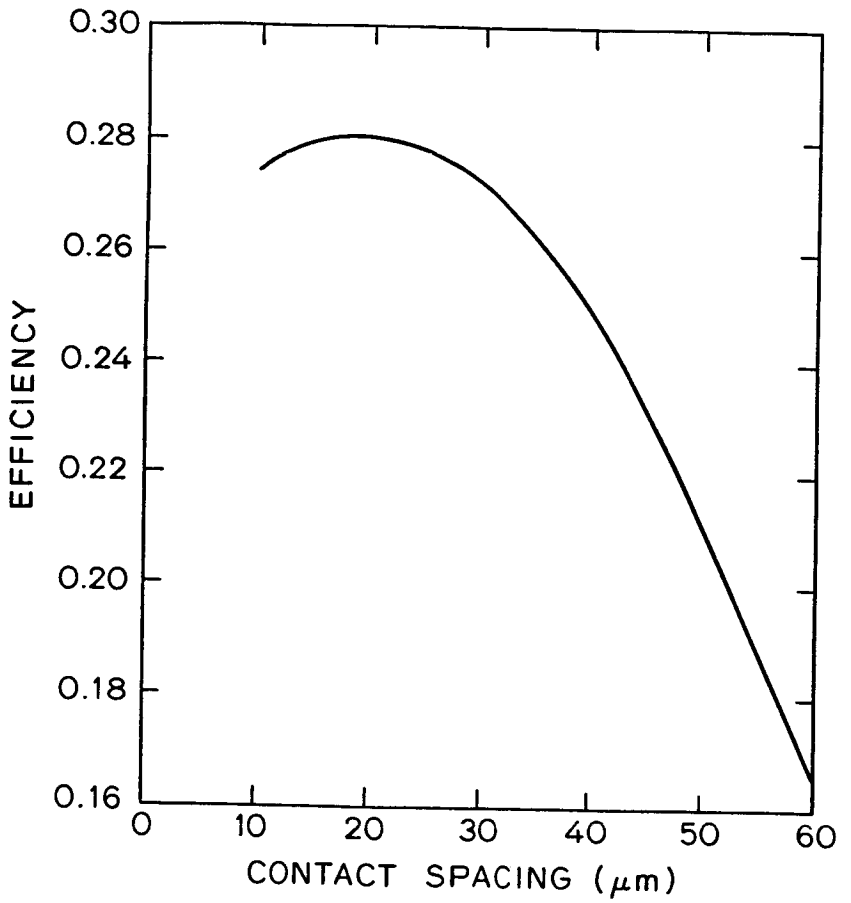

Figure 4: A three dimensional model has been developed to explore the potential of the cell and optimize the design. Important findings are:

- The contact spacing must be rather small to prevent excessive losses through base spreading resistance at the contact diffusions.
- The cell must be thin, in the 60 to 100 μm range, in order to keep the front surface carrier density low enough that Auger recombination (which goes as the third power of carrier density) does not excessively limit collection efficiency.
- The base lifetime must be over 500 μsec.
- The surface recombination velocity must be less than 10 cm/sec.
- The cell is capable of efficiencies of around 29 percent at 27 °C if the above conditions are met.

This figure shows the calculated efficiency versus contact spacing at a cell temperature of 330 K.

One Sun Results AM1.5 100 mW/cm^2								
Cell	Thickness	Texturized	Efficiency	V_{oc}	J_{sc}	V_{mp}	Fill Factor	Temp
11-3B	112 μm	Yes	22.2%	.681 V	41.5 mA/cm^2	.582 V	.786	24 °C
11-1A	152	No	18.5%	.678	35.0	.570	.778	26

Figure 5: Important one sun parameters of the test cells are shown. This table illustrates the importance of texturizing for improving the short circuit current.

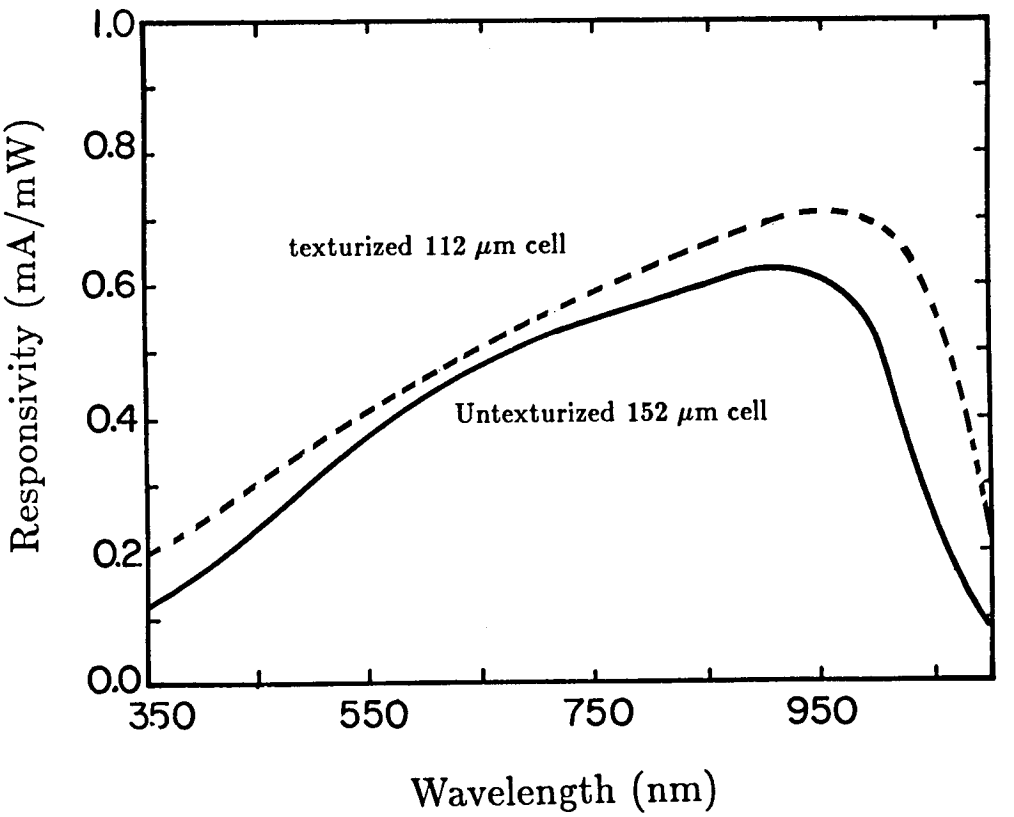

Figure 6: The spectral responsivity of a texturized and untexturized cell is shown. At shorter wavelengths the texturizing has reduced the reflectivity, resulting in improved response. Near the bandgap, however, the response has been dramatically increased due to light trapping.

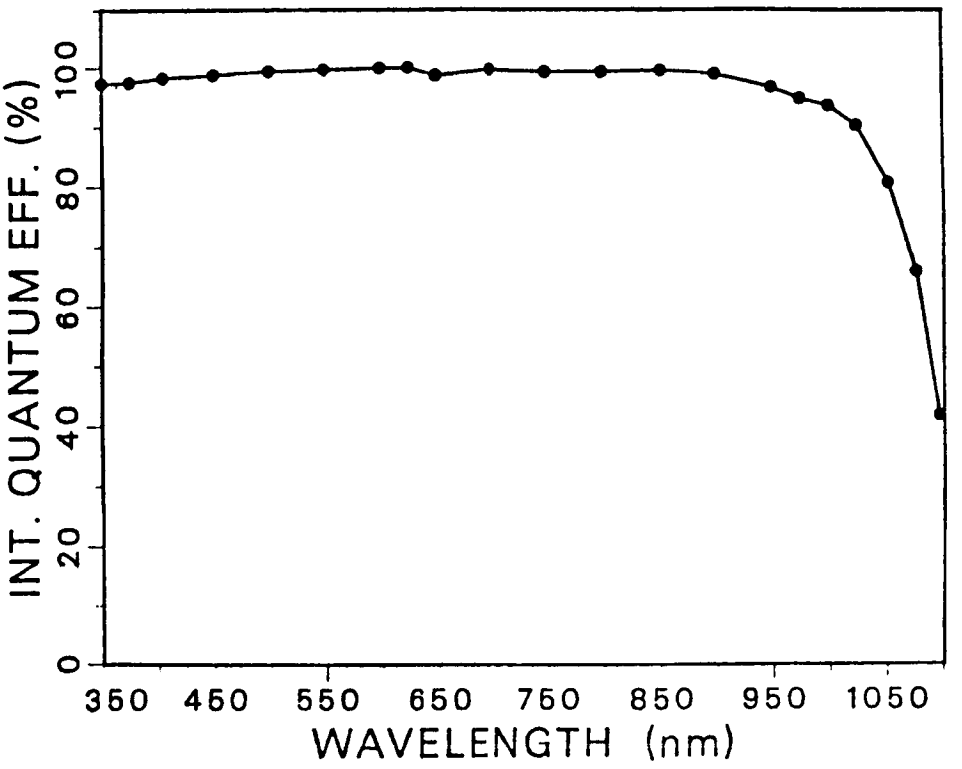

Figure 7: The internal quantum efficiency is essentially unity until near the bandgap, where competing absorption mechanisms, such as absorption in the back surface mirror, become comparable to photo-absorption.

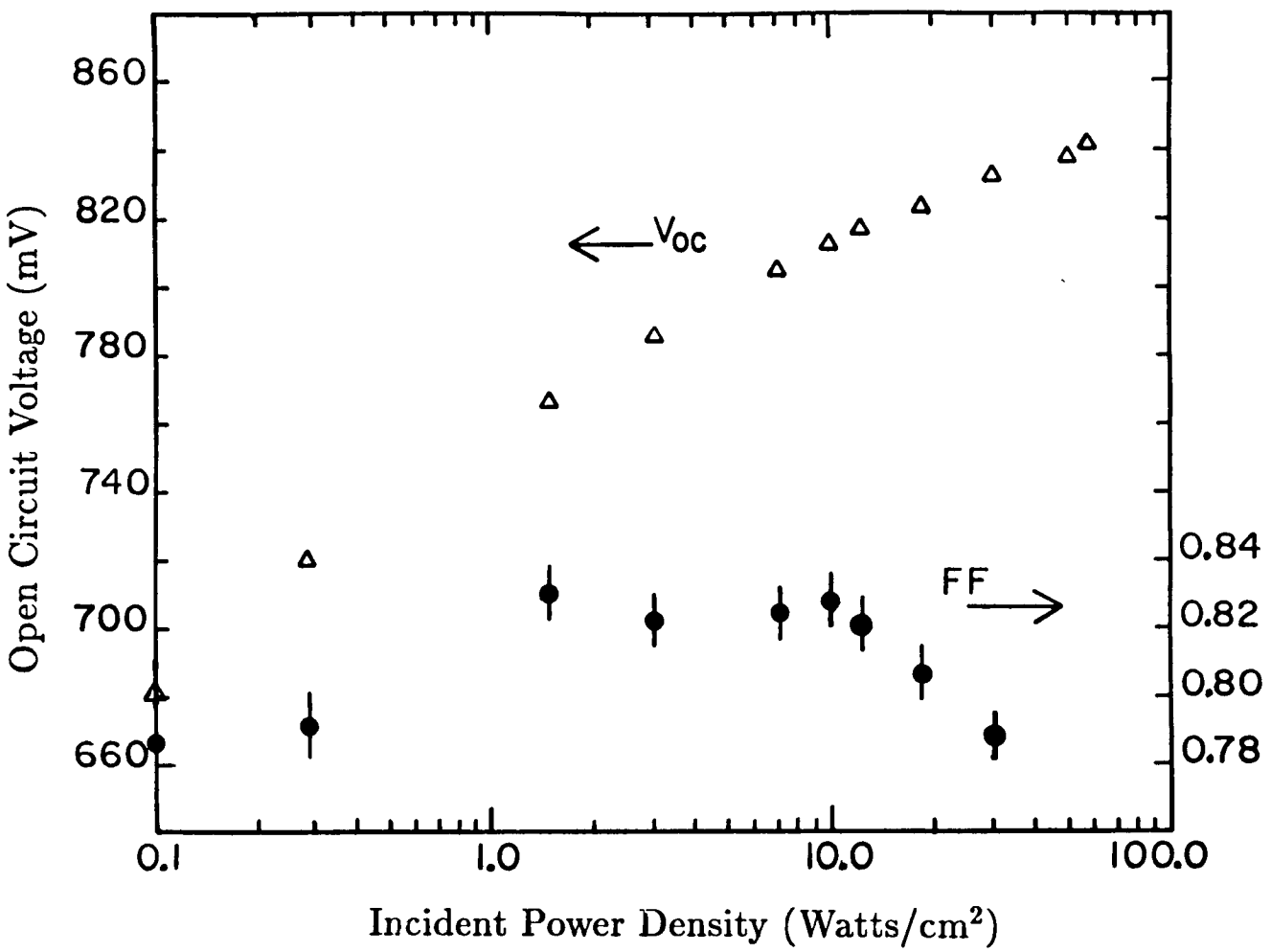

Figure 8: The measured open circuit voltage and fill factor of a 113 μm texturized cell is illustrated.

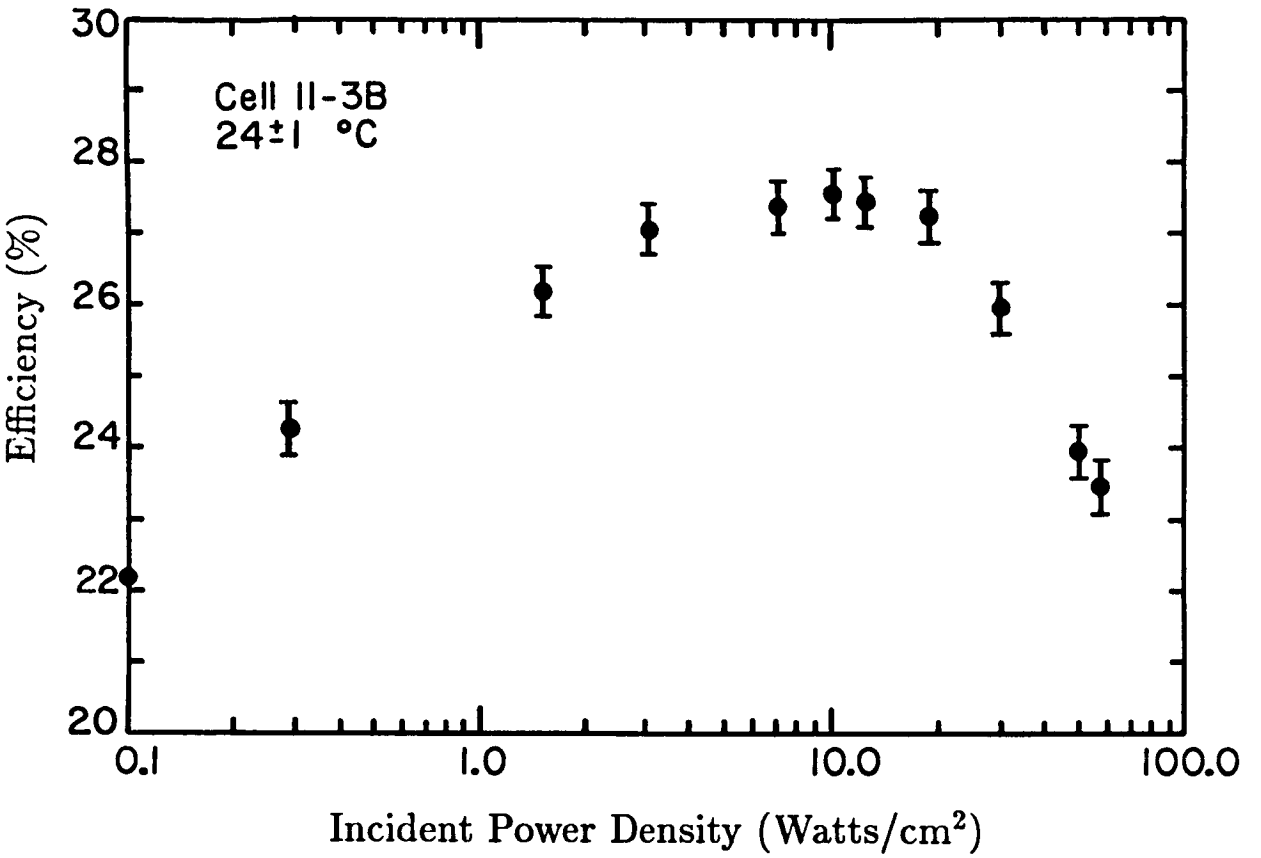

Figure 9: The measured efficiency of the cell from the previous figure is presented. The one sun efficiency is 22%, increasing to 27.5% at 100 suns. The major portion of the drop-off above 100 suns is due to metal series resistance; however, a significant portion results from a decrease in internal quantum efficiency at high intensity due to Auger recombination in the dense electron-hole plasma generated by the light. A thinner cell will reduce this effect. By decreasing the metal series resistance, thinning the cell to 80 μm, and providing a double layer anti-reflection coating it is expected that efficiencies over 29% can be reached.

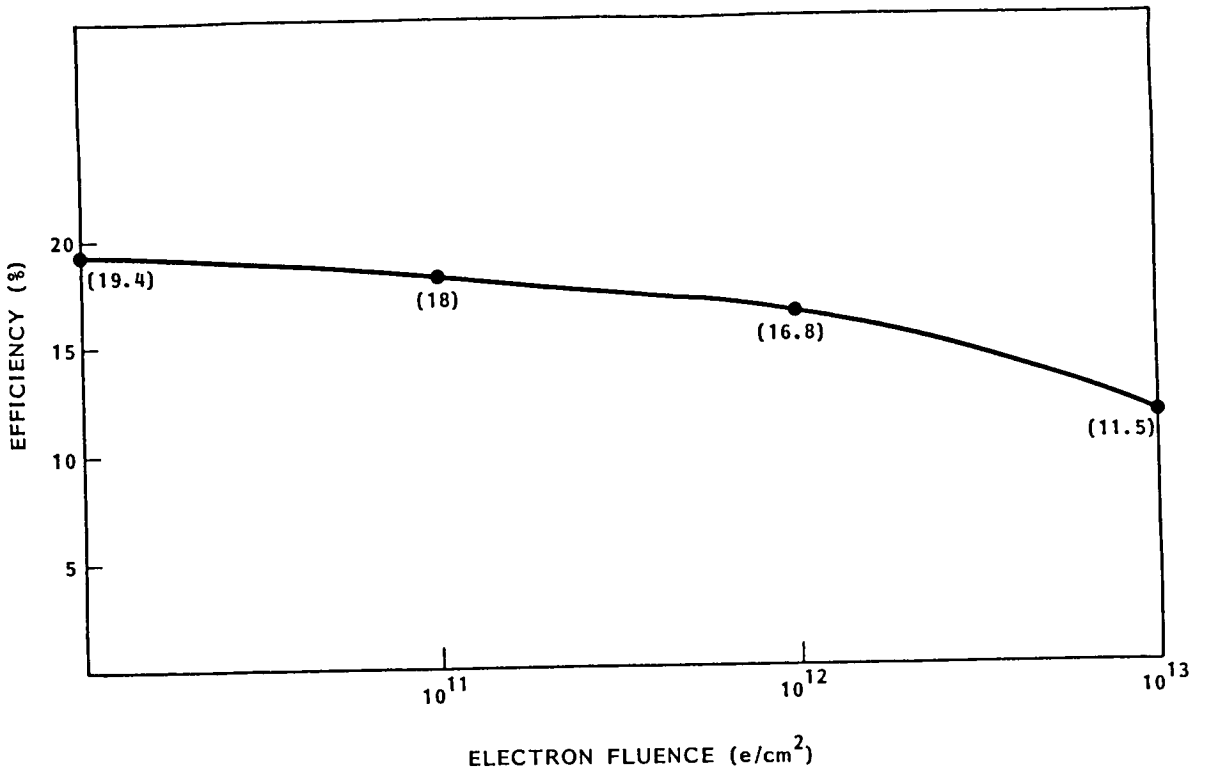

Figure 10: This figure shows the measured AM0 efficiency versus 1 MeV electron fluence. The radiation was done at Boeing under the direction of Lockheed and the measurements were performed at Lockheed. It is expected that much improved radiation sensitivity can be achieved through the use of doped substrates and front surface fields.

HIGH-EFFICIENCY GaAs CONCENTRATOR SPACE CELLS

J.G. Werthen, G.F. Virshup, H.F. MacMillan, C.W. Ford, and H.C. Hamaker
Varian Research Center
Palo Alto, California

High-efficiency $Al_xGa_{1-x}As$/GaAs heteroface solar concentrator cells have been developed for space applications. The cells, which were grown using metalorganic chemical vapor deposition (MOCVD), have been fabricated in both the p-n and n-p configurations. Magnesium and zinc are used as p-type dopants, and Se is used as the n-type dopant. The space cells, which are designed for use in a Cassegrainian concentrator operating at 100 suns, AMO, have a circular illuminated area 4 mm in diameter on a 5 mm x 5 mm cell. These cells have exhibited flash-tested efficiencies as high as 23.6% at 28°C and 21.6% at 80°C.

INTRODUCTION

Solar energy systems using GaAs cells in a concentrator array offer the potential for very high conversion efficiency along with low array costs. Several concepts for light-weight, radiation-resistant space concentrators have been proposed such as the point-focus miniature Cassegrainian array (Ref. 1) and the parabolic trough design (Ref. 2). GaAs devices have greater potential than Si cells in such applications due to their more optimal bandgap and more favorable temperature behavior. The latter factor enables the GaAs cells to operate efficiently at extreme concentrations ~1000 suns or at the higher operating temperatures which are inherent to concentrator systems. In this paper, we report $Al_xGa_{1-x}As$/GaAs heteroface solar concentrator cells grown by metalorganic chemical vapor deposition (MOCVD) for use in Cassegrainian arrays.

CELL DESIGN AND FABRICATION

The concentrator cells were designed with the aid of a detailed computer model. The model simulates the performance of GaAs solar cells and can be used to optimize the relevant cell parameters, e.g., layer thicknesses, doping levels of the emitter and base, grid pattern, and antireflection (AR) coating. Details of the model may be found elsewhere (Ref. 4). The design conditions for the Cassegrainian cell were defined to be 100 suns, AMO at an operating temperature T = 80°C, with a circular illuminated area of 0.126 cm^2 (4-mm diameter) on a 5 mm x 5 mm die. Under such conditions, it is crucial that the emitter and the grid pattern each have very low series resistance. At the same time, the spectral response should remain high and the obscuration must be minimized. The structures of the cells that resulted from these computer optimizations are very similar; this structure is shown in Fig. 1. In addition to the emitter and base, the devices include a highly doped buffer layer to minimize surface recombination effects at the back of the base and to provide a smooth surface upon which the overlying structure is grown. The $Al_{0.9}Ga_{0.1}As$ window layer passivates the front surface of the emitter and, in combination with the single-layer AR coating, minimizes the reflectance. Finally, the GaAs cap layer enables excellent ohmic contact by the top grid pattern while simultaneously minimizing the possibility of the grid metallization diffusing into the semiconducting

materials during processing. The cap layer is selectively etched away between the grid lines prior to the application of the AR coating. Doping levels for the cells are approximately 2 x 10^{18} and 7 x $10^{17}cm^{-3}$ in the emitter and base, respectively. For the n-p cells, the emitter thickness was reduced to about 0.15 μm.

The multilayer structure was grown in a horizontal rf-heated MOCVD reactor at 730°C, as described in Ref. 5. Growth rates were 0.06 μm/min. In the p-n cells, Mg and Se were used as the dopants, whereas Se and Zn were used as the dopants in the n-p cells. Conventional photolithographic techniques were used to lay down the top grid pattern. Metallizations, which were deposited by evaporation, were Au/Ge/Ni/Au and Pd/Au for n- and p-type GaAs ohmic contacts, respectively. The front grid pattern was subsequently plated with Ag and/or Au to a total thickness of 2 μm. The AR coating was deposited by plasma deposition at 350°C.

TESTING

One-sun efficiencies were determined using Spectrolab XT-10 simulators both at Varian and at Sandia National Laboratories. For AMO measurements, the simulator intensity was set using a balloon-flight-calibrated GaAs p-n solar cell which had a similar spectral response to the concentrator cells. A xenon-lamp flash tester was used to determine device performance under concentration. The incident power upon the cell in the flash tester was determined by assuming that the short-circuit current I_{sc} was linearly dependent upon the solar concentration. The exposed scribing streets at the edges of the cells were masked off from any light to assure the accuracy of the measurements. Efficiencies were based on the total illuminated area, and no correction was made for obscuration.

RESULTS OF CASSEGRAINIAN CELLS

Figure 2 shows the current-voltage (I-V) characteristics of one of the best p-n Cassegrainian cells at one-sun, AMO, and T = 28°C. The efficiency η = 20.8% is quite high, with a particularly high value of the fill factor FF = 0.86. Such a value for FF is attainable due to the low series resistance which results from the optimization of the grid pattern for high concentration. The open-circuit voltage V_{oc} is 1.02 V, and J_{sc} = 32.2 mA/cm^2. As shown in Fig. 3, the same cell at a concentration of 91 suns has η = 23.3%, while maintaining the good fill factor. Curve fitting of these data yield an estimate of ~5 mΩ for the series resistance in this cell. The conversion efficiency versus concentration is plotted in Fig. 4. The data show that η has its maximum value near 100 suns, which is very near the intended operating concentration. However, comparable performance is attainable over a comparatively wide range between 80 and 200 suns, and even at 400 suns, η exceeds 22%.

The temperature dependence of the cell at 94 suns, AMO is shown in Fig. 5. As expected, η drops linearly with increasing temperature, and a least-squares fit to the data yields a temperature coefficient of -0.036%/°C. At the intended operating conditions of ~100 suns and T = 80°C, η = 21.6%. Radiation damage experiments have been performed on similar Varian Cassegrainian p-n cells at NASA-Lewis (Ref. 6). After a fluence of 1 x $10^{15}cm^{-2}$ 1-MeV electrons on the bare cells, the 100-sun efficiency was reduced to 79% of its initial value. Using this result and those presented above, end-of-life (EOL) efficiencies could potentially exceed 17% under operating conditions. Since in the Cassegrainian module the cells are shielded from much of the radiation, as shown in Ref. 1, the actual EOL efficiency could be significantly higher.

Although the data presented in Figs. 2-5 indicate the performance of one of the best cells, the results are reproducible. Figure 6 shows the distribution of one-sun efficiencies for all cells, including the one discussed above, fabricated from the same wafer. Of the forty-eight devices which were obtained, twenty-seven exhibit $\eta > 20\%$, and eighty-five percent have $\eta > 17\%$. Lower cell efficiencies are almost invariably due to lower values of FF and, to a lesser extent, V_{oc}. The observed values of I_{sc} are relatively unchanged from cell to cell. When the values of η under concentration are used, the yield is even more impressive, as shown in Fig. 7. Over half of the tested devices have $\eta > 23\%$, and ninety-three percent exceed $\eta = 22\%$. Several other wafers have shown similar efficiency distributions, thus indicating the feasibility of producing these high-efficiciency cells in large quantities using MOCVD.

Although most of the Cassegrainian cells which have been fabricated to date have had the p-n configuration, several n-p cells have also been made. Figure 8 shows the one-sun I-V characteristics of one of these cells. Comparison with the data in Fig. 2 shows that the performance of this cell is very similar to the best p-n cells. The η versus concentration data for another n-p device, which is plotted in Fig. 9, shows an even higher peak efficiency of 23.6%. Furthermore, the decrease in η at greater concentrations is less pronounced, presumably due to the superior majority-carrier mobility in the n-type emitter. The computer modeling results indicate that the n-p structures may potentially have higher efficiencies than p-n, primarily due to better quantum efficiencies.

CONCLUSIONS

High-efficiency GaAs concentrator cells have been developed for both space and terrestrial applications. Their optimal structures were determined with the aid of a computer model which realistically simulates the performance of $Al_xGa_{1-x}As/GaAs$ heteroface cells. Cassegrainian cells have shown 100-sun, AMO efficiencies as high as 23.6% at T = 28°C and 21.6% at T = 80°C. The space cells have shown excellent radiation resistance to 1-MeV electrons, so in combination with the protective design of the magnifying element, the Cassegrainian arrays should offer excellent end-of-life performance. Although most of the development efforts have focused on the p-n configuration, several high-efficiency n-p cells were also fabricated. The computer modeling indicates that even higher efficiencies may be obtained in the latter case.

This research was supported in part by NASA/Lewis under contract No. NAS3-23876.

REFERENCES

1. Patterson, R. E.; Rauschenbach, H. S.; and Cannady, M. D.: Conference Record of the 16th IEEE Photovoltaic Specialists Conference, IEEE, New York, 1982, p. 39.

2. Stern, T. G; and Hayes, E. W: Conference Record of the 17th IEEE Photovoltaic Specialists Conference, IEEE, New York, 1984, p. 326.

3. Arvizu, D. E.; and Edenburn, M. W.: Proc. 105th ASME Winter Annual Meeting, 1984, 84-WA/SOL-13.

4. Hamaker, H. C.: J. Appl. Phys. 58, 2344, 1985.

5. Lewis, C. R.; Dietze, W. T.; and Ludowise, M. J.: J. Electron. Mater. 12, 507,

1983.

6. Curtis, H. B.; and Swartz, C. K.: Conference Record of 18th IEEE Photovoltaic Specialists Conference, IEEE, New York, 1985, p. 356.

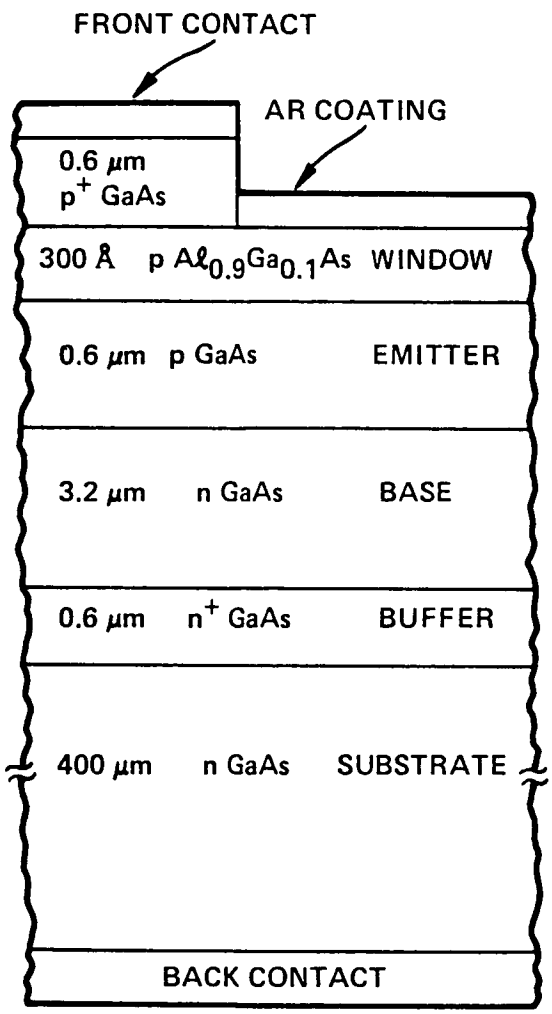

Figure 1: Optimized p-n solar cell structure obtained from the computer model.

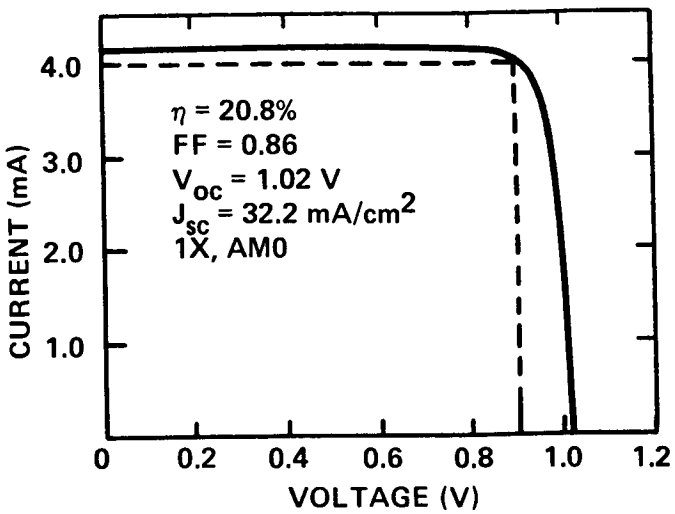

Figure 2: Current vs voltage for a p-n Cassegrainian solar cell at T = 28°C and 1-sun, AMO. The dashed lines indicate voltage and current at maximum power point.

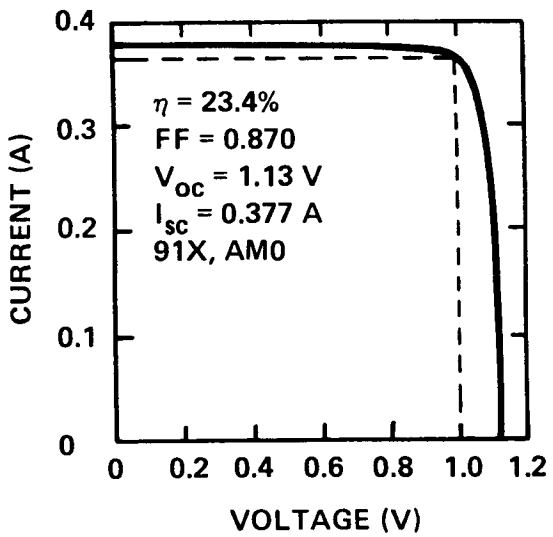

Figure 3: Current vs voltage for cell discussed in Fig. 2 at 91 suns. Dashed lines indicate voltage and current at maximum power point.

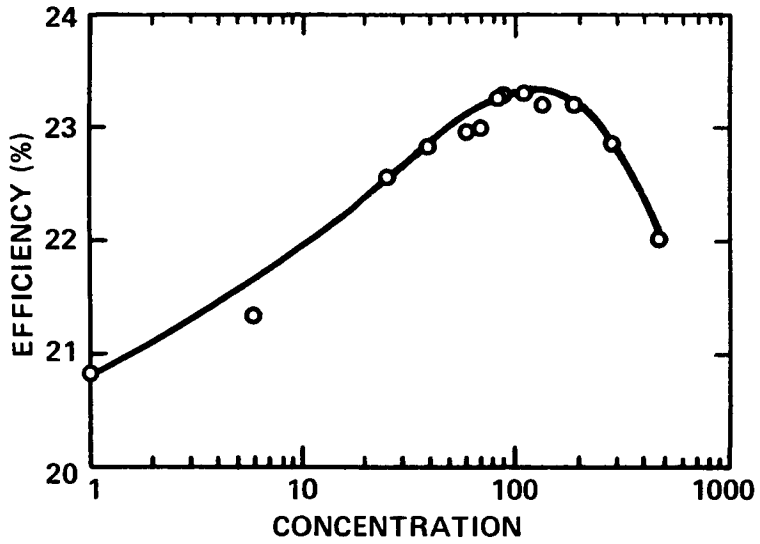

Figure 4: AMO efficiency versus solar concentration for cell discussed in Fig. 2 at T = 28°C.

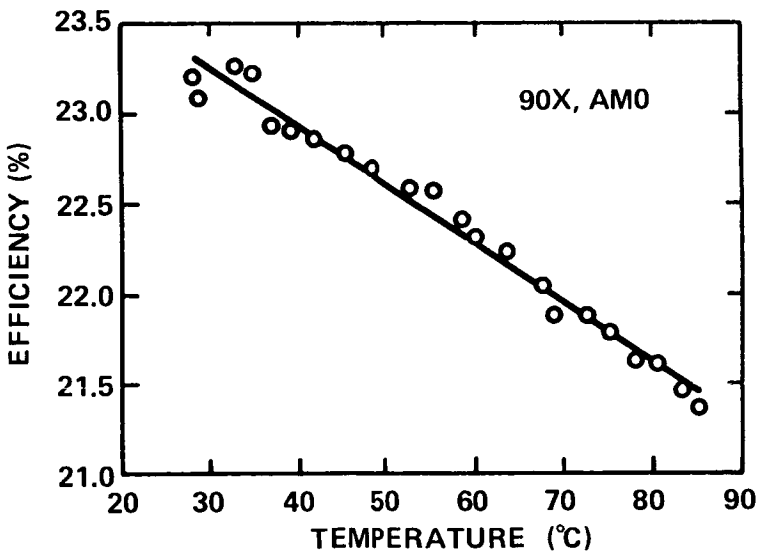

Figure 5: AMO efficiency versus temperature at 94 suns for cell discussed in Fig. 2. The line represents a least-squares fit to the data and has a slope of -0.036%/°C.

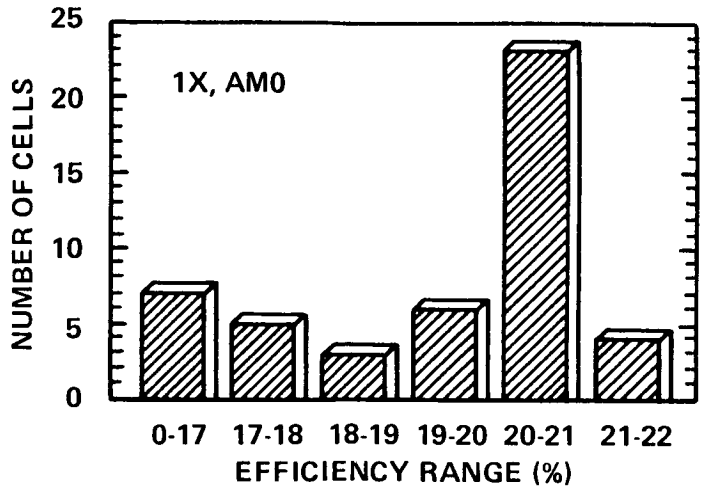

Figure 6: One-sun, AM0 efficiency distribution of all Cassegrainian cells processed from a single wafer, including cell discussed in Fig. 2.

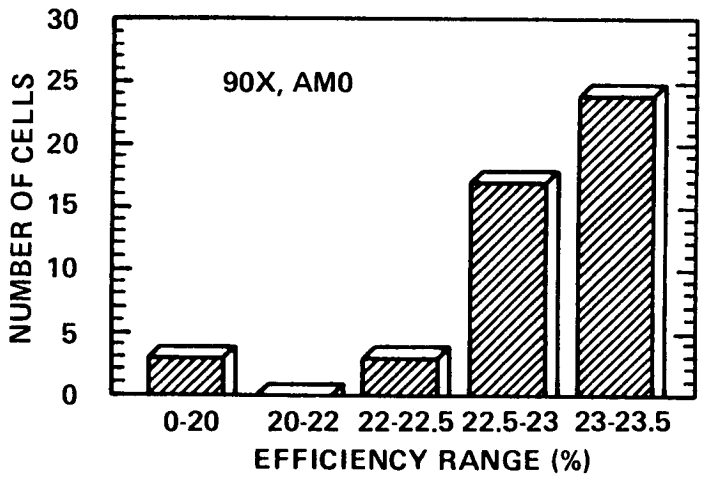

Figure 7: Efficiency distribution of all Cassegrainian cells processed from wafer of Fig. 6 at 90 suns, AM0 and T = 28°C.

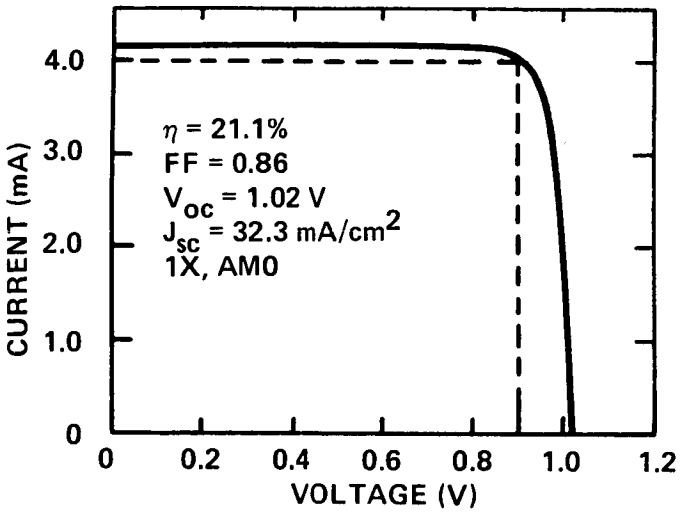

Figure 8: Current versus voltage for n-p Cassegrainian solar cell at T = 28°C and 1-sun, AMO. The dashed lines indicate voltage and current at the maximum power point.

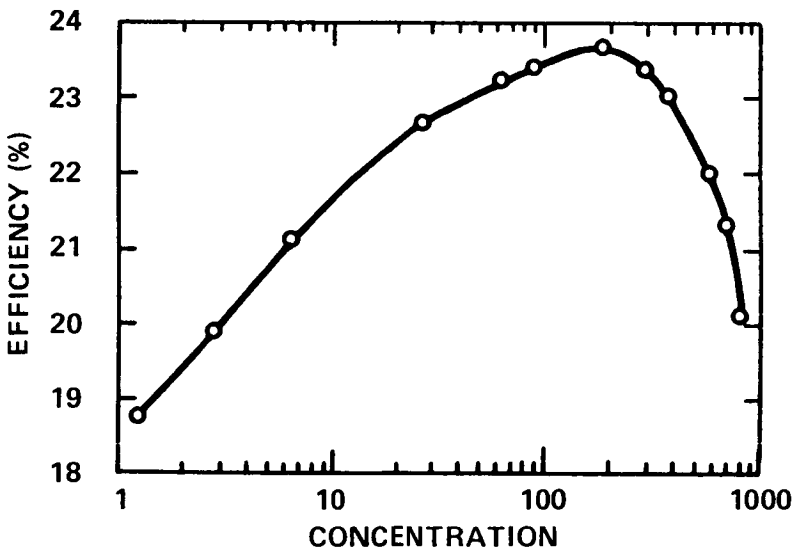

Figure 9: AMO efficiency versus solar concentration for a n-p Cassegrainian solar cell at T = 28°C.

THERMAL STRESS CYCLING OF GaAs SOLAR CELLS

Robert W. Francis
The Aerospace Corporation
Los Angeles, California

Introduction

Thermal stress cycling has been performed on gallium arsenide (GaAs) solar cells to investigate their electrical, mechanical and structural integrity. Sponsored by the Defense Meteorological Satellite Program, cells were cycled under low earth orbit (LEO) simulated temperature conditions in vacuum. Over 15,000 thermal cycles from -80°C to +80°C have been imposed which equates to a three year mission in LEO. The test matrix consisted of thirty single junction GaAs solar cells (ten each from Applied Solar Energy Corporation (ASEC), Hughes Research Laboratories (HRL), and Varian Associates) which were characterized before, during and after the thermal cycling to establish performance parameters and trends. Cell evaluations consisted of measured AMO power output values, i.e., short-circuit current, open circuit voltage, fill factor, and efficiency, as well as spectral response, optical microscopy, and ion microprobe mass analysis (IMMA) depth profiles on both front surface inter-grid areas and metallization contact grid lines.

Cells were examined for performance degradation after 500; 5,000; 10,000 and a total 15,245 thermal cycles. Within the limitations of the experimental analysis, no indication of performance degradation was observed for any vendor's cell lot. The results presented here establish that, after 15,000 thermal stress cycles, the equivalent of three years in LEO, the cells have retained their power performance output with no loss of structural integrity or physical change in appearance.

Solar Cell Characteristics

All thirty (30) solar cells received for the thermal cycling experiment were single junction GaAs with a minimum of 16% (AMO) solar conversion efficiency reported by each vendor. Cells were 2 X 2 cm in area with a nominal 12 mil thickness, were fabricated in a P on N configuration and were supplied unglassed. Evaluation and analyses were carried out at various periods throughout the duration of the thermal stress cycling. Power output I/V measurements, spectral response, and optical microscopy were performed initially and after the 500; 5,000; 10,000 and 15,245 thermal cycles; whereas, cells were subjected to IMMA only initially and after thermal cycling was complete to minimize damage potentially incurred by the ion probe. Details of the preliminary results after 5,000 cycles utilizing these same analytical techniques have been published by B.K. Janousek et al, (Reference 1). A review of the beginning of life solar cell characteristics is presented below for completeness.

Each cell's current vs. voltage and spectral response signature were measured at the Jet Propulsion Laboratory (JPL). A 1-sun illumination AMO spectral content was established by a Spectrolab X-25 solar simulator. The cell temperature was maintained at 28°C. Beginning-of-life (BOL) efficiencies confirmed values measured at each vendor. These efficiencies were 16% and above and are listed in Table 1 along with the other pertinent parameters. Cells are listed in descending efficiency value with no correlation to vendor. The average efficiency for the total thirty cell lot at BOL was 16.66% with a 0.53% standard deviation.

External quantum efficiency or spectral response measurements were also performed at the Jet Propulsion Laboratory on two solar cells from each of the three vendors. Spectral response signatures exhibit the quantum efficiency as a function of photon energy and permit the cell's electrical performance to be probed as a function of the device's optical absorption characteristic in a specific layer. Thus, the spectral response signatures enable evaluation of potential factors that contribute to performance losses by determining which interior region of the

cell has degraed. BOL spectral response signatures all exhibit a sharp rise at approximately 900 nm to a maximum response of about 0.55 mA/mW followed by a gradual down slope in response at shorter wavelengths and then finally a sharp drop in response at less than 450 nm.

Due to potential device damage created by oxygen-18 ion drilling during the IMMA concentration depth profile analysis, only one sample from each of the three vendors was investigated. To minimize electrical damage to the cell the probed area was only 100 X 20 μm and located at the lower end of a grid line opposite the bus bar. Since front contact metal migration and diffusion into the junction region could be enhanced by temperature differential stress cycling, this needed to be considered as a possible degradation mechanism in GaAs causing cell shunting. IMMA metallization depth profiles were obtained on the p-contact side both on and between the grid lines. Concentration depth profiles were obtained before cycling, after 5,000 cycles and at cycling termination. Comparison of the signature curves gives a good indication of only enhanced metal diffusion or interfacial structural changes due to the imposed thermal stresses.

Finally, optical photomicrographs were taken on all 30 cells before and after completion of each cycle period. These photographs served as a historical record to compare the cell surface morphology, topography and potential grid line delamination caused by the thermal cycling stresses.

Thermal Stress Cycling

Temperature cycling is being conducted in The Aerospace Corporation's Aerophysics Laboratory. A picture of the apparatus is shown in Figure 1. The temperature oscillates from -80°C to +80°C with a sinusoidal temperature vs. time profile. No temperature dwell time is imposed at the temperature extremes. One cycle period is 0.5 Hr. and the operation is continuous and automatic. The cells thermal cycle in vacuum at a pressure less than 10^{-6} torr. Several safety features are

built into the microprocessor control unit. If the temperature approaches +100°C or -100°C, a fail-safe feature prohibits operation beyond these temperature extremes; if the vacuum system fails, cell cycling is discontinued and the chamber is returned to ambient temperature. A call-in feature allows equipment status checking during off hours. Monitoring and control thermistors are mounted at nine locations both inside and outside the temperature control block (Figure 2).

During temperature cycling, the solar cells occupy individual square slots in a covered aluminum picture frame configuration that is mounted to the temperature control block. There are a total of 36-1.0 in^2 slots for cells. Three 2 X 2 cm silicon solar cells provided by ASEC are also included in the thermal cycling test to provide a standard and enable an internal comparison for the GaAs thermal stress evaluation. The remaining three slots were occupied with electrically inactive mechanical GaAs cell blanks with thermistors attached with thermal conductive epoxy. This permitted active cell temperature monitoring by similarity. Three additional backup beaded thermocouples were mounted to the top of the cover plate by washers on the temperature control block and the final three thermocouples were also washer mounted on the cover plate top to provide temperature control and uniform temperature monitoring.

The thermal data obtained during the total 15,245 cycles is described in Table 2. T6 and T8 are thermocouples mounted on the cover plate at each end and T7 is mounted in the middle section. Thermistors attached to the GaAs mechanical blanks (T0, T1 and T2) were not utilized for temperature monitoring due to difficulty with maintaining an adherent thermistor contact to the GaAs surface during the temperature cycling. As a result, this resulted in anomalous temperature readings from these sensors.

Performance Results After 15,245 Thermal Cycles

Cell efficiency data after 500, 5,000, 10,000 and 15,245 cycles are listed in Table 3. In Table 4 are the performance parameters after 15,245 cycles for comparison of the BOL data in Table 1. Again, cells are listed in the same order as Table 1 with no correlation to vendor. One cell examined by IMMA demonstrated anomalous efficiency values when measured at each 5,000 cycle period, and the other two vendors' cells broke into 2-3 pieces each, possibly due to cracks initiated during IMMA analysis and propagating during temperature cycling. Thus, electrical performance data as a function of cycle number is not given for these three IMMA analyzed cells. In addition, three cells were unintentionally broken when the thermal vacuum chamber was last opened at 15,245 cycles. Fortunately, however, the three broken cells are spread evenly among each of the suppliers. A total of six cells, therefore, are not included in the final analysis. With a total of two cells each from three vendors excluded from the final cycle period data base the statistical comparison is maintained. This brings the total number to twenty-four cells which have successfully completed over 15,000 thermal cycles. These twenty-four solar cells have an average efficiency of 16.6% with a standard deviation of 0.6%. This is compared to an average efficiency of 16.7% with a 0.6% standard deviation for the same twenty-four cells (or a 16.7% and 0.5% standard deviation for all thirty cells) prior to thermal cycling. Within the experimental error of the efficiency measurement ($\pm 0.3\%$) no performance degradation is demonstrated after the total 15,245 LEO simulated thermal cycles. The average efficiency of the three reference silicon solar cells also compared closely within experimental error to the value of 13.4% before thermal cycling.

Both the external spectral response curves and IMMA depth profile signatures after 15,245 cycles indicated negligible change. The curves and signatures from pre and post cycling could, for the most part, be superimposed with no differences exhibited. Thermal stress cycling apparently has no effect on the optical absorption characteristics or

quantum efficiency of the devices nor has it any influence on enhancing the intermetallic contact diffusion, or changing the interlayer or interface structure. No indication of material redistribution was apparent as a result of thermal stress.

The optical micrographs taken after the 15,245 cycles demonstrated no change in the surface morphology or the topography of any cell. Furthermore, no grid line delamination was noticeable from temperature cycling.

Summary/Conclusions

Thermal stress cycling has been performed on GaAs solar cells under LEO simulated temperature conditions in vacuum. Over 15,000 cycles have been imposed which simulates a three year mission. The test matrix consisted of thirty GaAs solar cells (ten each from three suppliers) which were characterized and evaluated before, during and after completion of the thermal cycling. For reasons unrelated to the thermal stress cycling experiment, six cells were eliminated from the final cycle period data base. After a total 15,245 thermal cycles, the remaining twenty-four solar cells have an average efficiency of 16.6% compared to a 16.7% average efficiency prior to cycling. About three years of simulated thermal eclipses in LEO have been demonstrated with no performance degradation on ASEC, HRL, and Varian GaAs solar cells. This establishes the electrical, mechanical, and structural integrity during thermal stress cycling of single junction GaAs solar cells alone, i.e., without interconnects and coverglass.

No continued thermal cycling of the individual cells is presently being planned. At this time, the thermal cycling apparatus has been modified to accommodate panels fabricated by RCA Astro-Electronics and Spectrolab. These panels consist of both soldered and welded interconnected GaAs solar cell circuits. Preliminary thermal stress cycling results and analysis indicate stable performance.

References:

1. B.K. Janousek, R.W. Francis, and J.P. Wendt, "Thermal Stress Cycling of GaAs Solar Cells", Space Photovoltaic Research and Technology 1985, NASA CP-2408, April 1985, pp. 231-238.

TABLE 1

SOLAR CELL PRE-CYCLING ELECTRICAL PERFORMANCE PARAMETERS

Cell	Voc	Isc	FF	η
1.	1.015	116.8	0.814	17.82
2.	1.038	118.9	0.774	17.66
3.	1.031	119.4	0.776	17.65
4.	1.001	116.5	0.818	17.64
5.	1.017	112.7	0.814	17.24
6.	1.034	118.9	0.750	17.04
7.	1.030	117.8	0.759	17.03
8.	1.005	114.1	0.800	16.96
9.	1.018	119.8	0.750	16.90
10.	1.018	113.7	0.788	16.86
11.	0.993	114.3	0.804	16.86
12.	0.976	117.1	0.793	16.74
13.	1.013	111.3	0.803	16.73
14.	0.974	117.1	0.787	16.58
15.	1.033	117.1	0.740	16.55
16.	0.952	117.4	0.800	16.52
17.	1.018	118.0	0.743	16.50
18.	1.021	112.0	0.778	16.44
19.	0.950	115.2	0.808	16.34
20.	1.024	119.1	0.725	16.33
21.	0.987	111.6	0.802	16.32
22.	0.968	115.0	0.793	16.31
23.	1.005	110.6	0.793	16.29
24.	1.006	115.6	0.752	16.16
25.	1.009	113.0	0.766	16.14
26.	0.982	114.5	0.777	16.14
27.	1.006	111.2	0.780	16.11
28.	1.000	109.1	0.798	16.08
29.	0.989	113.7	0.773	16.07
30.	1.012	111.4	0.766	15.95
	1.004	115.1	0.781	16.66
	s=0.023	s=3.0	s=0.024	s=0.53

TABLE 2: TEMPERATURE VALUES FOR THE TOTAL 15,245 CYCLES

Minimum Temperatures (°C)

	T6	T7	T8
Average	-82.9	-81.1	-86.9
Standard Deviation	2.3	2.8	4.2
Minimum Minimum	-77.8	-62.3	-55.2
Maximum Minimum	-94.9	-91.9	-96.7

Maximum Temperatures (°C)

Average	84.8	86.9	85.9
Standard Deviation	2.8	2.7	3.4
Minimum Maximum	75.9	78.3	72.3
Maximum Maximum	90.7	93.1	93.8

TABLE 3

SOLAR CELL EFFICIENCY VS. CYCLING

Cell	η (0)	η (500)	η(5,000)	η(10,000)	η(15,245)
1.	17.82	17.62	17.45	17.53	17.71
2.	17.66	17.72	17.74	17.52	17.56
3.	17.65	17.56	17.64	17.51	17.65
4.	17.64	17.55	17.54	17.55	17.53
5.	17.24	17.05	17.00	17.00	-
6.	17.04	17.06	17.06	17.04	17.09
7.	17.03	16.95	17.00	16.82	16.94
8.	16.96	16.55	16.77	16.63	16.35
9.	16.90	(16.62)	-	-	-
10.	16.86	17.00	16.78	16.80	16.66
11.	16.86	16.86	16.90	16.80	16.88
12.	16.74	16.67	16.67	16.66	16.74
13.	16.73	16.54	16.69	16.81	16.67
14.	16.58	16.55	16.50	16.46	16.51
15.	16.55	16.64	16.53	16.43	16.66
16.	16.52	16.46	16.41	16.35	16.46
17.	16.50	16.52	16.40	15.80	15.95
18.	16.44	16.39	16.33	16.57	16.30
19.	16.34	(13.95)	-	-	-
20.	16.33	16.28	16.25	16.29	-
21.	16.32	16.32	16.20	16.31	16.26
22.	16.31	16.37	16.37	16.44	16.39
23.	16.29	(16.13)	-	-	-
24.	16.16	16.14	16.19	16.13	16.22
25.	16.14	16.18	16.05	16.00	15.68
26.	16.14	16.12	16.14	16.09	-
27.	16.11	15.94	16.00	15.88	15.82
28.	16.08	16.03	15.97	16.03	15.97
29.	16.07	16.18	16.09	16.05	16.04
30.	15.95	16.31	15.99	16.18	15.99
	16.66	16.65	16.62	16.58	16.58
	s=0.53	s=0.51	s=0.53	s=0.52	s=0.59

( ) ≡ AFTER IMMA

TABLE 4

SOLAR CELL PARAMETERS AFTER 15,245 CYCLES

Cell	Voc	Isc	FF	η
1.	1.012	118.3	0.801	17.71
2.	1.035	119.3	0.770	17.56
3.	1.029	119.0	0.780	17.65
4.	0.999	116.7	0.814	17.53
5.	-	-	-	-
6.	1.032	118.7	0.755	17.09
7.	1.027	118.0	0.757	16.94
8.	1.009	114.2	0.768	16.35
9.	-	-	-	-
10.	1.016	113.1	0.785	16.66
11.	0.991	115.3	0.799	16.88
12.	0.973	117.0	0.796	16.74
13.	1.011	111.3	0.802	16.67
14.	0.967	116.8	0.791	16.51
15.	1.031	117.5	0.744	16.66
16.	0.950	117.5	0.798	16.46
17.	1.013	118.5	0.719	15.95
18.	1.017	112.6	0.770	16.30
19.	-	-	-	-
20.	-	-	-	-
21.	0.985	111.5	0.802	16.26
22.	0.965	115.8	0.794	16.39
23.	-	-	-	-
24.	1.004	115.9	0.754	16.22
25.	1.006	112.2	0.752	15.68
26.	-	-	-	-
27.	1.002	110.7	0.772	15.82
28.	0.997	109.1	0.795	15.97
29.	0.986	113.0	0.780	16.04
20.	1.008	112.2	0.766	15.99
	1.003	115.2	0.778	16.58
	s=0.023	s=3.0	s=0.023	s=0.59

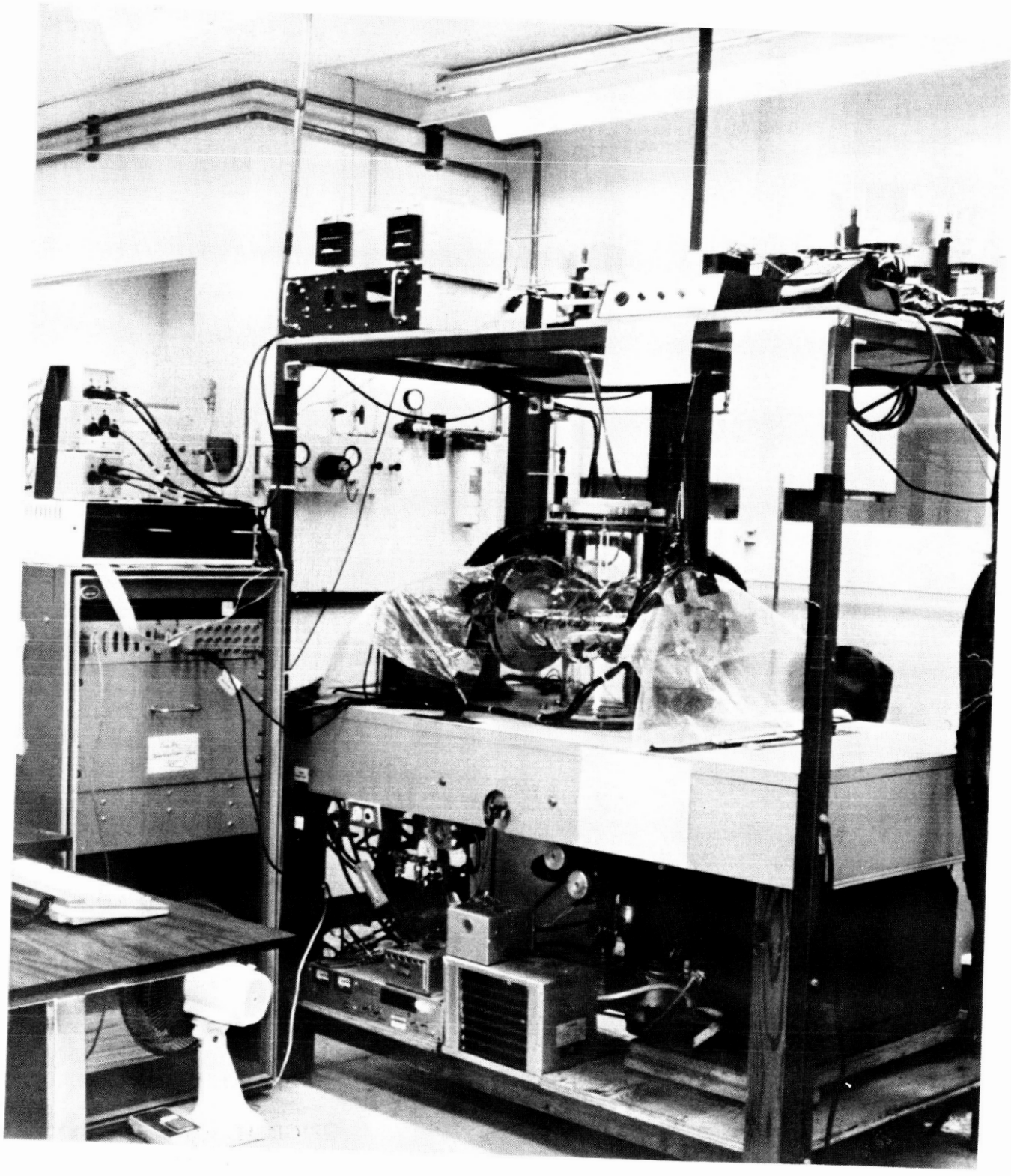

Figure 1

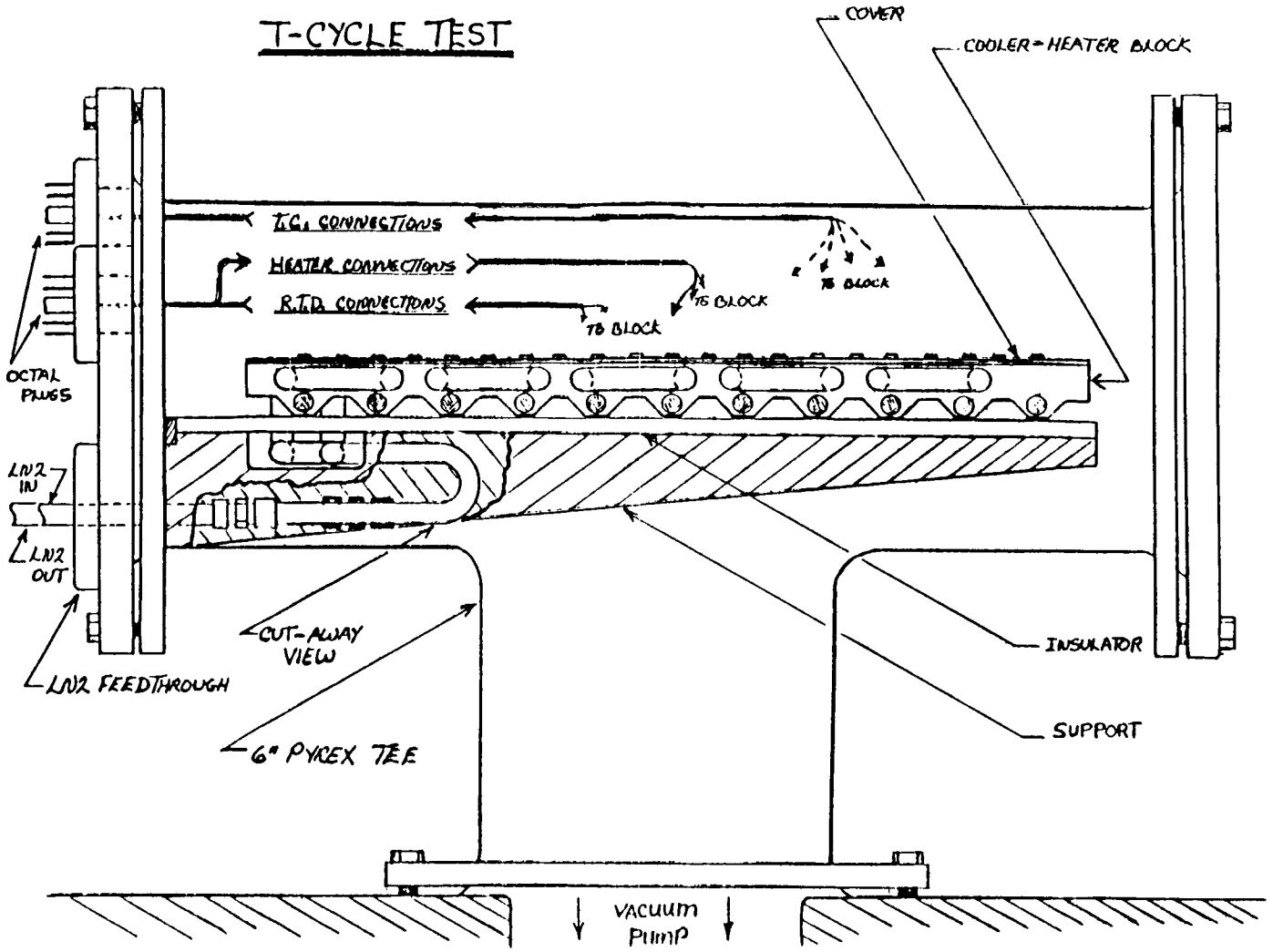

Figure 2

ORIGINAL PAGE IS
OF POOR QUALITY

HETEROSTRUCTURE SOLAR CELLS*

K.I. Chang, Y.C.M. Yeh and P.A. Iles
Applied Solar Energy Corporation
City of Industry, California

and

R.K. Morris
Air Force Wright Aeronautical Laboratories
Wright Patterson AFB, Ohio

This paper presents the performance of GaAs solar cells grown on the Ge substrates, in some cases the substrate was thinned to reduce overall cell weight with good ruggedness. The conversion efficiency of 2x2cm cells under AMO reached 17.1% with the cell thickness of 6 mils. The experience gained in this structure will be used to increase GaAs cell efficiency. Also the work described forms the basis for future cascade cell structures, where similar interconnecting problems between the top cell and the bottom cell must be solved. The details include discussion of substrate properties, growth conditions of GaAs cells, and cell construction including possible substrate thinning. A discussion will follow regarding applications of the GaAs/Ge solar cell in space and expected payoffs over present solar cell technologies.

INTRODUCTION

It has been known that GaAs solar cells have higher conversion efficiency and higher radiation resistance than Si solar cells. However, GaAs solar cells are more than twice as heavy as Si cells. For space applications it is desirable that the solar cell is lightweight, have high efficiency, and high radiation resistance. In order to meet all these requirements GaAs solar cells have to be fabricated on a substrate which is not only lighter or thinner than GaAs, but also more rugged than GaAs. Both silicon and germanium were considered as the starting substrates on which the GaAs solar cell may be fabricated. Because of the huge lattice mismatch between Si and GaAs the silicon substrate was ruled out. Germanium was selected because Ge and GaAs have very close lattice constants and thermal expansion coefficients. Also, Ge is a very rugged material so that it can be thinned to reduce the overall cell weight without introducing any mechanical problem. In this paper, we present the results of p on n GaAs solar cells on n-type Ge substrates.

* This work was supported by the Department of Air Force under Contract F33615-84-C-02403.

CELL FABRICATION

The structure of the p on n GaAs/Ge solar cell is shown in Figure 1. The n-type Ge substrate is doped with Sb and the electron concentration is in the middle of $10^{17}cm^{-3}$. The starting Ge wafer is approximately 7 mil thick and the crystal orientation is 4 degrees off the (100) direction. The heteroface GaAs/AlGaAs solar cell structure was deposited by the low pressure organometallic vapor phase epitaxy (OMVPE) technique. First an n-type GaAs buffer layer doped with Se was grown on top of the n-type Ge wafer. Then a p-type GaAs emitter and a thin p-type window layer were deposited and the p-type dopant was Zn. During the OMVPE growth the chamber pressure was 130 torr and the growth temperatures were 720 and 680°C. The 720°C was used to take advantage of the Ge auto-doping effect so that the electron concentration in the initial buffer layer was so high that it eases the electric properties at the hetero-interface between the Ge substrate and the GaAs buffer layer. This auto-doping effect was ceased by lowering the growth temperature to 680°C. The actual GaAs homojunction was grown at this temperature to obtain higher short-circuit current. The typical thickness for the buffer layer, the emitter, and the window layer is 9, 0.5, and 0.1um, respectively.

After layer growth the front p-contact made of Au/Zn and Ag were deposited onto the revealed p-emitter and the grid pattern was defined by the liftoff process. The multiple layer AR coatings made of TiO and A10 were next deposited on the window layer. At this point the GaAs/Ge structure was further thinned to 3 mils by removing Ge from the backside. Then the back n-contact made of Au/Ge, Ni, and Ag was deposited and sintered. Finally, the cell was cut into size. The entire cell fabrication sequence is shown in Figure 2.

RESULTS

Doping Profiles

The doping profile of the typical GaAs/Ge solar cell was measured using a Polaron C-V profiler. Figure 3 shows the doping profile of both the hole concentration in the emitter and the electron concentration in the buffer layer. The hole concentration was about $1.3 \times 10^{18}cm^{-3}$. The electron concentration was $2 \times 10^{17}cm$ for the first 3um near the junction and it increased to $1 \times 10^{18}cm^{-3}$ for the remaining 6um. This higher electron concentration was due to the auto-doping (out-diffusion) by Ge which is an n-type dopant in GaAs for the OMVPE growth. The difference in the electron concentration in the buffer layer was due to the growth temperatures. The growth temperature, Tg, was 720°C for the initial 6um and it was 685°C for the remaining 3um and the p-layer.

Modeling

The reason that the GaAs/Ge cell had high open circuit voltage and lower fill-factor is due to electric properties of the interface between the n-type Ge substrate and the n-type GaAs buffer layer. An experiment was performed to analyze the interface properties. An as-grown cell structure was etched in a 3:1:1 solution to remove the window layer and the p-emitter. N-type ohmic contacts were deposited and sintered on the GaAs buffer layer and the backside of the Ge substrate. The sample was cut into 5x5mm after sintering the n-contacts. A typical dark I-V characteristics of the isotype heterojunction interface is shown in Figure 4. The I-V characteristics are non-linear and the resistance of the 5x5mm sample was approximately 2 ohms near the origin. Therefore the series resistance of the isotype heterojunction between GaAs and Ge was high enough to result in low fill-factor.

Also a third terminal was made to the (n)GaAs buffer layer of a GaAs/Ge cell to evaluate the photovoltaic effect at the (n)GaAs/(n)Ge isotype heterojunction. It was found that Voc was 0.035V and that the polarity of this photovoltage agreed with that of the p/n GaAs cell. The polarity of this photovoltage suggests that the junction between the (n+)GaAs and (n)Ge be an n-type Schottky barrier. Figure 5 shows the band structure of the GaAs p/n junction and the (n+)GaAs/(n)Ge Schottky barrier. The degenerated (n+)GaAs acts as a metal on the (n)Ge semiconductor. The magnitude of the barrier height affects the collection photocurrent; i.e. Cff. The Schottky barrier height can be reduced by lowering the resistivity of the Ge substrate. It has been verified that better CFF for GaAs/Ge cells has been obtained by using low resistivity Ge wafers.

Light I-V Characteristics

The 2x2cm GaAs/Ge solar cells made on the 0.015 ohm-cm Ge substrates were tested under an AMO simulator at 28°C. Figure 6 shows the light I-V characteristics of a 2x2cm GaAs/Ge cell. The conversion efficiency of the cell was 17.1%; the open-circuit voltage 1.075V; the short-circuit current 115.9mA; and the fill-factor 0.742. The thickness of this cell was approximately 7 mils.

Table I lists the performance of the GaAs/Ge cells fabricated in the same lot. All cells have efficiency higher than 16% under AMO at 28°C. At 50% cummulative yield the cell efficiency was 16.8%; the open-circuit voltage 1.088V; the short-circuit current 115.7mA; and CFF 0.722. The thickness of these cells was about 7 mils.

Contact Integrity

The contact integrity is defined by low contact resistance, good adhesion, solderability, and weldability. The Ag-plated tabs were soldered onto the p-contact ohmic pads of a GaAs/Ge solar cell with 16% efficiency. The light I-V curves of the cell before and after soldering the tabs are shownin Figure 7. No degradation in electrical output of the cell was introduced by soldering process. The soldered tabs were pulled at 45 degrees with respect to the cell surface. The pull strength was 925 and 475 grams. The separation between the tabs and the cell was caused by divots in GaAs. Figure 8 shows the microphotograph of the large divots in GaAs after pulling off the tab on the p-contact ohmic pad. This kind of failure mode is acceptable because the pull strength was higher than 250 grams, which was the criteria for GaAs solar cells, and because the separation was due to large divots in GaAs.

Applications

It has been recognized that development of a lightweight GaAs solar cell is critical for achieving arrays with specific power approaching 300 W/kg (Ref. 1). The work presented here is a major step in approaching this type of performance. With the thin GaAs/Ge solar cell, a 50% improvement over silicon in EOL output can be realized with about the same cell weight. Table 2 outlines the relative performance of three cell technologies; silicon, gallium arsenide, and gallium arsenide on germanium. All values represent solar cells with 150 micron (6 mil) coverglasses in a 5 year, mid altitude orbit.

Further weight reduction and thermal survivability could be achieved by the use of deposited integral coverglasses. The relatively low tensile strength of standard GaAs cells inhibits use of integral covers due to cell bowing (Ref. 2). Use of a germanium substrate, with its higher strength, should allow for integral covers to be deposited on the thin GaAs cells, eliminating the need for adhesives. Further work is required in this area to ensure that the cover deposition temperature does not cause germanium diffusion into the GaAs buffer layer.

Other areas which warrant further research include fabrication and processing of the germanium substrate, larger area ($\geq 4cm^2$) device fabrication, and a cell interconnect process. Optimization of these processes would result in a planar solar array specific power of about 290 W/kg using present array blanket technology. This value compares to about 185 W/kg for a silicon array of the same basic design.

Use of the thin GaAs/Ge solar cells would not have to be limited to planar arrays or single junction applications. These cells could be used in concentrator arrays as well, although their advantages over conventional GaAs cells diminishes in this configuration. One remaining advantage, which could become significant, would be a reductiion in cost due to the substrate. The present cost of germanium is about half that of gallium-arsenide. Finally, the design of the thin GaAs cells lends itself well to multi junction cell applications. The materials technology developed for this cell could be applied to an AlGaAs/Ge monolithic multi-juncton cell design promising even higher efficiencies. In addition, the thin cell technology would yield a lightweight multi-junction solar cell.

CONCLUSION

In conclusion, the conversion efficiency of 2x2cm GaAs/Ge solar cells under AMO at 28°C reached 17.1% and a lot average of 16.8% has been demonstrated. It was found that the fill factor of the cell could be improved by reducing the barrier height at the isotype heterojunction between the Ge substrate and the (n) GaAs buffer layer.

This solar cell design presents many significant options for application to future space power systems. The most obvious use would be in ultra lightweight arrays, where the thin cell's high efficiency and radiation resistance would greatly improve power densitites. The GaAs/Ge solar cell could also be used in concentrators, where the biggest contribution would probably be in cell cost reduction. Additionally, the technology developed for this work represents an important step in the development of high efficiency monolithic multi-junction solar cells.

REFERENCES

1. Scott-Monck, J.; Stella, P.: Recent Developments in High Performance Planar Solar Array Technology. Proc. 19th IECEC, Vol. I, August 1984.

2. Fodor, J.S.: High Efficiency Solar Panel (HESP)-Final Report. AFWAL-TR-81-2050, June 1981.

3. Wolff, G.: Kamath, S.; Vedura, G.J.: HESP-Phase II, Gallium Arsenide. AFWAL-TR-80-2128, March 1981.

4. Anspaugh, B.E.; Downing, R.G: Radiation Effects in Silicon and Gallium Arsenide Solar Cells Using Isotropic and Normally Incident Radiation. JPL Pub. 84-61, September 1984.

5. Gurev, H.S.: Integral Covers for Solar Cells - Interim Report. AFWAL-TR-85-2024, May 1985.

TABLE 1

PERFORMANCE OF 2x2cm GaAs/Ge CELLS UNDER AMO AND 28°C

INDIVIDUAL CELL PERFORMANCE						CUMMULATIVE CELL PERFORMANCE					
CELL #	Voc (mV)	Isc (mA)	CFF (%)	Vm (mV)	EFF (%)	Yield (%)	Voc (mV)	Isc (mA)	CFF (%)	Vm (mV)	EFF (%)
12	1075	115.9	74.2	856	17.1	8.3	1075	115.9	74.2	856	17.1
5	1101	115.1	72.0	856	16.9	16.7	1088	115.5	73.1	856	17.0
2	1091	116.6	71.7	860	16.8	25.0	1089	115.9	72.6	857	16.9
6	1092	115.2	72.5	864	16.8	33.3	1090	115.7	72.6	859	16.9
7	1083	116.1	71.8	856	16.7	41.7	1088	115.8	72.4	858	16.9
4	1094	115.5	71.2	824	16.6	50.0	1089	115.7	72.2	853	16.8
1	1092	115.5	71.1	868	16.6	58.3	1090	115.7	72.1	855	16.8
9	1098	116.4	70.0	856	16.5	66.7	1091	115.8	71.8	855	16.8
11	1061	116.3	72.0	828	16.4	75.0	1087	115.8	71.8	852	16.7
10	1096	113.3	70.9	864	16.3	83.3	1088	115.6	71.7	853	16.7
3	1080	116.2	693	828	16.2	91.7	1088	115.7	71.5	851	16.6
8	1088	115.1	69.1	824	16.0	100.0	1088	115.6	71.3	849	16.6

TABLE 2

COMPARISON OF SOLAR CELL TECHNOLOGY PERFORMANCE

CELL TYPE	CELL THICKNESS (MICRONS)	TOTAL WEIGHT (GRAMS)	η %	
			BOL	EOL[3]
Si	100	0.35[1]	15	5.4
GaAs	305	0.82[2]	17	9.5
GaAs/Ge	78	0.35	18.5	10.4

[1] From Ref. 2
[2] From Ref. 3

[3] EOL values based on data in Ref.4; values for GaAs/Ge cells are calculated assuming agreement with data for GaAs performance.

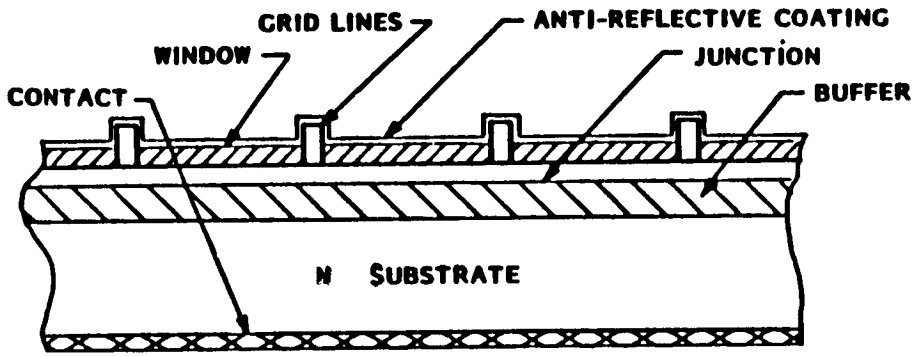

ELEMENT	THICKNESS (μm)	COMPOSITION	DOPANT CONCENTRATION (x 10^{18} cm^{-3})
GRID (p-CONTACT)	4.4	Ag – Au Zn Au	–
AR COATING	0.1	Ti O_x/Al_2 O_3	–
WINDOW (p^+)	0.1	$Al_xGa_{1-x}As$ (Zn)	2 TO 4
JUNCTION (p)	0.05	GaAs (Zn)	2
BUFFER (n)	9	GaAs (Se)	0.2 TO 0.5
SUBSTRATE (n^+)	75	Ge (Sb)	–
n – CONTACT	3.38	Ag – Au Ge Ni Au	–

FIGURE 1

GaAs/Ge SOLAR CELL STRUCTURE

1. Thin Ge Substrates to 7-8 Mils.
2. Prepare the surface of Ge wafers.
3. Grow GaAs and AlGaAs by MOCVD technique.
4. Etch window layer.
5. Deposit front p-contacts.
6. Deposit AR coating.
7. Thin GaAs/Ge cells to 3 mils.
8. Deposit back n-contacts.
9. Cut cells to size.
10. Test

FIGURE 2

PROCESS STEPS FOR THIN GaAs/Ge SOLAR CELLS

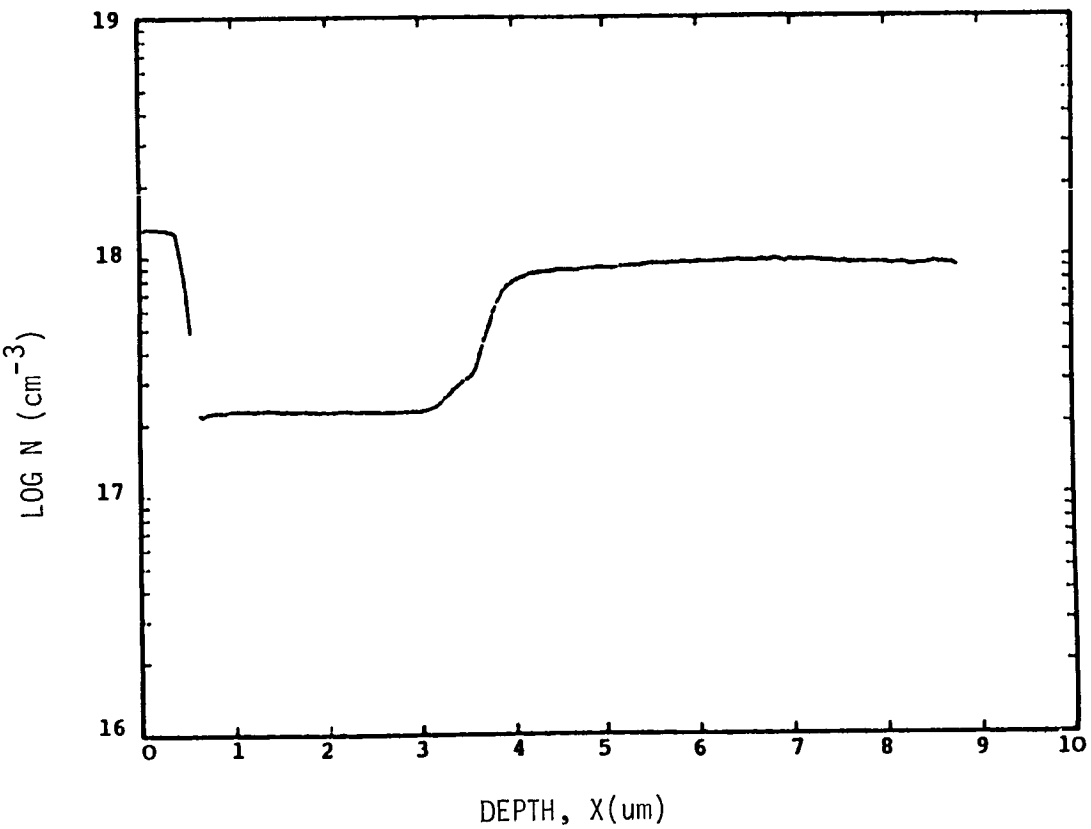

FIGURE 3

DOPING PROFILE OF A GaAs P/N JUNCTION GROWN ON A Ge SUBSTRATE

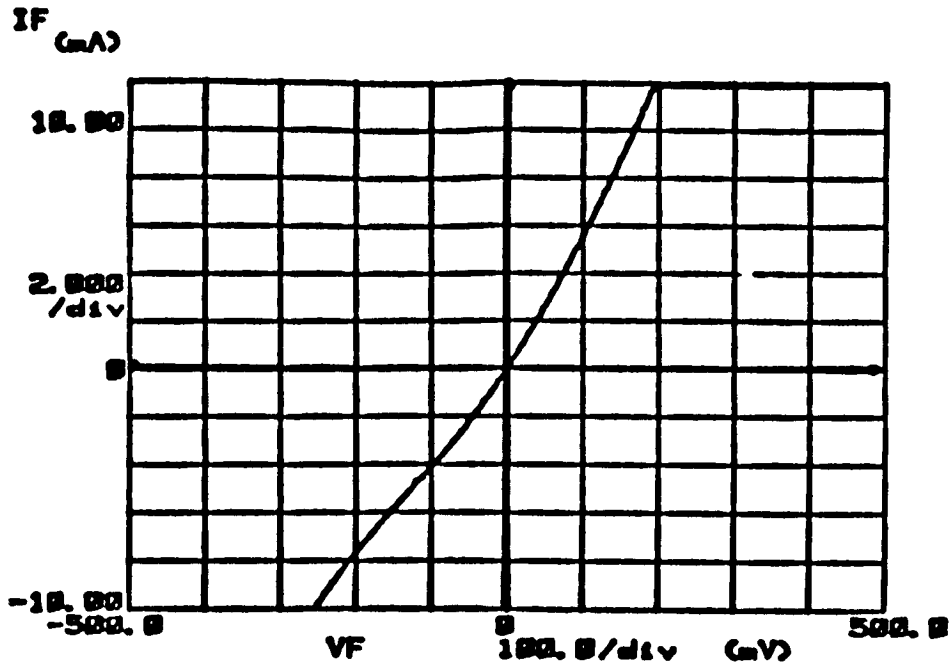

FIGURE 4

DARK I-V CHARACTERISTICS OF A (n)GaAs/(n)Ge ISOTYPE HETEROJUNCTION. THE SIZE OF THE DEVICE IS 5mm SQUARE

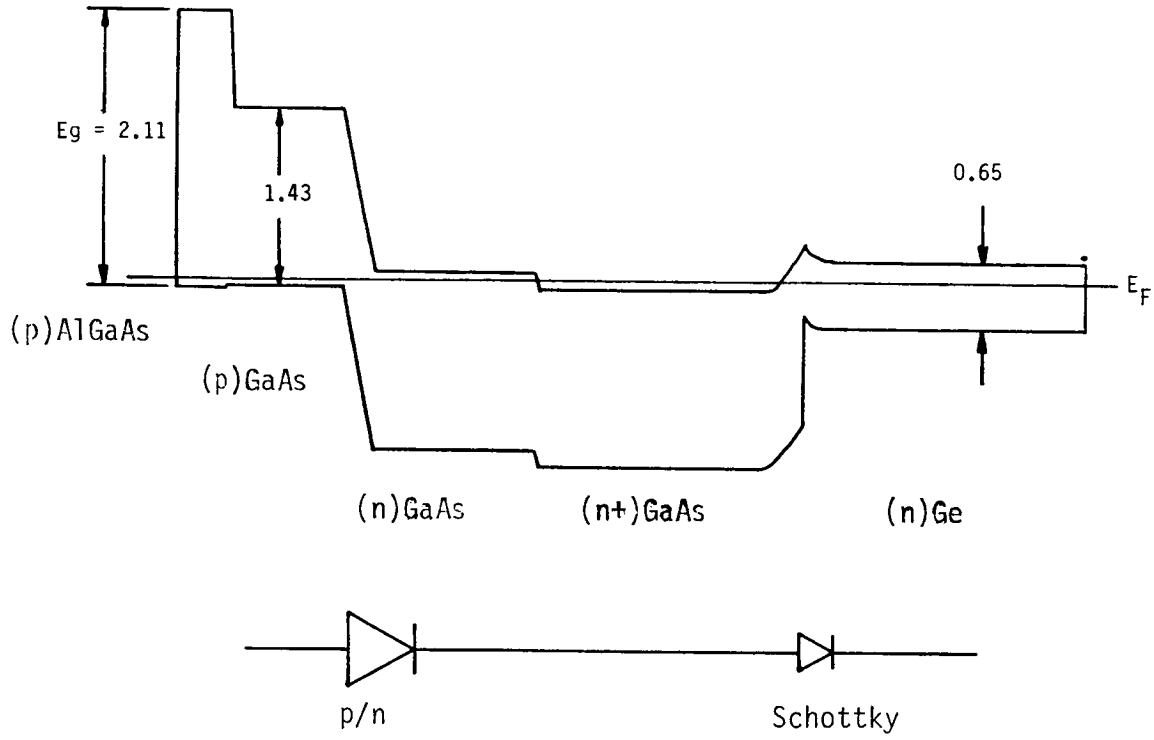

FIGURE 5

BAND STRUCTURE OF THE GaAs/Ge SOLAR CELL

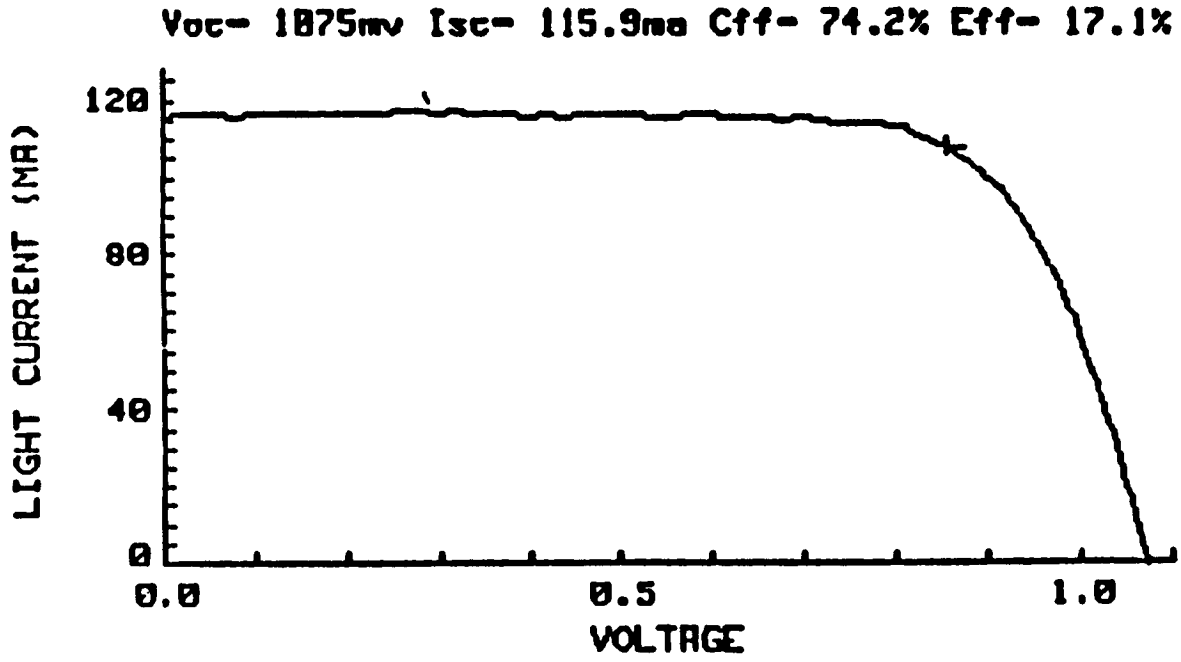

FIGURE 6

LIGHT I-V CURVES OF A 2x2cm P ON N GaAs/Ge SOLAR CELL (#12) TESTED UNDER AMO AND 28°C. THIS CELL IS 6 MIL THICK.

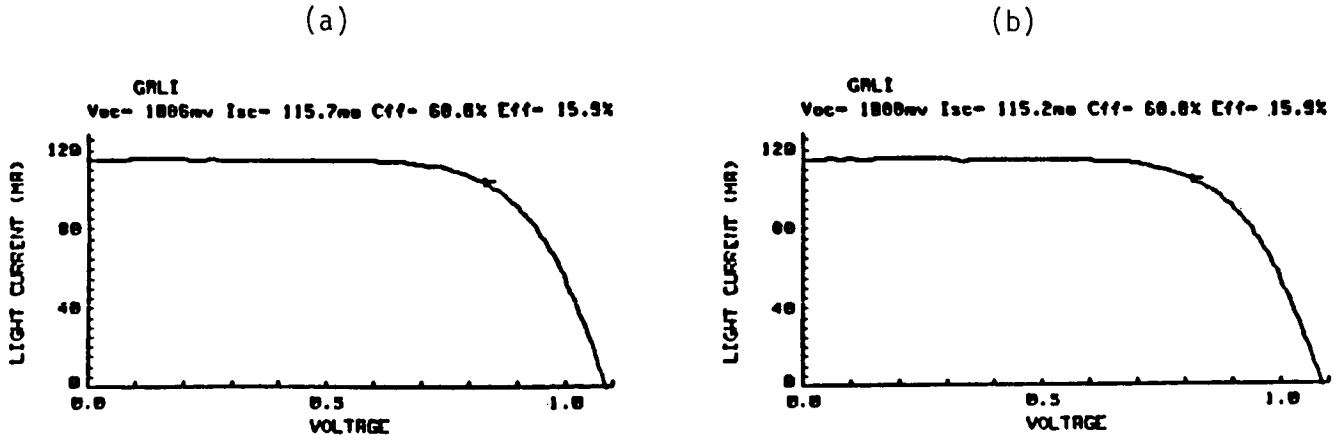

FIGURE 7

LIGHT I-V CHARACTERISTICS OF A GaAs/Ge SOLAR CELL #8 (a) BEFORE AND (b) AFTER SOLDERING TABS TO THE FRONT P-OHMIC CONTACTS.

(a)

(b)

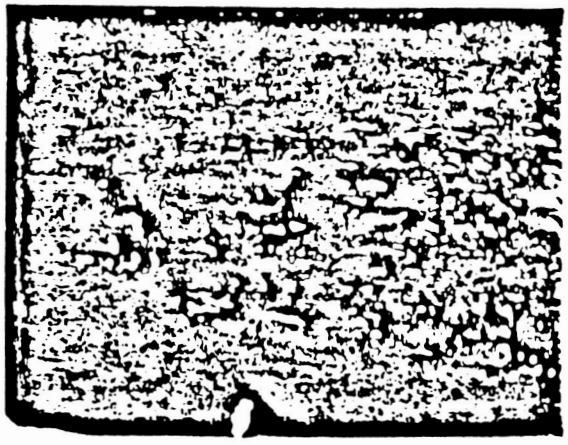

FIGURE 8

MICROPHOTOGRAPHS (50X) OF (a) THE PAD AND (b) THE TAB AFTER PULL TEST FOR CELL #8.

MECHANICALLY-STACKED TANDEM SOLAR CELLS WITH GaAsP ON GaP AND SILCON*

Gerald H. Negley, James B. McNeely, Patrick G. Lasswell, and Edgar A. Gartley
Astrosystems, Inc.
Newark, Delaware

and

Allen M. Barnett
University of Delaware
Newark, Delaware

The development of GaAsP top solar cells for mechanical attachment to silicon bottom solar cells can lead to AM0 conversion efficiency increases of 48% to 76% over the best state-of-the-art single junction silicon solar cells. These tandem solar cells can also be expected to be more radiation-resistant and mechanically and electrically stable.

Design rules are presented for the development of a high efficiency tandem stack. The system efficiency can range from 26.7% to 29.4% depending on the performance of the bottom solar cell. Consideration of the near term goal of a 25% efficient tandem solar cell is addressed. Guidelines for the achievement of this near term goal are given in terms of device parameters.

Liquid phase epitaxy is being used for this development of GaAsP on GaP top solar cells. Considerable progress has been demonstrated in the liquid phase epitaxial growth of GaAsP on GaP substrates. Multiple graded layers of GaAsP with up to 65% GaAs have been prepared with surface quality equivalent to commercial GaP on GaP epitaxial wafers. Techniques for stacking fault and dislocation density reduction are being developed. High quality active layers have been prepared with lattice parameters that differ from the GaP substrate by 2.41%.

The first experimental two-junction, four-terminal tandem cells with a GaAsP top solar cell on a conventional silicon bottom solar cell have been fabricated. Top solar cell transmission of 95% of the photons less energetic than the top cell bandgap has been accomplished. Initial results for these tandem solar cells will be presented. Future work will focus on increasing current in the top cell and increasing the device area.

*This work was supported in part by the Air Force AeroPropulsion Laboratory under contract No. F33615-86-C-2605.

Introduction

The addition of a GaAsP on GaP top solar cell over existing silicon solar cells has the potential of increasing the power output of a practical system by 48 to 76%. This is dependent on the bottom solar cell performance. The tandem solar cell efficiency can range from 26.7 to 29.4%. In this paper the design rules for the achievement of these performance levels are discussed. Next, those performance requirements necessary to achieve the near term goal of 25% are addressed. These performance goals can be described in terms of transparency, voltage, fill factor and current. Liquid phase epitaxy is being used for the growth of GaAsP on GaP. The progress in the development of a GaAsP top solar cell is presented.

Design

The design of the mechanically stacked GaAsP on GaP top cell is based on a model used to calculate theoretical maximum efficiencies of tandem solar cell systems. The model that is being used is by Nell (1) and is based upon tabulated standard spectra, the fit of experimentally achieved open-circuit voltages, and assumes unit quantum efficiency.

Using solar irradiance information, the performance is calculated for the top solar cell. The remaining part of the spectrum, $E < Eg$ (top), is then used to calculate the performance of the bottom cell. In this way, a complete set of isoefficiency curves is generated for various energy bandgap combinations. Assuming unit quantum efficiency and no losses, the model predicts a maximum solar cell efficiency of 35.8% at AMO and one sun insolation. This performance is based upon a four-terminal configuration for the tandem stack.

The maximum theoretical efficiency of 35.8% corresponds to a 1.97eV top solar cell and a 1.12eV bottom solar cell. This is equivalent to a $GaAs_{.54}P_{.46}$ top cell and a conventional silicon bottom solar cell. The device parameters for the "ideal" tandem stack are shown in Table I.

Table I

Predicted Theoretical Maximum Efficiency for the Four-Terminal Configuration according to Nell's Model

Bandgap (eV)	Voc (volts)	Jsc (mA/cm^2)	FF	Efficiency (%)
1.97	1.53	20.75	.91	21.4
1.12	.71	32.68	.84	14.4
				35.8

Anticipated Performance for a Practical System

To obtain the maximum efficiency for a practical system both the top and bottom solar cells must be state-of-the-art. The overall efficiency of the tandem stack must include electrical and optical losses. Loss calculations for

this tandem structure have been anticipated by others (2). In this work, the performance of other types of solar cells is used as the basis for predicting feasible system performance.

To obtain the maximum practical efficiency, both the top and bottom solar cells must be approaching their theoretical limit. The maximum efficiency predicted by the model for a silicon space solar cell is 23.9% at AMO and one sun (1). Swanson's (3) record efficiency concentrator solar cell is equivalent to 19.9% efficient for an AMO spectrum at one sun, while Green's (4) best results correspond to an efficiency of 18.6% (AMO, 1 sun). These results are 22% to 31% better than the average commercial silicon space solar cells. Table II shows a comparison of these results.

Table II

Modelled Theoretical Maximum for Silicon Space Solar Cells Compared to Actual Silicon Results

	Voc (volts)	Jsc (mA/cm^2)	FF	Efficiency (%)
Model	.710	53.43	.840	23.9
Swanson	.681	50.30*	.784	19.9
Green	.663	45.40*	.833	18.6
Commercial	.595	46.00	.750	15.2

*Corrected from AM1.5G to AMO

The modelled theoretical efficiency of the 1.97eV top solar cell is 21.4%. Again, losses must be included to obtain the best "real" case. Since the $GaAs_{.54}P_{.46}$ top solar cell is still in the experimental stages, tabulation of the limit predicted by the model with the best results to date does not allow a fair comparison of the overall tandem stack. However, if one surveys the literature and compares the performance of well-developed solar cells with their expected limit, one may easily predict the expected performance of the 1.97eV GaAsP top cell. Mid-range achievements of open-circuit voltage, short-circuit currents and fill factors are 96%, 91%, and 96%, respectively, of the expected limits from the model. Using these assumptions, the best case 1.97eV GaAsP top solar cell should peak at 17.9% efficiency. This is shown in Table III.

Table III

Expectation of Best Case $GaAs_{.54}P_{.46}$ (1.97eV)

	Voc (volts)	Jsc (mA/cm^2)	FF	Efficiency (%)
Model	1.53	20.75	.91	21.4
Best Case	1.47	18.90	.87	17.9
% Theoretical	96%	91%	96%	

With the expectations of the top and bottom solar cells, one can view the performance of the GaAsP-Si tandem stack. The best case tandem structure with various bottom solar cells is shown in Table IV. The tandem stack efficiencies range from 29.4% to 26.7% depending on the bottom solar cell.

Table IV

Best Case Tandem Solar Cell with
Various Silicon Bottom Solar Cells
(AMO)

	Swanson	Green	Commercial
GaAsP Top Cell	17.9	17.9	17.9
Si bottom cell	11.5*	10.8*	8.8*
Stack Efficiency (%)	29.4	28.7	26.7

*Includes an extra 5% reduction in Jsc due to optical transmission losses.

Requirements for a 25% Efficient Tandem Solar Cell

The near term goal is a 25% efficient solar cell at AM0. An inherent requirement to achieve this goal is the utilization of a state-of-the-art bottom solar cell. From Table II, the choice is the 19.9% efficient solar cell produced by Swanson. The performance requirements necessary for achievement of a 25% tandem device can be described in terms of transparency, voltage, fill factor and current.

The transparency can be determined once the choice of the energy bandgap for the top solar cell is made. From solar spectral irradiance data (5), one determines the portion of the spectrum absorbed in the top solar cell. The remaining part of the spectrum may be utilized by the bottom solar cell. However, due to loss mechanisms, such as free carrier absorption, the actual transmitted light may be less than that predicted by the solar spectral irradiance data. The ratio of the actual transmitted light to the theoretical maximum predicted by the irradiance data gives the overall transparancy of the material for photons less energetic then the bandgap.

The transparency of the top solar cell determines the overall reduction in performance of the bottom solar cell. This reduction is in the short-circuit current. Allowing for an additional 5% loss due to optical losses, the best state-of-the-art silicon solar cell should be 11.5% efficient when placed under a $GaAs_{.54}P_{.46}$ top solar cell. Hence, a 13.5% efficient top solar cell is needed to achieve the goal of a 25% efficient tandem stack.

To achieve a 13.5% efficient top solar cell, an open-circuit voltage of 1.46 volts, a short-circuit current density of 14.9 mA/cm^2 and a fill factor of 0.84 are needed. This short-circuit current density corresponds to a total quantum efficiency of 71.8%.

A comparison of the best case GaAsP solar cell parameters to those required for the achievement of a 25% efficient tandem solar cell is shown in Table V.

Table V

Comparison of Best Case GaAsP to Requirements
for a 25% Efficient Tandem Solar Cell

	Voc (volts)	Jsc (mA/cm^2)	FF	Efficiency (%)
Best Case	1.47	18.9	.87	17.9
Required	1.46	14.9*	.84	13.5

*Requires total quantum efficiency of 71.8%.

Progress of GaAsP Top Cell Device Fabrication

The GaAsP solar cell structure is being grown by liquid phase epitaxy (LPE). Liquid phase epitaxial crystal growth has, in general, produced devices that are superior in performance to those grown by other methods (6, 7). The superior performance of LPE devices when compared to vapor phase or diffused devices can be attributed to fewer deep level impurities, longer diffusion lengths and the fact that the impurities tend to segregate to the liquid rather than the solid.

The actual crystal growth of the multi-layer GaAsP on GaP structure is achieved using the slider method for LPE growth (8). The slider apparatus serves as a substrate holder and melt container for the growth solutions. Advantages of the slider method over other techniques are 1) the substrate can be brought in and out of contact with the melts, 2) several melts can be used, 3) growth is restricted to a single side of a wafer, 4) substrate - solution contact is from the bottom of the melts where there are no floating oxides or other contaminants, 5) excess solution can be wiped off by the sliding action of the apparatus, and 6) thermal equilibration and temperature profiling are easily facilitated. The slider assembly fits into a temperature gradient or cooling furnace. The zones of the furnace are controlled to better than $1^{o}C$. Currently, in our furnace, we use a high purity hydrogen atmosphere which sweeps the growth apparatus and tube during the growth process.

The slider assembly contains up to nine melts and consists of a graded well design such that each successive layer is narrower than the former layer. This can be seen in Figure 1. This allows testing and analysis of each individual layer. Individual melts are composed of approximately eight grams of solvent with appropriate amounts of GaP and GaAs - determined by phase equilibria data for the compositions desired. Growth is achieved by placing the GaP substrate under the first melt to grow a transition layer of $GaAs_xP_{1-x}$ by controlling the temperature level, cooling rate, and time of exposure. This procedure, continues, in turn, to each melt in the growth apparatus. Since GaP segregates preferentially over GaAs in metallic systems, melt depletion can be used to grade the layers from pure GaP to the desired final layer composition.

Figure 1

Slider Boat Growth Apparatus Showing
the Graded Well Width

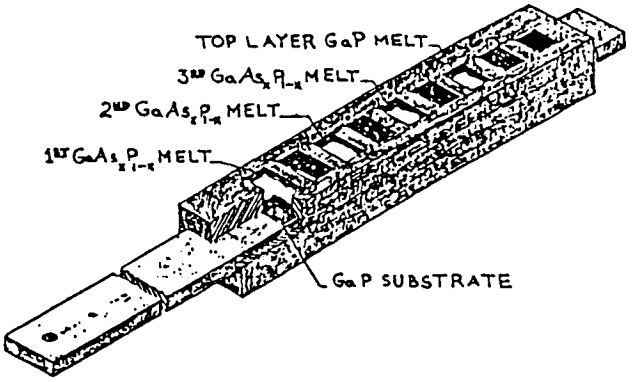

Multiple graded structures of GaAsP with up to 65% GaAs have been grown in our laboratories with surface qualities equivalent to commercial GaP on GaP epitaxial wafers. Currently, a combination of melt depletion and step grading has produced the best surface morphologies. This consists of a 10% GaAs layer grown on the GaP substrate. This 10% GaAs layer is depleted to approximately 12% GaAs before moving the substrate to the next melt for another step grade. The following step is to a 15% GaAs layer which, in turn, is depleted to about 17% GaAs. Then, the substrate is contacted to a 20% GaAs melt and melt depletion is used to grade to about 40% GaAs. At this point, the substrate is contacted with another melt to achieve the final GaAsP composition. Since melt depletion is used to grade the final two layers, the ending composition is determined by the final temperature. Modelling has been done to anticipate the temperature at which the final desired composition will be achieved. Table VI shows various expected vs. measured compositions.

Table VI

Comparison of Expected vs. Measured
Composition of Grown GaAsP

Sample	Design % GaAs	Energy Gap (eV) Expected	Measured
PT#66	50	2.01	2.01
PT#101	47	2.03	2.01
PT#104	79	1.69	1.69
PT#117	65	1.85	1.88
PT#193	54	1.97	1.98
PT#198	54	1.97	1.98
PT#200	54	1.97	1.96
PT#209	54	1.97	1.97

Since the LPE boat assembly has a graded well design (which allows easy access to the individual grown layers), optical transmission is used to determine the compositions of the grown layers. A typical structure determined by optical transmission is shown in Figure 2.

Figure 2

OPTICAL TRANSMISSION OF FOUR LAYER STRUCTURE

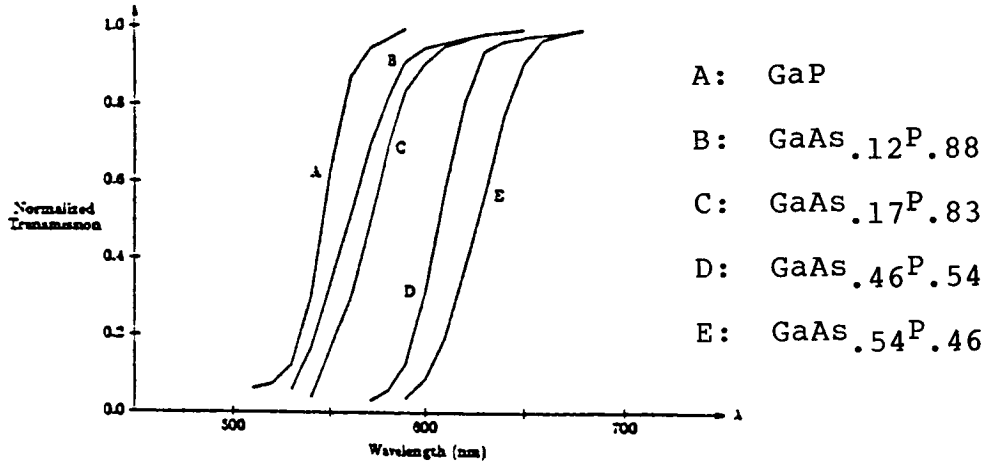

The preferred solvent for the GaAsP-GaP solvent system is gallium. When tin is used as a solvent, the grown layer is n-type with a carrier concentration of $6x10^{18}$/cc, which is too high for our solar cell design.

We are currently working on p/n structures, with the preparation of the thin emitter layers being accomplished by solid state diffusion techniques. This process was developed in our laboratory and is very similiar to diffusion from spin-on silica glasses (9). However, our process consist of a SiO_2 passivation layer to protect the crystal surface, a Zn_3P_2 layer for the zinc source, and a SiO_2 capping layer for the entire structure. The SiO_2 enhances the diffusion of a relatively low concentration of zinc (thereby minimizing wafer surface damage while facilitating high surface concentrations (10)). These diffusions are leading to open-circuit voltages in excess of 1.4 volts; however, the short-circuit current has been low.

Figure 3 shows the spectral response of two of our devices compared to a GaAs standard. Sample PT#184 has a 1.84eV composition, which shows a low quantum yield and a flat response. It is believed that part of this low yield is due to a dead layer resulting from the solid state diffusion process.

Sample H041886 has a 2.08eV composition and shows a more peaked response. This sample peaks in the region corresponding to the direct bandgap. Hence, some efficiency is lost in the indirect composition region. The poor blue response of H041886 is most likely due to a deep junction.

Figure 3

SPECTRAL RESPONSE OF TWO GaAsP DEVICES

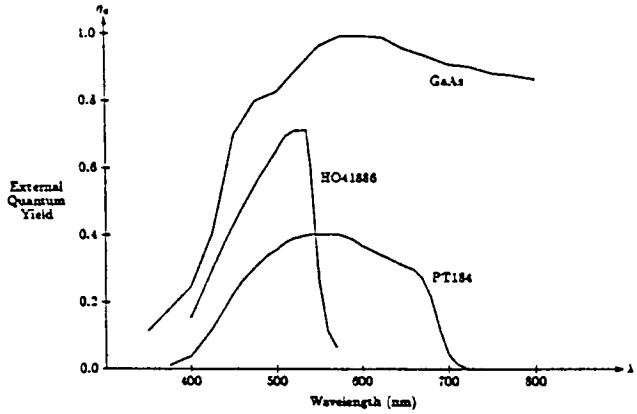

To achieve the 71.8% quantum efficiency needed for the attainment of a 25% tandem solar cell, the flat response of PT#184 must be brought up to the level of the H041886 peak. We are currently investigating the spectral response of MIS devices and grown p/n junctions in order to achieve this.

The near term goal of a 25% efficient tandem solar cell requires a 13.5% efficient top solar cell. Table VII shows our best parameters to date.

Table VII

Best GaAsP on GaP Solar Cell Parameters

	Target	Actual
Transparency below Eg (%)	95	92.3*
Voc (volts)	1.46	1.43
Jsc (mA/cm^2)	14.9	14.6**
FF	.84	.84

*Single layer AR coating
**MIS Device

The first experimental two-junction, four-terminal tandem cells with GaAsP top solar cell on a conventional silicon bottom cell has been prepared. The top cell has an open circuit voltage of 1.397 volts and a fill factor of 0.81, although the current was low. Nonetheless, the tandem stack outperformed the conventional silicon solar cell by more than 10%. If the GaAsP top solar cell were stacked on a state-of-the-art silicon solar cell, an efficiency approaching 20% would have been achieved. A transparency of 95.0% has been achieved with this tandem structure - this includes grid shading but neglects busbar losses.

Conclusions

Preliminary results are encouraging for the achievement of high conversion efficiencies using a GaAsP top solar cell mechanically stacked on a conventional silicon solar cell. A realistic maximum of 29.4% is suggested when both the top and bottom solar cells are state-of-the-art. Practical system efficiencies

greater than 25% are attainable in the near future with the use of a state-of-the-art bottom solar cell.

References

(1) M.E. Nell and A.M. Barnett, "The Spectral p-n Junction Model for Tandem Solar Cell Design", Conf. Rec. 18th IEEE Photovoltaic Specialist Conference, 116, Las Vegas (1985).

(2) A.M. Barnett, M.G. Mauk, J.C. Zolper, I.W. Hall, W.A. Tiller, J.B. McNeely and R.B. Hall, "Thin Film Silicon and GaAs Solar Cells", Conf. Rec. 17th IEEE Photovoltaic Specialist Conference, 747, Orlando (1984).

(3) R.A. Sinton, Y. Kwark, J.Y. Gan, and R.M. Swanson, "27.5% Silicon Concentrator Solar Cells", IEEE Electron Device Letters, EDL-7 (#10), 567-569, 1986.

(4) M.A. Green, A.W. Blakers, S.R. Wenham, S. Narayanan, M.R. Willison, M. Taouk, and T. Szpitalak, "Improvements in Silicon Solar Cell Efficiency", Conf. Rec. 18th IEEE Photovoltaic Specialist Conference, 39, Las Vegas (1985).

(5) NASA Space Vehicle Design Criteria (Environment), Solar Electromagnetic Radiation, NASA SP-8005, May 1971.

(6) L.R. Dawson, "Liquid Phase Epitaxy", Progress in Solid State Chemistry, Chapter 4, 7, 117, Pergamon Press (1972).

(7) R.L. Moon, "Liquid Phase Epitaxy", Chapter 11, Crystal Growth, ed. B.Pamplin, 2nd ed., p.421, Pergamon Press (1980).

(8) H. Nelson, "Depositing Successive Epitaxial Layers from the Liquid Phase", U.S. Patent 3,565,702 issued February 23, 1971.

(9) Emulsitone Co., "Deposition of Doped and Undoped Silica Films on Semiconductor Surfaces", U.S. Patent 3,615,943 issued October 26, 1971.

(10) Filmtronics, Inc., "Semiconductor Diffusant Products", processing information, p.35.

SUPERSTRUCTURE HIGH EFFICIENCY PHOTOVOLTAICS*

M.Wagner, L.C. So, and J.P. Leburton
University of Illinois
Urbana, Illinois

A novel class of photovoltaic cascade structures is introduced which features multijunction upper subcells. These Superstructure High Efficiency Photovoltaics (SHEP's) exhibit enhanced upper subcell spectral response because of the additional junctions which serve to reduce bulk recombination losses by decreasing the mean collection distance for photogenerated minority carriers. Two possible electrical configurations were studied and compared: a three-terminal scheme that allows both subcells to be operated at their individual maximum power points and a two-terminal configuration with an intercell ohmic contact for series interconnection. The three-terminal devices were found to be superior both in terms of Beginning-of-Life efficiency and radiation tolerance. Realistic simulations of three-terminal AlGaAs/GaAs SHEP's show that one sun AMO efficiencies in excess of 26% are possible.

INTRODUCTION

Although considerable effort has been devoted to the development of monolithic III-V cascade cells with two energy gaps, experimentally attainable conversion efficiencies have, to date, been substantially lower than the best single-gap cells. The highest reported efficiency for a two-terminal AlGaAs/GaAs cascade cell under one-sun AMO conditions is 15.1% [ref. 1]. Lattice-mismatched AlGaAs/InGaAs cells have achieved efficiencies of only 13.6% (under one sun AM1.5 conditions) [ref. 2].

There are two principal obstacles which must be surmounted before practical monolithic cascade cells can become realizable: upper subcell quality must be improved and a low-resistance intercell ohmic contact (IOC) technology must be developed [ref. 1]. In this paper we present a novel class of cascade cells designed to overcome both problems. These superstructure high efficiency photovoltaics (SHEP's) feature an upper subcell with multiple junctions for improved performance. Previous work by the authors has shown that multiple junctions in a single-gap cell can substantially improve spectral response, particularly for AlGaAs cells of the composition needed for the upper subcell of a cascade device.

A two-terminal configuration is possible for the SHEP's, but they lend themselves most naturally to a three-terminal configuration. This might seem a serious drawback since three-terminal photovoltaics have been dismissed as impractical by many authors [refs. 1,2,4]; however, this apparent difficulty lead us to an approach which circumvents the need for an IOC with its attendant electrical and optical losses. Complementary pairs (npn and pnp) of three-terminal cells in which the upper-subcell short-circuit current of one is matched to the lower-subcell short-circuit current of the other can be used to obtain a two-terminal output. Figure 1 shows the electrical configuration and one possible physical configuration of this scheme. We found only one reference to this idea in the literature [ref. 5], so it appears to have been largely overlooked.

* Work supported by the National Aeronautics and Space Administration

DEVICE STRUCTURE AND MODELLING

Cross-sectional views of two possible SHEP structures are shown in figure 2. The five- and seven-layer structures allow both the upper-subcell emitter and lower-subcell base to be p-doped, which is desirable for optimum spectral response (electron diffusion lengths are usually longer than hole diffusion lengths in III-V compounds). Additional junctions in the upper subcell of the seven-layer structure prevent transport of collected carriers in the direction transverse to the layers, as occurs in conventional solar cells. Instead, carriers must be transported in the layer planes to heavily doped contact regions extending vertically through the superstructure. These regions are known as selective electrodes since they connect to layers of like doping, while forming reverse-biased junctions (during normal operation) with layers of opposite doping type. By allowing collected carriers to be transported in the layer planes, selective electrodes make it possible to incorporate any number of epitaxial layers in the upper subcell. Fabrication of selective electrodes in structures with doping concentrations similar to what one would expect for photovoltaics ($> 10^{18} cm^{-3}$) was recently reported [ref. 6].

The performance potential of the cells was evaluated by means of a detailed computer model, which allows a wide variety of multilayer, multi-bandgap structures to be investigated. Effects of the selective electrode regions on the minority-carrier distribution are assumed to be negligible, permitting a one-dimensional analysis. Doping and composition profiles are assumed to be uniform within each layer and abrupt at junctions. These assumptions allow closed-form expressions to be used for the contributions of each layer to short-circuit current, injection current, and space-charge recombination, so that layer thicknesses can be rapidly optimized. The optimization criterion used was to maximize beginning-of-life (BOL) efficiency with the subcells operating at their respective maximum-power points. This criterion does not yield a precise estimate of cell performance in a complementary configuration, which will require the pnp and npn cells to be simultaneously optimized because of the current-matching requirement already discussed. However, it will provide a basis for comparing the five- and seven-layer structures as well as a rough prediction of the efficiency in the complementary configuration (within 1% AMO).

The current-voltage (I-V) characteristics of the three-terminal SHEP's are represented by an Ebers-Moll model. The coupled-diode equations are:

$$J_1(v_1,v_2)=J_{sc_1}-J_{o_{11}}e^{\lambda v_1}-J_{o_{12}}e^{\lambda v_2}-\sum_m J_{gr_m}\left|\frac{e^{\frac{\lambda v_1}{2}}}{v_{b_m}-v_1}\right| \tag{1}$$

$$J_2(v_1,v_2)=J_{sc_2}-J_{o_{21}}e^{\lambda v_2}-J_{o_{22}}e^{\lambda v_1}-\sum_m J_{gr_m}\left|\frac{e^{\frac{\lambda v_2}{2}}}{v_{b_m}-v_2}\right| \tag{2}$$

where λ = q/kT and the subscript one refers to the upper subcell. The terms J_{SC_1} and J_{SC_2} represent the upper and lower subcell short-circuit current densities, respectively. Coefficients $J_{o_{11}}$, $J_{o_{12}}$, $J_{o_{21}}$ and $J_{o_{22}}$ determine the dependence of the injected component of the dark current on the subcell terminal voltages. Coupling of the I-V equations arises from interaction of the injected minority-carrier populations across the heterojunction separating the upper and lower subcells. The space-charge recombination component of the dark current is represented by the remaining terms. Each summation is over the homojunctions contained in the corresponding subcell. Note that it is necessary to have a term for each junction because, in general, the barrier potentials (V_{b_m}'s) will not be the same for all junctions in a particular subcell. If they were identical, the voltage dependent terms would factor out and one could simply sum over the J_{gr_m}'s to obtain a composite coefficient as in the case of the short-circuit and injected current terms. To compute the J_{gr_m}'s we use Choo's theory of space-charge recombination for abrupt, asymmetrical junctions [ref 7].

Expressions for the contributions of the window, emitter (upper subcell), and base (lower subcell) to the short-circuit and injected currents are well known and have been published elsewhere [8]. Contributions of layers bounded above and below by homojunctions are easily derived from the minority-carrier continuity and current-density equations with the boundary condition of zero excess carrier density at the depletion-region edges. The contributions of layers adjacent to the isotype heterojunction which separates the upper and lower subcells are considerably more complicated to calculate because one must account for interaction between the minority-carrier populations in the layers above and below the heterojunction. The barrier seen by minority carriers at the heterojunction is the junction built-in potential. This holds under all bias conditions since doping concentrations in the layers forming the heterojunction are sufficiently high that junction bias will be effectively zero for typical current densities. The boundary conditions on the minority- carrier populations are therefore

$$\frac{P_{n_2}}{P_{n_1}} = \exp[q\,(E_{F_1} - (\Delta E_v + E_{F_2}))/kT] \tag{1}$$

$$D_{P_1} \nabla P_{n_1} = D_{P_2} \nabla P_{n_2} \tag{2}$$

The fermi levels E_{F_1} and E_{F_2} are measured from the respective valence band edges. Subscript one denotes the higher gap layer of the upper subcell. These boundary conditions are nearly identical to those described for low-high junctions [ref. 9]. The only difference is the ΔE_v term which must be included in the expression for the junction barrier potential to account for the valence band edge discontinuity at the heterojunction. We assume that ΔE_v is 40% of the energy gap difference in accordance with recent experimental work [ref. 10].

For all designs studied, the top layer is specified to be a 300 Å $Al_{0.9}GA_{0.1}As$ window with a surface recombination velocity of $10^6 cm/s$. The antireflection coating is Si_3N_4 and grid obscuration is assumed to be 4%, attainable with existing grid array technology [ref. 11]. The absorption coefficient is modelled as in reference 12.

RESULTS AND DISCUSSION

We found that efficiencies of optimized SHEP structures vary gradually with upper subcell composition (figure 3). Broad peaks occur at AlAs mole fraction x = 0.36 for both the five- and seven-layer structures with maximum BOL one-sun AMO efficiencies predicted to be slightly in excess of 26%. Dependence of efficiency on composition is expected to become more critical when the current-matching constraints of the complementary design are imposed. The spectral response of a five-layer SHEP with optimum upper subcell composition (x = 0.36) is shown in figure 4. Curves for the individual layer contributions include both depletion and quasi-neutral region response.

The performance, as diffusion lengths are degraded, of two SHEP structures and a five-layer, series-connected AlGaAs-GaAs cascade cell is shown in figure 5. With space-charge recombination suppressed (fig. 5a) the seven-layer SHEP has considerably higher BOL efficiency than the five-layer structure. This is because the injection component of the dark current depends strongly on layer thicknesses, so that the effect of thinner layers in the upper subcell more than offsets the effect of having two additional junctions in that subcell. Unfortunately, the space-charge recombination component of the dark current, which tends to dominate the injection component at the maximum- power point in AlGaAs cells, is quite independent of layer thicknesses. The seven-layer SHEP is, therefore, at a slight disadvantage in BOL efficiency because of the two additional junctions if the effects of space-charge recombination are included (fig. 5b), but its overall performance is still seen to be superior to that of the five-layer SHEP.

Although simulation of a complementary pair has not yet been performed, the efficiency is expected to be very close to that of an AlGaAs-GaAs cascade cell with an ideal IOC. The curves in figure 5 were calculated using this assumption of an electrically and optically lossless IOC. The BOL efficiency of this

cell is slightly less than 27% without space-charge recombination, which is somewhat lower than the value of 27.6% found in an earlier study of AlGaAs-GaAs cascade cells (this study neglected effects of space-charge recombination) [13]. The optimum upper-subcell composition predicted by our model (x = 0.38) was also found to be somewhat lower than that of the previous study (x = 0.41). These differences are probably accounted for by the assumption in our model that diffusion lengths fall exponentially with increasing AlAs mole fraction, which tends to skew the optimum upper-subcell composition to smaller values.

It is interesting to compare the degradation curves of the two five-layer structures. The slopes are seen to be almost identical. This shows that the number of layers is more important than electrical configuration (two-terminal vs. three-terminal) in determining radiation tolerance. It should be noted that the IOC of the series-connected cell is assumed to remain ideal even as layer diffusion lengths are degraded. We therefore anticipate that complementary pairs of multilayer SHEP's will decisively outperform cascade cells with monolithic IOC's, because of the additional layers and the lack of an IOC which could undergo degradation.

CONCLUSIONS

We have presented a class of structures designed to surmount the principal difficulties facing the development of practical lattice-matched monolithic cascade cells. Upper subcell quality is improved by multiple junctions, and the problem of an IOC is completely circumvented by using complementary pairs of three-terminal cells. Although simulation of complementary cells has not yet been performed, results from series-connected structures with an ideal IOC indicate that BOL efficiencies in excess of 25% under one-sun AMO conditions should be attainable. With higher concentration factors we anticipate conversion efficiencies approaching 30%. The seven-layer SHEP appears most advantageous, at present, for space applications because of its superior tolerance to radiation degradation. If the effects of space-charge recombination were reduced, which would entail reduction of deep level impurities and vacancies, structures with even greater numbers of thinner layers could substantially increase performance.

References

1. Hutchby, J. A.; Markunas, R. J.; Timmons, M. L.; Chiang, P. K.; and Bedair, S. M.: A Review of Multijunction Concentrator Solar Cells. Proc. 18th IEEE Photovoltaic Spec. Conf. (IEEE, New York, 1985), p. 20.
2. Lewis, C. R.; Ford, C.W.; Virshup, G. F.; Arau, B. A.; Green, R. T.; and Werthen, J. G.: A Two-Junction Monolithic Cascade Solar Cell in a Lattice-Matched System. Proc. 18th IEEE Photovoltaic Spec.Conf. (IEEE, New York, 1985), p. 20.
3. Wagner, M. and Leburton, J. P.: Superstructures and Multijunction Cells for High Efficiency Energy Conversion. Proc. 18th IEEE Photovoltaic Spec. Conf. (IEEE, New York, 1985), p. 157.
4. Fan, J. C. C.; Tsaur, B-Y. and Palm, B. J.: Optimal Design of High-Efficiency Tandem Cells. Proc. 16th IEEE Photovoltaic Spec. Conf. (IEEE, New York, 1982), p. 692.
5. Sakai, S. and Umeno, M.: Theoretical Analysis of New Wavelength-Division Solar Cells. J. Appl. Phys., 51, p. 5018 (1980).
6. Dohler, G. H.; Hasnain, G.; and Miller, J. N. In Situ Grown-In Selective Contacts to NIPI Doping Superlattice Crystals Using Molecular Beam Epitaxial Growth Through a Shadow Mask. Appl. Phys. Lett., 49, p. 704 (1986).

7. Choo, S. C.: Carrier Generation-Recombination in the Space-Charge Region of an Asymmetrical p-n Junction. Solid-State Electron., 11, p. 1069 (1968).

8. Hovel, H. J.: Semiconductors and Semimetals. (Academic Press, New York, 1975) Vol. 11.

9. Godlewski, M. P.; Baraona, C. R.; and Brandhorst, H. W.: Low-High Junction Theory Applied to Solar Cells. Proc. 10th IEEE Photovoltaic Spec. Conf., p. 40 (1973).

10. Wang, W. I.: On the Band Offsets of AlGaAs/GaAs and Beyond. Solid-State Electron. Vol. 29, p. 133 (1986).

11. Werthen, J. G.; Virshup, G. F. ; Ford, C. W.; Lewis, C. R.; and Hamaker, A. C.: 21% (One-Sun air mass zero) 4 cm^2 GaAs Space Solar Cell. Appl. Phys. Lett. 48, 74 (1986).

12. Hutchby, J. A.; and Fudurich, R. L.: Theoretical Analysis of $Al_x Ga_{1-x}$ As-GaAs Graded Bandgap Solar Cell. J. Appl. Phys. 47, p. 3140 (1976).

13. Lamorte, M. F.; and Abbott, D. H.: Window Losses and Current Mismatch Computer Modeling Studies in AlGaAs-GaAs Cascade Solar Cell. IEEE Trans. Electron Devices. ED-30, p. 1313 (1983).

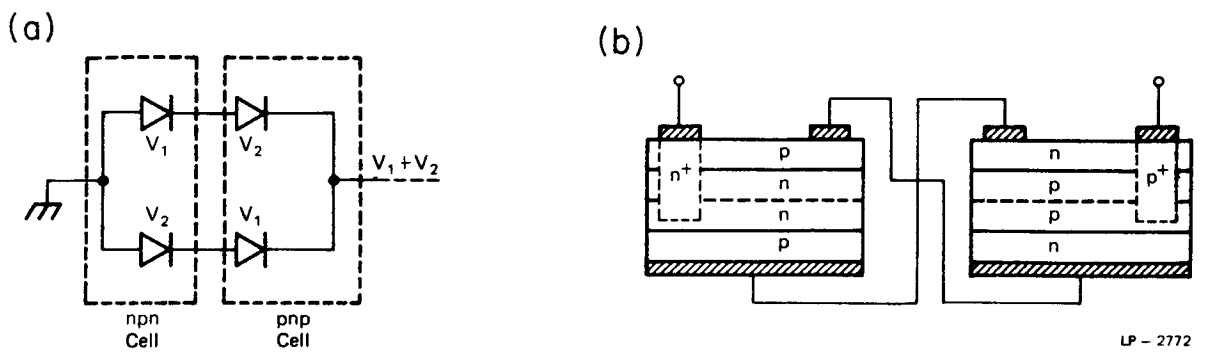

Figure 1. Complementary interconnection scheme for three-terminal photovoltaics showing a) electrical configuration and b) one possible physical configuration.

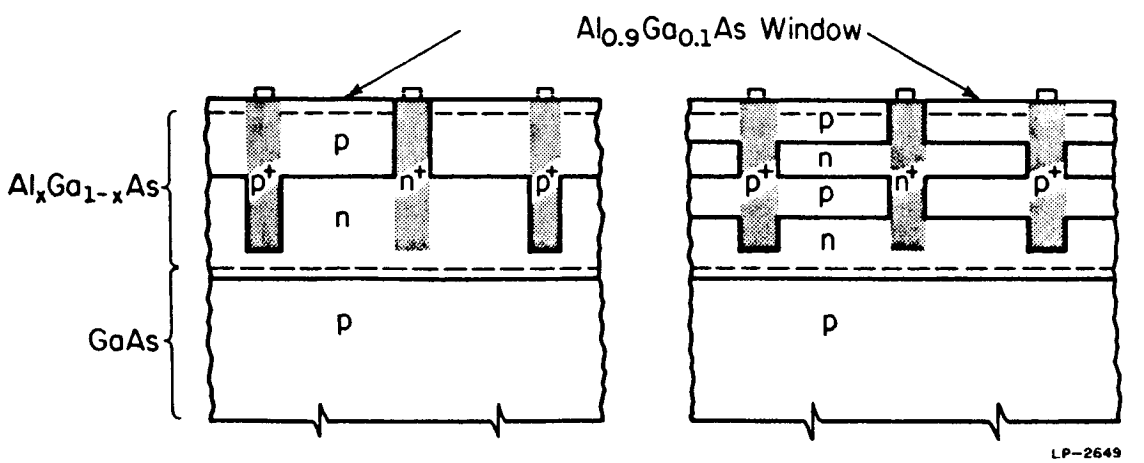

Figure 2. Cross-sectional views of five- and seven-layer SHEP structures. Isotype heterojunctions are represented by dashed lines.

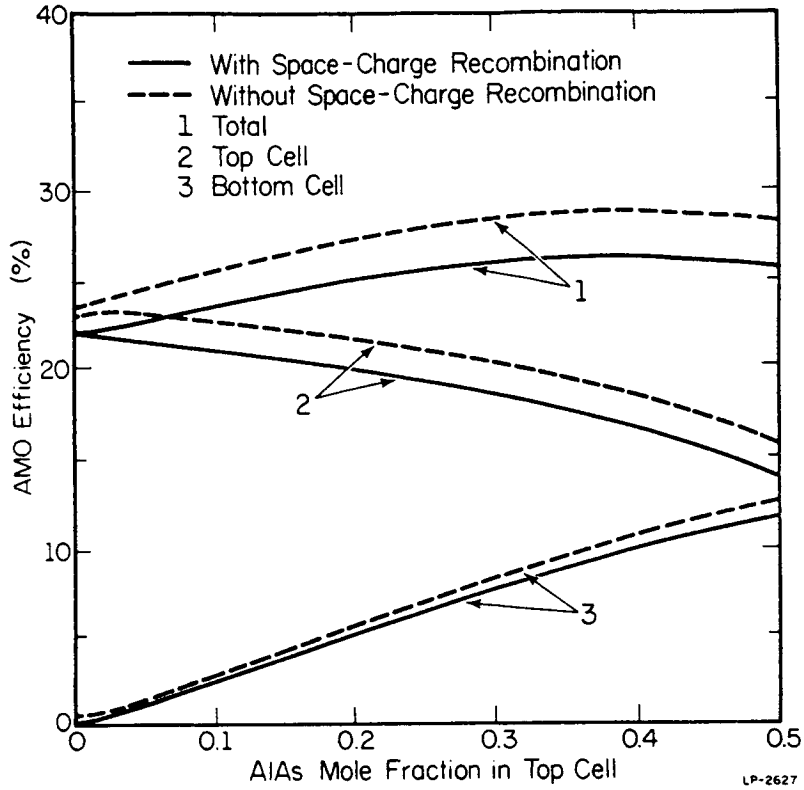

Figure 3. Performance of seven-layer SHEP structures under one-sun AMO illumination at 300 K.

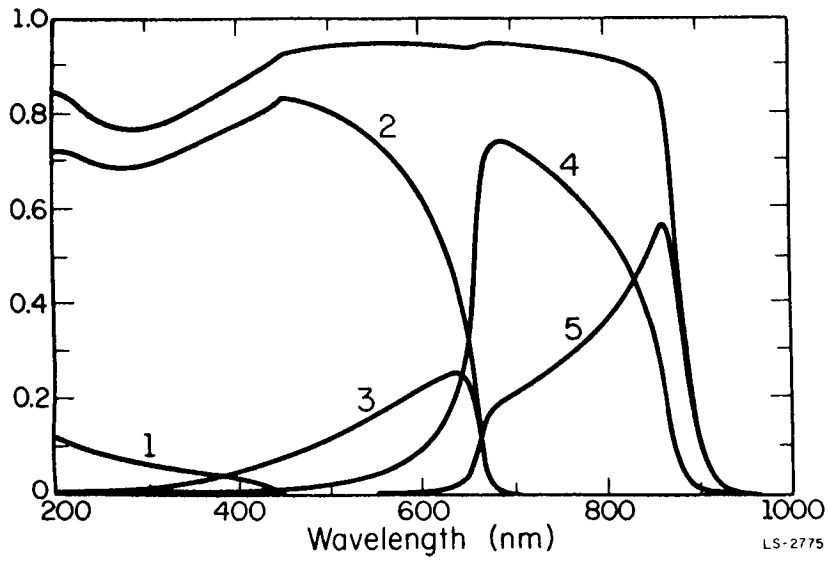

Figure 4. Spectral response of a five-layer SHEP with upper subcell composition x = 0.36. Individual layer contributions are shown as well as overall spectral response. Layers one, two, and three are the window, emitter, and base, respectively, of the upper subcell; layers four and five are the emitter and base of the lower subcell.

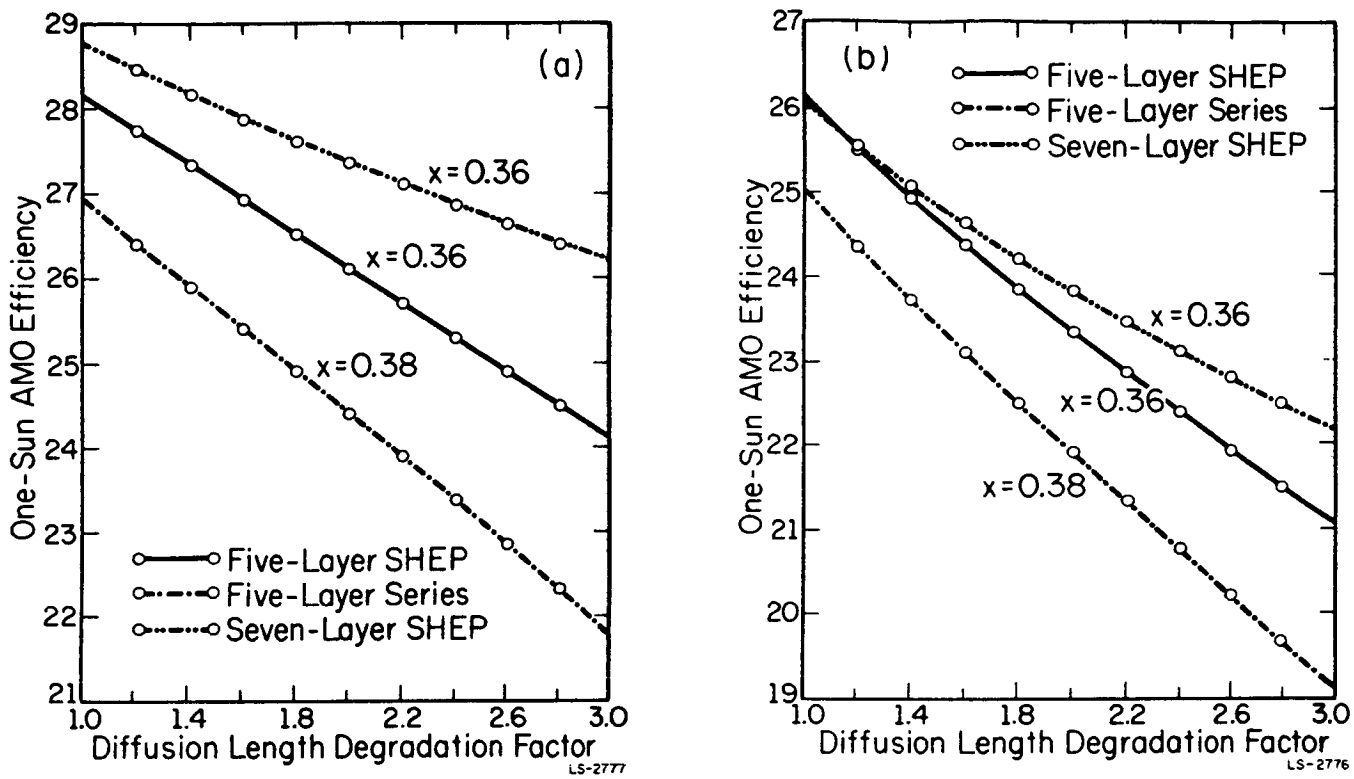

Figure 5. Performance as diffusion lengths are degraded of five- and seven-layer SHEP designs and a five-layer series-connected cascade cell with ideal IOC a) with space-charge recombination suppressed and b) including space-charge recombination.

DESIGN CONSIDERATIONS FOR A GaAs nipi DOPING SUPERLATTICE SOLAR CELL

Ralph Clark and Chandra Goradia
Cleveland State University
Cleveland, Ohio

and

David Brinker
NASA Lewis Research Center
Cleveland, Ohio

A new GaAs nipi doping superlattice solar cell structure is presented, which holds promise for a high efficiency coupled with very high radiation tolerance. This structure uses the CLEFT process and has all contacts on the unilluminated side. It is different from our structure proposed at the last SPRAT conference. Next, design constraints are presented which this structure must satisfy in order to exhibit high efficiency and high radiation tolerance. Finally, results of self-consistent quantum mechanical calculations are presented which show that a viable design of this cell would include relatively thick (~500 Å) n and p layers which are fairly heavily doped ($2x10^{18}$ to $5x10^{18}/cm^3$).

INTRODUCTION

At the previous SPRAT conference in 1985, we presented a GaAs nipi doping superlattice solar cell structure which showed promise for high efficiency and very high radiation tolerance (ref. 1). This structure is shown in figure 1. A unique feature of this structure was that photogenerated carriers are very quickly separated by the built-in electric field in times ranging from 10^{-12} sec to 10^{-10} sec and that these carriers then flow parallel to the superlattice layers, a direction of easy carrier flow. This is in contrast to strained-layer and other superlattice solar cell structures that have carrier flow normal to the layers, a direction of difficult carrier flow. However, it was also pointed out then that one major drawback of this structure was that, even after separation, the carriers could recombine across the "indirect gap in real space" before they reached their respective selective ohmic contacts. In addition, the photocurrent flows along the length of the thin layers between neighboring selective ohmic contacts and may lead to a severe series resistance problem. These two facts put constraints on the minimum lifetime of already-separated carriers across the indirect gap in real space, on the maximum distance between adjacent selective ohmic contacts, and on the minimum two-dimensional carrier densities in the n and p layers.

In order to calculate the lifetime across the indirect gap in real space, it is necessary to calculate the overlap integral of the electron and hole wavefunctions over one period of the superlattice, averaged over all the subbands of the conduction and valence bands. This requires self-consistent calculations between Schrödinger's equation and Poisson's equation, since the potential function in the

former equation is the solution to Poisson's equation and the charge density function in the latter depends on the solution to Schrodinger's equation. These calculations are rather difficult and time-consuming, and we had just begun them at the time of the previous SPRAT conference.

CELL STRUCTURE

We have now completed these self-consistent quantum mechanical calculations for a large number of combinations of layer thicknesses of the n, i, and p layers and of dopings in the n and p layers. These results have shown that our original structure of figure 1 would not work efficiently. We have come up with the modified structure of figure 2 which is based on the CLEFT process (ref. 2) and has all contacts on the back side, making it possible to have closely spaced contacts without having to worry about grid shadowing.

Figure 2(a) gives a basic idea of the method of cell fabrication. Starting with a GaAs substrate, a thin epitaxial layer of GaAs is grown as in the CLEFT process (ref. 2). On this is grown an undoped AlGaAs layer of appropriate thickness (0.2 to 0.5 μm); this layer will serve as a window for the finished cell. On the AlGaAs layer is grown the GaAs nipi superlattice with 10 periods of 0.1- to 0.2 μm each for a total thickness of 1 to 2 μm. V-grooves are photolithographically etched in the superlattice (ref. 3), and alternate grooves are ion-implanted n^+ and p^+ in an interdigitated fashion. The grooves are then metallized to form ohmic contacts to the n^+ and p^+ selective contacts. A rigid backing is then applied for structural support, leaving only the n^+ and p^+ bus bars exposed for external contacts. The backing material should be a good thermal conductor but an electrical insulator. The cell is then cleaved off the GaAs substrate by the CLEFT process (ref. 2), and the GaAs layer above the AlGaAs window is etched off. Finally, an antireflection coating is applied over the AlGaAs window. The finished cell is shown in figure 2(b), with light entering through the AlGaAs window.

DESIGN CONSTRAINTS

We have taken a close look at the design constraints that must be satisfied in order for the cell to exhibit high efficiency and high radiation tolerance. We have derived expressions for the minimum lifetime across the indirect gap in real space, and the minimum values of carrier concentrations in the n and p layers required to keep series resistance and recombination losses within acceptable levels. All of the design constraints are treated in detail in reference 4. Here, we summarize these constraints for the GaAs nipi superlattice solar cell of figure 2(b), operating at 20 AMO, 27 °C (300 K). They are as follows:

(1) total superlattice height or thickness of at least 1- to 2-μm to absorb most of the incident photons;

(2) at least 8 to 10 superlattice periods in order for our quantum mechanical calculations to apply;

(3) a distance between neighboring selective ohmic contacts of about 20 μm;

(4) highly reflecting rear metallization;

(5) thicknesses of n, i, p layers and dopings in n and p layers such that under operating conditions at a forward voltage of about 1.00 V (estimated to be the maximum power voltage at 20 AMO, 300 K) the average electron and hole concentrations are at least $5 \times 10^{17}/cm^3$ and the lifetime for recombination across the indirect gap in real space is at least 10 μsec;

(6) thicknesses of the n and p layers no larger than about 600 Å, so that even after irradiation to a fluence of 1×10^{16} 1 MeV electrons/cm^2 or 1×10^{13} 10 MeV protons/cm^2, the maximum distance a carrier has to diffuse in a low-electric field region is shorter than the carrier diffusion length.

RESULTS

Table I shows the various combinations of layer thicknesses and dopings considered. The lifetimes of already-separated carriers are plotted versus the forward voltage in figure 3. For an open circuit voltage of 1.1 V and an operating voltage (at maximum power) of about 1.0 V, it is seen that most combinations give lifetimes of about 10 msec or larger. Figure 4 shows the average hole concentration in the p layers versus the forward voltage. For the CLEFT type structure of figure 2(b), operating at 20 AMO and 27 °C, we have calculated that for a 20-μm spacing between adjacent contacts, the required minimum lifetime of already-separated carriers is ~10 μsec and the required average hole concentration is $5 \times 10^{17}/cm^3$, in order to keep the ohmic voltage drop across the series resistance to about 20 mV at short circuit. From figure 4, combinations 1, 2, and 15 from table I appear promising, 15 being perhaps the most promising. It then appears that, in order to meet the design constraints outlined earlier, the most convenient design of this cell would have the n and p layers of thickness around 500 Å, with relatively heavy dopings of 2×10^{18} to $5 \times 10^{18}/cm^3$, and i layers may be thin or thick (~500 Å). The lifetime requirement is easily met by just about any combination of thicknesses and dopings; the constraint on minimum carrier concentrations to minimize the series resistance loss is the more stringent requirement.

We have not yet theoretically generated the illuminated I-V characteristics of this device so as to give us the calculated performance parameters, both at beginning of life and after irradiation. Hence, at the present time, we cannot provide any calculated numbers on the expected efficiency and radiation tolerance of this device. This is an extremely difficult and laborious problem requiring 2 to 3 more years of work. However, it is possible to argue on theoretical grounds, as we have done previously (refs. 1 and 4), that this structure should exhibit a beginning-of-life efficiency that is nearly the same but somewhat smaller than that of a well-designed conventional GaAs concentrator solar cell operating under the same conditions and should exhibit a very high radiation tolerance. The next step is the actual fabrication and testing of this structure.

REFERENCES

1. Goradia, C.; Clark, R.; and Brinker, D.: A Possible Radiation-Resistant Solar Cell Geometry Using Superlattices. Space Photovoltaic Research and Technology 1985, NASA CP-2408, 1985, pp. 111-118.

2. McClelland, R.W.; Bozler, C.O.; and Fan, J.C.C.: A Technique for Producing Epitaxial Films on Reusable Substrates. Appl. Phys. Lett., vol. 37, no. 6 Sept. 15, 1980, pp. 560-562.

3. Leon, R.P., et al: Formation of a pn Junction on an Anisotropically Etched GaAs Surface Using Metalorganic Chemical Vapor Deposition, Appl. Phys. Lett., vol. 49, no. 15, Oct. 13, 1986, pp. 945-947.

4. Clark, R.O.: Self-Consistent Calculations and Design Considerations for an nipi Doping Superlattice Solar Cell. Master's Thesis, Cleveland State University, 1986.

TABLE I. - COMBINATIONS OF LAYER THICKNESSES AND DOPINGS CONSIDERED FOR SELF-CONSISTENT CALCULATIONS AND USED IN PLOTTING FIGURES 3 AND 4

Superlattice	d(A)	d_n	d_p	d_i	N_d	N_a
1	800	175	175	225	5×10^{18}	5×10^{18}
2	1000	469	469	31	2×10^{18}	2×10^{18}
3	1200	338	338	262	1.5×10^{18}	1.5×10^{18}
4	1200	562	562	38	1×10^{18}	1×10^{18}
5	1400	656	656	44	1.1×10^{18}	1.1×10^{18}
6	1400	656	656	44	8×10^{17}	8×10^{17}
7	1400	394	394	306	1×10^{18}	1×10^{18}
8[a]	1400	394	394	306	1×10^{18}	1×10^{18}
9	1400	394	394	306	2×10^{18}	2×10^{18}
10	1400	219	219	481	2×10^{18}	2×10^{18}
11	1400	394	1006	0	2×10^{18}	6.7×10^{17}
12	1600	450	450	350	8×10^{17}	8×10^{17}
13	1300	750	750	50	1×10^{18}	1×10^{18}
14	2000	562	562	438	5×10^{17}	5×10^{17}
15	2000	562	562	438	5×10^{18}	5×10^{18}
16	4000	1875	1875	125	1.6×10^{17}	1.6×10^{17}

[a]Superlattice 8 used $m_e^* = m_h^* = 0.067m_e$.

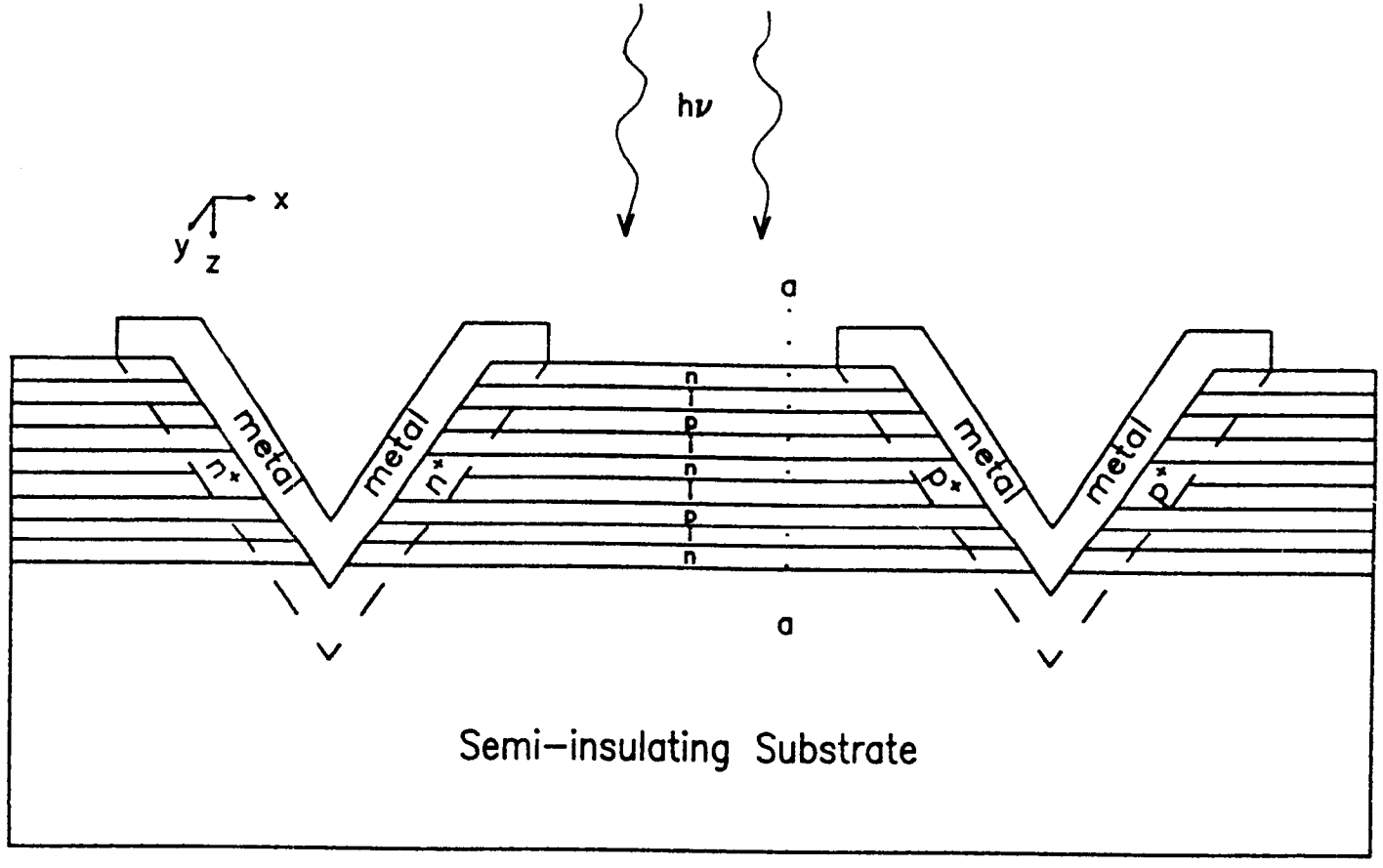

Figure 1. - Doping superlattice solar cell structure as originally proposed.

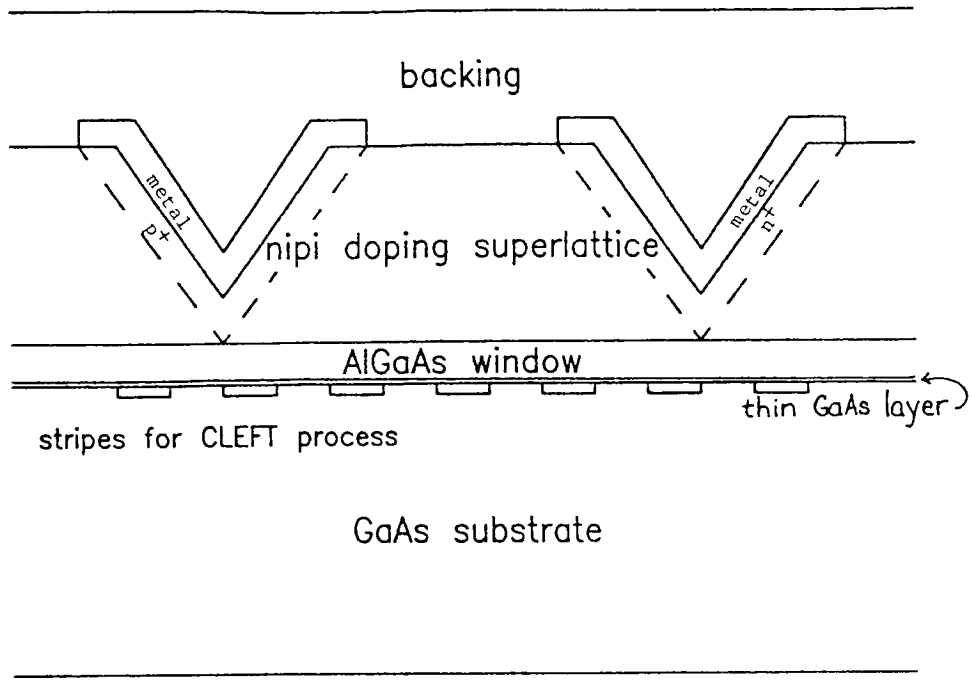

(a) Schematic of fabrication procedure.

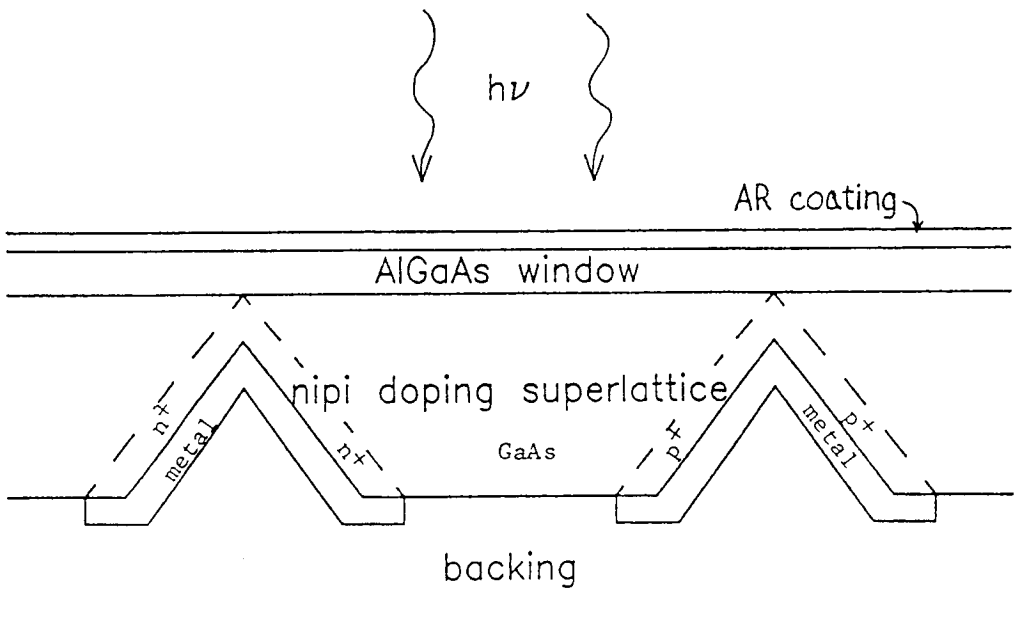

(b) CLEFT superlattice solar cell in use.

Figure 2. - Improved solar cell structure using CLEFT process.

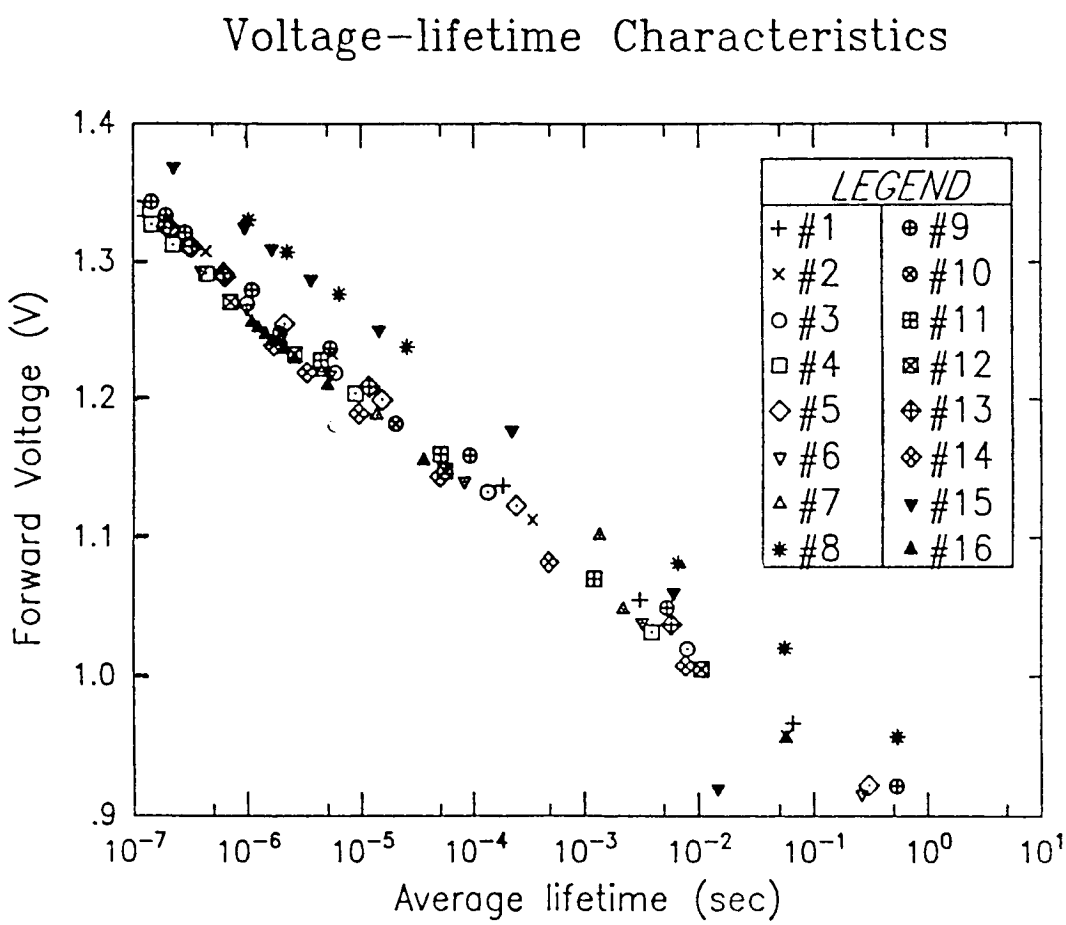

Figure 3. - Lifetime versus forward voltage characteristics for the superlattices in table I.

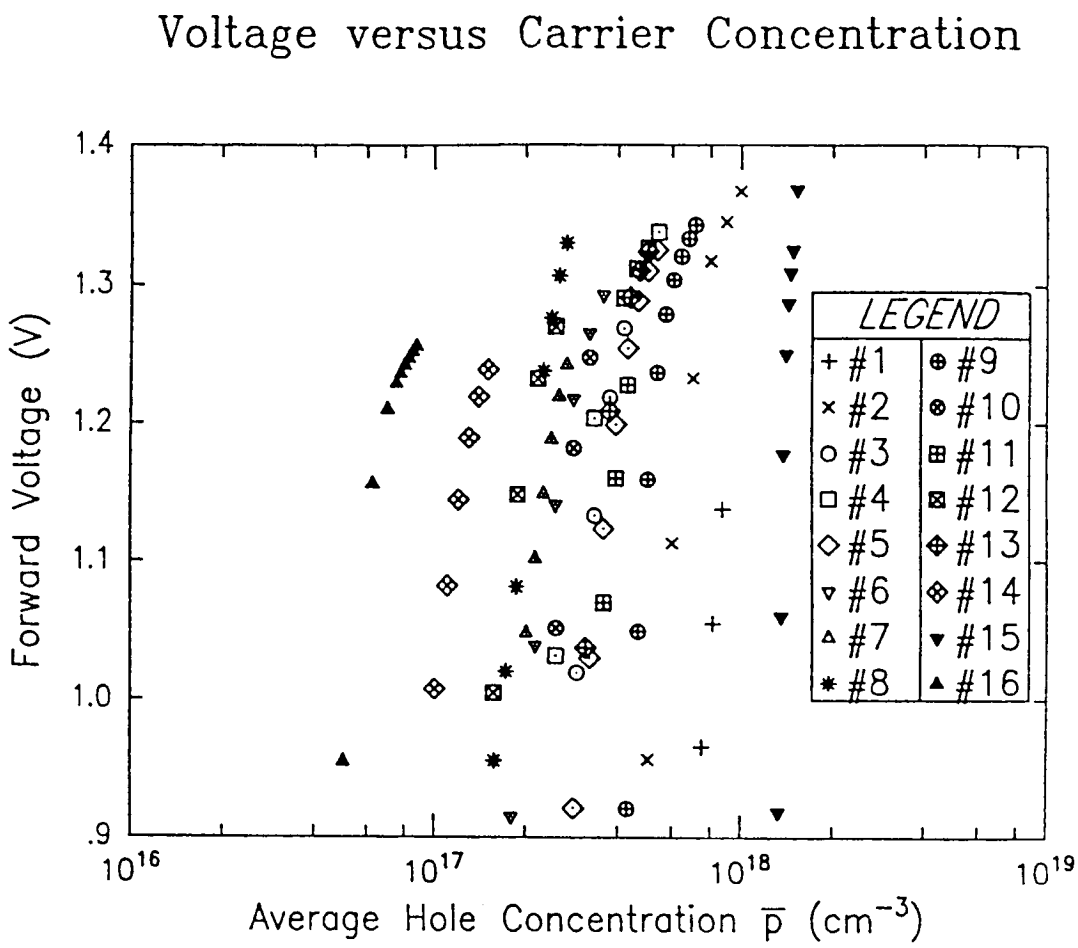

Figure 4. - Carrier concentration versus forward voltage for the superlattices in table I.

PROCESSING AND CHARACTERIZATION OF HIGH-EFFICIENCY SILICON SOLAR CELLS FOR SPACE

G. T. Crotty
California Institute of Technology
Jet Propulsion Laboratory

Silicon solar cells with AM0 efficiencies ranging from 17 to 17.7% are described. These cells were processed on low-resistivity FZ substrates using techniques recently developed for high-efficiency terrestrial silicon solar cells. Not surprisingly, preliminary results indicate that the JPL high efficiency cell is more susceptible to radiation damage in that it retains a smaller proportion of its original power output when compared to conventional space cells after exposure to 5 x 10^{14} 1 MeV electrons. However, the JPL cell does maintain a greater overall power output than the conventional cells to which it was compared. Furthermore, this cell does not demonstrate post-electron irradiation photon decay as has been described for cells processed on 1-10 ohm-cm float zone silicon.

INTRODUCTION

To meet NASA goals for high performance, arrays of 300 W/kg will require thin solar cells with BOL efficiencies >20%, or thin film devices with equivalent power-to-weight ratios (ref. 1). A number of technologies such as GaAs, thin film multijunction cells, indium phosphide and a-Si:H show promise of meeting or exceeding these goals and are currently in various stages of development.

Until these technologies mature, however, silicon will continue to be the workhorse of the space photovoltaics industry. This is most likely to be the case for some time and silicon should be expected to maintain a place in spacecraft power systems even as other technologies begin to prove themselves as viable alternatives.

The theoretical maximum efficiency for a silicon solar cell at AM0 is between 21 to 24%. Actual achievable efficiency will be considerably lower, but it is probably not unrealistic to strive for 18 to 19%. Recently, considerable progress in increasing terrestrial silicon solar cell efficiency has been made. JPL's DOE-supported efforts have resulted in silicon solar cells with AM1.5, global efficiencies as high as 20%. At AM0, these same cells measure 17.7%.

These cells, although initially designed primarily for terrestrial use, may conceivably find application in space. This paper will describe the design and processing of the JPL high-efficiency cell. Also discussed, will be preliminary tests of these cells to moderate 1 MeV electron radiation and comparison to conventional space cells. Post-electron irradiation photon degradation will also be discussed.

DESIGN AND PROCESSING

The JPL high-efficiency silicon solar cell incorporates many of the recent developments in solar cell processing technology designed to reduce minority carrier recombination in the bulk, at the front surfaces and under the contacts. Figure 1 is a diagrammatic view of the JPL high-efficiency cell. The structure of this cell is similar to the microgrooved PESC cell reported by Green, et al. (ref. 2), in that the contacts rest on mesas above a textured surface. The mesas offer two advantages. One is that since the surface is not textured, it reduces the total surface area contacted by the metal. The other advantage is that they aid in the alignment of the masks during various photolithography steps.

Following texturing, the N-type emitter is formed using a phosphine source at 825°C. Total diffusion time is 15 minutes. After removing the diffusion glass, the wafers are oxidized at 900°C in an atmosphere composed of 94.5% N_2, 4.5% O_2, and 1% HCl. This step results in an oxide that has been measured on planar <100> surfaces to be 100-120 Å thick. Following oxidation, the wafers are annealed at 600°C for one hour. The furnace is then cooled to 450°C. After cooling, the wafers are kept at 450°C for one hour, and then pulled from the furnace. This annealing step was chosen because it has been found to recover the minority carrier lifetimes in float zone ingots after high temperature treatments (ref. 3).

Ohmic back contacts are formed by electron beam evaporation of Al, Ti, Pd and Ag followed by a 20 minute sinter at 490°C in hydrogen. Front contact to the cells is made by opening 4-μm-square contact windows in the oxide and then evaporating the Ti, Pd and Ag grid lines and bus bar over the windows. These windows were spaced at 50, 100, 200 and 400 μm centers for each of the four cells processed on an individual wafer. This spacing results in actual contact areas of 0.575 to 0.075% of the total cell surface. Table I lists the spacing percent contact area for each cell measured. Shadowing from the front contact grid amounts to approximately 3.3% of the total cell surface.

The primary purpose for varying the contact area was to determine the effect of contact area on V_{oc} and series resistance. From Table I, V_{oc} does not show the expected increase with decreasing contact area. This may be because recombination in the base and emitter, along with band bending effects have begun to dominate so that recombination under the contacts is no longer relevant. As can be seen from the fill factors in Table I, series resistance does not increase with decreasing area.

RADIATION TESTS

To gain some understanding of the extent to which these cells might degrade in the space environment, cell 2B from Table 1 was irradiated with 5×10^{14} 1 MeV electrons. Light I-V data for this cell is summarized in Table II.

The power degradation of the JPL cell was compared to that of two types of cells routinely used in space photovoltaic arrays (ref. 4). K6-3/4 is a 2-mil cell with a dual layer AR coating. K7 is similar in design to the JPL cell in that it is textured, has a dual layer AR coating and is 8 mils thick. Both K6-3/4 and K7 were fabricated on 10 ohm-cm base material and have back surface fields and reflectors.

Figure 2 exhibits the power loss of cells K6-3/4 and K7 through a range of 1 MeV electron fluences along with the JPL cell before and after 5 x 10^{14} 1 MeV electrons. Cells K-6/34 and K7 retained 75 to 85% of their original power. The JPL cell exhibits considerably more deterioration in that it maintains only 67% of its original power output. Nevertheless, the power output of this cell is still 2.3% greater than for cell K6-3/4 and 4.3% greater than cell K7.

Float zone silicon has not typically been used on space arrays in part because of the additional photon degradation observed for devices made on 1-10 ohm-cm FZ material (ref. 5). Even though devices processed on float zone material may initially demonstrate higher performance than devices made on Cz material, after electron irradiation, the performance of the float zone devices deteriorates to where they are comparable to Cz devices after photon irradiation. Therefore, Cz is the material of choice since it is less costly and easier to obtain.

Photon degradation was also expected for the JPL cell. Table II summarizes the light I-V data for cell 2B following a 24-hour photon irradiation period carried out after 5 x 10^{14} 1 MeV electron irradiation. Surprisingly, no further degradation is observed for this cell processed on low-resistivity float zone material.

These radiation studies to date are encouraging, even though the results are very preliminary. If the trend toward higher post-irradiation power output continues, it is possible that this material and device structure may find future mission applications.

CONCLUSION

The significant increase in efficiency exhibited by the JPL high-efficiency cell is derived primarily from optimization of relatively conventional design approaches. These include very high-quality starting material, textured surfaces, front surface passivation, reduced contact area and reduced contact shadowing.

The behavior of these cells in radiation is encouraging in that they maintain a higher power output after 5 x 10^{14} 1 MeV electrons than for conventional space cells and do not suffer from photon degradation.

REFERENCES

1. Scott-Monck, J. A.; and Stella, P. M.: Advanced Photovoltaic Solar Array Program--A Preliminary Assessment. Proceedings of the 21st IECEC, San Diego, California, August 1986, p. 1458.

2. Green, M. A.; Blakers, A. W.; Wenham, S. R.; Narayanan, S.; Wilson, M. R.; Taouk, M.; and Szpitalak, T.: Improvements in Silicon Solar Cell Efficiency. Proceedings of the 18th IEEE Photovoltaics Specialists Conference, Las Vegas, Nevada, October 1985, p. 39.

3. Graff, K.; Peiper, H.; and Goldbach, G.: Carrier Lifetime Doping of P-Type Silicon by Annealing Processes. Semiconductor Silicon 1973, Edited by Howard R. Huff and Ronald Burgess, The Electrochemical Society, Princeton, New Jersey, p. 170.

4. Anspaugh, B. E.; Downing, R. G.; Tada, H. Y.; and Carter, J. R., Jr.: Solar Cell Radiation Handbook, Third Edition, JPL Publication 82-69, pp. 3-60 to 3-162.

5. Crabb, R. L.: Photon Induced Degradation of Electron Irradiated Solar Cells. Proceedings of the 9th IEEE Photovoltaic Specialists Conference, May 1972, p. 329.

Table I - AM0 I-V Data for 7 of the JPL High-Efficiency Silicon Solar Cells

Cell ID	S* (μm)	Contact Area (%)	V_{oc} (mV)	I_{sc} (mA)	Fill Factor	Effic. (%)
1A	400	0.575	647.0	179.4	0.799	17.14
1D	50	0.075	649.2	179.2	0.804	17.27
2B	200	0.29	650.4	176.8	0.810	17.20
3B	200	0.29	652.8	178.1	0.802	17.23
3C	100	0.15	660.1	178.4	0.815	17.74
4A	400	0.575	649.2	178.9	0.801	17.20
4D	50	0.075	649.7	178.9	0.805	17.30

*S = contact spacing

Table II - I-V Data for Cell #2B

V_{oc} (mV)	I_{sc} (mA)	Fill Factor	Effic. (%)	Remarks
650.4	176.8	0.810	17.2	Prior to 5 x 10^{14} 1 MeV electron irradiation
587.2	126.3	0.795	11.50	After irradiation
588.7	127.7	0.794	11.51	After 24-hr photon irradiation

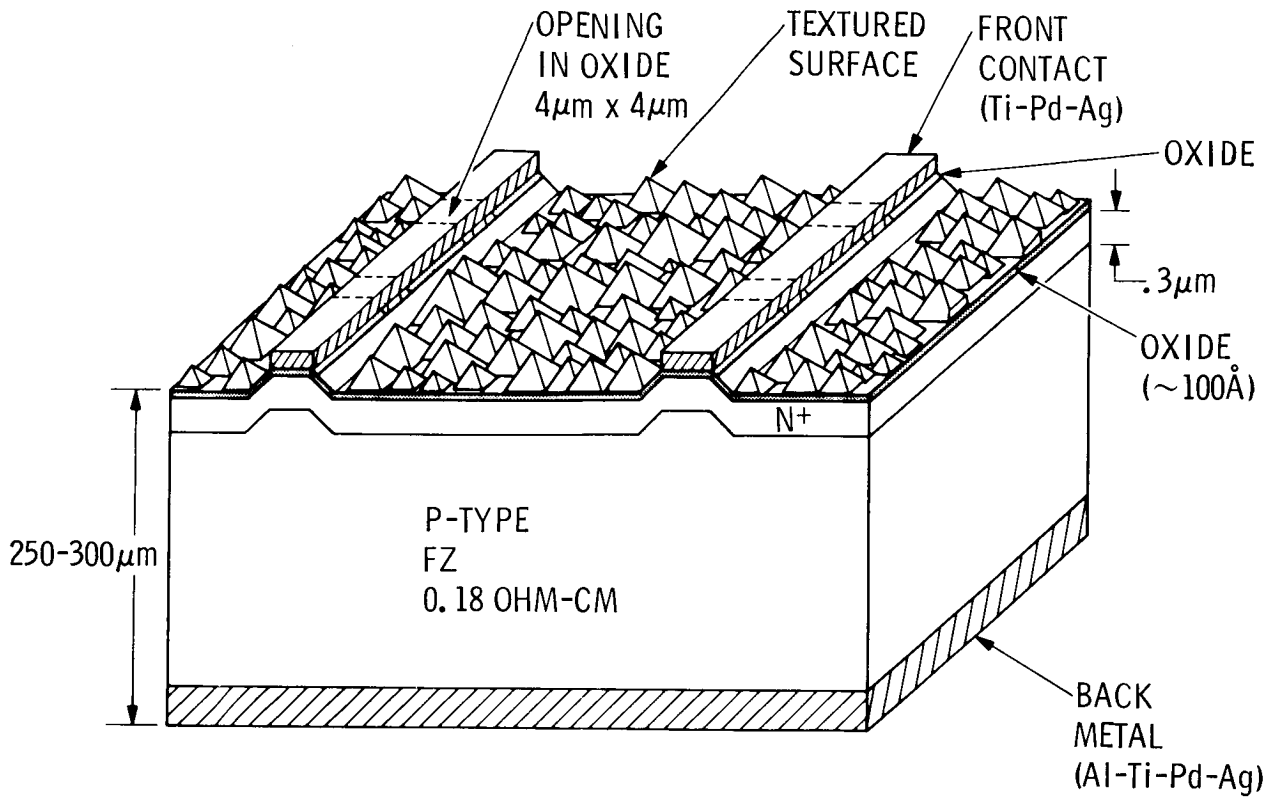

Figure 1. Schematic diagram of the JPL high-efficiency silicon solar cell

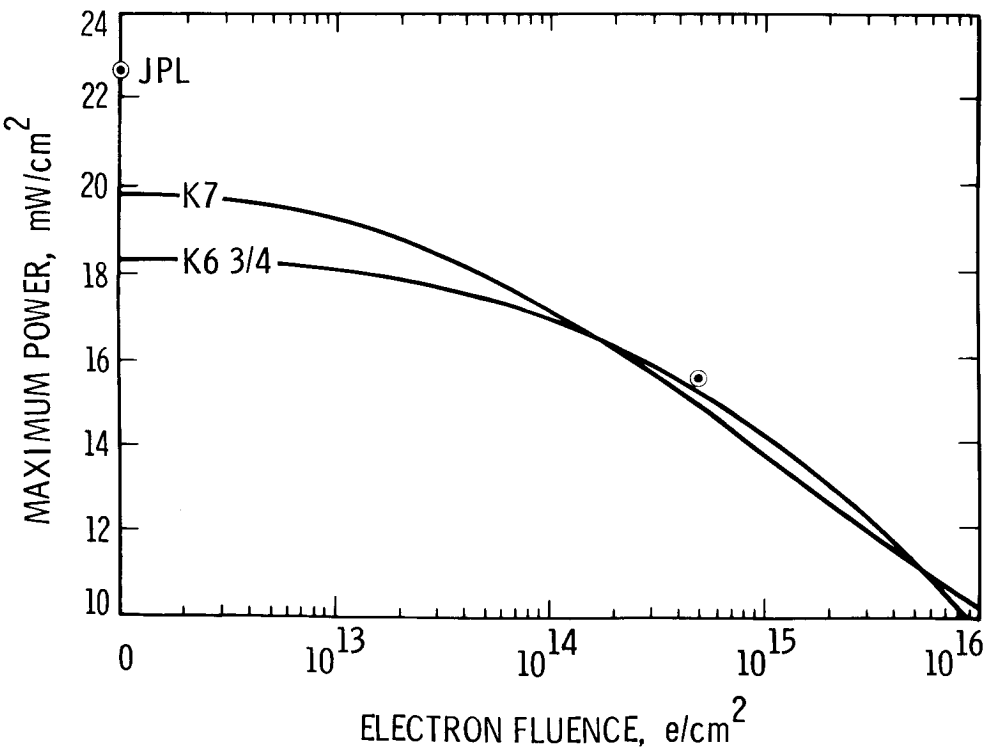

Figure 2. Maximum power vs. 1 MeV electron fluence for JPL high-efficiency cell and 2 conventional space cells. Maximum power after 5 x 10^{14} e/cm^2 is 15.6 mW/cm^2 for the JPL cell, 15.2 mW/cm^2 for K6-3/4 and 14.9 mW/cm^2 for K 7.

C-2

DESIGN STUDY OF LARGE AREA 8 cm x 8 cm WRAPTHROUGH CELLS FOR SPACE STATION

George F.J. Garlick and David R. Lillington
Spectrolab, Inc.
Sylmar, California

This paper reports on the design of large area silicon solar cells for the projected NASA Space Station. It is based on the NASA specification for the cells which calls for an 8 cm x 8 cm cell of wrapthrough type with gridded back contacts. The Beginning of Life (BOL) power must be 1.039 watts per cell or larger and maximum End of Life (EOL) after ten years in the prescribed orbit under an equivalent 1MeV electron radiation damage fluence of $5x10^{13}$ e/cm^2. On orbit efficiency is to be optimized by a low thermal absorptance goal (thermal alpha) of .63.

Within the above specification there is some latitude left to the designer in such factors as choice of cell type e.g. base resistivity, thickness and presence or absence of a back surface field (BSF) and planar or textured front surface. Emphasis is also placed on fabrication cost and power/weight ratio.

The design study was carried out under Task I of NASA contract NAS3-24672. This task covered a period of three months. It combined detailed computer modeling with input of actual data from previous cell diagnostics for factors such as radiation hardness, antireflection coating optimization and thermal alpha tests.

The relatively novel features of such cells are their large size, gridded back contacts and wrapthrough system. In this study, computation is extended beyond the required limits for completeness. For example cell performance was considered out to fluences of 10^{14} and 10^{15} 1 MeV e/cm^2 and the effects of front and back surface passivations were found.

THE DESIGN STUDY

Choice of Cell Type

Choice of cell type is strongly influenced by the radiation damage (EOL) after $5x10^{13}$ 1 MeV e/cm^2 fluence. However, this is small enough to include BSF cells in the considerations and also cells with lower base resistivities. Thus we considered cells of both 2 and 10 ohm-cm resistivities and in relation to manufacturing costs we considered both thin (4 mil) and thick (8 mil) cells. As shown below these choices can yield cells which lie above the minimum BOL power requirements. Textured and planar front and back surfaces were also considered. The various possibilities are shown schematically in Figures 1a through 1d.

The Modeling Basis

Computer programs have been developed which are based on the accepted analytical equations for cell transport processes. Typical parameters entered into the programs for cells are given in Table 1. The emitter characteristics are very similar to those optimized for space cells by Spectrolab after many years of experience. Variables of particular importance are the front and back surface recombination velocities. The usual front surface value is 5.10^4 cm/s when the emitter is thin but

for thicker emitters (deeper junctions) this velocity becomes critical and must be reduced to around 1000 cm/s. In the case of the back surface without BSF we find that the P-silicon to aluminum contact has a recombination velocity of about 1500 cm/s. When a BSF is present, best values are 10 cm/s but having in mind the use of a boron diffused or implanted BSF considered for the Space Station cells we adopted a more conservative estimate of 100 cm/s.

With respect to the antireflection coatings on front and back surfaces we again used data from previous work adding to them the analysis of the situation where a passivation layer of relatively low refractive index underlies the A.R. coating. The A.R. reflection spectra of actual cell types and also those computed for cells with the added passivation layers were used in the cell performance computations.

In order to maximize cell power when gridded front and back contacts are used the series resistance must be minimized. Spectrolab has computer models which, given a specific grid geometry, carry out optimization analysis to minimize resistive losses. Consideration of deeper junctions was included since these will reduce the sheet resistance of the emitter layer. However, as shown later and mentioned above, there is then a critical need to lower front surface recombination velocities by passivation.

Modeling Results

In this section we present the results of modeling for the cells at 25°C. These are then used in the next section to determine on orbit performance.

Series Resistance Minimization

Figure 2 gives the important parameters for the model which gives optimum grid geometry for minimum series resistance. They comprise the grid line dimensions and grid spacing, sheet resistance of the emitter region and ohmic bar dimensions. Grid line tapering is also taken into account. Effects of base and gridded back structure are also included. The latter is not as critical as the front grid structure.

To use the results for each design of wrap structure a value for series resistance so derived is used in obtaining an I-V curve for each cell and so cell power is found. The grid analysis involves an iterative nodal approach along each grid line. A favorable set of dimensions is a grid height of 10μM, a width of 25μM (average along taper) and a grid spacing of 800μM. A similar set of dimensions was chosen for the back contact grid system positioned to match the front structure.

Figure 3 shows one possible approach to the front and back contact designs for an 8 cm x 8 cm cell. Eight P+ contacts are provided with 4 N+ contacts. The series resistance for each of various cell types are later included in the cell performance assessment in Table 3. Other wrapthrough options such as small laser drilled holes which may reduce the wrapthrough contact area and shunt leakage losses are also currently being considered for the cell design.

Input Power Optimization

Optimization of input power is critically dependent on the attainment of minimum reflection of solar flux at the front surface by suitable antireflection coatings (A.R.) which may have to be deposited onto a passivation layer of lower refractive

index formed on the emitter surface. Programs exist at Spectrolab which, given the solar irradiance spectrum, the reflection spectrum of the silicon itself and the nature of any passivation layer, can by an iterative process determine the optimum thicknesses of dual A.R. layers of given materials. Figure 4 gives an illustration of their efficacy. A standard A.R. dual layer coating on top of a 100Å passivating silicon dioxide layer will greatly offset the A.R. performance. However, application of the programs gives adjusted A.R. coating thicknesses which can restore the performance.

Linked to the optimization of front surface A.R. coatings to minimize reflection across the active cell spectrum is the need to maximize transmission of the unwanted radiation through the back surface. In this way the thermal alpha for the cell is minimized. Figure 5 gives an empirical comparison of planar and textured cells with 'glassed' gridded back cells and A.R. coatings on both faces. The cells were 2 cm x 2 cm and boron was used as the BSF dopant where appropriate. The coverglass used was OCLI fused silica with a multilayer UVR coating on the backside and MgF_2 A.R. coating on the front side. The cells were glassed on the front side only. The excellent minimization of thermal alpha for the planar cells is very evident and is unaffected by the use of boron as a BSF dopant. The effects of these front and back surface reflection optimizations on cell peformance, particularly on orbit is brought out in Table 2.

Cell Performance Optimization

The reflection spectra of Figure 3 can be used together with the solar irradiance spectrum in the main cell computer programs to compute the operational parameters of the cells. The specifications required by NASA are for cells operating at 25°C and so the first five columns of data are for this case. However, it is important to determine what the "on orbit" cell performance will be and so using the thermal alpha value determined for each cell type from data such as those of Figure 5 we have calculated the on orbit temperature and then the cell efficiencies on orbit, by means of the formula:

$$T^4 = \frac{S(\alpha-\eta)}{\sigma(\varepsilon_1+\varepsilon_2)}$$

where S = radiant energy falling on cell equal to the solar constant for normal incidence,

α = solar absorptance of the incident surface or thermal alpha,
ε_1 = hemispherical emittance of front surface,
ε_2 = hemispherical emittance of back surface,
σ = Stefan's constant and
T = operating temperature of the cell in °K.

Figure 6 depicts the dependence of cell on orbit temperature on thermal alpha for a number of different cell photovoltaic efficiencies. Positions are indicated for different cell types chosen in our design study and for an ideal cell. It should be noted that the ideal thermal alpha is higher than the planar cell case. This is because perfect absorption is not attained over the cell active response spectrum in practice. Figure 7 gives other essential information namely the dependence of cell efficiency on temperature for various cell types and also indicates the temperature appropriate to each type as given by the respective thermal alpha value. These determinations enable us to compute the on orbit performance of the cells which is presented in the last two columns of Tables 2a and 2b.

From the results shown in Tables 2a and 2b it was possible to eliminate certain cell types from the list of possible candidates. It is clear, for instance, that sculptured cells, although providing a high efficiency at 25°C, currently have too high thermal alpha to be useful in a planar array since the on orbit operating temperature is too high. This results in the 'on orbit' efficiency being lower for sculptured cells than for planar cells. However, there is some evidence that the thermal alpha of gridded back sculptured cells may be significantly improved by further process modification. This work continues to be supported under NASA LeRC contract NAS3 24672 but will not be reported on here.

Further, more detailed modeling was performed on planar cell typoes considered to be most promising for use on Space Station given present thermal alpha data. These types were 2 ohm-cm 8 mil planar, 2 ohm-cm 4 mil planar BSF, 2 ohm-cm 8 mil planar BSF, and 10 ohm-cm 4 mil planar BSF. Additionally detailed grid modeling was performed on these cell types to differentiate between wraparound (WA) and wrapthrough (WT) cell types since there are some series resistance implications. The 25°C and on orbit (approximately 20°C) data for these cells is shown in Table 3. We discuss the tabled results below.

DISCUSSION

From the results of our modeling shown in Table 3 it is apparent that the choice of cell most suitable for Space Station is determined to some extent by the projected lifetime of the cell. If a 10 year lifetime is considered, corresponding to a fluence of approximately 5.10^{13} 1 MeV electrons cm^{-2}, then the 2 ohm-cm planar 4 mil cell with boron BSF has an EOL efficiency significantly greater than the 8 mil 2 ohm-cm planar non-fielded part. This is because the degradation in diffusion length at 5.10^{13} 1 MeV electrons cm^{-2} is not sufficient to have significantly reduced the effect of the BSF. At 10^{14} 1 MeV fluence (corresponding to 20 year life) the effect of the BSF is almost eliminated and the efficiencies of the fielded and non-fielded parts begin to converge. Generally the 10 ohm-cm 4 mil part does not maintain power to EOL as well as the 2 ohm-cm parts. We believe this is due to the higher doping concentration in the 2 ohm-cm substrate which suppresses I_{01} (the first diode saturation current). Based on current radiation damage coefficient data for 2 ohm-cm silicon we do not see a catastrophic fall in diffusion length with radiation which would otherwise increase I_{01}.

In terms of cell configuration it is clear that the wrapthrough design consistently yields higher values of efficiency than the wraparound design. This is a direct result of reduced resistive losses in the grids due to the shorter average distance that current has to flow to the ohmic current collection bar. This is evidenced by the value of R_s shown in column 3 of Table 3.

The decision whether or not to produce a 4 mil product for Space Station (vs 8 mil) is predicated largely on yield arguments. In efficiency terms there appears to be little difference between a 2 ohm-cm 4 mil, K6 wrapthrough cell and a 2 ohm-cm 8 mil wrapthrough cell. For instance at BOL the efficiencies are 14.7% and 14.5% for the 4 mil and 8 mil cells respectively, whilst at 1E14 1 MeV electron fluence the efficiencies are 13.5% and 13.1% respectively. Since cost will be a major issue for the Space Station cell and since yield is certain to be higher on the 8 mil cell, it was decided jointly by NASA and Spectrolab, with input from other aerospace companies, to pursue the 8 mil K6 planar cell in the Task II engineering development phase.

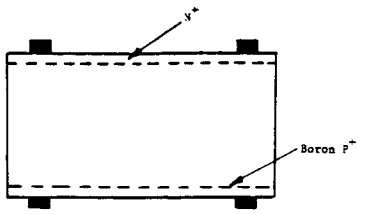

Figure 1a: SCHEMATIC OF GRIDDED P^+ BACK K6 CELL WITH PLANAR FRONT AND BACK

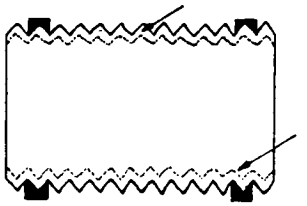

Figure 1b: SCHEMATIC OF GRIDDED P^+ BACK K7 CELL WITH SCULPTURED FRONT AND BACK

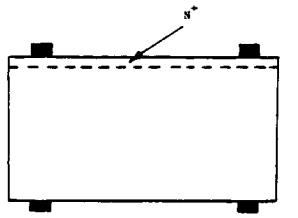

Figure 1c: SCHEMATIC OF GRIDDED BACK K4 CELL WITH PLANAR FRONT AND BACK

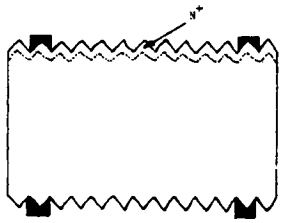

Figure 1d: SCHEMATIC OF GRIDDED BACK K5 CELL WITH SCULPTURED FRONT AND BACK

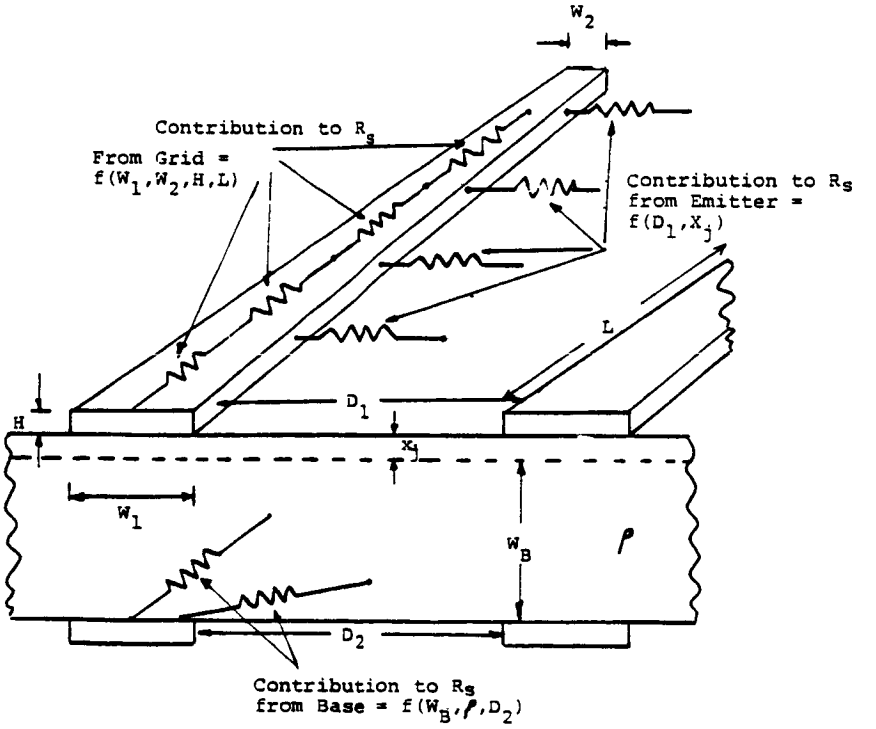

Figure 2: IMPORTANT PARAMETERS CONTROLLING GRID LINE OPTIMIZATION

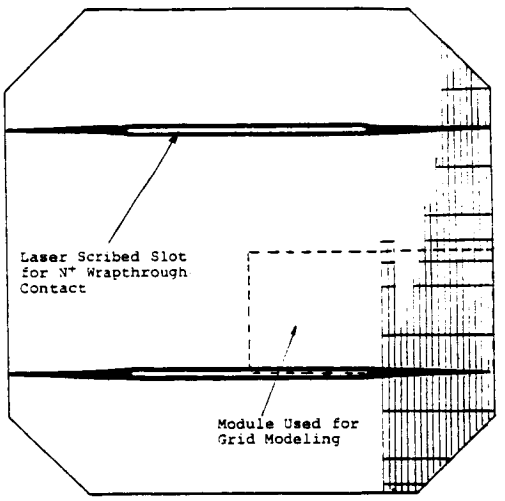

FIGURE 3a: PROPOSED FRONT CONTACT DESIGN FOR 8 CM X 8 CM WRAPTHROUGH CELL

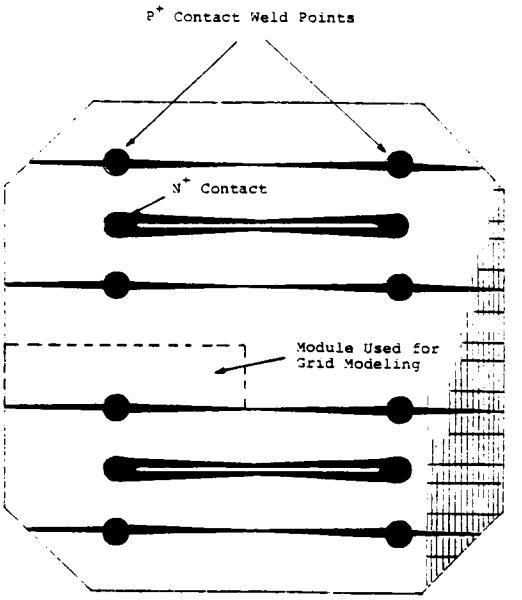

FIGURE 3b: PROPOSED BACK CONTACT DESIGN FOR 8 CM X 8 CM WRAPTHROUGH CELL

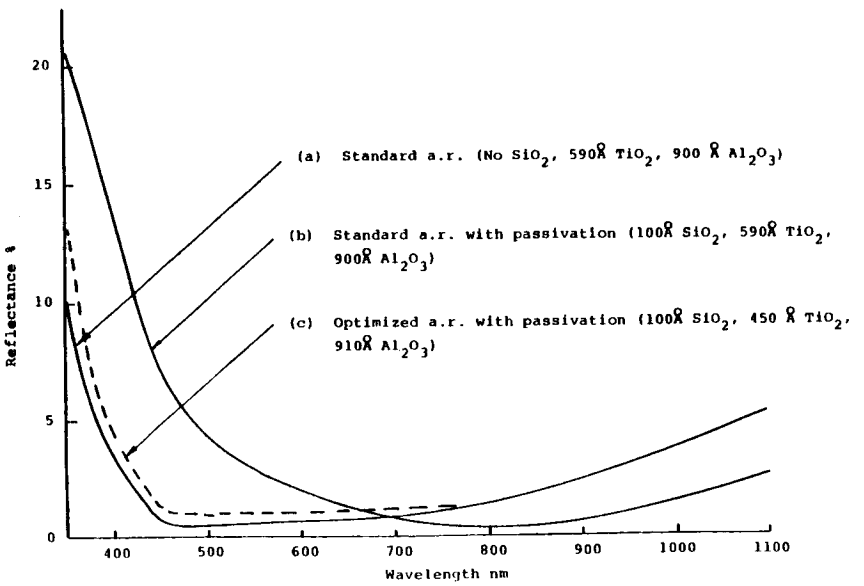

FIGURE 4: COMPUTED SPECTRAL REFLECTANCE FROM DC 93500 COVERED K4 SURFACE FOR DIFFERENT A.R. COATING AND PASSIVATION OXIDE THICKNESSES

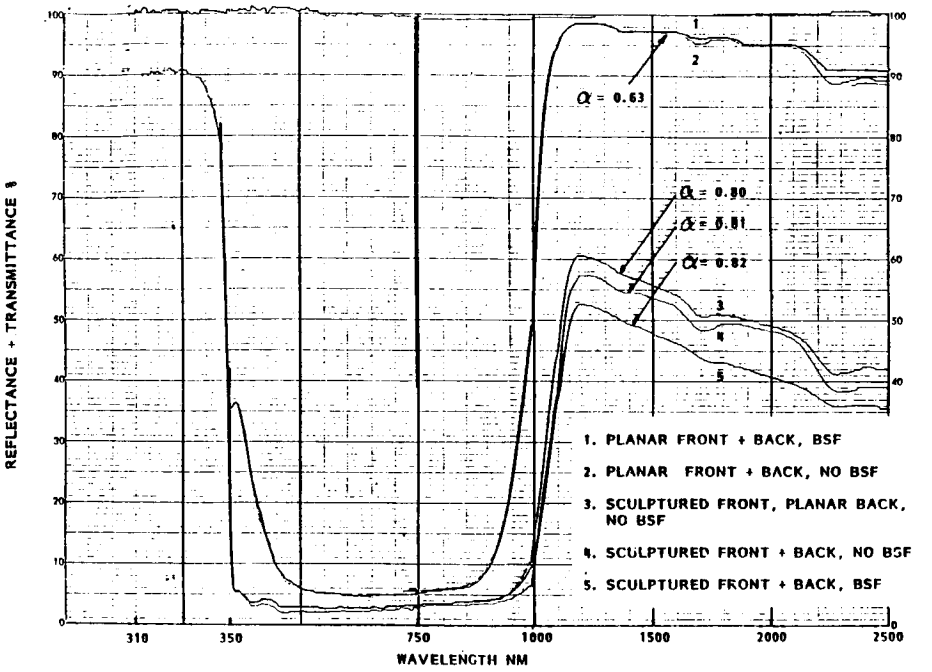

FIGURE 5: MEASURED SPECTRAL REFLECTANCE + TRANSMITTANCE OF GLASSED GRIDDED BACK CELLS WITH DUAL A.R. COATING BOTH SIDES

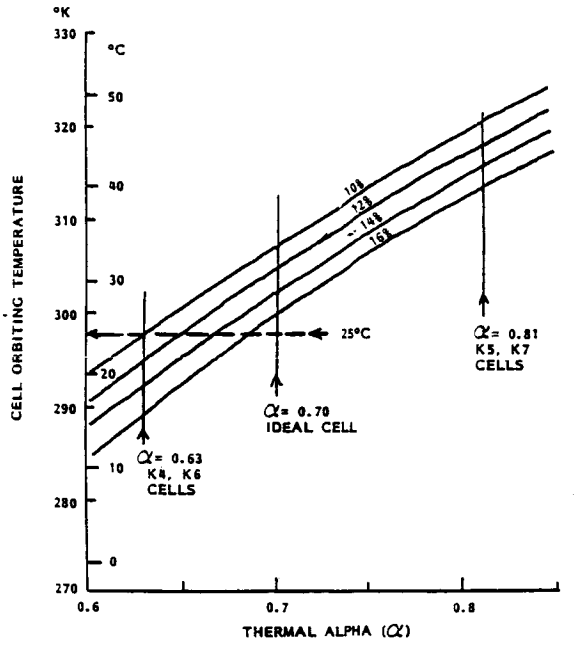

FIGURE 6: CALCULATED CELL ORBITING TEMPERATURE AS A FUNCTION OF THERMAL ALPHA AND EFFICIENCY. OPERATING POINTS FOR IDEAL CELL AND GRIDDED BACK K4, K5, K6, AND K7 CELLS ARE ALSO SHOWN

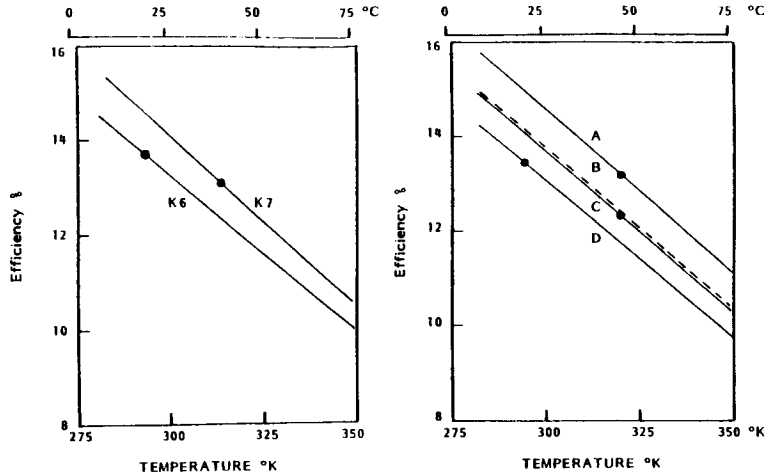

Fig 7a

Fig 7b

Fig 7a & 7b COMPUTED DEPENDENCE OF BOL CELL EFFICIENCY ON TEMPERATURE

Fig 7a 10 OHM-CM, 8 MIL, BSF K6 and K7 CELLS (S_{back} = 100 CM SEC^{-1})

Fig 7b 2 OHM-CM CELLS: A - 4 MIL K7, B - 4 MIL (BROKEN LINE)
C - 8 MIL K5, D - 8 MIL K4

o DENOTES ON ORBIT OPERATING TEMPERATURE AND EFFICIENCY BASED ON MEASURED THERMAL ALPHA (See Fig 5)

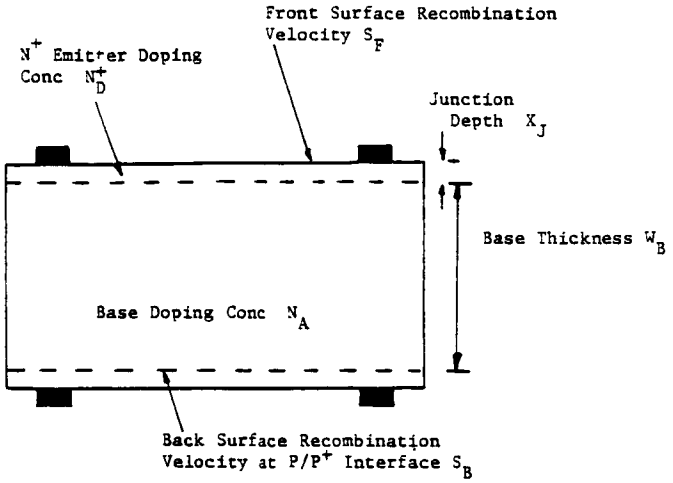

PARAMETERS USED IN MODELING OF TABLE 1

Emitter	10 Ohm-cm Base	2 Ohm-cm Base
X_J = 0.15 microns	L_N = 700 microns	L_N = 300 microns
L_P = 2.38 microns	D_N = 35 $cm^2\ s^{-1}$	D_N = 28 $cm^2\ s^{-1}$
D_P = 1.74 $cm^2\ s^{-1}$	S_B = 100 cm s^{-1}	S_B = 100 cm s^{-1}
S_F = 5E4 cm s^{-1}	N_A = 1.4 E15 cm^{-3}	N_A = 7.5E15
N_D^+ (mean) = 5E18 cm^{-3}		

TABLE 1: SCHEMATIC OF SOLAR CELL STRUCTURE SHOWING MOST IMPORTANT MODELING PARAMETERS AND THOSE VALUES USED IN OBTAINING PRELIMINARY RESULTS OF TABLE 1.

Cell Type	Fluence ϕ(e cm^{-2})	V_{oc} mV	J_{sc} mA cm^{-2}	Effy @ 25°C %	P/P_o	FF*	Thermal Alpha	Effy On Orbit %
2 ohm-cm, 8 mil, K4	0	595.0	38.3	13.1	1	0.780	0.63	13.5
" "	5×10^{13}	583.0	37.6	12.5	0.96	0.775	0.63	12.8
" "	1×10^{14}	576.1	37.1	12.2	0.93	0.773	0.63	12.6
2 ohm-cm, 8 mil, K5	0	583.3	42.1	14.0	1	0.770	0.81	12.5
" "	5×10^{13}	571.3	41.3	13.2	0.96	0.761	0.81	12.0
	1×10^{14}	564.3	40.8	13.0	0.93	0.763	0.81	11.6
2 ohm-cm, 4 mil, K6	0	618.6	38.6	13.8	1	0.783	0.63	14.1
" "	5×10^{13}	596.3	38.0	13.0	0.94	0.777	0.63	13.2
" "	1×10^{14}	585.5	37.6	12.6	0.91	0.774	0.63	12.9
2 ohm-cm, 4 mil, K7	0	606.7	42.2	14.7	1	0.774	0.81	13.2
" "	5×10^{13}	584.4	41.6	13.8	0.94	0.768	0.81	12.3
" "	1×10^{14}	573.5	41.1	13.3	0.91	0.763	0.81	12.0

*Assumes series resistance = 800 mohm-cm^2

Table 2a: Computed AMO Cell Characteristics of Different Cell Types as a Function of 1 MeV Electron Fluence Using Reflectance and Transmittance Data of Figure 5.

Cell Type	Fluence ϕ(e cm^{-2})	V_{oc} mV	J_{sc} mA cm^{-2}	Effy @ 25°C %	P/P_o	FF*	Thermal Alpha	Effy On Orbit %
10 ohm-cm, 8 mil, K6	0	592.4	39.6	13.4	1	0.776	0.63	13.7
" "	5×10^{13}	553.6	38.8	12.1	0.90	0.764	0.63	12.6
" "	1×10^{14}	541.3	38.2	11.6	0.87	0.761	0.63	11.9
10 ohm-cm, 8 mil, K7	0	580.9	43.7	14.4	1	0.767	0.81	12.9
" "	5×10^{13}	541.7	42.8	12.9	0.90	0.755	0.81	12.0
" "	1×10^{14}	529.4	42.1	12.4	0.86	0.751	0.81	11.6
10 ohm-cm, 4 mil, K6	0	599.4	38.8	13.4	1	0.778	0.63	13.7
" "	5×10^{13}	565.8	38.5	12.3	0.92	0.767	0.63	12.8
" "	1×10^{14}	557.6	38.2	11.9	0.89	0.763	0.63	12.5
10 ohm-cm, 4 mil, K7	0	587.6	42.5	14.2	1	0.770	0.81	13.0
" "	5×10^{13}	552.9	42.1	13.1	0.92	0.758	0.81	12.1
" "	1×10^{14}	539.4	41.8	12.6	0.88	0.753	0.81	11.7

*Assumes series resistance = 800 mohm-cm^2

Table 2b: Computed AMO Cell Characteristics of Different Cell Types as a Function of 1 MeV Electron Fluence Using Reflectance and Transmittance Data of Figure 5.

Table 3: Predicted AMO 25°C and 'On Orbit' Performance of Selected Cell Structures with Optimized Grid Designs

Cell Type	Fluence ø(e cm^{-2})	R_s milliohm cm^{-2}	P_{max}W (25°C)	Effy (25°C)	FF (25°C)	Effy on Orbit (~20°C)
2 ohm-cm 8 mil K4 WA	0	504	1.09	13.4	0.80	13.8
	5 x 10^{13}	504	1.04	12.82	0.79	13.2
	1 x 10^{14}	504	1:01	12.5	0.79	12.8
2 ohm-cm 8 mil K4 WT	0	268	1.11	13.6	0.81	14.0
	5 x 10^{13}	268	1.06	13.0	0.81	13.4
	1 x 10^{14}	268	1.03	12.7	0.80	13.0
2 ohm-cm 4 mil K6 WA	0	454	1.13	14.2	0.80	14.5
	5 x 10^{13}	454	1.09	13.4	0.80	13.7
	1 x 10^{14}	454	1.05	12.9	0.79	13.3
2 ohm-cm 4 mil K6 WT	0	260	1.17	14.3	0.81	14.7
	5 x 10^{13}	260	1.10	13.5	0.81	13.9
	1 x 10^{14}	260	1.07	13.0	0.80	13.5
10 ohm-cm 4 mil K6 WA	0	619	1.10	13.5	0.79	13.8
	5 x 10^{13}	619	1.02	12.5	0.78	12.9
	1 x 10^{14}	619	0.98	12.0	0.77	12.4
10 ohm-cm 4 mil K6 WT	0	289	1.12	13.8	0.81	14.2
	5 x 10^{13}	289	1.04	12.8	0.80	13.2
	1 x 10^{14}	289	1.00	12.3	0.79	12.7

Total Cell Area 60.14 cm^2. WA = Wraparound. WT-Wrapthrough

ULTRALIGHT AMORPHOUS SILICON ALLOY PHOTOVOLTAIC MODULES FOR SPACE APPLICATIONS

J.J. Hanak, Englade Chen, C. Fulton, and A. Myatt
Energy Conversion Devices, Inc.
Troy, Michigan

and

J.R. Woodyard
Wayne State University
Detroit, Michigan

Ultralight modules based on amorphous silicon alloys have been described recently as potentially useful for photovoltaic (PV) space arrays (ref. 1). They consist of thin-film multijunction solar cells deposited on polymeric substrates and interconnected in series and in parallel in a monolithic manner. Because of their extreme thinness, as small as 8 μm, very high specific power, in excess of 2.4 kW/kg and high stowability of 6.5 MW/m^3 have already been achieved. The modules are also flexible, so that they can be rolled up repeatedly to diameters of 3 cm or less. They are highly tolerant of physical damage, such as piercing by projectiles. They show improved radiation resistance to 1-MeV electrons and protons, by as much as 3 and 50 times, respectively, compared with crystalline Si and GaAs cells and also an improvement over $CuInSe_2$. Decreases in performance from exposure to light and ionizing radiation can be completely reversed by annealing at 160 to 200°C. Therefore, use of deployable and retractable arrays is proposed, which would not use glass covers and instead could be periodically annealed by solar heat inside their canisters. The monolithic structure facilitates design and fabrication of high voltage arrays required for high power systems. Large gains have also been made in the conversion efficiency and stability of a-Si alloy cells. A 13% AM1 efficiency and excellent optical stability have been already reported in devices consisting of a triple stacked cell structure and dual band gap materials a-Si:F:H and a-Si:Ge:F:H. AMO efficiency of 10% has been measured over active areas for similar cells. An update is given on the progress in this rapidly developing field, with emphasis on irradiation damage with 0.2 and 1-MeV protons and subsequent annealing behavior. Conceptual designs of large arrays, up to 1 MW, based on present engineering data are also presented.

INTRODUCTION

The development of ultralight, large-area, monolithic, flexible, roll-up modules, reported recently (ref. 1), is based on the unusual properties of the a-Si alloys and the rapid advances in PV technology based on them. Because of their very high optical absorption, solar cells made of a-Si alloys are less than one micrometer thick and their specific power exceeds 60 kW/kg, which is by far greater than for any crystalline material. Recent advances in device performance include exceeding of AM1 conversion efficiency of over 11% for single, wide-bandgap NIP cells of a-Si:F:H and reaching 10% with narrow-gap

*This work has been done for Sovonics Solar Systems

a-Si:Ge:F:H NIP cells (2, 3). These cells play an important role in achieving high efficiency with spectrum-splitting, multijunction devices. Next is the development of multijunction (ref. 4), multigap cells which have yielded AM1 efficiency of 13% with excellent stability (ref. 5). Efficiency of 30% has been forecast for such cells (ref. 6). The third is the achievement of excellent optical stability (ref. 7) with Sovonics multijunction cells using fluorine in the alloys (ref. 8). The fourth is the development of monolithic solar cell panel (ref. 9). The fifth is the development by Sovonics Solar Systems of a roll-to-roll continuous deposition process for multijunction cells onto a moving web (ref. 10). The sixth finding is that a-Si cells are about 3 times as resistant to 1-MeV electrons and more than 50 times to 1-MeV protons than crystalline silicon and GaAs and that the damage can be easily annealed out (refs. 11, 12, 13).

REVIEW OF THE FABRICATION AND THE FEATURES OF THE ULTRALIGHT MODULE

A summary of the description of the fabrication and of the features of the ultralight module published recently (ref. 1) follows. In order to take advantage of the high specific power inherent in the a-Si alloy solar cells, PV cell structures have been formed on thin foil substrates having thicknesses from 7.5 to μ25 m. The substrates included thin metals, metals clad with polyimide and polyimide films. A convenient thin metal substrate is electroformed nickel (ref. 14) or stainless steel, thinned by etching. The preferred substrate used in the present work for stowable, ultralight arrays is polyimide. Previous use of polyimide substrates has been limited to single cells and only of modest size (ref. 15). Normally, textured metal layers were coated on the substrates to enhance reflectively and promote light trapping (ref. 16). The material for the fabrication of the modules was produced by the Sovonics process (ref. 10) for continuous roll-to-roll deposition of thin-film, tandem-junction, PV cells onto webs 35 cm wide over 300 m long. A continuous layer of indium-tin oxide (ITO), about 60 nm thick, serving as the top transparent electrode was deposited by another roll-to-roll process.

A monolithic PV module structure has been designed which employs series and parallel cell interconnections (refs. 1, 17, 18) shown in figure 1. In this design the effect of an electrical shorting defect on the performance of the module is essentially limited to the defective cell. An analysis of such defects in the series-parallel module design is given elsewhere (ref. 19).

The processes for the fabrication of the module consisted of patterning of the continuous, deposited layers into arrays of cells by masking and etching or by scribing, screen-printing of current-collecting grids of silver paste, which also act as cell interconnections, application of electrical terminals, and encapsulation in polymeric sheets by lamination, as described in greater detail elsewhere (ref. 14).

To date, only single-gap a-Si:F:H alloys and single- or tandem- junction PV cell structures have been used for the development of the ultralight modules. Monolithic modules up to 61 x 30.5 cm^2 in area have been made on substrates 7.5 um thick, with or without top encapsulation, including a 37.5 m thick polyester or Tedlar. The module consists of 20 parallel strings of cells, with 12 cells in series per string, each cell having an area of 6 cm^2. PV performance data for the best module are given in table I. A comparison with specific power data reported by NASA for developmental "blankets" (ref. 22) and

NASA milestones for 1995 (ref. 23) with stowability data are shown in figures 2 and 3, respectively.

A photograph of an ultralight module in a roll, clearly demonstrating the features of flexibility, high specific weight, portability and stowability is shown in fig. 4. Another feature is the tolerance to physical damage, such as piercing by projectiles (ref. 1).

Because of the small thickness, such modules can be rolled up and unrolled repeatedly, without damage, to diameters as small as 3 cm (ref. 26). The results of such a test in which a module 31 cm x 31 cm in area and 50 μm in total thickness are shown in fig. 5.

CHARACTERISTICS AND PV PERFORMANCE OF PV CELLS AND MODULES

Although excellent progress has been made toward achieving high performance for the ultralight, monolithic modules, higher power output per area is needed to compete with existing PV arrays used in space. An intensive program has been underway at Sovonics toward developing advanced a-Si alloy materials and PV multijunction cell structures having high efficiency and stability. The status of this effort has been reported previously (refs. 2, 3, 5, 7, 20, 21) and the highlights are given in table II.

As indicated, the data in tables I and II are for AM1 illumination. Samples of 1-cm^2, dual-gap, triple cell, having AM1 active area efficiency of 12.5% have been measured at JPL by B. Anspaugh at AMO and shown to have a 10.0% efficiency (9.1% for total area) as shown in fig. 6.

SURVIVABILITY OF a-Si ALLOY SOLAR CELLS

A prerequisite for space PV arrays is a continuous operation over extended periods of time, ranging from days to tens of years, in the harsh environment of photon, electron and proton irradiation, bombardment by atomic oxygen, extremes of temperature excursions and physical damage due to surrounding equipment or meteorites. For high power arrays, high voltage arrays must be developed. Some of these issues have been addressed here and elsewhere, with remarkable success as described below.

Optical Stability of Multijunction PV Cells

Outstanding progress has been reported in achieving optical stability in Sovonics multijunction, dual-gap PV cells (refs. 5, 21) with respect to the Staebler-Wronski effect. Results for a triple-stacked, dual-gap cell with initial efficiency of 11.2% retained over 90% of its initial performance after 2500 hours of continuous illumination.

Stability of a-Si Alloy Cells in Ionizing Radiation

Studies of the effect of 1-MeV electrons on a-Si:H cells up to a fluence of 10^{16} electrons cm^{-3} have indicated approximately a threefold tolerance, compared with crystalline silicon cells (refs. 11, 12). Moreover, the damage was found to be fully annealable under conditions used to anneal the S-W effect.

Irradiation studies with 1-MeV protons (ref. 13) have been reported with

fluences ranging from 10^{11} to 1.6 x 10^{15} cm^{-2} on single cells of a-Si:F:H, a-Si:Ge:F:H, and single-gap, tandem-junction cells of a-Si:F:H*. More than a 50-fold greater tolerance to this radiation has been found in comparison with crystalline silicon and GaAs (ref. 24). Moreover, a total recovery of conversion efficiency has been attained after a one-hour anneal at 160°C, for fluences up to 10^{14} and 75% recovery for fluences up to 10^{15}. After 3-hour and 23 hour anneals, 90% and 97% recoveries, respectively, are reported for fluence of 10^{15} protons cm^{-2}. These results are shown again for the single-gap, a-Si:F:H tandem cells in fig. 7.

Additional radiation experiments with 200-keV protons have been reported (ref. 26) on the same set of samples after the annealing treatment. The effect of 200-keV proton irradiation on the performance of the three types of cell studied is shown in fig. 8, which also includes data for 1-MeV protons from reference 13. A comparison of the 1-MeV and 200-keV irradiation data for the dual-gap tandem cells alone is shown in fig. 9. A comparison with fig. 8 shows that the results are very similar to the single-gap a-Si:F:H tandem cells. As expected from other work (ref. 25), the lower-energy protons give rise to a somewhat increased rate of damage than for 1-MeV protons. The relative radiation tolerance to 200-keV protons is still much greater than for crystalline silicon or GaAs solar cells (refs. 24, 25). Figure 10 gives a comparison for irradiation of crystalline Si, GaAs, $CuInSe_2$ and a-Si alloy cells with 1-MeV protons and shows superior radiation resistance of the a-Si alloy, dual-gap, tandem cells.

The results of the annealing experiments on the tandem cells for the 200-keV proton irradiation are shown in fig. 11. Results are shown for various temperatures and times as a function of fluence. As with the 1-MeV proton irradiation shown in fig. 7, the damage is fully annealable at a modest temperature of 160°C up to a fluence of 10^{14} cm^{-2} and up to 79% of initial efficiency at 10^{15} cm^{-2}.

We have considered some of the mechanisms which lead to the decrease of the efficiency resulting from proton bombardment. Figures 8 and 9 show that 200-keV protons of a given fluence have about the same effect on the relative efficiency as 1-MeV protons with ten times the fluence. Thus the relative efficiency curves of the 1-MeV proton irradiations, when shifted to the left by one order of magnitude in fluence, compare favorably with the 200-keV data except for the highest fluences. Table III shows the results of our calculations to determine the nuclear recoil cross sections for the displacement of the various atoms in the cells. Displacement energies of 3.5 eV for hydrogen and 13 eV for Si and Ge were used in the calculations and only primary collisions are considered. The displacement cross sections are about five times larger at 200-keV as compared with 1-MeV. There are deficiencies in the analysis due to the uncertainty in the displacement energies, the electronic stopping of the protons and the displacement of atoms by the recoiling atoms. We believe that the agreement is adequate to suggest that the reduction in the relative efficiency is due to defects created by nuclear collisions. Our measurements show that the V_{oc} is insensitive to the proton fluence suggesting that the defects are produced primarily in the intrinsic region of the cell. Further confirmation of the suggestion is manifested by the relative effect of the protons on cells with different thicknesses; the

*In Reference 13, the proton radiation results for the tandem-junction cells have been reported by error as for tandem-junction, dual-gap cells.

measurements show that protons of the same energy and fluence degrade the efficiency of thicker cells to a greater extent.

The cells have been isochronally annealed for three hours at temperatures in the range of 60 to 160°C in an effort to determine if the knock-on of hydrogen or Si and Ge results in the defects. In a simple model where the protons are assumed to knock-on the hydrogen and create dangling bonds, the bonds should be passivated by the diffusion of hydrogen upon annealing. If this were the case, the annealing data should behave in a simple Arrhenius fashion. Our annealing data cannot be characterized by an Arrhenius plot over the range of fluences we studied; an approximate fit to an Arrhenius plot can be obtained at low fluences with an activation energy of the order of 0.1 eV. At higher fluences the cells are very resistant to isochronal annealing except at 160°C. We therefore conclude that the primary mechanism for the reduction of the relative efficiencies is not the creation of dangling bonds by the displacement of hydrogen. The complexity of the annealing data suggests that the defects are created by the displacement of Si and Ge and that a number of different types of defect configurations are produced by the recoiling atoms. The resistance to annealing at the higher fluences may be due to the overlapping of the damage zones; ion implantation studies show that damage produced at fluences where the damage zones overlap is more resistant to annealing than damage produced at fluences sufficiently low to insure that the damage zones do not overlap. If our suggestion is correct we expect that tandem cells made from several thin PIN tandems should be more radiation resistant than either tandems or single PINs made with thick intrinsic layers. An analysis of Figures 7, 8 and 9 confirms this suggestion.

High Voltage Arrays

In the monolithic structure of the ultralight modules shown in fig. 1 the cells as well as the cell interconnections are encapsulated in a continuous, transparent flexible cover, so that no bare electrical leads are exposed to the external environment. This structure is very amenable to design and fabrication of a high-voltage array.

CONCEPTUAL DESIGN OF LARGE SPACE ARRAYS

Because of high radiation resistance of Sovonics solar panels with respect to 1-MeV electron and 1-MeV and 200-keV proton irradiation and high optical stability, it appears that protection of the a-Si alloy PV arrays by cover glass is not required. Instead, the use of rollup, deployable and retractable arrays is recommended, so that if necessary, the arrays can be annealed periodically in their canisters under modest conditions of time and temperature. An example of such a concept is shown in fig. 12. A system of this type would be useful for electrical propulsion of vehicles which would be used to traverse high radiation zones, such as future Earth-Moon shuttles.

Another concept design, shown in figure sequence 13 a, b, c, and d, is for a 1 megawatt array, either for defense purposes or for interplanetary electrical propulsion.

CONCLUSIONS

Ultralight and ultrathin, flexible, rollup monolithic PV modules have been developed consisting of multijunction, amorphous silicon alloys for either terrestrial or aerospace applications. The rate of progress at Sovonics of increasing conversion efficiency of stable multijunction and multigap PV cells indicates that arrays of these ultralight modules can be available for NASA's high power systems for the 1990's. Already NASA's goals for specific power for 1990's have been nearly doubled. Because of the extremely light module weight and highly automated process of manufacture, the monolithic a-Si alloy arrays are expected to be strongly competitive with other systems, either photovoltaic, solar dynamic or nuclear for use in NASA's Space Station or other large aerospace uses in the years to come. For similar reasons extensive use of the monolithic ultralight arrays is expected for terrestrial applications as mobile high-power supplies.

REFERENCES

1. J. J. Hanak, Conf. Record 18th IEEE PVSC, 1985, 89.
2. S. R. Ovshinsky and J. Young, SPIE Proceedings, Vol. 706 edited by David Adler (SPIE, Bellingham, WA, 1986) in press.
3. J. Yang, T. Glatfelter, J. Burdick, J.P. Fournier, L. Boman, R. Ross and R. Mohr; Proceedings of the 2nd International PVSEC, Beijing, China, 1986, p. 361.
4. J. J. Hanak, J. Non-Cryst. Solids, 35 & 36, 755 (1980), North-Holland Publishing Co.,; Y. Hamakawa, H. Okamoto and Y. Nitta, ibid., 749.
5. Jeffrey Yang, Robery Ross, Ralph Mohr, and Jeffrey Fournier, 1986 Materials Research Society Spring Meeting, Palo Alto, CA.
6. Stanford R. Ovshinsky, Tech. Digest Int. PVSEC-1, Kobe, Japan, Nov. 13-16, 1984, 577.
7. J. Yang, R. Mohr and R. Ross, Tech. Digest Int. PVSEC-1, Kobe, Japan, Nov. 13-16, 1984, Late News, A-II-L 6.
8. S. R. Ovshinsky and A. Madan, Nature 276, 482 (1978).
9. J. J. Hanak, Solar Energy, 23, 1456 (1979).
10. Masat Izu and S. R. Ovshinsky, Thin Solid Films, 119 (1984); S. R. Ovshinsky, Proc. SPIE 407, 5 (1983); Masat Izu and S. R. Ovshinsky, ibid., 42.
11. C. F. Gay, R. R. Potter, D. P. Tanner and B. E. Anspauch, Conf. Record 17th IEEE PVSC, 1984, 151.
12. C. E. Byvik, W. Slemp, B. T. Smith and A. M. Buonchristiani, ibid., 155.
13. J. J. Hanak, A. Myatt, Prem Nath, and J. R. Woodyard, Conf. Record 18th IEEE PVSC, 1985, 1718.
14. H. Okaniwa, M. Asano, K. Nakatano, M.Yano, and K. Suzuki, Jpn. J. Appl. Phys. Suppl. 21-22 (1982) 239.
15. J. J. Hanak, M. Izu, Prem Nath and J. Young, U.S. Patent 4,530,739, July 23, 1985.
16. H. W. Deckman, C. B. Roxlo, C. R. Wronski, and E. Yablonovitch, Conf. Record 17th IEEE PVSC, 1984, 955.
17. Yuan-sheng Tyan and Evelio A. Perez-Albuerne, ibid., 961.
18. J. J. Hanak, U.S. Patent 4,514,579, April 30, 1985.
19. Troy Glatfelter and W. Czubatyj, Conf. Record 18th IEEE PVSC, 1985, 1186.
20. Prem Nath and M. Izu, ibid., 939
21. S. Guha, J. Non-Cryst. Solids 77-78, 1451 (1985).
22. D. J. Flood, private communication.

23. J. P. Mullin, J. C. Loria and H. W. Brandhorst, Conf. Record 17th IEEE PVSC, 1984, 12.
24. B. E. Anspaugh and R. G. Downing, ibid., 23.
25. J. Y. Yaung, Space Photovoltaic Research and Technology 1983, NASA Conference Publication 2314, p.56.
26. J. J. Hanak, C. Fulton, A. Myatt, Prem Nath, and J. R. Woodyard, 21st IECEC, San Diego, CA, August 25-29, 1986.

Table I
PV Data of a-Si Alloy Ultralight Module at AM1
(Area = 61 x 30.5 cm^2)

Voc	16.4 V
Isc	1.05 A
Fill Factor	0.56
Power	9.69 W
Power/weight	2.4 kW/kg
Power/area	52 W/m^2
Power/Volume	6.5 MWm^3

Table II
Highlights of the Status of Sovonics PV Cells

AM1 Conversion Efficiency (%)	Cell Type	Size (cm^2)	Reference
13.0	dual-gap, triple	1	5
12.0	single-gap, triple	1	2
11.1	dual-gap, triple	930	20
12.5	dual-gap, tandem	1	5
10.4	dual-gap, tandem	930	20
11.8	single-gap, tandem	1	2
9.0	single-gap, tandem	*	21

*35-cm wide, continuous web, in production

Table III
Results of Cross Section Calculations

System	Energy	E_d	$\sigma(\Delta Q)$
H→ H	200 keV	3.5 eV	9.3E-20 cm^2
H→ Si	200 keV	13 eV	1.8E-19 cm^2
H→ Ge	200 keV	13 eV	3.5E-19 cm^2
H→ H	1.00 MeV	3.5 eV	1.9E-20 cm^2
H→ Si	1.00 MeV	13 eV	3.4E-20 cm^2
H→ Ge	1.00 Mev	13 eV	6.9E-20 cm^2

Figure 1. Monolithic module structure consisting of four parallel strings of four series-connected cells in each string.

Figure 2. Specific power data for various types of PV modules or "blankets".

Figure 3. Stowability data for PV modules and blankets.

Figure 4. Ultralight, monolithic PV module on a roll (module only on the top three wraps); a full roll would have a power output of about 35 kW, compared with 10 kW for the diesel generator in the background.

Figure 5. Test of the effect of repetitive rolling and unrolling of an ultralight module around a cylindrical mandril on its PV performance.

Figure 6. Current-voltage and cell performance data for dual-gap, triple stacked cell under AM0 illumination (for active cell area).

Figure 7. The effect of 1-MeV proton irradiation on the conversion efficiency of tandem, single-gap, a-Si:F:H cells and the effect of subsequent annealing at 160°C (ref. 13).

Figure 8. The effect of 200-keV and 1-MeV proton irradiation on the conversion efficiency of single a-Si:F:H and a-Si:Ge:F:H and tandem single-gap a-Si:F:H cells.

Figure 9. The effect of 200-keV and 1-MeV proton irradiation on the conversion efficiency of dual-gap, tandem cells of of a-Si:F:H and a-Si:Ge:F:H alloys.

Figure 10. Comparison of the effect of 1-MeV proton irradiation on the efficiency of crystalline Si, GaAs, $CuInSe_2$ and amorphous dual-gap tandem cells.

Figure 11. The effect of 200-keV proton irradiation on the conversion efficiency of tandem, single-gap, a-Si:F:H cells and the effect of subsequent annealing at various temperatures and times.

Figure 12. Ultralight PV system concept for the Space Station. A pair of counter-rotating a-Si alloy arrays deployed by means of centrifugal force.

Figure 13. A design concept for a 1-MW, ultralight PV array.
Volume: 1 cubic meter; area: 100 x 100 meters; thickness: 75 μm;
Voltage: 10,000 Volt; current: 100 A; deployment: 30s.
a. Array in stowed condition
b. Deployment of folded array in x direction
c. Deployment in y direction
d. Fully deployed array

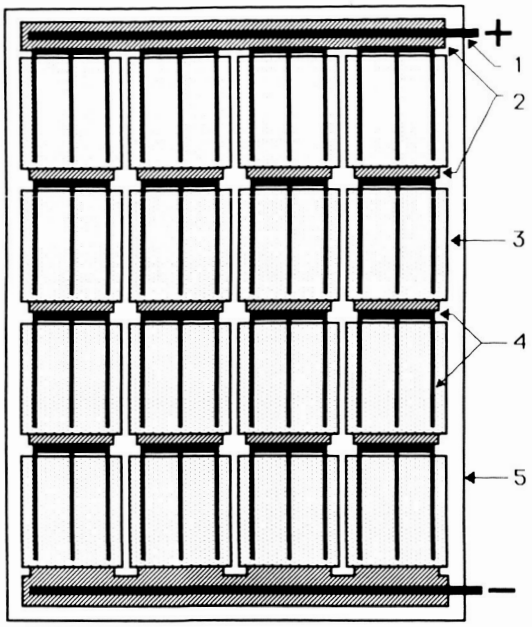

Figure 1. Monolithic module structure consisting of four parallel strings of four series-connected cells in each string. Legend: (1) busbar, (2) rear electrode layer, (3) cell, (4) metallic grid, (5) front and rear encapsulant.

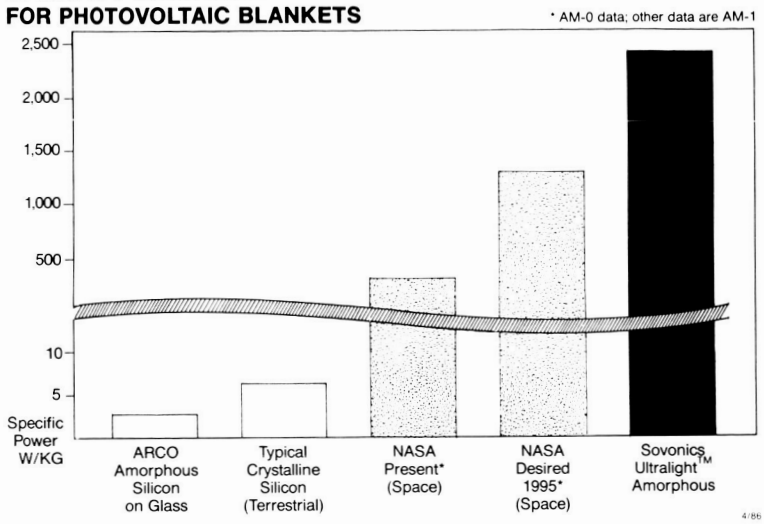

Figure 2

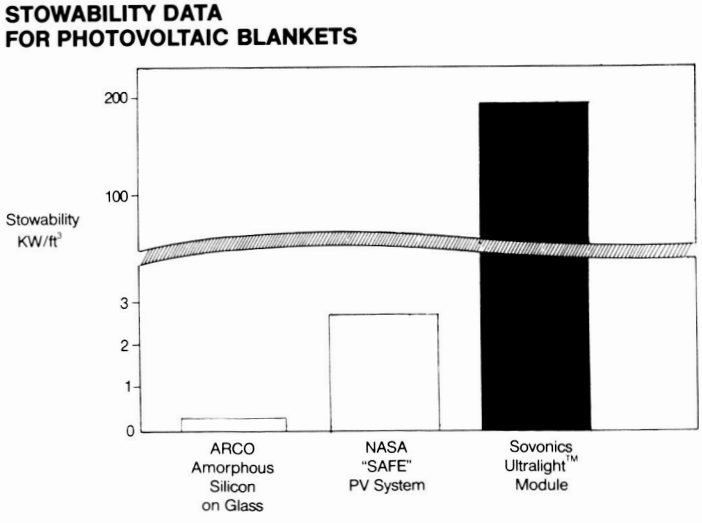

Figure 3

Figure 4

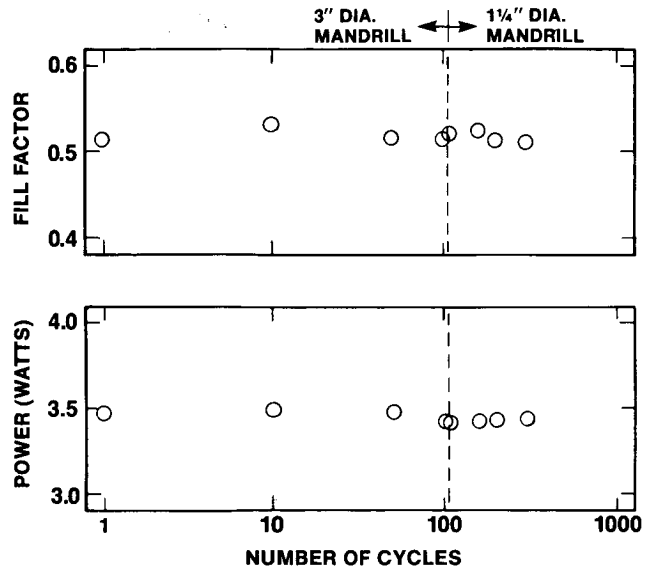

Figure 5

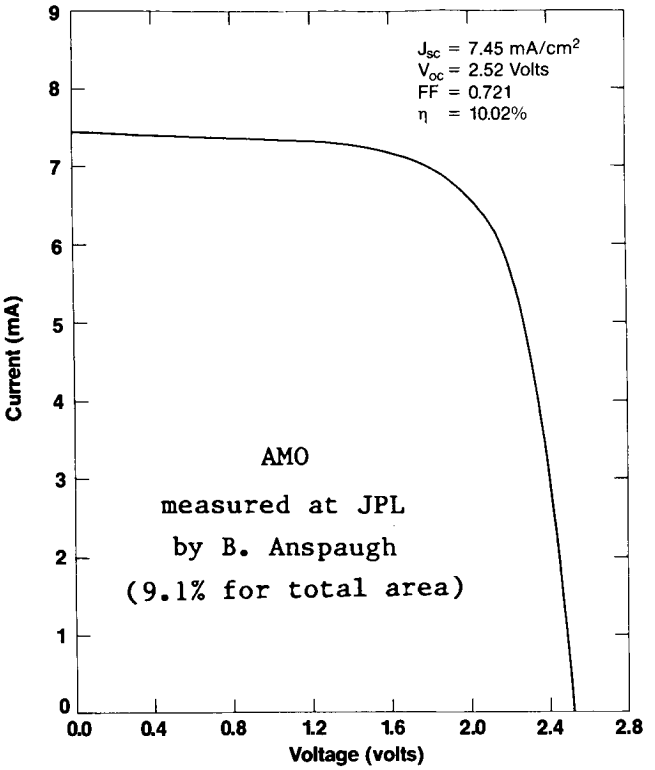

Figure 6

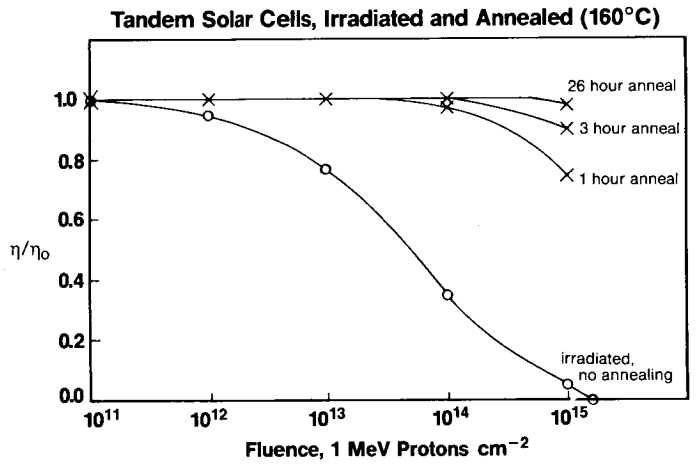

Figure 7

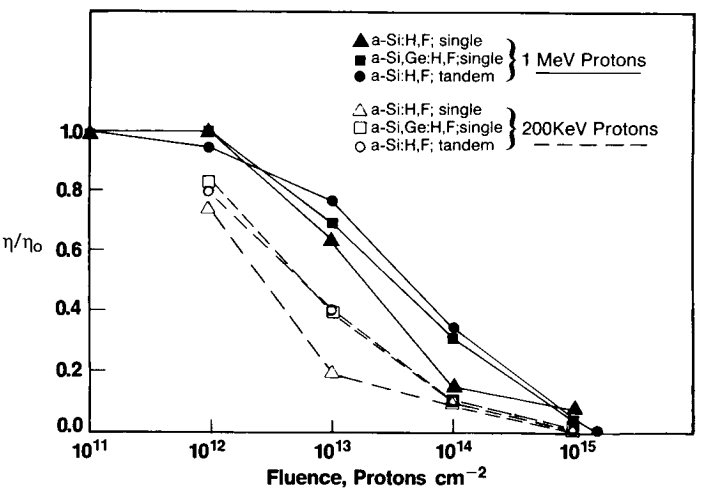

Figure 8

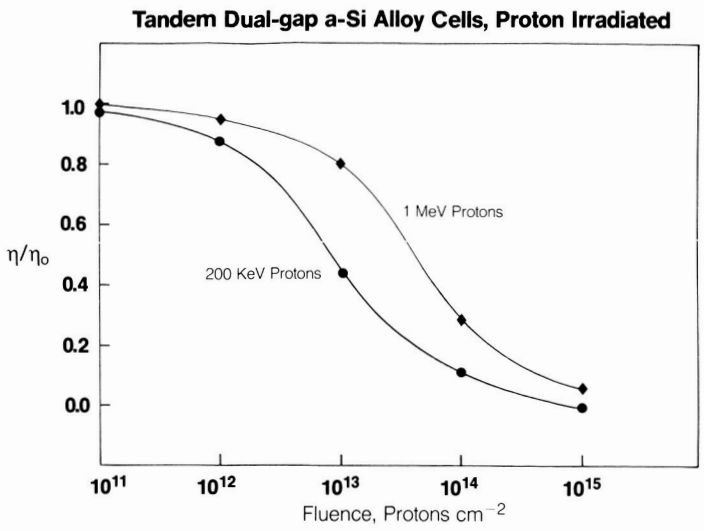

Figure 9

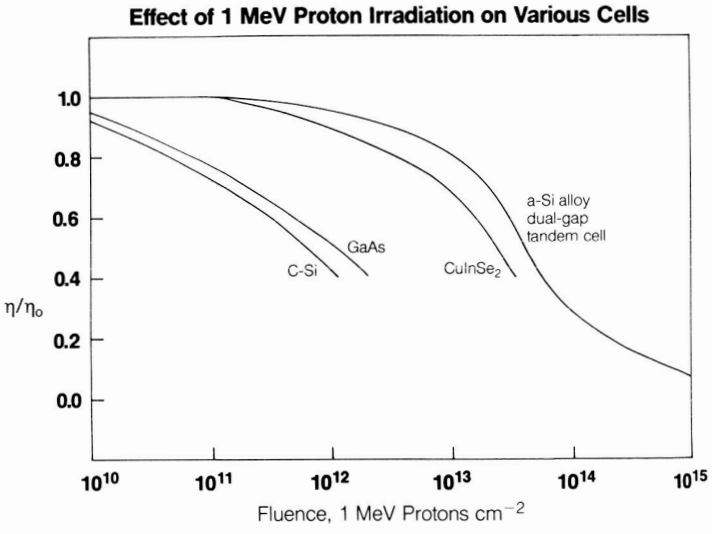

Figure 10

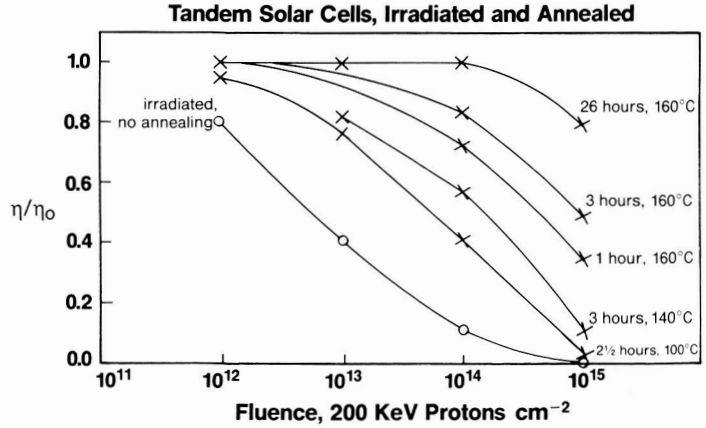

Figure 11

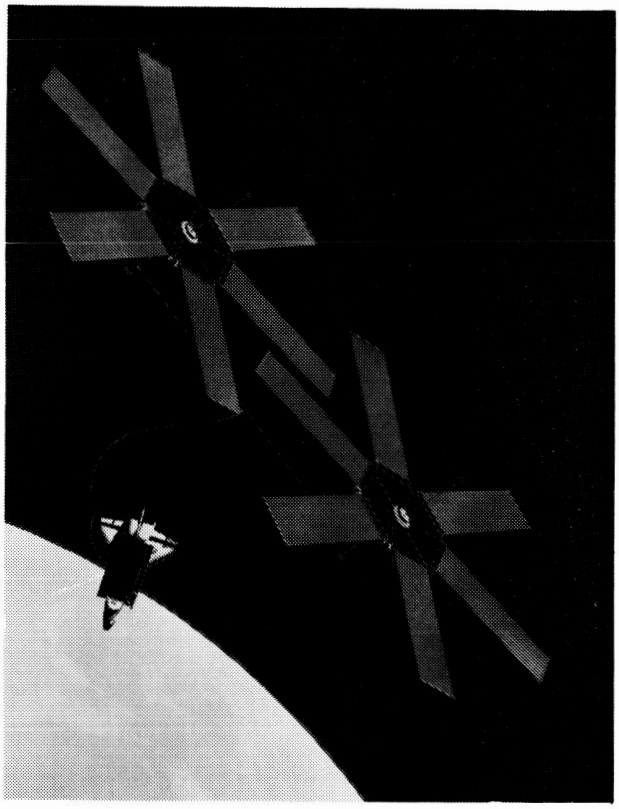

Figure 12

ORIGINAL PAGE IS
OF POOR QUALITY

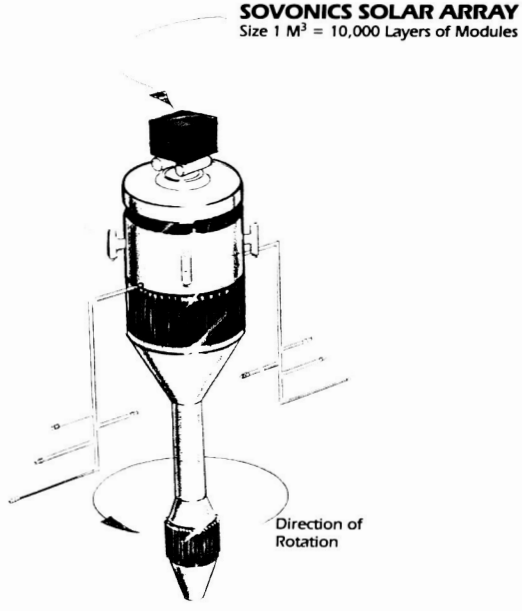

Figure 13 a

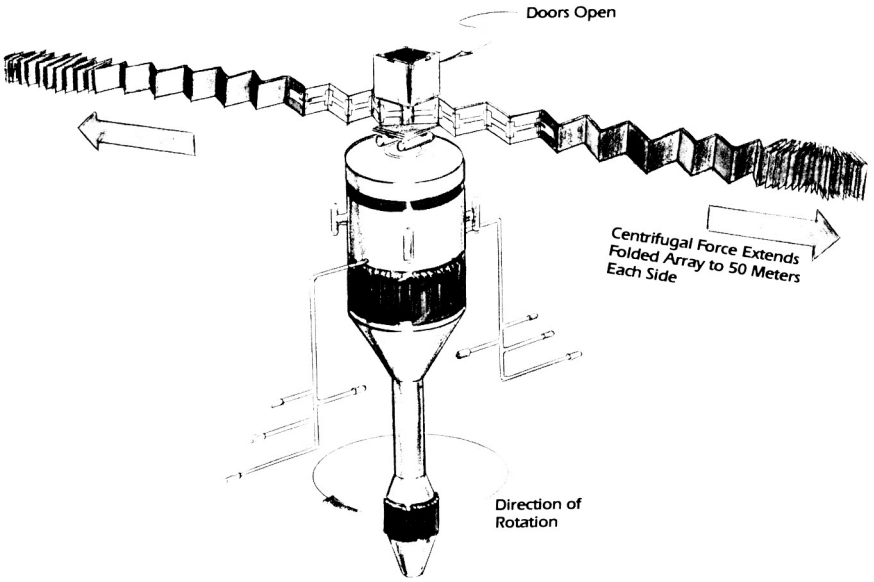

Figure 13 b

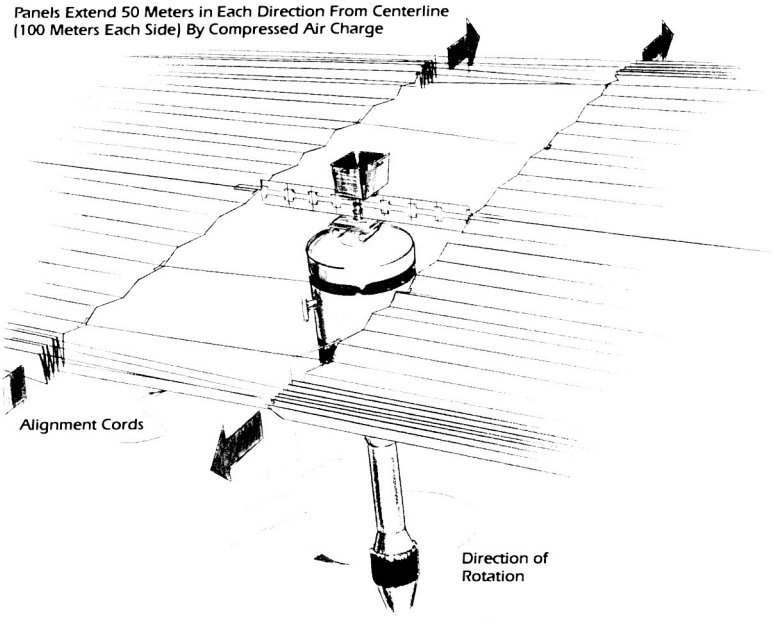

Figure 13 c

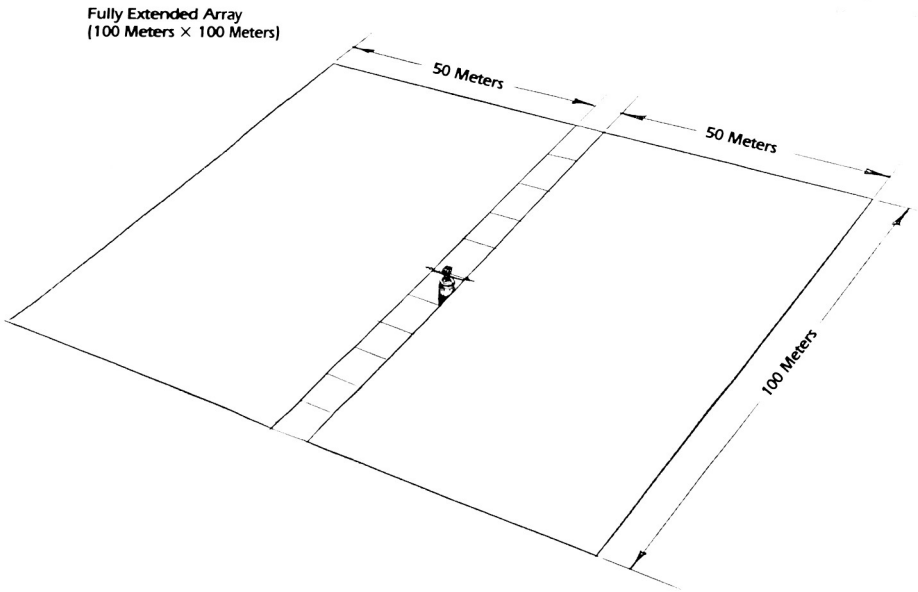

Figure 13 d

THE AIR FORCE CONCENTRATING PHOTOVOLTAIC ARRAY PROGRAM

Jack W. Geis
AF Wright Aeronautical Laboratories
Wright Patterson AFB, Ohio

The history of the Air Force solar concentrator project goes back to FY77 when an initial concentrator study program was conducted with Rockwell International Space Systems. The conclusions drawn from the study were that solar concentrator arrays have the potential to survive severe nuclear, particulate, and laser radiation environments which no planar solar array of comparable weight could tolerate. Concentrator arrays also offer the advantage over planar arrays of higher power per unit area than conventional planar array designs because the higher photovoltaic efficiency of the concentrator cells more than offsets the optical loss of the concentrator system.

Cell costs can be reduced significantly compared to costs for planar cells because a concentrator designed at a given Concentration Ratio (CR) will require approximately 1/CR the area of solar cells to produce the same electrical power output. Because concentrator cells operate at higher efficiency and degrade less in hazardous nuclear environments (concentrator shielding protects cells), the required End-Of-Life (EOL) array size can be 30-60% smaller than that required by planar solar cell arrays.

Satellite vehicles requiring high efficiency, low life cycle cost and maximum W/m^2 capability, and which must operate in high intensity natural radiation belts, could profitably use concentrator array systems. The high performance, high radiation resistance, but high cost gallium arsenide solar cell will find a natural application in the concentrating photovoltaic array where the cost of the solar cells themselves becomes secondary to other system costs.

AFWAL/ML funded TRW systems on the Satellite Materials Hardening Programs (SMATH). Although the major effort under SMATH IV in the power hardening area was to explore and develop techniques for hardening planar solar cell array power systems to the combined nuclear and laser radiation threat environments, a portion of the program dollars was devoted to developing a preliminary design for a hardened solar concentrator. The TRW design that was selected was a Cassagrainian configuration that utilized a narrow light acceptance angle to advantage for front side laser protection, and a deployable metal foil shutter for backside protection. The AFWAL/APL (Aero Propulsion Laboratory), as a result of the SMATH program, initiated several efforts to design, fabricate, and test concentrating photovoltaic devices which are survivable to hazardous nuclear and radiation environments. The first contract was awarded to TRW Systems, Inc., "Multi-Threat Hardened Concentrating Development" (F33615-81C-2055). The Laboratory has also sponsored concentrator feasibility and development work with General Dynamics Corporation on contract F33615-83C-2319, "SLATS Concentrator Development Program," and on contract F33615-84C-2420, "SLATS PHASE II."

More recently efforts have been directed toward transitioning the exploratory development efforts to advanced development through the initiation of the "Survivable Concentrating Photovoltaic Array" (SCOPA) program. This program, which is expected to begin in FY87, will result in the design, fabrication, test, flight qualification, and subsequent flying of a 500 watt concentrator panel in a low-altitude orbit. This paper discusses the general program objectives and overall performance goals of the program.

THE SURVIVABLE CONCENTRATING PHOTOVOLTAIC ARRAY (SCOPA) PROGRAM

Concentrator development has progressed substantially under the above mentioned contracts with TRW systems and the general Dynamics Corporation. Estimated performance capabilities for low to moderately hardened configurations are shown in Table I (General Dynamics Corporation briefing to AFWAL/POOC April, 1984). Subsequent designs to meet increasingly higher laser irradiation threats will reduce concentrator specific power and weight values due to higher mass density optical and thermal radiator components, and higher temperatures for the concentrator cells. It should also be noted here that post-laser irradiation performance levels of planar arrays under low to moderate laser irradiation levels may decrease drastically, or the array may fail catastrophically, compared to concentrators. The objectives of the two Air Force sponsored programs were to develop designs that are survivable to high level laser weapon, nuclear weapon, and background particulate irradiations, while maintaining reasonable electrical performance.

Air Force plans for FY87 and beyond are to initiate a five-year, multi-million dollar program to transition hardened concentrator elemental and modular technology from exploratory development to advanced development, and subsequent flight test of a hardened 500W concentrator panel. The program is divided into four phases: Phase I - Critical Hardened Component Development and Preliminary Panel Design; Phase IIA - Design, Fabrication, and Flight Qualification of Hardened Concentrator Panel; Phase IIB - Hardened Flight Panel Acceptance Testing and Spacecraft Integration; and Phase IIC - Flight Support of Hardened Concentrator Panel.

PHASE I - CRITICAL HARDENED COMPONENT DEVELOPMENT AND PRELIMINARY PANEL DESIGN

The intent is to award dual contracts for this 1 1/2 - 2 year effort. SCOPA performance and survivability objectives have been discussed through numerous meetings with various Satellite Program Offices (SPO's). As a result of these meetings, there has arisen a general understanding of the need for near-term development of space power systems that will be survivable to natural threats that may exist in space in the 1990's and beyond. SCOPA can meet these threats, and has been defined as a enabling space power technology.

Stringent and demanding threat requirements support the development of two competing concepts for Phase I to maximize the probability of program success. Concepts proposed for SCOPA by the various bidders on this multi-source procurement vary greatly in design, and each has its own strengths and weaknesses.

The major objectives of Phase I will be to establish confidence in concentrator designs and fabrication/manufacturing processes necessary to meet the program performance and survivability requirements and goals. Concentrator elements and modules will be subjected to vacuum chamber irradiation exposures from continuous wave and pulsed wave laser sources that simulate irradiation intensities and exposure times of ground-based and space-based lasers. Modules will also be subjected to thermal cycling, proton, electron, and space plasma environments such as might be encountered in Mid-Earth-Orbit (MEO) and Low-Earth-Orbit (LEO). A 500 W panel preliminary design will be accomplished near the end of Phase I. At the end of Phase I the best concentrator concept will be carried into Phase II A.

PHASE IIA - DESIGN, FABRICATION, AND FLIGHT QUALIFICATION OF HARDENED CONCENTRATOR PANEL

Under Phase IIA the contractor will fabricate at least one hardened 500 W panel, based on the test results and preliminary design work of Phase I. The panel will represent structurally and thermally the characteristics of a multi-kilowatt concentrator array. The contractor will conduct ground-based qualification of the 500 W panel. Qualification test guidelines will be based on a possible future space shuttle launch with subsequent deployment in a LEO orbit for a one-year (nominal) operation. Tests will include but not be limited to thermal, vibration, deployment and dynamic/static loading, and electrical performance verification tests.

PHASE IIB - HARDENED FLIGHT PANEL ACCEPTANCE TESTING AND SPACECRAFT INTEGRATION

Under Phase IIB, the contractor will refurbish the hardened concentrator panel developed and tested under Phase IIA, or build another unit and perform flight acceptance tests in accordance with acceptance test guidelines.

PHASE IIC - FLIGHT SUPPORT OF HARDENED CONCENTRATOR PANEL

The final phase of the program will be involved with providing the necessary supporting personnel for experiment data collection, reduction, and analysis resulting from a low-altitude "proof-of-concept" flight experiment. The experiment will be designed to determine the operational envelope of hardened concentrating photovoltaic arrays operating in space. Table II lists the Survivable Concentrating Photovoltaic Array Performance Verification Flight Experiment (AFWAL - 501) characteristics, (AFWAL/POOC briefing to Space Test Program Tri-Service panel, June, 1986).

HARDENED CONCENTRATOR DESIGN

REQUIREMENTS AND GOALS

The achievement of the concentrator design requirements and goals will permit the development of high performance, survivable, multi-kilowatt concentrator arrays for operation in hazardous natural and artificial space environments. In addition, the achievement of these requirements and goals will demonstrate significant survivability and performance improvements compared to conventionally hardened planar solar arrays, and will satisfy the requirements of several Air Force satellite systems.

In addition to continuous and pulsed wave laser, nuclear, and pellet threat hardening requirements and goals, the concentrator must be survivable to natural background radiation and space plasma environments as shown in Table III (AFWAL/POOC SCOPA Requirements and Goals, 1986).

SCOPA requires that a concentrator system be capable of surviving, with no more than 20% electrical power degradation, one exposure from each of the background radiations described in Table III. The tests represent five-year fluences in a 5600 NMI orbit at 60% inclination. The test exposures are not to be cumulative.

The hardened arrays are to be designed for Beginning-Of-Life (BOL) performance goals of 15W/kg (including pointing and tracking mechanism), and 120W/m^2. Although the performance design goals are very conservative, the laser and nuclear requirements and goals are not! The severe threat conditions imposed on the design result in a relatively heavy system, but the hardened design requirements and goals, if achieved, will permit the future development of multi-kilowatt concentrating photovoltaic arrays that will be survivable to artificial threat environments projected for the 1990's and beyond, and to natural threat environments that may be encountered in MEO missions and which cannot be accomplished with planar solar cell arrays. Projections of performance improvements possible with concentrator systems, when compared to planar array systems, are shown in Figure 1 and Figure 2 (Reference 1).

CONCLUDING REMARKS

The SCOPA program is very ambitious, especially from a survivability standpoint. However, a successful program will enable the Air Force to provide a survivable space power system that will have the capability of performing a variety of missions in hazardous environments, including those missions previously thought incapable of being accomplished by photovoltaic arrays (e.g., 5600 NMI missions). In addition, the concentrator will be capable of being designed as a lightweight system (50-100W/kg) through the use of thinner, low mass density materials and configurations, and may find applications in such missions as high power, lightweight electric propulsion orbital transfer where weight is a critical factor.

REFERENCES

1. Spacecraft Subsystem Survivability, R. M. Kurland, J. S. Archer, W. R. Hardgrove, TRW Systems, Inc., 30 March 1986.

TABLE I - EFFECT OF IMPROVED
EFFICIENCY ON OVERALL CONCENTRATOR PERFORMANCE

Parameter	Planar *	Cassegrainian	SLATS	SLATS W/DUAL-BANDGAP
Optical Efficiency	.98%	.80%	.92%	.92%
Cell Efficiency	.10% @ 65°C	.20% @ 85°C	.18% @ 85°C	.25% @ 85°C
Packing Factor	.86	.85	.95	.9
Radiation Deg (5 yr, 600 NMi, 60°)	.76	.92	.92	.86
Net Array EOL Effic.	6.4%	12.5%	14.5%	17.8%
Specific Power	87 W/m²	169 W/m²	196 W/m²	240 W/m²
Specific Weight	18.8 W/kg	24.8 W/kg	48.8 W/kg	59.9 W/kg

* INSAT ARRAY

Note: Data presented are for 1984 concentrator designs, based on survivability background radiation environment, and moderate laser irradiation threat environment only.

TABLE II - SURVIVABLE CONCENTRATING
PHOTOVOLTAIC ARRAY PERFORMANCE VERIFICATION
FLIGHT EXPERIMENT (AFWAL-501)
CHARACTERISTICS

- Experiment only, free flyer out-of-space shuttle bay, or on another spacecraft, up to 12 month in LEO
- 3-axis spacecraft stabiliation to within ±1°
- -20°C to +125°C, nominal thermal environment
- 500 W panel, 35 kg nominal, 454 X 92 cm
- Panel pointing and tracking (± 1½°)
- Temperature, current/voltage measurements
- Sun sensor
- Mirror/cell degradation sensor

TABLE III
GEOMAGNETICALLY TRAPPED PROTONS AND ELECTRONS
(OMNIDIRECTIONAL FLUENCES), AND
SPACE CHARGE/SPACE PLASMA EFFECTS CONDITIONS

- o 1 Mev, 1 X 10^{15} protons/cm^2
- o 5 Mev, 8.6 X 10^{12} protons/cm^2
- o 10 Mev, 5 X 10^{11} protons/cm^2
- o These tests represent 5-year fluences in a 5600 NMi orbit at 60° inclination

(a) PROTON TEST CONDITIONS

- o 1 Mev, 7.5 X 10^{13} electrons/cm^2
- o 3 Mev, 7.5 X 10^{12} electrons/cm^2
- o 5 Mev, 7.4 X 10^{11} electrons/cm^2
- o These tests represent 5-year fluences in a 5600 NMi orbit at 60° inclination

(b) ELECTRON TEST CONDITIONS

- o 10^3 - 10^6 electrons, and nitrogen (or argon) ions per cm^3
- o 0.1 - 1.0 volt, individual particle energies
- o Test to be performed in 10^{-7} torn, with test article biased + 500V relative to tank

(c) SPACE CHARGE/SPACE PLASMA EFFECTS TEST CONDITIONS

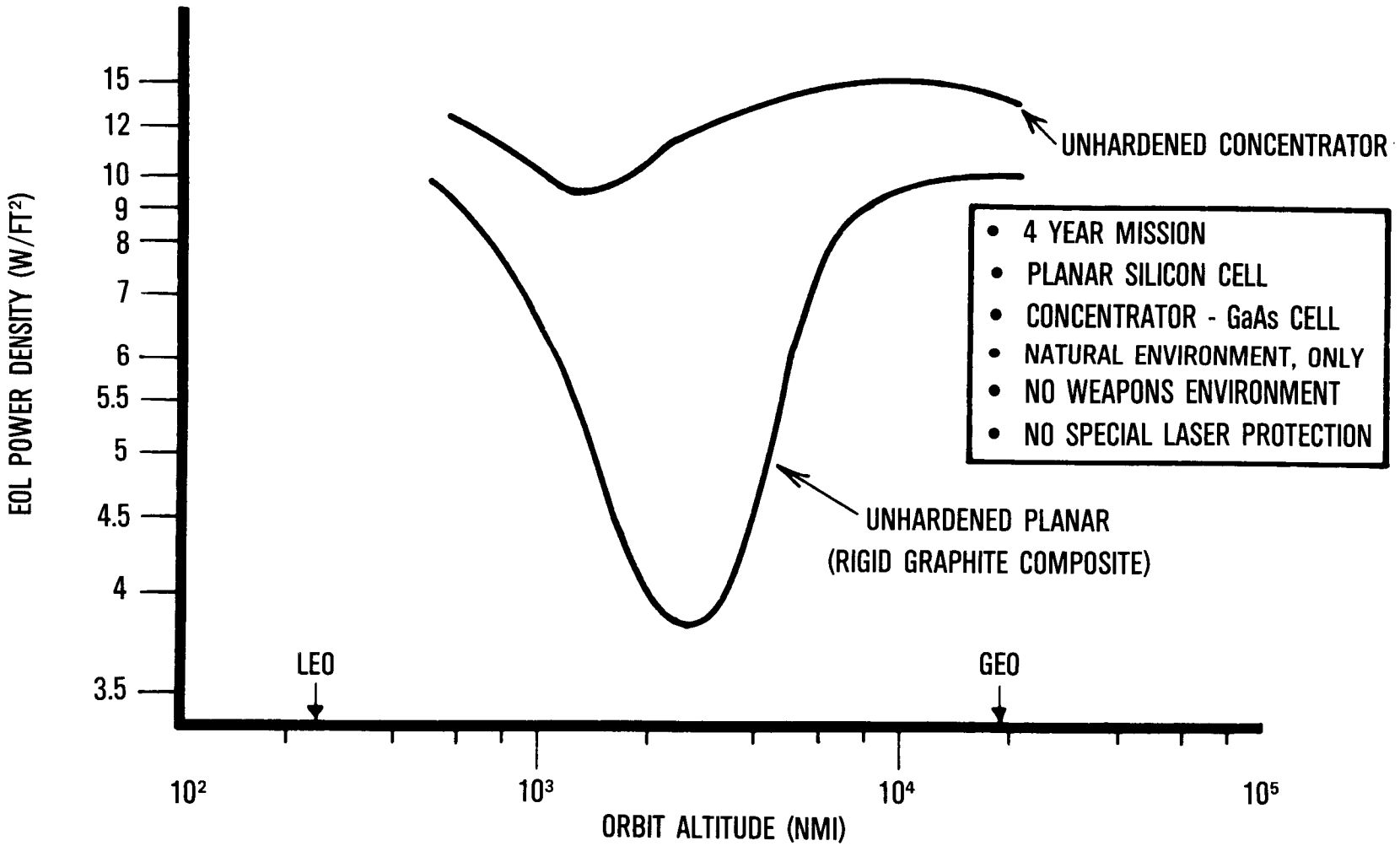

FIGURE 1. EOL PLANAR AND CONCENTRATOR PERFORMANCE

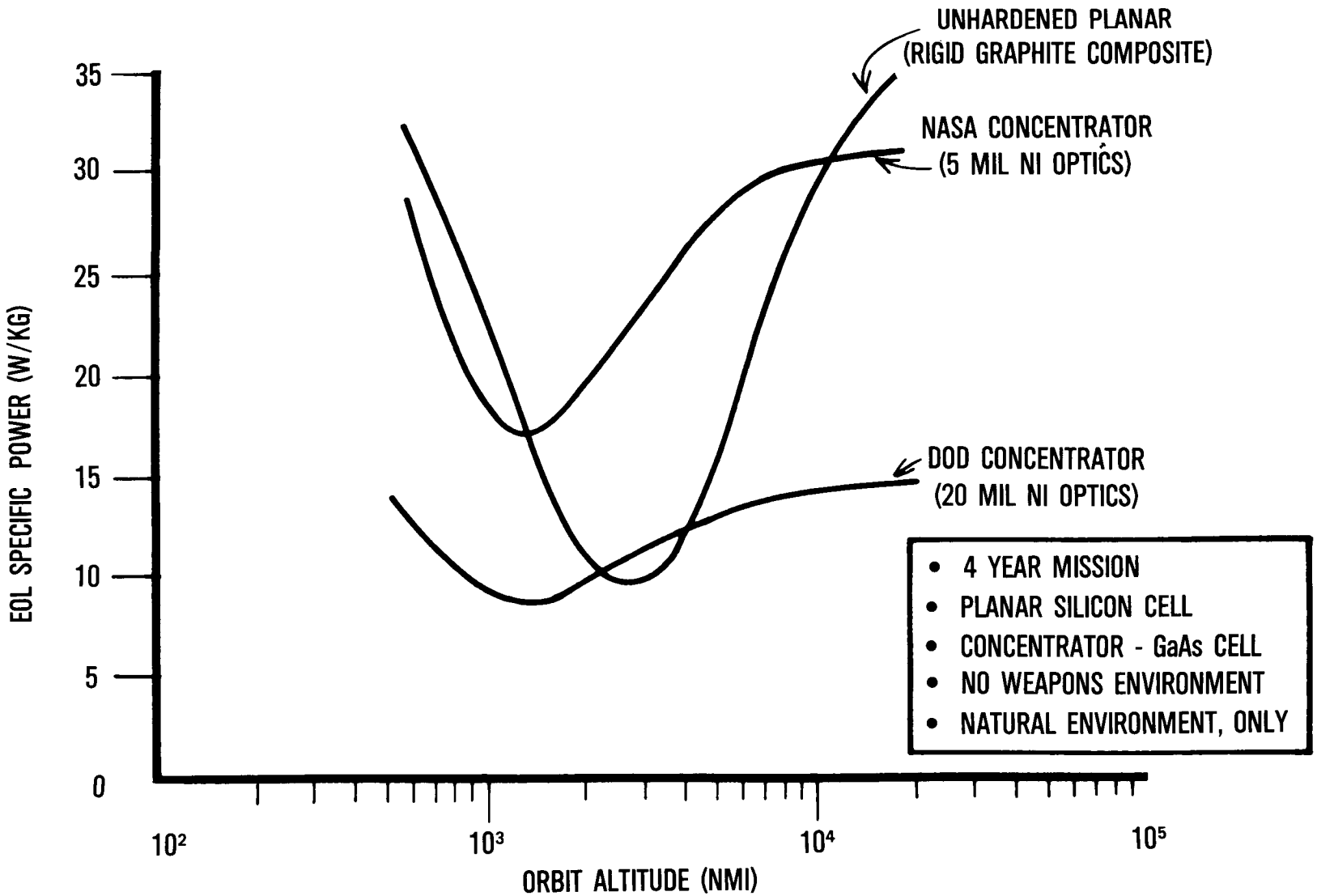

FIGURE 2. EOL PLANAR AND CONCENTRATOR PERFORMANCE

DEVELOPMENT OF A FRESNEL LENS CONCENTRATOR FOR SPACE APPLICATION*

Mark J. O'Neill
ENTECH, Inc.
Dallas-Fort Worth Airport, Texas

Michael F. Piszczor
NASA Lewis Research Center
Cleveland, Ohio

EXTENDED ABSTRACT

Since 1977, ENTECH (including its predecessor organization, E-Systems Energy Technology Center) has been actively developing, refining, and commercializing Fresnel lens photovoltaic concentrator systems for terrestrial applications. These systems are all based on a unique, transmittance-optimized, error-tolerant, Fresnel lens optical concentrator, which has been patented in fifteen countries (e.g., U.S. Patent No. 4,069,812). Much of this terrestrial development effort has been carried out as part of the Department of Energy's National Photovoltaic Program, under the Photovoltaic Concentrator Project administered by Sandia National Laboratories in Albuquerque. A typical ENTECH line-focus silicon cell concentrator array is shown in Figure 1. The first major installation of this type of equipment is represented by the 25 KWE system at DFW Airport's Central Utility Plant. This system has operated efficiently and reliably since 1982. Using low-cost, 15% efficient, linear Fresnel lens/polycrystalline silicon concentrator modules, ENTECH is currently offering utility-scale terrestrial systems at prices approaching $3 per peak DC watt, about one-third the price of terrestrial flat-plate photovoltaic systems.

In early 1986, ENTECH was selected under NASA's Small Business Innovative Research (SBIR) program, to perform a conceptual design study of a Fresnel lens photovoltaic concentrator system for space application, based on the successful terrestrial technology background described above. After evaluating both line-focus and point-focus approaches, ENTECH and NASA jointly selected a mini-dome lens point-focus concentrator with gallium arsenide cells (Figure 2) as near-optimal for space applications. The selected approach uses a square-aperture dome Fresnel lens (smooth exterior surface/prismatic interior surface) to focus incident sunlight onto a small gallium arsenide cell, which is mounted to a thin aluminum backplane radiator for cooling. The shape of the lens (defined in U.S. Patent No. 4,069,812) is non-spherical, such that solar rays make equal angles of incidence and emergence with each prism in the lens. This refractive symmetry minimizes reflection losses, sun image size, and the effects of aberrations and manufacturing inaccuracies. For example, the effect of slope errors (shape errors) is 200 times less for the dome lens than for any reflective concentrator. Using a simple aluminum "egg-crate" honeycomb structure, a matrix of individual concentrator modules can be combined into a larger panel (Figure 3). To allow panel stacking during transport, the honeycomb structure is slightly taller than the lens (Figure 4). Cells may be connected in any desired series/parallel arrangement to provide the proper current/voltage output.

* NASA Lewis Research Center Contract No. NAS3-24871.

Panels can be combined to provide larger area assemblies (Figure 5). Finally, many panels can be integrated with a lightweight, automatically deployable structure, such as the Astro Aerospace Extendible Support Structure (ESS), to provide multi-kilowatt arrays (Figure 6). The dome lens concentrator (DLC) panel is remarkably light (Figure 7), weighing only 2.5 kg/sq.m. for the current design. With further optimization, this weight could easily be reduced. The ESS support structure is also light, weighing less than 0.7 kg/sq.m. of DLC panel aperture. Thus the total array weight for the current design is only 3.2 kg/sq.m., which is equivalent to the Space Station lightweight Kapton-blanket, planar-silicon array weight. Furthermore, the DLC honeycomb panel is extremely stiff structurally. Under 16g launch loads, maximum stresses correspond to a factor of safety of four. Under 1g terrestrial testing, maxiumum panel deflections correspond to panel slope errors of only 0.05 degree.

The key component of the DLC system is the mini-dome lens (Figure 8). While much work remains to be done in selecting the optimal lens material(s), the current leading candidate is Kel-F fluoropolymer. Kel-F has excellent optical properties, can be mass-produced into lenses by compression or injection molding, has a wide operating temperature range, and has an excellent outdoor lifetime in the terrestrial environment. However, for space applications, a protective coating (candidates: microglass, magnesium fluoride, silicon oxide, sol-gel, etc.) will be required to minimize degradation due to monatomic oxygen, ultraviolet radiation, particulate radiation, and other hostile environmental factors. The 3.7 cm square-aperture mini-dome lens has been sized for use with a 0.4 cm diameter gallium arsenide concentrator cell, since much effort has been expended over the past several years by NASA and its cell suppliers in developing such a cell for use at 100 sun irradiance. Without antireflection coatings, the selected lens (Figure 8) will provide 91.5% net optical efficiency. With a geometric concentration ratio (lens aperture area/cell active area) of 109X and an optical efficiency of 91.5%, a net irradiance of 100 suns will intercept the cell. Using a dispersive cone optics computer code, which has been validated through testing of several versions of terrestrial lenses, the dome lens design has been optimized to provide the desired focal plane irradiance profile. The individual prisms which comprise the lens have been designed to place the focussed sunlight onto a target area (0.26 cm diameter) which is smaller than the cell active area (Figure 9). The non-illuminated annular ring (0.07 cm in extent) around the edge of the target area has been sized to tolerate the lateral motion of the image in the event of a 1 degree sun-tracking error. Essentially no energy (less than 0.2%) is lost due to such a tracking error, by using this "guard band" lens design approach.

The selected cell design (Figure 10) is the same size and shape as the cell which has been developed by NASA for use in the TRW mini-Cassegrainian concentrator (MCC). However, for the dome lens application, the cell will utilize a parallel gridline geometry rather than a radial "wagon-wheel" gridline geometry. Also, the new cell will have 20% of its active area covered by gridlines, rather than the 14% coverage used in the MCC cell. By using a prismatic cell cover (the effectiveness of an example cover is shown in Figure 11 for a terrestrial line-focus silicon cell), the obscuration loss due to gridlines will be eliminated by redirecting incident sunlight onto active cell area between gridlines. The ability of the prismatic cell cover (patent pending) to eliminate gridline obscuration losses has been fully validated in tests at ENTECH, Sandia, and elsewhere, for several types of terrestrial cells. The performance parameters for the new prismatically covered cell (Figure 10) are based on measured cell parameters for a 1984-vintage Hughes gallium arsenide cell. The cell should provide a 24.7% conversion efficiency at 25C cell temperature under a uniform 100 sun irradiance. However, detailed cell modeling under the current program has

shown that the cell performance will fall to 24.0% under the non-uniform irradiance produced by the lens (Figure 9). This decrease in performance is due to increased voltage drops in the emitter sheet, along the gridlines, and in the bulk material, due to the relatively high irradiance over the small illuminated cell area (Figure 9).

While a 1 degree maximum tracking error is anticipated by NASA for most space applications, larger tracking errors can be readily accommodated by making the cell active diameter slightly larger (Figure 12), i.e., by decreasing the geometric concentration ratio from 109X to lower values. For example, with a 26X geometric concentration ratio (0.82 cm active cell diameter), a 4 degree tracking error can be tolerated, while maintaining the overall lens/cell module efficiency above 21% at 25C cell temperature (Figure 12). Thus, with slight modification in cell size, very large tracking errors can be tolerated if mission requirements so dictate.

The conceptual design and thermal performance of the cell-to-radiator mount have also been investigated (Figure 13). By using a top-metallized, plasma-sprayed alumina mount, the cell-to-radiator temperature differential can be maintained at about 4C. The backplane radiator has also been thermally analyzed (Figure 14) to define the effect of radiator thickness on cell operational temperature. The thermal analysis results have been interpreted in terms of cell operational efficiency, by using the measured gallium arsenide efficiency/temperature coefficient (-0.035% per degree C), resulting in the selection of a 200 micron thick radiator as near-optimal (Figure 15). This thickness corresponds to a cell temperature of 100C, and a cell efficiency of 21.4%.

In summary, the selected conceptual design of the dome lens concentrator uses a 3.7 cm square aperture dome lens to focus onto a 0.4 cm active diameter gallium arsenide cell. The selected configuration will provide 91.5% lens optical efficiency and 21.4% cell efficiency at 100 suns irradiance and 100C cell temperature, for an overall lens/cell module efficiency of 19.6%. The selected configuration will tolerate 1 degree tracking errors with negligible loss of performance. The selected panel weight is 2.5 kg/sq.m. The selected ESS support structure weight is 0.7 kg/sq.m. These performance and weight parameters have been compared to state-of-the-art planar silicon and mini-Cassegrainian gallium arsenide arrays (Figure 16). In addition, improved versions of the three technologies have been included in the comparisons. For planar silicon, the major anticipated improvement in technology relates to a more efficient cell (8 cm square with chopped corners). For the Cassegrainian and dome lens concentrators, improved cell technology has recently been demonstrated by Varian, and improved optical performance is expected (higher reflectance Cassegrainian components and anti-reflection coatings for the lens). After including packing factor and wiring/mismatch losses for all three technologies, the dome lens concentrator clearly offers higher performance (w/sq.m.) and higher specific power (w/kg) than the planar silicon or Cassegrainian approaches, for both current and improved technology versions of the three approaches. With further development (i.e., multi-junction cells), the dome lens concentrator approach should provide 300 w/sq.m. in performance, and 100 w/kg in specific power. In final summary, the dome lens concentrator system represents an exciting new space power option.

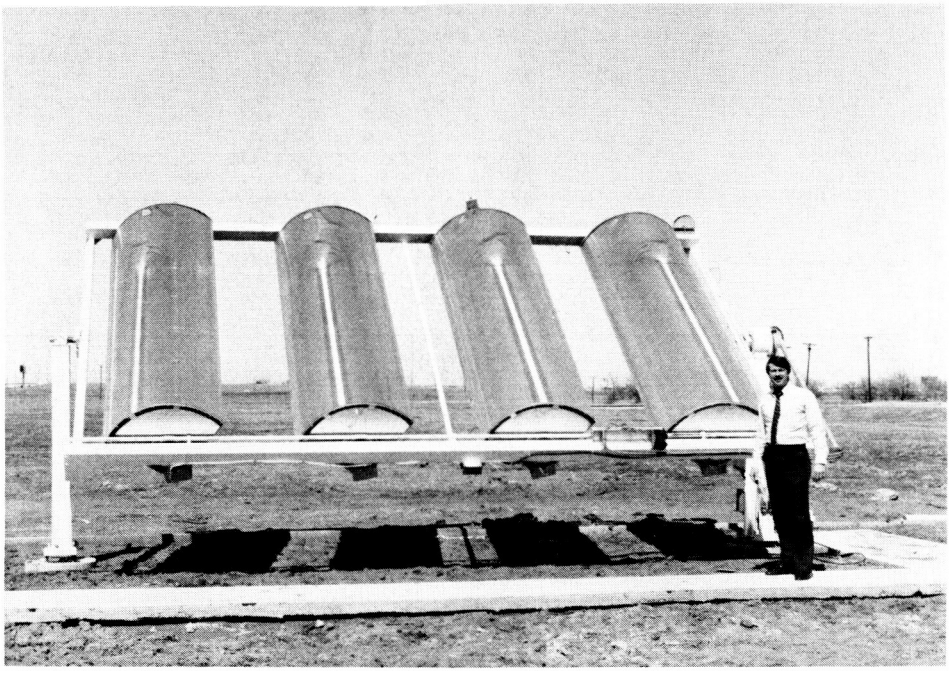

FIGURE 1 - TYPICAL ENTECH TERRESTRIAL PHOTOVOLTAIC CONCENTRATOR ARRAY

DOME LENS PV MODULE CONCEPTUAL DESIGN

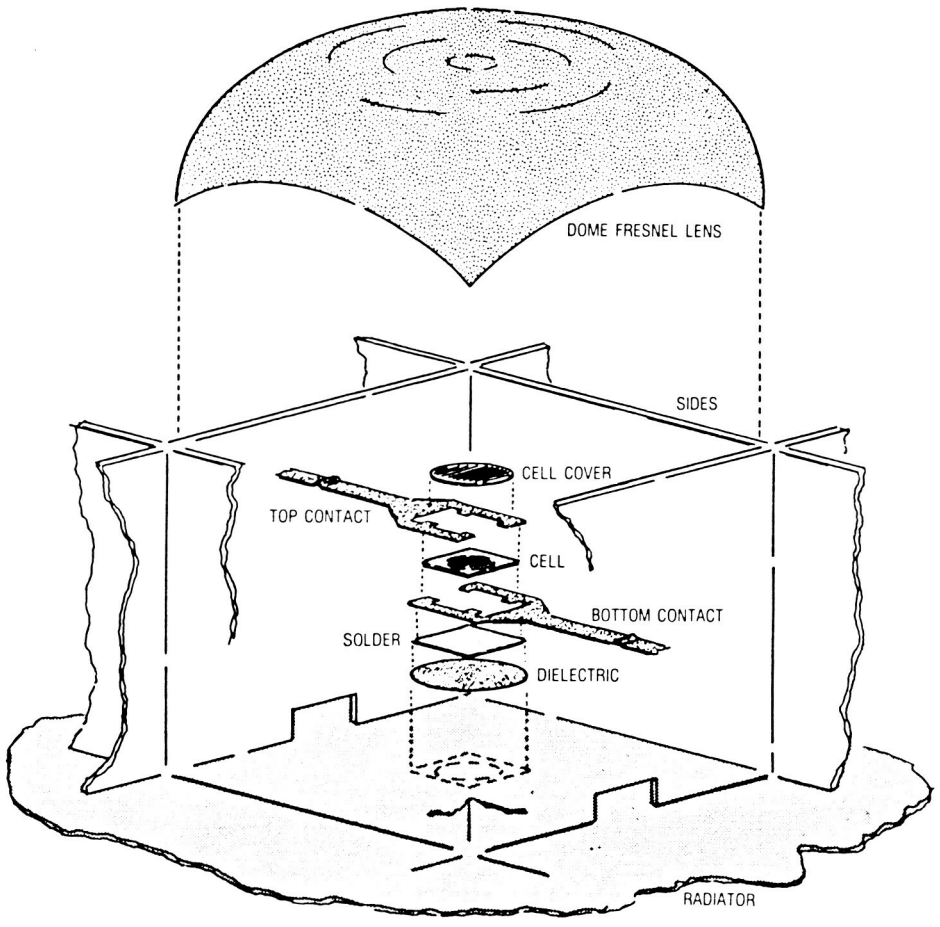

FIGURE 2

ENTECH DOME LENS PV CONCENTRATOR PANEL CONCEPTUAL DESIGN (1/4 PANEL)

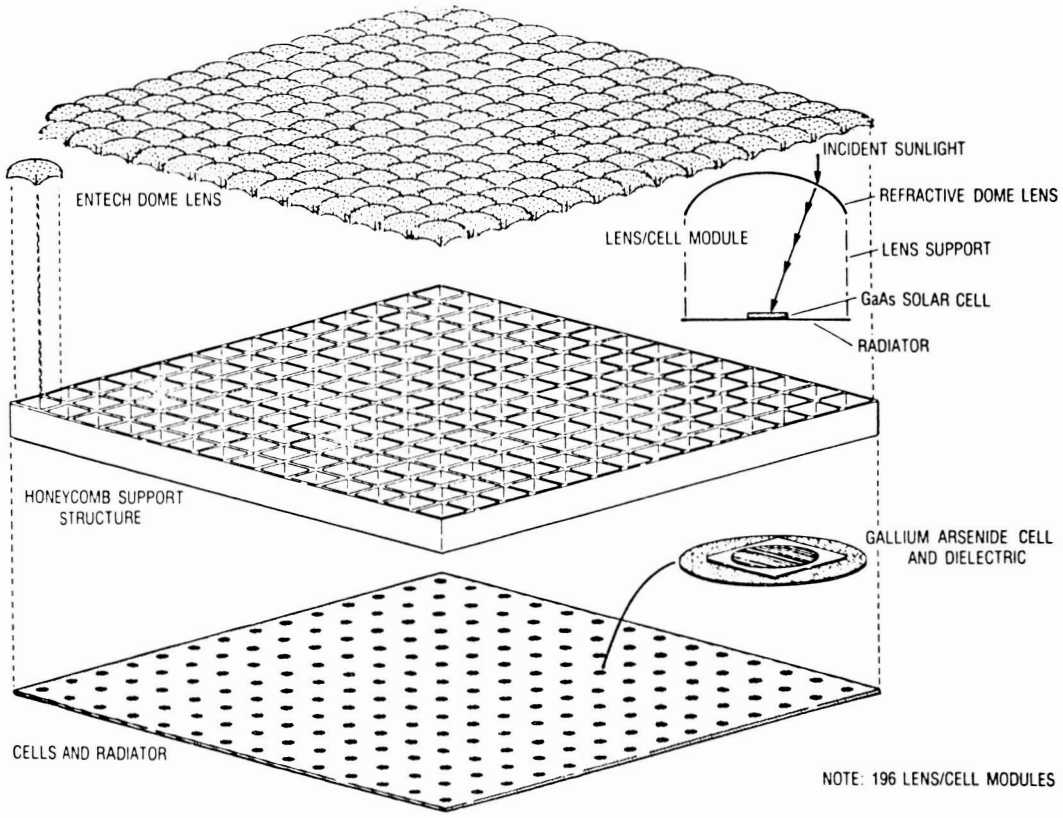

FIGURE 3

CROSS - SECTIONAL VIEWS OF DOME LENS PV PANEL

FIGURE 4

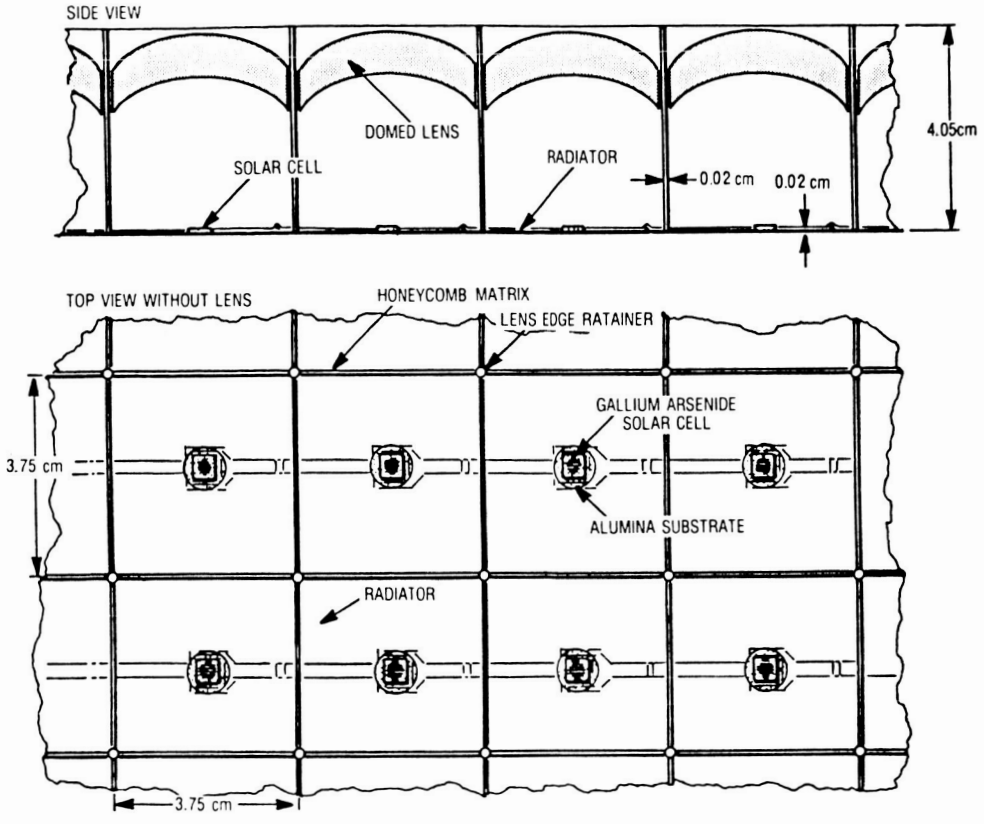

THREE DOME LENS PV PANELS

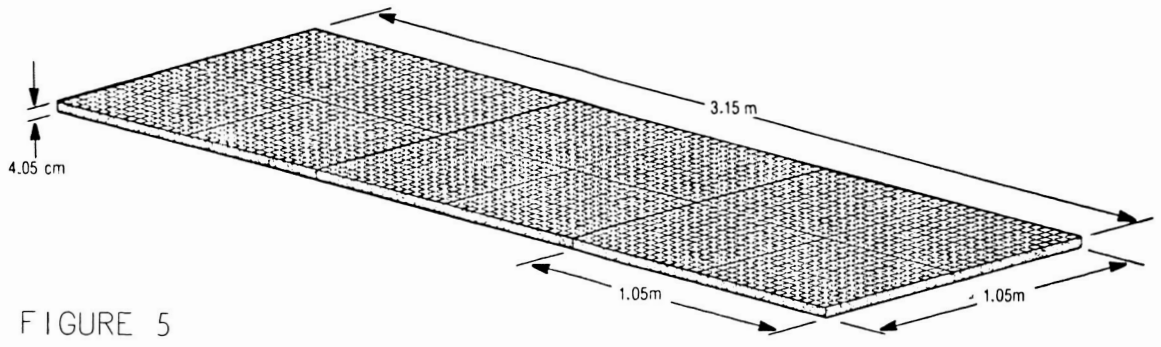

FIGURE 5

DOME LENS
PV ARRAYS ON ESS SYSTEM
ATTACHED TO SPACE STATION

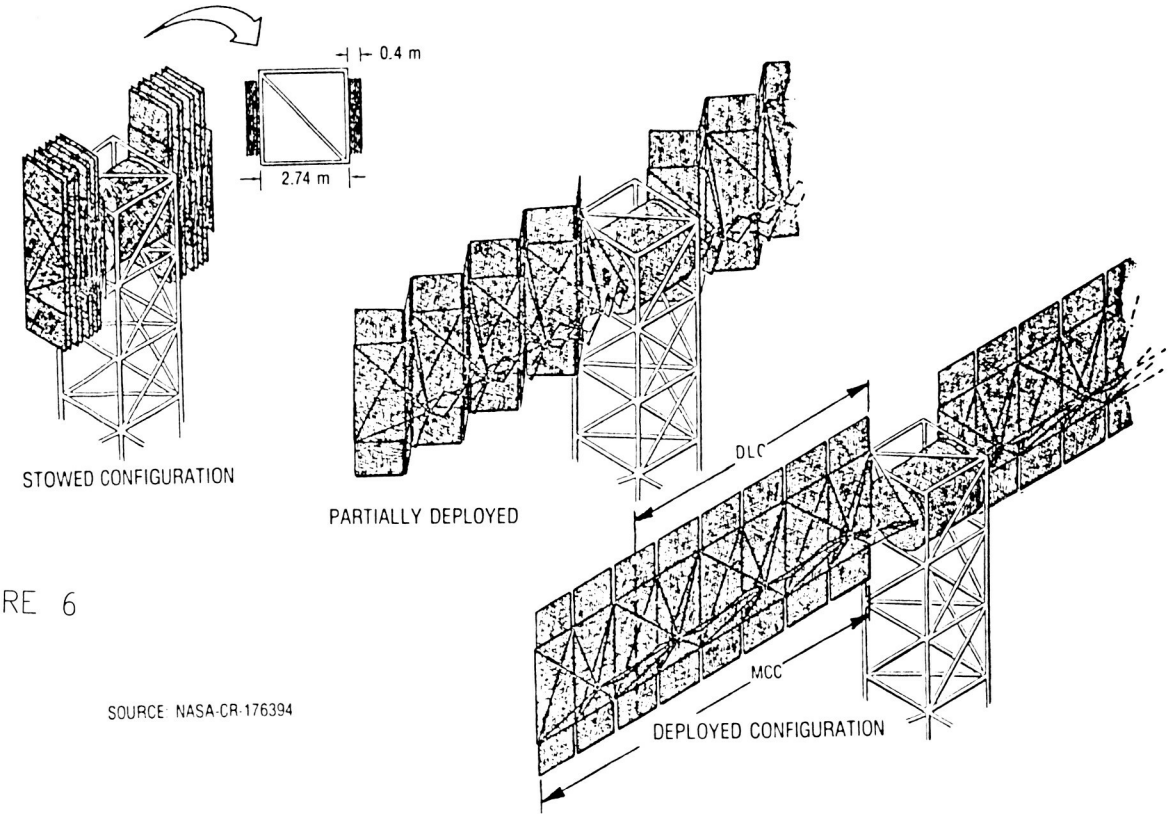

FIGURE 6

SOURCE NASA-CR-176394

DOME LENS CONCENTRATOR (DLC)
PANEL WEIGHT ESTIMATE

PANEL COMPONENT	WEIGHT/PANEL AREA (KG/SQ.M.)
LENS	0.68
RADIATOR	0.54
CELL/MOUNT/INTERCONNECTS	0.05
ALUMINUM MATRIX	0.62
ATTACHMENTS	0.14
ADHESIVES	0.34
MISCELLANEOUS	0.13
TOTAL	2.50

FIGURE 7

SELECTED LENS DESIGN

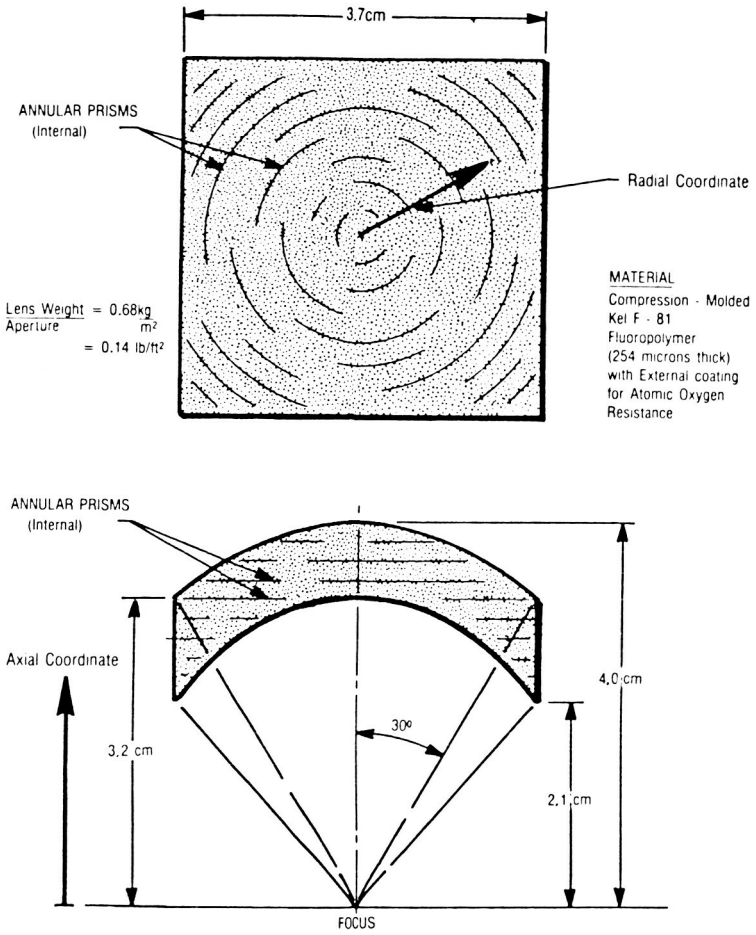

FIGURE 8

FLUX PROFILE FOR THE SELECTED SQUARE DOME LENS
DESIGNED FOR 1 DEGREE TRACKING ERROR GUARD BAND

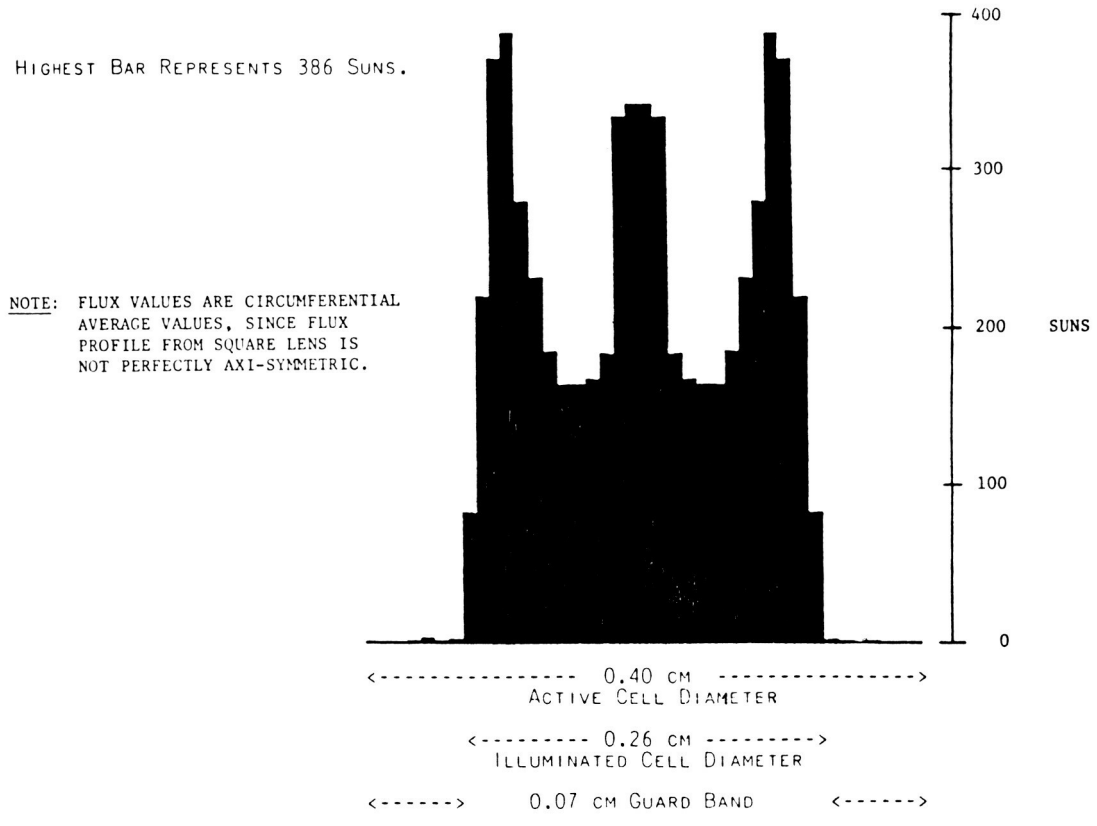

FIGURE 9

SELECTED 100X GALLIUM ARSENIDE CELL
FOR USE WITH ENTECH DOME LENS CONCENTRATOR
AND WITH ENTECH PRISMATIC CELL COVER

FIGURE 10

CELL GEOMETRY

TOTAL AREA: SQUARE, 0.5 CM PER SIDE, 0.2500 SQ.CM. AREA
ACTIVE AREA: CIRCLE, 0.4 CM DIAMETER, 0.1257 SQ.CM. AREA

METALLIZATION PATTERN (SHOWN IN WHITE)

NO. OF GRIDLINES:	31
GRIDLINE CENTERLINE SPACING:	127 MICRONS
GRIDLINE WIDTH:	25 MICRONS
GRIDLINE HEIGHT:	10 MICRONS
BUSBAR AROUND CELL PERIPHERY	

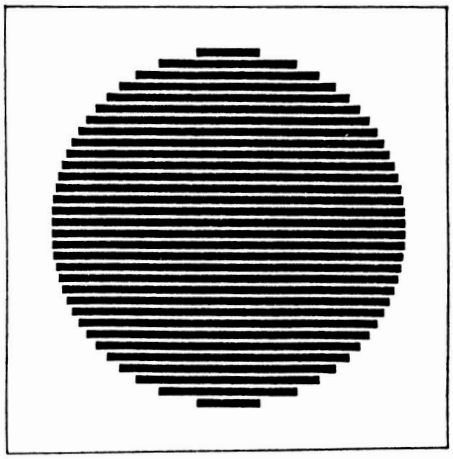

ELECTRICAL CHARACTERISTICS (@ AMO, 100 SUNS, 25 C)

PARAMETER	UNIFORM ILLUMINATION	LENS ILLUMINATION
ISC:	0.415 AMP*	0.415 AMP*
VOC:	1.154 VOLTS	1.154 VOLTS
FF:	0.877	0.852
EFFICIENCY:	0.247	0.240

*WITH PRISM COVER; 0.332 AMP WITHOUT COVER.

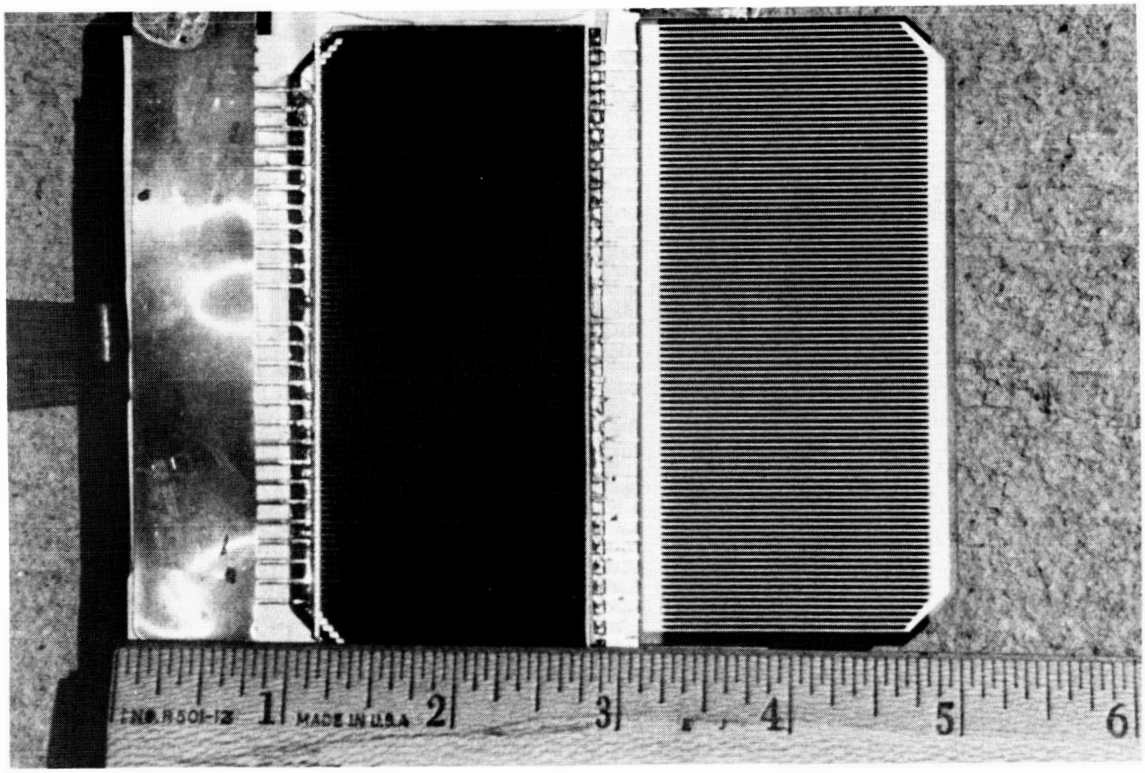

FIGURE 11 - EFFECTIVENESS OF ENTECH PRISMATIC CELL COVER FOR A 25% METALLIZED TERRESTRIAL SILICON CONCENTRATOR CELL

TRACKING ERROR TOLERANCE WITH VARIOUS CELL SIZES — ALL USING THE SELECTED LENS DESIGN

FIGURE 12

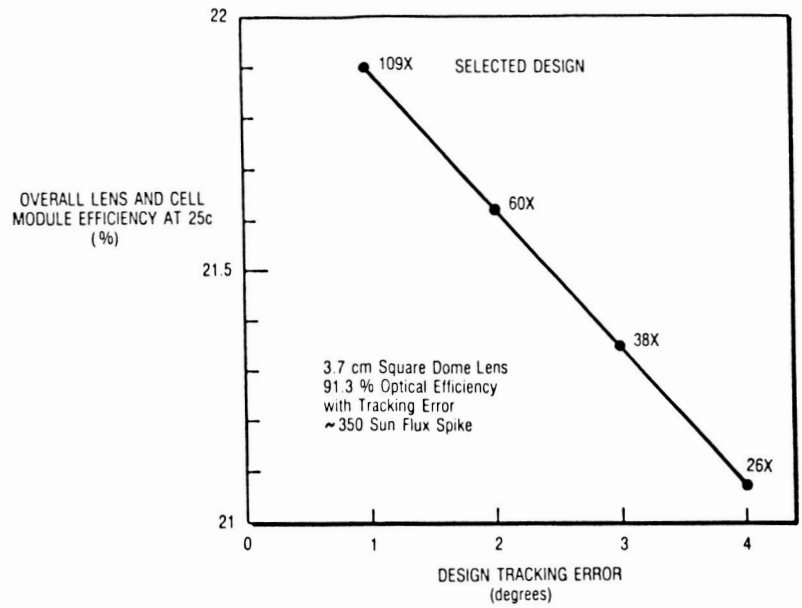

CELL MOUNT THERMAL ANALYSIS

FIGURE 13

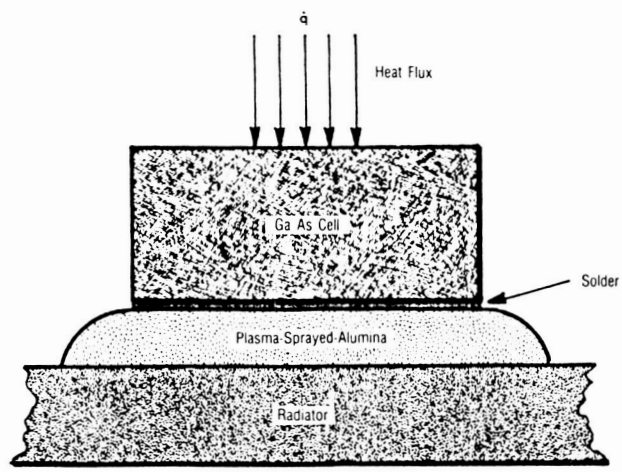

ELEMENT	THICKNESS	THERMAL CONDUCTIVITY	t/k
Cell	0.0305 cm	0.39 w/cm °c	0.078 cm².°c/w
Solder	0.0025 cm	0.32 w/cm °c	0.008 cm².°c/w
Alumina	0.0127 cm	0.35 w/cm °c	0.036 cm².°c/w
Radiator	0.0102 cm*	1.73 w/cm °c	0.006 cm².°c/w
		TOTAL	0.128 cm².°c/w

$\dot{q}$ = 350 suns * 0.1353 w/cm² * (0.95 - 0.24) = 33.6 w/cm²

$T_{cell} - T_{radiator} = \dot{q} * t/k = 4.3°c$

* ½ thickness of radiator, since heat radiates from both sides, and average radiator temperature is of interest.

RADIATOR THERMAL ANALYSIS RESULTS

FIGURE 14

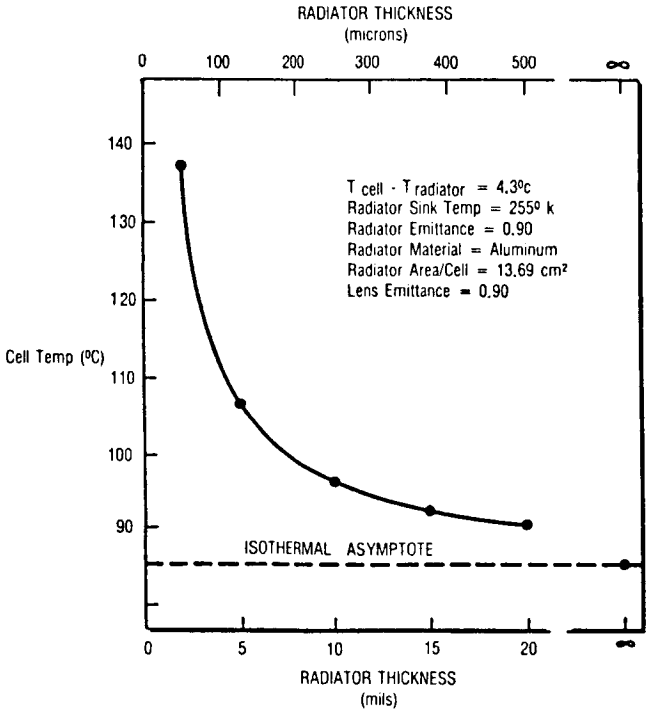

RADIATOR THICKNESS SELECTION

FIGURE 15

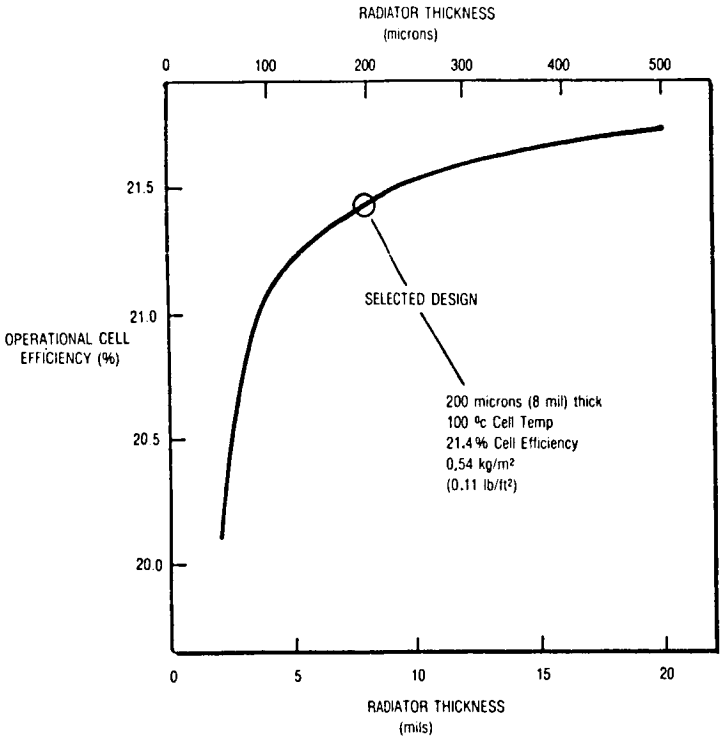

PERFORMANCE COMPARISON OF THREE COMPETING
TECHNOLOGIES FOR SPACE PHOTOVOLTAIC POWER

ITEM	LOCKHEED SPACE STATION* FLAT SILICON ARRAY (1 Sun, 20 C Cell)		TRW MINI-CASSEGRAINIAN** GaAs CONCENTRATOR ARRAY (100 Suns, 85 C Cell)		ENTECH DOME LENS GaAs CONCENTRATOR ARRAY (100 Suns, 100 C Cell)	
	Current	Improved	Current	Improved	Current	Improved
Cell Oper. Effy.	13.4%	14.6%	18.9%	21.2%	21.4%***	24.0%***
Optical Effy.	100.0%	100.0%	70.0%	80.0%	91.5%	96.0%
Packing Factor	96.0%	91.0%	88.0%	88.0%	97.0%	97.0%
Mismatch/Wiring	93.0%	93.0%	93.0%	93.0%	93.0%	93.0%
Array Efficiency	11.8%	12.4%	10.8%	13.9%	17.7%	20.8%
Watts/Sq.M.	160	168	146	188	239	281
Panel Kg/Sq.M.	N/A	N/A	5.7	5.7	2.5	2.5
Structure Kg/Sq.M.	N/A	N/A	0.7	0.7	0.7	0.7
Array Kg/Sq.M.	3.0	3.0	6.4	6.4	3.2	3.2
Watts/Kg	53	56	23	29	75	88

* R.V. Elms, LMSC, "Solar Arrays for Space Station and Platforms," IECEC-86, August 1986.

** R.E. Patterson, TRW, "Design, Performance Investigation, and Delivery of a Miniaturized Cassegrainian Concentrator Solar Array," Final Report, NASA Contract NAS8-35635, May 1985.

*** Cell performance using ENTECH's prismatic cell cover to eliminate gridline obscuration.

FIGURE 16

PHOTOVOLTAIC CONVERSION OF LASER POWER TO ELECTRICAL POWER

Gilbert H. Walker
NASA Langley Research Center
Hampton, Virginia

and

John H. Heinbockel
Old Dominion University
Norfolk, Virginia

Photovoltaic laser to electric converters are attractive for use with a space-based laser power station. This paper presents the results of modeling studies for a silicon vertical junction converter used with a Nd laser. A computer code was developed for the model and this code was used to conduct a parametric study for a Si vertical junction converter consisting of one p-n junction irradiated with a Nd laser. These calculations predict an efficiency over 50 percent for an optimized converter.

INTRODUCTION

Space-based laser power stations will require converters at the receiving spacecraft to convert the laser radiation to electricity. Photovoltaic converters are promising devices for this use (ref. 1). Special considerations must be given to the laser wavelength and to the laser power density. Figure 1 shows some laser photon energies compared to selected semiconductor bandgap energies. The semiconductor, for use as the photovoltaic converter, must be chosen so that its bandgap energy is slightly less than the energy of the laser photons to be converted into electricity (ref. 2). Incident power densities may be as high as 1×10^3 watts cm^{-2}. In a previous paper (ref. 2) vertical junction converters were suggested as appropriate for use as laser photovoltaic converters. A promising solar-pumped laser for use on a laser power station is a Nd laser (ref. 3). From figure 1, silicon is the appropriate semiconductor for use with a Nd laser. The Si bandgap energy is 1.11 eV, slightly less than the 1.17 eV energy of the photons from the Nd laser. The maximum power density assumed in this study is 1×10^3 watts cm^{-2} at 1.06 μm or 3.47×10^{21} photons cm^{-2} sec^{-1}. The photons are absorbed at an appreciable depth into the semiconductor rather than absorbed near the top surface. This paper describes a model developed to study vertical junction laser-photovoltaic converters and the application of this model to the Nd laser-Si single vertical junction photovoltaic converter.

MODEL

The model (described in detail in Appendix A) for this vertical junction converter uses the device geometry shown in figure 2 and assumes a generation rate at a depth β given by

$$g(\beta) = \phi_0(1 - R_e)\ \alpha\ e^{-\alpha\beta} \qquad (1)$$

where ϕ_0 is the number of incident photons [cm^{-2} sec^{-1}], α is the absorption coefficient [cm^{-1}], and R_e is the reflection coefficient. The basic equations for a n/p device involve the photocurrent from the n and p materials as well as the photocurrent from the depletion regions. Current is assumed to flow in sheets parallel to the top surface of the converter; thus, the model contains no diffusion between sheets. These currents, when summed, produce the total short circuit current. At this depth (β), we assume that a narrow strip exists which behaves like a conventional photoconverter. The short circuit current and dark currents are used in the equivalent circuit diagram of figure 3 together with the effects of the series resistance (R_S) and shunt resistance (R_{Sh}) to obtain a current-voltage relationship.

The temperature of the photoconverter is determined by the balance between the rate of heat production due to the fraction of absorbed laser power which is degraded to heat and the rate of heat loss by conduction. The model includes a heat-transfer calculation from the converter to a heat pipe at the back face of the device. The device temperature may be controlled by varying the heat pipe temperature and the heat-transfer coefficient.

APPROACH

Using the computer code developed for the model, a study of the Nd laser-Si vertical junction photovoltaic converter was conducted. (Table I shows the baseline parameters used in this study.) In this study, these baseline parameters were varied individually in order to determine the optimum value for each parameter.

RESULTS

Wavelength

Figure 4 shows the efficiency as a function of wavelength. The efficiency varies from 8 percent at a wavelength of 0.6 μm to 54 percent at a wavelength of 1.05 μm. At the wavelength of the Nd laser (1.06 μm), the converter efficiency is 53 percent at baseline conditions.

Converter Width

Figure 5 shows the effect of increasing the converter width with the p-n junction located 10 μm from one edge. The efficiency is highest for the smaller widths. The efficiency is about 56 percent for a width of 20 μm, and it remains above 50 percent for widths as great as 55 μm. Based on these data, for a small sacrifice of efficiency, wider single-crystal converters can be used. Thus, for a series-connected, multijunction device, a range of currents and voltages can be achieved. Although smaller width converters can produce slightly higher efficiencies, for the purpose of this study, the optimum achievable width is 20 μm.

Junction Position

The efficiency for the baseline converter is a strong function of the width of the p-region (here called junction position). Figure 6 shows this efficiency as a function of junction position for the 20 μm wide baseline converter. As the junction position is changed from 2 μm to 16 μm, the efficiency increases from approximately 38 percent to 57 percent. As the junction position is moved to greater values, the width of the p-region increases. The p-region has longer minority carrier diffusion lengths thus accounting for an increased efficiency (ref. 4). For our optimum cell, the junction position is chosen to be 16 μm.

Converter Thickness

Figure 7 shows the efficiency as a function of converter thickness for the baseline converter. Thickness is the distance in the direction of travel of the laser light within the converter. The efficiency increases from less than 2 percent at a thickness of 1×10^{-3} cm to greater than 53 percent at a thickness of 1.5×10^{-1} cm. The photons from the 1.06 μm laser are absorbed relatively deep in the semiconductor. From this the thickness of our optimum cell is 1.5×10^{-1} cm.

Temperature and Heat-Transfer Coefficient

The interface between the heat pipe and the converter must be an electrically insulating, thermally conducting surface. However, the major emphasis of our investigations has been on the structure and performance of the converter. The baseline heat-transfer coefficient was chosen to be 100 cal sec^{-1} cm^{-2} $°C^{-1}$, corresponding to a layer of insulating material. By varying the heat-transfer coefficient and the heat-pipe temperature, the converter temperature can be varied. Figure 8 shows the efficiency as a function of temperature. The efficiency at our baseline temperature of 293 K is 52 percent. This efficiency decreases to 28 percent at 500 K with a temperature coefficient of approximately -0.13 percent/K. Our optimum cell uses a heat-transfer coefficient of 40 cal sec^{-1} cm^{-2} $°C^{-1}$ to maintain the operating temperature of 293 K.

Power Density

Lasers in space for power-transmission applications may provide power densities up to 1×10^3 watt/cm^2 at the receiver. Figure 9 shows the efficiency as a function of power density for baseline conditions. The efficiency increases from about 41 percent at 1 watt/cm^2 to about 53 percent at 1×10^3 watts/cm^2. Not only the current, but also the voltage increases with increasing absorbed power to produce this increased efficiency. The incident power density for our optimum cell is chosen as 1×10^3 watts/cm^2. For a 50 percent efficient converter a heat transfer rate of 5×10^2 watts/cm^2 would be required.

Series Resistance

At high-power densities, the series resistance is one of the most important photovoltaic converter parameters. The vertical junction converter minimizes series resistance by minimizing the current path from the junction to the contact. Figure 10 shows the efficiency as a function of series resistance. As

the series resistance increases from 1×10^{-3} ohm to 1 ohm, the efficiency decreases from 53 percent to less than 10 percent. The series resistance chosen for our optimum converter is 1×10^{-2} ohms, well above the bulk resistance of 9×10^{-5} Ω.

Carrier Concentration

Figure 11 shows the converter efficiency as a function of acceptor concentration for four different donor concentrations. The peak efficiency of 59 percent is reached for both a donor and acceptor concentration of 1×10^{17} carriers cm^{-3}. Therefore, for our optimum converter we have chosen both a donor and acceptor concentration of 1×10^{17} carriers cm^{-3}.

Surface Recombination Velocity

The effect of surface recombination velocity on the converter efficiency is shown in Figure 12. Increasing the surface recombination velocity on the n-contact surface from 1 cm sec^{-1} to 1×10^{5} cm sec^{-1} decreases the efficiency from 53 percent to 29 percent. Increasing the surface recombination velocity on the p-contact surface from 1 cm sec^{-1} to 1×10^{4} cm sec^{-1} decreases the efficiency from 53 percent to 38 percent. Recombination velocities of 5×10^{2} cm sec^{-1} are required to keep the calculated efficiency above 50 percent. For our optimum converter we have chosen a recombination velocity of 1×10^{2} cm sec^{-1} (ref. 4) on both the n and p contact surfaces.

CONCLUSIONS

Table II shows the parameter values for our optimum single p-n junction converter. The parameter values chosen for our optimum converter are considered attainable. For example, a converter width of 20 μm was chosen as an attainable dimension, although narrower converters have a higher theoretical efficiency. In reality, a practical device would be composed of multiple p-n junctions connected in series. This has been accomplished previously by mechanically stacking silicon wafers (each containing a p-n junction) and providing a metal contact between each unit (ref. 5); however, the silicon wafers were 240 μm wide. The narrower width of fragile silicon p-n junctions in our proposed converter would probably require a substantially different method of fabrication. It has recently been demonstrated that an epitaxial single crystal composite of silicon and metallic $CoSi_2$ can be fabricated (ref. 6). This opens the possibility of fabricating a series-connected multiple p-n junction device where all the elements of the device, even the metal contacts, are single crystal. The shunt resistance for our optimum converter was realistically chosen as 1×10^{6} ohm (ref. 4). A converter thickness of 1.5×10^{-1} cm will allow for absorption of the 1.06 μm Nd laser radiation. The junction position of 16 μm provides the maximum output for this width converter. Carrier concentrations of 1×10^{17} carriers cm^{-3} attain the highest efficiency. The optimized converter has a calculated efficiency of 55 percent for the 1.06 μm Nd laser radiation.

APPENDIX A

MODEL

The model for this vertical junction converter uses the device geometry shown in figure 2 and assumes a generation rate at a depth β given by

$$g(\beta) = \phi_o(1 - Re)\ \alpha e^{-\alpha\beta}$$

where ϕ_o is the number of incident photons [cm^{-2} sec^{-1}]; α is the absorption coefficient [cm^{-1}]; and Re is the reflection coefficient. The basic equations for a n/p device involve the photocurrent from the n and p materials as well as the photocurrent from the depletion region. The currents, when summed, produce the total short circuit current. Following reference 7, we assume that there exists a narrow strip at a depth β below the surface which behaves like a conventional photoconverter. At this depth β, we have the hole excess in the n-region given by

$$D_p \frac{d^2}{dX^2}(P_n - P_{no}) - \frac{(P_n - P_{no})}{\tau_p} = -g(\beta),\ Xj + Xn \leq X \leq B$$

which is subject to the boundary conditions

$$- D_p \frac{d}{dX}(P_n - P_{no}) = S_p(P_n - P_{no})\Big|X = B$$

and

$$P_n - P_{no}\Big|X = Xj + Xn = 0 \quad .$$

This produces the current density

$$Jp = qD_p \frac{d(P_n - P_{no})}{dx}\Big|X = X_j + n = -qg(\beta)L_p f(S_p, D_p/L_p, (B-X_j-X_n)/L_p)$$

where $f(a,b,c) = \dfrac{a - a\cosh(c) - b\sinh(c)}{b\cosh(c) + a\sinh(c)}$.

Similarly, the electron excess in the p-region is given by

$$D_n \frac{d^2}{dX^2}(n_p - n_{p_o}) - \frac{(n_p - n_{p_o})}{\tau_n} = -g(\beta),\ 0 < X < X_j - X_p$$

with boundary conditions

$$D_n \frac{d}{dX}(n_p - n_{p_o}) = S_n (n_p - n_{p_o}) \Big| X = 0$$

$$n_p - n_{p_o} \Big| X = X_j - X_p = 0 \ .$$

This produces the current density

$$J_n = -qD_n \frac{d}{dX}(n_p - n_{p_o}) \Big| X = X_j - X_p = -qg(\beta)L_n f(S_n, D_n/L_n, (X_j - X_p)/L_n)$$

where Xj is the junction depth and Xp,Xn define the space charge region. The photocurrent from the depletion region is neglected, and we have the total short circuit current density as a function of β

$$J_{sc} = J_{sc}(\beta) = J_n(\beta) + J_p(\beta) \ .$$

The total current is obtained by integrating these current densities over the depth of the photoconverter and

$$I_{sc} = \int_0^A J_{sc}(\beta)d\beta \ .$$

Following reference 4, the dark current is given by $I = Ip^* + In^*$ where we have assumed a photoconverter depth in the Z-direction of 1 cm to obtain the dark currents:

$$Ip^* = \frac{gD_p}{L_p} P_{n_o} F\left(\frac{B - X_j - X_n}{L_p}, \frac{S_p L_p}{D_p}\right) \cdot (e^{qV/kT} - 1)A$$

and

$$I_{n*} = \frac{qD_n}{L_n} n_{p_o} F\left(\frac{X_j - X_p}{L_n}, \frac{S_n L_n}{D_n}\right) \cdot [e^{qV/kT} - 1]A$$

which gives the injection current

$$I_{inj} = I_{p*} + I_{n*} = I_o (e^{qV/kT} - 1) ,$$

where

$$F(A,B) = \frac{B + \tanh(A)}{1 + B \tanh(A)} .$$

Also, from reference 4, we use the recombination current density of

$$J_{rec} = \frac{\pi q n_i W \sinh(\frac{qV}{2kt})}{\sqrt{(\tau_p \tau_n)}\ q(V_{bi} - V)/kT}$$

where V_{bi} is the built in voltage, n_i is the intrinsic carrier density, W is the width of the depletion region, T is temperature, q is electron charge, τ_p and τ_n are lifetimes, V is voltage, and k is Boltzmann's constant. The short circuit currents and dark currents are used in the equivalent circuit diagrams of figure 3, and we obtain the current voltage relation

$$I(1 + \frac{Rs}{Rsh}) = I_{sc} - V/R_{sh} - I_o[e^{\frac{q(V+IRs)}{kT}} - 1] - I_{rec} .$$

which includes the effects of the series resistance R_s and shunt resistance R_{sh}.

Table I

Baseline Parameters

Series Resistance	0
Heat Pipe Temperature	20°C
Heat-Transfer Coefficient	100 cal sec^{-} cm^{-} °C^{-1}
Surface Recombination Velocity on n-surface	0 cm sec^{-1}
Surface Recombination Velocity on p-surface	0 cm sec^{-1}
Input Power	1 x 10^{3} w/cm^{2}
Laser Wavelength	1.06μm
Converter Thickness	1.3 x 10^{-1} cm
Converter Width	2.0 x 10^{-3} cm
Converter Length	1 cm
Junction Position	1 x 10^{-3} cm
Acceptor Carrier Concentration	1.25 x 10^{17} cm^{-3}
Donor Carrier Concentration	5.0 x 10^{19} cm^{-3}
Reflection Coefficient	0.05
Shunt Resistance	1 x 10^{6} ohms

Table II

Parameters for Optimized Converter

Series Resistance	1 x 10^{-2} ohms
Heat Pipe Temperature	20°C
Heat-Transfer Coefficient	40 cal sec^{-1} cm^{-2} °C^{-1}
Recombination Velocity on n-Surface	100 cm/sec
Recombination Velocity on p-Surface	100 cm/sec
Input Power	1 x 10^{3} watts/cm^{2}
Laser Wavelength	1.06 μm
Converter Thickness	1.5 x 10^{-1} cm
Converter Width	20 μm
Converter Length	1 cm
Width of the p-region	16 μm
Acceptor Carrier Concentration	1 x 10^{17} carriers/cm
Donor Carrier Concentration	1 x 10^{17} carriers/cm^{3}
Reflection Coefficient	0.05
Shunt Resistance	1 x 10^{6} ohms

REFERENCES

1. DeYoung, R. J.; Tepper, W. D.; Conway, E. J.; and Humes, D. H.: "Preliminary Comparison of Laser and Solar Space Power Systems." Proceedings of the 18th Intersociety Energy Conversion Engineering Conference. Orlando, FLorida; August, 1983; pp. 983-989.

2. Walker, G. H.: "Photovoltaic Conversion of Laser to Electrical Power." Proceedings of the 18th Intersociety Energy Conversion Engineering Conference. Orlando, Florida; August, 1983; pp. 1194-1199.

3. Williams, M. D.; Zapata, L.: "Solar-Pumped Solid State Lasers." NASA TM87615, 1985.

4. Hovel, H. J.: Semiconductors and Semimetals, Volume 11, Solar Cells, Academic Press, 1975.

5. Sater, B. L.; Brandhorst, H. J., Jr.; Riley, T. J.; Hart, R. E., Jr.: "The Multiple Junction Edge-Illuminated Solar Cell," Conference Record of the 10th Photovoltaic Specialist Conference, Nov., 1973, Palo Alto, California, p. 181.

6. Hensel, J. C.; Levi, A. F. J.; Tung, R. T.; and Gibson, J. M.: "Transistor Action in Si/$CoSi_2$/Si Heterostructures," Appl. Phys. Lett. 47, July 15, 1985, p. 151.

7. Grover, A.; Stella, P.: "Vertical Multijunction Solar Cell One Dimensional Analysis," IEEE Transactions on Electron Devices, Vol. ED-21, June, 1974, p. 351-356.

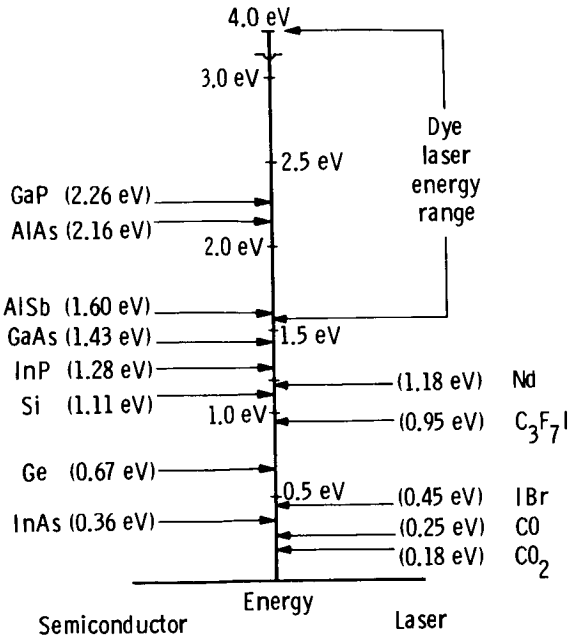

Figure 1 - Semiconductor bandgap energy - laser photon energy relationship

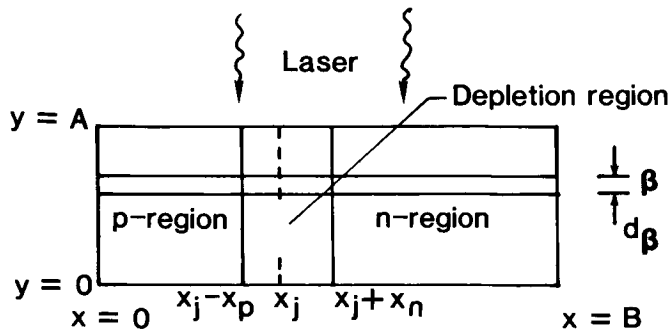

Figure 2 - Converter geometry

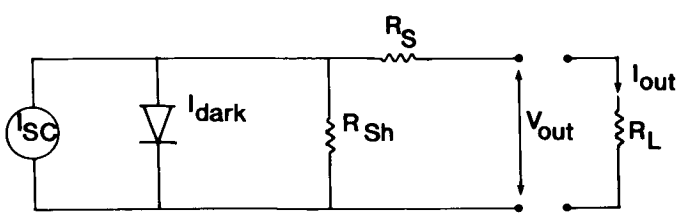

Figure 3 - Equivalent circuit

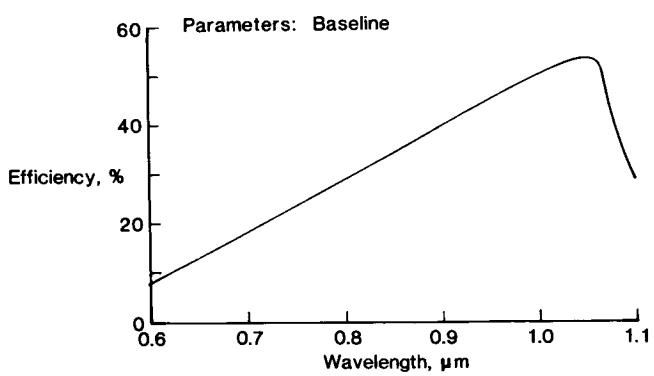

Figure 4 - Converter efficiency vs. laser wavelength

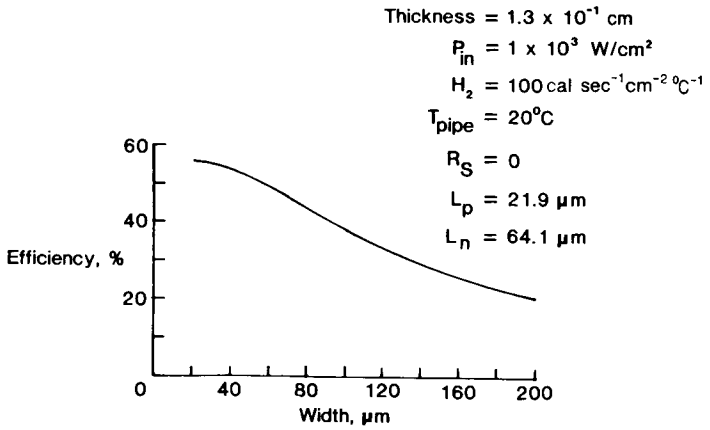

Figure 5 - Converter efficiency vs. converter width

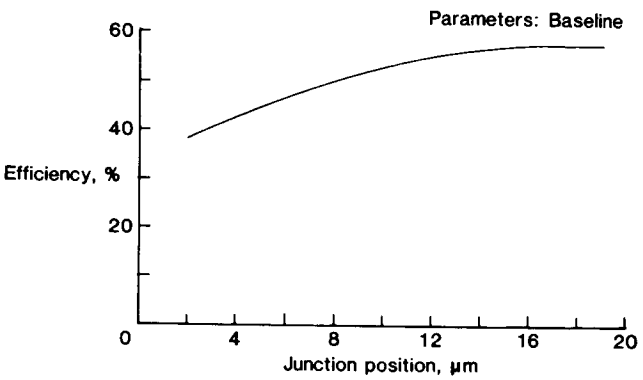

Figure 6 - Converter efficiency vs. junction position for a 20 μm-wide converter

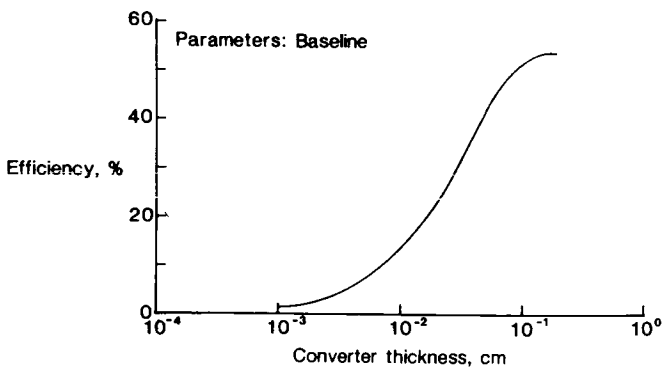

Figure 7 - Converter efficiency vs. thickness

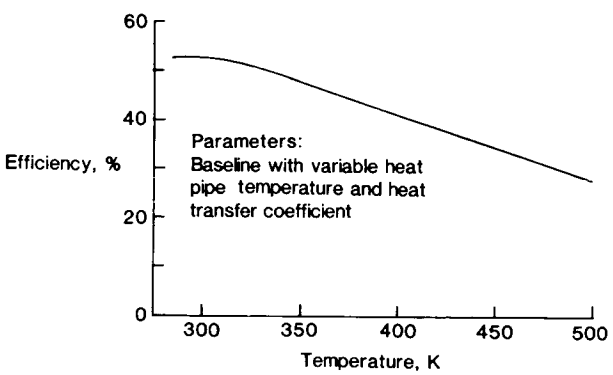

Figure 8 - Converter efficiency vs. temperature

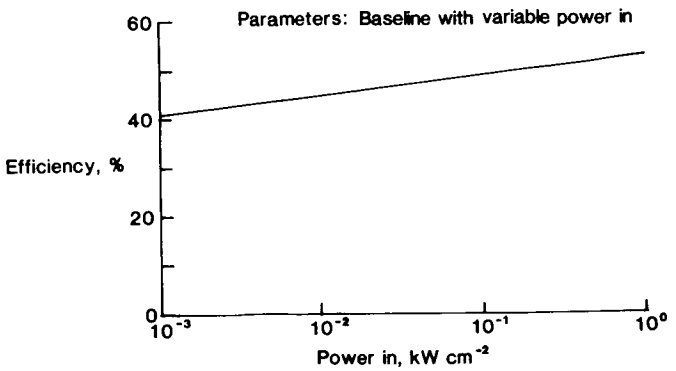

Figure 9 - Converter efficiency vs. input power density

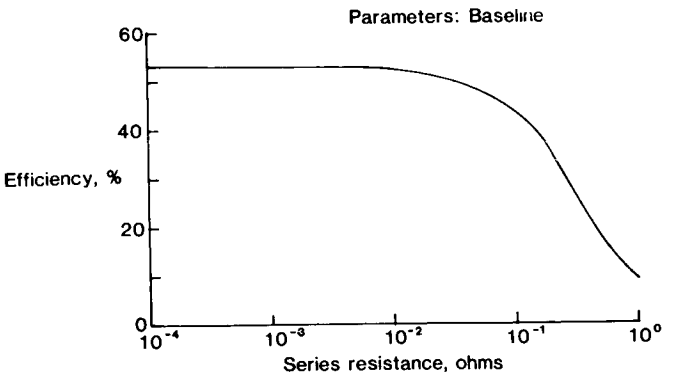

Figure 10 - Converter efficiency vs. series resistance

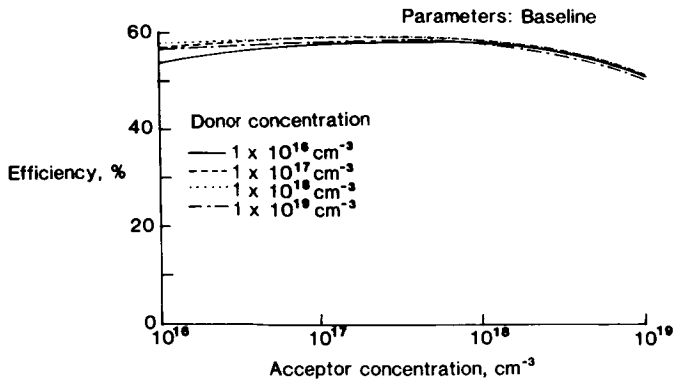

Figure 11 - Converter efficiency as a function of acceptor concentration for four different donor concentrations

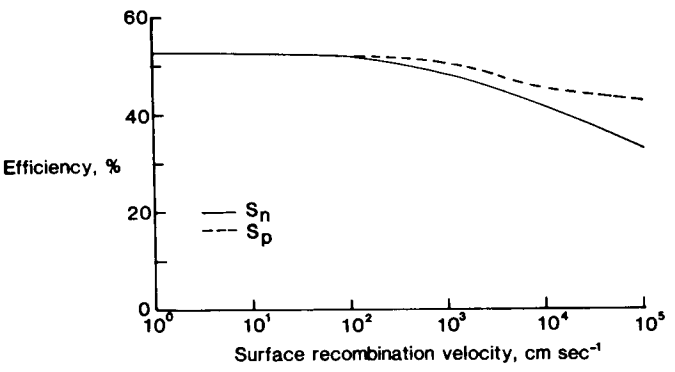

Figure 12 - Converter efficiency vs. surface recombination velocity on the n- and p-contact surfaces

ADVANCED PHOTOVOLTAIC SOLAR ARRAY DESIGN ASSESSMENT

Paul Stella and John Scott-Monck
Jet Propulsion Laboratory
Pasadena, California

The Advanced Photovoltaic Solar Array (APSA) program seeks to bring to flight readiness a solar array that effectively doubles the specific power of the SAFE/SEP design that was successfully demonstrated during the Shuttle 41-D mission. APSA is a critical intermediate milestone in the NASA-OAST effort that has, as its goal, to demonstrate solar array technologies capable of 300 W/kg and 300 W/m^2 at beginning of life. The APSA program, at its completion, should yield a flight ready, high performance solar array that can efficiently accommodate the types of solar cells required to provide either a 300 W/kg or 300 W/m^2 array.

The genesis for such ambitious goals was the demonstration that ultrathin (50 μm) silicon solar cells with very high (~15 percent) conversion efficiency could be fabricated (ref. 1). During the nearly 10 years that it took to bring the prototype cell to a state of flight readiness, parallel activities addressing ultrathin cell laydown and interconnection, suitable flexible blanket substrates and covers (ref. 2), plus compatible, efficient array structures (ref. 3) were conducted. The success of these programs led to the decision to commit to the APSA program.

PROGRAM DEFINITION

APSA was conceived as a multiyear three-phase effort. The initial phase was to address the development of a realistic design that would incorporate existing elements of advanced array technology and was capable of accommodating anticipated advancements. This would be followed by a fabrication phase in which, as a goal, protoflight hardware would be demonstrated on a scale that would assure user confidence in manufacturing the technology. This would then lead to a ground test phase in which the protoflight hardware would be subjected to the types of generic tests required for space-qualified arrays.

Establishing meaningful, challenging goals for the APSA Program was considered essential for success. Generic targets such as W/kg and W/m^2 would not be sufficient to assure that the technology would be considered by the users for future mission applications. Orbit, mission duration and spacecraft function were other factors that had to be addressed. These, in turn, would influence array stiffness and circuit architecture at one level and cell and coverglass selection at another.

In order to involve the community in the process of goal definition, a survey was taken where the respondents were asked to not only provide array design targets but justify them in terms of perceived missions. The entire space community was invited to participate, even though the array technology to be developed was for NASA specific mission objectives. This was done in the hope that the APSA baseline array technology would have a wide appeal to mission users, thus enhancing its prospects for flight use.

APSA DESIGN REQUIREMENTS

Performance requirements were then established by JPL for the APSA design based partially upon the results of the survey. In addition, an analysis was performed to establish the array performance that would be anticipated from the component characteristics developed as part of the OAST advanced array technology program. A third aspect of the requirements was to limit the scope of the two contractors' efforts so as to remain within the overall available budget and still determine a "highly probable" advanced array design with acceptable detail.

These considerations led to the following design requirements:

8 to 12 kW BOL
130 W/kg BOL
105 W/kg EOL
110 W/m^2 EOL

with EOL defined to be 10 years in the baseline geosynchronous orbit. Although the restriction to geosynchronous orbit eliminates many other important future missions from detailed analysis, it did contain two important features. First, the most frequently mentioned use of an advanced high performance array with power level on the order of 10 kW is for geosynchronous communications satellites. Second, this type of orbital environment is more closely related to the environment expected for interplanetary array use, an obviously important consideration for NASA-OAST developed technology. Naturally, other orbital environments can be imposed on the developed designs by interested parties to determine suitable "scaling factors." Other requirements included the need for shuttle launch environment compatibility and the the demonstration of technology maturity so as to allow for a subsequent fabrication of protoflight hardware based on the advanced array technology.

Once the contracted efforts began, some additional requirements were developed to assure that the merits of the competing designs could be meaningfully compared. These were as follows:

(1) Deployed wing frequency to be evaluated over the range 0.01 Hz to 0.10 Hz (cantilevered).
(2) On-orbit wing loads to be evaluated over the range 10^{-3} to 10^{-2} g ultimate.
(3) Partial extension, partial and full retraction, and full restowage were not required.
(4) Array voltage levels shall not exceed 200 volts BOL open circuit at normal operating temperature.
(5) Array shadowing is not to be assumed.
(6) Trapped radiation and solar flare environments are as specified by JPL.

CANDIDATE DESIGNS AND SELECTION

Figure 1 summarizes the two final designs. Not unexpectedly, there was some degree of similarity in that both decided to propose a basic array structure featuring a coilable longeron mast deployed from a canister. Each blanket design employed 65 μm silicon solar cells, thin ceria-doped microsheet covers and a Kapton-based substrate.

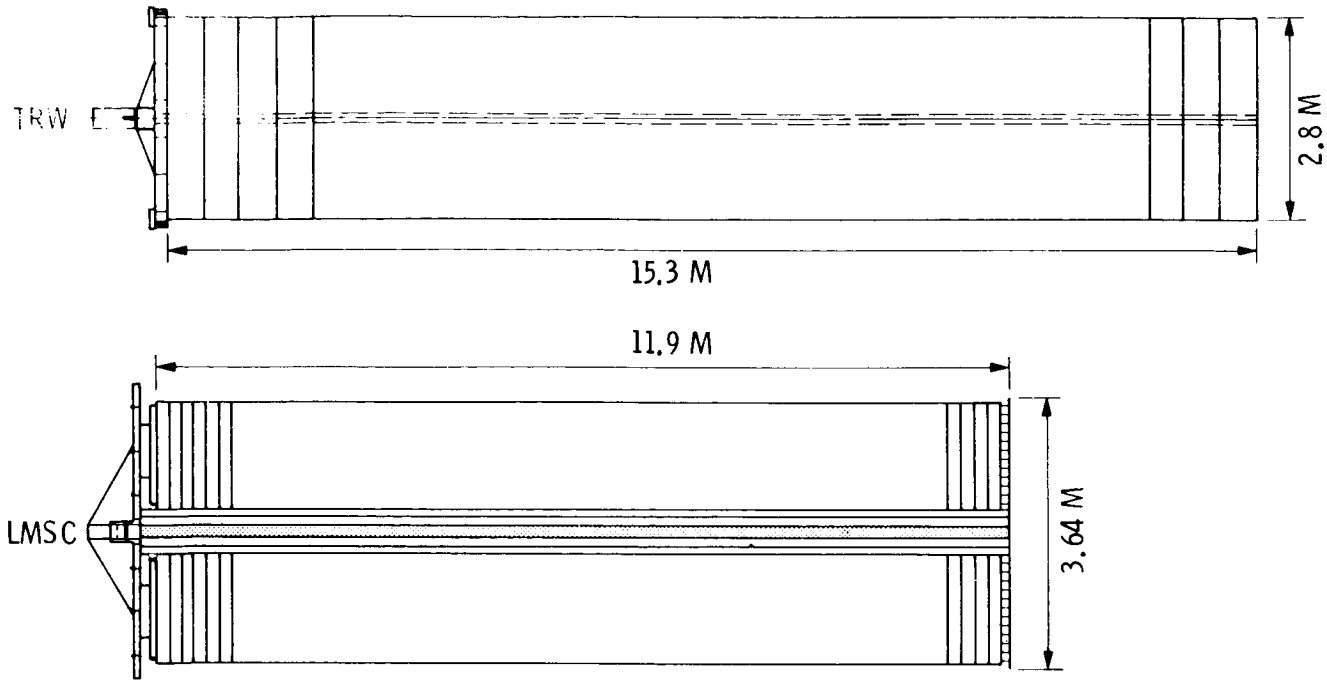

	LMSC	TRW
CELL	7.1 X 7.1 CM X 65 μM WRAPTHROUGH CONTACT η = 13.3%	2 X 4 CM X 65 μM η = 13.5%
COVER	16 X 35.7 CM X 75 μM Ce MICROSHEET	2 X 4 CM X 50 μM Ce MICROSHEET
SUBSTRATE	74 μM THICK PRINTED CIRCUIT, Cu/KAPTON	50 μM THICK CARBON LOADED KAPTON
DEPLOYMENT MAST	CONTINUOUS LONGERON 16.3 CM DIAM. 3.8 MM D. LONGERON	CONTINUOUS LONGERON 20.8 CM DIAM. 3.8 MM D. LONGERON
CANISTER	GRAPHITE/EPOXY	ALUMINUM
CONFIGURATION	ACCORDIAN FOLD DUAL BLANKET IN PLANE MAST	ACCORDIAN FOLD SINGLE BLANKET REAR SIDE MAST
SPECIFIC PERFORMANCE, BOL WITH 5% CONTINGENCY	138 W/KG	145 W/KG

Figure 1. APSA Design Candidates

There were also some interesting differences in that one proposed a single blanket wing as opposed to the other's dual blanket approach. Although there was only a one percent difference in total wing area, the selected wing aspect ratios were quite dissimilar. There was also a wide divergence in opinion on cell size and configuration, as shown in Figure 1. Perhaps the greatest surprise was the fact that there was not agreement on the method of cell interconnecting; one opting for welded, the other solder.

The selection process focused on technical maturity (risk) since protoflight hardware was required in the second phase of the APSA program. Cost constraints were also a significant factor in the selection process, since it was considered essential that the protoflight hardware include all the components that constitute an operating array. This was mandated by the architecture and total funding of the APSA program which must culminate in ground-based testing of the total array design.

Even though only one design could be chosen, it should be noted that the APSA design phase has shown that at least two solar array design options exist for meeting this critical NASA-OAST milestone for advanced solar array technology. Hopefully, other agencies or flight program offices that require this type of solar array improvement will give attention and support to the alternate APSA design.

APPROACHES TO ENHANCING APSA PERFORMANCE

The APSA design represents a significant improvement in array specific power performance, but substantial work remains in order to achieve the ambitious 300 W/kg and 300 W/m^2 goals set by NASA-OAST. Analysis of the APSA components shows that solar cell performance improvements offer the greatest leverage for future progress. It should be noted at this point that the NASA-OAST goal of 300 W/kg was established for an array capable of delivering 25 kW at beginning of life. Thus, in the subsequent discussion of APSA, all quoted specific power forecasts should be escalated by approximately 15 percent to account for the advantages (deployment and stowage mass contributions) associated with scaling this design to the appropriate NASA-OAST power level goal.

Figure 2 depicts the APSA performance that would be achieved by the substitution of higher efficiency and lower mass (equivalent to 10 μm of silicon) solar cells with no other array changes made. Based on previous results in developing high efficiency 62 μm silicon cells (ref. 1) and recent work demonstrating efficiencies approaching 18 percent for 300 μm silicon cells (ref. 4), it would appear reasonable to forecast that 16 percent 62 μm silicon cells could be mass produced in the near term. This would raise the APSA specific power to at least 175 W/kg, translating to approximately two-thirds (200 W/kg) of the NASA-OAST goal.

Thin film solar cells appear to hold the most promise for going beyond the 200 W/kg performance level. To give some perspective to this statement, the current status of various thin film solar cell candidates is included in Figure 2. It should be mentioned that these efficiency values represent the best that have been achieved to date under laboratory conditions. It would not be unrealistic to anticipate that a single crystal, thin film solar cell could achieve a realistic (manufacturable) conversion efficiency of 18 percent provided that sufficient resources were devoted to its development. This would likely satisfy the NASA-OAST goal of 300 W/kg.

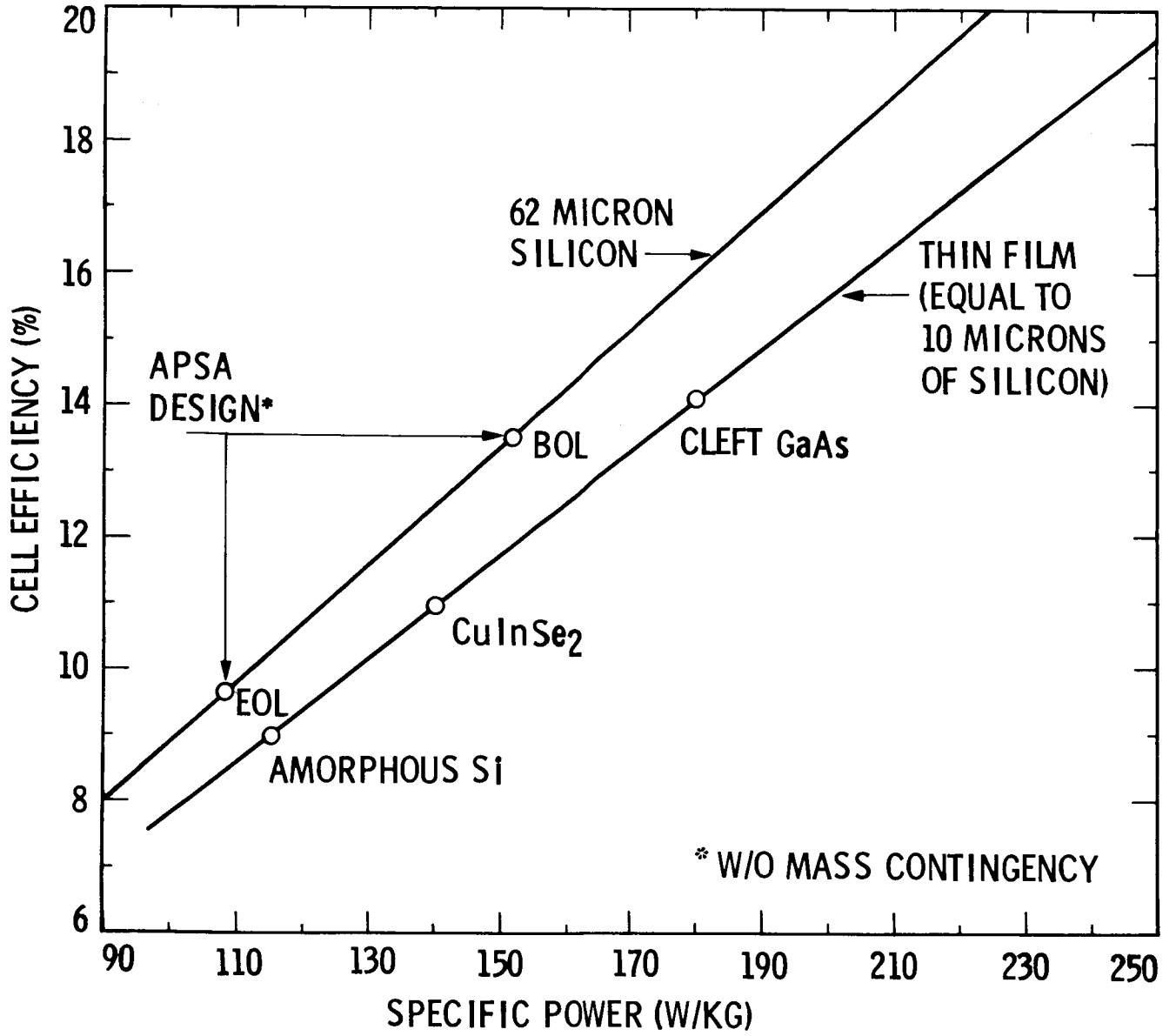

Figure 2. Impact of Advanced (Thin) Cells on APASA Design

Although the OAST goals are expressed in terms of beginning-of-life (BOL), it is necessary, when actually evaluating a mission, to design the array for maximum specific power at end-of-life (EOL). From this perspective, many of the thin film solar cells look potentially attractive for high performance solar arrays. Based on admittedly limited radiation test data, materials such as amorphous silicon and $CuInSe_2$ show considerable promise, especially for missions that would experience very high (approaching 1×10^{16} e/cm^2) radiation environments. For example, a thin film solar cell that yields 9 percent conversion efficiency after an equivalent 1 MeV fluence of 1×10^{15} e/cm^2 would result in greater than 200 W/kg specific power at EOL for a solar array operating for 10 years in a geosynchronous orbit.

In summary, it is not unreasonable to anticipate the development of solar array designs capable of 300 W/kg at BOL for operational power levels $\geqslant 25\ kW_e$. It is also quite reasonable to expect that high performance solar arrays capable of providing at least 200 W/kg at EOL for most orbits now being considered by mission planners will be realized in the next decade.

REFERENCES

1. Gay, C.: "Thin Silicon Solar Cell Performance Characteristics," Proc. 13th IEEE Photovoltaic Specialists Conf., June 1978.

2. Patterson, R.; Mesch, H.; and Scott-Monck, J.: "Development of Flight Ready Fifty-Micron Silicon Solar Array Module Technology," Proc. 21st IECEC, Aug. 1986.

3. Adams, L.: "STACBEAM: An Efficient, Low Mass, Sequentially Deployable Structure," Proc. 17th IECEC, Aug. 1982.

4. Crotty, G.: "Processing and Characterization of High-Efficiency Solar Cells for Space," Space Photovoltaic Research and Technology Conference, Oct. 1986.

THE EFFECT OF INTERNAL STRESSES ON SOLAR CELL EFFICIENCY

Victor G. Weizer
NASA Lewis Research Center
Cleveland, Ohio

Diffusion induced stresses in silicon are shown to result in large localized changes in the minority carrier mobility which in turn have a significant effect on cell output. Evidence is given that both compressive and tensile stresses can be generated in either the emitter or the base region. Tensile stresses appear to be much more effective in altering cell performance. While most stress related effects appear to degrade cell efficiency, this is not always the case. Evidence is presented showing that arsenic induced stresses can result in emitter characteristics comparable to those found in the MINP cell without requiring a high degree of surface passivation.

INTRODUCTION - COMPRESSIVE STRESSES

Evidence was presented in a recent publication indicating that the high voltages obtained from the MINP solar cell are due not only to its highly optimized emitter region but to improvements in its base region as well. (ref. 1) The analysis further suggested, albeit on the basis of indirect evidence, that the MINP cell base enhancement is due to a lower value of minority carrier mobility in that region as compared to cells of the same material but fabricated at other laboratories.

Subsequent measurement of the base region minority carrier mobility in the MINP cell as well as in other cells made from similar material, confirmed the suggestions of the preceding analysis (ref. 2). The MINP cells were indeed found to have a lower base mobility than the other cells tested. However, rather than finding a lower than normal mobility in the MINP cells, it was discovered that the other cells possessed anomalously high mobility values. Figure 1, taken from reference 1, shows these differences and indicates further that the anomalously high mobility (diffusivity) values are localized in the near-junction base region.

The MSD cell data in figure 1 can be fit quite well using a model that assumes a narrow region of high diffusivity (D) near the junction. Figure 2 shows such a fit assuming, for ease of calculation, an infinite value of D in a 15 μm thick region adjacent to the depletion region. A detailed calculation of the variation of the base component of the dark saturation current J_{ob} as a function of the magnitude of D in the near-junction region indicates that an increase of only 12x is required to explain the measured factor of two difference between the MINP and the MSD base saturation current components. This is illustrated in figure 3 where J_{ob}' and J_{ob} are the base components of the dark saturation current with and without the high D region, respectively. Although it was not possible to take measurements on samples thinner than 20 μm or so, extrapolation of the MSD cell data in figure 1 indicates that D increases of this magnitude are indeed feasible.

The mechanism responsible for the localized increases in D has been identified as the effect of diffusion induced stress (ref. 2). Emitter contraction due to phosphorus diffusion causes tensile stresses to be generated in that region. These stresses in turn cause compressive stresses to be generated in the adjacent lattice, i.e., in the near-junction base region. Since silicon is a piezoresistive material,

these base region stresses result in localized disturbances in the minority carrier diffusivity in that region.

If the above mechanism is correct, if the high diffusivity values measured in the base regions of these cells are due to stresses originating in the emitter, then it is reasonable to believe that removal of some or all of the highly stressed emitter should result in a lowering of the base diffusivity. When the emitter surface is chemically etched, however, just the opposite effect is found. When the surface of the emitter is removed the measured diffusivity shows an abrupt increase. Also, as seen in figure 4, the increase is not limited to the near-junction region. Diffusivity levels throughout the base are raised by the etching process. Concurrent with these changes in D are a sizable decline in the red response (fig. 5), confirming that the etching operation performed on the emitter does affect the base region, and a drop in the open circuit voltage.

Upon thermal annealing (110 °C, 30 min.) the etched cell characteristics return to normal. Diffusivity levels throughout the cell drop to values typical of an unetched thick base cell, and the voltage and the red response recover. Measurement of the activation energy for thermal recovery (fig. 6) yields a value close to the energy for divacancy migration, indicating that atomic motion (silicon self diffusion) is involved in the recovery process.

TENSILE STRESSES

While the mechanism of stress generation in an as-diffused cell is rather straightforward, an explanation of cell behavior subsequent to emitter etching and annealing appears to be somewhat involved. In order to describe the etch and anneal phenomenon it appears that we must postulate that as the cell is lowered from the diffusion temperature and is still in a plastic state, a limited amount of plastic deformation takes place to relieve some of the diffusion induced stress. The resulting room temperature situation is described schematically in figure 7(a). As shown, there is a region near the surface in a state of tension that is balanced by other regions in various states of compression.

When a part of the surface region (in tension) is removed by the etching process, the tension-compression couple becomes unbalanced, allowing the compressed region to expand (fig. 7(b)). The slipped region, being at room temperature and unable to flow plastically, merely transmits the expansion to the adjacent base region. The near-junction base region is thus put into a state of tension. It is this etch induced tensile stress that is proposed as the cause of the drastic post-etch increase in D. Further evidence supporting a tension based mechanism will be presented further on in the discussion.

When the etched cell is annealed at elevated temperatures, the stresses are relieved by a rearrangement of the lattice and the various cell characteristics return to, or close to, normal.

We can thus state at this point that both tensile and compressive stresses can be generated in the base region and that both types of stress degrade cell operation. It is also evident that tensile stresses are appreciably more damaging than compressive stresses.

Another means of reducing diffusion associated lattice stress, according to conventional wisdom, is to use a diffusant that is dimensionally compatible with the silicon lattice. One such element is arsenic, which has, according to the literature, a tetrahedral radius very close to that of silicon (ref. 3).

Following this line of reasoning we prepared a number of arsenic diffused solar cells from 0.1 ohm-cm float zone material. To ensure that the diffusant and the lattice were in as close to an equilibrium state as possible, we performed a low temperature deposition (850 °C, 150 min), and then subjected the wafers to a long (65 hr.), high temperature (950 °C) drive in with the arsenic source removed.

Upon measuring the base region diffusivity in these cells we found, to our surprise, that the situation was worse than it was with the phosphorus diffused cells. Figure 8 is a plot of the measured diffusivity as a function of base width for one of the arsenic diffused cells. For comparison the figure also shows the corresponding data for a MINP cell. As can be seen, not only is there a wide region of high diffusivity adjacent to the junction, but the high D values persist deep into the cell. The plot is quite similar to that found for the etched phosphorus diffused cell (fig. 4).

An estimate of the increase in the base component of the dark saturation current caused by the diffusivity profile of figure 8 can be made by assuming a base region composed of two regions of constant D. If we assume a base with a 30 to 40 μm thick near-junction region where D is 15 to 20 times that in the rest of the base, and assume (from fig. 8) a value of 35 cm^2/sec in the rest of the cell, a 5x to 8x enhancement in J_{ob} should be expected. This is considerably greater than the twofold increase found for the phosphorus diffused cells.

These unexpected results prompted a return to the literature. What one finds upon closer scrutiny is that although arsenic is well matched dimensionally to the silicon lattice, a substantial fraction (as much as 35 to 40 percent (ref. 4)) of the absorbed material goes into the lattice non-substitutionally. At least a portion of this non-substitutional fraction becomes incorporated in the lattice in the form of lattice expanding precipitates (ref. 5), as evidenced by the increased lattice parameters which have been measured in arsenic diffused silicon. (ref. 6) Thus, contrary to the situation found in the phosphorus diffused emitter, the arsenic diffused emitter is a region of compressive stress, and as such should be expected to cause tensile stresses to be generated in the adjacent base region.

The evidence strongly suggests, therefore, that the extremely high values of D found in the base region of the arsenic diffused cell are due to the existence of tensile stresses in that region which, in turn, are the result of compressive stresses in the emitter region. The similarity between the diffusivity versus base width plots of the arsenic diffused cells and those of the phosphorus diffused, emitter etched cells suggests that the same mechanism is active in both cases. The arsenic diffused cell data thus support the mechanism proposed earlier to explain the behavior of the emitter etched, phosphorus diffused cells.

Although an attempt to lower base stress levels in phosphorus diffused cells by chemically removing highly stressed emitter regions resulted instead in an unexpected increase in stress, a similar effort with arsenic diffused cells proved to be successful. Figure 9 shows plots of D versus base width for an arsenic diffused cell before and after the emitter etch procedure. As can be seen, the etching process reduces stress levels to such an extent that the measured diffusivity profile after etching is quite similar to that found in the low stress MINP cell (fig. 1).

Another major difference between the phosphorus and arsenic diffused cells is the fact that the dark saturation current of the former cell rose abruptly after emitter etching whereas for the arsenic diffused cell it remained constant. This is shown in table I where the etched arsenic diffused cell characteristics can be seen to be even slightly better than those of the unetched cell. This is in contrast to the sharp drop in the output characteristics of the etched phosphorus diffused cell.

The fact that the total dark saturation current of the arsenic diffused cell is not affected by the etching process while at the same time the base component undergoes a significant change, permits us to draw some interesting conclusions concerning the emitter region.

EFFECT OF STRESS ON EMITTER CHARACTERISTICS

Up to this point we have limited our discussion to diffusivity changes taking place in the base region. While we cannot measure D in the emitter region, it is obvious that similar, possibly even greater changes are taking place there. Fortunately, we can get some insight into what is happening from an analysis of the variation of the cell electrical characteristics during the emitter etching procedure.

As mentioned with respect to figure 9, the base diffusivity profile of the etched arsenic diffused cell is very similar to that measured for the low stress MINP cell. If we make the reasonable assumption that the etched arsenic diffused cell has a value of J_{ob} comparable to that found in the MINP cell, we can, as shown in table II, separate the dark saturation current of the etched arsenic diffused cell into its base and emitter components.

As discussed earlier, there is a difference of a factor of at least 5 between the J_{ob} values of the etched and the unetched arsenic cells. If this is true, and if J_{ob} in the etched cell is 0.85×10^{-13} A°/cm^2, then in the unetched cell (table II) $J_{ob} = J_o$. The emitter component (J_{oe}) must therefore be negligibly small. It thus appears that the stresses in the unetched arsenic diffused cell are capable of producing an emitter with characteristics as good as those found in the MINP cell emitter without requiring MINP-type surface passivation.

As is evident in table II, however, the good news of an improved emitter region is accompanied by the bad news that the emitter improvement is coupled with a degradation in base characteristics. To realize the potential gains involved here, a means would have to be developed to decouple base and emitter stresses, eliminating the harmful base region stresses while at the same time maintaining the beneficial emitter region stresses.

BIPOLAR DEVICES

While the unetched arsenic diffused device in figure 9 would not make a very good solar cell, it would have a distinct advantage if it were incorporated into a bipolar transistor.

It is well known that the common emitter current gain of a bipolar transistor is directly proportional to the ratio of the minority carrier diffusivity in the base to that in the emitter. It is reasonable to assume that the extremely low value of J_{oe} found for the unetched arsenic cell in table II is due to a stress induced reduction in the emitter diffusivity. The exact magnitude of the reduction is hard to determine but an estimate of about 10x would certainly be compatible with the data in table II. Conversely, for the same cell a 10x diffusivity increase in the near-junction base region would not be excessive. A ratio of the diffusivities thus indicates a two order of magnitude increase in transistor current gain should be possible through the use of a properly diffused arsenic emitter.

SUMMARY

The results of the preceeding analysis can be summarized as follows:

1) Anomalously high values of minority carrier diffusivity have been measured in both phosphorus and arsenic diffused silicon.

2) The cause of the diffusivity anomalies is diffusion induced stress.

3) Both tensile and compressive stresses can be generated in the base region, tensile stresses being more degrading.

4) Arsenic related stresses can greatly improve emitter characteristics.

5) Emitter improvements in present cells are coupled with base degradation. There is a need to develop techniques to decouple base and emitter stresses.

6) Current gain increases of 100x are possible in bipolar transistors incorporating properly designed arsenic diffused emitters.

REFERENCES

1. Weizer, V.G., et al.: Voltage-Controlling Mechanisms in Low-Resistivity Silicon Solar Cells - A Unified Approach. IEEE trans. Electron Dev., vol. 33, no. 1, Jan. 1986, pp. 156-158.

2. Weizer, V.G.; and DeLombard, R.: Minority-Carrier Mobility Anomalies in Low-Resistivity Silicon Solar Cells. Appl. Phys. Lett., vol. 49, no. 4, July 28, 1986, pp. 201-203.

3. Pauling, L.: Nature of the Chemical Bond. 3rd. ed., Cornell University Press, 1960.

4. Chou, S.; Davidson, L.A.; and Gibbons, J.F.: A Study of Diffused Layers of Arsenic and Antimony in Silicon Using the Ion-Scattering Technique. Appl. Phys. Lett., vol. 17, no. 1, July, 1970, pp. 23-26.

5. Natsuaki, N.; Tamura, M.; and Tokuyama, T.: Nonequilibrium Solid Solutions Obtained by Heavy Ion Implantation and Laser Annealing. J. Appl. Phys., vol. 51, no. 6, June, 1980, pp. 3373-3382.

6. Miyamoto, N.; Kuroda, E.; and Yoshida, S.: The Behavior of Arsenic in Silicon During Heat-Treatment. Proceedings of the 5th International Conference on Solid State Devices, Jpn. J. Appl. Phys. Suppl., vol. 43, Japan Society of Applied Physics, Tokyo, 1974, pp. 408-414.

TABLE I. - AMO OUTPUT CHARACTERISTICS FOR AN ARSENIC DIFFUSED CELL, BEFORE AND AFTER EMITTER ETCHING

Etched	V_{oc}(V)	I_{sc}(A)	J_o(A/cm^2)
Yes	0.648	0.127	3.52×10^{-13}
No	.644	.122	3.95×10^{-13}

TABLE II. - CALCULATED BASE AND EMITTER DARK SATURATION CURRENT COMPONENTS

	J_o(A/cm^2)	J_{ob}(A/cm^2)	J_{oe}(A/cm^2
MINP cell	0.85	0.85	(0)
Arsenic emitter - etched	3.52	.85	2.67
Arsenic emitter - unetched	3.95	3.95	(0)

All values x 10^{-13}

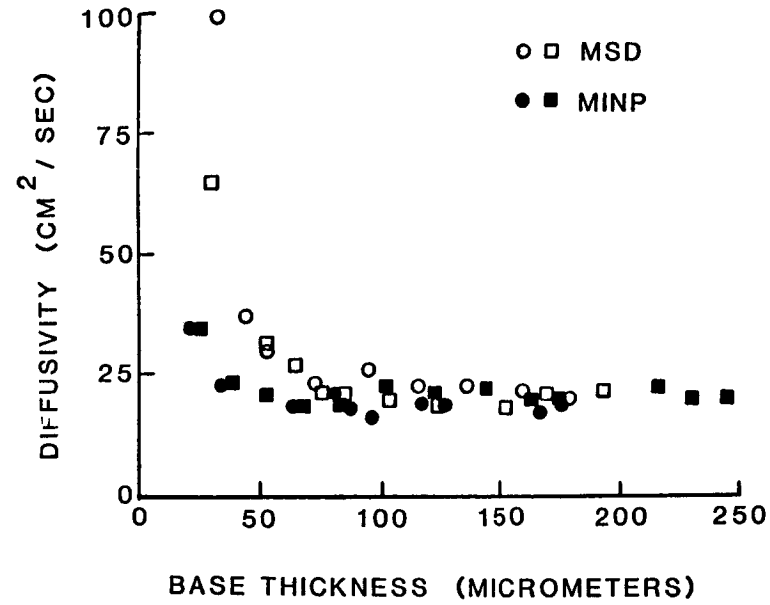

Figure 1. Measured base diffusivity as a function of base width for MINP and MSD cells.

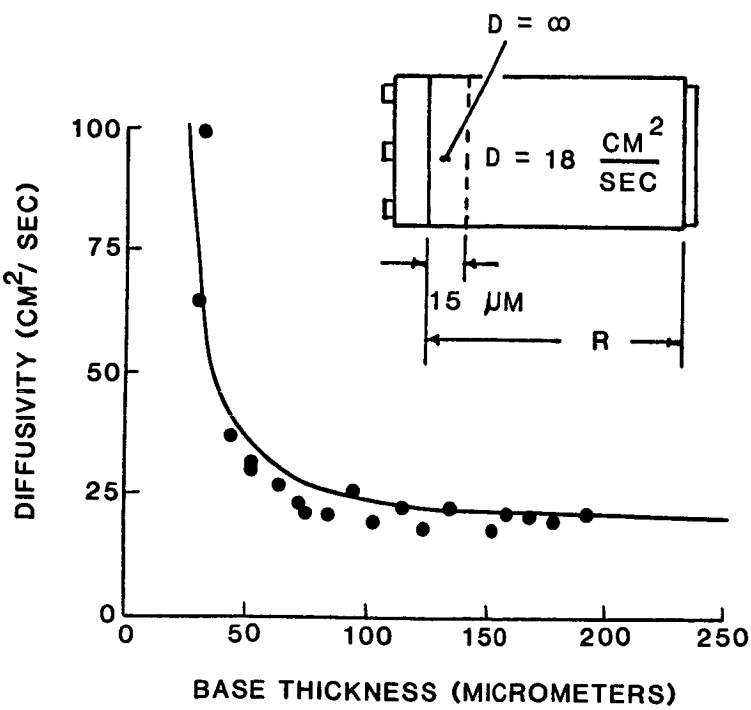

Figure 2. Theoretical fit to MSD cell diffusivity data.

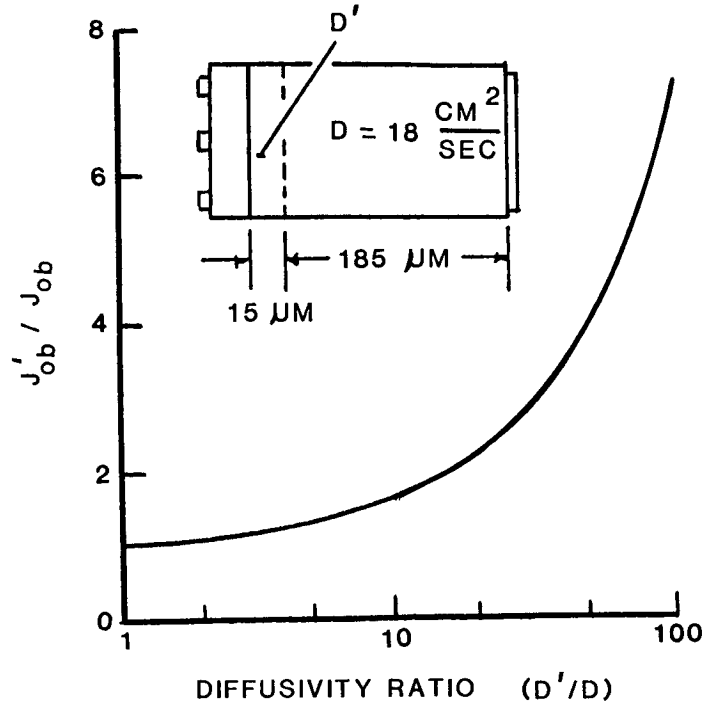

Figure 3. Calculated variation of base saturation current component with diffusivity ratio.

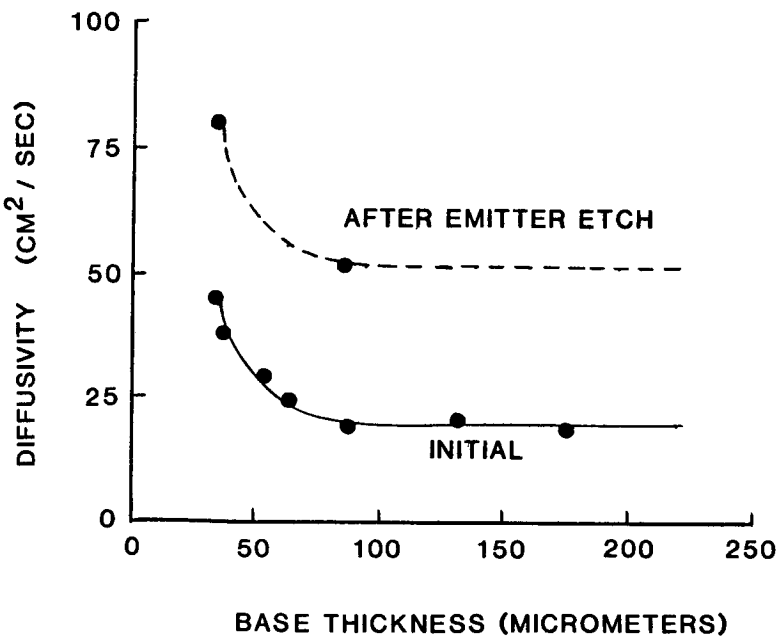

Figure 4. Effect of emitter surface etch on base diffusivity.

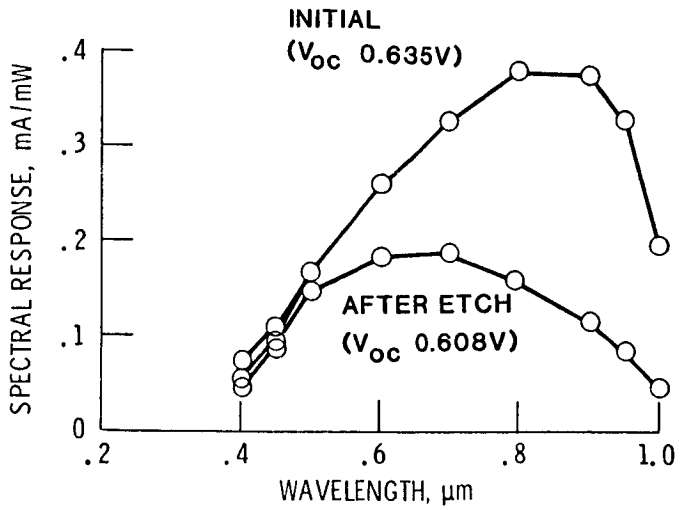

Figure 5. Measured spectral response changes with emitter surface etch.

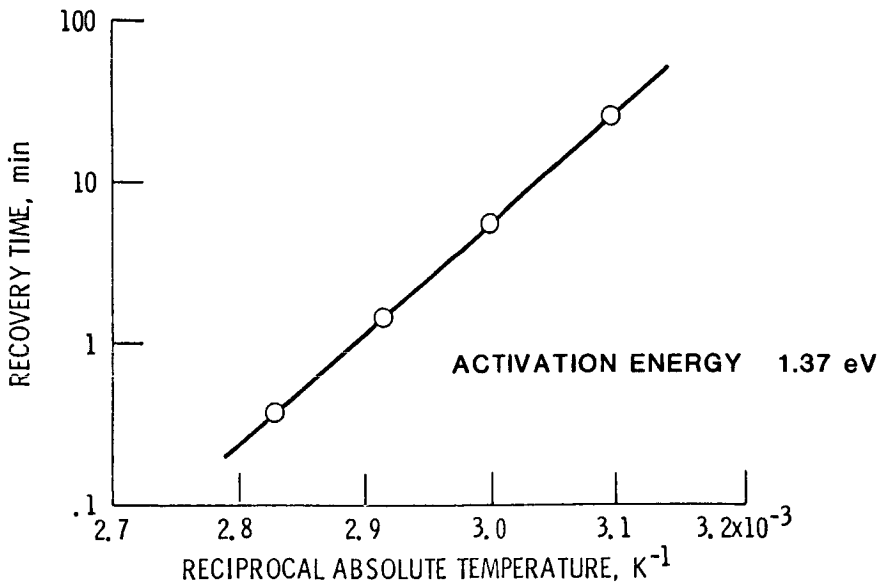

Figure 6. Thermally activated recovery time as a function of reciprocal temperature.

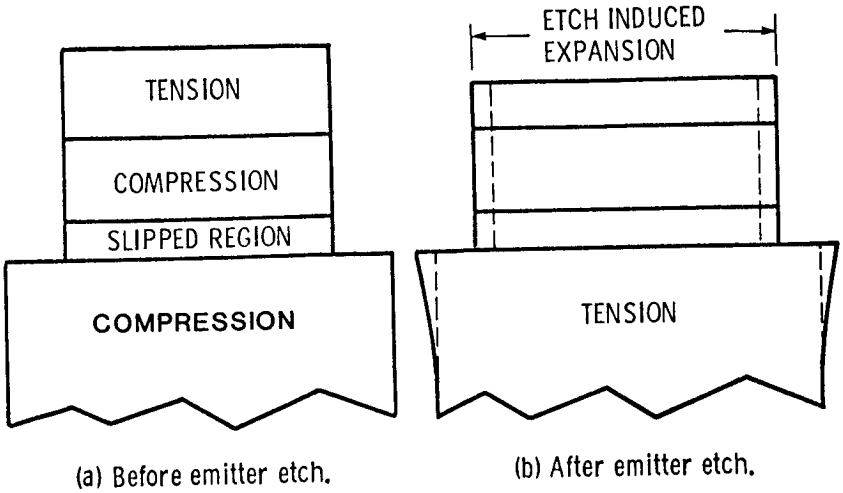

Figure 7. Schematic description of etch induced stress generation mechanism.

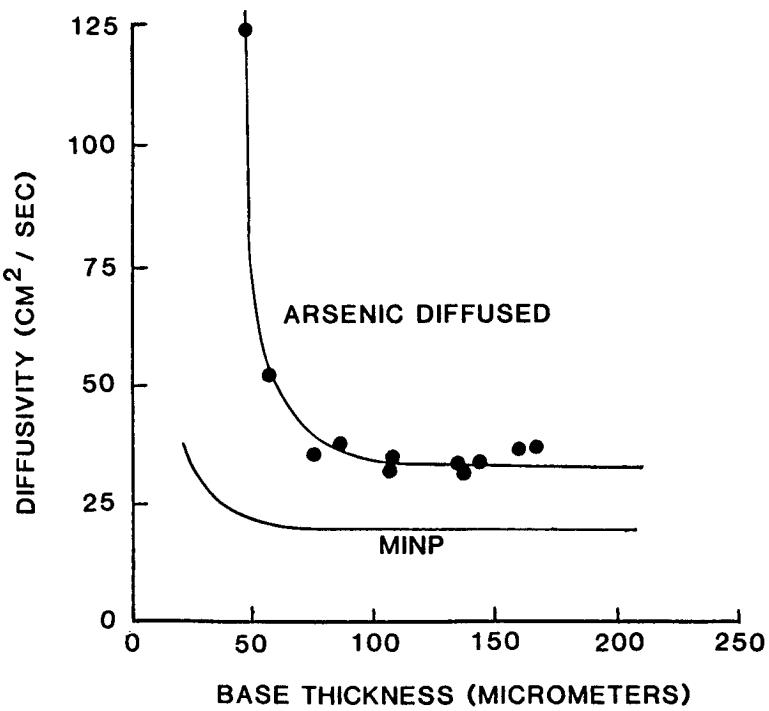

Figure 8. Measured base diffusivity as a function of base width for arsenic diffused cell.

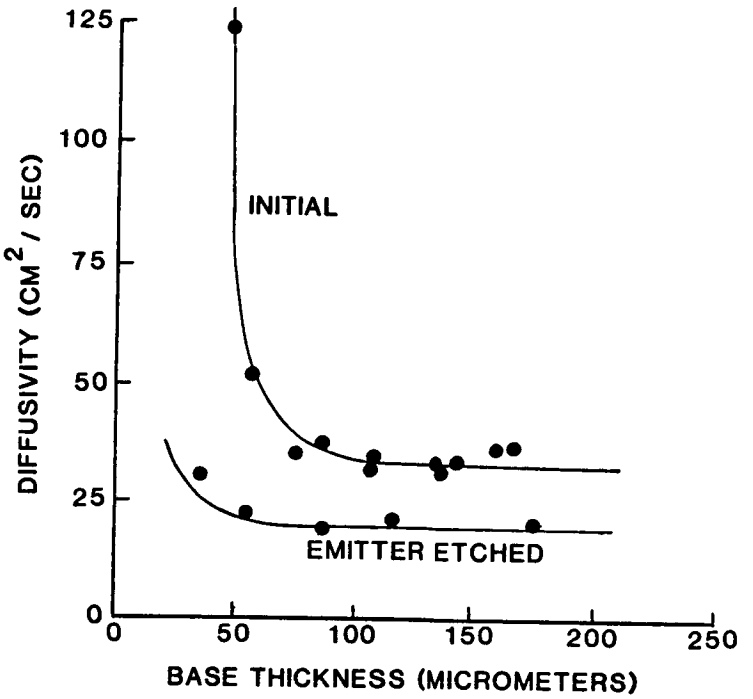

Figure 9. Effect of emitter surface etch on base diffusivity in an arsenic diffused cell.

RECOMBINATION IMAGING OF III-V SOLAR CELLS

G.F. Virshup
Varian Research Center
Palo Alto, California

An imaging technique based on the radiative recombination of minority carriers in forward-biased solar cells has been developed for characterization of III-V solar cells. The initial use of this technique has been to determine the quality of 1.93-eV AlGaAs solar cells grown by metalorganic chemical vapor deposition (MOCVD). The solar cells are forward biased until the J_{sc} reaches a threshold of approximately 100 mA/cm^2. At this current, the light emitted by 1.93-eV AlGaAs cells due to radiative recombination is sufficiently bright to be seen visually. Variations in the intensity of the light across the wafer and individual cells correlates well with various loss mechanisms. The technique is especially suited to high-bandgap cells because the emitted radiation is visible in the spectrum and the image can be recorded using regular photographic film. GaAs cells have been studied with this technique using vidicon tubes with responsivity as low as 1.15 eV.

INTRODUCTION

III-V solar cells are being developed at Varian for use in multijunction solar cells. The successful development of these cells requires an understanding of the loss mechanisms which detract from the optimal performance of the cells. Imaging the photons generated by recombination of injected minority carriers during forward biasing of solar cells has led to the identification of various loss mechanisms. Recombination images are spatial views of cell current and loss mechanisms which simplify the interpretation of complementary electrical data such as open circuit voltage, short circuit current, efficiency, and fill factor. Data which lead to the identification of three loss mechanisms in 1.93-eV AlGaAs cells grown by metalorganic chemical vapor deposition (MOCVD) is presented.

EXPERIMENTAL DESCRIPTION

Recombination imaging (RI) is based on the radiative recombination of minority carriers in forward-biased solar cells. This process occurs in direct-gap solar cells such as those in the GaAs material system. When these cells are forward biased, there is injection of minority carriers across the p-n junction. As seen in Ref. 1, these carriers recombine by both radiative and nonradiative processes, relative occurences of which are dependent on the two associated lifetimes.

The radiative recombination process yields photons having bandgap energy of the semiconducting material. A fraction of these photons escape the semiconductor. For high-bandgap materials such as 1.93-eV AlGaAs, the emitted photons can be detected by the human eye; however, an infrared viewing scope is required for viewing images from lower energy bandgap materials. For permanent images, photographic paper can record visible photons and vidicon camera image photons with energies as low as 1.15 eV.

The spatial variations of the recombination image intensity indicate regions of high or low radiative recombination, which allows qualitative evaluation of the cell quality. A schematic for setting up a RI system is shown in Fig. 1. The power supply forward biases the cell under test to a predetermined current or voltage level, at which time the imaging system produces a recombination image.

CHARACTERIZATION OF III-V SOLAR CELLS

Initial use of recombination imaging at Varian has been in the characterization of AlGaAs solar cells with bandgaps of 1.93 eV. The cells are grown by MOCVD on Bridgman D-shaped GaAs wafers. Under forward biasing, these cells emit 642-nm photons which are visible as red light.

Figures 2 and 3 are composites of recombination images of the solar cells processed from two different MOCVD growths. The cells in these figures were imaged using forward bias currents of 100 and 400 mA/cm^2, respectively. The composites allow us to see growth nonuniformities over the entire wafer. Gas flows were from right to left during the growth of both wafers.

The left side in Fig. 2 shows reduced intensity of light emission. This is interpreted as a downstream depletion of trimethylgallium and consequently higher aluminum fraction in the AlGaAs layers during growth, which results in a transition from direct to indirect AlGaAs. The recombination image of indirect gap material is of extremely low intensity due to the radiative lifetime in indirect material, as seen in Ref. 2. AlGaAs makes the transition from direct-gap material to indirect-gap material near 1.94 eV. These results are supported by photoluminescence measurements of these samples.

Table I contains the efficiency, open circuit voltage (V_{oc}), short circuit current (J_{sc}), and fill factor (FF); the information corresponds to the cells in Fig. 2. The efficiencies of the cells ranges from 2% to over 10%, with 50% of the cells between 9 and 10.5% efficiency. The average current density of these cells over the wafer is 12 mA/cm^2, while the average V_{oc} is 1.37 volts. The poor cells (efficiencies < 9%) all exhibit lower fill factors, but some (2, 6, 7, 11) have low values of I_{sc} and others (cells #9, 10) have low V_{oc}. The terminal electrical characteristics identified a problem with some of the cells, but did not explain the cause of the loss mechanisms. The causes only became clear when recombination images were compared to the electrical characteristics.

The cells with reduced image intensity (cells #2, 6, 7, 11) have an average current density of only 8 mA/cm^2. The lower current density correlates well with either a higher bandgap semiconductor or a lower quantum yield, both of which are expected for the indirect-bandgap material.

Another loss mechanism seen in Fig. 1 is the existence of point defects. These are visualized as localized dark regions scattered over the wafer. Some point defects were found to be shorting paths which lowered the open circuit voltage of the cells. Other point defects are just surface defects which block light from exiting or entering the cells. Cells 9 and 10 exhibit low open circuit voltages due to the shorting defects, while their current density is not affected. The point defects seen in cells 8 and 14 are surface defects. Also seen in Fig. 1 are disconnected grid lines which are visualized as dark regions due to the lack of current flow in the nearby regions.

Similar loss mechanisms have been seen with recombination imaging in other 1.93-eV AlGaAs growths. Figure 3 shows a wafer with downstream direct-to-indirect transition, but few point defects.

Recombination imaging has been implemented for GaAs cells whose bandgap radiation of 870 nm is beyond the sensitivity of regular photographic paper. Figure 4 is a recombination image of a GaAs space cell made using a vidicon camera with sensitivity to wavelengths as long as 1100 nm. Figure 4 also shows that point defects and disconnected grid lines can be detected in GaAs solar cells.

SUMMARY

Recombination imaging of solar cells is a simple technique that allows visual identification of direct-gap solar cell loss mechanisms. When used in mapping of whole wafers, it has helped identify three independent loss mechanisms (broken grid lines, shorting defects, and direct-to-indirect bandgap transitions), all of which resulted in lowered efficiencies. The imaging has also lead to improvements in processing techniques to reduce the occurrence of broken gridlines as well as surface defects. The ability to visualize current mechanisms in solar cells is an intuitive tool which is powerful in its simplicity.

REFERENCES

1. Sze, S. M.: Physics of Semiconductor Devices, Second Edition, John Wiley and Sons, New York, 1981.

2. Muller, R. S.; and Kamins, T. I.: Device Electronics for Integrated Circuits, John Wiley and Sons, New York.

TABLE I: Map of current-voltage measurement results from wafer shown in Fig. 2.

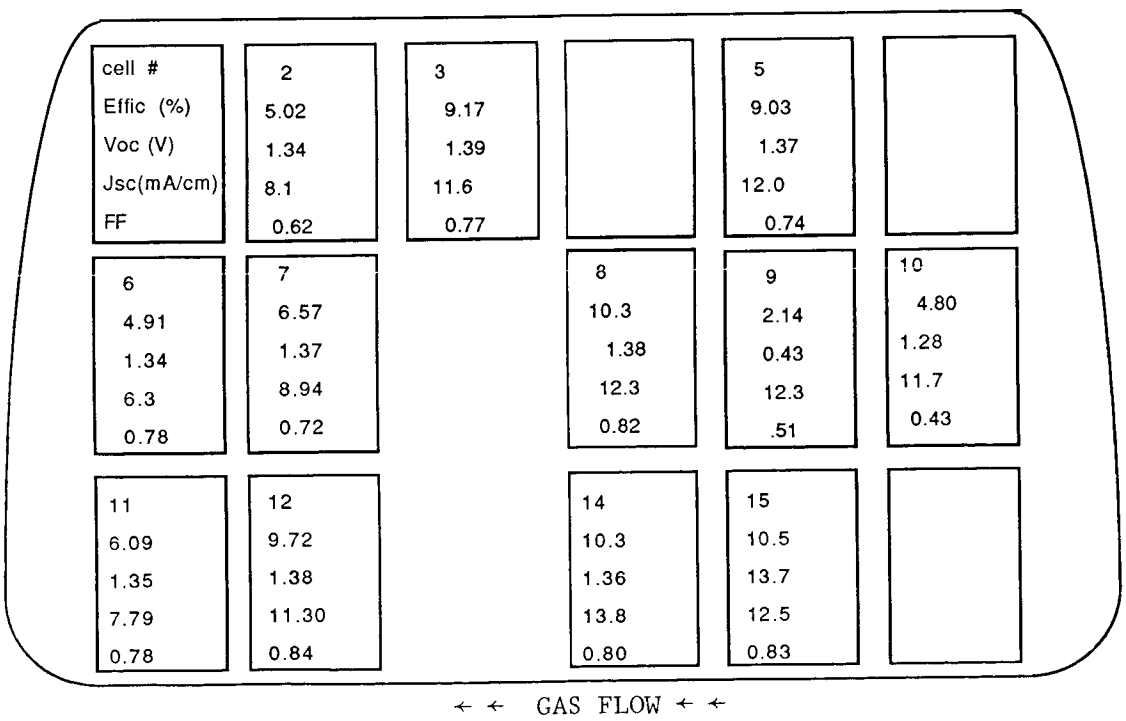

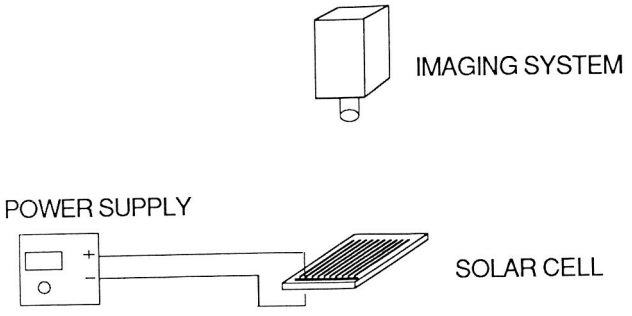

Fig. 1 Schematic of recombination imaging system.

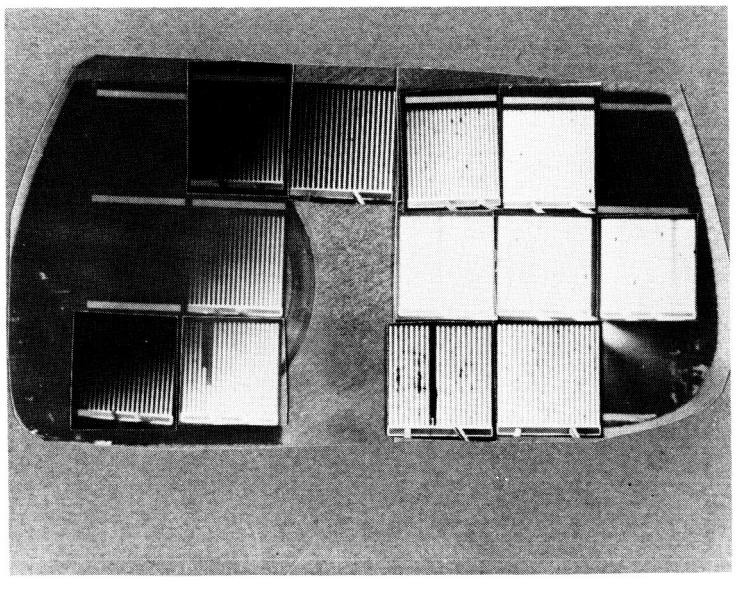

Fig. 2 Recombination image of 1.93-eV AlGaAs solar cells with 100 mA/cm^2 forward current.

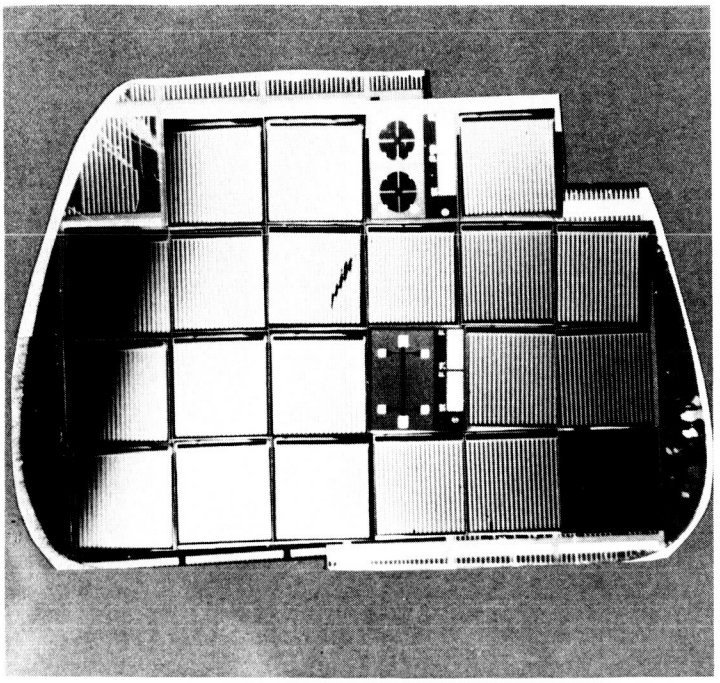

Fig. 3 Recombination image of 1.93-eV AlGaAs solar cells with 400 mA/cm^2 forward current.

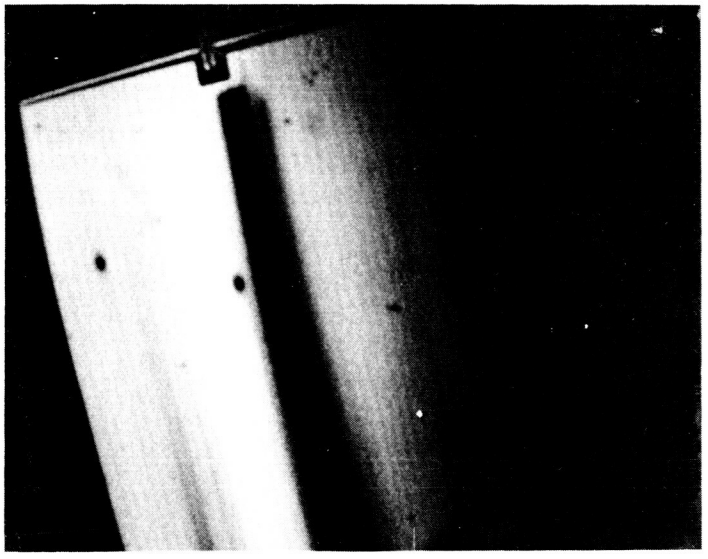

Fig. 4 Recombination image of GaAs space cell. Imaged using vidicon tube.

Light Emission as a Solar Cell Analysis Technique

Christiana Honsberg and Allen M. Barnett
University of Delaware
Newark, Delaware

1. Solar Cells and Light Emitting Diodes

Since solar cells and light emitting diodes first came into common use, they have largely been considered separate areas. The information determined from one was not directly applicable to the other. However, there are many similarities between solar cells and light emitting diodes (LEDs) which suggest the potential use of light emission for solar cell analysis. Solar cells and LEDs both operate in forward bias. However, solar cells absorb light to generate current whereas LEDs require injected current to generate light. In other words, light drives a solar cell into forward bias and generates energy in the form of current at a certain voltage. In contrast, injected current in a LED drives the LED into forward bias and generates energy in the form of light. The use of light emitted from the surface of the solar cell has not been widely used as a technique to analyze solar cells.

In order to determine if a solar cell would indeed emit usable light as expected, a GaAs solar cell was forward biased and examined with an infrared viewer. The light emitted from the solar cell was not uniform, even though the I-V curve of the solar cell displayed no defects.

2. Solar Cell Background

A solar cell, like a LED, is a semiconductor p-n junction. However, the structure of the solar cell is somewhat different than a standard semiconductor diode, since the depletion region must be near the surface in order to efficiently collect photogenerated carriers. This special structure, which in practical terms implies a very thin collector, makes the solar cell vulnerable to certain defects. Most of these defects can be simply modeled and affect the I-V curve. However, the model does not distinguish between microscopic and macroscopic defects, while the I-V curve will detect only macroscopic defects. Nevertheless, microscopic defects (which can include shunt defects) can lead to device failure. Defects which lead to device failure (mostly shunts and irregularities at the junction) are the subject of this work.

3. Light Emission

Since light emission begins at the junction and passes through the collector to the surface, any defects in this region will affect the pattern of light emission. Two types of light emission can be used to analyze solar cells. The first, forward biased light emission is the radiative recombination of carriers and is the mechanism operating in LEDs. In order for a semiconductor to emit light in forward bias, there must be sufficient radiative recombination of carriers and

incomplete absorption of the radiative recombination. This works well if the material has a direct band gap, and if enough carriers can be injected and radiatively recombine so that the light can be detected at the surface of the solar cell. Additionally, the collector must not be so thick that all the light is internally re-absorbed.

Forward biased light emission is strongly dependent on the threshold current density flowing through each part of the solar cell. In areas of the solar cell with a higher current density, the light will be emitted with greater intensity than in areas with a lower current density. Consequently, the overall current flowing through the device alone does not provide much information, but must be used only in conjunction with the pattern of the light emitted from the surface. The threshold current density also determines, by the diode equation, what the threshold voltage for light emission will be. Light emission is sensitive to local variations in the current and voltage that will not affect the overall I-V curve.

The reverse biased light emission is also strongly dependent on the localized current density. However, the mechanism by which current flows across the junction and by which light is emitted is quite different than that involved in forward bias light emission. Current begins to flow across the junction due to avalanche breakdown. However, avalanche breakdown does not occur uniformly across the junction, but begins where the applied voltage is higher or the voltage required to begin avalanche breakdown is lower. Consequently, current flows only through certain small areas of the junction. Due to the carrier multiplication in avalanche breakdown, large amounts of current flow through the small areas undergoing avalanche breakdown. This high current (and power) density heats the lattice to the point where the areas undergoing avalanche breakdown begin to emit black body radiation in the visible region.

4. Mechanisms Affecting Light Emission

A solar cell completely free from any defects should emit light uniformly across the entire surface in forward bias. However, there are several mechanisms which will cause variations in the ideal uniformity of the light. Of major importance are those due to defects which may lead to catastrophic failure. One such defect is a shunt defect. Shunt defects, which greatly reduce the power available from a solar cell, are very common and with the advent of new thin film solar cells may become even more frequent. Shunts are usually caused by punch-through of the metal grid-pattern across the very thin collector. As can be seen from the model of a solar cell, a shunt defect acts like a current divider between the shunt defect and the area of the junction without the shunt defect. At a fixed voltage, lower shunt resistance results in more current flow through the shunt, but not less across the junction unaffected by the shunt. Consequently, the total current flowing through the solar cell when light emission begins increases while the voltage present across the solar cell remains the same. The total current will be inversely proportional to the shunt resistance, while the current density flowing across the junction needed to begin light emission remains the same.

The area near a shunt defect will not emit light. Since there are no injected minority carriers in the region of a shunt, there are no carriers to recombine and cause radiative recombination. The location of the shunt affects the pattern of light emission from the surface of the solar cell. If the shunt occurs in the bulk of the material, the solar cell will behave in the way the ideal

model predicts, and only the small area around the shunt will not emit light. Shunts in the bulk of the material may migrate to the grid pattern and cause device failure.

If the shunt occurs along the grid pattern, portions of the solar cell will be shorted out and will remain dark. If the shunt occurs along the grid line, no current will flow through the entire region from which the grid line previously collected current. In other words, the shunt on the grid bar shorts out this entire region, much the same way in which many resistors in series will be shorted if a much lower resistor is put in in parallel with some of them. Consequently, all areas of the solar cell from which the grid line collected current will remain dark. In addition, the current going through the entire device will be much larger than if a shunt is not present, or if the shunt was only in the bulk of the material. The voltage measured at the probe will be slightly higher than a solar cell without a shunt, due to current crowding at the probe. The voltage is measured only at a single point, the probe. The entire current flowing throughout the device must flow through the probe. The higher current creates a larger voltage drop vertically across the grid bar. Since the measured voltage at the probe takes into account this voltage drop, the actual voltage across the junction unaffected by the shunt is somewhat less than the measured voltage. The voltage is higher only along the path from the shunt to the bus bar. The rest of the junction has the threshold voltage present across it.

The third place a shunt can form is on the bus bar. In this case, the entire junction is shorted out. This implies only that the majority of the current flows through the shunt rather than across the junction of the solar cell. If enough current flows through the shunt, the voltage can increase until the necessary current density to begin light emission is forced across the junction. Again, as in the case with the shunt occurring on the grid line, the voltage will be higher along the the path through which the shunt current flows, due to current crowding.

A second mechanism which affects the light emitted from the surface of the solar cell is the presence of irregularities at the junction. These defects are not detectable under examination of the I-V curve, but can also lead to catastrophic failure by lowering the reverse breakdown voltage, a key parameter in nearly all applications of the solar cell. In all practical applications the solar cells are grouped into arrays, usually groups in series and these groups parallel. If shade covers a solar cell, the solar cells that are still in the sun will drive the shielded solar cell into reverse breakdown, and possibly catastrophic failure. This will reduce the power from the entire array. It can be very difficult to test for this defect. The areas containing irregularities will not emit light, or may emit light at a higher (or lower) current.

Another mechanism which will affect the pattern of light emission from the surface of the solar cell is an non-uniformly applied voltage. The voltage may be unevenly applied due to current crowding, series resistance, or cracks.

Finally, the light may be altered by some of the light being blocked. This can be due either to dirt or to an excessively thick collector.

All these types of defects can be distinguished from each other by examining the current density needed to begin light emission and the pattern of the light emission. A shunt defect is the only type of defect which will increase the current density and possibly voltage needed to begin light emission. Any cracks can be distinguished from other defects by the fact that the

region between a light area and a dark area is very sharply defined. Additionally, dark areas will extend to the edges of the solar cell in at least one direction. A close visual examination may reveal a crack. Dirt on the surface of the solar cell should also have sharply defined edges but in an irregular pattern and may also be visible upon a close visual examination. Light blocked by a collector that is too thick will have very fuzzy edges, and the dark areas should become slightly smaller as the current is increased. Also, cracks, dirt, and uneven collector will all lower the short circuit current. Irregularities in the junction will affect the reverse breakdown voltage of the solar cell, but not the forward characteristics. They may have either a regular shape or an irregular shape. The edges as well may appear to be slightly fuzzy.

5. Experimental Procedure and Results

Light emission is especially useful for detecting defects that can lead to catastrophic failure. The two major types of defects that can lead to catastrophic are shunt defects and irregularities at the junction. In order to test for shunt defects, solar cells free from shunt defects were obtained from Joseph F. Wise of the U.S. Air Force Wright Aeronautical Laboratories. Shunt defects were then induced, and based on the light emission, the location of the shunt defect was determined and the shunt removed. The presence and location of irregularities was also determined. The procedure to demonstrate this is given below.

1. The I-V curves of the solar cells were measured to insure that there were no shunt defects present.

2. The forward biased light emission was recorded to determine the presence of any irregularities.

3. The solar cell was reverse biased until avalanche breakdown occurred.

4. The light during avalanche breakdown emission was photographed to confirm the presence and location of irregularities.

5. In order to induce a shunt defect, the avalanche current through the solar cell was increased until irreversible breakdown occurred, and the light emitted was again photographed.

6. The solar cell was forward biased and the light emission photographed.

7. The I-V characteristics of the solar cell were measured.

8. The solar cell was cut were the forward and reversed biased light emission predicted the shunt to be.

9. Both halves of the solar cell were re-examined.

All the solar cells behaved very similarly except where avalanche breakdown occurred, and the value of the reverse breakdown voltage. Both depend on the presence of irregularities at the junction.

The solar cell shown in Figs. 1 to 4 contains many irregularities at the junction, probably doping variations or dirt at the junction of the solar cell. The many dark areas in Fig 1b predict the presence of irregularities. Theoretically, these irregularities should correspond to regions where the avalanche breakdown voltage is lower, and they should begin to conduct current sooner than the rest of the junction. Since the reverse bias light emission is dependent on the current density through each area, regions with irregularities should emit light in reverse breakdown. Consequently, Fig 1c confirms the prediction of Fig 1b that there are many irregularities at the junction. The avalanche breakdown voltage was rather low, approximately 2.5 V. The solar cell in Fig 1c has not suffered irreversible breakdown, only avalanche breakdown. In order to induce a shunt defect, the current in avalanche breakdown was increased until irreversible breakdown occurred. Once the shunt was induced, the resistance in this region became lower, so most of the current began to flow through the newly created shunt defect. This accounts for the greater intensity of the light being emitted at one location once irreversible breakdown occurred. Due to the heating of the grid pattern through which the shunt current flowed, some areas of the grid pattern also became shunted. The extent to which this happened depended on how long the irreversible breakdown current was flowing through the solar cell. The shunting happened first where the power density (corresponding to the current density) was the highest. Consequently, the light seemed to move from its original location to the probe. This accounts for the slightly oval shape of the light in Fig 2a. Fig 2b, like Fig. 2a, predicts that the shunt occurred on the second grid line from the left. This location of the shunt defect was confirmed by removing the region expected to contain the shunt. The area predicted to contain the shunt did indeed display severely shunted characteristics (Fig. 4b compared to Fig. 3b) while the other region regained nearly identical characteristics to those of the original solar cell. Some shunting effects are present due to heating of the bus bar, while the current is slightly lowered due to cutting damage or inaccuracies in area measurement.

The other sample shown behaved similarly except that there were fewer irregularities at the junction. The light emitted in forward bias predicts fewer irregularities. Fewer spots suffering avalanche breakdown (see Fig 6a), combined with a higher avalanche breakdown voltage (5 V) confirms the prediction of fewer irregularities. Again, the forward bias light emission and reverse bias light emission both indicated that the shunt was on the third grid bar from left. When this area was removed, half of the solar cell displayed normal I-V characteristics (Fig. 7a compared to 8a) while the half which was predicted to contain the shunts, showed severely shunted characteristics (Fig. 7b compared to Fig. 8b).

6. Conclusion

Solar cells and light emitting diodes are similar devices. A solar cell, if under light, can charge a battery, while the battery in turn can cause the solar cell to emit light like an LED. Since the solar cell can be used as two separate devices, it can be used to test itself.

Two types of light emission, forward bias and revrese bias, can be used to test the solar cell. Defects which are not readily apparent when examining the I-V curve (but can lead to device failure) can be detected using light emission. Two such common defects are irregularities at the junction and shunt defects. Both forward and reverse bias light emission can detect these types of shunts. Other, grosser defects are also readily apparent using light emission. These can include shunt defects, cracks, dirt, and an excessively thick collector. By examining the I-V

characteristics of the solar cell, and the current density needed to begin light emission, localized information about the solar cell can be obtained and the type of defect can be determined.

Further work would include investigation into the nature of the irregularities that lower the reverse breakdown voltage. In addition, quantification of this method can lead to the development of a useful quality assurance procedure which can evaluate and predict the performance of solar cells.

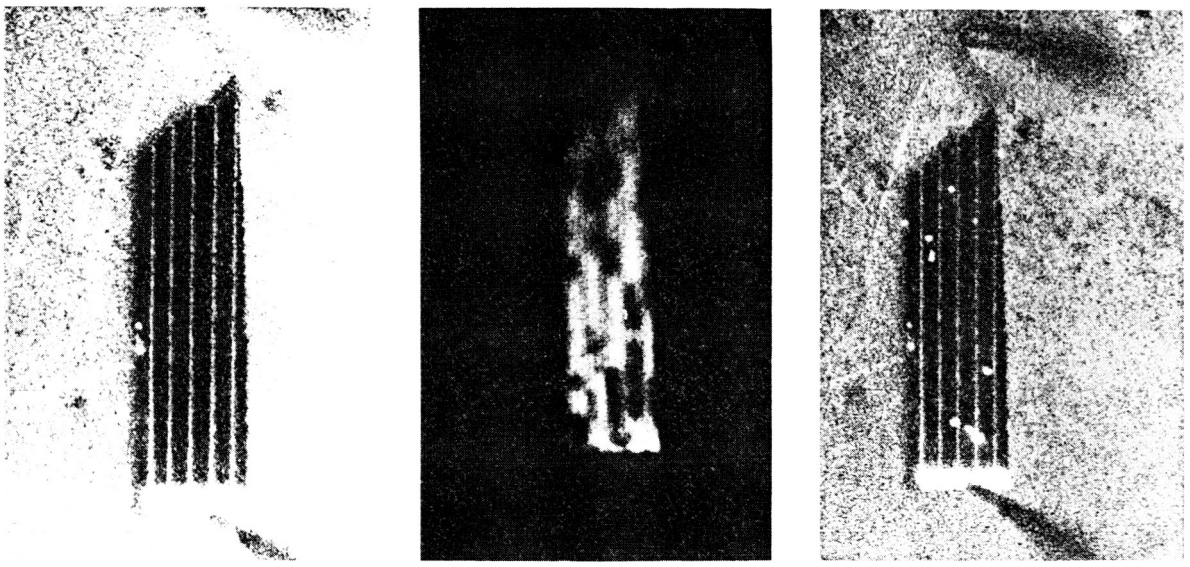

a) b) c)

Figure 1 Sample h332d a) The solar cell with no bias present across it. b) The forward bias light emission before a shunt was induced. The dark rectangle at the bottom is the bus bar. The faint vertical lines are the grid lines. The irregular dark areas correspond to irregularities at the junction. c) Reverse bias light emission before the shunt defect was introduced. The white areas are emitting light. As the theory predicted, the dark areas in b) and the light areas in c) are in similar locations.

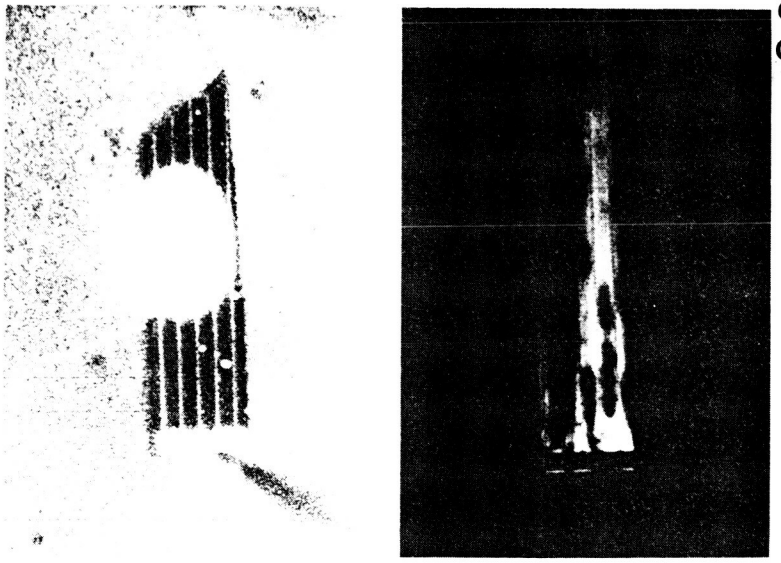

a) b)

Figure 2 Sample h332d a) The reverse bias light emission when the shunt was induced. The light emission appears to be oblong because the shunt is beginning to burn its way to the probe. b) The forward bias light emission after the shunt was induced. The light emission predicts the shunt to be on the second grid bar from the left. The shunt is further down than Fig. 1c suggests because the shunt continued to move towards the probe after the picture was taken.

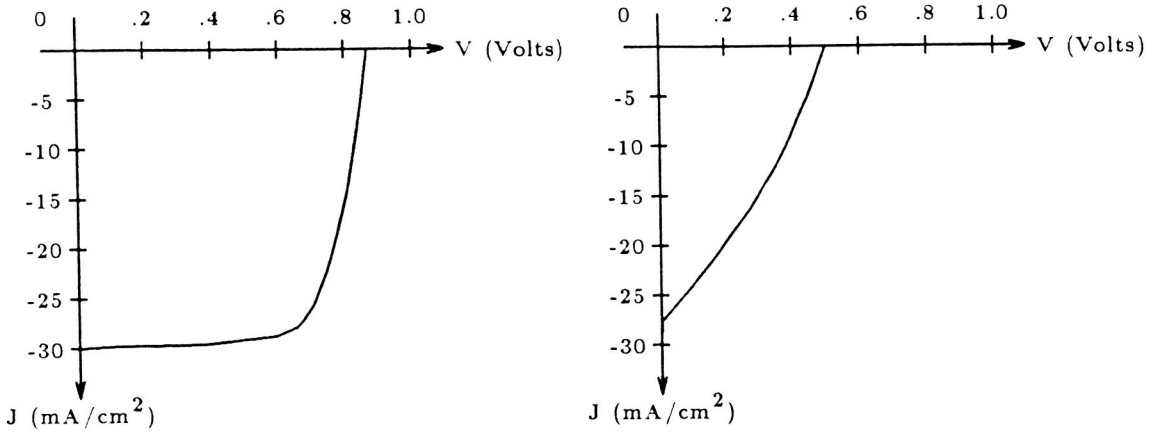

a) b)

Figure 3 Sample h332d a) The I-V curve of the solar cell before the shunt was induced. b) The I-V curve of the solar cell after the shunt was induced.

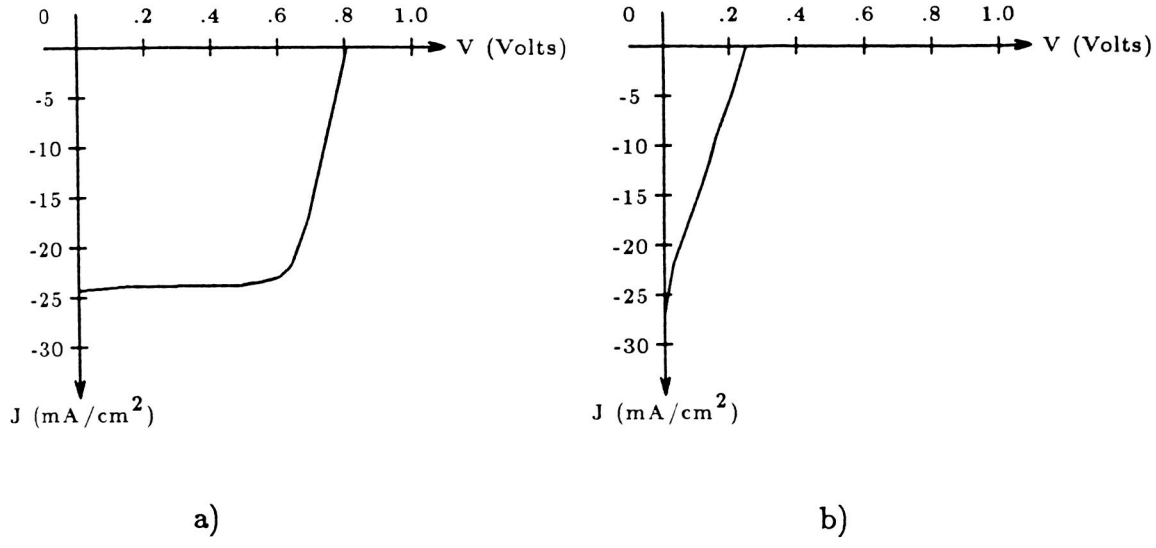

Figure 4 Sample h332d a) The I-V curve of the area predicted not to contain the shunt. The curve is not identical to that in Fig. 3a due to heating of the bus bar and cutting damage. b) The I-V curve predicted to contain the shunt.

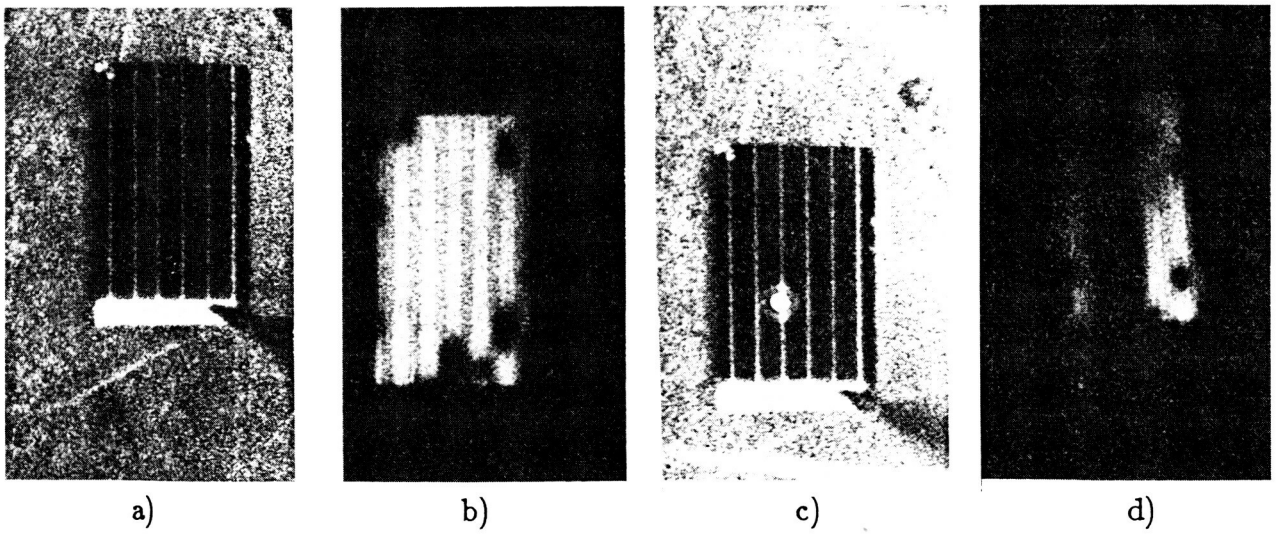

Figure 5 Sample h339d a) The solar cell without any applied bias. b) The in forward bias light emission. The light emission is fairly uniform. c) The reverse bias light emission. Since the light from forward bias light emission is fairly uniform, there should be few areas emitting light in reverse bias. In this sample, only one area underwent avalanche breakdown, so the reverse bias light emission before and after the shunt was introduced will be the same. d) The forward bias light emission. The shunt was predicted to be on the third grid bar from the left, near the bottom of the solar cell.

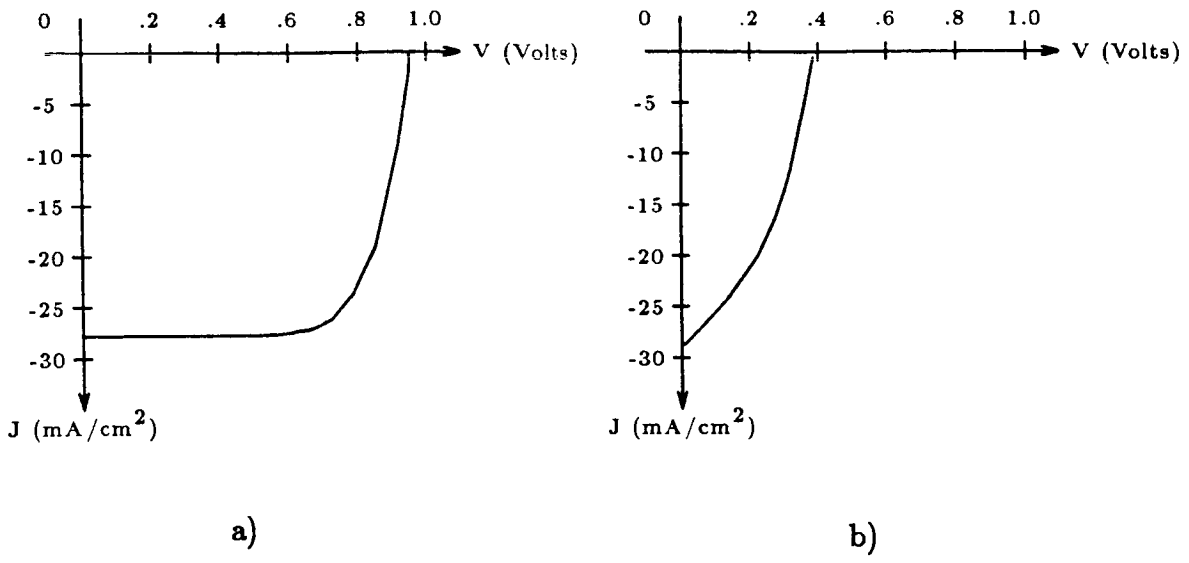

Figure 6 Sample h339d a) The I-V curve of the solar cell predicted to contain the shunt. b) The I-V curve after the shunt was induced.

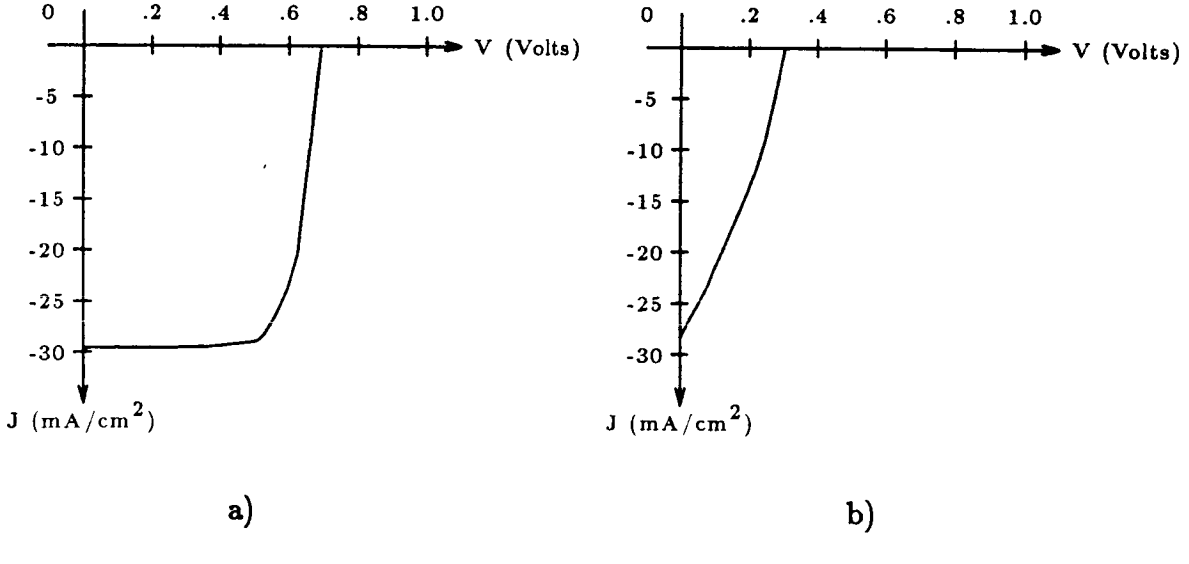

Figure 7 Sample h339d a) The I-V curve of the area predicted not to contain the shunt. b) The I-V curve of the area predicted to contain the shunt.

C-3

ELECTRO-OPTICAL CHARACTERIZATION OF GaAs SOLAR CELLS*

Larry C. Olsen, Glen Dunham, F.W. Addis, Dan Huber, and Dave Daling
University of Washington
Seattle, Washington

This paper concerns electro-optical characterization of MOCVD GaAs p/n solar cells. The objectives of these studies are to identify and understand basic mechanisms which limit the performance of high efficiency GaAs solar cells. The approach involves conducting photoresponse and temperature dependent current-voltage measurements, and interpretation of the data in terms of theory to determine key device parameters. Depth concentration profiles are also utilized in formulating a model to explain device performance.

CELL FABRICATION AND PERFORMANCE

Solar cell structures studied are described by figure 1. MOCVD film structures were grown according to specifications by industrial suppliers. Metallization, cap removal, and AR layer deposition are done at the Center. SiN_x deposited by plasma-enhanced CVD (PECVD) is utilized as a single AR coating. AM1 efficiencies in the range of 17% to 18% have been achieved with cells fabricated as discussed. Cells are typically 1.5 cm x 1.5 cm.

PHOTORESPONSE

Spectral photoresponse studies are used to determine values for the front recombination velocity, S(F), the emitter minority diffusion length, L(F), and the base minority carrier diffusion length, L(B). We typically find L(F) to be 3 to 5 μm, and S(F) in the range of 10^4 to 10^5 cm/sec. The devices under study are emitter dominated cells. As a result, the internal photoresponse is rather insensitive to the base diffusion length. Two particularly interesting results have been obtained, namely: a light biasing effect; and the apparent existence of a 'dead layer' in the p-GaAs region, adjacent to the AlGaAs layer.

The internal photoresponse is plotted for a cell under dark and biased conditions in figure 2. Under dark conditions, the surface recombination velocity is on the order of 10^6 cm/sec. With the cell illuminated by approximately AM1 illumination, the internal photoresponse indicates S(F) = 10^4 cm/sec. The light biasing effect is observed to occur after SiN_x deposition. Prior to silicon-nitride deposition, the value of S(F) is typically in the range of 10^4

* Work supported by the Air Force Office of Scientific Research, Grant AFOSR-84-0355.

to 10^5 cm/sec, and is the same under both dark and illuminated conditions. Depth concentration profiles taken by Auger spectroscopy indicate that a significant level of oxygen exists at the SiN_x-AlGaAs interface after silicon-nitride deposition. A possible explanation for the light biasing effect is that excess oxygen exists at the GaAs-AlGaAs interface giving rise to recombination centers that saturate when cells are subjected to AM1 illumination. We are not aware of any other reports of this light biasing effect in GaAs cells.

Figure 3 describes calculated internal photoresponse curves assuming S(F) = 2×10^5, L(F) = 5 μm, and four thicknesses for the 'dead layer'. Referring to figure 4, layer 2A is the so-called dead layer. It is assumed that this region of GaAs is characterized by a negligible minority carrier lifetime. As indicated in figure 3, it is found that the experimental curve for the internal photoresponse can only be fit by selecting a finite value for the dead layer thickness. We interpret this result as indicating that the transition region between GaAs and AlGaAs is very defective. This conclusion is supported by depth concentration profiles obtained by Auger spectroscopy.

T-I-V ANALYSES

Current-voltage analyses have been carried out at various temperatures between 250°K and 400°K. Data are taken under dark and illuminated conditions. A computer based data acquisition system is utilized to obtain data points as desired at each temperature. Data are then interpreted in terms of theory. We find that I vs. V under dark conditions and I_{LOSS} vs. V (where $I_{LOSS} = I_{PH} - I$) under illuminated conditions can be interpreted in terms of two current mechanisms acting in parallel, one dominant at low voltages and one dominant at high voltages. Figure 5 describes typical results for the loss current vs. voltage measured under illuminated conditions. The two mechanisms are apparent. The low voltage mechanism can usually be interpreted as involving multiple-step tunneling. The upper mechanism is due to minority carrier injection or space charge recombination. In cases for which the high voltage mechanism is due to minority carrier injection, $n = 1.00$ and $J_0 \simeq 3 \times 10^{-19}$ A/cm^2. When space charge recombination is dominant, n takes on values anywhere between 1.0 and 2.0, indicating that a wide range of recombination levels may be active in the junction regions. These investigations suggest that the device edges are the sources of loss currents due to multiple-step tunneling, as well as loss currents resulting from space charge recombination.

PHYSICAL CHARACTERIZATION

Depth concentration profiles for the same device for which internal photoresponse data is described in figure 2 are depicted in figure 6. The GaAs-AlGaAs transition region appears to be on the order of 400 Å wide. Furthermore, as noted above, a relatively high concentration level of oxygen exists in the top layers of the device. In particular, these results suggest that a relatively high level of oxygen may exist in the GaAs-AlGaAs transition region. It is proposed that the wide transition region and oxygen impurity level are responsible for both the light biasing effect and the dead layer.

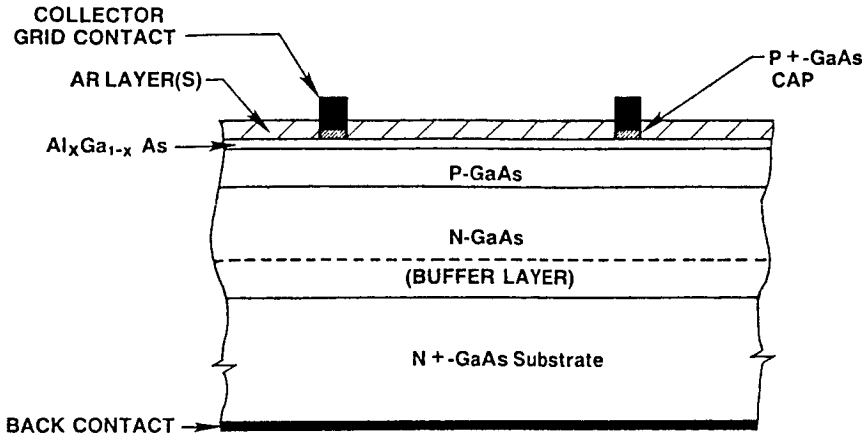

LAYER	LAYER DESCRIPTION	DOPANT CONCENTRATION (cm^{-3})	LAYER THICKNESS
4	CAP : GaAs (P)	$>10^{18}$	.10
3	Al_xGa_{1-x}, x = .85	$>10^{18}$	.025
2	GaAs (P)	10^{18}	1.0
1	GaAs (N)	10^{18}	3.0
SUBSTRATE	GaAs (N)	$>10^{18}$	15 mils

Figure 1. GaAs Solar Cell Structure.

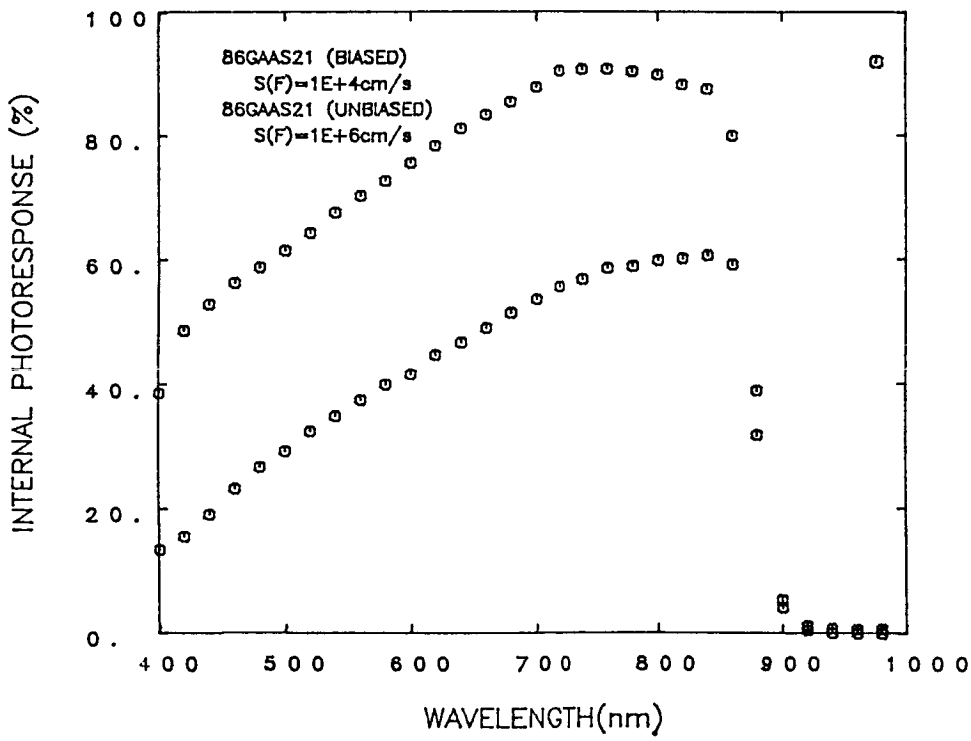

Figure 2. Internal Photoresponse of GaAs Cell Exhibiting Light Biasing Effect.

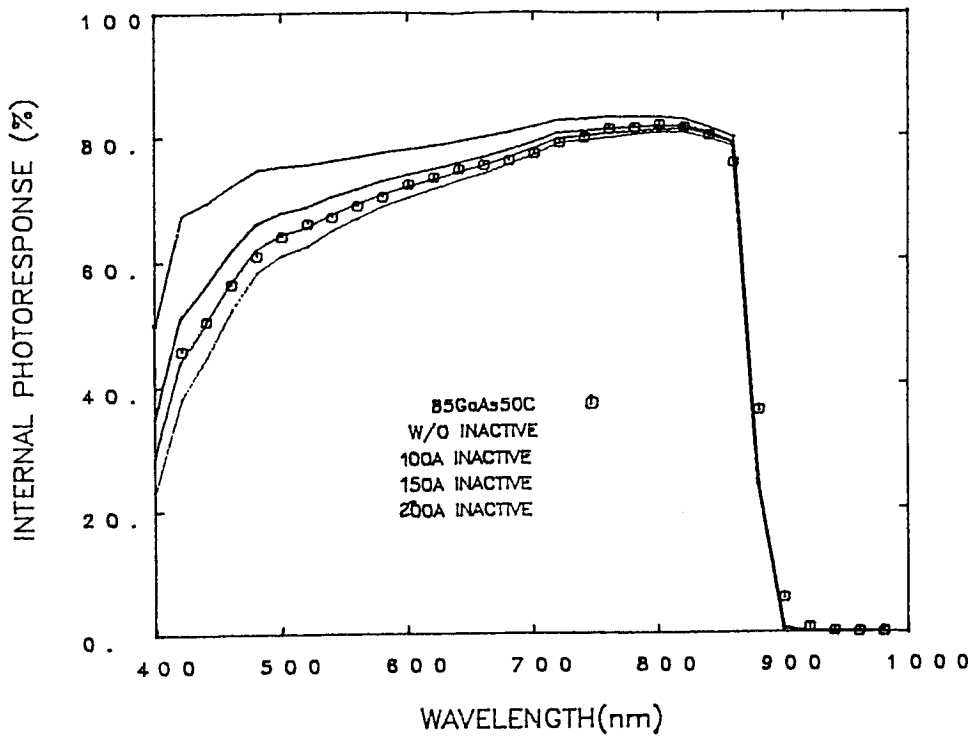

Figure 3. Effect of 'Dead Layer' on Fitting of Photoresponse Data.

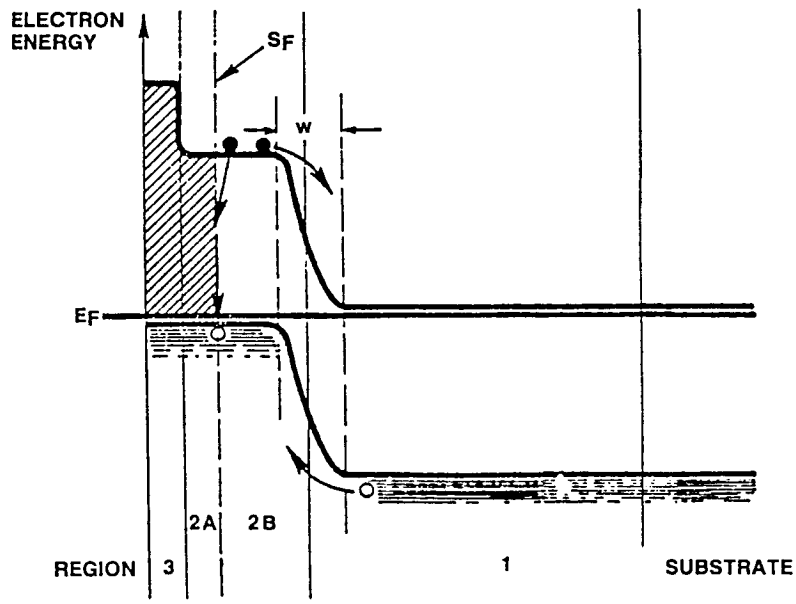

Figure 4. Electron Band Diagram Showing Location of 'Dead Layer'.

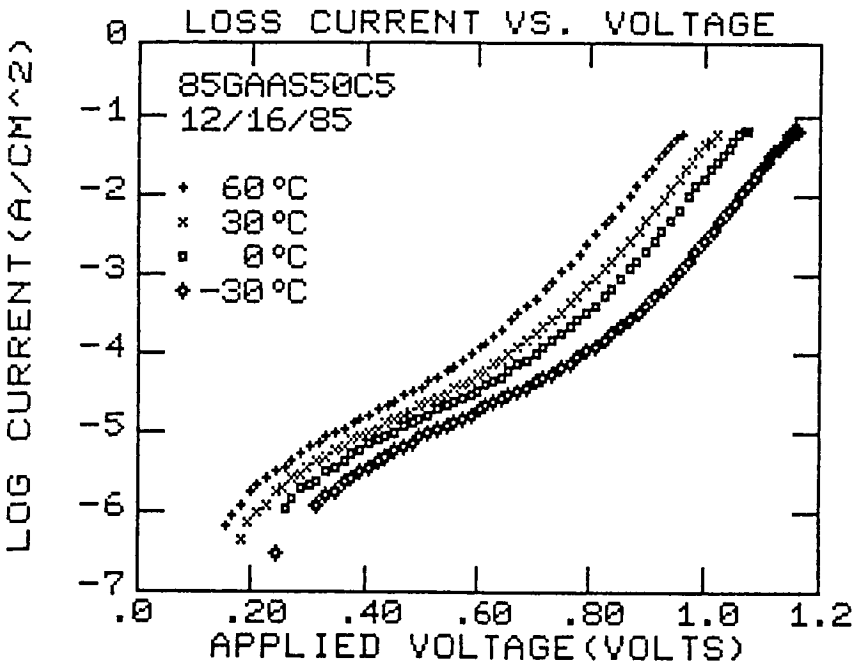

Figure 5. T-I-V Data for GaAs Cell.

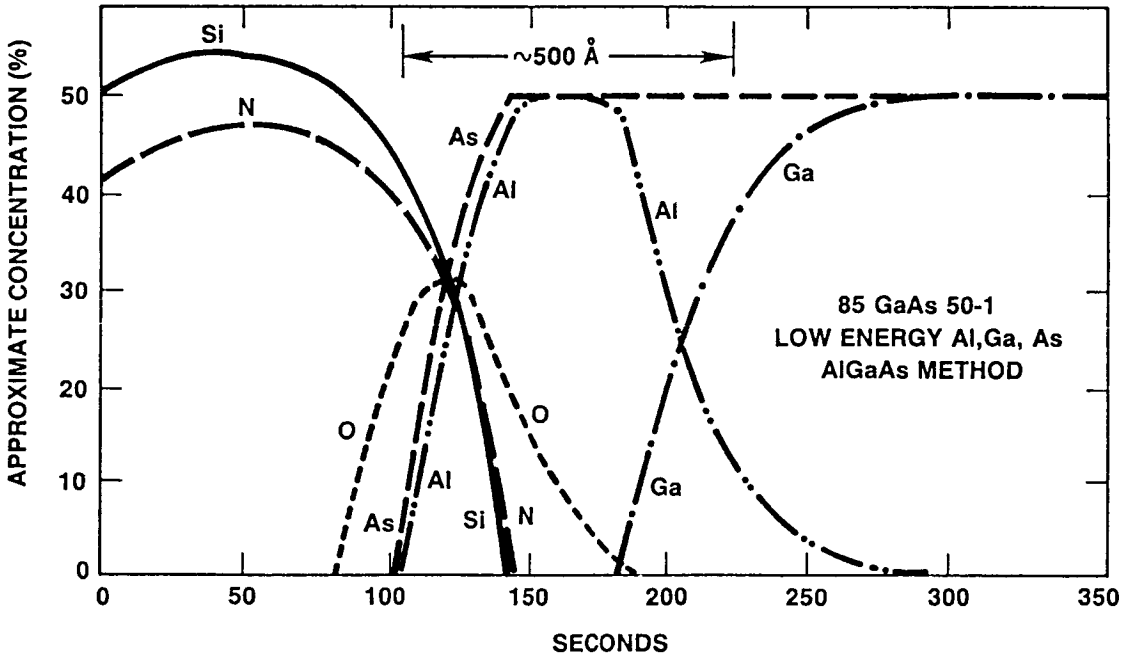

Figure 6. Depth Concentration Profiles Through Heteroface Region of GaAs Cell with 500 Å $Al_{.85}Ga_{.15}As$ Window.

THE USE OF MULTIPLE EBIC CURVES AND LOW VOLTAGE ELECTRON MICROSCOPY IN THE MEASUREMENT OF SMALL DIFFUSION LENGTHS

R.P. Leon
NASA Lewis Research Center
Cleveland, Ohio 44135

Diffusion length measurements were made in highly doped and radiation damaged III-V semiconductors using the technique of charge collection microscopy (sometimes known as electron beam induced current (EBIC)). EBIC curves were plotted while using the SEM on a line scan mode. Values of the currents read from these curves were then equated to expressions obtained from the solution of the diffusion equation for a thick sample. An extended generation function was used in order to account for the finite volume of the induced minority carriers. The surface recombination velocity was either treated as an unknown in a system of two integral equations, or measured directly using low accelerating potentials for the electron beam.

With the emergence of III-V compounds in the field of photovoltaics, it has become increasingly more important to have accurate methods for determining small (1 to 10 μm) diffusion lengths L. A reliable determination of the values of L is necessary in device modeling, radiation damage studies, and device fabrication since it is quite important to be able to assess the damage to the electronic properties of materials subject to certain processes.

Figure 1 shows the configuration that has been used to make these measurements. The depicted geometry was chosen to permit direct measurements to be made on finished solar cells. The contacts used were ohmic ones made with evaporated thin films of gold. The current amplifier had fast response, low noise, low input imped ance, and the gain was calibrated. The leads were shielded, and the circuit ground was separated from the SEM ground.

When energetic electrons impinge on semiconducting material, electron hole pairs are created. The required ionization energy is a function of the bandgap (ref. 1). In GaAs it takes 4.5 eV of incoming radiation energy to create a minority carrier. If one assumes no surface recombination, and point generation of minority carriers, the collected current follows a simple exponential decay form:

$$I_{cc} = I_o e^{-x/L} \qquad (1)$$

where

I_o maximum current collected (PN junction)
L diffusion length
X distance from PN junction

However, the surface recombination can be very large in III-V's, and its effect (ref. 2) cannot be neglected in the measurement of L. Increasing the accelerating potential for the electron beam minimizes the effect of surface recombination velocity S. Unfortunately, this approach diminishes the resolution of this technique, since for small L's the electron range then becomes comparable to the

value of L. Figure 2 shows that at 30 kV - the most commonly used accelerating potential in routine SEM operation - the electron range R_e is about 3 μm.

For these reasons low accelerating potentials have been used to obtain the charge collection microscopy curves used in these measurements and calculations. The integral solution of the two-dimensional diffusion equation with semi-infinite thickness and an extended generation function (ref. 3) in the form of a three-dimensional gaussian distribution have been used here. Figure 3 shows an experimental EBIC plot of the ratio of collected current to maximum current (in the depletion region). At any x_o, this ratio can be expressed as (ref. 4)

$$\frac{I_{cc}(x_o)}{I_o} = \frac{2}{\pi}\int_o^\infty \frac{udu}{(u^2+1)}\left\{\exp\left(-\frac{u^2\sigma^2}{2L^2}\right) - 0.57\exp\left(\frac{\sigma^2}{2L^2} - \sqrt{u^2+1}\,\frac{z_o}{L}\right)\right.$$
$$\left. X\,\frac{\eta}{\eta+\sqrt{u^2+1}}\,\mathrm{erfc}\left[\frac{\sigma}{\sqrt{2}L}\left(\sqrt{u^2+1} - \frac{z_o}{L}\,\frac{L^2}{\sigma^2}\right)\right]\right\}\sin\left(u\,\frac{x_o}{L}\right) \qquad (2)$$

where

$$z_o = 0.3\,R_e$$

$$\sigma = \frac{R_e}{\sqrt{15}}$$

$$\eta = \frac{LS}{D}$$

As can be seen one can measure or assume reasonable values for all the variables in equation (2) except for the surface recombination velocity S, an unknown whose effect is not negligible. Hence, two different approaches that allow the determination of S were undertaken, so that equation (2) could be solved numerically, and the value of L could be extracted from the integral form.

Assume two different accelerating potentials (E_1 and E_2) for the electron beam impinging on the same semiconductor. In functional form, the normalized current at a given x_o can be rewritten as

$$\frac{I_{cc1}(x_o)}{I_{o1}} = \int f(L,E,S,x_o,\ldots) \qquad (3)$$

$$\frac{I_{cc2}(x_o)}{I_{o2}} = \int f(\ldots,E_2,\ldots) \qquad (4)$$

Figure 4 shows two of the experimentally obtained EBIC curves at the different potentials. The same x_o is used, so one can assume the same value for the diffusion length. This applies even in the case of graded doping or other nonuniformities. At the same x_o, one can also assume that S will be the same, even for different values of the recombination across the surfaces of the samples analyzed. This allows the treatment of equations (3) and (4) as two integral equations with two unknowns.

The value for S can then be obtained by using an iterative process, where an initial value for S is guessed. Holding S constant in equation (3), an L is found that satisfies the condition

$$\left| I_{cc(calculated)} - I_{cc(measured)} \right| \leq \text{TOLERANCE} \qquad (5)$$

This value for L is then used in equation (4), where S is next varied to satisfy equation (5). This process is repeated as necessary until an L and an S are found which satisfy both equations (3) and (4). Numerical integration was done using the Romberg method where the upper limit was increased until the last two computed integrals differed by a negligible value. The roots (values of L and S) were searched by using the Regula Falsi Method. The integral form for the complementary error function was used. Figure 5 shows a flowchart for the numerical calculations performed here.

The second method uses less computer time but requires a more sophisticated SEM. It makes use of the result (ref. 5)

$$\frac{\partial}{\partial z} \ln I_{cc} \Big|_{z \to 0} = \frac{S}{D} \quad (\text{as } E \to 0) \qquad (6)$$

which allows a more direct determination of the value of S while the sample is inside the SEM specimen chamber. In order to use equation (6) and obtain accurate values, one must have low voltage capabilities and the ability to vary the beam accelerating potential without changing the total beam current. Figures 6 and 7 show the determination of S/D for the devices that were analyzed here. The GaAs diode was P on N. The N region was silicon doped, with a carrier concentration of about 1×10^{18}. The junction was very abrupt. The InP solar cell had a P-type base, doped at about 1×10^{17}. The cell had been subject to $10^{12}/cm^2$ 10 MeV proton irradiation.

Figures 8 and 9 show the measured values for diffusion length, as a function of distance from the PN junction, for the same devices. The spread in the data points from the different accelerating voltages (which ideally, would coincide for a given x_0) has been used to assign a value to the uncertainty. The reported value has been chosen as the L that is reached asymptotically as x_0 gets farther from the junction, since other workers (ref. 6) have observed that the measured value of L is more reliable if a larger x_0 is used.

In summary, accurate evaluations of diffusion lengths for heavily to moderately doped III-V semiconductors and/or radiation damaged solar cells have been made possible by using the experimental and numerical techniques described.

ACKNOWLEDGMENT

Navid Fatemi's contribution in the formation of ohmic contacts on one of the samples was very helpful. We thank the Magnetics Technology Center at Carnegie Mellon University for making their field emission SEM available for this work. We also appreciate Suresh Santhanam's help in the collection of the EBIC data that was used. Ralph Thomas' measurements of carrier concentrations are also appreciated.

REFERENCES

1. Klein, C.A.: Bandgap Dependence and Related Features of Radiation Ionization Energies in Semiconductors. J. Appl. Phys., vol. 39, no. 4, Apr. 1968, pp. 2029-2038.

2. Van Roosbroeck, W.: Injected Current Carrier Transport in a Semi-Infinite Semiconductor and the Determination of Lifetimes and Surface Recombination Velocities. J. Appl. Phys., vol. 26, no. 4, Apr. 1955, pp. 380-391.

3. Fitting, H.J.; Glaefeke, H.; and Wild, W.: Electron Penetration and Energy Transfer in Solid Targets. Phys. Stat. Sol. (a), vol. 43, 1977, pp. 185-190.

4. Donolato, C.: On the Analysis of Diffusion Length Measurements by SEM. Solid-State Electronics, vol. 25, no. 11, Nov. 1982, pp. 1077-1081.

5. Watanabe, M.; Actor, G.; and Gatos, H.C.: Determination of Minority-Carrier Lifetime and Surface Recombination Velocity with High Spacial Resolution. IEEE Trans. Electron Devices, vol. 24, no. 9, Sept. 1977, pp. 1172-1177.

6. Luke, K.L.; von Roos, O.; and Cheng, L.: Quantification of the Effects of Generation Volume, Surface Recombination Velocity, and Diffusion Length on the Electron-Beam-Induced Current and its Derivative: Determination of Diffusion Lengths in the Low Micron and Submicron Ranges. J. Appl. Phys., vol. 57, no. 6, Mar. 15, 1985, pp. 1978-1984.

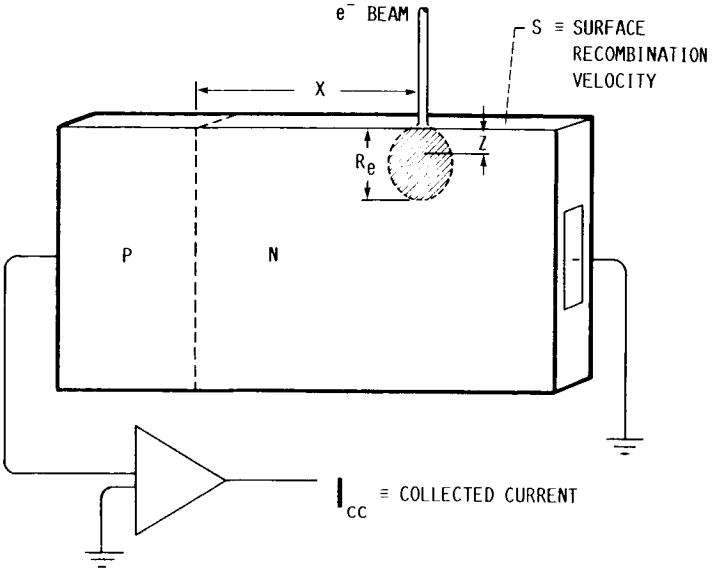

FIGURE 1. - EXPERIMENTAL SETUP FOR CHARGE COLLECTION MICROSCOPY.

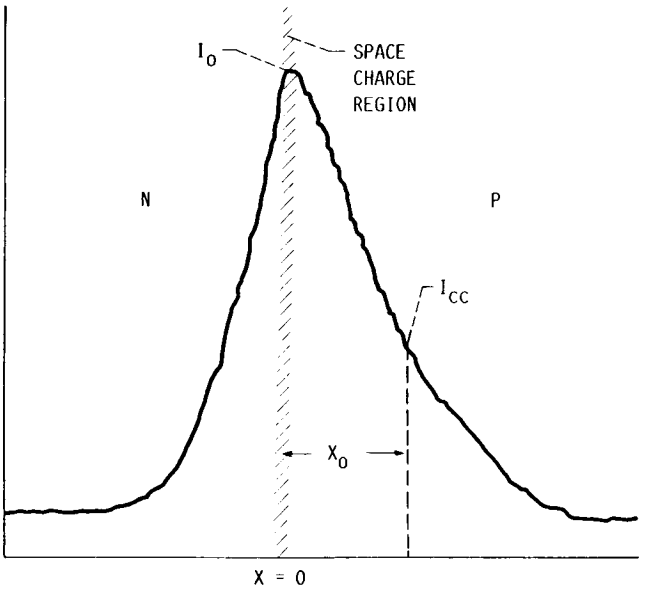

FIGURE 3. - EBIC PLOT FOR A PN JUNCTION.

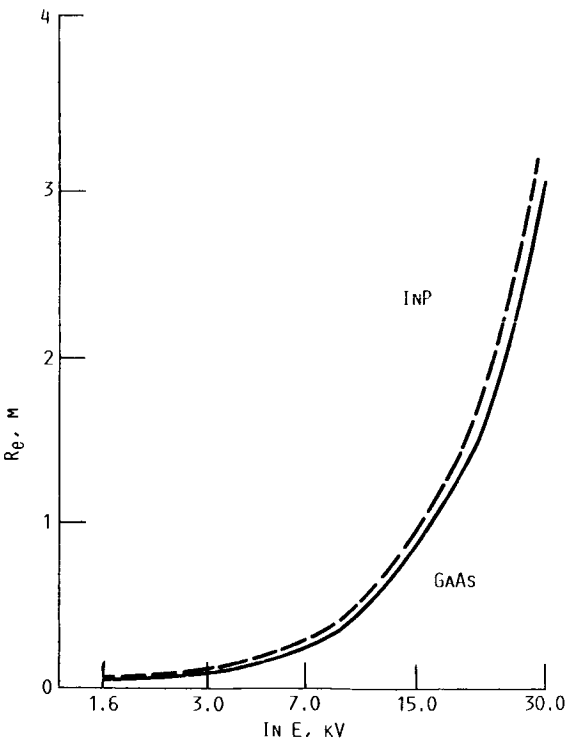

FIGURE 2. - ELECTRON RANGE AS A FUNCTION OF ACCELERATING VOLTAGE.

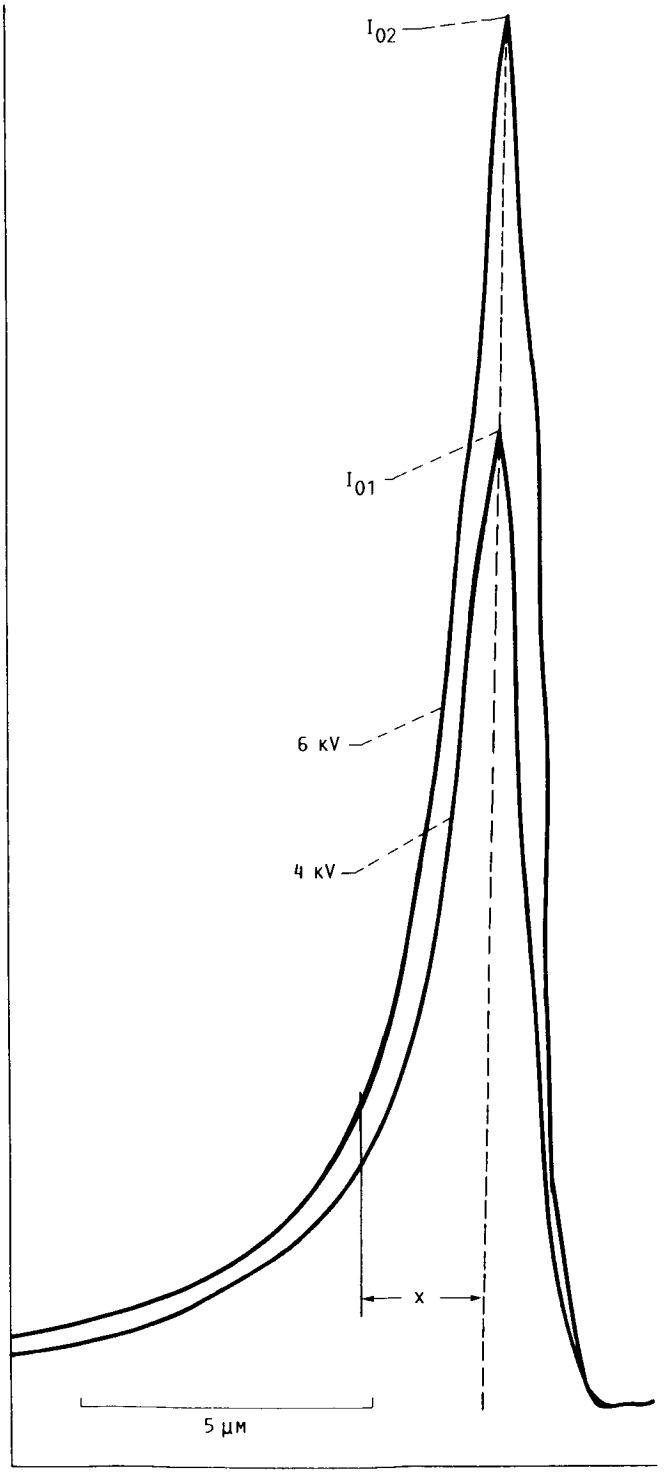

FIGURE 4. - EBIC CURVES AT 4 AND 6 kV.

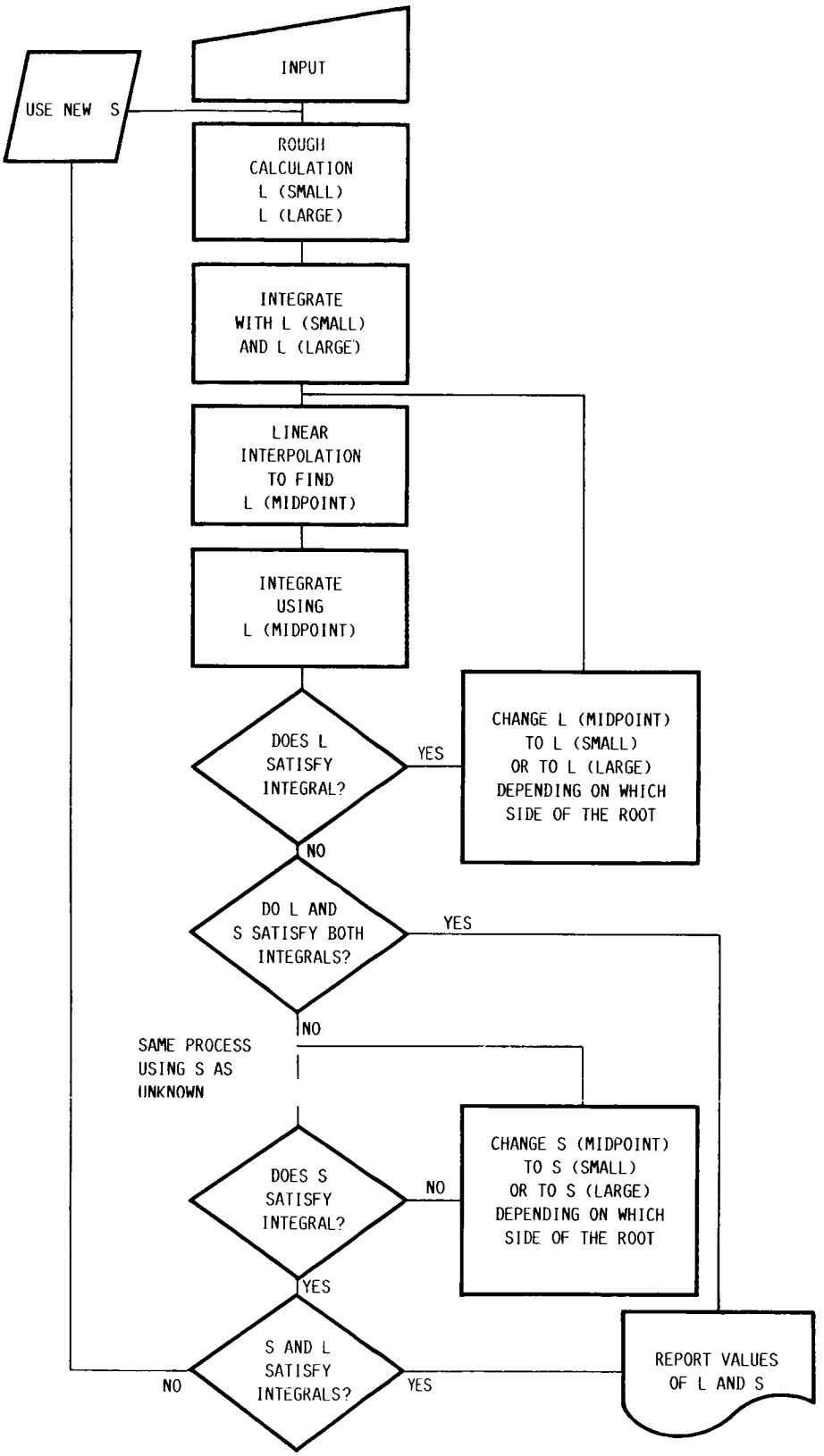

FIGURE 5. - FLOWCHART FOR NUMERICAL CALCULATIONS. USER INPUTS X_0, NORMALIZED CURRENTS, AND ELECTRON BEAM POTENTIALS FOR TWO CURVES.

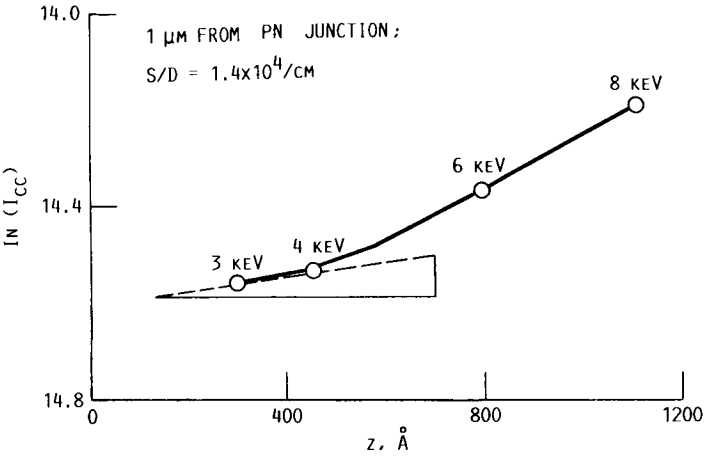

FIGURE 6. - DETERMINATION OF S/D FOR AN INP CELL.

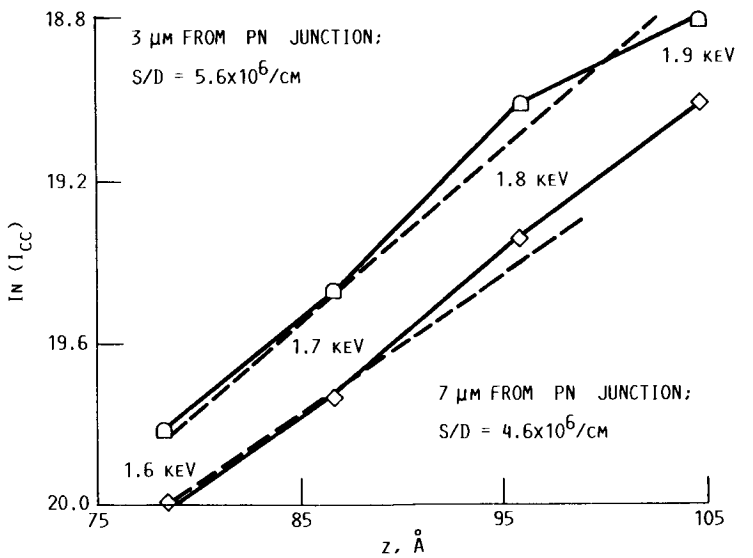

FIGURE 7. - DETERMINATION OF S/D FOR A GAAS DIODE.

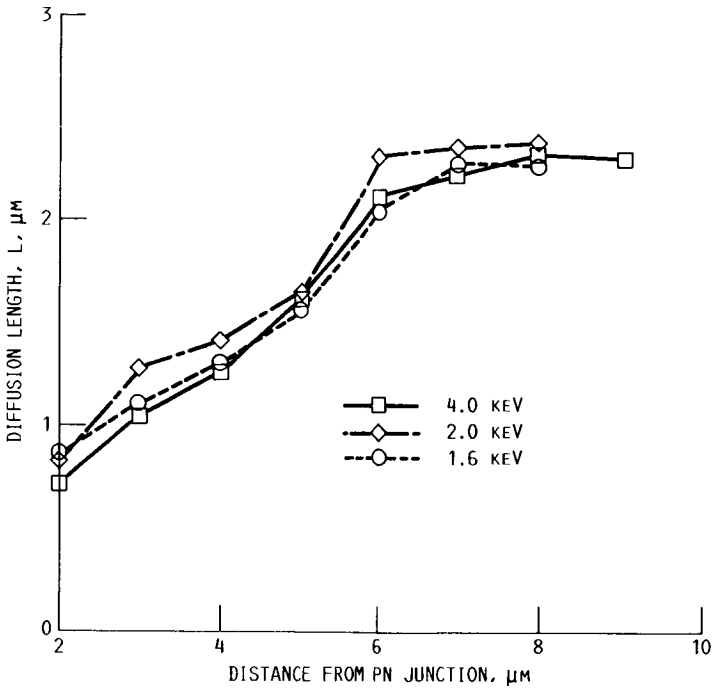

FIGURE 8. - VALUES OF DIFFUSION LENGTHS IN THE GaAs DIODE. N TYPE; $N_A = 1 \times 10^{18}/cm^3$; L = 2.3 μM±0.15 μM.

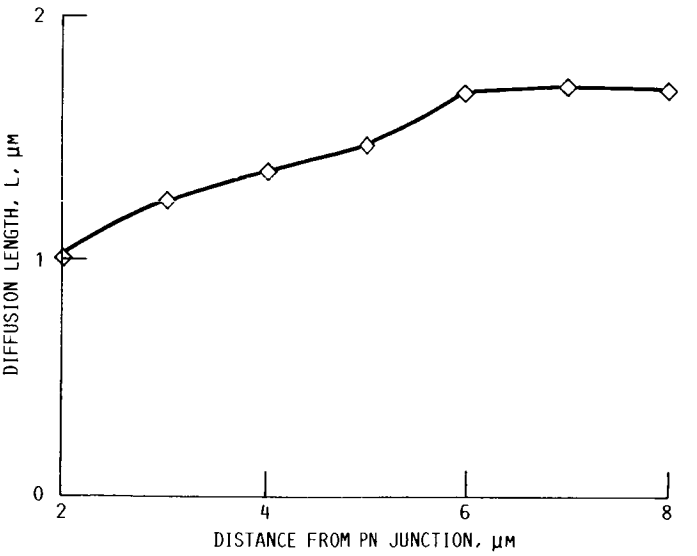

FIGURE 9. - VALUES OF DIFFUSION LENGTHS IN AN IRRADIATED InP SOLAR CELL. P TYPE; $N_A \cong 10^{17}/cm^3$; (AFTER $10^{12}/cm^2$ 10 MeV PROTON IRRADIATION). L = 1.7 μM±0.15 μM.

RESULTS OF 1 MeV PROTON IRRADIATION OF FRONT AND BACK SURFACES OF SILICON SOLAR CELLS

B.E. Anspaugh and R. Kachare
Jet Propulsion Laboratory
Pasadena, California

V.G. Weizer
NASA Lewis Research Center
Cleveland, Ohio

Several silicon solar cells with and without back surface fields (BSF), having thicknesses of 200 μm and 63 μm were irradiated with 1 MeV protons having fluences between 1 x 10^{10} and 1 x 10^{12} p/cm^2. The irradiation was performed using both normal and isotropic incidence on the front as well as back surfaces of the solar cells. The results of the back surface irradiations are analyzed by using a model in which irradiation-induced defects across the high-low (BSF) junction are considered. It is concluded that degradation of the high-low junction is responsible for the severe performance loss in thinner cells when irradiated from the rear.

INTRODUCTION

For the past several years most solar cell manufacturers have incorporated a back surface field in their solar cells in order to boost power output. The BSF has been particularly important in thin solar cells where the minority carrier diffusion length may be much larger than the thickness. Significant increases in power (as much as 28% for 63 μm thick cells) are achieved when the field is incorporated. However, BSF cells lose their output at a greater rate than their non-field counterparts when exposed to ionizing radiation typical of space exposures (ref. 1). The degradation of BSF cells with radiation has not been adequately modeled, and it is the purpose of this paper to explore the cell degradation with one specific energy of protons and compare the results with the predictions of a recent model describing the behavior of cells with defective BSFs (ref. 2).

EXPERIMENTAL PROCEDURE

The solar cells tested were made from 10 ohm-cm silicon. They all had dual antireflection coatings and aluminum back surface reflectors (BSR). Two thicknesses of solar cells were used, 63 μm and 200 μm. Half the cells of each thickness had back surface fields applied using aluminum paste, and half had no BSF. The cell manufacturer estimated that the junction depths were 0.25 μm, the BSFs penetrated into the cell ~ 5 μm and the thicknesses of the aluminum BSRs were 0.2 μm. All cells measured 2 x 2 cm.

The 1 MeV proton irradiations were performed at the Caltech 1 MeV van de Graaff accelerator facility using the techniques described in reference 3. The protons were spread out into a uniform beam at the target plane by use of a gold scattering foil about 2 μm thick. Two groups of cells were irradiated during each run, one group under front normal incidence, and the other group under simulated front isotropic incidence using the omnidirectional fixture (ref. 3). After the two groups of cells were irradiated in this manner, the irradiation was repeated with another two groups of cells with the protons incident on the rear cell surfaces. Light I-V curves before and after irradiation were taken with an X25 Solar Simulator simulating the air mass zero solar spectrum. This procedure was repeated 7 times with the same solar cells, increasing the fluence level each time until a total fluence of 1×10^{12} p/cm^2 had been accumulated. The cells were not annealed after irradiation, and in most cases were measured within an hour of the irradiation.

RESULTS AND DISCUSSION

Protons having an energy of 1 MeV will penetrate to different depths in silicon solar cells, depending on whether they are incident on the front or rear surfaces. They will go into the silicon 16.5 μm (ref. 4) when incident on the front, but due to the presence of the rear metal contact, they will only go into the silicon ~ 4 μm when incident on the rear. When protons are incident normally, they produce most of the displacement damage very near the end of their track, essentially producing a recombination zone which inhibits passage by minority carriers. But when protons are incident isotropically, they produce a rather smeared out damage profile which will be easier for minority carriers to cross. The use of 1 MeV protons was made in this investigation to selectively examine the effect of irradiation on the front portion of the cells where the junction is involved, and on the rear portion of the cells where the back surface field is involved.

Tables I and II show the values of I_{sc}, V_{oc}, P_{max}, and FF of 200 μm and 63 μm silicon solar cells respectively before and after 1 MeV proton irradiation to fluences of 1×10^{12} p/cm^2. The pre-irradiation data shows the advantage of using the BSF structures. For example, the fields increased cell performance in the 200 μm cells by ~ 20 mA in I_{sc}, 69 mV in V_{oc}, and 17 mW in P_{max} while in the 63 μm cells, the fields gave corresponding increases of ~ 15 mA, 90 mV, and 16 mW.

The advantage of the field is given up after front surface irradiations, however. As shown in the Tables, the electrical parameters of the 63 μm cells are essentially the same after either normal or omni irradiation, regardless of whether the cells began life with a BSF. In contrast, the thicker 200 μm cells with BSF retain slightly higher outputs cells after the 1 MeV front irradiations. This behavior is also depicted in figures 1 and 2 where P_{max} is plotted as a function of 1 MeV proton fluence. The data is illustrating that as the proton fluence is increased, the effectiveness of the BSF is reduced and nearly the same values of P_{max} should be observed irrespective of BSF and cell thickness.

A comparison of the differences between front surface omni vs. normal incidence irradiation reveals some interesting differences. For both cell thicknesses, the omni irradiation is not as damaging for either I_{sc} or P_{max}. But for V_{oc}, the end result after $\Phi = 1 \times 10^{12}$ p/cm^2 is exactly the same.

When the non-BSF cells of either thickness are irradiated from the rear with omnidirectional protons, there is almost no degradation of the solar cell parameters. This is not true of the BSF cells, however. The 63 μm BSF cells with fields degrade more than the non-BSF cells under these conditions. The opposite

is true of the 200 μm BSF cells where the BSF cells retain higher outputs after the rear omni irradiations.

Examining the case for rear normal irradiation, we find degradation in all cell types. Here too, the 63 μm cells with fields degrade more than their non-BSF counterparts. The 200 μm cells with fields degrade at a faster rate than their non-field counterparts, but they retain more absolute power. Figures 3 through 5 illustrate the degradation of the various cell parameters under normal rear incidence irradiation. Figure 3 illustrates that negligibly small changes occurred in the I_{sc} values of non-BSF cells of either thickness. However, significantly large degradations in I_{sc} values are seen in both thicknesses of BSF cells. The 63 μm BSF cells retain their I_{sc} advantage over the non-BSF cells until fluences greater than 1×10^{11} p/cm^2 are reached, but from then on, the non-BSF cells were superior. This behavior, which has been observed a sufficient number of times to establish statistical validity, is not understood. The I_{sc} values for 200 μm BSF cells also degrade under this irradiation geometry, but they retain their advantage over the non-BSF cells over the entire fluence range. The I_{sc} degradation curves for both thicknesses of BSF cells appear to exhibit a plateau effect such that after reaching a certain fluence, no further degradation will occur. For 200 μm cells, this plateau occurs at $\sim 3 \times 10^{11}$ p/cm^2 and for the 63 μm cells, the plateau is not fully developed, but appears to occur at slightly higher fluences.

The variation of V_{oc} as a function of 1 MeV protons normally incident on the rear cell surfaces is presented in figure 4. Negligibly small changes in V_{oc} for non-BSF cells were observed. However, dramatic reductions in the V_{oc} values with increasing fluence in 63 μm BSF cells were noted and V_{oc} was reduced to less than the corresponding V_{oc} values of non-BSF cells after $\Phi > 2 \times 10^{11}$ p/cm^2.

Figure 5 gives the change in P_{max} as a function of 1 MeV proton fluence incident normally on the rear surfaces. As for I_{sc} and V_{oc}, the non-BSF cells do not degrade with fluence, but here that is only true for fluences less than 1×10^{11} p/cm^2, after which they begin degradation. The P_{max} degradation for 63 μm BSF cells occurs at a more rapid rate than for any other cell type, and these cells lose their power advantage over the 63 μm non-BSF cells after $\Phi > 2 \times 10^{11}$ p/cm^2.

Figure 6 depicts the variation of P_{max} as a function of fluence of 1 MeV protons with omnidirectional incidence on the rear surfaces. Here there is no P_{max} degradation of cells without BSF, nor do the BSF cells degrade as severely as observed for the rear normal incidence cases shown in figure 5. Also, the BSF effect in 63 μm cells is preserved up through $\Phi = 5 \times 10^{11}$ p/cm^2.

The important point to be made here is that though significant improvement in 63 μm cell performance is achieved by using a BSF, it is totally reduced to less than the non-BSF cell performance level after high fluences of low energy protons. Fields in the thicker cells do not enhance the cell performance quite as markedly as they do for thinner cells, but the thicker cells retain some of their advantage after irradiation to these same levels.

MODEL CALCULATIONS

Front Surface Irradiations

Since the projected range of 1 MeV front surface normally incident protons is 16.5 μm, we attempted to analyze the data by dividing the cell into two regions, one inner irradiated region (16 μm thick) and the other consisting of a deeper non-damaged region (184 μm thick). As a first approximation, we assumed that in the damaged region only the minority carrier lifetime is uniformly degraded throughout the 16 μm layer. We also assumed that with a proton fluence of 1×10^{12} p/cm^2, heavy damage has been introduced at the end of the proton track and consequently

for front surface irradiations, the BSF and non-BSF cells are similar. This rationale appears to be acceptable based on the results shown in figures 1 and 2.

The experimental I_{sc} and V_{oc} values before irradiation were fitted to the standard solar cell equations (ref. 5) using suitable values for 10 ohm-cm silicon, e.g. the diffusion constant D = 30 cm^2/sec, the dopant concentration, N_A = 1.3 x 10^{15} cm^{-3}, and back surface recombination velocities, S_B values of 10 cm/sec and 10^8 cm/sec, for BSF and non-BSF cells respectively. Minority carrier diffusion length (L_n) values of 600 μm were found to fit the pre-irradiation data for both BSF and non-BSF cells.

Various calculations were made to fit the post-irradiation I_{sc} and V_{oc} values. In these calculations, only L_n values for the inner layer were varied in order to fit the data. The calculated I_{sc} and V_{oc} values were significantly affected only when L_n values for the inner layers were made less than 16 μm. For both BSF and non-BSF cells under normal incidence, L_n values of 4 μm for the inner layer gave good fits to the data, and L_n values of about 6 μm gave good fits to the omnidirectional data.

It should be pointed out that if values of D, L_n, S_B, and intrinsic carrier concentration (n_i), are varied, then several sets of these parameters could conceivably give fits to the experimental data. This problem in the calculation can be reduced by subdividing the damaged layer into multi-layers (refs. 6 and 7) which take into account the non-uniformity of proton irradiation, and assigning appropriate parameters to each layer. However, such calculations are highly complicated and are not considered here.

Back Surface Irradiations

Figures 3 through 6 show that rear surface normal and omnidirectional protons do not degrade non-BSF cells except for fluences greater than 1 x 10^{10} p/cm^2 at normal incidence. As can be seen in Tables I and II, the fill factors (FF) of these cells are significantly reduced after normal incidence irradiation of 10^{12} p/cm^2. This change in FF could be due to an increase in dark saturation current in the base, I_{ob}, an increase in series resistance, R_s, or a decrease in the shunt resistance, R_{sh}. Changes in R_{sh} and I_{ob} will have a major effect on the degradation of V_{oc} and an increase in R_s will degrade I_{sc} (ref. 5). Since significant reductions in V_{oc} are observed compared to those in I_{sc}, it would appear that major changes in R_{sh} and I_{ob} are occurring. Also some increase in R_s may be expected with such a high fluence due to majority carrier removal (ref. 8). I_{ob} will increase due to decreases in L_n and D due to radiation-induced defects. Since the non-BSF cells are not degraded as badly as the BSF cells, we will focus our attention on the degradation in the BSF cells.

Since the 1 MeV protons are stopping in the pp+ region, they will produce maximum damage to the high-low junction. The energy levels and density of these defects depend strongly on the fluence and irradiation configuration. Omni-directional incidence protons will induce defects that are spatially smeared in the entire BSF region whereas normal incidence protons will produce highly localized large defect concentrations in the vicinity of the pp+ junction. Consequently, a more defective BSF is produced by the normal incidence protons than by the omni protons. This is reflected in the experimental data of figures 3 through 6.

Attempts were made to explain the degradation of BSF cells using the existing models (refs. 2 and 9). In the Sah model (ref. 9) the effects of defects distributed in the bulk across the BSF are analyzed by using three regions in a defective unit cell containing one defect. The width of the first region surrounding the defect is characterized by the distance-of-influence which is about two diffusion lengths. The defect itself is characterized by three parameters, namely, defect density, defect area and the surface recombination velocity at the

defective area. The model predicts very substantial degradation of V_{oc} even if there are only 40 defects/cm^2 (ref. 9). If this would have been the case, then the V_{oc} values shown in figure 4 and the P_{max} values shown in figures 5 and 6 would have been rapidly degraded with fluences less than 1 x 10^{11} p/cm^2. Since this is not so, this model apparently over-estimates the cell degradation (ref. 2).

The other model is described in detail in reference 2. The important finding of this model analysis is that it is possible to have a fully effective BSF region, regardless of the spatial distribution of the defective areas as long as the total defective area is reduced below certain limits. A case of distributed defects discussed in reference 2 closely matches the defect geometry induced in the BSF region by low energy protons. Modifying eq. 8 (ref. 2) for the distributed defect case to match the degradation in V_{oc} by low energy protons in BSF cells, we obtain:

$$dV_{oc} = KT \ln \left[\frac{J_{sc1} \left(S' + \tanh d/L_n \right)}{J_{sc2} \left(\tanh d/L_n + S' \tanh^2 d/L_n \right)} \right] \qquad (1)$$

where J_{sc1} and J_{sc2} are the short circuit currents of the BSF cells before and after irradiation respectively and

$$S' = 5 \times 10^6 \left[\frac{f}{2 - f} \right] \frac{L_n}{D_n} \qquad (2)$$

where S' is a normalized rear surface recombination velocity, S_B, f is the fraction of the BSF area which is defective, and d is the cell thickness.

The change in S' as a function of Φ can be calculated using equation (1) and the corresponding value of f can then be obtained from equation (2). S_B is given by (ref. 2):

$$S_B = \frac{V}{2} \left[\frac{f}{2 - f} \right] \qquad (3)$$

where V is the carrier thermal velocity which for silicon is ~ 10^7 cm/sec.

Several runs were made using various values of L_n while holding D constant at 30 cm^2/sec. Figure 7 illustrates the results of our model calculation where the back surface recombination velocity plots as a function of proton fluence are given for 200 μm and 63 μm BSF cells having L_n = 800 and 600 μm respectively. As can be seen, S_B increases with Φ, and it increases at a different rate for normal incidence than it does for omnidirectional incidence. These results clearly demonstrate that as the BSF becomes defective, S_B tends to increase. Thus the cell performance which has been improved by using a BSF has been mostly degraded after irradiation. In general, for a given fluence there is more increase in S_B for rear normal incidence than that for omnidirectional irradiation. S_B values of 5.36 x 10^5 cm/sec and 1.07 x 10^4 cm/sec were calculated for 200 μm and 63 μm BSF cells respectively after rear normal irradiation with Φ = 1 x 10^{12} p/cm^2.

It is gratifying to find that such a simple model can provide quantitative changes in the trend of S_B as a function of fluence. However, to obtain an in-depth understanding of damage mechanism of the BSF, the model would probably have to be refined to take into account the leakage in the high-low junction, changes in the recombination velocity at the pp+ junction, and the change in L_n in the p+ region with fluence. In addition it may be necessary to consider imperfections in the Al paste alloying, impurities in the paste, and an imperfect Al profile.

CONCLUSIONS

Of the four radiation geometries observed, the front surface normal incidence irradiation was the most effective in producing degradation in both thick and thin cells with and without BSF.

No significant cell degradation was observed in either thick or thin non-BSF cells when irradiated from the rear surface with 1 MeV protons.

After rear surface normal and omnidirectional irradiation with fluences of 1 x 10^{12} p/cm^2, all the BSF cells degrade at a faster rate than cells without BSF. However, the 200 μm BSF cells retain more absolute power than comparable non-BSF cells, but 63 μm BSF cells retain less absolute power than comparable non-BSF cells.

A simple model was used to calculate the back surface recombination velocity and explain the rear incidence proton irradiation damage in both thick and thin BSF cells.

Additional rear surface irradiation experiments with the cells having BSF made by boron diffusion, ion implantation and Al diffusion coupled with a refined model which will take into account high-low junction related device parameters will be required to fully understand the defective BSF and its role, particularly in thin cells.

REFERENCES

1. H. Y. Tada, Jr. R. Carter, Jr., B. E. Anspaugh, and R. G. Downing, Solar Cell Radiation Handbook, JPL Publication 82-69, Jet Propulsion Laboratory, Pasadena, California, Nov. 1982.
2. V. G. Weizer, "The Effect of a Defective BSF Layer on Solar Cell Open Circuit Voltage," Solar Cells, 14, 1985, p. 241.
3. B. E. Anspaugh and R. G. Downing, "Radiation Effects in Silicon and Gallium Arsenide Solar Cells Using Isotropic and Normally Incident Radiation," JPL Publication 84-61, Jet Propulsion Laboratory, Pasadena, California, Sept., 1984.
4. J. F. Janni, "Proton Range-Energy Tables, 1 keV-10GeV," Atomic Data and Nuclear Data Tables, 27, Nos. 4/5, July/Sept., 1982.
5. H. J. Hovel, Semiconductors and Semimetals, Vol. 11, Solar Cells, Academic Press, New York, 1975.
6. I. Nashiyama, E. Teranishi, and M. Kageyama, "Protons and Deuteron Irradiation Damage in Silicon Solar Cells," Jap. Jour. of Appl. Physics, 10, No. 11, Nov., 1971, p. 1564.
7. D. L. Crowther, E. A. Loda, J. DePangher, and A. Andrew, "An Analysis of Non-Uniform Proton Irradiation Damage in Silicon Solar Cells," IEEE Transactions on Nuclear Science, NS-13, Oct., 1966, p. 37.
8. E. Stofel and D. Joslin, "Low Energy Proton Irradiation of Solar Cell Back Contacts," Proc. IEEE Eighth Photovoltaic Spec. Conf., 1970, pp. 209.
9. C. T. Sah, K. A. Yamakawa, and R. Lutwack, "Reduction of Solar Cell Efficiency by Bulk Defects Across the Back-Surface-Field Junction," J. Appl. Phys. 53(4), April, 1982.

Table I. Light I-V Data (AMO, 28° C) of 200 μm Thick Silicon Solar Cells Before and After 1 MeV Proton Irradiation

Irradiation Configuration	BSF	Fluence (p/cm^2)	I_{sc} (mA)	V_{oc} (mV)	P_{max} (mW)	FF
Front Normal	No	0	150.1	539.3	63.23	0.78
		1×10^{12}	89.9	437.6	27.61	0.70
	Yes	0	171.0	608.4	80.78	0.78
		1×10^{12}	95.1	441.1	29.88	0.71
Front Omni	No	0	150.9	538.2	63.15	0.78
		1×10^{12}	104.4	437.9	32.86	0.72
	Yes	0	170.9	607.4	80.48	0.78
		1×10^{12}	113.1	440.4	35.94	0.72
		---	---	---	---	---
Rear Normal	No	0	151.9	537.1	63.28	0.78
		1×10^{12}	150.0	524.0	54.45	0.69
	Yes	0	173.5	605.8	80.99	0.77
		1×10^{12}	158.6	530.7	63.23	0.75
Rear Omni	No	0	152.0	536.8	63.35	0.78
		1×10^{12}	151.4	535.3	62.86	0.78
	Yes	0	171.7	606.4	80.62	0.78
		1×10^{12}	159.4	542.1	67.23	0.77

Table II. Light I-V Data (AM0, 28° C) of 63 μm Thick Silicon Solar Cells Before and After 1 MeV Proton Irradiation

Irradiation Configuration	BSF	Fluence (p/cm^2)	I_{sc} (mA)	V_{oc} (mV)	P_{max} (mW)	FF
Front Normal	No	0	144.5	509.9	56.43	0.77
		1×10^{12}	96.3	434.1	28.43	0.68
	Yes	0	161.2	600.2	72.53	0.77
		1×10^{12}	95.8	434.5	28.59	0.69
Front Omni	No	0	144.9	510.3	56.68	0.77
		1×10^{12}	107.7	435.2	33.60	0.72
	Yes	0	160.2	600.3	72.33	0.75
		1×10^{12}	111.0	436.5	34.97	0.72

Rear Normal	No	0	143.6	511.5	56.03	0.76
		1×10^{12}	138.9	493.2	46.13	0.67
	Yes	0	161.7	597.9	72.29	0.76
		1×10^{12}	133.9	485.5	43.97	0.67
Rear Omni	No	0	144.7	511.3	56.09	0.76
		1×10^{12}	142.2	506.5	54.31	0.75
	Yes	0	160.5	601.5	72.41	0.75
		1×10^{12}	137.8	504.2	[illegible]	0.77

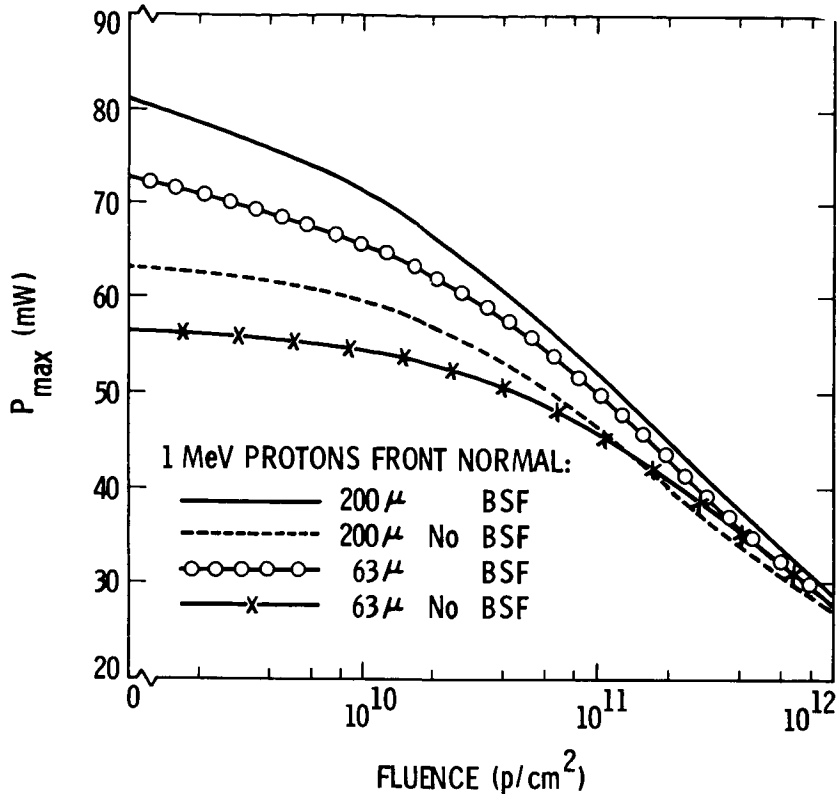

Figure 1. P_{max} of 200 μm and 63 μm BSF and Non-BSF Solar Cells as a Function of Fluence of 1 MeV Front Surface Normal Incident Protons.

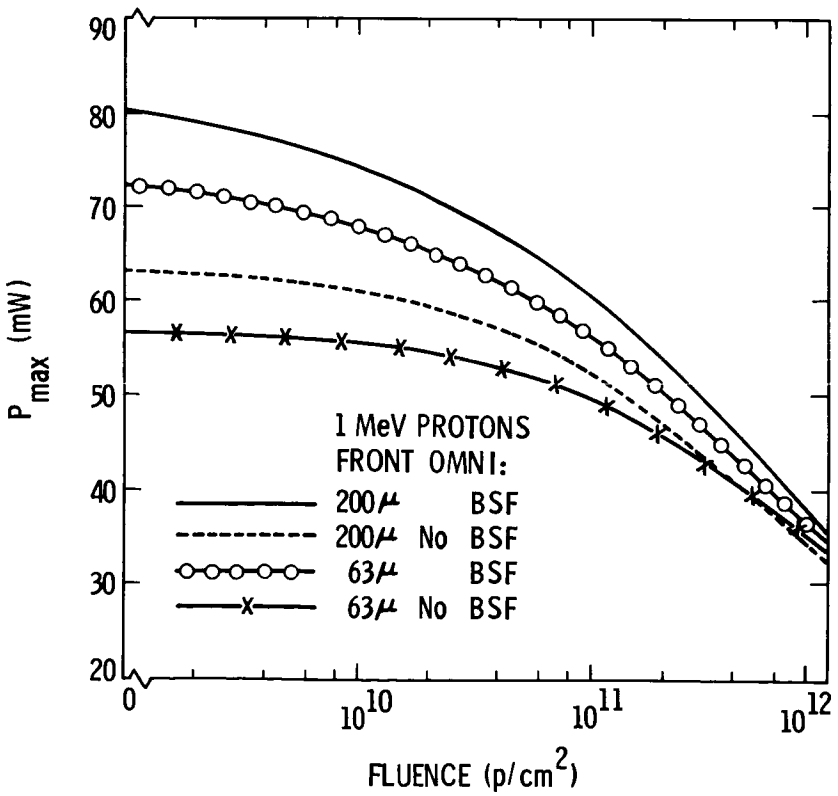

Figure 2. P_{max} of 200 μm and 63 μm BSF and Non-BSF Solar Cells as a Function of Fluence of 1 MeV Front Surface Omnidirectional Incident Protons.

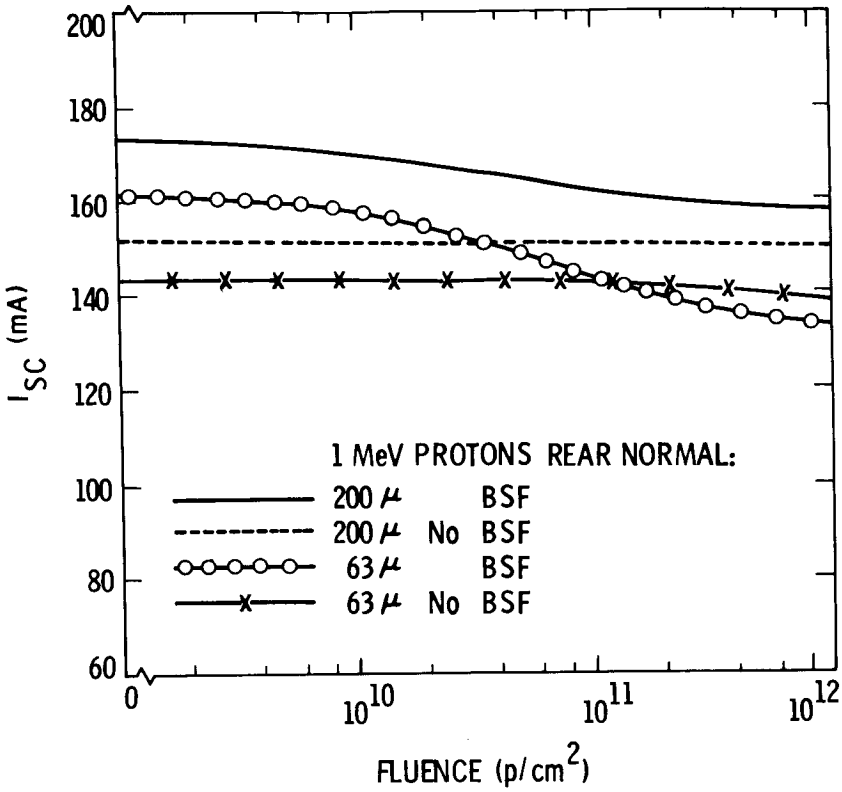

Figure 3. I_{SC} of 200 μm and 63 μm BSF and Non-BSF Solar Cells as a Function of Fluence of 1 MeV Rear Surface Normal Incident Protons.

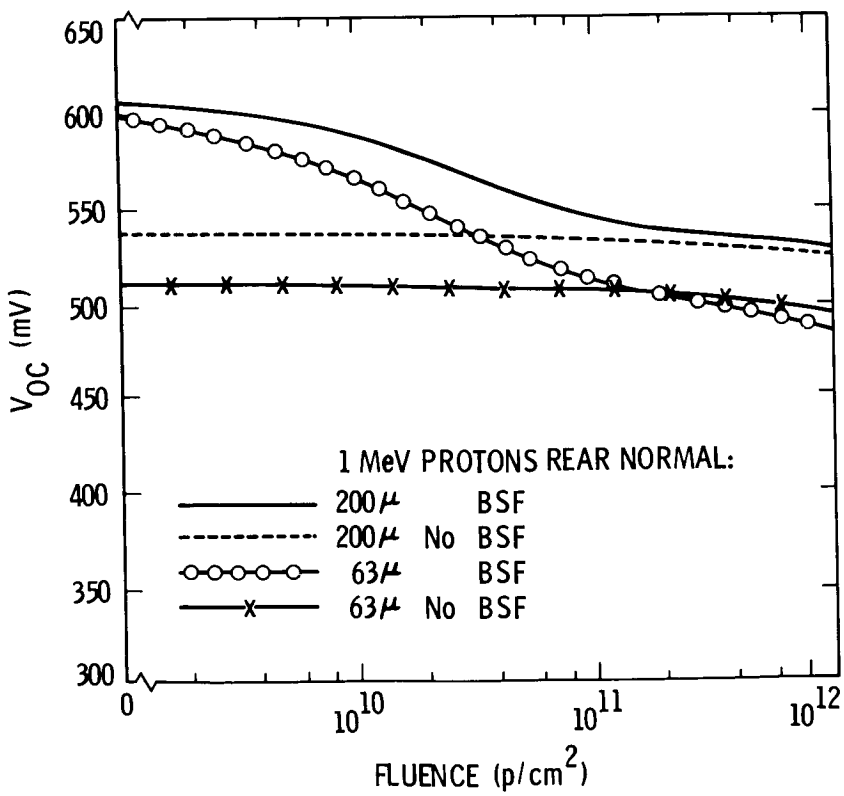

Figure 4. V_{OC} of 200 μm and 63 μm BSF and Non-BSF Solar Cells as a Function of Fluence of 1 MeV Rear Surface Normal Incident Protons.

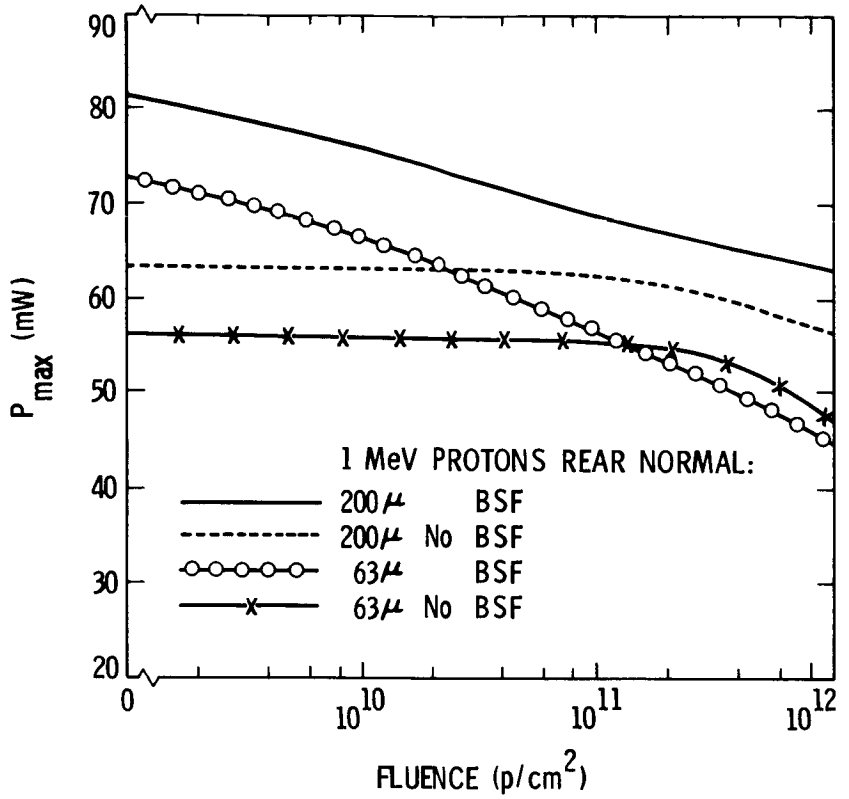

Figure 5. P_{max} of 200 μm and 63 μm BSF and Non-BSF Solar Cells as a Function of Fluence of 1 MeV Rear Surface Normal Incident Protons.

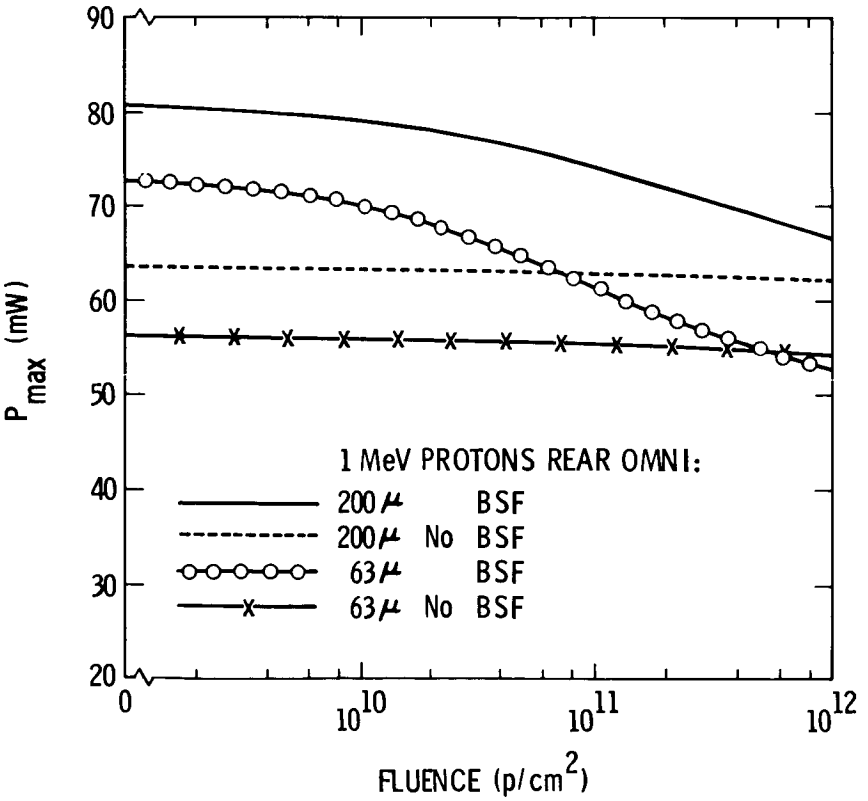

Figure 6. P_{max} of 200 μm and 63 μm BSF and Non-BSF Solar Cells as a Function of Fluence of 1 MeV Rear Surface Omnidirectional Incident Protons.

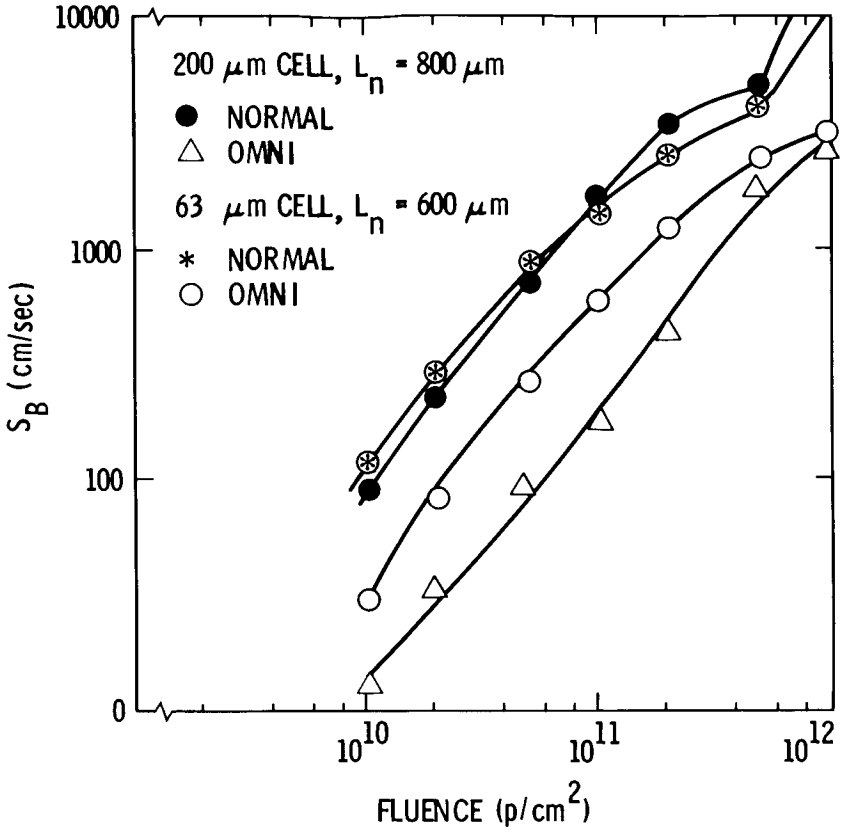

Figure 7. Calculated Back Surface Recombination Velocity of 200 μm and 63 μm Solar Cells as a Function of Fluence of 1 MeV Rear Surface Normal and Omni Incident Protons.

EFFECT OF 1.0 MeV ELECTRON IRRADIATION ON SHUNT RESISTANCE IN Si-MINP SOLAR CELLS*

Wayne A. Anderson and Sonali Banerjee
State University of New York at Buffalo
Amherst, New York

Shunt resistance from 100 K-400°K is compared for diffused and ion-implanted cells, before and after irradiation. R_{sh} decreases from $>10^7 \Omega\text{-cm}^2$ for T<250°K to $10^4 \Omega\text{-cm}^2$ at 400°K for non-irradiated diffused cells. Electron irradiation causes a more rapid decrease in R_{sh} for T>250°K. Ion-implanted cells exhibit a similar trend except that R_{sh} is significantly less for T<250°K and is more sensitive to irradiation at these low temperatures. The mechanism of R_{sh} appears to be a combination of multistep tunneling and trapping - detrapping in the defect states of the semiconductor. Radiation serves to increase the density of these states to decrease R_{sh}.

INTRODUCTION

Metal-Insulator-N^+ silicon -p silicon (MINP) solar cells are basically a surface passivated cell offering high efficiency due to a reduction in loss mechanisms such as surface recombination. This type of cell now produces an efficiency in excess of 20% which makes it a likely candidate for space applications. Thus, a study of radiation effects becomes important.

This paper deals with the effects of 1.0 MeV electron irradiation on the shunt resistance (R_{sh}) of MINP solar cells which has not previously been well characterized. Since R_{sh} must be high to avoid loss in efficiency, any decrease in high R_{sh} due to irradiation becomes an area of concern for the designer of solar cells for space applications.

EXPERIMENTAL TECHNIQUES

MINP solar cells were fabricated by ion implantation or diffusion. Diffused junctions were formed in 0.1-0.3 Ω-cm, (100), p-type Si using a Carborundum phosphorous solid source at 950°C for 5 minutes (ref. 1). A junction depth of about 0.3 μm gave good UV response. Figure 1 shows the cell structure which utilizes a reduced-area Al ohmic contact, Yb-Cr-Al layered grid, and a single layer SiO antireflection (AR) coating. Other cells were implanted through the

* Sponsored in part by Office of Naval Research
Contract No. N0001485K0727.

courtesy of Mark Spitzer of Spire Corp., with 5 keV phosphorous to a dose of about $2.5 \times 10^{15}/cm^2$. After annealing (ref. 1), the cells were completed as described above. Total area efficiency up to 17% was achieved.

Solar cells were irradiated by 1.0 MeV electrons at fluence levels of $1 \times 10^{14}/cm^2$, $1 \times 10^{15}/cm^2$, and $1 \times 10^{16}/cm^2$. Standard measurements were made of dark I-V, I_{sc}-V_{oc}, spectral response, diffusion length, and photovoltaic response at AM1.5 and AMO using an ELH lamp source. In addition, R_{sh} was determined by low voltage dark I-V data or low illumination I_{sc}-V_{oc} date (ref. 2) from 100 K to 400 K. A liquid nitrogen cryostat was utilized for refrigeration and a Keithley Model 480 picoammeter for measuring low current values.

EXPERIMENTAL DATA

Photovoltaic data for a diffused MINP cell, edge-exposed implanted cell, and non-passivated implanted cell are given in Table 1. The diffused cell gave the highest value of R_{sh} before and after irradiation. It also suffered a greater loss in PV data since it was more finely tuned in the initial design. Previous studies (ref. 3) show MINP cells to outperform N^+-P cells for electron fluence levels $<1 \times 10^{15}/cm^2$. The lower R_{sh} for implanted cells indicates effects of bulk damage from the implantation.

Figure 2 shows R_{sh} for the diffused cell with temperature as a variable. R_{sh} is independent of T for $T<250\,^{\circ}K$ and decreases thereafter. Irradiation causes a more rapid loss in R_{sh} at increased T. Implanted cell data of Figure 3 indicate R_{sh} to decrease with increased T for $T>100\,^{\circ}K$. Again, irradiation served to further reduce R_{sh}. Shunt current (I_{sh}) was seen to depend linearly upon voltage and super-linearly upon radiation fluence as seen in Figure 4.

DISCUSSION

A number of observations regarding R_{sh} may be listed and compared to a theoretical model.

1) R_{sh} of diffused cells is greater than for implanted ones. This suggests remaining implantation damage after annealing.

2) R_{sh} is independent of temperature below a threshold (T_t) after which it decreases rather rapidly with T (ref. 2).

3) Shunt current (I_{sh}) is linearly dependent on voltage but increases with T in a super-linear fashion (ref. 2).

4) Electron irradiation causes a decrease in R_{sh} below T_t, little change in T_t, and a superlinear increase in I_{sh}.

A previous publication (ref. 2) explained temperature dependence of R_{sh} by examining the influence of defect states on a captured

carrier. A carrier may traverse the space charge region via multistep tunneling which explains the temperature independence for $T<T_t$. Alternatively, R_{sh} may be due to thermal re-emission, the probability of which increases at increased temperatures. The following equations then prevail (ref. 4):

$$N_t(T)=N_{to}\exp[-A\exp(-E/kT)]t \quad (1)$$

where $N_t(T)$ = # carriers trapped
N_{to} = initial # trapped carriers
E = energy of the state.
t = time

Also, $A = N_{eff}\, Sv_{th}$ (2)

where N_{eff} = density of states
S = capture cross section
v_{th} = thermal velocity

Conductivity due to released trapped charge is then given by

$$\Delta\sigma = \Delta N_t(T) q\, \Delta\mu \quad (3)$$

These equations predict an increase in free carriers above a certain threshold temperature. This increase is dependent upon the defect energy level, defect density, capture cross section, and temperature. Linear dependence on voltage satisfies V=IR. A super-linear dependence of R_{sh} and I_{sh} on temperature fits equation 1. The rapid increase of I_{sh} and decrease in R_{sh} with electron fluence indicates the role of defects introduced by irradiation and enforces the original premise that R_{sh} arises from defects in the bandgap.

REFERENCES

1) B. B. Rao, S. Banerjee, W. A. Anderson, and M. K. Han, "Excess Currents in MINP-Type Solar Cells", IEEE Trans. Elec. Rev., ED-32, 817-821, 1985.

2) S. Banerjee and W. A. Anderson, "Temperature Dependence of Shunt Resistance in Photovoltaic Devices", Appl. Phys. Lett., 49, 38-40, 1986.

3) M. Thayer, W. A. Anderson, and B. B. Rao, "Reliability of MINP Compared to MIS, SIS, and N/P Silicon Solar Cells Under 1.0 MeV Electron and Environmental Effects", IEEE Trans. on Elec. Dev., ED-31, 619-621,1984.

4) R. H. Bube, Photoconductivity of Solids, John Wiley & Sons, New York, 273-299, 1960.

TABLE 1

Photovoltaic Data Before and After Irradiation by 1.0 MeV Electrons to $10^{16}/cm^2$

	V_{oc}(V)		J_{sc}(mA/cm^2)[d]		Shunt Resistance[e] (Ω - cm^2)	
Sample	Before	After	Before	After	Before	After
1[a]	0.632	0.494	43.1	19.7	8.4×10^6	9.3×10^5
2[b]	0.608	0.506	40.8	23.8	5.0×10^4	1.6×10^4
3[c]	0.626	0.489	42.9	25.7	2.4×10^5	1.2×10^5

a) Diffused MINP cell with diffusion performed through a window in the oxide. Area = 2.0 cm^2.

b) Ion-implanted MINP cell where junction edges are exposed. Area = 2.1 cm^2.

c) Ion-implanted without passivation. Area = 4.0 cm^2.

d) Illuminated at 135 MW/cm^2.

e) @ 300 °K.

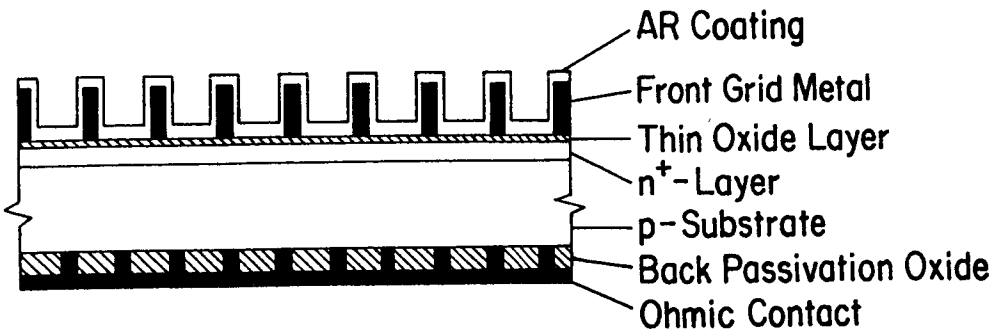

Figure 1. Diagram showing MINP solar cell design.

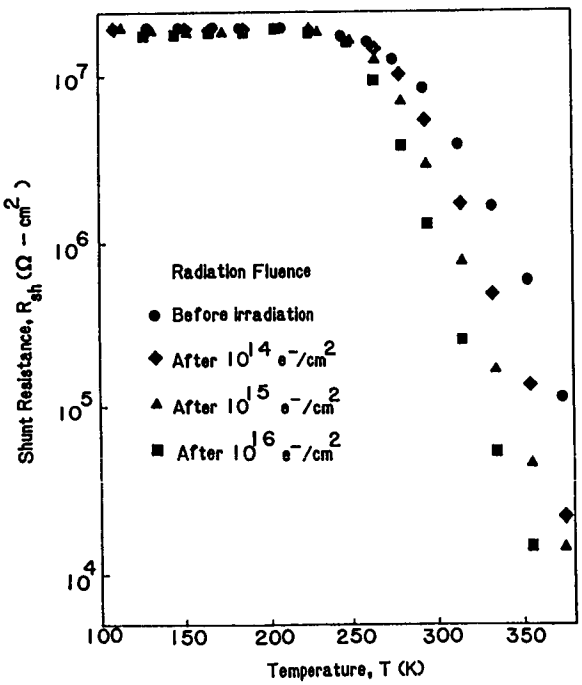

Figure 2. Temperature dependence of R_{sh} for a diffused cell as a function of 1.0 MeV electron fluence.

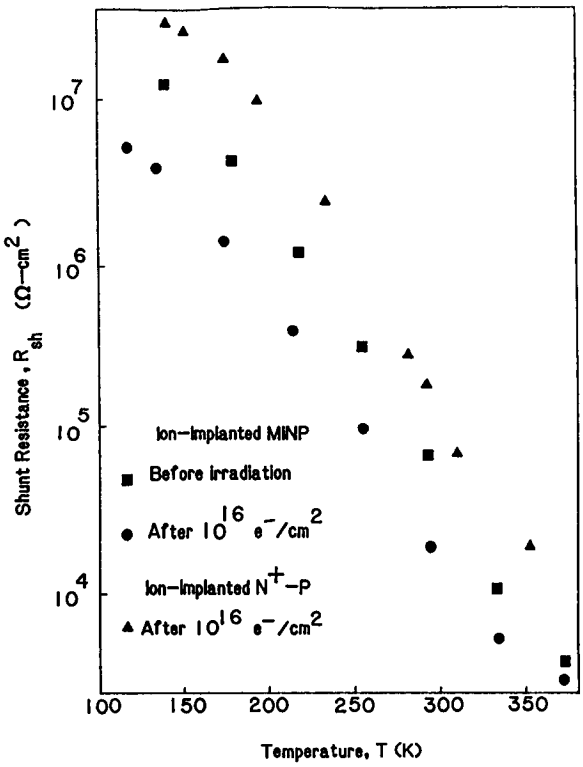

Figure 3. Temperature dependence of R_{sh} for ion-implanted cells as a function of 1.0 MeV electron fluence.

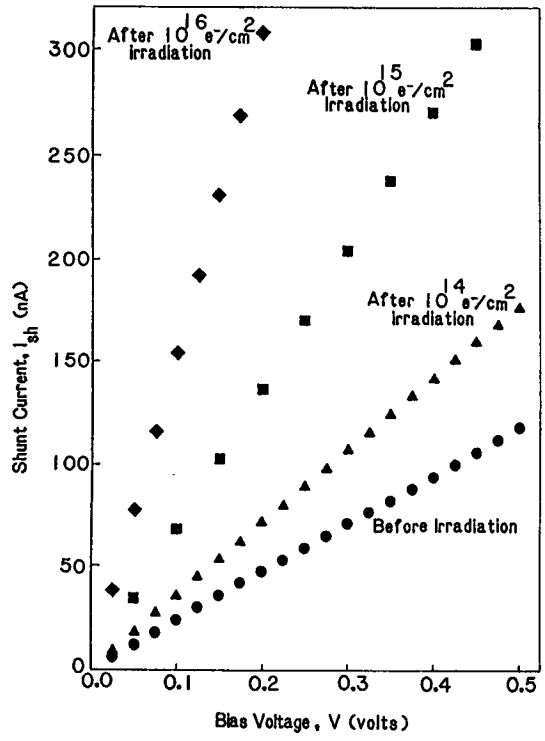

Figure 4. Shunt current variation with bias voltage for a diffused cell as a function of 1.0 MeV electron fluence.

RADIATION DAMAGE OF GALLIUM ARSENIDE PRODUCTION CELLS

N. Mardesich, D. Joslin, J. Garlick, D. Lillington, M. Gillanders, B. Cavicchi
Spectrolab, Inc.
Sylmar, California
and
J. Scott-Monck, R. Kachare, and B. Anspaugh
Jet Propulsion Laboratory
Pasadena, California

In 1985 a process for manufacturing gallium arsenide solar cells by Liquid Phase Epitaxy (LPE) was transferred from Hughes Research Laboratories, Malibu to Spectrolab, Inc. The process, involving the growth of GaAs and AlGaAs from a super cooled liquid gallium semi-infinite melt has been described elsewhere (Reference 1) and will not be repeated here. Existing facilities allow the fabrication of up to 15,000, 2 cm x 4 cm (or equivalent area) GaAs cells of 17% nominal efficiency with the provision for rapid scale-up when required.

In a joint study with Jet Propulsion Laboratory (JPL) we have irradiated high efficiency LPE GaAs cells made on our manufacturing line with 1 MeV electrons up to fluences of $1x10^{16}$ cm^{-2}. Measurements of spectral response and dark and illuminated I-V data were made at each fluence and then, using computer codes developed here for our HP3000 "in-house" computer, we have fitted experimental data to our GaAs cell models. In this way it has been possible to determine the extent of the damage, and hence damage coefficients in both the emitter and base of the cell.

CELL DESCRIPTION

Cells manufactured for this test were produced on Spectrolab's GaAs LPE production line. The cross-sectional view of the device is illustrated in Figure 1, where a nominal 300 μm substrate was used to produce a 7 μm buffer, 0.45 μm emitter and 0.40 μm window. The typical dopant concentrations in the substrate, buffer and emitter were $2x10^{18}$ Si/cc, $2x10^{17}$ Sn/cc and $2x10^{18}$ Be/cc respectively. The ohmic contacts were made directly to the P- GaAs and N+ GaAs (substrate) for the front and back respectively.

Typical production cells of 16.7% (AM0) average efficiency, (22.6 mW/cm^2), were used in the radiation evaluation. I_{sc} and V_{oc} were nominally 28.7 mA/cm and 985 mV respectively.

With the limited number of pilot runs which have been produced, the typical electrical yield of devices above 16.0% (average above 16.5%) was 75%. Figure 2 is a composite graph of 5 lots manufactured over the period from July through September.

THEORETICAL BASIS FOR ANALYSIS

Computer models have been developed by Spectrolab for windowed gallium arsenide cells (Reference 2). These can provide from basic cell parameters (see Table 1) such as diffusion lengths for carriers in the various cell layers, a prediction of cell performance. These outputs give overall parameters such as I_{sc}, V_{oc}, P_{max}, CFF, etc., as well as spectral response for cells, as functions of radiation damage. The models

give the component spectral response due to window, emitter, junction and buffer as well as the overall spectral response. A typical output is shown in Figure 3 for BOL and for EOL (ϕ = 1E16 e/cm^2). An important feature of the spectral analysis is that at a wavelength of .5 μm the response is almost entirely due to the emitter. This makes it possible to deduce the emitter damage coefficient separately from that in the buffer. Then since the analysis gives the component ratios for the long wavelength response (.88 μm) the .5 μm data can be used to find the emitter component at .88 μm and hence to determine the buffer damage coefficient.

The modeling (as discussed in Reference 2) examines the effect of first diode (diffusion limited behavior) and of the second diode (depletion layer recombination limited behavior). The latter is important in high band gap cells such as gallium arsenide. In addition to the obvious parameters I_{sc}, V_{oc}, etc., the model analysis also gives the saturation currents for the first and second diodes (I_{01} and I_{02} respectively) as functions of the radiation damage.

TEST EQUIPMENT AND SET-UP

The current-voltage (I-V) characteristic, as recorded for cells before and after irradiation, was accomplished with the aid of a computerized data acquisition system. The system acquires 300 data points, which are stored into memory and then manipulated to produce the I-V curve, short circuit current (I_{sc}), open circuit voltage (V_{oc}), and maximum power operating point (P_{max}).

The simulator used in this test is designated Spectrolab X-25. It's AMO intensity was set using a GaAs encapsulated secondary standard 83-156 traceable to balloon flown standard 80-132. However, unirradiated sister cells to the ones tested were measured before and after irradiation to verify simulator intensity. Irradiated balloon flown standard 85-132 was also used to verify correct blue-red color ratio. The sample temperature on the test block was held to 28 $\pm$ 1°C by water cooling the block.

The instrumentation used to measure the spectral irradiance of the simulator was an Optronics Spectroradiometer with a Hewlett Packard 85 computer used for converting detector current to irradiance values, and for system control. The lower and upper limits of the range was 280 nm and 1050 nm, respectively. The slit width on the monochrometer and the wavelength interval was 5 nm during both the calibration and the actual scan.

Spectrolab has developed a computerized data acquisition system for dark I-V measurement. The system based on a 10 bit D/A and A/D interface is driven by an Apple IIe computer and enables rapid I-V measurement to be made over six orders of magnitude of current. Algorithms within the computer code allow the determination I_{01}, I_{02} and shunt resistance to be made and also a hard copy may be made on an HP X-Y recorder. The system is bipolar, enabling forward and reverse measurements to be made with ease.

Spectral response measurements were made by use of a computer controlled multifilter system. Twenty optical filters cover the expected cell response range with "crowding" filters at crucial parts of the spectrum for gallium arsenide cells (.4 - .5 and .8 to .9 μm respectively). At each filter position many readings are taken and averaged to increase accuracy and the system is calibrated by a sub-standard silicon cell with a spectral range much greater than that of gallium arsenide. This cell was calibrated against a silicon diode calibrated at Optoelectronics Laboratories

and also had formed one of a group of cells circulated among various establishments by Spectrolab in an attempt to standardize interlaboratory results. The system output gives cell response in mA/mW and also the quantum efficiency at each wavelength. An integration procedure gives an estimate of I_{sc} at AMO from the spectral data and this can be compared with I_{sc} data from the AMO simulator.

RESULTS

The cells used for irradiation were divided into four groups. The first group were held as standards and were not irradiated. The second group were irradiated to 10^{14}, $9X10^{14}$, $2.0x10^{15}$ and $7x10^{15}$ e^-/cm^2. The cells were tested at every level and a few cells were held as controls at each level. The third group were irradiated to $9X10^{14}$, $2.0x10^{15}$ and $7x10^{15}$ e^-/cm^2 for a total dosage of $9.9x10^{15}/cm^2$. Cells at each dosage level were also held as controls. The fourth and final group were irradiated to $7x10^{15}$ e/cm^2. The average P/P_o, J_{sc}/J_{sco} or V_{oc}/V_{oco} of the total starting group were within $\pm$ 0.3% of the final diminished group receiving the total dosage.

Table 2 and Figure 4 represent the degradation of the average cell and typical I-V curve for cells in group 2. This data is plotted in Figure 5 as a function of fluence. Representative spectral response curves for the range of fluence are plotted in Figure 6. Table 2 includes predicted values (in brackets) from the cell model using the parameters of Table 1.

From the response spectra of cells under the various fluences the variation at certain chosen wavelengths was determined. The results are plotted in Figure 7 for the wavelengths of .5 μm and .88 μm together with the overall I_{sc} calculated from the full spectral response. Also included is the plot for I_{sc} taken from the X-25 simulator measurements. These curves now have to be compared with those deduced from the modeling. The main cell specifications are as in Table 1 but parameters such as damage coefficients are varied to test fits with data. The broken curves in Figure 7 give the modeling curves for emitter and buffer damage coefficients of $3.5.10^{-8}$ and 2.10^{-7}/e respectively. A discussion of the comparative behavior is given below.

DISCUSSION

As shown by Table 2 the results of the 1 MeV electron irradiation tests can be predicted by the model using appropriate damage coefficients for emitter and buffer. We have chosen first to match these to prediction of I_{sc} values which depend on the total surface interface velocity between emitter and window. The model V_{oc} values at BOL are then too large but this is likely to be due to the fact that under the front grid contacts which penetrate into the emitter much higher velocities occur. Computation then shows that under V_{oc} conditions the experimental BOL value of V_{oc} would be obtained if the velocity averages 2.10^6 cm/s indicating much higher values under the contacts.

From dark state current-voltage curves we have computed the second diode (depletion layer recombination) saturation currents (I_{02}) as functions of damage. Initially, for the model parameters of Table 1 the value of I_{02} is about $5\text{-}6.10^{-11}$ A/cm^2 and at EOL (10^{16} e/cm^2) it is about $8\text{-}9.10^{-10}$ A/cm^2 i.e. a factor of 7 higher. The model gives a BOL value of 5.10^{-11} A/cm^2, close to the experimental value; at 10^{16} e/cm^2 fluence it is also about 7 times higher.

The extensive spectral response measurements in this work afford an opportunity to test the model. The data in Figure 7 at .5μm give the ability to see damage in

the emitter almost exclusively while the data at .88μm give the combined buffer, junction and emitter effects. In this region the discrepancies between model and experiment are evident. To match the .88μm values the damage coefficient for emitter would have to be increased so much that the .5μm data would not correlate with the model. There is clearly a situation here which needs to be followed up by model review and by further, more detailed analysis of the spectral data.

In conclusion we have carried out extensive studies of the effects of 1 MeV electron damage in gallium arsenide windowed cells. Overall the results are very similar to those published earlier by Mitsubishi (Reference 3) and by Hughes Research Laboratories (Reference 4). This is very significant since these devices were manufactured by us and these companies at different times; only the LPE layer growth is similar. We have extended diagnostics to include dark current-voltage curves and to detailed spectral analysis. What has been revealed is that overall modeling is satisfactory but that there are significant and interesting discrepancies which demand further attention.

Reference 1 - Mardesich, N. IEEE Proc. 18th PVSC, P.105 (1985)

Reference 2 - Garlick, G.F.J. IEEE Proc. 18th PVSC, P.854 (1985)

Reference 3 - Kato, M. IEEE Proc. 18th PVSC, P.652 (1985)

Reference 4 - Anspaugh, B. et al. Solar Cell Radiation Handbook 3rd Ed. JPL Publication 82-69 1982

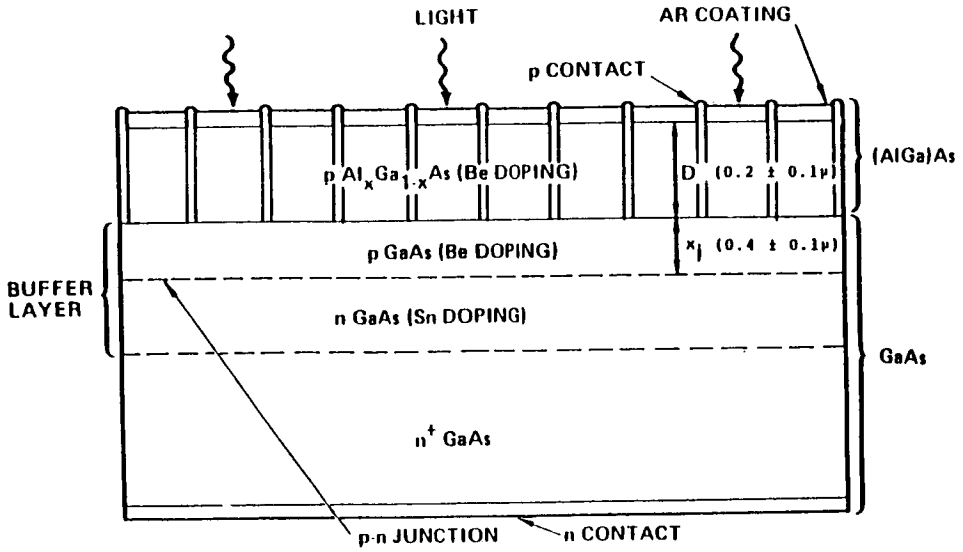

FIGURE 1. CROSS-SECTIONAL VIEW OF GaAs SOLAR CELL

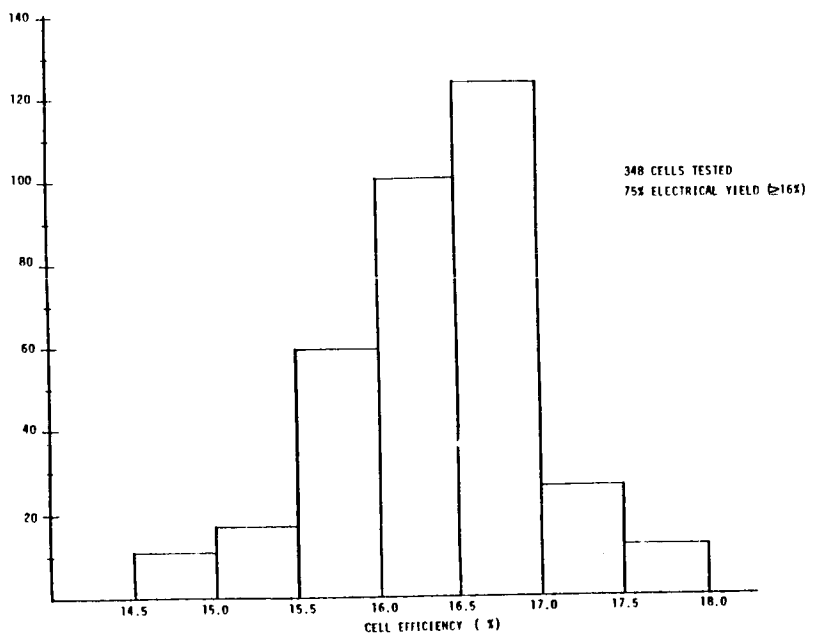

FIGURE 2. EFFICIENCY DISTRIBUTION OF GaAs CELL (4.30 CM^2)

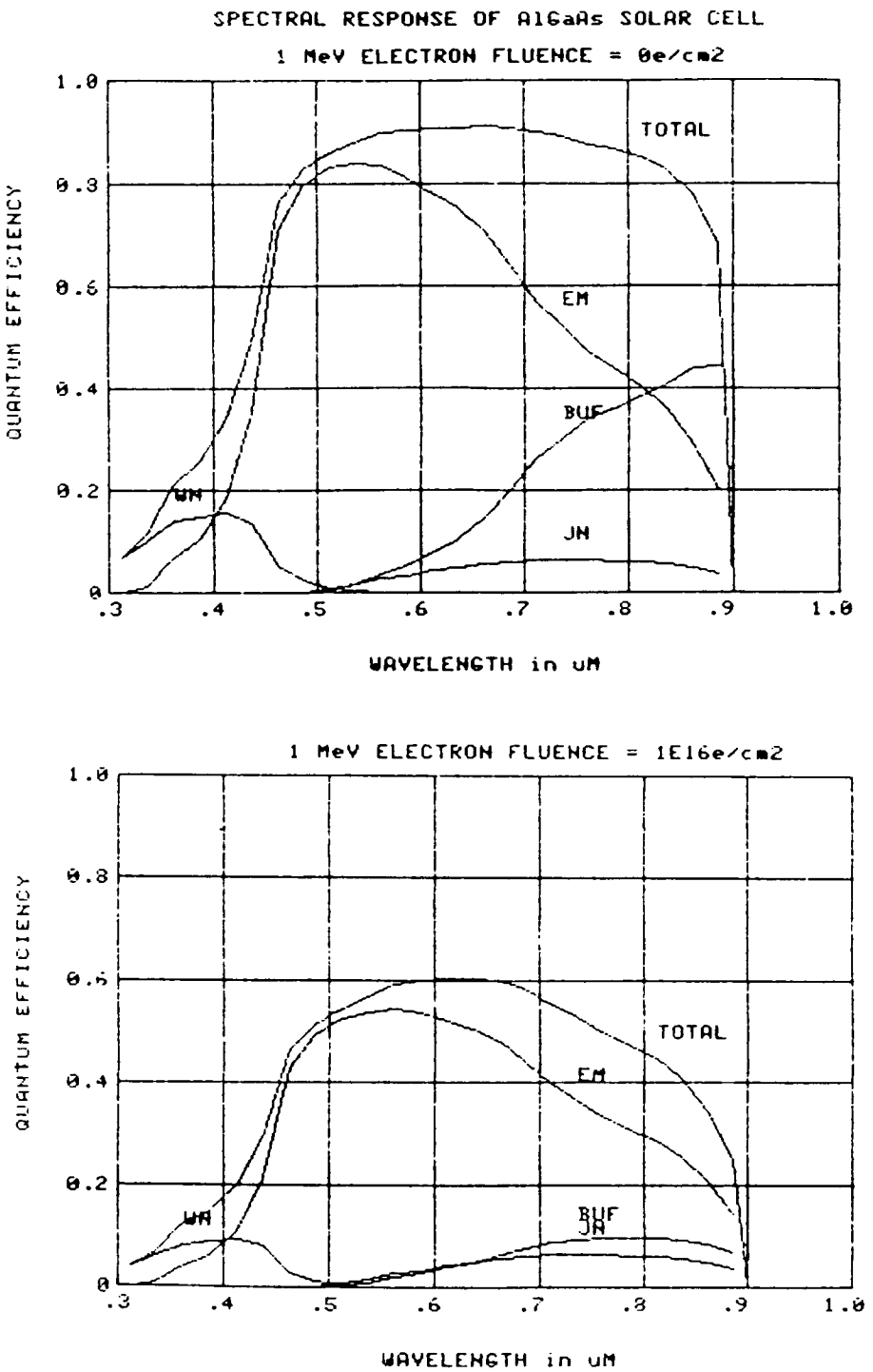

FIGURE 3. CALCULATED SPECTRAL RESPONSE OF GaAs CELL AT ZERO AND 10^{16} e-/cm^2 FLUENCE

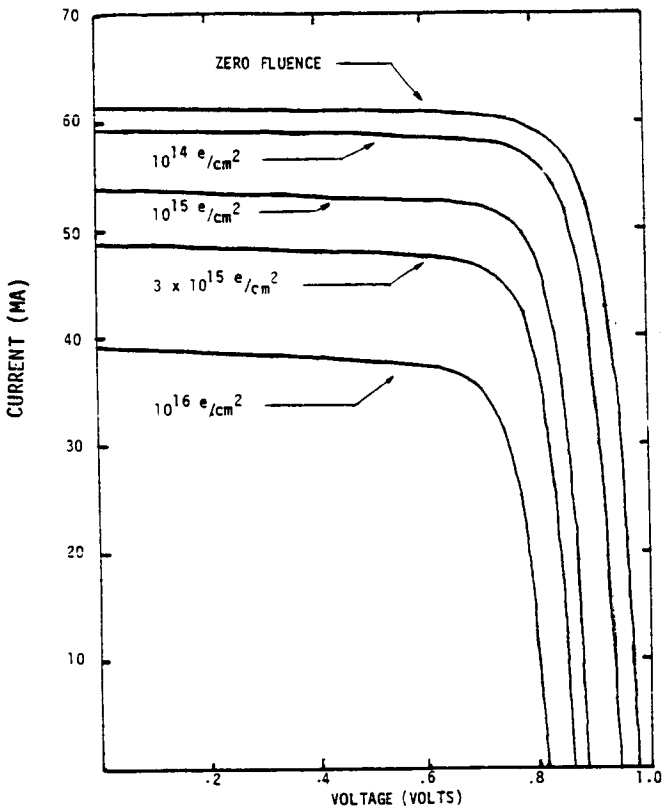

FIGURE 4. I-V CURVE OF A TYPICAL GaAs CELL AT VARYING 1 MeV FLUENCE

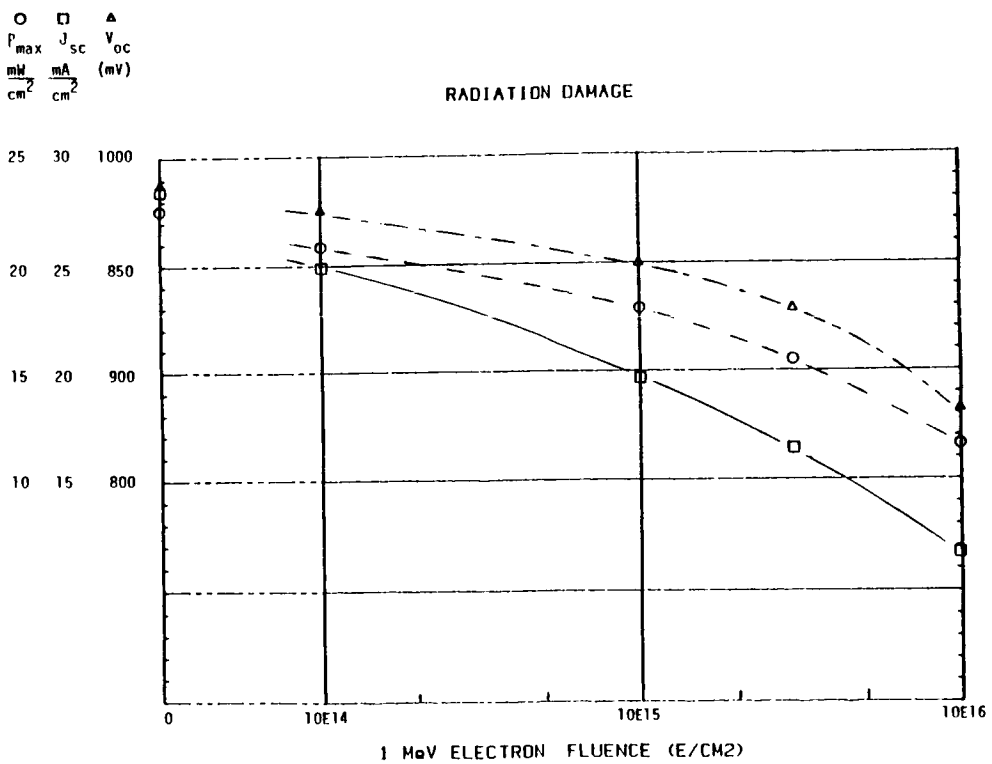

FIGURE 5. P_m, I_{sc}, AND V_{oc} vs. 1 MeV ELECTRON FLUENCE FOR TYPICAL GaAs CELL

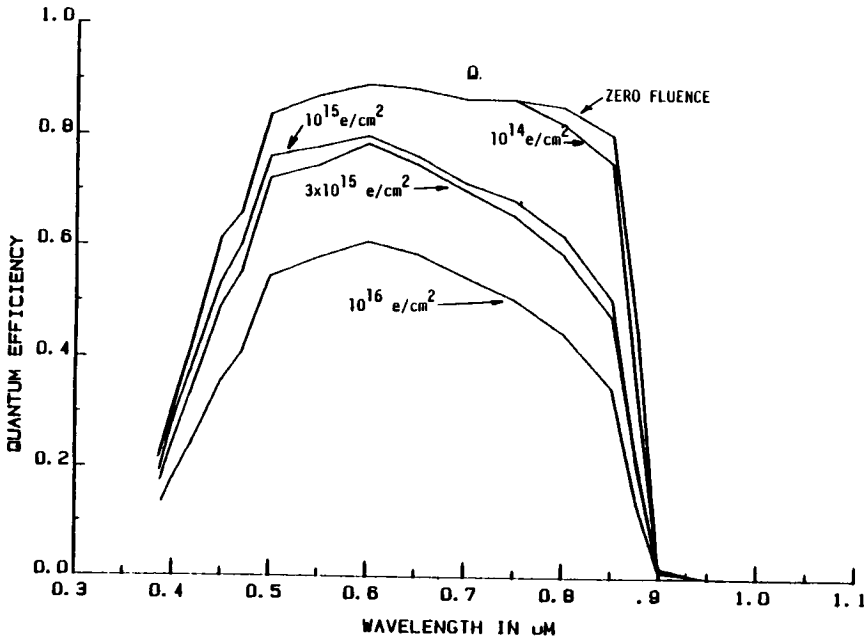

FIGURE 6: QUANTUM EFFICIENCY DEGRADATION AS A FUNCTION OF 1 MeV ELECTRONS

RADIATION DAMAGE

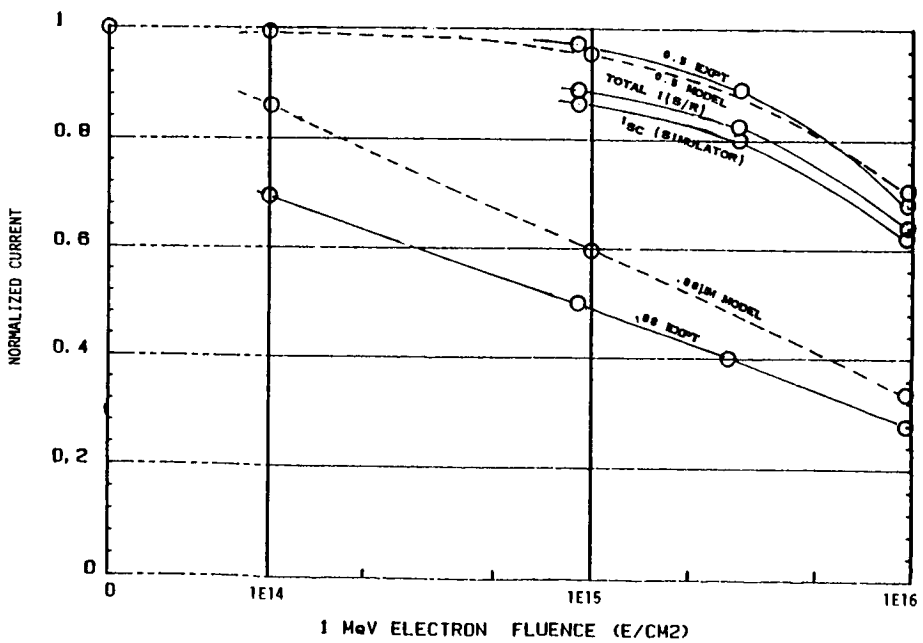

FIGURE 7: I_{SC} (AMO) I_{SC} (SPECTRAL RESPONSE), I_{SC} (.5μm) AND I_{SC} (.88μm) AS A FUNCTION OF 1 MeV ELECTRONS COMPARED TO THEORETICAL MODEL

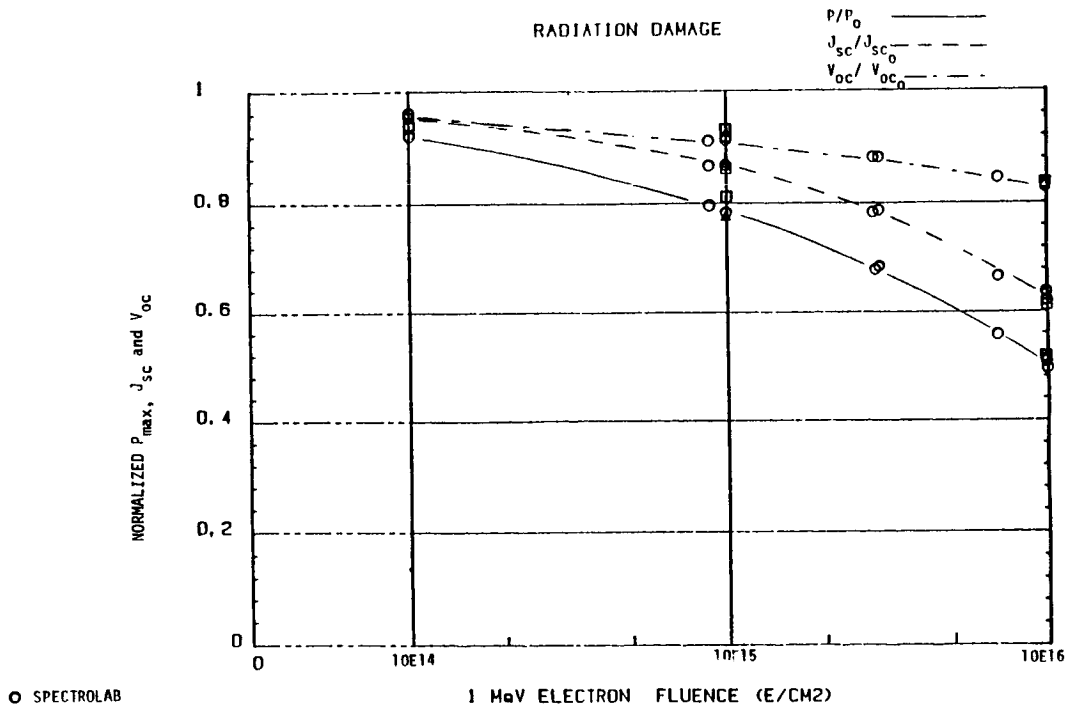

FIGURE 8. NORMALIZED P_{max}, I_{sc}, AND V_{oc} AS A FUNCTION OF 1 MeV ELECTRONS FOR RECENT TEST AND PUBLISHED DATA

TABLE 1

TYPICAL CELL PARAMETERS FOR MODELING OF CHARACTERISTICS TO MATCH EXPERIMENTAL DATA

WINDOW LAYER	
Thickness	.5 µm
Diffusion length	.2 µm
Diffusion coefficient	.27cm^2/s
Surface recombination velocity	10^6 cm/s
Doping concentration	2.10^{18}/cm^3
EMITTER LAYER	
Thickness	.5 µm
Diffusion length	5 µm
Diffusion coefficient	90cm^2/s
Interface recombination velcity	3.10^5 cm/s
Doping concentration	2.10^{18}/cm^3
BUFFER LAYER	
Thickness	7 µm
Diffusion length	2 µm
Diffusion coefficient	5 cm^2/s
Doping concentration	2.10^{17}/cm^3
DAMAGE COEFFICIENTS	
Emitter	$3.5.10^{-8}$/e
Buffer	$1.8.10^{-7}$/e

TABLE 2

FLUENCE (e/cm^2)	V_{oc} (mV)	I^{sc} (mA/cm^2)	P_{max} (mW/cm^2)	FF
0	984	28.7	22.6	.800
	(1006)	(28.0)	(22.8)	
10^{14}	948	27.5	20.9	.802
	(992)	(27.63)	(21.86)	
10^{15}	896	25.0	17.9	.800
	(933)	(25.77)	(18.5)	
3×10^{15}	863	22.7	15.4	.788
10^{16}	817	18.3	11.5	.769
	(812)	(18.14)	(11.09)	

*Bracketed values are model predictions

AVERAGE V_{oc}, J_{sc}, P_{max}, FF OF GROUP 2 GaAs SOLAR CELLS AFTER 1 MeV FLUENCE

N87-26438

PERFORMANCE OF AlGaAs, GaAs, AND InGaAs CELLS AFTER 1 MeV ELECTRON IRRADIATION

Henry B. Curtis and Russell E. Hart Jr.
NASA Lewis Research Center
Cleveland, Ohio

Electron irradiations (1 MeV) were made on three different types of III-V cells. AlGaAs, GaAs, and InGaAs cells with bandgaps of approximately 1.72, 1.43, and 1.1 eV, respectively, were tested. All of the cells were concentrator cells and performance data from 1 sun to beyond 100x AM0 were taken. The total 1 MeV electron fluence was $3x10^{15}$ e/cm^2 with data taken at several intermediate fluences. Cell performance is presented as a function of electron fluence for various concentration ratios and two different temperatures (25 and 80 °C). Since these three cell types are potential candidates for the individual cells in a cascade structure, it is possible to calculate the loss in performance of cascade cells under 1 MeV electron irradiation. Data are presented which show the calculated performance of both series-connected and separately connected cascade cells.

INTRODUCTION

For many years concentrator photovoltaic (PV) systems have been under strong consideration for use in space. The advantages of concentrator PV include higher cell efficiency, better radiation resistance, and a cost effective way of using advanced PV technology such as multijunction cells. Several optical designs are being studied such as the minature Cassegrainian system developed by TRW (ref. 1) and the SLATS trough system developed by General Dynamics. Both designs utilize small cells with illuminated areas that are a fraction of a square centimeter.

One of the concerns about concentrator PV is the effect of particle radiation on the cell performance at concentrated light levels. As part of an ongoing program at NASA Lewis Research Center, we have irradiated several types of concentrator cells with 1 MeV electrons and measured the performance degradation. Results for several GaAs cells were presented at the 18th IEEE Photovoltaic Specialists Conference (PVSC)(ref. 2). The results presented here are for AlGaAs, GaAs, and InGaAs cells irradiated with 1 MeV electrons to a fluence of $3x10^{15}$ e/cm^2. Results are also given for the calculated performance of multijunction cells under 1 MeV electron irradiation.

CELL DESCRIPTION

All the cells used in these irradiations were made by Varian. The bandgaps were 1.72 eV for the AlGaAs cells, 1.43 eV for the GaAs cells, and 1.1 eV for the InGaAs cells. The cells are all OM-VPE grown with an appropriate AlGaAs window. The AlGaAs cells were n/p while the GaAs and InGaAs cells were p/n. The GaAs cells had a junction depth of 0.5 μm, and the AlGaAs and InGaAs were about the same. There were a minimum number of cells available for this effort and some care should be taken in analyzing the data. There were four GaAs cells irradiated along with

two each of the AlGaAs and InGaAs cells. A summary of cell bandgaps and illuminated diameters is given in table I.

EXPERIMENTAL DESCRIPTION

All small area concentrator cells were individually mounted in separate cell holders. For the GaAs and AlGaAs cells, the holders consisted of a small bottom metal base and a washer-like metal top with a beveled hole slightly larger than the illuminated area of the cell. These two pieces supplied both a permanent support for the cell and an area for the four-wire electrical attachment. There was no soldering or welding of any contact to any cell. The InGaAs cells were mounted in Varian holders with top contacts attached directly to the outer busbar. The cells remained in their holders throughout all electron irradiations and performance measurements. There were no cover glasses attached to the cells, nor was there any shielding by optical elements during the irradiations.

Electron irradiations using 1 MeV electrons were performed at the NASA Lewis dynamitron and at the Naval Research Laboratory (NRL) Van de Graff generator. The cells were irradiated to a total fluence of 3×10^{15} e/cm^2, with performance measurements made at several intermediate fluence levels. The performance measurements consisted of the following:

1) Current-Voltage (I-V) data at 25 °C and 1 AM0 using an X-25 xenon solar simulator and a reference cell.

2) I-V data at 25 °C at several concentrations up to 100x AM0 and above using a pulsed xenon solar simulator and the linear assumption between irradiance and short-circuit current.

3) Short-circuit current data at one fixed concentration at both 25 and 80 °C in order to set the current scale at the elevated temperature.

4) I-V data at 80 °C at several concentrations as in step 2.

During I-V measurements the cells in their holders are mounted to a temperature-controlled block. The concentration level on the cell is varied by changing the distance from the light source and by using a Fresnel lens. Since the duration of the light pulse from the flash simulator is just 2 msec, there is no heating effect from the concentrated light. The elapsed time at 80 °C was about 30 min for each cell. Several repeat measurements were made at 1 sun and 25 °C after the elevated temperature measurements, in order to determine if any annealing had taken place.

RESULTS AND DISUSSION

Table II shows the average starting electrical parameters (before electron irradiation) for the three different cell types. Data are presented for 100x concentration levels at both 25 °C and 80 °C, and at AM0 25 °C. At the 100x concentration level, the cells show excellent efficiencies with the GaAs cells averaging over 21 percent at 25 °C and 20 percent at 80 °C. At 1 sun, the efficiencies were somewhat low because of shunting effects, which are unseen at the normal operating concentration levels.

Tables III, IV, and V show the ratios of short-circuit current, open-circuit voltage, fill factor, and maximum power after irradiation to the unirradiated values for several fluence levels at three different measurement conditions. Table III shows data for 25 °C at 1 sun, while tables IV and V show data for 100x concentration at 25 °C and 80 °C respectively. The ratios for short-circuit current at 25 °C are the same for both solar irradiation levels because of the linear current-irradiance assumption. The tables indicate that the bulk of the degradation is in the current with much smaller degradation in voltage and fill factor.

Figure 1 shows plots of normalized maximum power as a function of 1 MeV electron irradiance for the three cell types at 25 °C and 100x AM0. The InGaAs cells show more degradation at the higher fluences than the AlGaAs or GaAs cells. It is difficult to draw conclusions from these curves because they are based on a small number of cells (two each of AlGaAs and InGaAs and four of GaAs). However there may be a trend of more radiation resistance with increasing bandgap. If so, this would be beneficial for multijunction cells where the higher bandgap cells produce more of the power. Figures 2, 3, and 4 show similar data for short-circuit current (I_{SC}), open-circuit voltage (V_{OC}), and fill factor respectively. These curves show the major drop in power is due to loss of current as the 1 MeV fluence level increases.

Figures 1 to 4 show data taken at 25 °C. Typical operating temperatures on concentrator cells in space will be dependent on orbit, concentration level, cell size, and concentrator design. During this investigation data were taken at 80 °C, which would be a typical operating temperature. Figure 5 shows normalized maximum power at 100x AM0 for the AlGaAs cells as a function of 1 MeV electron fluence for two temperatures, 25 °C and 80 °C. The difference between data at the two temperatures is not that large. From tables IV and V, the spread in degradation between 25 °C and 80 °C for GaAs cells is smaller than the AlGaAs spread in figure 5, while it is a little larger for the InGaAs cells.

All the data presented have been for individual cells and are actual measured data. Since we have data for cells of different bandgaps, we can calculate the performance of multijunction cells under 1 MeV electron irradiation. The AlGaAs/InGaAs pair is a good candidate for this calculation since the bandgaps, 1.72 eV and 1.1 eV, are near the ideal pair for optimum multijunction performance. When the AlGaAs and InGaAs cells are operating as a multijunction cell, the bottom cell (InGaAs) is filtered by the AlGaAs cell and has less sunlight incident upon it. Since the bandgaps are near optimum for a series-connected multijunction cell, we reduced the irradiance on the bottom cell until the currents matched at the unirradiated fluence level. With 100x concentration on the AlGaAs cell, we had about 56x on the InGaAs cell. Since data were taken at several concentration levels at 25 °C at each fluence, we can readily obtain data for the InGaAs cell at 56x for all fluence levels.

Figure 6 shows normalized maximum power for the top AlGaAs cell and the "filtered" bottom InGaAs cell as a function of 1 MeV electron fluence. The curves are normalized to 1 for the top cell. Note that although the two curves look parallel, there is a much greater percentage drop for the InGaAs bottom cell as fluence increases. Figure 7 is a similar curve showing short-circuit current for the AlGaAs top cell and the "filtered" InGaAs cell. For the current data, the two curves diverge a large amount while starting at the same value at zero fluence.

There are two cases of multijunction cells of interest. One is the separately connected or 4-terminal structure, and the second is the series-connected structure. In the separately connected case, the performance of the multijunction cell can be calculated just by adding the maximum powers of the individual cells shown on figure 6. The series connected structure requires adding actual I-V curves in series. In this case, if the currents are mismatched, the output power will be less than the simple sum of the individual cell powers.

The diode equation was used to obtain I-V curves for the series connected case. The light-generated current was set to the desired short-circuit current while the coefficients of the injection term and space-charge recombination term were varied to match V_{OC} and fill factor. A series resistance of less than .05 ohm-cm^2 was used. We were than able to calculate an entire I-V curve to match any set of parameters. In order to add I-V curves with different currents, a reverse characteristic is required. For this work we assumed the curves broke down between -2 and -3 V.

Figure 8 shows the calculated degradation in maximum power (Pmax) for both the series-connected and separately connected (four-terminal) multijunction cells under 1 MeV electron irradiance. The operating conditions are 25 °C and 100x AM0 incident on the top cell. We also show the individual curves for the top AlGaAs and the "filtered" bottom InGaAs cells. Note that for very low fluences, the difference between series and separate connections is quite small. However as the currents of the two cells diverge at higher fluence levels, the series connected case falls to a point where the multijunction cell delivers less power than a bare AlGaAs cell would. This is due to the limiting action of the large current mismatch between the two individual cells.

The results of figure 8 indicate that for high-radiation missions, it may be necessary to use the separately connected version of multijunction cells because of the problems created by current mismatch. For shorter missions in a low radiation orbit, the series connected version would perform just as well as the four-terminal case. It must be noted that this work is based on 1 MeV electron irradiations only on a small number of cells. Further work is required to more completely investigate the radiation performance of multijunction cells.

ACKNOWLEDGMENTS

The electron irradiation facilities at NRL were made available through the cooperation of Richard Statler and Robert Farr.

REFERENCES

1. Patterson, R.E.: Preliminary Concept of a 100-Kilowatt Miniaturized Cassegrainian Concentrator Solar Array. Space Photovoltaic Research and Technology 1983, NASA CP-2314, 1983, pp. 157-162.

2. Curtis, H.B.; and Swartz, C.K.: Performance of GaAs and Silicon Concentrator Cells Under 1 MeV Electron Irradiation. 18th IEEE Photovoltaic Specialists Conference, IEEE, 1985, pp. 356-361.

TABLE I. - DESCRIPTION OF CELLS

Cell type	Bandgap, eV	Diameter, mm
AlGaAs	1.72	6.3
GaAs	1.43	4.0
InGaAs	1.10	6.3

TABLE II. - INITIAL I-V DATA

	Short-circuit current/cm^2, A	Open-circuit voltage, V	Fill factor	Efficiency, percent
100x AMO, 25 °C				
AlGaAs	1.996	1.376	0.836	16.9
GaAs	3.174	1.143	.792	21.2
InGaAs	3.580	.859	.794	18.1
100x AMO, 80 °C				
AlGaAs	2.069	1.264	0.802	15.5
GaAs	3.309	1.059	.772	20.0
InGaAs	3.648	.774	.775	16.2
AMO, 25 °C				
AlGaAs	19.96×10^{-3}	1.200	0.772	13.7
GaAs	31.74	.898	.762	16.0
InGaAs	35.80	.613	.655	10.6

TABLE III. - RATIOS OF IRRADIATED TO INITIAL VALUES FOR SEVERAL 1 MeV ELECTRON FLUENCES AT 25 °C and 1X

Fluence level, e/cm^2	Short-circuit current I_{sc}	Open-circuit voltage V_{oc}	Fill factor	Power Maximum
AlGaAs				
$1x10^{13}$	1.002	0.998	1.005	1.007
$3x10^{13}$	.998	.999	1.008	1.007
$1x10^{14}$	.993	.997	1.003	.993
$3x10^{14}$	.968	.987	1.003	.959
$1x10^{15}$	.909	.938	.986	.868
$3x10^{15}$	.821	.938	.971	.747
GaAs				
$1x10^{13}$	0.989	1.002	1.000	0.991
$3x10^{13}$	.978	.994	1.009	.981
$1x10^{14}$	.965	.993	1.007	.965
$3x10^{14}$	.927	.977	1.011	.923
$1x10^{15}$	.875	.957	1.020	.860
$3x10^{15}$	.776	.928	1.036	.750
InGaAs				
$1x10^{13}$	0.974	1.006	0.995	0.976
$3x10^{13}$	.973	.999	.996	.969
$1x10^{14}$	.942	.989	.995	.929
$3x10^{14}$	.879	.980	.998	.860
$1x10^{15}$	.687	.929	.995	.637
$3x10^{15}$	.460	.857	.989	.393

TABLE IV. - RATIOS OF IRRADIATED TO INITIAL VALUES FOR SEVERAL 1 MeV ELECTRON FLUENCES AT 25 °C and 100x

Fluence level, e/cm^2	Short-circuit current I_{sc}	Open-circuit voltage V_{oc}	Fill factor	Power Maximum
AlGaAs				
$1x10^{13}$	1.002	0.987	0.990	0.979
$3x10^{13}$	.998	.988	.977	.966
$1x10^{14}$	.993	.983	.975	.953
$3x10^{14}$	.968	.979	.963	.913
$1x10^{15}$	.909	.963	.969	.849
$3x10^{15}$	.821	.948	.938	.730
GaAs				
$1x10^{13}$	.989	.991	1.010	.989
$3x10^{13}$	.978	.975	1.029	.978
$1x10^{14}$	.965	.954	1.030	.947
$3x10^{14}$	.927	.925	1.027	.881
$1x10^{15}$	.875	.893	1.033	.807
$3x10^{15}$	.776	.859	1.029	.687
InGaAs				
$1x10^{13}$	.974	.996	.995	.963
$3x10^{13}$	.973	.998	.997	.968
$1x10^{14}$	.942	.988	.997	.926
$3x10^{14}$	.879	.971	.994	.847
$1x10^{15}$	.687	.933	.975	.623
$3x10^{15}$	.460	.889	.953	.389

TABLE V. - RATIOS OF IRRADIATED TO INITIAL VALUES FOR SEVERAL 1 MeV ELECTRON FLUENCES AT 80 °C and 100x

Fluence level, e/cm^2	Short-circuit current I_{sc}	Open-circuit voltage V_{oc}	Fill factor	Power Maximum
AlGaAs				
$1x10^{13}$	1.004	0.992	0.991	0.991
$3x10^{13}$	.996	.994	.988	.982
$1x10^{14}$	.998	.990	.983	.972
$3x10^{14}$	.977	.983	.979	.943
$1x10^{15}$	.926	.967	.970	.871
$3x10^{15}$	.839	.943	.968	.767
GaAs				
$1x10^{13}$	.988	.992	.999	.980
$3x10^{13}$	.980	.971	1.015	.966
$1x10^{14}$	.965	.947	1.024	.939
$3x10^{14}$	.925	.916	1.036	.871
$1x10^{15}$	.872	.879	1.025	.786
$3x10^{15}$	.779	.840	1.020	.670
InGaAS				
$1x10^{13}$	.977	.999	.986	.963
$3x10^{13}$	.976	.998	.986	.963
$1x10^{14}$	.951	.995	.990	.939
$3x10^{14}$	.899	.981	.985	.870
$1x10^{15}$	.748	.922	.968	.666
$3x10^{15}$	.527	.884	.946	.441

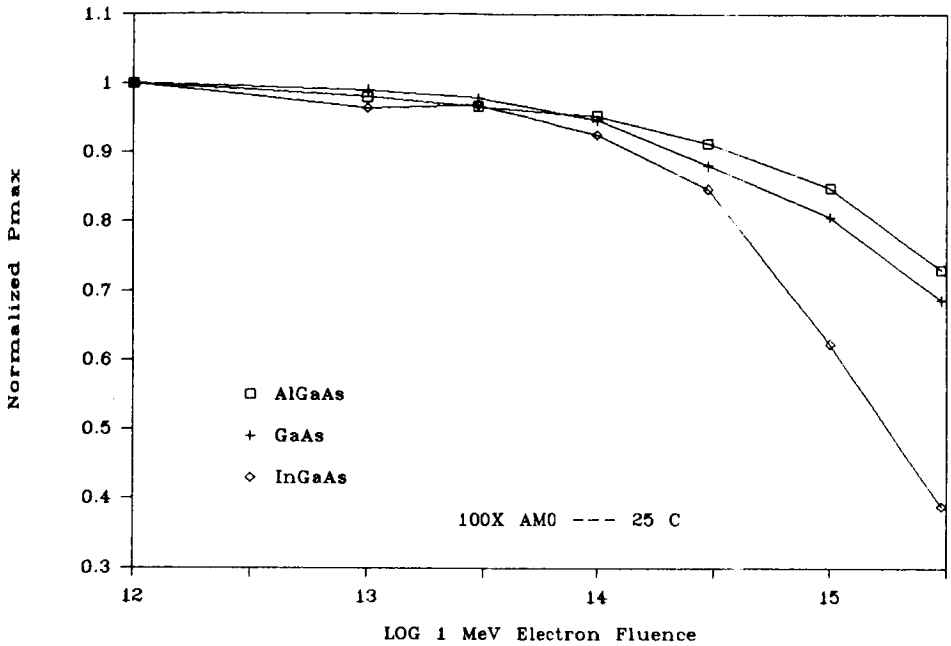

Figure 1. - Normalized maximum power for AlGaAs, GaAs, and InGaAs cells as function of 1 MeV electron fluence. (100x AM0, 25 °C)

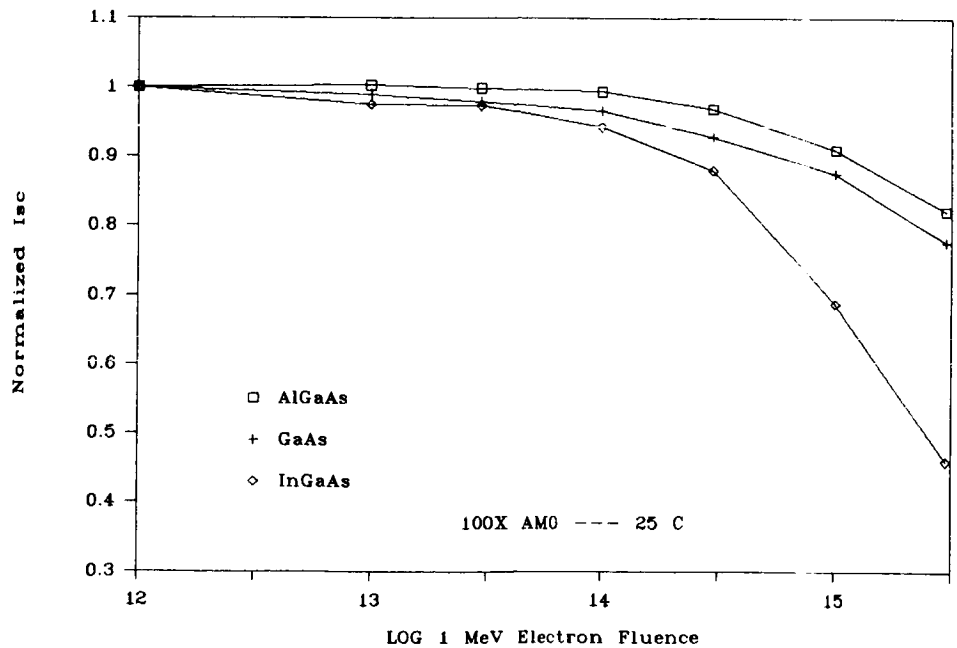

Figure 2. - Normalized short-circuit current for AlGaAs, GaAs, and InGaAs cells as function of 1 MeV electron fluence. (100x AM0, 25 °C)

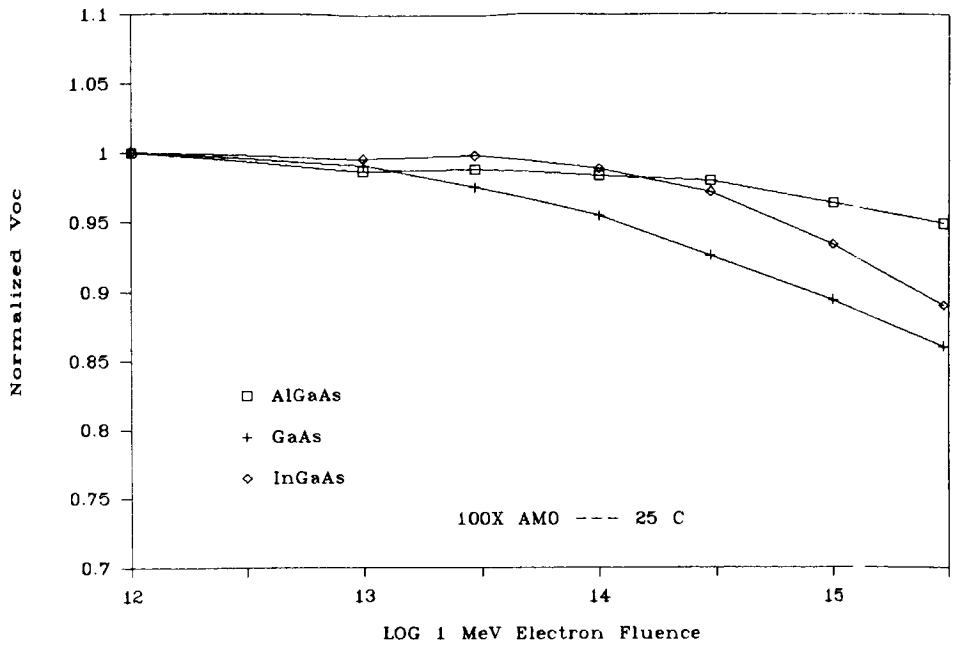

Figure 3. - Normalized open-circuit voltage for AlGaAs, GaAs, and InGaAs cells as function of 1 MeV electron fluence. (100x AMO, 25 °C)

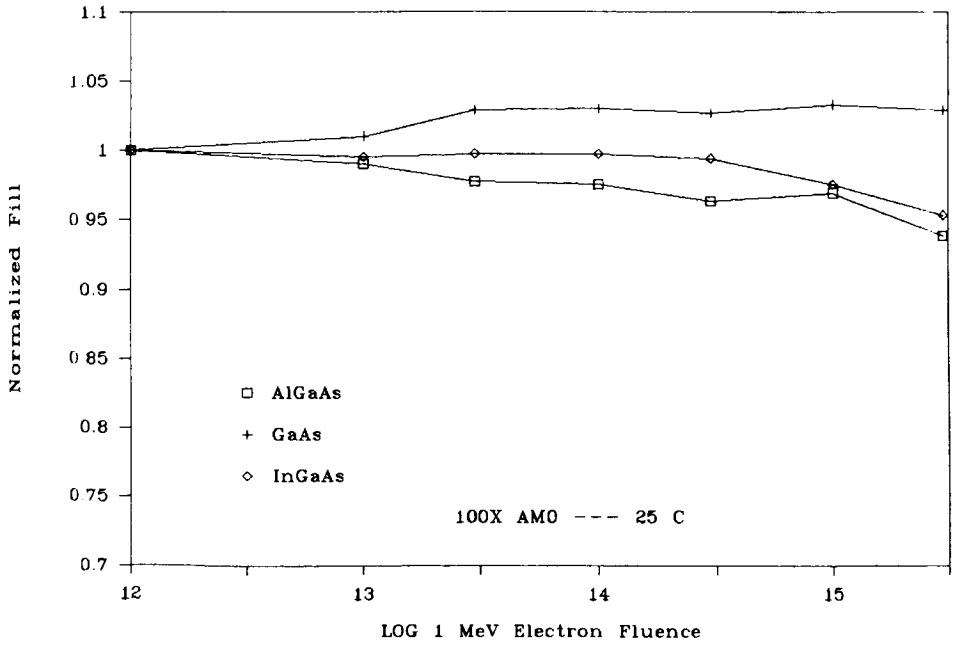

Figure 4. - Normalized fill factor for AlGaAs, GaAs, and InGaAs cells as function of 1 MeV electron fluence. (100x AMO, 25 °C)

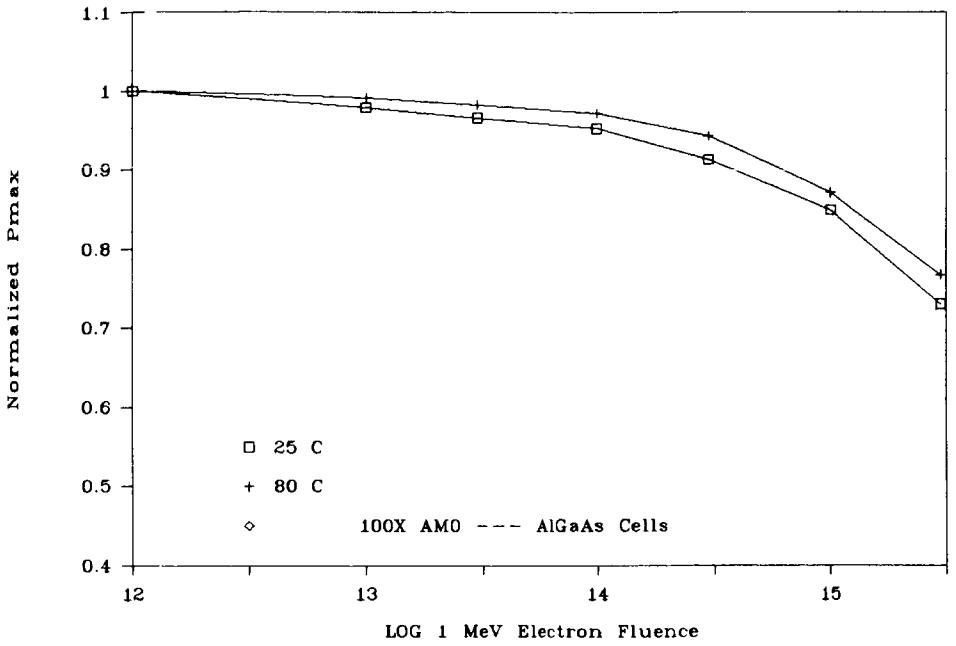

Figure 5. - Normalized maximum power for AlGaAs cells at 25 °C and 80 °C as function of 1 MeV electron fluence.

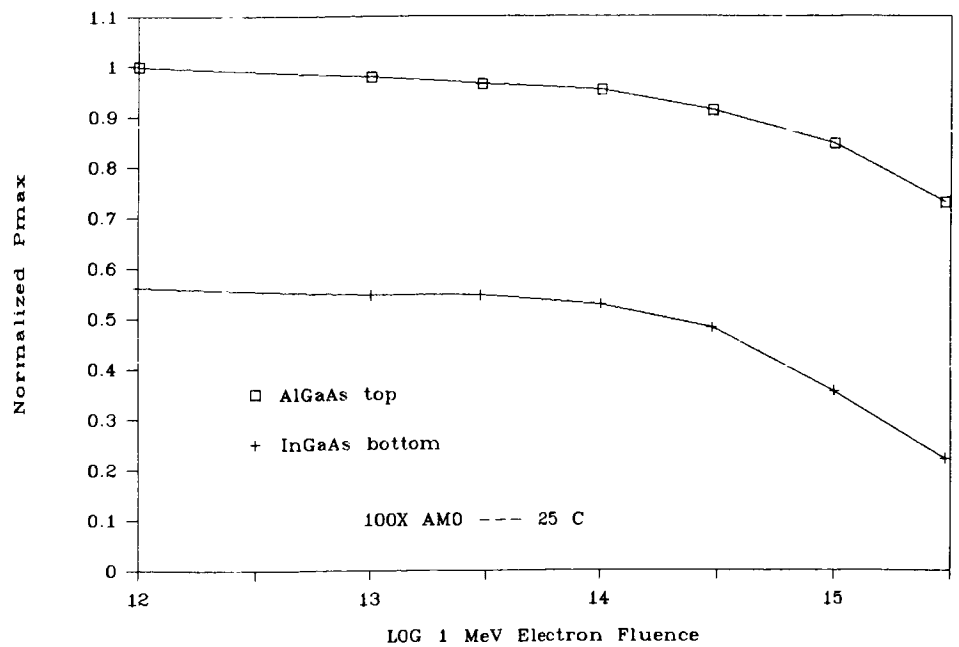

Figure 6. - Normalized maximum power for AlGaAs top cell and an InGaAs bottom cell at 25 °C with 100x AMO incident on top cell as function of 1 MeV electron fluence.

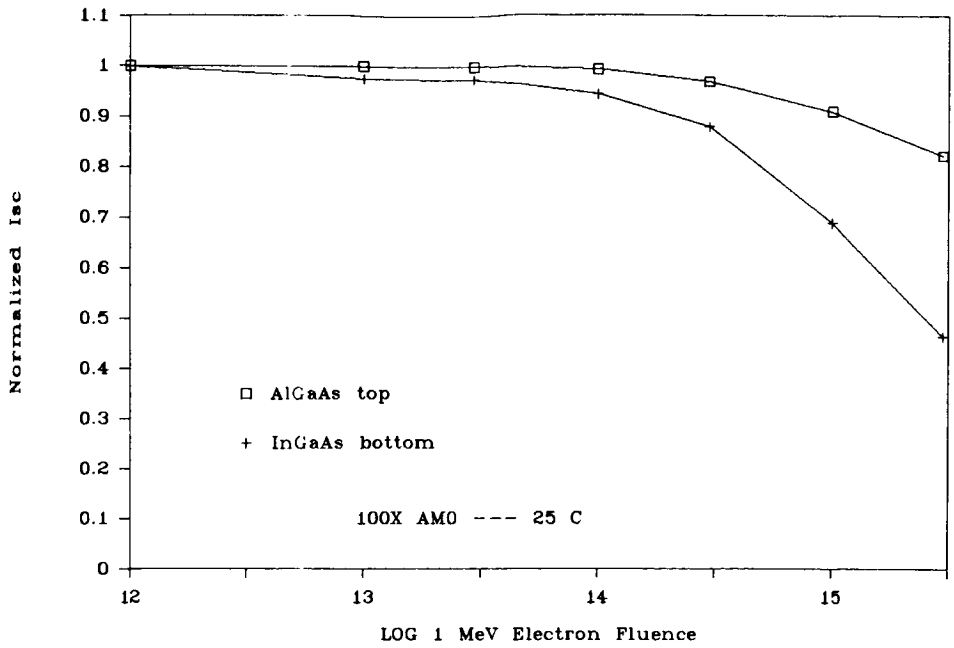

Figure 7. - Normalized short-circuit current for an AlGaAs top cell and an InGaAs bottom cell at 25 °C with 100x AM0 incident on top cell as function of 1 MeV electron fluence.

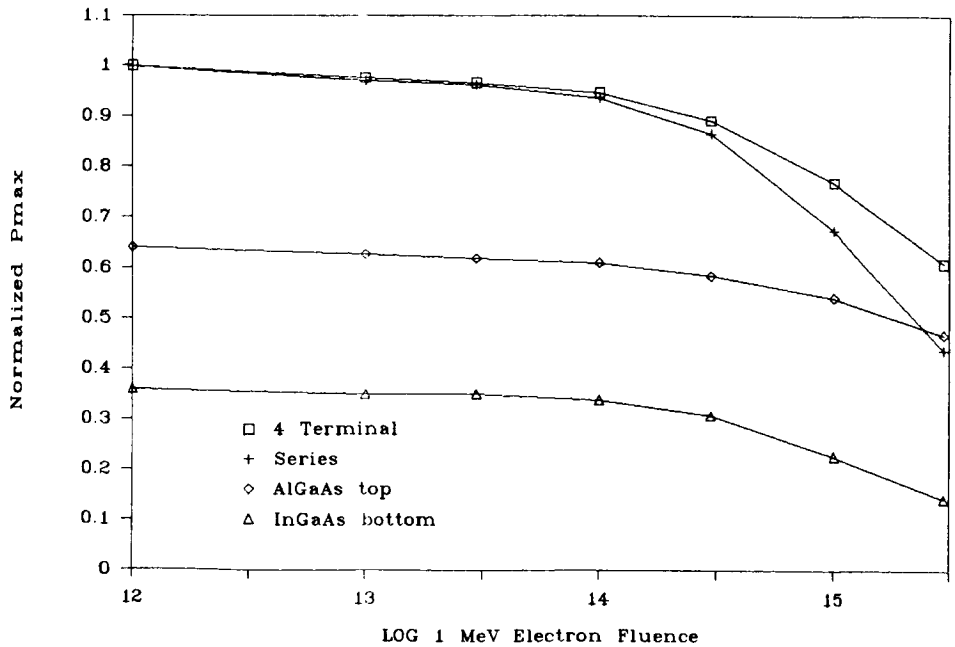

Figure 8. - Normalized maximum power for an AlGaAs/InGaAs cascade cell (series and separately connected) at 25 °C and 100x AM0 as function of 1 MeV electron fluence.

CALCULATIONS OF THE DISPLACEMENT DAMAGE AND SHORT-CIRCUIT CURRENT DEGRADATION IN PROTON IRRADIATED (AlGa)As-GaAs SOLAR CELLS

C.S. Yeh and S.S. Li*
University of Florida
Gainesville, Florida

and

R.Y. Loo
Hughes Research Laboratories
Malibu, California

A theoretical model for computing the displacement damage defect density and the short-circuit current (I_{sc}) degradation in proton-irradiated (AlGa)As-GaAs p-n junction solar cells is presented in this paper. Assumptions were made with justification that the radiation induced displacement defects form an effective recombination center which controls the electron and hole lifetimes in the junction space charge region and in the n-GaAs active layer of the irradiated GaAs p-n junction cells. The degradation of I_{sc} in the (AlGa)As layer was found to be negligible compared to the total degradation. In order to determine the I_{sc} degradation, the displacement defect density, path length, range, reduced energy after penetrating a distance x and the average number of displacements formed by one proton scattering event were first calculated. The I_{sc} degradation was calculated by using the electron capture cross section in the p-diffused layer and the hole capture cross section in the n-base layer as well as the wavelength dependent absorption coefficients. Excellent agreement was obtained between our calculated values and the measured I_{sc} in the proton irradiated GaAs solar cells for proton energies of 100 KeV to 10 MeV and fluences from 10^{10} p/cm^2 to 10^{12} p/cm^2.

INTRODUCTION

Although a handful of publications on the study of radiation damage in (AlGa)As-GaAs solar cells have been reported in the literature, there have been no accurate models for computing the short-circuit current (I_{sc}) degradation in the proton irradiated (AlGa)As-GaAs p-n junction solar cells. Wilson et al. [1-3] first proposed a simple model for calculating the I_{sc} degradation in the electron and proton irradiated GaAs solar cell. In their model they assumed that the radiation induced displacements within the solar cells formed recombination centers for the minority carriers produced by photon absorption. Yaung [4] modified Wilson's model

*This work was supported by Air Force Wright Aeronautical Laboratories under subcontract through Universal Energy Systems Inc.

including the wavelength dependent absorption coefficient of the GaAs cell. However, both these models did not consider the reduced energy of an incident proton after penetrating the (AlGa)As window layer, and hence the I_{sc} degradation calculated from these two models was found less satisfactory when compared with the experimental data for the proton irradiated (AlGa)As-GaAs solar cells [5]. The discrepancy found in both models is due primarily to the oversimplified assumptions made by Wilson and Yaung in which the recombination cross sections for both p-type and n-type GaAs were assumed equal and the empirical formulae for the path length (P) and the range (R) of an incident proton in resting in the (AlGa)As and GaAs solar cells were assumed the same. These assumptions are in fact not valid for the proton irradiated GaAs solar cells considered in this paper.

In this paper, we present a more rigorous model for the displacement damage calculations in the (AlGa)As-GaAs solar cells under normal incident conditions, and show the correlation between the defect parameters and the I_{sc} degradation for the proton irradiated (AlGa)As-GaAs solar cells. To facilitate our study, the experimental data on I_{sc} degradation in proton irradiated (AlGa)As-GaAs solar cells fabricated by Hughes Research Laboratories (HRL) were used for comparison with our theoretical calculations.

EXPERIMENTAL DETAILS

Figure 1 shows the physical structure and dimensions of the (AlGa)As-GaAs solar cells used in this study. The wide bandgap Be-doped $Al_{0.85}Ga_{0.15}As$ epi-layer was grown by infinite solution liquid-phase epitaxy (LPE) with dopant density of 3-5 x 10^{18} cm^{-3} and used as a window layer to reduce the surface recombination at the p-GaAs surface. During the window layer growth, a p-n junction was formed by Be diffusion into the n-GaAs buffer layer. The hole density in the p-GaAs layer is around 10^{18} cm^{-3}. The Sn-doped n-GaAs buffer layer was grown on the n+-GaAs substrate by LPE technique, which has an electron density of around 2 x $10^{17}cm^{-3}$. The n-GaAs substrate was doped with tellurium with dopant density of 5 x 10^{17} cm^{-3}. A thin window layer of less than 0.5 μm thick and a diffused junction depth of less than 0.5 μm were used to ensure the low optical absorption loss and to increase radiation hardness [6]. The n-GaAs buffer layer is 10 um thick. No cover glass was used in this cell. AuZn ohmic contacts on the window layer were about 0.3 to 0.4 μm thick with an Ag overlay of about 4 μm. The n-substrate contact is AuGeNi of about 0.5 μm thickness with silver overlay. The anti-reflection coating is Ta_2O_5. The AMO conversion efficiency of around 16 to 17 percent was obtained for (AlGa)As-GaAs solar cells fabricated under these conditions.

The solar cells used in this study were irradiated at room temperature by protons with energies of 0.1, 0.2, 0.29, 2, 5 and 10 MeV and fluences varying from 10^{10} to 10^{12} p/cm^2.

THEORETICAL MODEL FOR I_{sc} DEGRADATION

Displacement Damage

A solid may be affected in two ways by the energetic particle bombardments as follows: [7]

(1) Lattice atoms are removed from their regular lattice sites, producing displacement damage.

(2) The irradiating particle causes change in the chemical properties of the solid via ion implantation or transmutation.

In the displacement model, it is assumed that the dominant defect produced by incident protons is due to lattice displacement. Under this assumption, an atom will be invariably displaced from its lattice site during collisions if its kinetic energy exceeds the threshold energy (T_d) for the atomic displacement to take place, and conversely will not be displaced if its kinetic energy is less than T_d [8]. We assume that the transferred energy (T) to the atom which was struck is transformed to the kinetic energy only. If T is sufficiently large (i.e., $T \gg T_d$), then additional displacement can be produced by the recoiling nucleus before coming to rest at an interstitial site. Therefore, for $T > T_d$, the total number of displacements produced by a normal incident proton to the solar cell can be calculated by using the expression

$$D(E_o) = \int_0^R N \sigma \overline{V} \, dR \qquad (1)$$

where $D(E_o)$ = number of displacement/incident proton,

Eo = initial energy of an incident proton,

N = number of atoms per unit volume of the solar cell,

σ = displacement cross section for energetic protons,

$\overline{V}$ = average number of displacements formed by one proton-scattering event,

R = range of the proton of energy E_o.

Since the mass of the proton is heavy, it is necessary to consider the multiple scattering effect of the proton. Therefore, $D(E_o)$ with multiple scattering effect is obtained by replacing R with path length P in Eq. (1). The difference however, between the path length and range of a proton coming to rest in the GaAs cell is less than 5 percent for those protons with energies greater than one MeV. Thus, the multiple scattering effect is important only for low energetic protons. The empirical formulae for the path length, range and reduced energy (E_{re}) after penetrating a distance x were obtained by fitting the data of Janni [9] as shown in Appendix.

CALCULATIONS OF I_{sc} DDGRADATION

The total I_{sc} in an (AlGa)As-GaAs solar cell is equal to the sum of I_{sc} in the (AlGa)As window layer, p-GaAs layer and n-GaAs layer as well as in the depletion region of the junction. Since the spectral response of the window layer is much less than that of the whole solar cells [10] and the thickness of the window layer is less than 0.5 μm, it is reasonable to assume that I_{sc} degradation of the window layer is negligible compared with the total I_{sc} degradation.

To derive an expression for the I_{sc} in a proton-irradiated GaAs p-n junction solar cell, the following assumptions are made: [1,11-13]

(1) radiation-induced defects do not alter the internal electric field,

(2) radiation-induced defects alter the cell performance mainly through change of minority-carrier lifetimes in the bulk, and

(3) radiation-induced displacements within the solar cell form recombination centers for the minority carriers of electron-hole pairs produced by photon absorption.

The short circuit current, I_{sco} for the unirradiated solar cell is given by:

$$I_{sco}(\lambda) = \int_0^t \eta_c(x)\, \rho\,(x,\lambda)\, dx \qquad (2)$$

and for the damaged cell, the I_{sc} can be expressed by [1, 4]

$$I_{sc}(\lambda) = \int_0^t \eta_c(x)\, [1 - F\,(x)]\, \rho\,(x,\lambda)\, dx \qquad (3)$$

The normalized I_{sc} degradation can thus be calculated by using the expression:

$$I_{sc}/I_{sco} = \int_{\lambda_1}^{\lambda_2} I_{sc}(\lambda)\, d\lambda \;/\; \int_{\lambda_1}^{\lambda_2} I_{sc,o}(\lambda)\, d\lambda \qquad (4)$$

where

$F(x) = 1 - E_2\,[\sqrt{6}\,\sigma_r\,\Phi\,|D(E_x) - D(E_{xj})|]$, the recombination loss coefficient

$E_2(z)$ = exponential integral of order 2,

σ_r = capture cross section; for electrons and holes σ_r is different,

Φ = proton fluence,

$D(E)$ = total number of displacements calculated from equation (1),

E_x = reduced proton energy after penetrating a distance, x.

x_j = junction depth,

$\rho(x,\lambda)$ = photo-absorption rate at depth x, $\rho(x,\lambda) = K\,\alpha\,\exp(-\alpha\,x)$,

K = integrated photon flux in the absorption band,

α = the absorption coefficient,

$\eta_c(x)$ = current collection efficiency,

Note that t is the thickness of the cell and λ_1 and λ_2 denote the short-wave and long-wave limits of the total useful solar spectra for the GaAs cell (i.e. λ_1 = 0.35 um and λ_2 = 0.9 um).

RESULTS AND DISCUSSION

The parameters involved in the I_{sc} degradation calculations are absorption coefficients of GaAs, current collection efficiency, electron and hole capture cross sections, total number of displacement defects formed and fluences and energy of protons. In order to calculate the total number of displacement defects, parameters such as P, R and E_{re} of incident protons should also be calculated. In our computer simulation, we have assumed that the absorption coefficient and current collection efficiency of the GaAs cell remain constant after irradiation. Thus, according to Eq. (3) it is obvious that the larger the recombination loss F(x), the smaller the I_{sc}, and the smaller the F(x), the larger the value of $E_2(z)$. Since the fluence of protons through the entire GaAs is constant, and the total number of displacement is bound to the initial energy of incident protons, the values selected for electron and hole capture cross sections are critical to the I_{sc} degradation calculations. The values of parameters used in our simulation are listed in Table 1.

Since the I_{sc} degradation in the (AlGa)As window layer is negligible, it is reasonable to calculate the I_{sc} degradation in the GaAs solar cell only. In our simulation we first calculated E_{re} after penetrating the window layer. If the E_{re} is equal to zero, then there is no damage to the GaAs solar cell. Otherwise, the E_{re} would be applied as the initial energy of the proton for the GaAs solar cell. According to our calculations, the proton would lose 50 KeV after penetrating a 0.34 μm thick window layer. Therefore, there is no damage to the GaAs solar cell if the incident proton energy is less than 50 KeV. It is appropriate to use two different recombination cross sections (i.e., σ_n in the p-region, and σ_p in the n-region of the solar cell) for our computer simulation since the recombination mechanism in the p-diffused region is controlled by the electron capture cross section and by the hole capture cross section in the n-region. We have chosen the best value of 1.8×10^{-14} cm^2 for the electron capture cross section in the p-region and 1.5×10^{-13} cm^2

for the hole capture cross section in the n-region in our calculations. These approximations are consistent with the fact that p-GaAs is more radiation hardness than that of n-GaAs, as confirmed by the deep-level transient spectroscopy. [13]

Figure 2 shows the range of proton irradiated $Al_{0.85}Ga_{0.15}As$-GaAs solar cells as a function of proton energy. Since the thickness of the window layer is assumed equal to 0.34 μm, for proton energies less than 50 KeV there will be no damage created by these protons. The 100 KeV protons are stopped at about 0.8 μm below the surface, creating damage close to the junction. The 200 KeV protons penetrate deeper into the GaAs cell and are stopped at about 1.34 μm below the surface, causing most of the damages throughout the junction. The 290 KeV protons are stopped at about 2.0 μm below the surface, producing damages to the bulk of the n-GaAs layer. The one Mev protons are stopped at about 10 μm which is equal to the thickness of the cell. For proton energies higher than one MeV, protons will penetrate the p-n junction cell, and hence create less damages to the cell.

It should be noted that the total number of displacement defects as shown in Fig. 3 are obtained from Eq. (1) by integrating along the path length if the multiple scattering effect is considered, and by integrating along the range if the multiple scattering effect is excluded. Thus, the accurate empirical formulae of path length and range for $Al_{0.85}Ga_{0.15}As$-GaAs solar cells are important for displacement defect density calculations. The reasons for using Janni's data [9] instead of the data given by Andersen and Ziegler [14] are twofold: (1) data of path length and range obtained by Janni are for GaAs instead of Ga and As elements, and (2) data of range included high energy multiple scattering correction, and are therefore applicable for proton energies above 100 KeV [9].

As shown in Fig. 4 the maximum I_{sc} degradation was created by the 200 KeV protons. The reason the 200 KeV protons create much more damage than those higher energy protons is that most of the damages caused by 200 KeV protons occurred in the junction and inside the active region of the n-GaAs layer. The solid dots shown in Fig. 4 for proton energies of 100 KeV, 290 KeV, 2 MeV, 5 MeV and 10 MeV are the experimental data for the proton irradiated (AlGa)As-GaAs p-n junction solar cells and the solid curves are calculated from Eq. (4).

SUMMARY AND CONCLUSIONS

A rigorous model for computing the I_{sc} degradations in proton irradiated AlGaAs/GaAs p-n junction solar cells has been developed in this work, and calculations of I_{sc} degradation in proton irradiated (AlGa)As-GaAs solar cells have been carried out for proton energies from 100 KeV to 10 MeV and fluences from 10^{10} to 10^{12} p/cm^2. In addition, the empirical formulae for the path length, range, total number of displacement defects formed and reduced energy after penetrating a distance have also been derived for the proton irradiated (AlGa)As-GaAs solar cells. The result shows that the I_{sc} degradations increases with increasing proton fluences. The results show an excellent agreement between our calculated values and the experimental data for the I_{sc} degradation in (AlGa)As-GaAs p-n junction solar cells.

REFERENCES

[1] J.W. Wilson, J.J. Stith, and L.V. Stock, A Simple Model of Space Radiation Damage in GaAs Solar Cell, NASA Technical Paper 2242, 1983.

[2] J.W. Wilson, G.H. Walker, and R.A. Outlaw, "Proton Damage in GaAs Solar Cells", IEEE Trans. on Electron Devices, Vol. ED-31, No. 4, p. 421, 1984.

[3] J.W. Wilson and L.V. Stock, "Equivalent Electron Fluence for Space Qualification of Shallow Junction Heteroface GaAs Solar Cells", IEEE Trans. on Electron Devices, Vol. ED-31, No. 5, p. 622, 1984.

[4] J.Y. Yaung, Model of Solar Cell Proton Damage, NASA Space Photovoltaic Research and Technology Conference, p. 56, 1983.

[5] R.Y. Loo, G.S. Kamath, and R.C. Knechtli, Low Energy Proton Radiation Damage to (AlGa)As-GaAs Solar Cells, NASA Final Report, January 1979.

[6] R.Y. Loo and G.S. Kamath, Radiation Damage in GaAs Solar Cells, 14th IEEE Photovoltaic Specialist Conference, p. 1090, 1980.

[7] N.L. Peterson and S.D. Harkness, eds., Radiation Damage in Metals, American Soc. for Metals, C, p.59, 1976.

[8] G.J. Dienes and G. H. Vineyard, Radiation Effects in Solids, Interscience Publishers Inc., New York, 1957.

[9] J.F. Janni, Proton Range-Energy Tables, 1 KeV - 10 GeV, Atomic Data and Nuclear Data Tables 27, p.147, 1982.

[10] R.C. Knechtli, R.Y. Loo, and G.S. Kamath, "High-Efficiency GaAs Solar Cells", IEEE Trans. on Electron Devices, Vol. ED-31, No. 5, p. 577, 1984.

[11] G.H. Walker and E.J. Conway, Short Circuit Current Changes in Electron Irradiated AlGaAs/GaAs Solar Cells, 13th IEEE Photovoltaic Specialist Conference, p. 575, 1978.

[12] G.H. Walker and E.J. Conway, "Recovery of Shadow Junction GaAs Solar Cells Damaged by Electron Irradiation", J. Electro. Chem. Soc., p. 1726, 1978.

[13] S.S. Li, Electronic Properties of Deep-Level Defects in Proton Irradiated AlGaAs-GaAs Solar Cells, NASA Final Report, September 1981.

[14] H.H. Andersen and J.F. Ziegler, Hydrogen Stopping Powers and Ranges in All Elements, Pergamon Press, Inc., c. 1977.

APPENDIX

1. Empirical Formulae for Path Length and Range

(i) $Al_{0.85}Ga_{0.15}As$ window layer:

$$P = \begin{cases} 3.300891\ E^{0.550212} & E \leq 0.15 \text{ MeV} \\ 10.79623\ E^{1.163227} & E \leq 1.25 \text{ MeV} \\ 9.963561\ E^{1.1565366} & E \leq 10.0 \text{ MeV} \end{cases}$$

$$R = \begin{cases} 5.010253\ E^{0.865712} & E \leq 0.175 \text{ MeV} \\ 10.31089\ E^{1.257302} & E \leq 1.500 \text{ MeV} \\ 9.561796\ E^{1.579760} & E \leq 10.00 \text{ MeV} \end{cases}$$

where P and R are in μm and E is in MeV. Unless specify otherwise, the unit of length is in μm and that of energy is in MeV.

(ii) GaAs solar cell:

$$P = \begin{cases} 3.859312\ E^{0.545909} & E \leq 0.150 \text{ MeV} \\ 11.85262\ E^{1.135261} & E \leq 1.250 \text{ MeV} \\ 10.92040\ E^{1.550638} & E \leq 10.00 \text{ MeV} \end{cases}$$

$$R = \begin{cases} 5.861370\ E^{0.878671} & E \leq 0.175 \text{ MeV} \\ 11.23652\ E^{1.243952} & E \leq 1.500 \text{ MeV} \\ 10.42719\ E^{1.567030} & E \leq 10.00 \text{ MeV} \end{cases}$$

2. Empirical Formulae for Reduced Energy

(i) $Al_{0.85}Ga_{0.15}As$ window layer:

With Multiple Scattering

$$E_{re} = \begin{cases} 0.00130 - 0.01750x + 0.22468x^2 - 0.10073x^3, & E_0 \leq 0.1 \text{ MeV}. \\ -0.01715 + 0.13045x - 0.00424x^2 + 0.000079x^3, & E_0 \leq 1.75 \text{ MeV} \\ 0.85196 + 0.04353x - 0.000087x^2 + 0.000000095x^3, & E_0 \leq 10 \text{ MeV} \end{cases}$$

where E_{re} is in MeV; E_0 is the initial energy in MeV, x is the distance in μm

Without Multiple Scattering:

$$E_{re} = \begin{cases} -0.00031 + 0.09588x + 0.159531x^2 - 0.120901x^3, & E_o \leqq 0.1 \text{ MeV} \\ 0.01389 + 0.13373x - 0.00462x^2 + 0.000091x^3, & E_o \leqq 1.75 \text{ MeV} \\ 0.67525 + 0.05087x - 0.000014x^2 + 0.000002x^3, & E_o \leqq 10 \text{ MeV} \end{cases}$$

(ii) GaAs solar cell:

Multiple Scattering:

$$E_{re} = \begin{cases} 0.00131 - 0.014452 + 0.155159x^2 - 0.0557547x^3, & E_o \leqq 0.1 \text{ MeV} \\ -0.02554 + 0.11890x - 0.00346x^2 + 0.000059x^3, & E_o \leqq 1.75 \text{ MeV} \\ 0.82870 + 0.04092x - 0.000076x^2 + 0.000000078x^3, & E_o \leqq 10 \text{ MeV} \end{cases}$$

Without Multiple Scatterins:

$$E_{re} = \begin{cases} -0.00027 + 0.08880x + 0.10807x^2 - 0.06943x^3, & E_o \leqq 0.1 \text{ MeV} \\ 0.01126 + 0.12242x - 0.00386x^2 + 0.000071x^3, & E_o \leqq 1.75 \text{ MeV} \\ 0.85343 + 0.04137x - 0.000078x^2 + 0.000000081x^3, & E_o \leqq 10 \text{ MeV} \end{cases}$$

Table 1. Input parameters for the calculations of the I_{sc} degradation of the proton irradiated (alGa)As-GaAs Solar Cells.

Cell	d(μm)	x_j(μm)	t(μm)	T_d(eV)	Z_2	M_2	$\sigma_n(cm^2)$	$\sigma_p(cm^2)$
(AlGa)As	0.34	-	-	-	-	-	-	-
GaAs	-	0.5	10	9.5	32	72.5	1.8×10^{-14}	1.5×10^{-13}

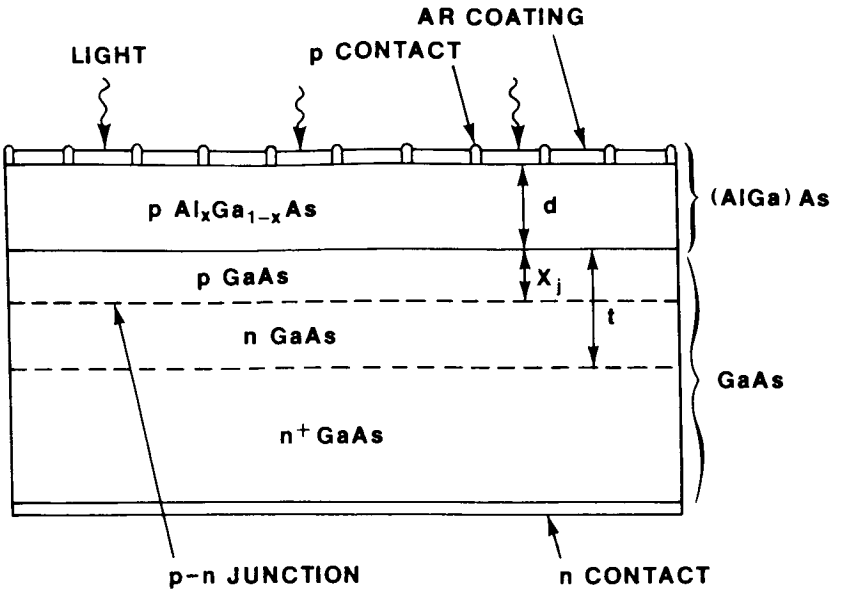

Fig. 1. The cross sectional view of a (AlGa)As-GaAs p-n junction solar cell.

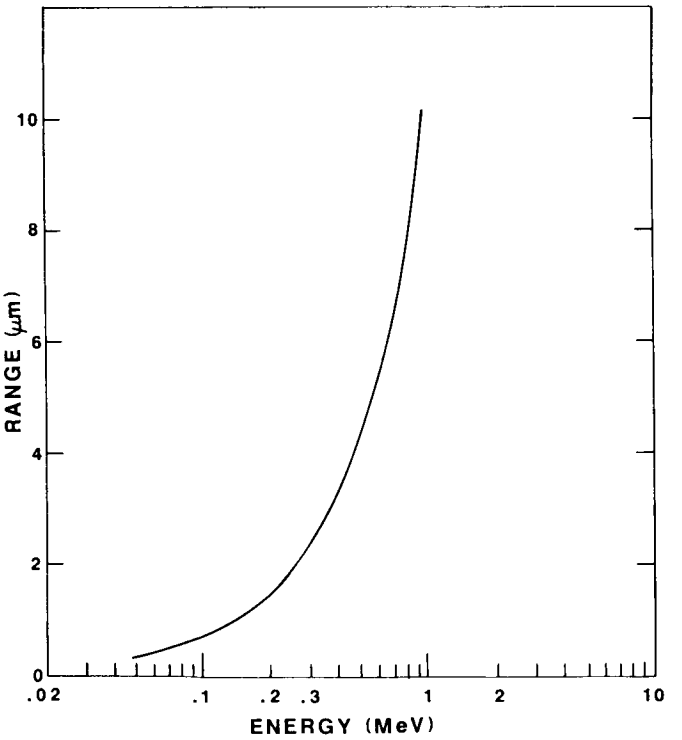

Fig. 2. The range of the $Al_{0.85}Ga_{0.15}As$-GaAs solar cell vs. incident proton energies.

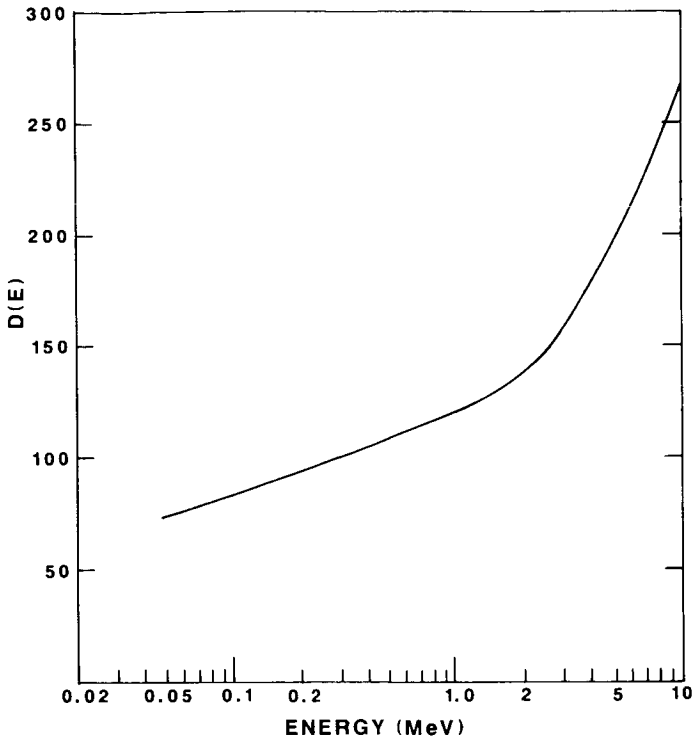

Fig. 3. The total number of displacement defect vs. incident proton energies for a GaAs p-n junction solar cell.

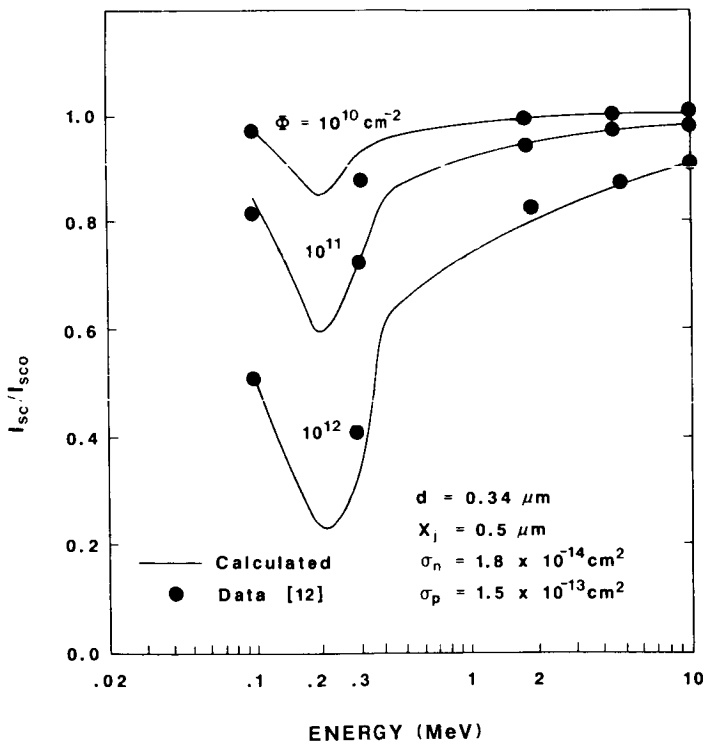

Fig. 4. The calculated I_{SC} degradation ratio in the $Al_{0.85}Ga_{0.15}As$-GaAs p-n junction solar cell. Solid curves are from our calculations, solid dots are the experimental data. The thickness of the window layer is 0.34 μm and the junction depth is 0.5 μm.

STATUS OF INDIUM PHOSPHIDE SOLAR CELL DEVELOPMENT AT SPIRE*

M.B. Spitzer, C.J. Keavney, and S.M. Vernon
Spire Corporation
Bedford, Massachusetts

On-going development of indium phosphide solar cells for space applications is presented. The development is being carried out with a view toward both high conversion efficiency and simplicity of manufacture. The cell designs comprise the ion-implanted cell, the indium tin oxide top contact cell, and the epitaxial cell grown by metal organic chemical vapor deposition. Modelling data on the limit to the efficiency are presented and comparison is made to measured performance data.

INTRODUCTION

The radiation sensitivity of space solar cells is a critical factor affecting many aspects of space power system design, and improvements to end-of-life cell efficiency offer numerous advantages in cost, weight and area. For the large power systems anticipated for future space projects (ref. 1), reduction of array area may be particularly important, owing to weight and drag considerations, and to the necessity of assembly and maintenance in space. This reduction of area is possible if end-of-life efficiency can be increased.

Recently, Yamamoto et al. (ref. 2) have reported that indium phosphide (InP) solar cells have remarkable radiation tolerance. Their results indicate that both electron and x-ray damage are completely annealed at 100°C. A further important result is that the radiation damage is annealed by minority carrier injection (ref. 3,4). These cells would therefore seem to have considerable promise as a new type of radiation-resistant space solar cell.

In the work to be reported here, our objective is first to reproduce the work of Yamamoto et al., and then to examine the generality of the findings regarding radiation tolerance. Our work is also carried out with a view toward high efficiency, and with a secondary goal being the identification of useful manufacturing techniques. The specific devices investigated by us are: (1) the ion-implanted cell, (2) the indium tin oxide (ITO) coated cell, and (3) epitaxial cells formed by metalorganic chemical vapor deposition. By investigating three

* This work is funded by NASA contract NAS3-24857.

manufacturing approaches, we intend to gain an understanding of the efficiency and radiation tolerance for various cell structures, and hence the generality of the findings of Yamamoto et al.

In this paper we will first present a review of our modelling of InP solar cells; this modelling has served as a basis for both cell design and analysis of loss mechanisms. We then present a description of our cell fabrication experiments. At the present time, we have fabricated test solar cells and are working on obtaining improvements in efficiency. Results obtained thus far will be presented.

MODELLING

To identify a high efficiency cell design for InP, we utilized a solar cell modelling code developed at Brown University (ref. 5). This code evaluates the solution of the one-dimensional time-independent inhomogeneous diffusion equation. This solution is integrated over the solar spectrum to determine the terminal characteristics of the device.

The code is based on the partition of the cell into three regions: the emitemitter, the space-charge region, and the base. The boundary conditions are the conventional Boltzmann conditions at the edges of the space-charge region, and the surface recombination velocity at the outside surfaces of the cell. The code also calculates generation in the space-charge region.

A literature search was carried out to determine up-to-date input parameters for the model. Optical data were obtained from reference 6. Data on the AM0 spectrum were obtained from M. Wolf (ref. 7). Mobility data were compiled from various sources, and figure 1 indicates the values used in the modelling. Owing to a lack of experimental data, it was necessary to assume that the minority carrier lifetime is inversely proportional to the majority carrier concentration. For a doping level of 2×10^{16} cm^{-3}, this assumption yields an electron diffusion length (L_e) of about 10 micrometers. At the present time, our assumption appears to be reasonable based on the dependence of lifetime upon doping in other semiconductors. We also assume an emitter doping level of 5×10^{18} cm^{-3} and a space-charge region (SCR) width of 0.25 micrometers. The junction depth is assumed to be 0.2 micrometers. Other parameters used for modelling are provided in table 1.

The model has been used to calculate the limit to the conversion efficiency as a function of resistivity. Since the dependence of L_e upon doping is not well established, we varied L_e over a wide range. The results of this calculation are shown in figure 2. We also have indicated the efficiency for values of L_e consistent with the lifetime given by our assumption that lifetime is inversely in proportional to carrier concentration; this result is shown as data points in the figure. This assumption yields the dashed line in figure 2, which shows that the optimum doping is in the range of 10^{16} cm^{-3} to 10^{17} cm^{-3}. This range is fortunately also approximately optimal for radiation hardness (ref. 8). For this

cell structure, the upper limit to the AM0 efficiency is then 18% (including 8% shadow loss). If higher lifetime can be obtained, AM0 efficiency of up to 20% may be possible.

We have also examined the importance of hole diffusion length (L_h) in the n-type emitter, for a junction depth of 0.1 micrometer. In this calculation, we assume that in the base the acceptor concentration is fixed at 2×10^{16} cm^{-3}. The result of this calculation is shown in figure 3. It can be seen that if L_h can be increased, the upper limit to the efficiency approaches 22%.

The theoretical external quantum efficiency (QE) of InP cells has been investigated to gain an understanding the way that L_e and junction depth (x_j) affect the efficiency of non-ideal experimental cells. Although antireflection (AR) coatings are necessary in the final cells, uncertainties in the optical properties increase the difficulty of the modelling and analysis. For this reason, many of our experiments involve non-coated cells. Therefore, in our QE calculations, measured reflectance of non-AR-coated InP was used to facilitate comparison of theory to actual cell data.

Figure 4 shows the calculated external QE as a function of L_e. It can be seen that varying L_e between 1 and 9.5 micrometer has only a small effect; this is a result of the fact that most of the current is generated in the emitter and space-charge region. For example, if one assumes a junction depth of 0.1 micrometer, one finds that a non-AR-coated cell with L_e=9.5 micrometer should have J_{sc} of 23.8 mA/cm^2. Of this total, only 5.8 mA/cm^2 is generated in the base. The emitter generates 8.7 mA/cm^2. The width of the space charge region is 0.25 micrometer, and 9.34 mA/cm^2 are generated within it. Thus, this modelling indicates the need for high quality near-surface regions. We note that these tentative findings are based on the optical data of reference 6, and that it would be desirable to obtain absorption data from crystals that are grown in the same manner and doped as the solar cells being investigated here.

CELL FABRICATION EXPERIMENTS

Experiments have been carried out on the fabrication of cells. The three cell designs are shown in figure 5. Note that the ion-implanted and ITO-coated cells utilize lightly-doped substrates whereas the epitaxial cell is grown on a p^{++} wafer, which has an orientation of 2° off <100>. The final cell area in our experiments is 0.5 cm x 0.5 cm.

Ion-Implanted Solar Cells

The use of ion implantation for junction formation in InP has received attention (ref. 9-14). Such junctions have been evaluated for application to cell fabrication. Table 2 summarizes the process parameters investigated, as well as the parameters that have yielded the best results thus far. The best parameters shown in the table yield a sheet resistance of 500 ohms-per-square, Hall mobility of 690 $cm^2/Vsec$, and junction depth estimated to be 0.2 micrometers. We have

investigated the use of C-V based junction profiling techniques, but at the present the application to very shallow junctions appears to be unreliable.

Fabrication of cells comprises ion implantation and annealing as shown in table 2. The wafers are then provided with front (Ge-Au) and back (Zn-Au) contacts. A mesa etch is used to separate the junctions. Finally, a multilayer AR coating is applied.

Characterization of the cells indicates that the primary loss mechanism in most of the cells is space-charge region recombination (n=2 over four decades). Quantum efficiency measurements indicate low blue response which may be attributable to either space-charge region recombination or possible emitter recombination (bulk or surface). Further experiments on junction formation are underway to improve the dark characteristics of the device. Nevertheless, AMO efficiency of over 13% has been obtained, as will be discussed in the next section.

ITO-coated Cells

The use of ITO as a top contact has recently gained attention, and highly efficient cells have been reported (ref. 15). We have therefore investigated ITO deposition by RF sputtering with a variety of process conditions. The best ITO films are approximately 0.1 micrometers thick and have sheet resistance of about 180 ohms-per-square. The absorption within the films is negligible in the range of 500 nm to 1000 nm.

Fabrication of cells begins with the formation of the Zn-Au back contact. Next, the ITO is deposited and front contacts are applied. A mesa etch is used to separate the cells. Finally, if desired, a single layer of MgF is applied to reduce reflection.

The best cells are presently characterized by low fill factor (FF) and low open circuit voltage (V_{OC}). The cause of the low performance has not been identified, but it is possibly the result of a high density of interface states which could cause the device to perform as a Schottky diode. Further work in this area is in progress.

Epitaxial Cells

We are presently investigating formation of both grown junctions and complete cells by metalorganic chemical vapor deposition. For the grown junctions, we are using <100> lightly doped p-type substrates, and the desired resultant structure is the same as is shown in figure 5a for the ion-implanted device. As in the ion-implanted cell, a large fraction of the space-charge region is formed in the starting wafer. We are also investigating the all-epitaxial cell shown in figure 5c, in which the emitter and base are formed in epitaxial material grown on a more highly doped photovoltaically-inactive substrate.

The source gases for this work are $(CH_3)_3In$ and PH_3. N-type dopants under evaluation are SiH_4, H_2Se and $(CH_3)_4Sn$. For p-type doping, we are investigating $(CH_3)_2Zn$ and CP_2Mg. The growth temperature is in the range of 600 to 650°C with a pressure of 76 torr.

The solar cell structures that have been investigated to date include thin abrupt homojunctions, graded emitters, and high-low emitters. The highest V_{OC} has been obtained with thin homojunctions, but the best J_{SC} is obtained with the high-low emitters. Further work is underway to better understand the performance of the grown junctions.

CELL PERFORMANCE

We have fabricated cells with each of the processes and designs described above. The ion-implanted cell has thus far yielded the best performance. The best cells of each type are summarized in table 3. It should be noted that the epitaxial cells are the results of our first cell fabrication run, and are rather good for a first attempt.

The illuminated current-voltage characteristic for the best cell is shown in figure 6. We have obtained AM0 efficiency of 13.3%. V_{OC} is 807mV and J_{SC} is 29.6 mA/cm^2. To understand the origin of the loss mechanisms, we measured the dark log current-voltage and V_{OC}-I_{SC} characteristics, shown in figure 7. Analysis shows that the fill factor is limited in part by junction recombination (n=1.7 at Vmp), and in part by series resistance. Calculations show that the ideal fill factor is 86.2%; this is reduced to 82.6% by leakage current, and to 81.8% by series resistance. The combined effects of series resistance and leakage reduce the fill factor to 76.1%. If such effects could be eliminated, efficiency would be raised to 15.3%. Examination of the data also shows that for this cell the V_{OC} is not limited by space-charge region recombination.

Measured external QE data are shown in figure 8. The low blue response indicates that the recombination in the emitter and/or space-charge region is limiting the J_{SC}. Development of improved epitaxial emitter structures is expected to correct this problem.

CONCLUSION

The status of our InP solar cell development has been presented. Efficiency of 13.3% (AM0) has been obtained and the manner in which greater performance could be obtained has been reviewed. It is expected that by improving the minority carrier properties of the emitter and space-charge region, AM0 efficiency of 16% can be achieved in the near future.

REFERENCES

1. Forestieri, A.F. and Baraona, C.R., "Space Station Power System," Rec. of the 17th IEEE Photovoltaic Specialists Conference, Orlando (1984), p. 7.

2. Yamamoto, A.; Yamaguchi, M.; Uemura, C., "High Conversion Efficiency and High Radiation Resistance InP Homojunction Solar Cells," Appl. Phys. Let. 44, 611 (1984).

3. Yamaguchi, M.; Andu, K.; Yamamoto, A.; and Uemura, C., "Minority-Carrier Injection Annealing of Electron Irradiation-Induced Defects in InP Solar Cells," Appl. Phys. Lett. 44, 432 (1984).

4. Yamaguchi,M.; Uemura, C.; and Yamamoto, A., "Radiation Damage in InP Single Crystals and Solar Cells," J. Appl. Phys. 55, 1429 (1984).

5. Spitzer, M.B., "The Upper Limit to the Theoretical Efficiency of P-N Homojunction and Interfacial Layer Heterojunction Solar Cells," Ph.D. Thesis, Brown University (1981).

6. Aspnes and Studinoff, Phys. Rev. B., 27, 985 (1983).

7. Wolf, M., private communication.

8. Yamaguchi, M.; Ando K.; and Uemura, C., "Carrier Concentration Effects on Radiation Damage in InP," J. Appl. Phys. 55, 3160 (1984).

9. Davies, D.E.; Lorenzo, J.P.; and Ryan, T.G., "N-type Doping of Indium Phosphide by Implantation," Solid-State Electronics 21, 981 (1978).

10. Donnelly, J.P. and Ferrante, G.A., "The Electrical Characteristics of InP Implanted with the Column IV Elements," Solid-State Electronics 23, 1151 (1980).

11. Kasahara, J.; Gibbons, J.F.; Magee T.J.; and Perry, J., "Ion Implantation of Sulfur in Cr-doped InP at Room Temperature," J. Appl. Phys. 51, 4119 (1980).

12. Inada, T.; Taka, S.; Yamamoto, Y. "Selenium Implantation in Indium Phosphide," J. Appl. Phys. 52, 4863 (1981).

13. Sussmann, R.S., "N-type Doping of InP by Io Implantation," J. of Elect. Mater. Vol. 12, No. 3, p. 603 (1983).

14. Gouskov, L.; Conjeud, A.L.; Dhouib, A.; Favenec, P.N.; Salvi, M.; L'Haridon, H.; Bastide G. and Bayaa, D., "n^+-InP (Silicon Implanted)/p-InP Homojunction: Minority Carrier Diffusion Length in the Implanted Layer," Solar Cells 11, 343 (1984).

15. Coutts, T. and Naseem, S., "High Efficiency Indium Tin Oxide/Indium Phosphide Solar Cells," Appl. Phys. Lett. 46, 164 (1985).

TABLE 1. MODEL INPUT PARAMETERS

PARAMETER	VALUE
Temperature, T	28°C
Intrinsic Concentration, n_i	2.6×10^7 cm^{-3}
Donor Concentration, N_D	5×10^{18} cm^{-3}
Acceptor Concentration, N_A	2×10^{16} cm^{-3}
Electron Diffusion Length, L_e	9.5 μm
Hole Diffusion Length, L_h	0.08 μm
Electron Mobility	3500 $cm^2/Vsec$
Hole Mobility	60 $cm^2/Vsec$
Input Spectrum	AM0, 135.3 mW/cm^2
Shadow Loss	8%
Reflection Loss	0

TABLE 2. DEVELOPMENT OF ION IMPLANTED JUNCTIONS

PROCESS PARAMETER	RANGE INVESTIGATED	BEST RESULT
Implant Energy (keV)	10 to 50	10
Implant Dose (cm^{-2}) (Si,Se, S)*	3×10^{14} to 10^{15}	10^{15}
Anneal Temp. (°C)	700 to 800	750
Anneal Time (min)*	1 to 15	15
Surface Protection	Flowing PH_3, PSG, Si_3N_4, Silox	Flowing PH_3

*Experiments in progress.

TABLE 3. SOLAR CELL PERFORMANCE DATA FOR THE BEST CELL OF EACH TYPE

Cell Type	V_{oc} (mV)	J_{sc} (mA/cm^2)	FF (%)	Eff (%)
Ion-implanted	807	29.6	75.2	13.3
ITO-coated	689	19.7	62.0	6.2
Epitaxial	721	23.6	73.0	9.2

Notes: AM0, 135 mW/cm^2. T = 25°C. Area = 0.25 cm^2.

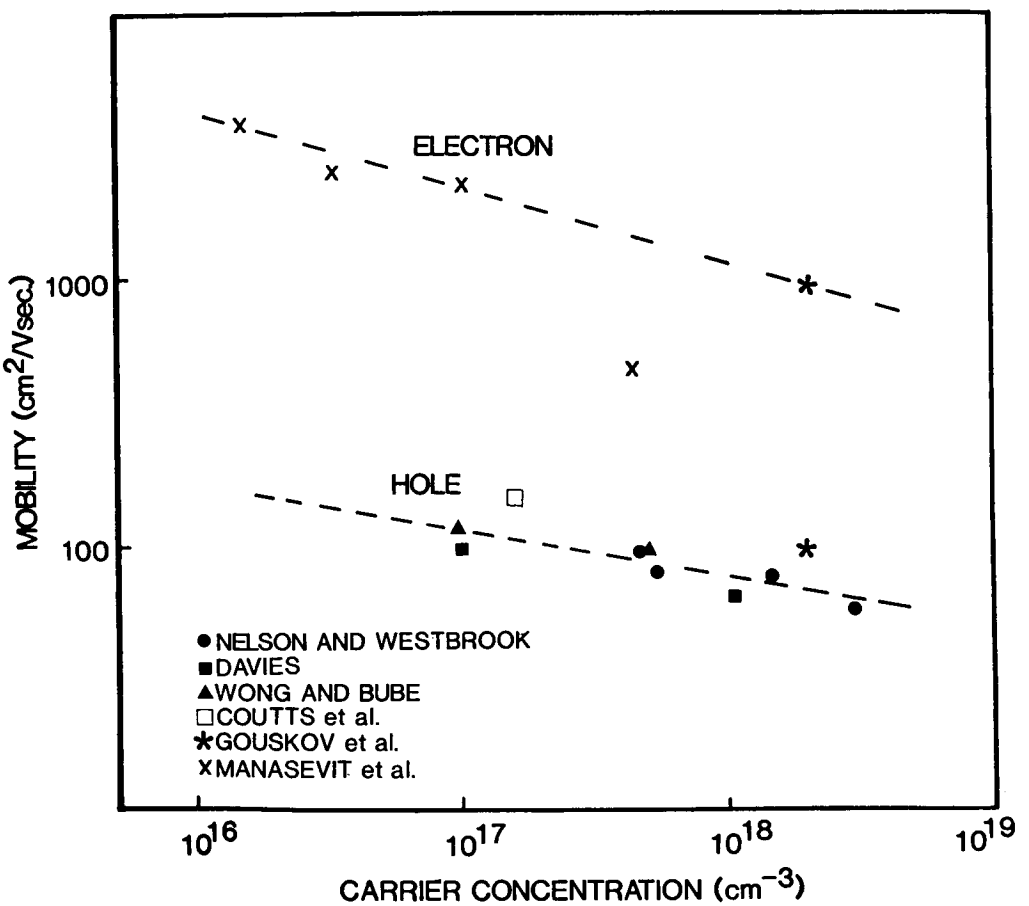

Figure 1. MOBILITY AS A FUNCTION OF CARRIER CONCENTRATION IN InP. The dotted lines indicate the values used in the model.

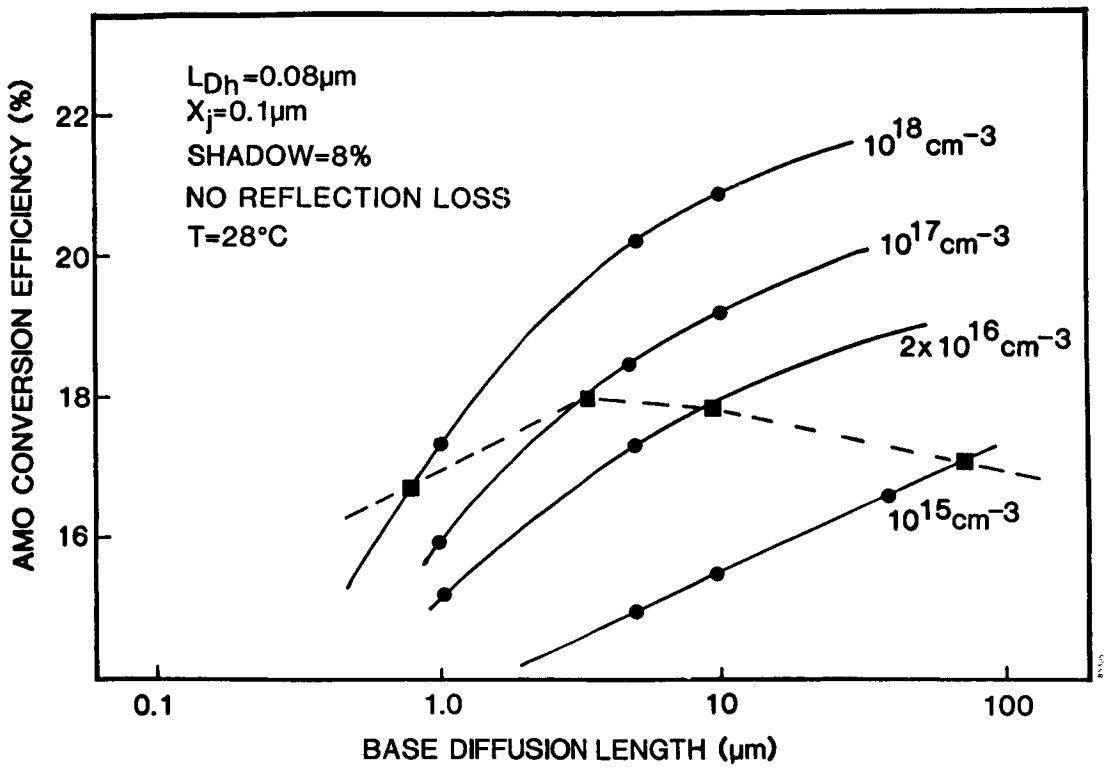

Figure 2. THEORETICAL AMO EFFICIENCY AS A FUNCTION OF L_e AND RESISTIVITY. The dotted line indicates the value of L_e associated with the assumed dependence of lifetime upon dopant concentration.

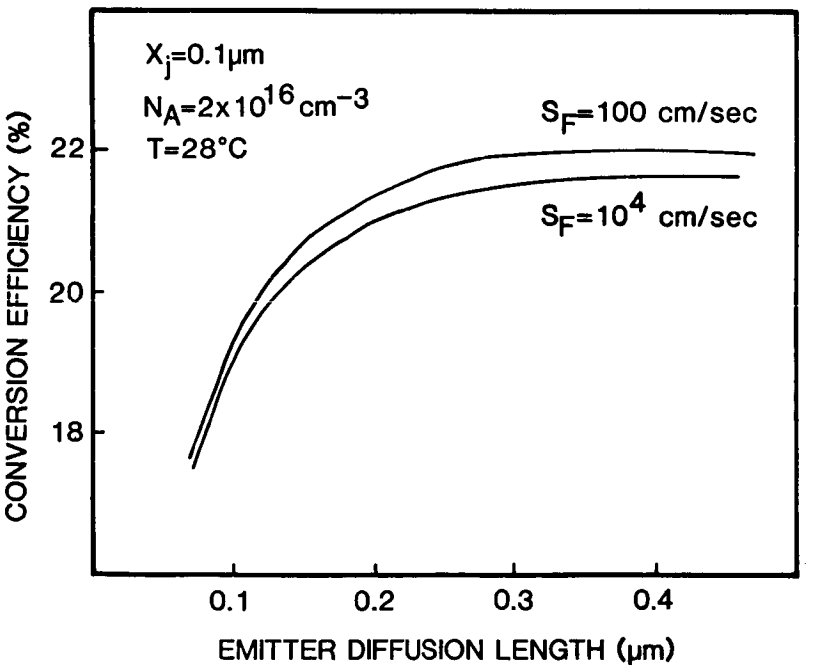

Figure 3. UPPER LIMIT TO THE AMO EFFICIENCY AS A FUNCTION OF HOLE DIFFUSION LENGTH IN THE EMITTER.

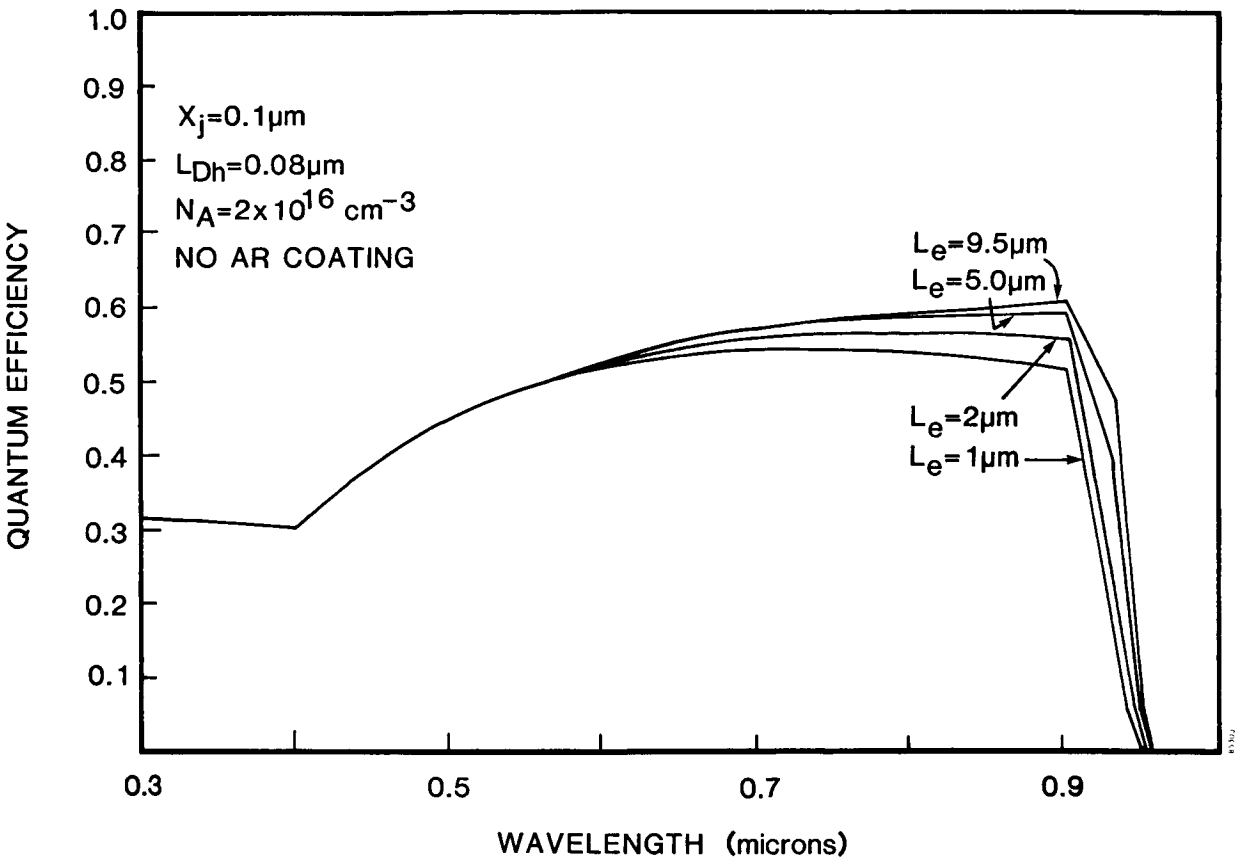

Figure 4. THEORETICAL EXTERNAL QUANTUM EFFICIENCY AS A FUNCTION OF WAVELENGTH AND BASE DIFFUSION LENGTHS.

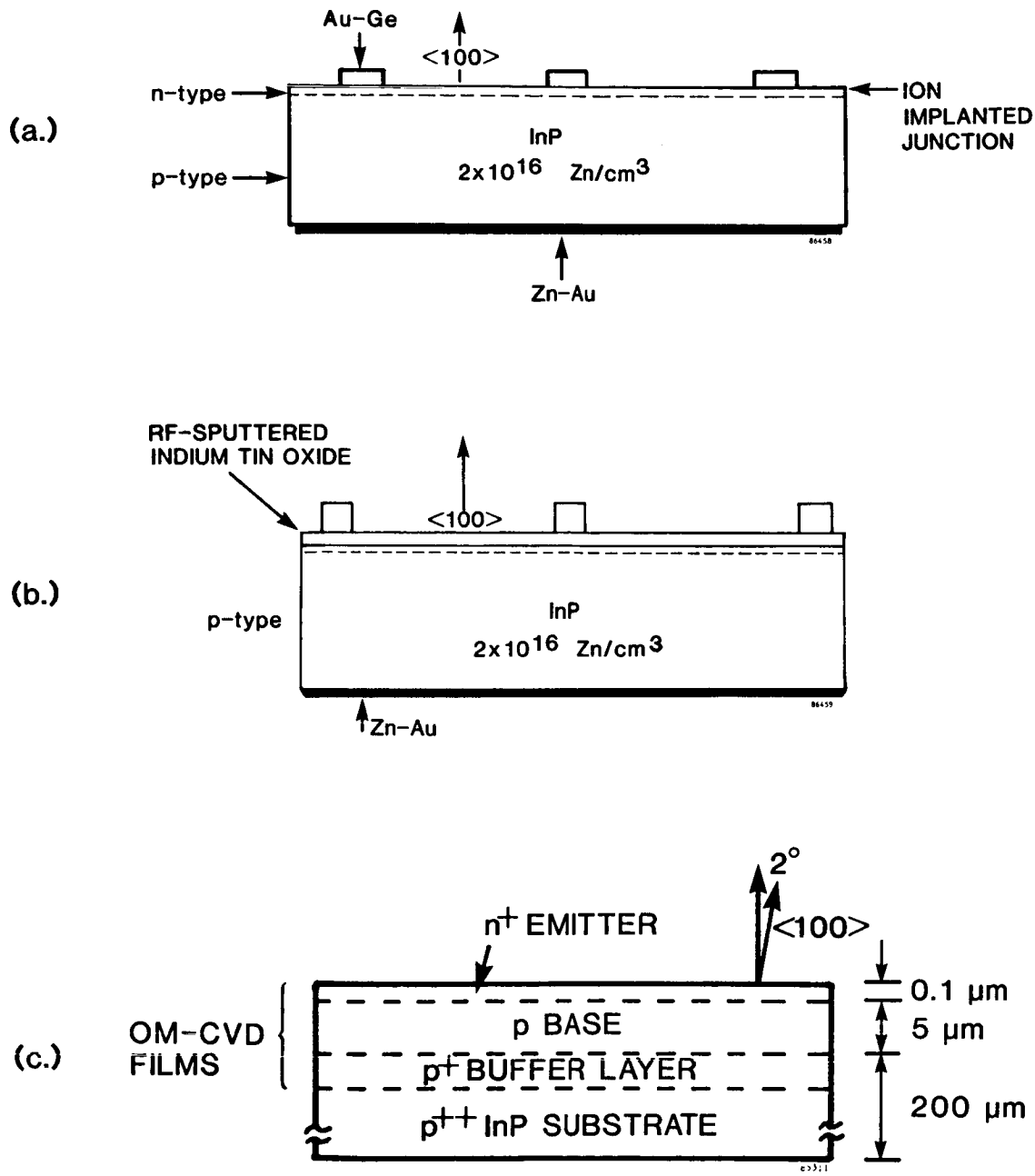

Figure 5. INDIUM PHOSPHIDE SOLAR CELL DESIGNS. (a) Ion-implanted cell, (b) Indium tin oxide coated cell, (c) Epitaxial cell.

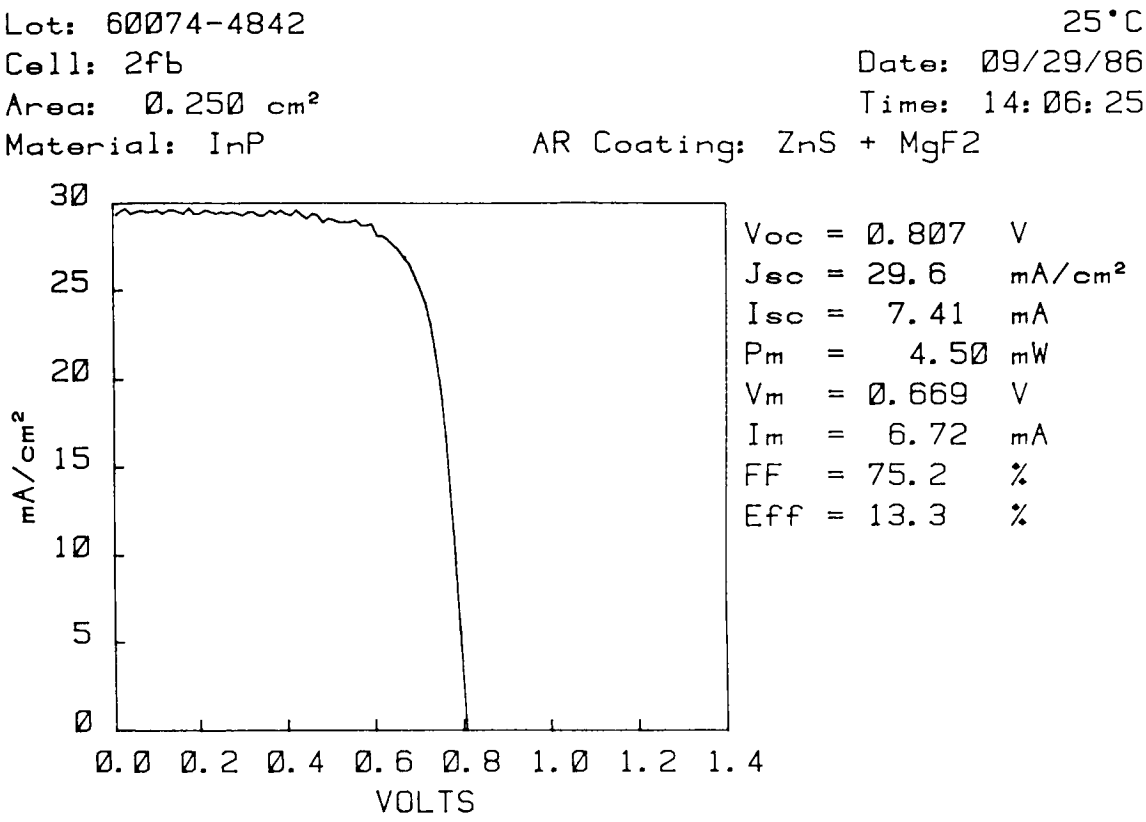

Figure 6. ILLUMINATED I-V CHARACTERISTIC FOR AN ION-IMPLANTED InP HOMOJUNCTION SOLAR CELL (AM0, 135 mW/cm^2)

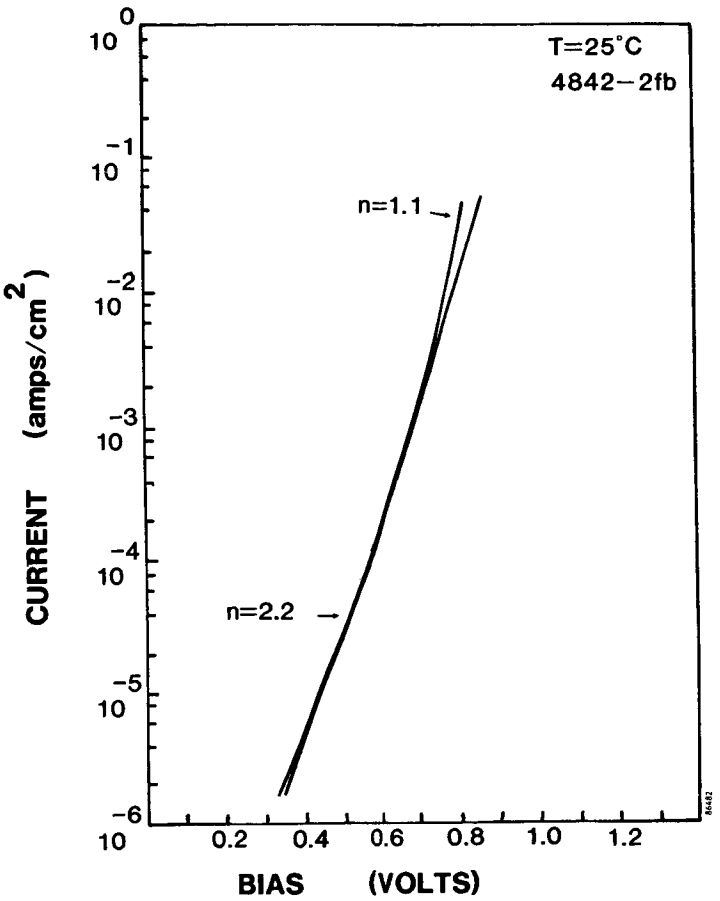

Figure 7. DARK LOG CURRENT VOLTAGE CHARACTERISTIC AND I_{sc} PLOT FOR DEVICE 4842-2fb

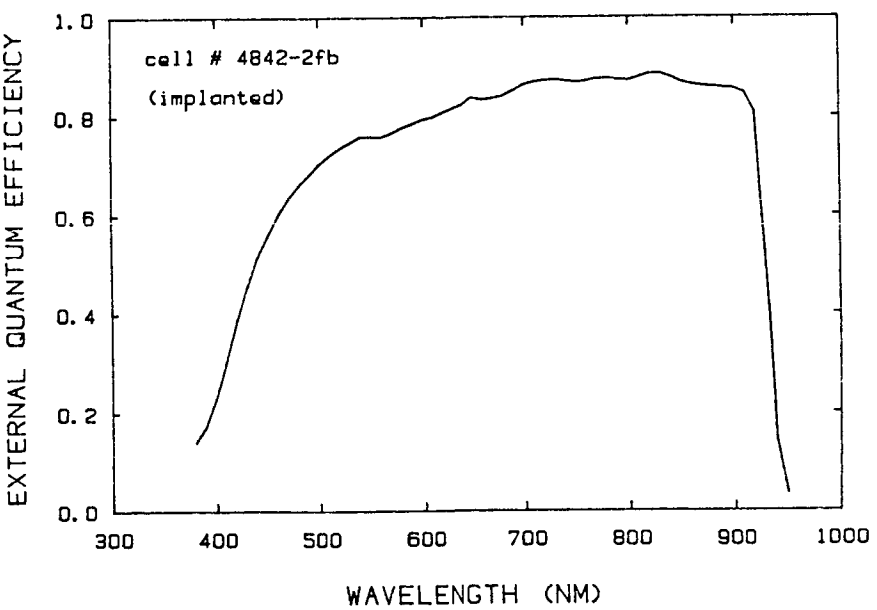

Figure 8. EXTERNAL QUANTUM EFFICIENCY OF DEVICE 4842-2fb

COMPARATIVE PERFORMANCE OF DIFFUSED JUNCTION INDIUM PHOSPHIDE SOLAR CELLS

I. Weinberg, C.K. Swartz, and R.E. Hart, Jr.
NASA Lewis Research Center
Cleveland, Ohio

and

S.K. Ghandhi, J.M. Borrego, and K.K. Parat
Rensselaer Polytechnic Institute
Troy, New York

A comparison was made between indium phosphide solar cells whose p-n junctions were processed by open tube capped diffusion, and closed tube uncapped diffusion, of sulphur into Czochralski grown p-type substrates. Air mass zero, total area, efficiencies ranged from 10 to 14.2%, the latter value attributed to cells processed by capped diffusion. The radiation resistance of these latter cells was slightly better, under 1 MeV electron irradiation. However, rather than being process dependent, the difference in radiation resistance could be attributed to the effects of increased base dopant concentration. In agreement with previous results, both cells exhibited radiation resistance superior to that of gallium arsenide. The lowest temperature dependency of maximum power was exhibited by the cells prepared by open tube capped diffusion. The average value of dPm/dT, including cells of both types, was found to be $-(5.3\pm 1.2)\times10^{-2}$ mW/cm^2 ^{o}K at 60^{o}C. Calculated values if dVoc/dT were in reasonable agreement with experimental values. However, contrary to previous results, no correlation was found between open circuit voltage and the temperature dependency of Pmax. It was concluded that additional process optimization was necessary before concluding that one process was superior to the other.

INTRODUCTION

It has been demonstrated that n/p homojunction indium phosphide solar cells have properties which make them excellent candidates for use in the space radiation environment.[1,2,3,4] This follows from their excellent radiation resistance, annealibility at relatively low temperatures and under the influence of light and their potentially high efficiencies.[1,5,6] These desirable properties have served as a stimulus for renewed InP solar cell research both in the USA and abroad.[3,4] However, due to the different ways in which results are reported, and the various standards and light sources used in measuring cell performance it is difficult to meaningfully compare the results emanating from different laboratories.[3] For example, results appear in the literature quoting active area efficiencies and under AM1.5, AM1 and AM0 light intensities. For space use, the latter spectrum with parameters reported in terms of total area has long been the sole accepted mode for reporting cell performance measurements. In the present case we compare the performance of indium phosphide solar cells processed by two different techniques, in two separate laboratories. Performance data are obtained, in the same simulator, under air mass zero conditions with efficiencies and current densities

reported in terms of total rather than active area. Our interest lies in comparing cell performance parameters of unirradiated cells and after exposure to 1 MeV electrons and the variations in performance under varying temperature conditions.

EXPERIMENT

The diffused junction InP cells differed principally in the method of p/n junction formation. Referring to Fig. 1, the cells whose junction were formed by closed tube diffusion (labeled J cells) were processed at the Nippon Telephone and Telegraph, Electrical Communication Laboratories in Ibaraki, Japan.[7] On the other hand, the cells processed by open tube capped diffusion (labeled R cells) were processed at the Rensselaer Polytechnic Institute.[8] In both cases, the starting material was p-type, zinc-doped Czochralski grown indium phosphide, sulphur being the n-dopant. Major cell fabrication details are shown in the figure. Additional processing details can be found in references 7 and 8. All performance measurements were carried out at NASA Lewis using an air mass zero X-25 zenon arc solar simulator with a gallium arsenide solar cell used as a standard. The standard cell was calibrated at air mass zero using the Lewis high altitude aircraft technique.[9]

The cells were irradiated by 1 MeV electrons in the Naval Research Laboratories Van De Graaf accelerator. Temperature dependency measurements on unirradiated cells were performed in a nitrogen atmosphere using a variable temperature chamber into which the X-25 simulator beam was introduced through a glass port built into the side of the simulator.

RESULTS

The performance parameters of several R and J cells, determined at 25°C, are shown in Table 1. The efficiencies of 14.2% for R cells and 13.6% for the J cells are the highest AMO, total area efficiencies, measured at 25°C, at NASA Lewis, for these cell types. However, these are not the highest efficiencies obtained for InP cells. For example, we have measured an AMO total area efficiency of 15.9%, at 25°C for a p^+n InP cell whose junction was formed by OMCVD.[10] On the other hand, AMO active area efficiencies of 18%, at 20°C, have been reported for a p^+-I-n cell also fabricated by OMCVD.[11] Since this latter cell had 10% front grid coverage, the total area AMO efficiency at 25°C is calculated to be 16%. To obtain this latter value at 25°C, we used the temperature correction factor $dPm/dT = -5.3 \times 10^{-2}$ mW/cm^2 °K where Pm is cell maximum power output. This numerical value is obtained in a following section of the present work.

Results of the 1 MeV electron irradiations are shown in Figs. 2, 3, and 4 for the InP cells listed in Table II. Also shown are results for state of the art GaAs cells, obtained from Varian.[12] Preirradiation cell parameters for the GaAs cells are shown in Table III. Since these latter cells had efficiencies close to 20%, they produce more output power over the present fluence range than do the InP cells. However, when plotted on a normalized basis, in terms of preirradiation output power, the InP cells exhibit greater radiation resistance. This latter result is in agreement with previous results.[1,2]

DISCUSSION

From Fig. 2, the cells processed by open tube capped diffusion have slightly higher radiation resistance, at the lower fluences, than the cells processed by closed tube diffusion. However, one cannot state from these results that one specific process inherently results in superior radiation resistance. This follows from the observation that, in the present concentration range, radiation resistance increases with base dopant concentration.[13]

Considering the remaining cell performance parameters it is seen that, for irradiated InP,the greatest drop occurs in Isc while for GaAs, the greatest drop occurs in Voc as a result of the irradiation. This would tend to indicate that a decrease in diffusion length with irradiation is a major factor in decreased output for the InP cells while for GaAs, the change in dark current with irradiation appears to be the major factor in decreased cell output.

Decreased cell output power with increasing temperature is an additional significant loss factor. An example of the variation in cell output power with temperature shown in Fig. 5, while Fig. 6 graphically summarizes the variation in cell maximum power, Pmax, with temperature determined for a number of R and J cells at 60°C. This temperature was chosen as representative of that experienced by solar cells in low earth and geosynchronous orbit. Cell performance parameters for these cells are listed in Table IV. From the table, the average value of dPm/dT for these cells is $-(5.3^{+}1.2) \times 10^{-2}$ mW/cm^2 °K.

To consider temperature effects in greater detail it is convenient to express the temperature dependencies of the cell performance parameters as relative variations, using the expression[14]

$$\frac{1}{Pm}\frac{dPm}{dT} = \frac{1}{Isc}\frac{dIsc}{dT} + \frac{1}{Voc}\frac{dVoc}{dT} + \frac{1}{FF}\frac{dFF}{dT} \qquad (1)$$

The temperature variation terms in the right hand side of Equation 1 are listed in Table V. In the past, the term in dVoc/dT was found to be a major factor in the variation of Pmax with temperature.[14,15] Hence, we examine this term in some detail using the expression[14]

$$\frac{dVoc}{dT} = \frac{Voc-Eg(T)}{T} - \frac{3k}{q} - \frac{\alpha T\,(T+2\beta)}{(T+\beta)^2} + \frac{kT}{I_{sc}}\frac{dIsc}{dT} \qquad (2)$$

where k is Boltzmann's constant and q is the electronic charge with,

Eg(T) = the band gap at temperature T in electron volts

$$Eg(T) = Eg(0) - \frac{\alpha T^2}{(T+\beta)} \qquad (3)$$

Eg(0) = 1.421 electron volts

α = 6.63×10^{-4} V/°K

β = 552 °K

It is noted here that, in reference 16, the value of β is given as 162°K. However, this latter quantity yields the value 1.292 eV for Eg at 300°K rather than the more correct value 1.351 eV.[16] The present value of β used in Eq. 3 yields the more correct bandgap value at 300°K.

Using the preceding set of equations, calculated values of dVoc/dT are found to be in reasonable agreement with experiment (Table VI). The success of equation 2 in predicting experimental values has led to the prediction of an inverse relation between Voc and the absolute magnitude of (1/Voc)(dVoc/dT).[14] From Fig. 7, it is seen that the present data is in rough agreement with the preceding statement. Also, if the term in dVoc/dT were dominant in Eq. 1, then there should be an inverse relation between Voc and the magnitude of (1/Pm) (dPm/dT).[14] However, as seen from Fig. 8, this is not the case for the present data. In fact, from the data of Table V, one cannot generalize and state that for InP, the temperature variation of any specific quantity is dominant in determing the temperature variation of Pmax. Noting however that the temperature dependencies in Table V are both positive and negative, it is desirable that dIsc/dT be as large as possible while the absolute magnitude of the negative terms in Voc and FF be as small as possible.

In general, the temperature dependence of Isc arises from the fact that diffusion length increases with temperature while band gap decreases with increasing temperature, the net result being an increase in current. With respect to the temperature dependence of Voc, from Eq. 2, it is seen that at fixed temperature, higher values of Voc lead to the desired lower values in the absolute magnitude of dVoc/dT. In this respect it is noted that, in Eq. 2, the term in dIsc/dT yields a relatively small contribution to dVoc/dT the principal contribution arising from the first term. The fill factor term in Eq. 1 is perhaps the most process dependent. Here one would expect shunt (Rsh) and series resistance (Rs) to play significant roles. However, a theoretical expression for dFF/dT is needed which includes the effects of Rs and Rsh.[14] Aside from this, the factors operative in determining the temperature dependencies of Voc and Isc are apparent from the preceding discussion and warrant further consideration in attempts to reduce the temperature dependency of Pmax.

CONCLUSION

In comparing the performance of these diffused junction cells one cannot conclude that either process is preferable in terms of increased radiation resistance. Although the cells prepared by open tube capped diffusion have slightly higher efficiencies, as measured at Lewis, it is possible that neither process was optimized at the time the present cells were processed. Hence a choice, based on efficiency, would be premature. The greatest difference appears in the temperature dependency, which favors the R cells. However the data is inconsistent in the sense that the present results do not show the dependency of dPm/dT on open circuit voltage which was observed in previous work.[14,15] In addition, the exact dependencies of the temperature variation of fill factor on Rs and Rsh is unclear at present. Thus, in summation, it can be stated that further efforts in both theory and experiment are required before concluding that one process is preferable to the other.

REFERENCES

1. Yamaguchi, M.; Uemura, C.; and Yamamoto, A.: Radiation Damage in InP Single Crystals and Solar Cells. J. Appl. Phys., vol. 55, no. 6, Mar. 15, 1984, pp. 1429-1436.

2. Yamamoto, A.; Yamaguchi, M.; and Uemura, C.: High Conversion Efficiency and High Radiation Resistance InP Homojunction Solar Cells. Appl. Phys. Lett., vol. 44, no. 6, Mar. 15, 1984, pp. 611-613.

3. Weinberg, I.; and Brinker, D.J.: Indium Phosphide Solar Cells - Status and Prospects for Use in Space. Advancing Toward Technology Breakout in Energy Conversion (21st IECEC), Vol. 3, American Chemical Society, 1986, pp. 1431-1435.

4. Weinberg, I.; Swartz, C.K.; and Hart, R.E. Jr.: Potential for Use of InP Solar Cells in the Space Radiation Environment. Proceedings of the 18th Photovoltaic Specialists Conference, IEEE, 1985, pp. 1722-1724.

5. Gordia, C.; Geier, J.V.; and Weinberg, I.: Near Optimum Design of InP Homojunction Solar Cells. Space Photovoltaic Research and Technology Conference, NASA CP-2475, 1986, to be published.

6. Ando, K.; and Yamaguchi, M.: Radiation Resistance of InP Solar Cells Under Light Illumination. Appl. Phys. Lett., vol. 47, no. 8, Oct. 15, 1985, pp. 846-848.

7. Yamamoto, A.; Yamaguchi, M.; and Uemura, C.: High Efficiency Homojunction InP Solar Cells. Appl. Phys. Lett., vol. 47, no. 9, Nov. 1, 1985, pp. 975-977.

8. Parat, K.K., et al.: Solar Cells in Bulk InP, Made by an Open Tube Diffusion Process. Solid State Electron., vol. 30, no. 3, Mar. 1987, pp. 283-287.

9. Brandhorst, H.W. Jr.; and Boyer, E.O.: Calibration of Solar Cells Using High-Altitude Aircraft. NASA TN D-2508, 1965.

10. Shen, C.C.: Arizona State University, Private Communication, 1986.

11. Yamaguchi, M., et al.: 22% Efficient and High-Radiation Resistant InP Solar Cells. Proceedings 2nd International Photovoltaic Science and Engineering Conference, Kobe, Japan, 1986, pp. 573-576.

12. Werthen, J.G., et al.: 21% (One Sun, Air Mass Zero) 4 cm^2 GaAs Space Solar Cells. Appl. Phys. Lett., vol. 48, no. 1, Jan. 6, 1986, pp. 74-75.

13. Yamamoto, A.; Yamaguchi, M.; and Uemura, C.: Fabrication of High-Efficiency n^+-p Junction InP Solar Cells by Using Group VIb Element Diffusion into p-Type InP. IEEE Trans. Electron Devices, vol. 32, no. 12, Dec. 1985, pp. 2780-2786.

14. Fan, J.C.C.: Theoretical Temperature Dependence of Solar Cell Parameters. Solar Cells, vol. 17, no. 2-3, Apr.-May 1986, pp. 309-315.

15. Weinberg, I; Swartz, C.K.; and Hart, R.E. Jr.: Performance and Temperature Dependencies of Proton Irradiated n/p and p/n GaAs and n/p Silicon Cells. Eighteenth IEEE Photovoltaic Specialists Conference, 1985, pp. 344-349.

16. Bachmann, K.J.: Properties, Preparation, and Device Applications of Indium Phosphide. Annual Reviews of Materials Science, Vol. 11, Annual Reviews, Inc., Palo Alto, CA., 1981, pp. 441-484.

TABLE I

AMO PERFORMANCE PARAMETERS OF InP CELLS

T=25°C

CELL	CARRIER CONC (cm^{-3})	EFFICIENCY (%)	Voc (mV)	Jsc (ma/cm^2)	FF (%)
R-1	$4.5X10^{16}$	14.2	814	30.5	78.5
R-2	$9.0X10^{16}$	13.7	825	28.8	79.1
R-3	$4.5X10^{16}$	12.9	815	26.3	82.6
J-1	$5.0X10^{15}$	13.6	826	27.6	81.8
J-2	$5.0X10^{15}$	13.3	823	28.0	79.0
J-3	$1.0X10^{17}$	10.05	812	22.6	75.1

TABLE II

PRE-IRRADIATION InP SOLAR CELL PARAMETERS

T=25°C

CELL	CARRIER CONC (cm^{-3})	EFFICIENCY (%)	Voc (mV)	Jsc (ma/cm^2)	FF (%)
R-3	$4.5X10^{16}$	12.9	815	26.3	82.6
R-4	$4.5X10^{16}$	12.7	814	26.0	82.6
J-2	$5.0X10^{15}$	13.3	823	28.0	79.0
J-4	$5.0X10^{15}$	12.1	813	27.8	73.5

TABLE III

PRE-IRRADIATION AMO PARAMETERS OF GaAs CELLS

T=25°C

EFFICIENCY (%)	Voc (mv)	Jsc (ma/cm^2)	FF (%)
19.6	1041	31.8	81.2
19.8	1044	32.1	81.1

TABLE IV

PERFORMANCE PARAMETERS OF InP CELLS

T=60°C

CELL	CARRIER CONC (cm^{-3})	Pm (mw/cm^2)	Voc (mv)	Jsc (ma/cm^2)	FF (%)	dPm/dT ($mw/cm^2\ ^oK$)
R-5	$4.5X10^{16}$	14.95	741	25.62	78.8	$-3.13X10^{-2}$
R-6	$4.5X10^{16}$	15.53	749	27	76.8	$-4.86X10^{-2}$
J-5	$5.0X10^{15}$	16.01	751	29.6	71.1	$-6.23X10^{-2}$
J-6	$5.0X10^{15}$	15.64	767	25.9	78.9	$-6.25X10^{-2}$
J-7	$1.0X10^{16}$	12.45	725	24.73	69.5	$-5X10^{-2}$
J-8	$1.0X10^{16}$	13.44	731	25.6	71.2	$-6.3X10^{-2}$

TABLE V

TEMPERATURE VARIATION TERMS

T=60°C

CELL	$\frac{1}{Isc}\frac{dIsc}{dT}$ ($^{o}K^{-1}$)	$\frac{1}{Voc}\frac{dVoc}{dT}$ ($^{o}K^{-1}$)	$\frac{1}{FF}\frac{dFF}{dT}$ ($^{o}K^{-1}$)
R-5	$12.6X10^{-4}$	$-3.12X10^{-3}$	$-3.71X10^{-4}$
R-6	$6.25X10^{-4}$	$-3.11X10^{-3}$	$-1.12X10^{-3}$
J-5	$7.67X10^{-4}$	$-3.09X10^{-3}$	$-1.63X10^{-3}$
J-6	$5.56X10^{-4}$	$-2.88X10^{-3}$	$-1.24X10^{-3}$
J-7	$9.66X10^{-4}$	$-3.28X10^{-3}$	$-1.35X10^{-3}$
J-8	$6.33X10^{-4}$	$-3.37X10^{-3}$	$-2.39X10^{-3}$

TABLE VI

CALCULATED AND MEASURED TEMPERATURE VARIATIONS OF Voc

T=60°C

CELL	$\frac{dVoc}{dT}$ ($mv/^{o}K$) MEASURED	CALCULATED
R-5	-2.31	-2.38
R-6	-2.33	-2.39
J-5	-2.32	-2.32
J-6	-2.21	-2.34
J-7	-2.38	-2.46
J-8	-2.46	-2.45

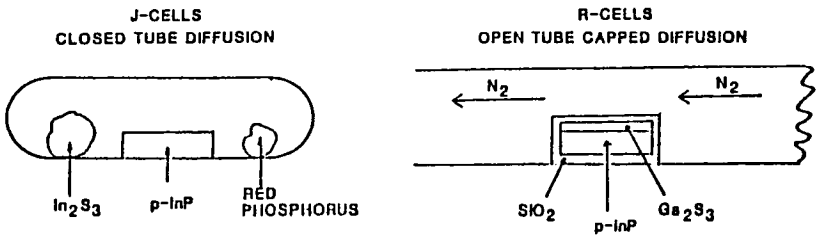

	J-CELLS	R-CELLS
DIFFUSION TEMP. (°K)	625	700
DIFFUSION TIME (min)	180	25
AR COATING	SiO	SiO
FRONT CONTACT	Au	Au
BACK CONTACT	Au/Zn	Au/Zn
CELL AREA (cm^2)	0.273	0.313

FIGURE 1.- JUNCTION FORMATION PROCESSES WITH ADDITIONAL InP CELL DETAILS.

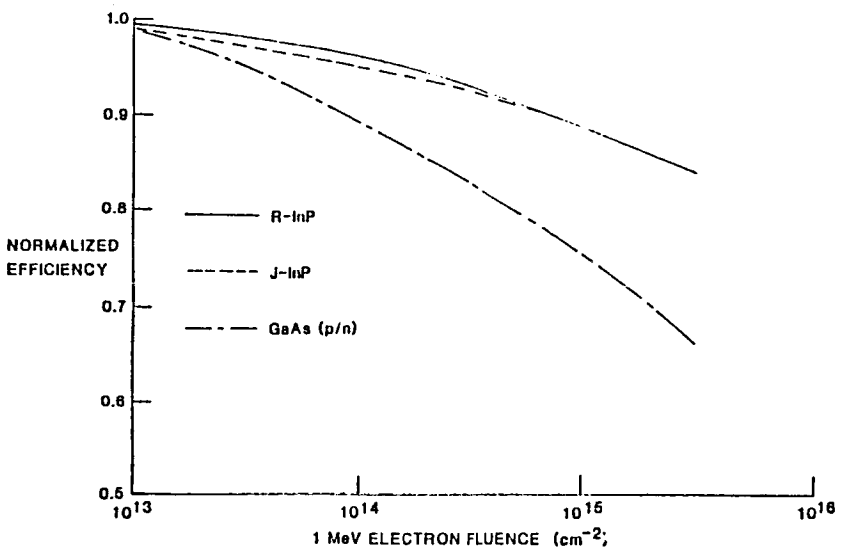

FIGURE 2.- NORMALIZED EFFICIENCY VS 1 MEV ELECTRON FLUENCE.

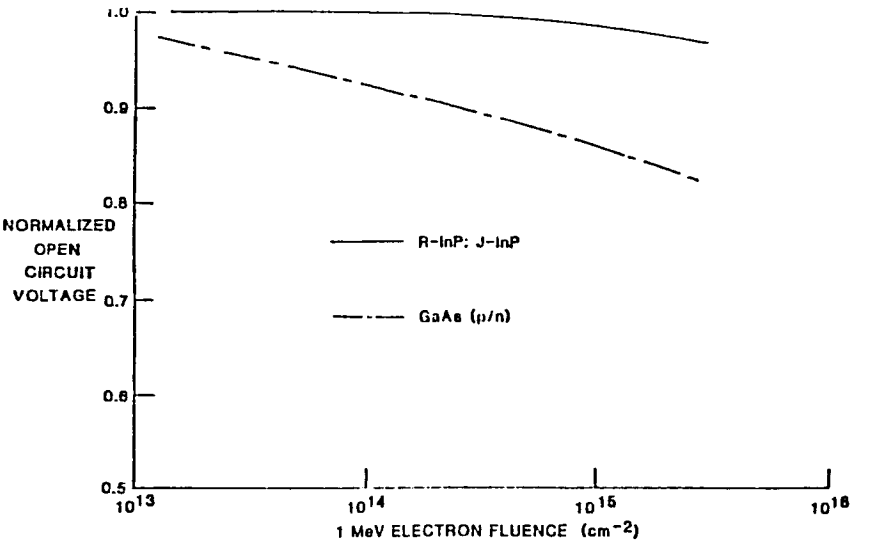

FIGURE 3.- NORMALIZED OPEN CIRCUIT VOLTAGE VS 1 MeV ELECTRON FLUENCE.

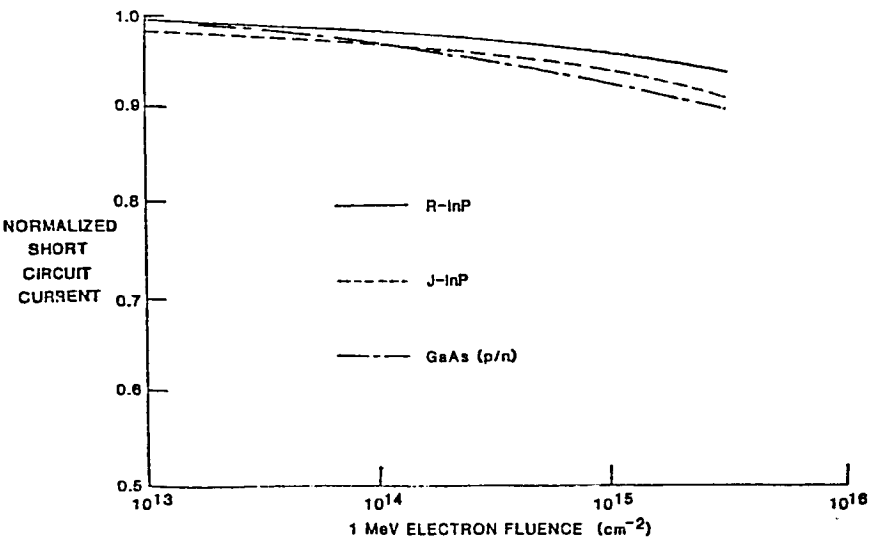

FIGURE 4.- NORMALIZED SHORT CIRCUIT CURRENT VS 1 MeV ELECTRON FLUENCE.

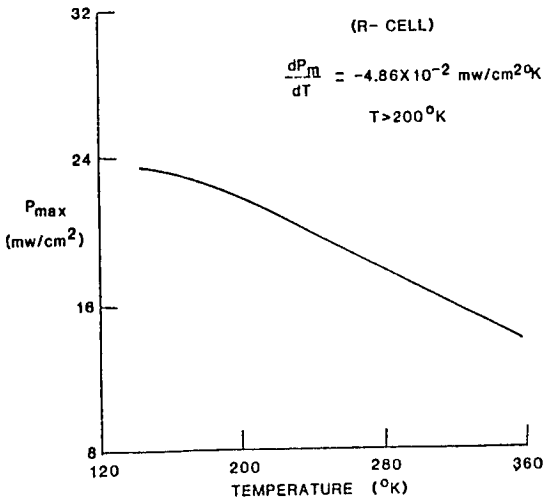

FIGURE 5. - VARIATION OF CELL MAXIMUM POWER WITH TEMPERATURE FOR A CELL PROCESSED BY OPEN TUBE DIFFUSION.

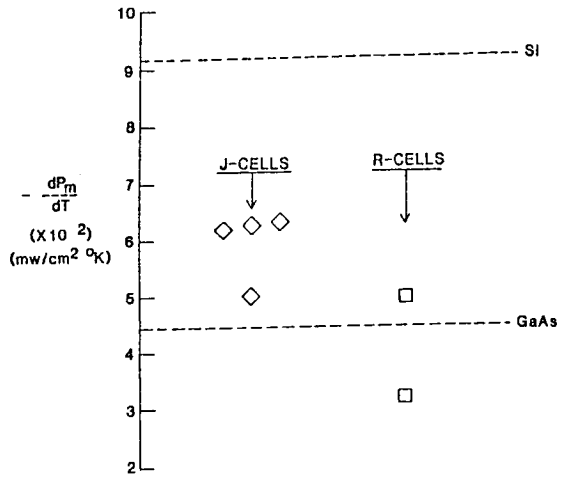

FIGURE 6.- TEMPERATURE DEPENDENCY OF CELL MAXIMUM POWER. GaAs AND Si DATA SHOWN FOR COMPARISION.

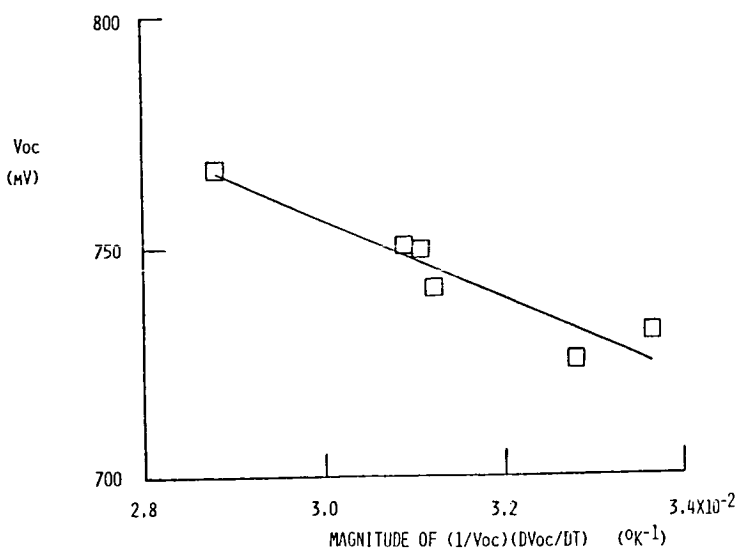

FIGURE 7.- Voc VS MAGNITUDE OF (1/Voc)(DVoc/DT).

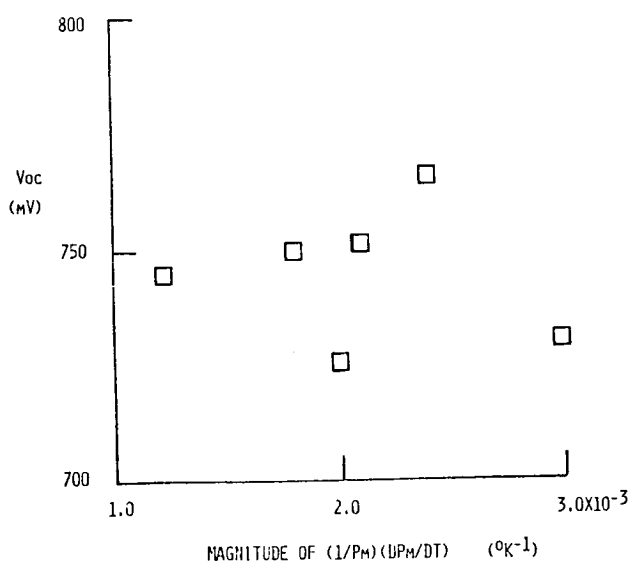

FIGURE 8.- Voc VS MAGNITUDE OF (1/PM)(DPM/DT)

ITO/InP Solar Cells: A Comparison of Devices Fabricated by Ion-Beam and RF Sputtering of the ITO

T.J. Coutts
Solar Energy Research Institute
Golden, Colorado

This work has been performed with a view to elucidating the behavior of ITO/InP solar cells prepared by rf and ion-beam sputtering. It is found that using rf sputter deposition of the ITO always leads to more efficient devices than ion-beam (IB) sputter deposition. An important aspect of the former technique is the exposure of the single crystal p-InP substrates to a very low power plasma, prior to deposition. Substrates treated in this manner have also been used for ion-beam deposition of the ITO. In this case the cells behave very similarly to the rf deposited cells, thus suggesting that the low power plasma exposure (LPPE) is the crucial process step.

Detailed analysis of the quantum efficiency of the cells shows that the LPPE causes the formation of a very thin type-converted surface layer on the p-type substrate, leading to a buried homojunction. These cells always had a much larger V_{oc} than the IB only cells, although the latter had a slightly larger J_{sc}. The largest J_{sc} achieved for the IB cells (of area nearly 1 cm^2) is 27.7 mA cm^{-2} (total area, 28°C, 100mW cm^{-2}, SERI/NASA direct normal spectrum). This is equivalent to 33.5 mA cm^{-2} (total area 28°C, 137.2 mW cm^{-2}, AMO WRRL-1985) which is, at the time of writing, the largest yet reported for any InP based cell. However the largest V_{oc} we have achieved is only 802 mV (28° C, for one of the rf cells), which is much less than should be expected for InP.

INTRODUCTION

Although the suitability of InP for solar cells has long been recognized, it has largely been ignored by the research community (principally because of its relatively high materials cost). In thin film form, where the cost considerations do not apply, it has also been discounted as an absorber for terrestrial solar cells because of unsolved problems of severe grain boundary recombination. The latter remains an outstanding question; why should grain boundary recombination be so severe when surface recombination is so minimal a problem? Hence, although InP has all the properties required for the fabrication of efficient solar cells (Eg=1.35 eV, direct band-gap and large absorption coefficient, low surface recombination velocity, and acceptably long minority carrier diffusion length), it has only been investigated by a relatively small number of research groups (1-5).

In recent years, however, this situation has begun to change, largely because of the extraordinary radiation resistance and annealing properties which InP exhibits (6-8). This has stimulated an appreciation of its potential for space applications which in turn may cause renewed interest in thin film cells for terrestrial application.

p-InP absorbers have been used with a variety of window-layers; e.g., with CdS (1), ZnO (9) and indium tin oxide (ITO) (2) being the most commonly studied. On the basis of elementary heterojunction design considerations, (lattice match, electron affinity match, window layer transmittance etc), one would expect the CdS/InP combination to have the highest efficiency of these three, whereas in practice it is the ITO/InP cell which has this record (2). The reasons for this somewhat unexpected

behavior have been the subject of considerable debate, and part of the objective of this paper will be the elucidation of ITO/InP junctions for cells in which the ITO has been deposited by either rf or ion-beam (IB) sputtering. This has established that the former are actually extremely shallow buried homojunctions, whereas the latter are more like true heterojunctions. However, it is concluded that in neither case will efficiencies approaching theoretical values be achieved. Rather, further advances will depend on optimizing the performance of n^+-p-p^+ cells, probably grown by OMCVD on the p^+ substrate.

EXPERIMENTAL

In this work, single crystal p-type InP has been used. The orientation was <100>; the crystals were zinc doped and two impurity concentrations were investigated; these being $N_A-N_D = 3x10^{16}$ cm^{-3} (purchased from Crysta Comm Inc.) and $3x10^{15}$ cm^{-3} (MCP Ltd.)

Device fabrication followed the sequence below:

i) Contact formation - after cleaving the as delivered wafer into substrates of approximately 1 cm^2 in area, the latter were chemo-mechanically polished with 0.25 μm diameter Al_2O_3 grit and 0.05 v/o Br: methanol. After this procedure the surface was examined ellipsometrically to check for residual roughness or contamination. Generally, it was found that the surface gave ellipsometric data close to that predicted for an ideal InP surface. Metal contacts were then deposited. In the work reported here, the metallization was 200Å of Zn (deposited by rf sputtering) followed by 2000Å of Au (deposited by thermal evaporation). The metallized substrate was then annealed in flowing forming gas for about one minute at a temperature of approximately 425°C. Contacts made this way tended to be somewhat variable and alternative systems based on Au:Be and Ni/Au:Be are now being studied.

ii) Active surface cleaning - because InP selectively loses phosphorus at quite low temperatures, it was always necessary to re-etch the front surface after contact formation. This was done in exactly the same manner as described above.

iii) Deposition of ITO - the ITO was deposited either by rf sputtering or by ion-beam sputtering. We have previously shown that exposure of the substrates to an extremely low power rf plasma, prior to deposition of the ITO, led to a great enhancement of device performance (10). To elucidate the effects of the low power plasma exposure (LPPE) we have made three types of cell. Type 1 cells were made entirely in the rf system. The ITO target was first sputter cleaned at full power for about thirty minutes, with the InP substrates protected by a shutter. The power was then reduced to a level at which no deposition was registered by a quartz crystal monitor. The shutter was then opened and the substrates subjected to LPPE for a pre-determined period. After this, the power was increased to give a rate of deposition of about 0.3-0.4Å s^{-1} and a film of ITO about 650Å grown. Type 2 cells were also subjected to the LPPE but after this were removed from the rf system and transferred to the ion-beam system for deposition of the ITO. Again, 650Å of ITO was used. Type 3 cells were not subjected to LPPE and the ITO was deposited by ion-beam sputtering.

iv) Gridding - was carried out using the temporary grids described elsewhere (11). The grids were electroformed from copper and were Au plated. They were held in close contact with the ITO using Scotch Tape. Although almost laughable in its lack of sophistication, this technique has proved remarkably successful as evidenced by the high device efficiencies achieved. However, the shadowing loss of these grids was 8-9% whereas recent calculations have shown that optimal grids would have shadow

losses of about 3%. More recent work on the electroplated grids will be published later.

v) Device characterization - the J/V, C/V and quantum efficiency of all the cells were measured. For efficiency measurements, standarized conditions of intensity, spectral content and temperature were used (total area, 28°C, 100mW cm^{-2}, SERI/NASA, direct normal spectrum). The C/V measurements were made using a Hewlett-Packard LCR bridge (Type 4274 A) at a frequency of 100 kHz. Reverse biases up to 10V have been used but were generally restricted to about 4V. The quantum efficiency measurements were made as a function of reverse voltage bias and light bias. It is the analysis of these measurements which will form the basis for most of the subsequent discussion.

RESULTS

The performance characteristics of all sixteen cells are summarized in tables 1 and 2; with the current/voltage characteristics of cells rf4 and IB1 (60 mins. LPPE, rf sputtered ITO; 0 mins. LPPE, IB sputtered ITO; respectively) being shown in Fig. 1. Cell rf4 had a value of J_{sc} = 27.7 mA cm^{-2} for the measurement conditions defined above. Using the spectral response of this cell, it was calculated that the AMO value of J_{sc} would be 33.5 mA cm^{-2} (using the total area of the cell = 0.981 cm^2, 28°C, 137.2 $mWcm^{-2}$ AMO WRRL - 1985). Since these cells had a grid shadow loss of about 8.5%, the actual active area current = 36.6 mA cm^{-2} which is to be compared with the theoretical maximum of 41.82 $mAcm^{-2}$.

The quantum efficiencies for cells rf1-4 are shown in Fig. 2 from which the completely systematic improvement with increasing LPPE is evident. This, of course is reflected in J_{sc}. Cells rf5-8 showed similar behavior although the optimum LPPE was 30 mins.

It should also be noted that all the rf series cells had $V_{oc} \geq 746$ mV whereas only those cells which had been rf plasma exposed, in the IB series, had relatively large V_{oc}. Cells IB1 and IB5 which had not been plasma exposed had high currents but low voltages. (Cell IB2 should not be included in this analysis since it was accidentally exposed to the ion-beam prior to deposition of the ITO). These key differences in the behavior of the two types of cell provide much information and they will be discussed later.

Plots of $1/C^2$ - V were also made and an illustrative example is shown in Fig. 3. The important feature to note here is that the IB cell gave nearly perfect linearity for the entire range of biases used whereas the rf cell showed a discontinuity. This behavior was typical.

DISCUSSION

It has previously been suggested that rf sputter deposition of any window layer material onto p-InP causes type conversion of the surface (9) and, indeed, direct evidence of phosphorus depletion has been obtained (12). In addition, "mixing" at the interface has been observed (13), as has the in-diffusion of tin (14), and the out-diffusion of dopants (15). Hence there are several processes known to take place at, or near, the interface which could radically influence the behavior of the cells. We believe that the larger values of V_{oc} and the lower values of J_{sc} are clear indications that the rf fabricated cells are buried homojunctions, while the IB cells, with their slightly larger J_{sc} (for the unexposed devices) and much lower V_{oc}, are probably heterojunctions.

In the absence of interface recombination, the internal quantum efficiency of a homojunction with disimilar diffusion lengths in the p- and n-regions, is

$$\eta_{int} = \left(\frac{e^{-\alpha d}}{1-\alpha L_p}\right) - \left(\frac{\alpha L_p e^{-d/L_p}}{1-\alpha L_p}\right) - \left(\frac{e^{-\alpha(d+W)}}{1+\alpha L_n}\right) \quad (1)$$

where α is the optical absorption coefficient, L_n and L_p are the minority carrier diffusion lengths, d is the thickness of the type-converted surface region, and W is the width of the space charge region. At the short wave-end of the spectrum, where α is large, it is straightforward to show that

$$\eta_{int} = \exp(-\alpha d) \quad (2)$$

provided that L_p is very small; i.e., that the surface is essentially "dead". From the measured reflectance spectrum of the cells we can calculate η_{int}, and these data can then be plotted in the form of $\ell n\ \eta_{int}$ ~α to obtain the thickness of the dead-layer. An example of such a plot is shown in Fig. 4 and it should be stressed that this technique worked only for the plasma exposed cells. IB1 and IB5 did not exhibit this behavior. In Fig. 5 we show the variation of the dead-layer thickness with plasma exposure time for the eight rf series cells. The striking feature is that the dead-layer decreases in thickness; monotonically for the more lightly doped material, and passing through a minimum for the 3×10^{16} cm^{-3} material (the latter observation is also reflected in the variation of J_{sc} with LPPE duration). The fact that cells rf1 and rf5 with no LPPE have the thickest dead-layers, and have relatively large voltages, whereas cells IB and IB5 (also without LPPE) have no dead-layer and have relatively low voltages, implies that most of the type-conversion mechanism takes place in the initial stages of the ITO deposition by rf sputtering. Hence the LPPE must somehow lessen the damaging effects of deposition, and we speculate that it somehow causes migration of acceptor impurities to the surface (as observed by SIMS (14)) which therefore makes the subsequent type-conversion of that region more difficult. The out-diffusion of acceptor species would also create a very lightly doped, graded sub-surface region which would have the effect of widening the space charge. This would lead to improved quantum efficiencies at all wavelengths.

To check this model we have examined the variation of dead-layer thickness with substrate impurity concentration. These data are shown in Fig. 6 for a fixed duration LPPE. As predicted by the model, the dead-layer thickness decreases as the impurity content of the substrates increase.

Finally, we have also made measurements of the dead-layer thickness as a function of reverse bias for one of the rf cells. The data are shown in Fig. 7 where d is plotted against W; the latter having been obtained from measurement of capacitance as a function of reverse bias. We interpret the decrease of d with increasing W as being due to the expansion of the space charge toward the surface of the type-converted region (i.e., toward the ITO interface) as well as into the p-type bulk. This, of course, also supports the homojunction model. If we assume that the change in the space charge width is proportional to the square root of the impurity concentration, then

$$\frac{\Delta d}{\Delta W} \approx \frac{|N_A - N_D|_p}{|N_D - N_A|_n}^{1/2} \quad (3)$$

For a reverse bias of 10V, $\Delta d \approx 80$ Å, $\Delta W \approx 0.5$ μm, and $|N_A-N_D|_p = 3\times10^{16}$ cm^{-3}. We have $|N_D-N_A|_n = 1\times10^{20}$ cm^{-3}. Dautremont-Smith et al have shown that deposition by rf sputtering of SiO_2 onto p-InP causes considerable disruption of the surface. Measured in terms of an areal density, the damage was of the order of 10^{15} cm^{-2}. If expressed in terms of a volume density, this number would be about 10^{22} cm^{-3} which could, therefore, be the donor concentration in the surface region. However, the net donor concentration, $|N_D-N_A|$, will actually be substantially less than this, due to compensation by out-diffusion acceptor species, and a value around 10^{20}cm^{-3} would not seem unreasonable. hence, it is believed that the benefits of the LPPE are due to making the surface strongly p^+ before being compensated to n^+ by damage due to the actual deposition of the ITO. This is more consistent with all the experimental observations than the in-diffusion of tin, suggested earlier (14,15), and is consistent with the recent observations of Olego et al (16). Hence, to summarize, the cells fabricated entirely in the rf system are essentially n^{++}(ITO)$|n^+$(InP)$|$p(InP), while those made using LPPE plus IB sputtering are possibly n^{++}(ITO)$|p^+$(InP)$|$p(InP). The IB only cells would be expected to be n^{++}(ITO)$|$p(InP). It is believed that this model explains all our observations.

CONCLUSIONS

This work has shown that ITO/InP cells, in which the ITO has been deposited by rf sputtering, are actually very shallow buried homojunctions. The influence of LPPE is to increase J_{sc}, particularly for the more lightly doped material. Substrates which were first plasma exposed on then had ITO deposited by IB sputtering, behaved similarly to the rf series cells. Conversely, IB sputtering and no LPPE, led to poor voltages and the largest J_{sc} of all. We conclude that these are actually true heterojunctions.

Measurement of the dead-layer thickness of the rf cells as a function of voltage has enabled us to estimate the effective concentration of donors in the type-converted surface layer. This is roughly in accordance with the damage estimates by Rutherford backscattering spectroscopy. Although we have made cells with efficiencies even higher than these (16.2% (2)), further substantial improvement is unlikely. The damage mechanism must inherently limit V_{oc} and the fill-factor and therefore we believe that realization of the full potential of this material will ultimately depend on optimization of OMCVD grown n^+-p-p^+ structures recently reported (7).

REFERENCES

1. S. Wagner, J.L. Shay, K.J. Bachmann, and E. Buehler, Appl. Phys. Letts., 26, 229 (1975).

2. T.J. Coutts and S. Naseem, Appl. Phys. Lett., 46, 164 (1985).

3. L. Gouskov, H. Luquet, J. Esta and C. Gril, Solar Cells, 5, 51 (1981).

4. T.L. Chu, S.S. Chu, C.L. Lin, C.T. Chang, Y.C. Tzeng and A.B. Kuper, Proceedings of the 14th IEEE PV Spec. Conf., San Diego, Jan. 7-10 (1980), p. 661.

5. N.G. Dhere, R.G. Dhere and H.R. Moutinho, Proceedings of the 18th IEEE PV Spec. Conf., Las Vegas, Oct. 21-25, (1985), p. 1423.

6. A. Yamamoto, M. Yamaguchi and C. Uemura, Appl. Phys. Lett., 44 611, (1984).

7. M. Yamaguchi, A. Yamamoto, Y. Itoh, and C. Uemura, Proceedings of the 2nd International Photovoltaic Science and Engineering Conference, Beijing, Aug. 19-22, (1986), p. 573.

8. I. Weinberg, C.K. Swartz and R.E. Hart, Proceedings of the 18th IEEE PV Spec. Conf., Las Vegas, Oct. 21-25 (1985), p. 1722.

9. M.J. Tsai, A.L. Fahrenbruch and R.H. Bube, J. Appl. Phys., 51, 2696, (1980).

10. T.J. Coutts and N.M. Pearsall, Proceedings of the IEE Meeting on Plasma Deposition Processes, London, (1982).

11. N.M. Pearsall, Ph.D. Thesis, Cranfield Institute of Technology, Cranfield, Bedfordshire, England, (1982).

12. W.C. Dautremont-Smith and L.C. Feldman, J. Vac. Sci. Technol. A 3, 873 (1985).

13. A. Swartzlander, T.J. Coutts, S. Naseem and T.P. Massopust, Thin Solid Films, 138, 65 (1986).

14. K.J. Bachmann, H. Schreiber, Jr., W.R. Sinclair, P.H. Schmidt, F.A. Thiel, E.G. Spencer, G. Pasteur, W.L. Feldmann, and K.S. Sree Harsha, J. Appl. Phys. **50**, 3441 (1979).

15. T.J. Coutts, S. Naseem and R.K. Ahrenkiel, Proceedings 6th European Communities Photovoltaic Solar Energy Conference, London, (1985), D. Reidel Publishing Co., pp. 174-178.

16. D.J. Olego, R. Schachter, M. Viscogliosi and L.A. Bunz, Appl. Phys. Lett., 49, 719 (1986).

Table I. Summary of parameters of solar cells prepared using rf sputtering.[a]

Supplier	Mining and Chemical Products ($3x10^{15}$ cm^{-3})				Crysta-Comm, Inc. ($3x10^{16}$ cm^{-3})			
Cell Ref.	rf1	rf2	rf3	rf4	rf5	rf6	rf7	rf8
LPPE (min)	0	15	30	60	0	15	30	60
J_{sc} (mA cm^{-2})	24.0	25.9	26.3	27.2	23.3	24.5	25.6	24.9
V_{oc} (mV)	746	761	760	785	760	756	759	765
FF (%)	69.3	65.4	66.7	72.2	66.2	73.9	73.7	61.1
η (%)	12.4	12.9	13.3	15.4	11.7	13.7	14.3	11.6

[a]All the cells whose properties are summarized in the table were made by rf sputter deposition of ITO onto the InP substrates immediately after exposure of the latter to the low power plasma. Their characteristics were measured at SERI at 28°C, using a standard spectrum, atmosphere, and other experimental conditions. There was an interval of approximately one month between their fabrication and characterization.

Table II. Summary of parameters of solar cells prepared using ion-beam sputtering.[a]

Supplier	Mining and Chemical Products ($3x10^{15}$ cm^{-3})				Crysta-Comm, Inc. ($3x10^{-16}$ cm^{-3})			
Cell Ref.	IB1	IB2[b]	IB3	IB4	IB5	IB6	IB7	IB8
LPPE (min)	0	15	30	60	0	15	30	60
J_{sc} (mA cm^{-2})	27.7	23.5	26.5	26.0	27.1	26.3	26.1	25.8
V_{oc} (mV)	674	676	773	768	693	758	765	756
FF (%)	65.4	67.1	64.4	65.1	63.9	69.8	64.9	70.8
η (%)	12.2	10.7	13.2	13.0	12.0	13.9	13.0	13.8

[a]These cells were prepared on substrates which had been given the LPPE treatment several weeks before the ITO was deposited by ion-beam sputtering. Therefore, it is possible that a surface oxide may have formed, thus increasing the series resistance and decreasing the fill-factor.

[b]Cell IB2 was accidentally exposed to the ion-beam for several seconds before deposition was begun; it cannot therefore be regarded as one of the family of cells.

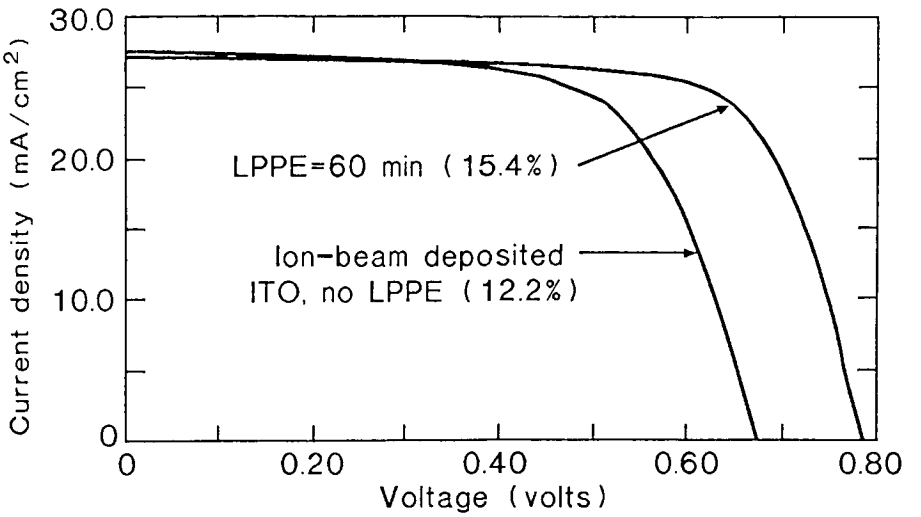

1. - Current/Voltage characteristics of cells 1B1 and rf4. Note that the use of the low-power plasma exposure resulted in a considerably larger V_{oc}.

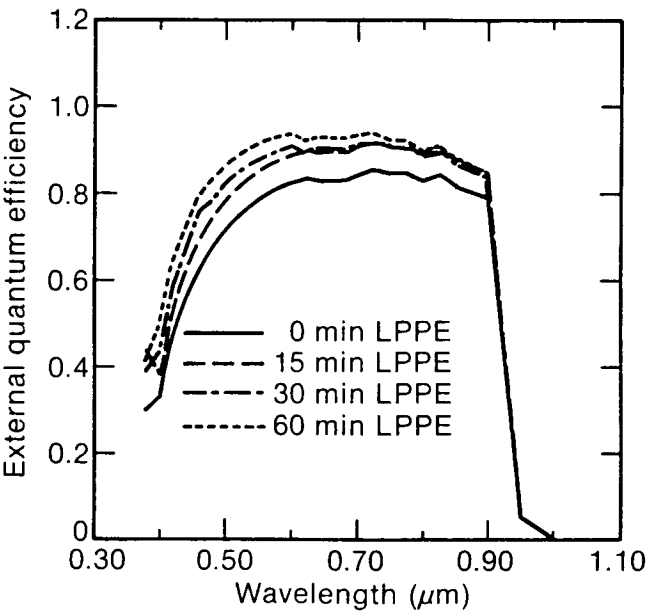

2. - External quantum efficiencies of cells rf1-4. Note the systematic improvement with the increasing duration of the low-power plasma exposure.

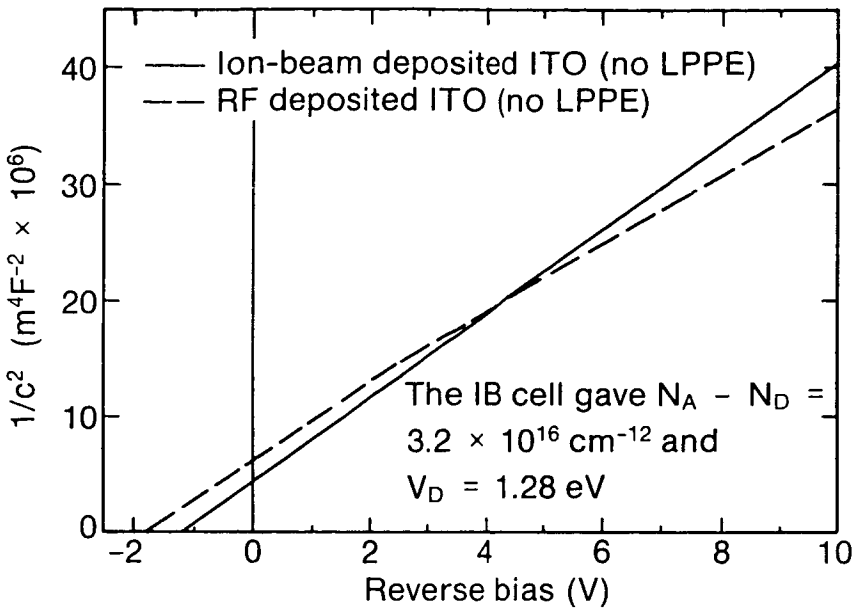

3. - Mott-Schottky plot for cells rf1 and IB1. Even without the plasma exposure, cell rf1 exhibited non-linearity which, it is believed, is indicative of homojunction formations.

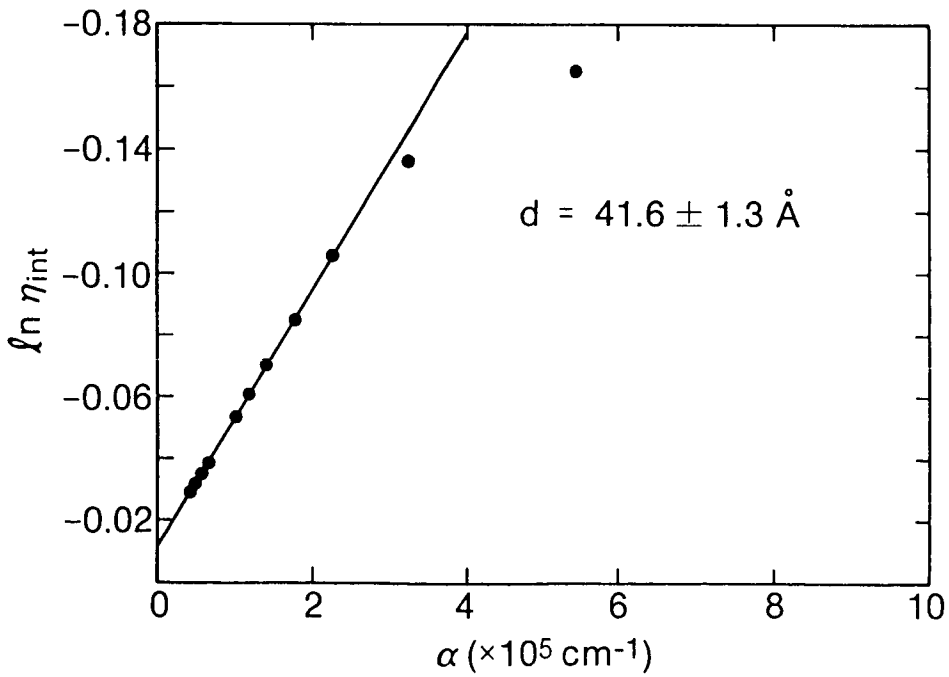

4. - "Dead-layer" plot for a typical cell.

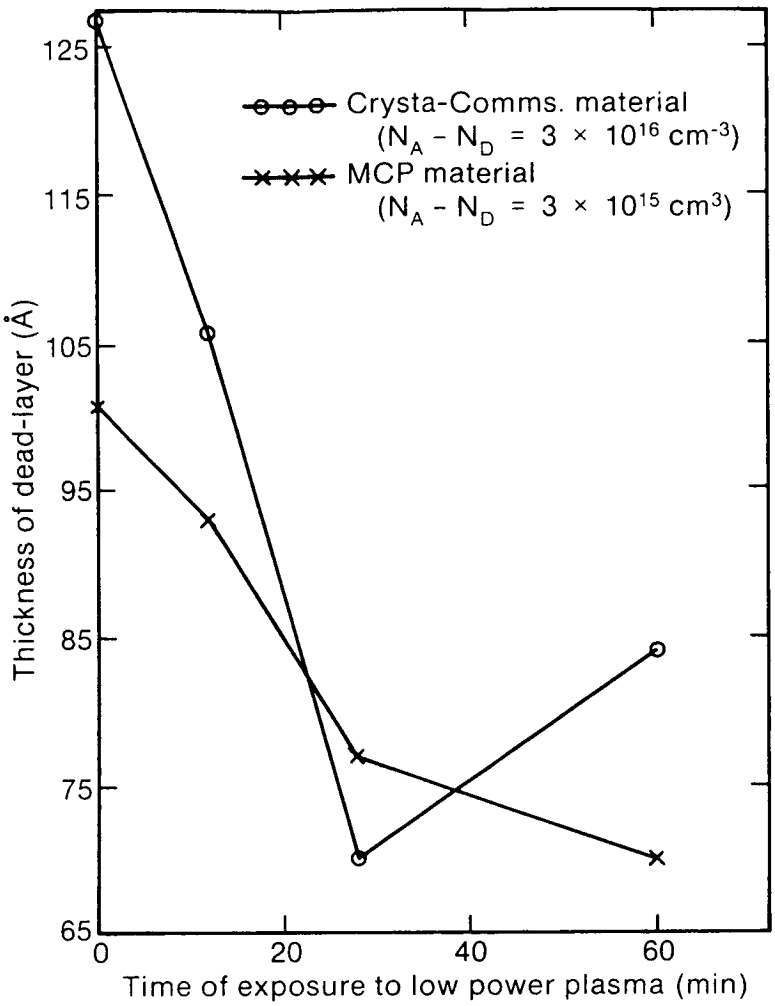

5. - Variation of dead-layer thickness as a function of the duration of the low-power plasma, for two values of $|N_A - N_D|$.

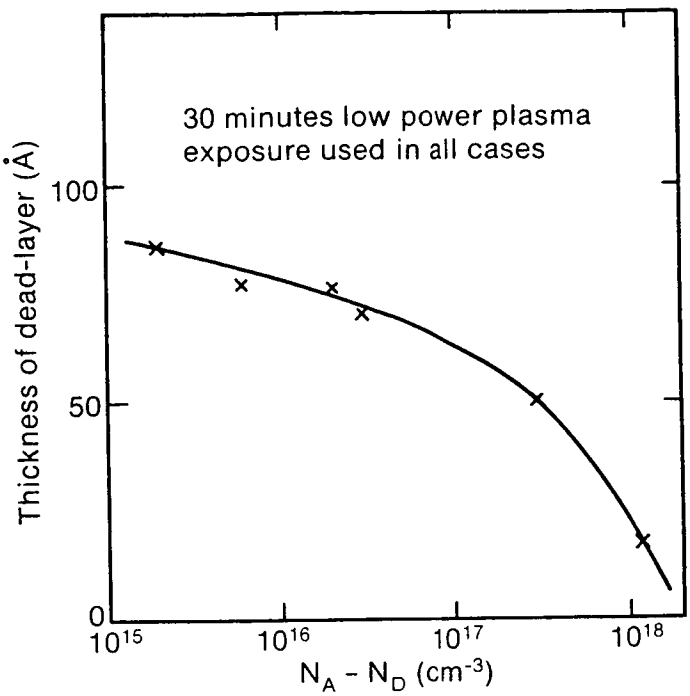

6. - Variation of dead-layer thickness as a function of substrate impurity concentration for a fixed duration plasma exposure.

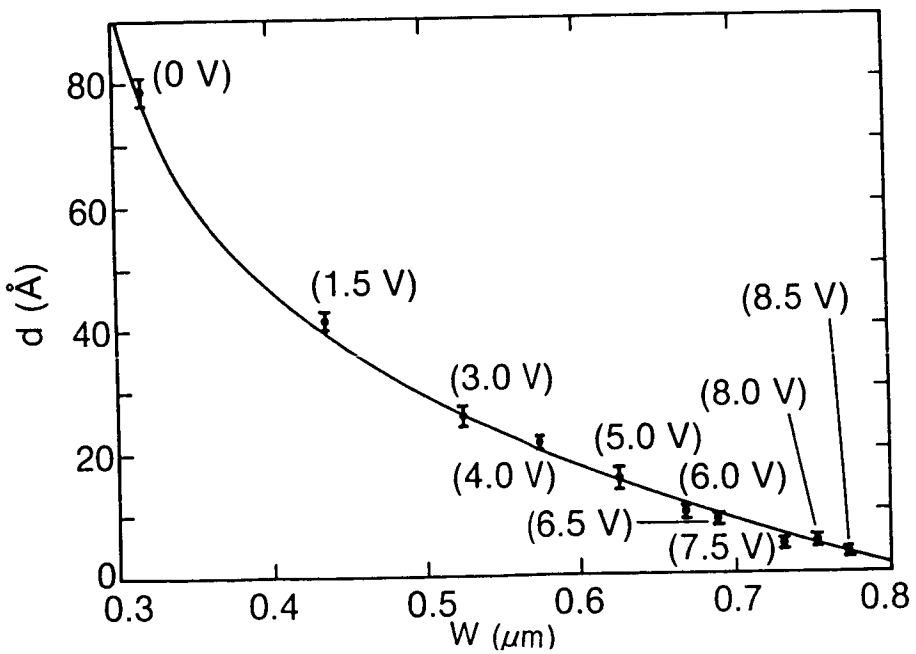

7. - Variation of dead-layer thickness as a function of the total width of the space charge region. It is believed that this result, for one of the rf series cells, indicates an expansion of the space charge toward the ITO/InP interface as well as into the p-InP substrate. This supports the buried homojunction model.

NEAR-OPTIMUM DESIGN OF THE InP HOMOJUNCTION SOLAR CELL

Chandra Goradia and James V. Geier
Cleveland State University
Cleveland, Ohio

Irving Weinberg
NASA Lewis Research Center
Cleveland, Ohio

Using a fairly comprehensive model, we have done a parametric variation study of the InP n+p homojunction solar cell for AMO, 25°C operation. The results of this study are presented. These results indicate that an efficiency of about 20.5% should be realistically possible in a shallow homojunction InP solar cell with near-optimum design.

INTRODUCTION

Results obtained so far indicate that InP solar cells show a much greater tolerance to 1MeV electron and 10MeV proton irradiation than Si and GaAs solar cells [1]. In addition, InP cells can be annealed at a relatively low temperature of about 100°C [2] and are even annealed under minority carrier injection under a forward bias [3]. For these reasons, InP cells show great promise for space applications and there is now considerable interest in developing these cells for high efficiency.

Currently, the best InP cells have exhibited a total area, AMO, 25°C efficiency of 16% [4]. This efficiency needs to be significantly improved in order for InP cells to meet the long-term kW/kg, kW/m^2 and $/kW goals for space cells. There is thus a need to theoretically assess the realistic improvements in efficiency that may be possible for InP cells. To this end, we undertook to answer the following two questions: 1) What is the maximum realistically achievable AMO, 25°C total area efficiency in InP cells? 2) What is the optimum or near-optimum design of the cell in terms of its geometrical and material parameters which will yield this maximum efficiency?

To help us answer the above questions, we have developed a fairly comprehensive one-dimensional computer simulation model for the InP solar cell. This model takes into account position- and wavelength-dependent optical generation in the emitter, base, space-charge and BSF/substrate regions, doping-dependent

mobilities and lifetimes (HSR and radiative) in all these regions, and realistic front and back surface recombination velocities. In addition, the model calculates the wavelength-dependent reflection coefficient for a given AR coating material and thickness and the series resistance for a given rectangular or circular grid design.

CALCULATED RESULTS

Using this model, we have done a parametric variation study to determine the maximum realistically attainable efficiency and near-optimum design of the cell. As a first step, to gain confidence in our model, we tried to fit our calculated results to the measured results on two InP cells made at Rensselaer Polytechnic Institute. Using only the diffusion lengths in the emitter and base and the effective lifetime in the space charge region as fitting parameters, we got excellent match with the measured curves of not just the illuminated I-V but also the spectral response and the I_{sc}-V_{oc}. In addition, our model predicted the same behavior of the performance parameters as a function of base doping as observed by Yamamoto et al [5].

Table 1 shows the near-optimum design parameters and best performance for each of three combinations of emitter and base dopings. It is seen that the best performance is obtained for relatively low emitter and base dopings of 5E17 and 1E16 cm^{-3} respectively, yielding a realistically attainable efficiency of ~20.5%. Our predicted values of V_{oc} are low because we have used conservatively low lifetimes and diffusion lengths. With somewhat longer lifetimes, V_{oc}'s up to about 915mV are predicted, with correspondingly higher efficiencies reaching 21.4%. Note the rather decent values of short circuit current density and fill factor, indicating that series resistance is not a problem even for the rather thin emitter of only 400Å.

Figures 1 and 2 show the cell output parameters versus emitter width and emitter doping respectively. The values of all other parameters are as listed under the Series C column in Table 1. The vertical arrows in these and other figures indicate nominal values of the independent variable.

It is seen from Figure 1 that for the chosen grid design the cell efficiency monotonically decreases with increasing width of the emitter, indicating that the emitter should be as narrow as is realistically possible, around 400 to 600Å. The primary cause of efficiency reduction with increasing emitter width is the reduced collection of photogenerated carriers, as evidenced by a significant decrease in the short circuit current density. A secondary cause is the increased recombination with a large emitter volume, causing a reduction in V_{oc} with increasing emitter width.

Figure 2 shows that there is a broad peak in the curve of

cell efficiency versus emitter doping, with best results for an emitter doping between 4E17 and 8E17 cm^{-3}. At the rather low emitter dopings, below 1E17 cm^{-3}, it is the V_{oc} and FF which are low; on the other hand, all parameters, J_{sc}, V_{oc} and FF, decrease with increasing doping above 1E18 cm^{-3}. Thus, a relatively low emitter doping of ~5E17 cm^{-3} is ideal.

Figure 3 shows the performance parameters versus front surface recombination velocity (SRV). It is very likely that the 1E4 cm/s value of front SRV which we have used in our calculations is perhaps too low and a more realistic value should have been 1E5 to 2E5 cm/s. If that be the case, then we see from this figure that the maximum efficiency would come down from 20.35% to ~19.7% or, for the case of longer lifetimes, from 21.4% to ~20.7%. Note that because of the rather large diffusion velocity D/L in the emitter ($\gtrsim$1E4 cm/s), cell performance is barely affected by front SRV values smaller than a few times 1E4 cm/s.

In Figures 4 and 5 we show cell performance parameters versus base width and base doping respectively. It is seen that, up to a base width of 4μm, the V_{oc} monotonically decreases because of increased volume recombination, since base diffusion length is greater than 4μm, while I_{sc} increases with base width. The efficiency goes through a broad peak at a base width between 2.0 and 3.0μm. More interestingly, the V_{oc} increases and I_{sc} decreases with increasing base doping in such a manner that the efficiency decreases with increasing base doping. The ideal base doping seems to lie in the range 5E15 to 5E16 cm^{-3}. This is in conformation with the observed dependence of performance on base doping. In the present effort, our emphasis has been on optimum design only with respect to efficiency. We are in the process of incorporating into our model the fluence dependence of lifetime (in all regions of the cell) and of the front SRV and doing radiation damage simulation of the cell. It may then turn out that from the radiation tolerance point of view, base dopings around 5E16 cm^{-3} or somewhat higher may be desirable, as has been experimentally observed.

Figure 6 shows the components of light-generated current ($\approx I_{sc}$) from the various cell regions and Figure 7 shows the loss current components at open circuit, both as functions of the base doping. In Figure 6 it is seen that for base dopings less than 2E16 cm^{-3} nearly two-thirds of the light-generated current comes from the space charge region, slightly less than one-third from the emitter and only a very small amount from the base. This in spite of a very thin (400Å) emitter. This is because of the very high optical absorption coefficient of InP. This is very different from silicon solar cells where practically all of the light-generated current comes from the base, and also somewhat different from gallium arsenide solar cells where the base contributes significantly to the light-generated current. This difference may have a bearing on the improved radiation tolerance of InP solar cells compared to Si and GaAs solar cells. We are in

the process of investigating this. On the other hand, as seen from Figure 7, the base is practically the sole contributor to the loss current at V_{OC}. This behavior is the same as in Si and GaAs solar cells. It is easily seen from Figures 6 and 7 why I_{SC} decreases and V_{OC} increases with increasing base doping.

CONCLUSIONS

Our theoretical modelling of the InP n^+ shallow homojunction solar cell allows us to draw the following inferences:

1. A maximum total area, 1AMO, 25°C efficiency slightly above 20% appears realistically possible.

2. A near optimum design of the cell would have emitter and base high quality layers (preferably, epitaxial) of thicknesses ~400Å and 2μm respectively and dopings 5E17 cm^{-3} and 1E16 respectively, with a good quality BSF/substrate layer of doping 2E18 to 5E18 cm^{-3}.

3. The light-generated current ($\sim I_{SC}$) is controlled primarily by the space charge and emitter regions while the open circuit voltage V_{OC} is controlled primarily by the properties of the base region.

REFERENCES

1. Yamaguchi, M.; Uemura, C.; and Yamamoto, A., "Radiation Damage in InP Single Crystals and Solar Cells," J. Appl. Phys. 55, 1429 (1984).

2. Yamaguchi, M.; Itoh, Y.; and Ando, K., "Room-Temperature Annealing of Radiation-Induced Defects in InP Solar Cells," Appl. Phys. Lett. 45, 1206 (1984).

3. Yamaguchi, M.; Ando, K.; Yamamoto, A.; and Uemura, C., "Minority-Carrier Injection Annealing of Electron Irradiation-Induced Defects in InP Solar Cells," Appl. Phys. Lett. 44, 432 (1984).

4. Yamaguchi, M.; Yamamoto, A.; Itoh, Y.; Uemura, C., "22% (AM 1.5, Active Area) Efficient and High Radiation Resistant InP Solar Cells," Proc. PVSEC II, Aug. 19-22, 1986, Beijing, China, pp. 573-576.

5. Yamamoto, A.; Yamaguchi, M.; and Uemura, C., "Fabrication of High-Efficiency n^+p Junction InP Solar Cells by Using Group VIb Element Diffusion into p-Type InP," IEE Trans. Elect. Dev. 32, 2780 (1985).

TABLE 1

Parameter	Series B	Series D	Series C
Performance:			
Short Ckt. Current Density J_{sc}, mA/cm^2	35.85	37.05	37.29
Open Ckt. Voltage V_{oc}, mV	875.1	877.4	877.7
Fill Factor FF, %	85.09	85.39	85.38
Conversion Efficiency η, %	19.44	20.22	20.35
General:			
Junction Area, cm^2	1.00	1.00	1.00
Total Illuminated Area, cm^2	0.94	0.94	0.94
Grid Coverage, %	6.00	6.00	6.00
SiO AR Coating, angstroms	750	750	750
Specific Contact Resistance, ohm-cm^2	1.0E-3	1.0E-3	1.0E-3
Intrinsic Carrier Concentration n_i, cm^{-3}	1.655E7	1.655E7	1.655E7
Calculated Series Resistance R_s, ohm	0.137	0.199	0.271
Front Surface Recombination Velocity S_F, cm/s	1.0E4	1.0E4	1.0E4
Space-Charge Region Dark Current Correction Factor	2.0E-2	2.0E-2	2.0E-2
n^+ Emitter:			
Width W_E, angstroms	400	400	400
Uniform Doping N_{dE}, cm^{-3}	5.0E18	1.0E18	5.0E17
Minority Carrier Mobility μ_{pE}, cm^2/Vs	40.0	75.0	100.0
Minority Carrier Lifetime τ_{pE}, ns	0.04	0.20	0.40
Minority Carrier Diffusion Length Length L_{pE}, μm	0.064	0.196	0.321
p Base:			
Width W_B, μm	2.00	2.00	2.00
Uniform Doping N_{aB}, cm^{-3}	5.0E16	5.0E16	1.0E16
Minority Carrier Mobility μ_{nB}, cm^2/Vs	3.55E3	3.55E3	4.25E3
Minority Carrier Lifetime τ_{nB}, ns	4.00	4.00	20.0
Minority Carrier Diffusion Length L_{nB}, μm	6.00	6.00	14.8
p^+ BSF/Substrate Layer:			
Width W_S, μm	250	250	250
Uniform Doping N_{aS}, cm^{-3}	5.0E18	5.0E18	5.0E18
Minority Carrier Mobility μ_{nS}, cm^2/Vs	2.46E3	2.46E3	2.46E3
Minority Carrier Lifetime τ_{nS}, ns	0.040	0.040	0.040
Minority Carrier Diffusion Length L_{nS}, μm	0.50	0.50	0.50
Effective SRV at BSF/Base Interface S_s, cm/s	1.26E4	1.26E4	2.51E3

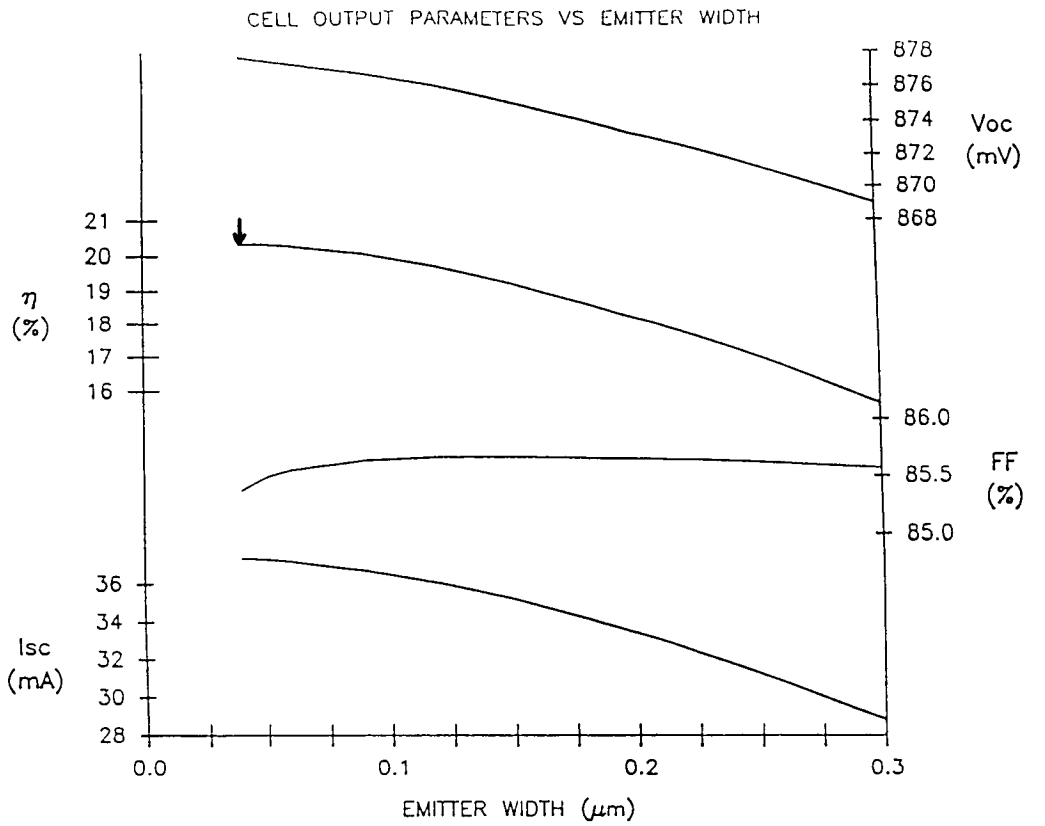

Figure 1

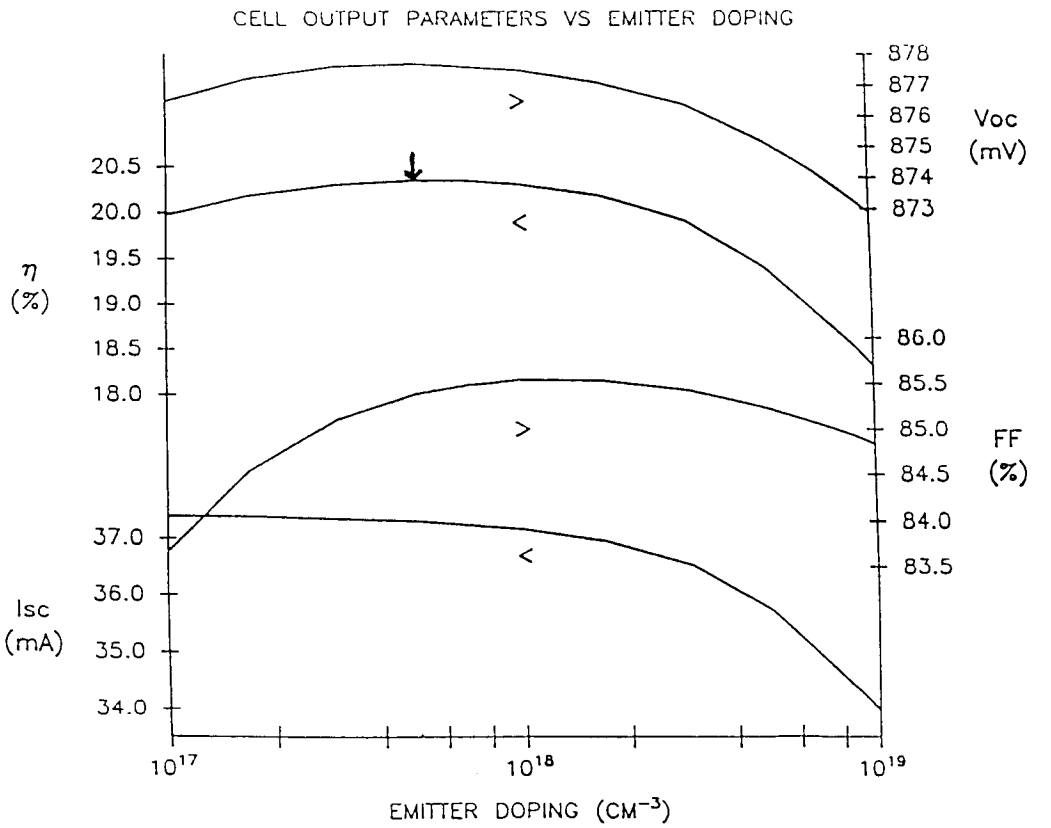

Figure 2

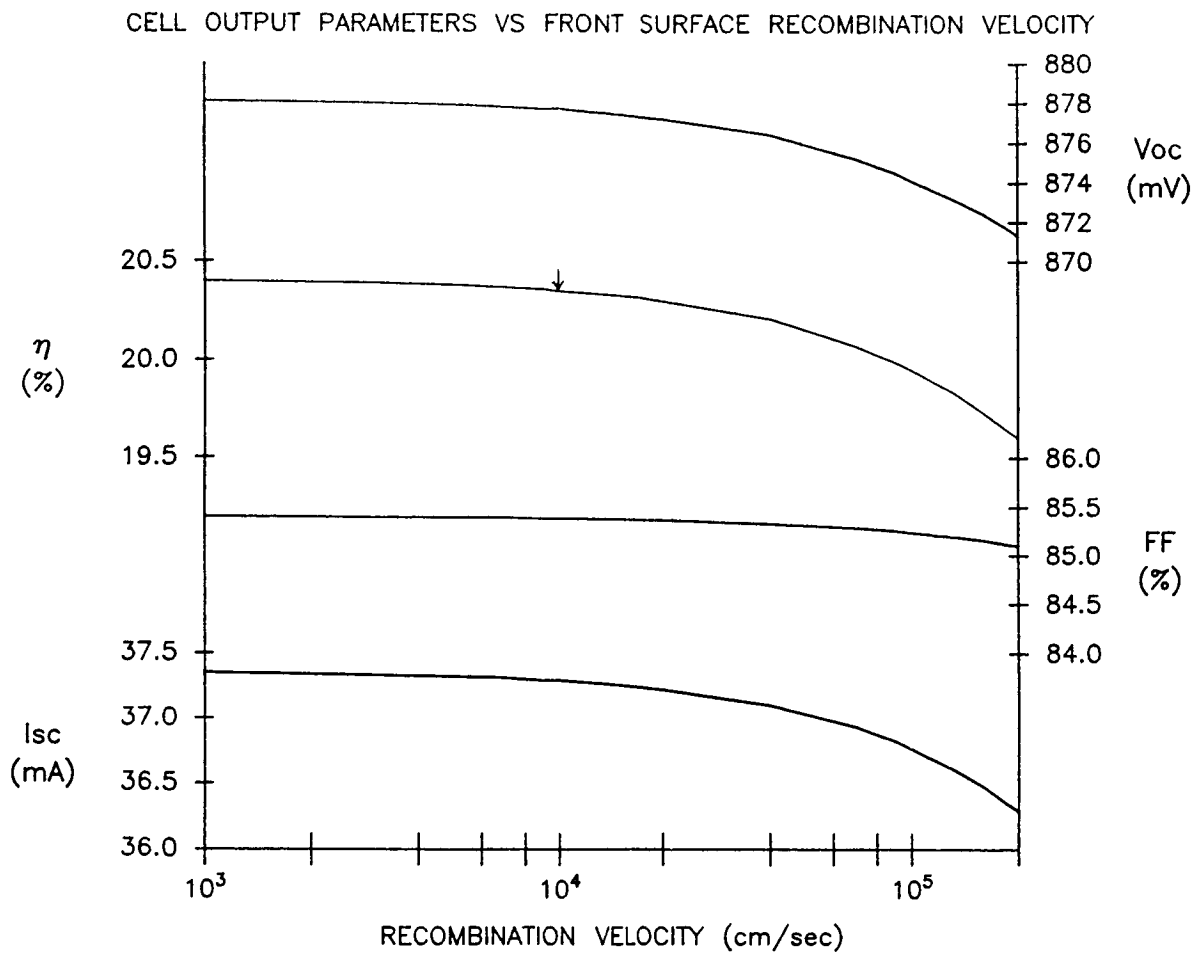
CELL OUTPUT PARAMETERS VS FRONT SURFACE RECOMBINATION VELOCITY
880
878
876
874
872
870
Voc
(mV)
20.5
η
(%)
20.0
19.5
86.0
85.5
85.0
84.5
84.0
FF
(%)
37.5
37.0
Isc
(mA)
36.5
36.0
10³
10⁴
10⁵
RECOMBINATION VELOCITY (cm/sec)

Figure 3

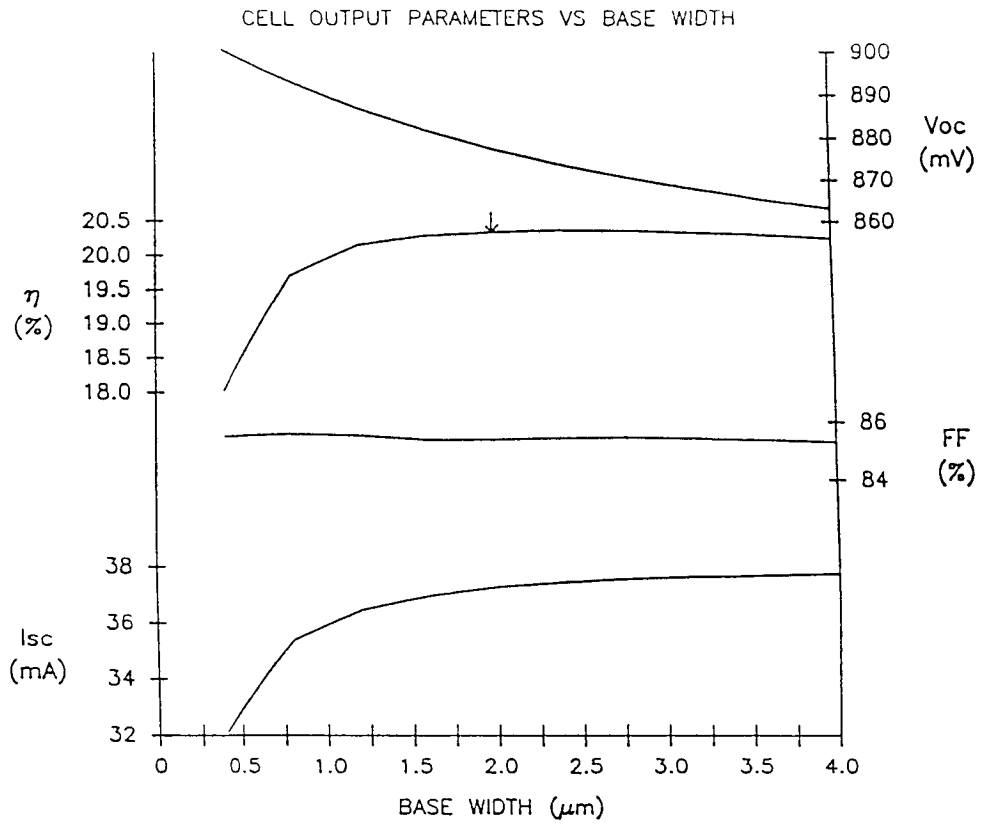

Figure 4

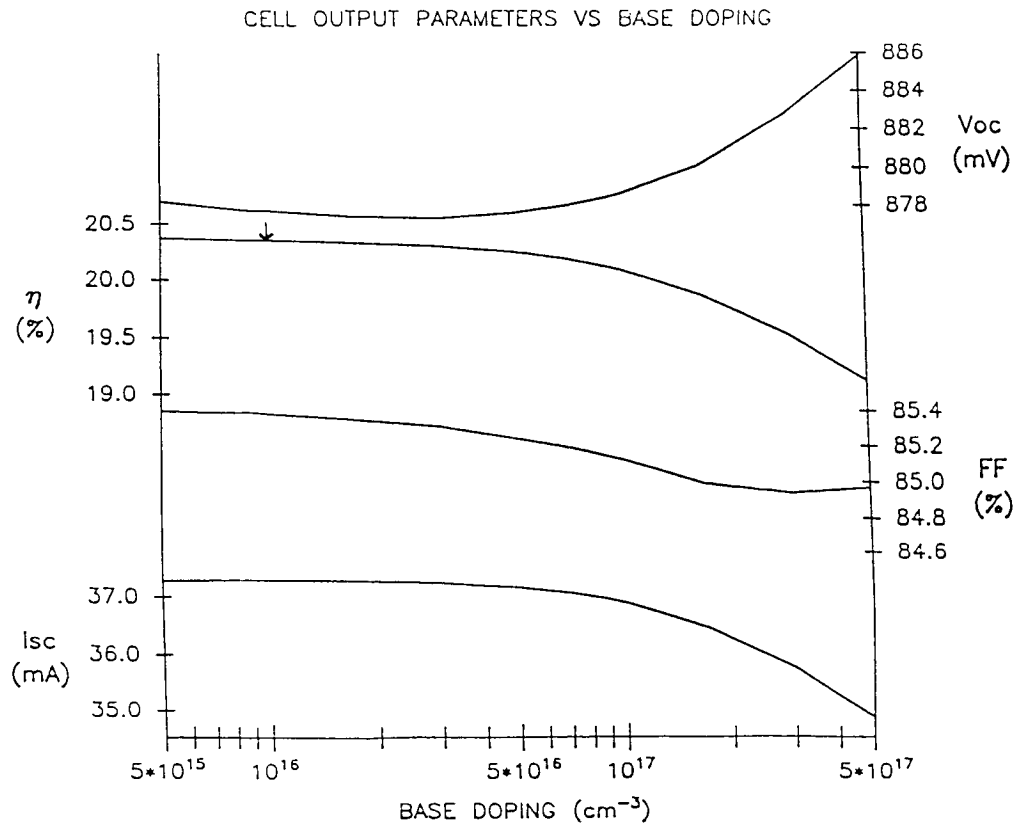

Figure 5

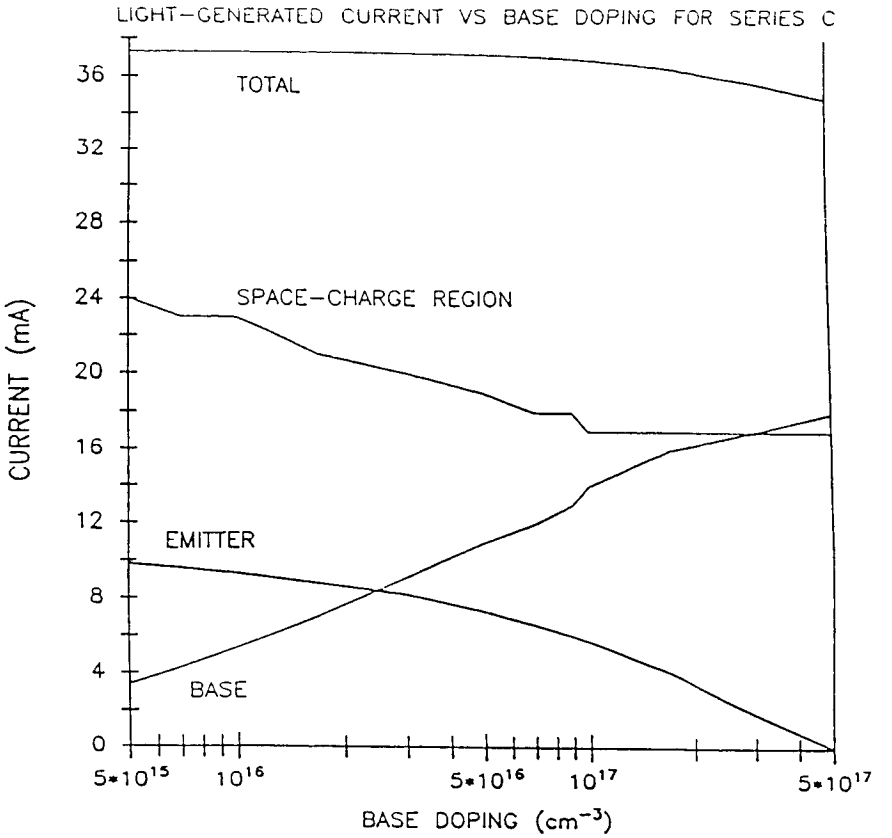

Figure 6

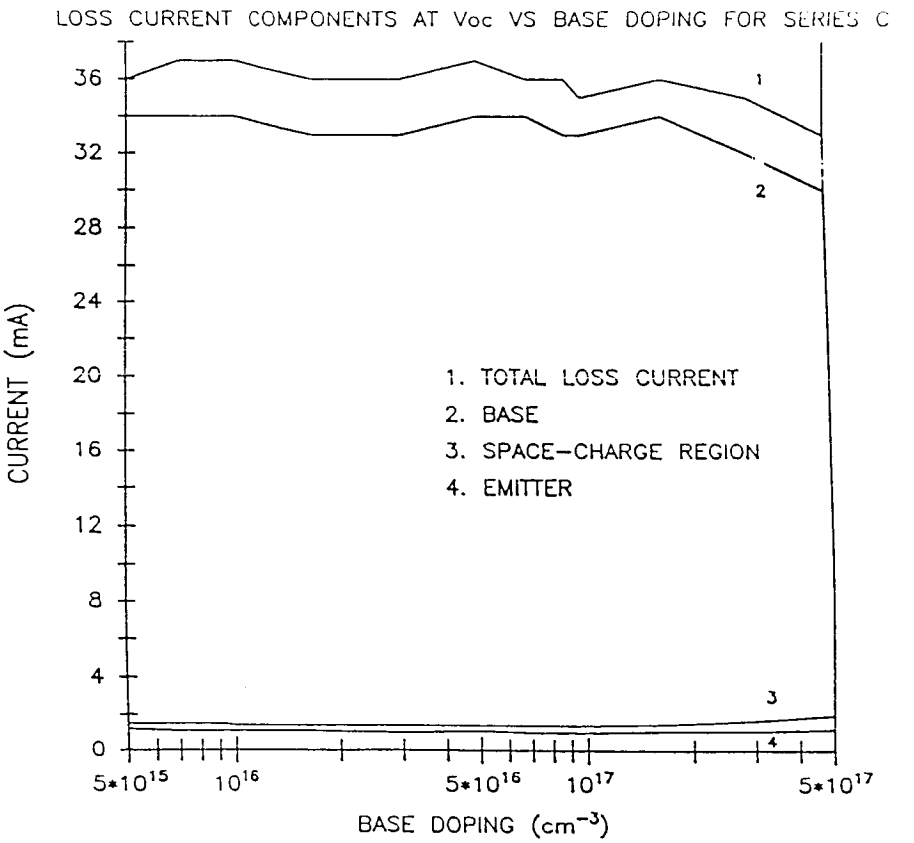

Figure 7

SOLAR CELLS IN BULK InP USING AN OPEN TUBE DIFFUSION PROCESS*

K.K. Parat, S. Bothra, J.M. Borrego and S.K. Ghandhi
Rensselaer Polytechnic Institute
Troy, New York

This paper describes a simple open tube diffusion technique for the fabrication of N+P junction solar cells. Large area (>0.25 cm^2) solar cells have been made by this process with a photovoltaic conversion efficiency of 15.2% under simulated AMO illumination. An ideality factor is 1.04 and a saturation current density of 9.6 x 10^{-16} A/cm^2 have been observed for these cells. These are the lowest (best) values reported to date for diffussed structures in bulk InP.

INTRODUCTION

At the present time there is large interest in the use of indium phosphide on solar cells for space applications. Besides being a direct band gap material with an energy gap of 1.34eV which is close to the one required for maximum efficiency under AMI illumination, it offers the possibility of low surface recombination velocity if properly passivated (ref. 1) and it has shown less degradation to gamma ray radiation than Si or GaAs cells of comparable junction depths (ref. 2).

InP solar cells previous reported had been fabricated by either epitaxial growth or by thermal diffusion in a closed box system (ref. 3, 4). In this paper we describe the fabrication and photovoltaic characteristics of n+p InP solar cells using a simple open tube diffusion process. Advantages of this technique are its case of implementation and potential for low cost.

DEVICE FABRICATION

The p-type InP substrates used for the fabrication were pre-polished LEC grown** 2" diameter wafers (100) misorientated 2° towards (110) and doped with Zn to a concentration of 5-6 x 10^{16} cm^{-3}. After degreasing the slices were etched in order to remove any residual poslishing damage. Before loading in the evaporator, the wafers were etched in 10% H_3PO_4 to remove any surface damage. A gallium sulphide (99.99% purity) film was evaporated onto the frontside which was used as the source for sulphur doping. To prevent degradation of the InP surface during diffusion the InP substrate was coated on top and back with a 0.5 um thick film of SiO_2. The silicon dioxide film was deposited on the wafer in a CVD reactor by the pyrolysis of silane and oxygen in an argon ambient. During the SiO_2 deposition the samples were held at 325°C. The sulphur diffusions were carried out for 20 to 60 minutes at 700°C in an open tube furnace with nitrogen gas flowing in order to prevent back diffusion of air. After diffusion the SiO_2 and Ga_2S_3 films were removed and a back ohmic contact

* Work performed under NASA-Lewis Grant No. NAG-3-604.
**Crystacom Inc., Mountain View, CA 94043.

made by evaporating a film of Au - 5% Zn and alloying it at 420°C in forming gas. The non-optimized top metallic grid was defined photolithographically and electroplated Au was used as the contact metal for the top n+ layer. The active area of the cell was delineated by a second photolithography step and it was mesa etched using a solution of iodic acid. The total area of the cell was 0.313 cm^2 which after substracting the area of the top metallic grid gives 0.265 as the active area of the cell. Since the refractive index of InP is approximately 3.5, the optimum values of the refractive index of a single layer AR coating is 1.9 which makes SiO a suitable choice for this purpose. An SiO layer of approximately 750 Å was evaporated over the whole cell to serve as an AR coating. No attempts were made to passivate the top n+ surface of the cell. A schematic diagram of the cell structure is shown in Fig. 1.

ELECTRICAL AND PHOTOVOLTAIC CHARACTERISTICS

Electrical characterization of the finished cells involved measurement of their photovoltaic performance of large area cells, their quantum efficiency as a function of wavelength and ln I vs V. Small area diodes were used for diagnostic purposes specially for determining the doping concentrations and doping profile in the vicinity of the junction. The photovoltaic performance of the large area solar cells was measured under simulated AM1 conditions in our laboratory and under simulated AM0 at NASA* and it is summarized in Table I using the active area of the cell. The short circuit is larger under AM0 conditions than under AM1 illumination but the fill factor and efficiency remain the same. Figure 2 shows the ln I vs V characteristics of a large area cell. For low forward biases the forward characteristics are determined by recombination in the depletion layer. At larger currents the ln I vs V characteristics are linear and show an ideality factor of n = 1.04 and saturation current density of $J_o = 9.6 \times 10^{-16}$ A/cm^2. The very low value of the saturation current density is responsible for the high open circuit voltage observed. The value of the ideality factor close to 1 indicates that the forward current characteristics are dominated by recombination in the neutral regions and not in the depletion layer of the junction which indicates a clean junction. The high value of the fill factor is a consequence of the ideality factor being close to 1 and that the top n+ layer is heavily doped so the series resistance is low even for the shallow junction used

Figure 3 shows the external quantum efficiency as a function of wavelength for typical AR and a non-AR coated cell. For the non-AR coated cell the quantum efficiency remains essentially constant for 500 nm to 850 nm where the efficiency drops very sharply and it is essentially zero at 920 nm which corresponds to the energy gap of InP.

The external quantum efficiency of the AR coated cell shows that the efficiency improves between 550 nm and 900 nm. This increase in efficiency is responsible for an increase of 37% in the short circuit current between AR coated and non-AR coated cells.

* The AM0 measurements were performed by Dr. I. Weinberg of NASA Lewis Research Center, Cleveland, Ohio.

COMPUTER SIMULATION

In our measurements the internal quantum efficiency η int was obtained from the measured external quantum efficiency η ext through the equation:

$$\eta \text{ int} = \eta \text{ ext}/(1-R) \quad (1)$$

where R is the reflection coefficient. This internal quantum efficiency was compared to a computer simulation in order to determine important cell parameters. The internal quantum efficiency at short wavelengths is determined mainly by the junction depth and the top surface recombination velocity. The hole diffusion length in the top n+ layer does not appear to affect the quantum efficiency as long as the diffusion length is longer than the junction depth. At long wavelengths the internal quantum efficiency depends upon the depletion layer width and the electron diffusion length in the p-region.

Figure 4 shows the comparison between a computer simulation and the measured internal quantum efficiency of one of the non AR coated cells. The same figure shows that the values of the parameters for a good match were junction depth of 0.06 μm top surface recombination velocity of 2×10^6 cm/sec, depletion layer width of 0.26 μm and electron diffusion length of 2.5 μm. Of the above parameters the depletion layer width was determined by measuring the depletion layer capacitance of small area diodes.

CONCLUSION

We have demonstrated an open tube diffusion technique for fabricating high efficiency n+p InP solar cells. Detailed evaluation of the electrical and photovoltaic characteristics of the cells shows that the fabrication techniques used give a clean junction with an ideality factor close to 1 and a very low value of the saturation current density. Comparison of the measured and simulated spectral response as a function of wavelength allowed the determination of important device and material parameters.

REFERENCES

1. H.C. Casey, Jr; and E. Buehler: Evidence for Low Surface Recombination on n-type InP. App. Phys. Lett. Vol. 30, No. 5, March 1977, pp 247-249.

2. A. Yamamoto; M. Yamaguchi; and C. Uemura: High Conversion Efficiency and High Radiation Resistance InP Homojunction Solar Cells. App. Phys. Lett. Vol. 44, No. 6, March 1984, pp. 611-613.

3. C.C. Shen; and K.Y. Choi: High Conversion Efficiency p-n+ InP Homojunction Solar Cells. Electron Devices Lett. Vol, EDL-6, No. 2, February 1985, pp. 78-80.

4. A. Yamamoto; M. Yamaguchi; and C. Vemura: Frabrication of High Efficiency n+-p Junction InP Solar Cells by Using Group V16 Element Diffusion into p-type InP, IEEE Trans. on Elec. Dev. Vol. ED-32, No. 12, December 1985, pp. 2780-2786.

TABLE I

Photovoltaic Performance of Bulk n+p InP Cells.

	J_{sc} (mA/cm^2)	V_{oc} V	FF -	Eff. (%)
AM - 1	24.7	0.800	0.815	16.3
AM-0 (NASA)	31.01	0.815	0.826	15.2

DEVICE STRUCTURE

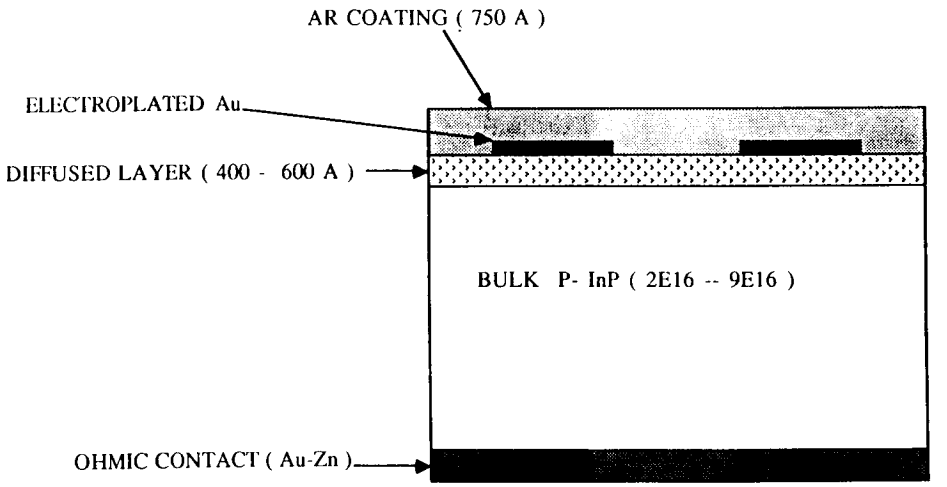

* MESA ETCH DEFINED * DEVICE AREA 0.313 CM^2

Fig. 1 - Schematic Diagram of Solar Cell Structure

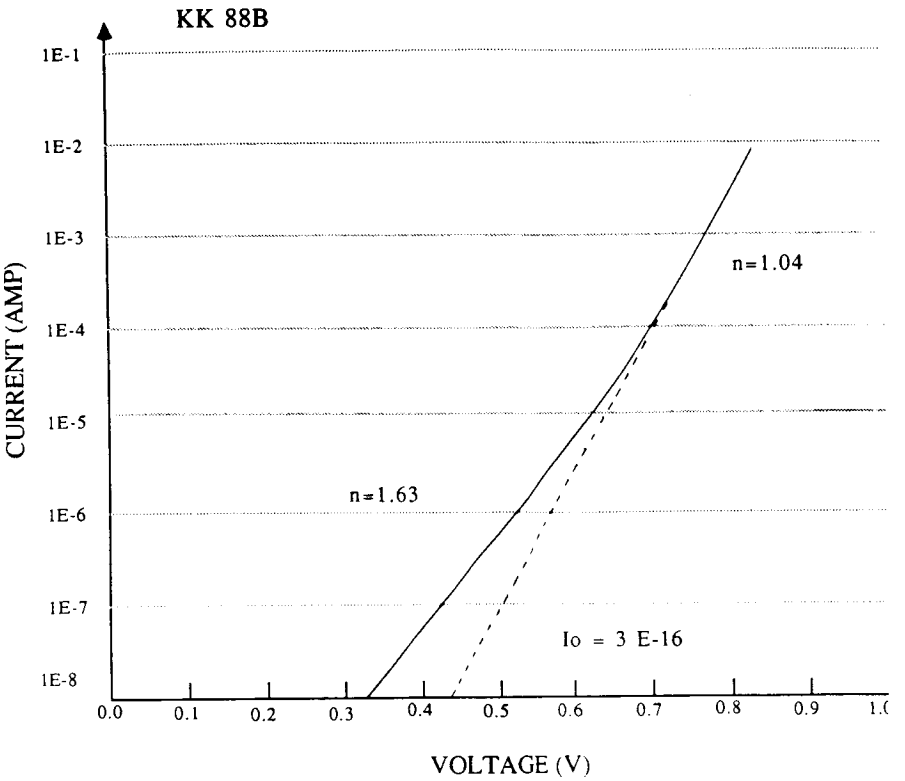

AREA = 0.313 cm^2

Jo = 9.58 E-16 A /cm^2

Fig. 2 - lnI vs V characteristics of large area solar cell

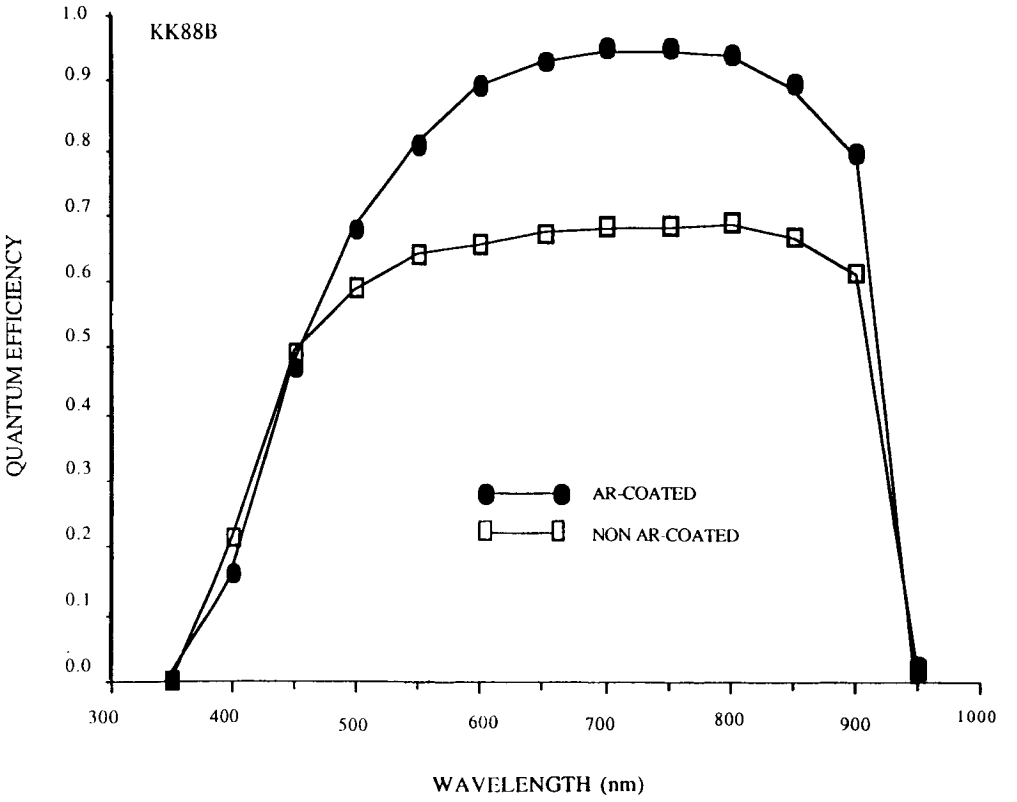

Fig. 3 - Quantum efficiency as a function of wavelength for n+p InP cells.

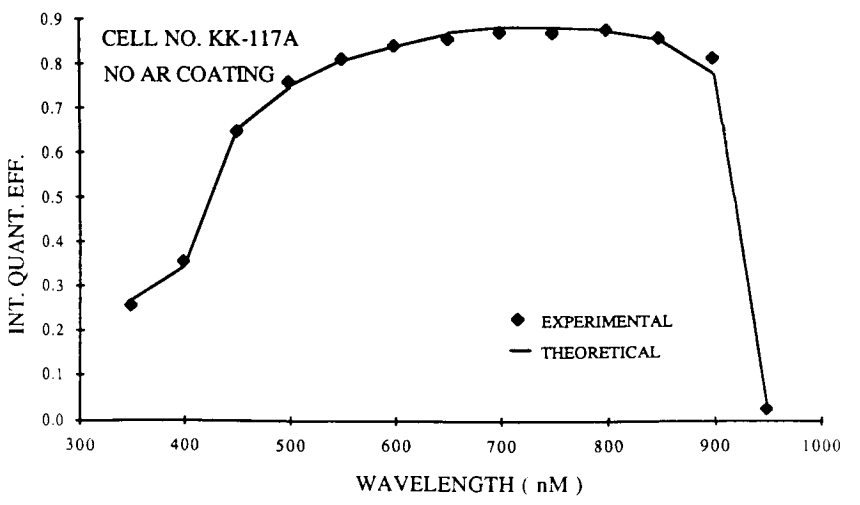

Fig. 4 - Comparison between measured and simulated internal quantum efficency for a non AR coated InP cell.

P/N InP HOMOJUNCTION SOLAR CELLS BY LPE AND MOCVD TECHNIQUES*

K.Y. Choi and C.C. Shen
Arizona State University
Tempe, Arizona
and
B.I. Miller
AT & T Bell Laboratories
Princeton, New Jersey

P/N InP homojunction solar cells have been prepared by using both Liquid Phase Epitaxy (LPE) and Metalorganic Chemical Vapor Deposition (MOCVD) growth techniques. A heavily doped p-$In_{0.53}Ga_{0.47}As$ contacting layer was incorporated in the cell structure to improve the fill factor and to eliminate surface spiking at the front surface. The best conversion efficiencies (total area) obtained under AM 1 illumination are 14.2% for a LPE cell and 15.4% for a MOCVD cell.

INTRODUCTION

Indium phosphide (InP) has recently emerged as an attractive solar cell material for space application, owing to the high conversion efficiencies (ref. 1) and radiation resistance (ref. 2) which were demonstrated in the past few years.

Most of the InP homojunction solar cells reported so far consist of a shallow homojunction. In order to obtain low contact resistance as well as low sheet resistance, the top layer was usually doped heavily; as a result, the minority-carrier diffusion length in this region is very short. To maximize the short-circuit current, the top layer has to be made very thin; however, the reverse saturation current and the diode's ideality factor of InP homojunction solar cells were observed to increase markedly when the p-n junction depth is less than 0.15 μm (ref. 3). Also, the surface spiking at the surface layer of shallow junction solar cells can sometimes cause the deterioration of diode characteristics (ref. 4). To circumvent these problems associated with shallow homojunction cells, we have modified the conventional InP homojunction solar cells by adding an additional contacting $In_{0.53}Ga_{0.47}As$ layer between the front grid contact and the thin top InP layer (This is an extension of our previous work (ref. 5), in which an InGaAsP layer was used as contacting layer). The advantages of this extra InGaAs contacting layer are twofold: firstly, the bandgap of $In_{0.53}Ga_{0.47}As$ (0.75 eV) is much smaller than that of InP (1.35 eV) at room temperature, so

*The work at Arizona State Univ. is supported by NASA Lewis Research Center.

it can be doped more heavily to facilitate the contacting processes. Secondly, the front grid contact is now in direct contact with the InGaAs layer instead of the InP surface layer, thus it eliminates possible surface spiking problems. In the following sections, we present the experimental details of the fabrication and characterization of this type of P/N InP homojunction solar cell prepared by LPE and MOCVD techniques.

EPITAXIAL GROWTH AND CELL FABRICATION

A schematic diagram of the cross section of a mesa-type P/N InP homojunction solar cell is shown in Figure 1. The cell contains an InP p-n junction and an InGaAs contacting layer. To eliminate optical absorption in the InGaAs layer, major portion of the InGaAs layer, which was not covered by the front grid contact, was etched away chemically. The two InP layers and the InGaAs layer were grown successively on a (100) oriented, n^+-InP single crystal substrate with a typical carrier concentration of 2×10^{18} cm^{-3} by either LPE or MOCVD growth techniques.

The LPE growth was performed using a conventional horizontal LPE system. Three epitaxial layers were grown successively on a n^+-InP substrate. An undoped n-type InP layer about 3 to 5 μm thick was grown first on the substrate, which was followed by a p-InP layer and a p^+-InGaAs layer. Zinc was used as p-type dopants for the second and the third epitaxial layers. For the samples we have prepared so far, the two p-type layers have typical thickness values of 0.5 μm. The LPE layers were grown by a supercooling growth technique with a cooling rate of 1°C/min. The growth temperature ranged from 650°C to 620°C. To suppress surface dissociation at the InP substrate surface, the substrate was covered by an InP cover piece during the saturation period, prior to the growth cycle.

The MOCVD wafer was grown in a horizontal atmospheric MOCVD system featuring a fast switching run-vent manifold, allowing for very abrupt interfaces. Trimethylindium (TMI) and trimethylgallium (TMG) were used as group III sources while pure arsine and phosphine were used as group V sources. Hydrogen sulfide (H_2S) and triethylzinc (TEZ) were used as n- and p-type dopant sources respectively. The growth temperature was around 625°C with a growth rate of 5 Å/sec for InP and a growth rate of 10 Å/sec for InGaAs. The background concentrations were about 5×10^{15} cm^{-3} for InP layers and 2×10^{15} cm^{-3} for InGaAs layers.

The layer thicknesses and p-n junction locations for several grown wafers were determined by using a scanning electron microscope. Figure 2 shows the electron-beam induced current (EBIC) signals superimposed on the secondary emission images for the cleaved and stained cross sections of a LPE sample (Fig. 2a) and a MOCVD sample (Fig. 2b). The gentle slopes of the EBIC signals in the lightly doped InP layers indicate that the minority carrier diffusion lengths in this region, which are estimated to be several microns long for both samples, are much longer than the minority carrier diffusion lengths in other layers as expected. The typical carrier

concentrations of the grown layers for the LPE samples are 3.5×10^{18} cm^{-3}, 4.0×10^{17} cm^{-3}, and 4.0×10^{16} cm^{-3} for p^+-InGaAs, p-InP, and n-InP layers, respectively; while those for the MOCVD samples are 10^{18} cm^{-3}, 10^{18} cm^{-3}, and 10^{16} cm^{-3} for p^+-InGaAs, p-InP, and n-InP layers, rspectively.

The ohmic contacts to the backside were obtained by thermal evaporation of Au/Sn alloy onto the entire substrate, while the front grid contacts were achieved by first evaporating Au/Zn alloy onto the front surface which was previously coated with photoresist and patterned by conventional photolithographic techniques. A subsequent lift-off process completed the deposition of the front contact. The cells were subsequently annealed at 250°C for 1 minute in a flowing nitrogen atmosphere. The contact grids are 50 μm wide and the spacings between the grid lines are 450 μm. The front contact for these cells covers about 12.5 percent of the whole surface. The cell area was defined photolithographically and the cells were made into mesa-type devices by etching the edges of the cells with 1N $K_2Cr_2O_7$: HBr : CH_3COOH (1 : 1 : 1 by volume). The surface area of InGaAs layer, which was not covered by the grid contact, was later removed by selective etching. The frontside of the cells were then covered with 650 A vacuum-deposited Sb_2O_3 as an antireflection (AR) coating. The photograph of the frontside of a completed cell processed from a MOCVD sample is shown in Figure 3. The total cell area for the MOCVD cells is 25 mm^2 while that for the LPE cells, which is 4 mm^2, is somewhat smaller.

DEVICE CHARACTERIZATION

The dark current density - voltage (J-V) characteristics under forward bias for two solar cells prepared by both LPE and MOCVD are shown in Figure 4. The diode's ideality factors are about 1.7 for both cells. The reverse saturation current densities are 3.97×10^{-11} A/cm^2 for the LPE cell and 1.67×10^{-11} A/cm^2 for the MOCVD cell.

The completed cells were tested under simulated sunlight using ELH lamp as light sources. The incident power density was adjusted to 100 mW/cm^2 using a calibrated silicon solar cell. The photovoltaic characteristics of six InP homojunction solar cells prepared from one LPE wafer are summarized in Table I. The average values for V_{oc}, J_{sc}, and FF are 0.812 volt, 25.0 mA/cm^2, and 0.63, respectively. In Table II, we list the photovoltaic characteristics of InP homojunction solar cells processed from one MOCVD wafer. The average values for V_{oc}, J_{sc}, and FF are 0.840 volt, 22.5 mA/cm^2, and 0.72, respectively. The highest conversion efficiencies (total area) achieved are 14.2% for a LPE cell and 15.4% for a MOCVD cell. Figure 5 shows the J-V characteristics under illumination of the best LPE cell and the best MOCVD cell.

The spectral responses for these cells were characterized by using a grating monochromator equipped with a calibrated tungsten light source. The spectral responses of a representative LPE cell and a representative MOCVD cell with and without AR coating are shown in Figure 6. For those uncoated

cells, the spectral response curves exhibit a peak at 0.9 μm, and then drop gradually as the wavelength decreases. The spectral response curves of those coated cells exhibit a flat zone for photon wavelengths between 0.6 and 0.9 μm, and drop off for wavelengths less than 0.6 μm. The overall efficiencies for our cells were improved more than 30% with the aid of an AR coating.

DISCUSSION AND CONCLUSION

Although the open-circuit voltages for our cells are excellent, the short-circuit current values are less than satisfactory. We believe that short-circuit current can be improved by optimizing the cell parameters such as layer thicknesses and doping levels of the epitaxial layers. A larger fill factor can also be expected by increasing the doping level of the InGaAs layer. We have observed very good yield for cells processed from grown wafers prepared by both LPE and MOCVD techniques. However, solar cells processed from MOCVD wafers exhibit better yield and uniformity regarding overall device performance. The preliminary experimental results we obtained from these modified P/N InP homojunction solar cells are encouraging. Such a structure can be easily extented to N/P InP homojunction solar cells. The technical advantages it offers may make it more suitable for large-scale production than the conventional shallow homojunction InP solar cells.

REFERENCES

1. Itoh, Y.; Yamaguchi, M.; and Uemura, C.: 17.2-Percent Efficient (AMO) p^+-i-n InP Homojunction Solar Cells. IEEE Electron Device Lett., vol. EDL-7, no. 2, Feb. 1986, pp. 127-128.

2. Yamamoto, A.; Yamaguchi, M.; and Uemura, C.: High Conversion Efficiency and High Radiation Resistance InP Homojunction Solar Cells. Appl. Phys. Lett., vol. 44, no. 6, Mar. 1984, pp. 611-613.

3. Sugo, M.; Yamamoto, A.; Yamaguchi, M.; and Uemura, C.: High-Efficiency InP Solar Cells with n^+-p-p^+ Structure Grown by Metalorganic Chemical Vapor Deposition. Jpn. J. Appl. Phys., vol. 24, no. 9, Sept. 1985, pp. 1243-1244.

4. Schroder, D. K.; and Meier, D. L.: Solar Cell Contact Resistance—A Review. IEEE Trans. Electron Devices, vol. ED-31, no. 5, May 1984, pp. 637-647.

5. Shen, C. C.; and Choi, K. Y.: High Conversion Efficiency p-n^+ InP Homojunction Solar Cells. IEEE Electron Device Lett., vol. EDL-6, no. 2, Feb. 1985, pp. 78-80.

Table I. Photovoltaic characteristics for InP homojunction solar cells prepared by LPE (AM1, 100 mW/cm^2 at 27°C).

Cell no.	V_{oc} (V)	J_{sc} (mA/cm^2)	FF (%)	Efficiency (%)
1	0.817	25.4	68.0	14.1
2	0.818	25.1	59.2	12.1
3	0.817	24.1	60.5	11.9
4	0.815	25.5	68.2	14.2
5	0.805	24.6	61.9	12.3
6	0.800	24.9	62.1	12.4

Table II. Photovoltaic characteristics for InP homojunction solar cells prepared by MOCVD (AM1, 100 mW/cm^2 at 27°C).

Cell no.	V_{oc} (V)	J_{sc} (mA/cm^2)	FF (%)	Efficiency (%)
1	0.832	21.9	70.4	12.9
2	0.840	21.6	77.9	14.1
3	0.845	22.6	69.4	13.3
4	0.849	22.7	79.7	15.4
5	0.840	22.8	76.5	14.7
6	0.844	22.2	76.6	14.4
7	0.837	22.7	68.9	13.1
8	0.840	23.8	63.8	12.8
9	0.832	23.0	72.0	13.8
10	0.839	21.7	66.8	12.1

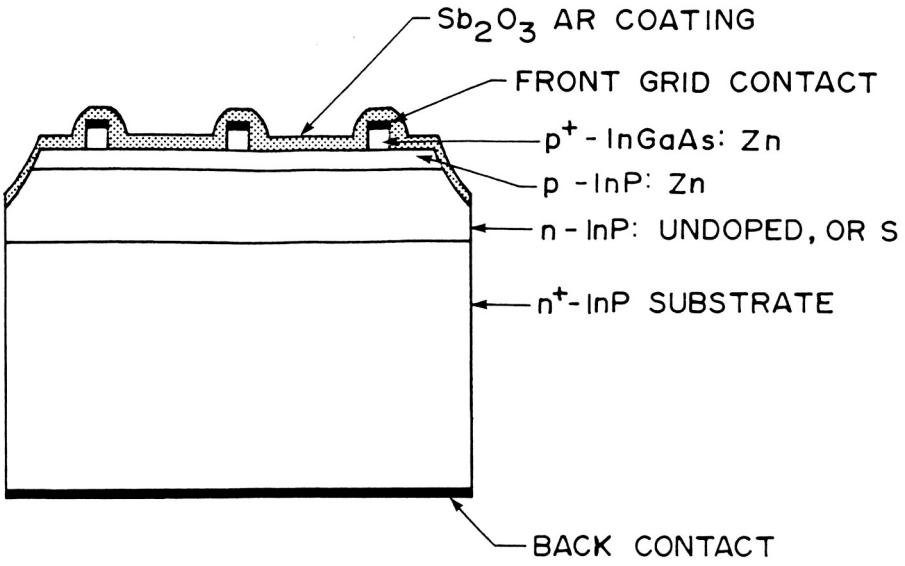

Figure 1. Schematic diagram of the cross section of a P/N InP homojunction solar cell.

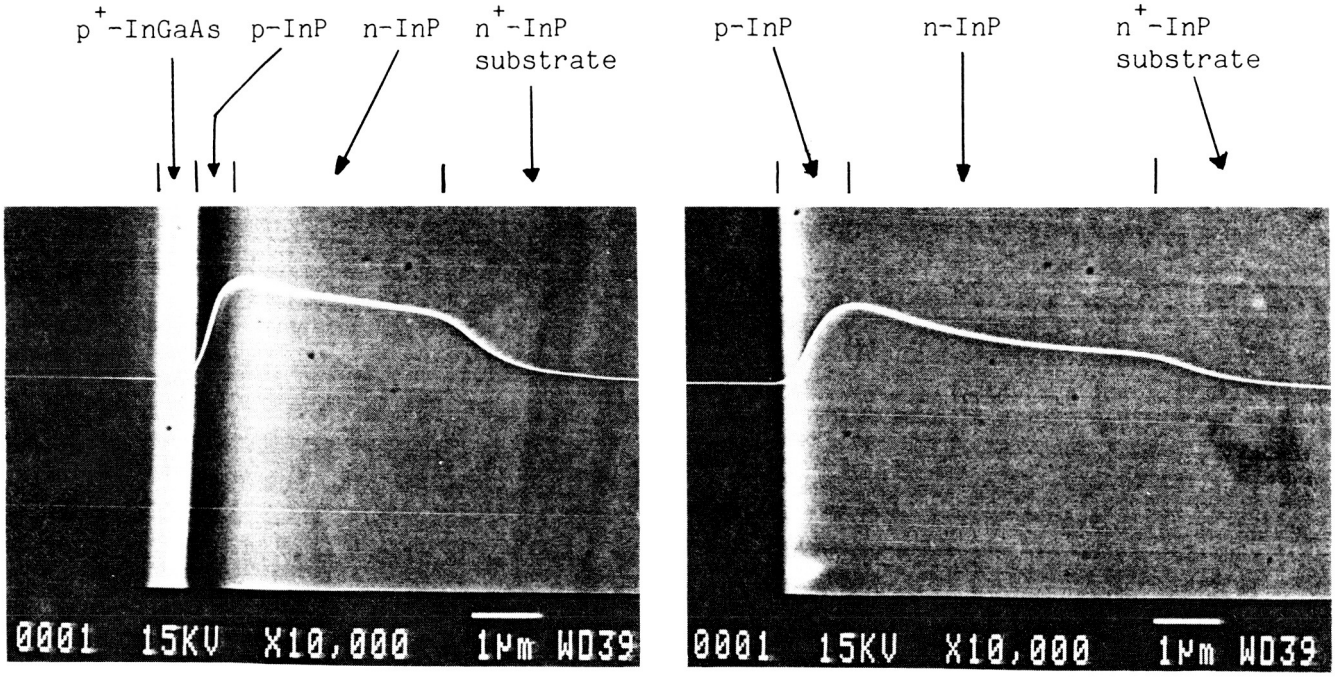

Figure 2. Secondary emission and EBIC images of the cross sections of two P/N InP solar cells prepared by (a) LPE and (b) MOCVD.

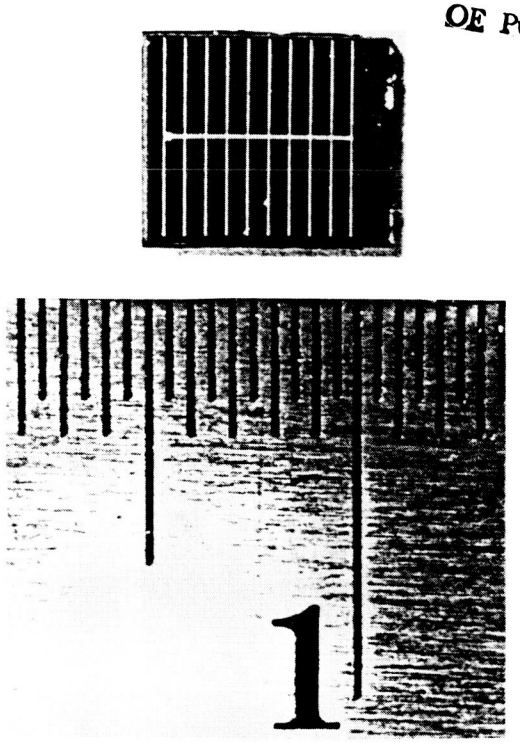

Figure 3. Photograph of the front side of a completed P/N InP homojunction solar cell.

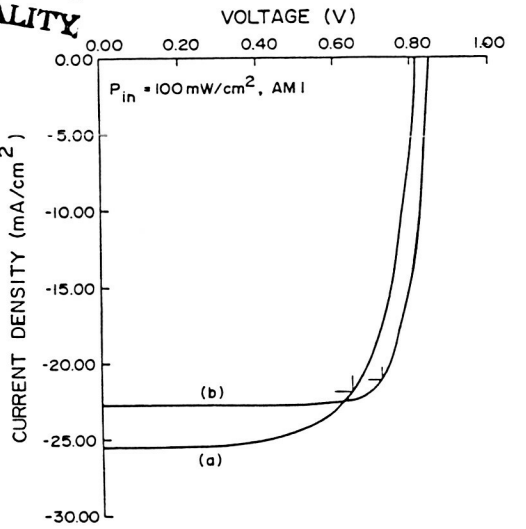

Figure 5. Current density versus voltage plot for two P/N InP homojunction solar cells prepared by (a) LPE and (b) MOCVD under AM 1 illumination. The conversion efficiencies for cells (a) and (b) are 14.2% and 15.4%, respectively.

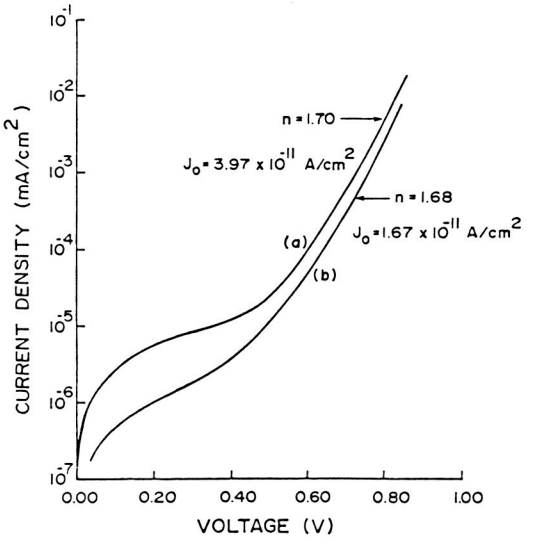

Figure 4. Dark current density versus voltage plot under forward bias for two P/N InP homojunction solar cells prepared by (a) LPE and (b) MOCVD.

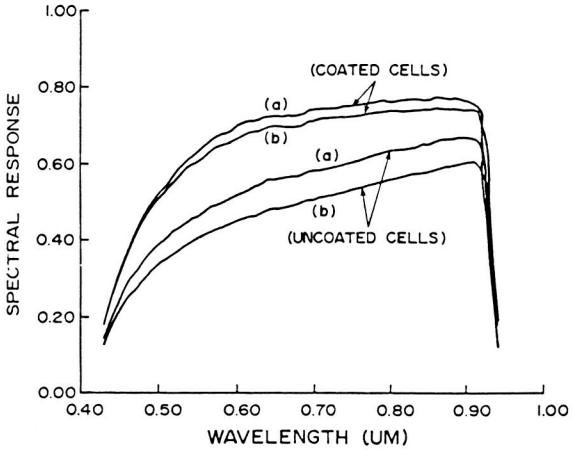

Figure 6. Spectral responses of two typical P/N InP homojunction solar cells prepared by (a) LPE and (b) MOCVD with and without AR coating.

AN OVERVIEW OF THE DOE TERRESTRIAL CRYSTALLINE SOLAR CELL RESEARCH PROGRAM *

James M. Gee and Dan E. Arivizu
Sandia National Laboratories
Albuquerque, NM

There has been significant progress in the crystalline solar cell area in the past two years that has rejuvenated interest in high efficiency devices for terrestrial photovoltaic systems. The most significant developments have been in the crystalline silicon cell area but progress in the III-V area has also been recorded. A review of terrestrial crystalline cell research is presented along with a description of future research directions.

INTRODUCTION

Photovoltaic systems are an attractive technology for electric power generation. The United States Department of Energy (DOE) has been pursuing PV research for over a decade with the long term goal of lowering the cost of PV systems such that they can be a cost effective option for utility applications. In order to position PV for a utility market, it will be necessary to reduce the cost of a PV system by a factor of 4 to 6 from current systems (1). In order to meet these long term goals, DOE is investigating two approaches for a cost effective PV device. In the first approach, thin films of amorphous or semicrystalline semiconductors which can be fabricated with low cost deposition techniques are used. This technology features low material costs; material costs are currently the most expensive component in PV commercial flat-plate modules. The DOE effort in thin films is managed by the Solar Energy Research Institute (SERI). Industry has become interested in the thin film approach recently and is making substantial investments in this new technology. While the cost of the materials are low and the initial progress is very promising, a significant challenge remains to improve the performance of thin film cells to levels appropriate for utility applications (>15%).

The second approach pursued by DOE is investigation of crystalline cells. These cells are composed of high quality materials and are capable of very high efficiencies. There is a very large technological base for development of crystalline cells. The concern with crystalline cells has always been

*This work was supported by the U.S. Department of Energy at Sandia National Laboratories under Contract DE-AC04-76DP00789.

material costs. However, with concentrator collectors or with advanced sheet growth processes, the material cost issue may be circumvented while the performance advantage of crystalline cells is retained. Most of the DOE crystalline cell research has been recently consolidated at Sandia National Laboratories, including the research on crystalline silicon one-sun and concentrator cells and advanced materials concentrator cells. This paper will briefly review the present status of terrestrial crystalline cell research and give an outline of future research directions.

SILICON CELLS

Silicon cells have received the bulk of the research effort among crystalline cells. In order to improve the cost effectiveness of crystalline silicon cells, it will be necessary to reduce the material and processing costs and to improve the cell performance. Past work that was managed by the Jet Propulsion Laboratory emphasized reducing the material and processing costs through source material and advanced crystal growth research and through research into low cost processing techniques (metallizations, boule wafering, etc.). An excellent review of this work can be found in reference 2. Future work in this area will emphasize fundamental studies of advanced silicon crystal growth processes and characterization and control of defects. This work can later be can later be transferred to industry. The silicon materials research will probably involve more university participation and fewer large engineering development efforts. In an era of reduced budgets, it is felt that this approach will have the greatest impact on achieving program goals.

A novel approach to improving the cost effectiveness of current one-sun crystalline silicon cell technology has been recently developed by ENTECH, which manufactures concentrator modules. ENTECH has developed a prismatic coverglass which effectively removes the grid obscuration (6). With the larger current densities produced under concentrated illumination, concentrator cells have typically featured relatively expensive metallizations with a narrow linewidth, high aspect ratio, and low contact resistance. With the greater grid coverage that is possible with the prismatic coverglass, it becomes possible to use the low cost metallizations typical of one-sun cell technology for a low concentration module. An installed system cost near $6/Wp has been estimated for a small utility scale application (300 kW) with a 20X module, one-sun cells, and the prismatic coverglass (6). Figure 2 presents results for a polycrystalline silicon cell fabricated by Solarex with and without the coverglass. The grid obscuration in this case was 20%. It is evident from the results presented in Figure 2 that the coverglass was effective in eliminating the grid obscuration.

The second approach to cost effectivenss of crystalline silicon cells is to increase the efficiency of both one-sun and concentrator cells. Modelling at both Stanford and Purdue have indicated that efficiencies in excess of 30% are possible with thin, high resistivity silicon concentrator cells (3,4). These cell designs were thought to require long minority carrier life-

times that are only available in expensive float zone material. Recent modelling at Iowa State University indicates that high efficiencies should also be possible with minority carrier lifetimes typical of Czochralski or polycrystalline material if sufficient light trapping and surface passivation schemes are employed (5). These same calculations project efficiencies around 25% at one-sun (Figure 1). A common feature in all these modelling results is that the high efficiency silicon cells will need to be very thin and will use high resistivity material.

Progress in experimental high efficiency silicon devices has been very encouraging recently. Researchers at the University of New South Wales (UNSW) under Sandia sponsorship have recently fabricated low resistivity 0.1 and 0.2 ohm-cm silicon concentrator cells that achieved 24.7% at 50X to 100X (7). (All measurements reported in this paper were made under an AM1.5 spectrum, with the irradiance at one-sun (1X) equal to 100 mW/cm^2.) Two improvements have been incorporated into these cells. The first improvement is the use of a passivated surface with reduced contact area in order to minimize recombination at the surface of the cell. The second improvement has been optimization of the optical properties of the front surface in order to minimize reflectance from both the active area and the grid lines. The surface has been anisotropically etched to form microgrooves that reduce the surface reflectance. The grid lines are defined at approximately a 45 degree angle with respect to the grooves so that light specularly reflected from the grids can be absorbed at the adjacent surface of the groove. The improved front surface design is illustrated in Figure 3 along with cell performance data. This cell uses essentially the same structure as commercial silicon concentrator cells (contacts on both the front and back surfaces with the back surface fully metallized) and could be incorporated into concentrator modules relatively easily. Using a similar approach for one-sun silicon cells, the researchers at UNSW have also achieved an efficiency of 21% and 19% at one-sun for cells fabricated in float-zone silicon and in solar-grade Czochralski silicon (8).

In another remarkable achievement, researchers at Stanford University have achieved 27.7% at 100X and 22.2% at one-sun with an unconventional cell structure (8). The new cell structure (see Figure 4) starts with a high-resistivity float zone silicon substrate. The substrate is first chemically etched to the desired thickness of about 100 microns. Both the n- and p-type diffusions are then made on the back surface. The area of the diffusions and of the metal/silicon contact area is minimized in order to reduce the recombination associated with the heavily doped regions and with the contacts. It is also very important to incorporate light trapping in order to maximize absorption of light in the thin silicon cell and to passivate the surfaces in order to minimize surface recombination. The high efficiency is due to both the high current densities (Jsc>40 mA/cm^2) and the high voltages (Voc>680 mV at 1X) achieved in this cell. The Stanford researchers project that efficiencies of 29% under concentrated sunlight are possible using the present design with reduction of the cell reflectance and grid resistance.

Figure 5 shows the progress of crystalline silicon cell efficiencies over the past 10 years. The increase in silicon cell performance has been due to both improvements in processing and improved cell designs. Future advanced silicon crystalline cells will be thin (<100 microns) and will include light trapping, passivated surfaces, and optimized emitter structures. Other areas that will also need to be addressed include heterojunction contacts to minimize contact recombination and issues regarding the module readiness (reliability, stability, mechanical mounting, etc.) of these advanced cells. Silicon cells with efficiencies in excess of 24% and 30% at one-sun and under concentration appear to be quite achievable.

ADVANCED MATERIAL CONCENTRATOR CELLS

By advanced materials, we refer to crystalline III-V compound semiconductors. These materials have been used for elecro-optical devices for over a decade due to their superior electro-optical properties compared to silicon. It is no surprise that these same qualities make these materials very effective for solar cells. The materials for these cells are significantly more expensive than for silicon cells, so that these cells can only be cost effective if their performance can be significantly increased over the projected silicon cell performance of 30% and if they can be operated at higher concentrations (>500X). Consequently, the long term goal of this task is to develop a highly efficient (>35%) multijunction (MJ) concentrator cell for operation at high concentrations (>500X).

An integral part of MJ cell development is to first develop optimized single-junction devices. The higher efficiencies of MJ cells compared to single-junction devices comes from the more efficient use of the broad solar spectrum. However, the projected high efficiencies can only be attained if the properties of each subcell in the MJ cell are nearly optimal. The latter requirement implies that the performance of a single-junction cell be well understood before an MJ cell can be optimized.

The high efficiencies that have been achieved with single-junction III-V solar cells despite the relative immaturity and modest support of this technology demonstrates the performance potential of III-V solar cells. Two years ago, Varian fabricated GaAs concentrator cells that achieved 26% at 700X (9). This cell had the highest reported efficiency of any photovoltaic device until the recent silicon cell results reported by Stanford. It should also be noted that on an active area basis, these cells are more efficient than the new silicon cells. GaAs solar cells are still the most efficient PV devices reported to date for one-sun illumination with an efficiency of 23% (10). Projections for GaAs cells also predict very high efficiencies for an optimized cell. By combining the best parameters (Voc, Jsc, and FF) observed on different GaAs cells, Fan has projected an efficiency of 26% for GaAs at one-sun (11). Similarly, the researchers at Purdue University project efficiencies near 34% for a GaAs cell operating at 500X using realistic values for the material parameters with a detailed computer modelling code (12).

Another demonstration of the high performance potential of III-V cells is the recent set of results with InGaAs concentrator cells. These cells were also fabricated by Varian and were developed as part of monolithic MJ work funded by SERI and by NASA. These InGaAs cells have a bandgap of 1.15 eV, which is close enough to silicon to allow a direct comparison of the relative merits of III-V and silicon cell technologies. The InGaAs concentrator cell achieved 24.4% at 400X despite a poor Jsc at one-sun of 31 mA/cm^2 (13). An efficiency in excess of 30% is projected for these cells if the Jsc can be improved to levels already demonstrated for silicon cells (36 to 40 mA/cm^2). The high performance of these cells was due to their high Voc, which under concentration is over 100 mV higher than the best silicon concentrator cell voltages (Figure 7).

In order to further improve single-junction GaAs and other III-V cells, it will be necessary to improve the short-circuit current density (Jsc). Unlike silicon cells, the open-circuit voltage (Voc) of III-V cells have traditionally been very good but have had a poor Jsc. For example, a compilation of reported Voc's for various III-V cells with bandgaps between 1.15 eV and 2.0 eV shows that the Voc is within 10% of the fundamental voltage limit imposed by radiative recombination (13). Some of the improvement in Jsc will come from techniques that remove some of the grid obscuration, such as the prismatic coverglass or use of a microgrooved surface. Some of the improvement of Jsc will also need to come from better material quality and device optimization since the peak internal quantum efficiency is generally below 95% and have poor response at short wavelengths (Figure 6). As was found to be very useful for silicon cell development, sophisticated models and advanced measurements are needed to help guide the device development.

The two approaches to achieving a high efficiency MJ cell are the monolithic MJ (MMJ) and the mechanically stacked MJ (MSMJ) cells. Research into MMJ cells for terrestrial applications is managed through SERI and has been reviewed at this conference in previous years (14). Sandia has been investigating MSMJ cells whose progress has been promising. A GaAs/silicon MSMJ cell was assembled at Sandia with the component GaAs and silicon cells fabricated by Varian and Applied Solar Energy Corporation, respectively. The GaAs cell had grids on the front and back surfaces in order to allow light transmission to the silicon bottom cell. The cells were not otherwise optimized for stacked cell operation. The GaAs/silicon MSMJ cell achieved 26.6% at 300X when the subcells were operated independently (Figure 8), which briefly held the record efficiency until the recent silicon cell results (15). We have estimated that this approach can obtain about 5% from the silicon cell and thereby over 30% for the GaAs/silicon MSMJ cell under concentration (16). Even higher performance is projected for an MSMJ cell using an optimized bandgap combination. Sandia is supporting development of a wide bandgap (1.75 eV) cell for stacking on top of a silicon cell and of a narrow bandgap (0.7 eV) cell for stacking underneath a GaAs cell.

Another important development in MJ cells has been the examination of new electrical configurations other than the series-connected configuration for MJ cells. In particular, a new voltage-matched configuration has been proposed by researchers at Chevron for MSMJ cells (18). Voltage-matched configurations can also be used with MMJ cells (17). The voltage-matched configuration connects the cells in parallel so that the bandgap selection criteria becomes matched voltages rather than matched currents as in series-connected MJ cells. This configuration has been recently modelled at Sandia and several advantages were found for the voltage-matched configuration (17). These advantages include wider selection of bandgaps for the component cells, less sensitivity to spectral variations inherent in terrestrial spectra, structures that avoid the difficult transparent ohmic interconnect required in series-connected MMJ cells, and possibly better radiation resistance for space applications. It is expected that the advantages of a voltage-matched configuration will make realization of an efficient MJ cell easier.

SUMMARY

We have reviewed recent developments and presented an outline of the research topics in the DOE terrestrial crystalline cell program. With an integrated program of material and device research, we feel that crystalline PV systems can become an important renewable energy source for the United States.

REFERENCES

1. D. E. Arvizu, submitted to the 1987 ASME-JSME-JSES Solar Energy Conference, Honolulu, HI, March 22-27, 1987. conference.

2. Elmer Christensen, Flat-Plate Solar Array Project: 10 Years of Progress, JPL 400-279, 1985.

3. R. M. Swanson, Proceedings of the 18th IEEE Photovoltaic Specialists Conference, Las Vegas, NV, October 1985, pg. 604.

4. J. L. Gray and R. J. Schwartz, Proceedings of the 17th IEEE Photovoltaic Specialists Conference, Kissimmee, FL, May 1984, pg. 1297.

5. P. A. Basore, Concentrator Solar Cell Research, Final Report for Sandia Contract 21-8779, to be published 1986.

6. Mark O'Neill, Photovoltaic Concentrator Technology Project: 14th Project Integration Meeting, Sandia Report SAND86-0058, 1986, pg. 173.

7. Martin A. Green, et al., IEEE Elect. Dev. Lett. EDL-7, 583(1986).

8. R. A. Sinton, ibid., pg. 567.

9. H. C. Hamaker, et al., in reference 3, pg. 327.

10. R. P. Gale, et al., in reference 3, pg. 296.

11. J. C. C. Fan, in reference 3, pg. 28.

12. P. D. DeMoulin, in reference 3, pg. 321.

13. J. M. Gee, private communication.

14. J. P. Benner, et al., Space Photovoltaic Research and Technology 1985, NASA Conference Publication 2408, 1985, pg.23.

15. D. L. King, private communication.

16. J. M. Gee, et al., in reference 3, pg. 546.

17. J. M. Gee, Proceedings of the 2nd International Photovoltaic Science and Engineering Conference, Beijing, China, August 1986.

18. L. D. Partain, et al., in reference 3, pg. 539.

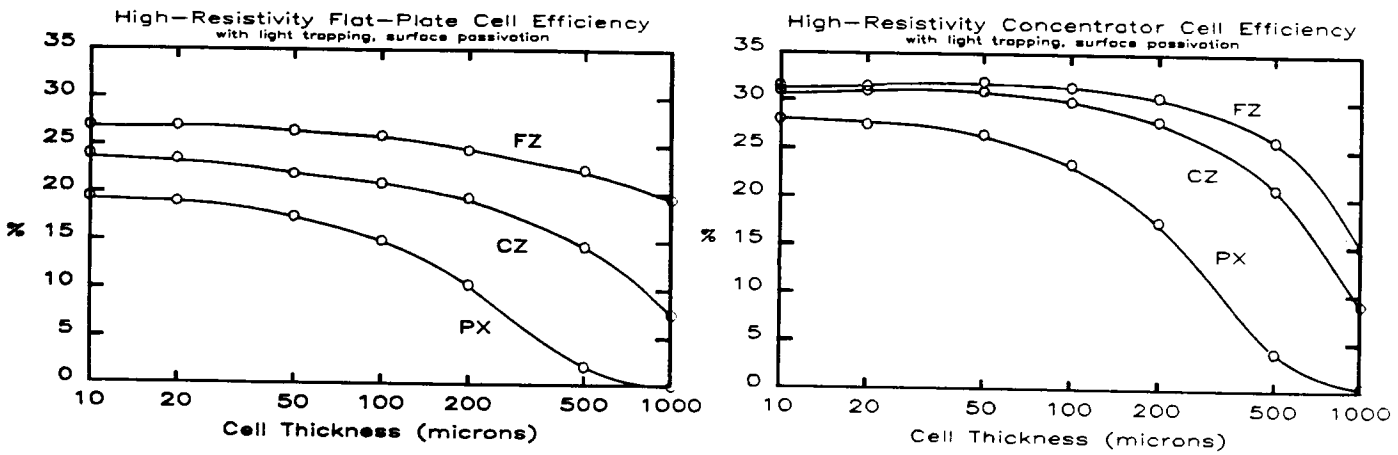

Figure 1. Iowa State University cell efficiency modelling results incorporating light trapping and surface passivation for minority carrier lifetimes typical of float-zone (FZ), Czochralski (CZ), and polycrystalline (PX) silicon. Results for one-sun and at 100X are presented.

ONE SUN PERFORMANCE

	SOLAREX (POLY SI)	ARCO (CZ)
A(CM^2)	39.5	39.4
Voc (V)	.572	.570
FF	.760	.74
I_{SC} (A)	1.18	.565
I_{SC}* (A)	1.42	1.38

*WITH PRISM COVER

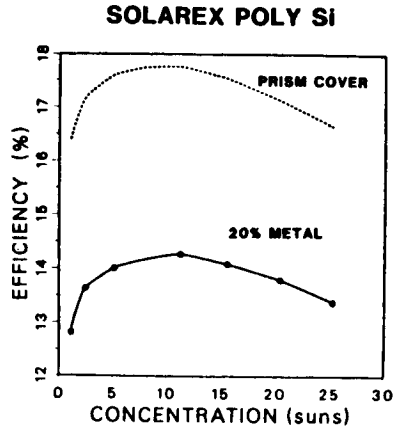

Figure 2. Results for silicon cells fabricated with one-sun silicon cell technology under low concentrations. The obscuration of the 20% metal grid coverage is removed with a prismatic coverglass.

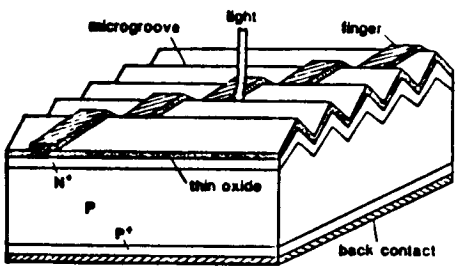

ONE SUN PERFORMANCE

	.1 Ω-CM	.2 Ω-CM
A (CM2)	.09	.09
Jsc (MA/CM^2)	38.8	40.2
Voc (v)	.663	.651
FF	.836	.825
η(%)	21.5	21.6

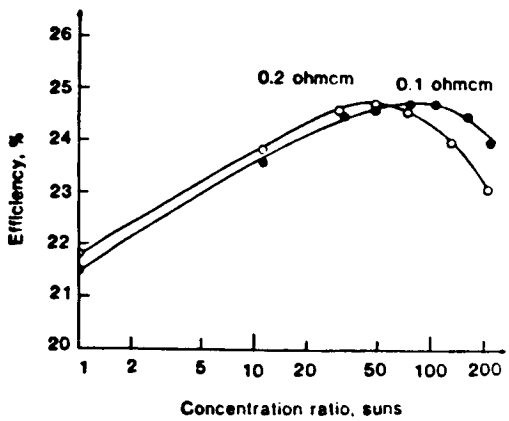

Figure 3. University of New South Wales low-resistivity silicon concentrator cell test results and cell structure.

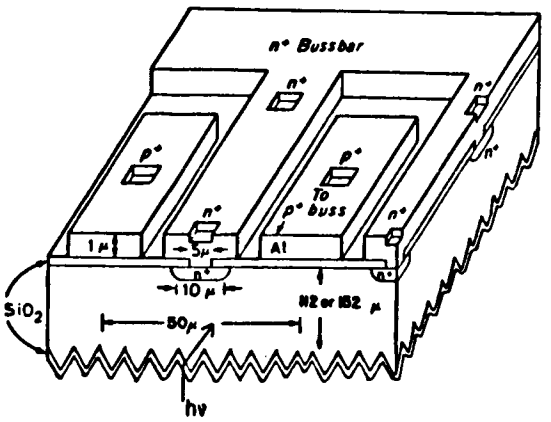

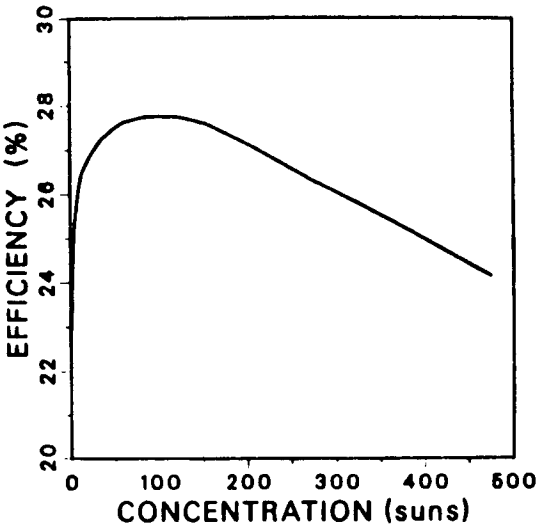

CELL PERFORMANCE

	1X	100X
AREA (CM^2)	.15	.15
J_{SC} (A/CM^2)	.0415	4.15
V_{OC}* (V)	.682	.809
FF	.785	.826
η (%)	22.2	27.7

Figure 4. Test results and cell structure for Stanford's Point Contact Concentrator (PCC) cell.

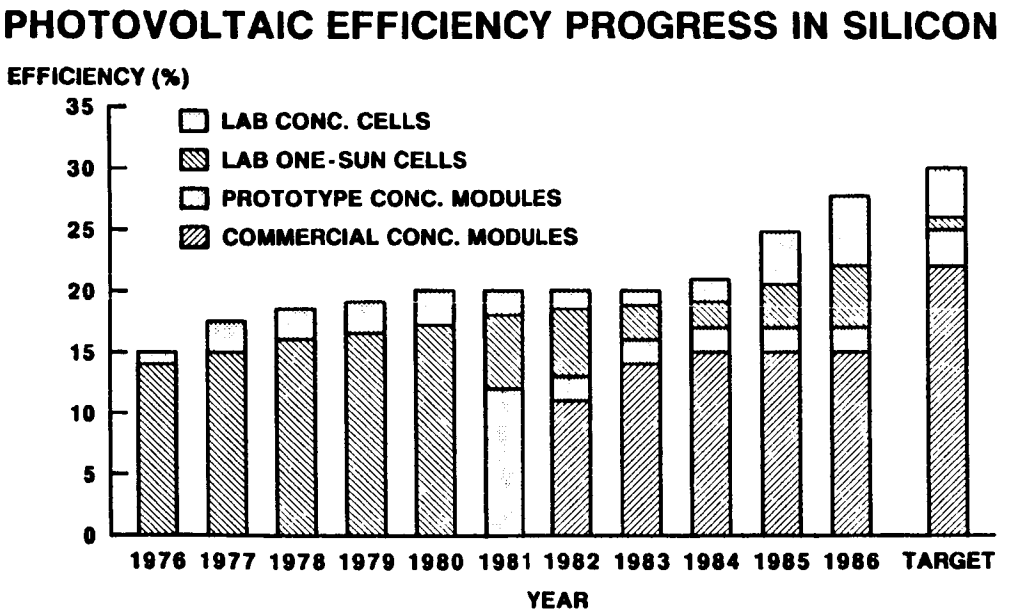

Figure 5. History of silicon cell and module efficiency improvements. All efficiencies measured at Sandia under standard test conditions.

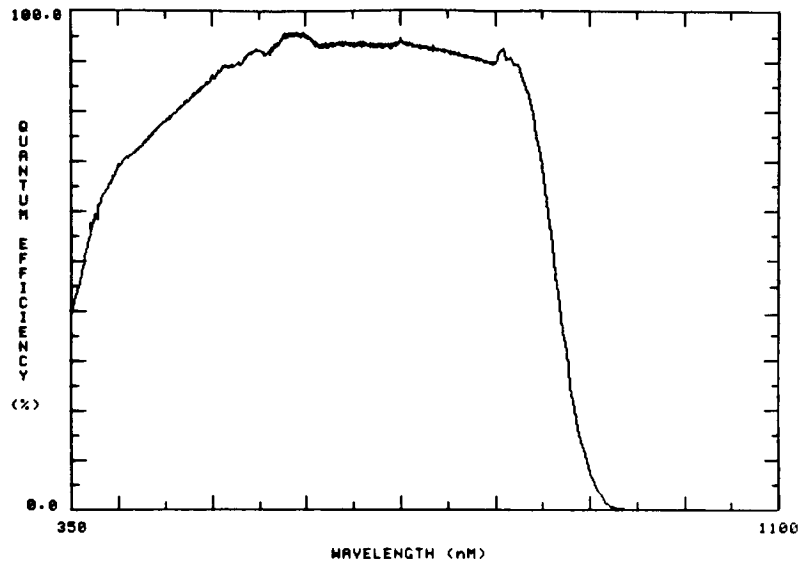

Figure 6. A plot of the internal quantum efficiency for a high efficiency GaAs concentrator cell fabricated by Varian.

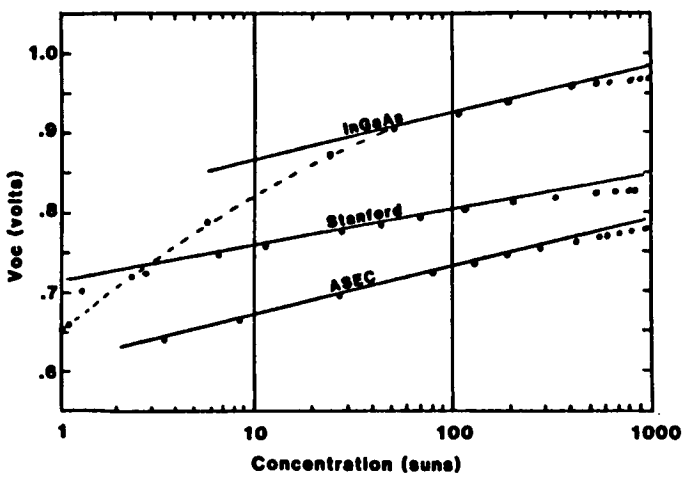

Cell	n	Voc@
Stanford	.76	.710
ASEC	1.0	.611
InGaAs	1.0	.804

Figure 7. Voc versus irradiance for an InGaAs cell, an advanced silicon cell (Stanford's PCC Cell), and a commercial low-resistivity concentrator cell (ASEC). The data are plotted as points and the solid lines are a fit of the data to the diode equation. The parameters for the fit are given in the adjacent table.

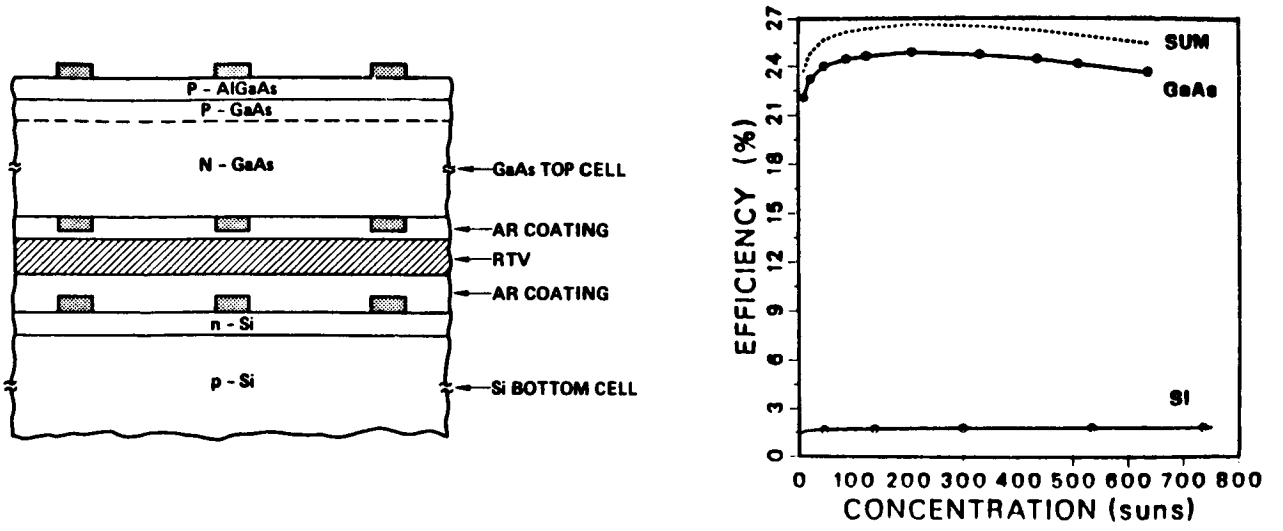

Figure 8. Test results for a MSMJ cell assembled by Sandia using component cells fabricated by Varian (GaAs top cell) and by ASEC (silicon bottom cell).

SPACE STATION POWER SYSTEM

Cosmo R. Baraona
NASA Lewis Research Center
Cleveland, Ohio

The manned space station is the next major NASA program. It presents many challenges to power system designers. The power system, in turn, is a major driver on the overall configuration. In this paper, the major requirements and guidelines that affect the station configuration and the power system are explained. The evolution of the space station power system from the NASA program development-feasibility phase through the current preliminary design phase is described. Several early station concepts, both fanciful and feasible, are described and linked to the present concept. The recently completed phase B trade study selections of photovoltaic system technologies are described in detail. A summary of the present solar dynamic system and the power management and distribution system is also given.

BACKGROUND

The space station system is the next major step in the manned space program. The space station will be a multipurpose facility that will enable advancements in science, technology, and space transportation capabilities. It will promote commercialization of space and open new avenues not yet fully explored.

Space stations have existed in the minds of writers, scientists, and engineers for decades. In a series of fictional articles beginning with the October 1869 issue of the Atlantic Monthly, a fanciful space station was described by the Rev. E.E. Hale from Boston. "The Brick Moon" articles described a hollow sphere 200 ft in diameter. It was whitewashed on the outside to serve as an aid to navigation and was launched into orbit by water wheels. The articles made no mention of a power source for the brick moon after it left the Earth. The brick moon concept did not have a sound basis by today's standards, but it was entertaining and thought provoking!

In 1928, Hermann Noordung published "Befahrung des Weltraums" (The Problem of Space Travel). He described a manned toroidal space station that rotated to produce artificial gravity. The idea was further developed in the March 22, 1952 issue of Collier's magazine and was described in the book, "Across the Space Frontier" (Viking Press, New York, NY 1952) (fig. 1). Walt Disney Studios produced television programs that were based on Noordung's concept. In this concept, power was produced by a large parabolic mirror which focused solar energy to heat steam and operate a turbine generator. In today's terminology, this was a form of a solar thermal-dynamic power system. At that time, practical photovoltaic (PV) cells had not yet been invented!

These early works, as well as numerous studies conducted in the 1960's and 1970's after the creation of NASA (ref. 1), helped establish a role for a manned space station. The solar dynamic power source described in 1952 was primitive but functional. However, most unmanned satellites launched since the beginning of the space age in 1957 have been powered by silicon solar-cell-based photovoltaic systems. A few deep space interplanetary missions and manned spacecraft like Mercury, Gemini, and Apollo are exceptions. During this era, technology has been developed

for photovoltaic, solar dynamic, and nuclear systems as well. The primary thrust of these developments has been toward lighter weights, lower volumes, higher efficiencies, longer lifetimes, and greater reliability. These technologies and flight experiences formed the starting point for establishing the feasibility of the current space station and for defining its power system.

FEASIBILITY PHASE

The current space station program had its beginnings in 1981, when technology steering committees were formed to identify candidate technologies. These committees were staffed with people from the NASA field centers. In early 1982, the Space Station Task Force was formed at NASA Headquarters, Washington, DC, to determine the feasibility of a space station. This was referred to as phase A in the program development process.

In August 1982, the task force sponsored contracts with eight major aerospace companies to analyze the uses or missions for a manned space station. Specific missions were determined and studied extensively, but these are too numerous to describe in detail here (ref. 2). These missions included materials processing, Earth and space observations, and servicing and repair of satellites and other payloads. The mission analysis studies showed that the station would serve as an assembly facility, a storage depot, and a transportation node (or way station) for payloads intended for higher Earth orbits or for interplanetary missions.

These diverse missions led to the space station complex shown in figure 2. It is composed of a manned core and an unmanned co-orbiting platform (both in a 28.5° orbit), another platform in a polar orbit, and a system of unmanned vehicles for maneuvering payloads near the station or for transferring them to other orbits.

The mission analysis studies identified resource requirements, such as crew time, thermal control, and power, for each projected experimenter and each scientific and commercial user of space station. The sum of the power requirements of each of these missions defined the total requirement for each station element. Power levels were determined as a function of time from the initial operational capability (IOC) through some future power level when the station and the number of missions would have grown. These power requirements have changed as the mission definition has evolved. The current user power levels are shown in table I. User power or bus power is expressed in kilowatts electric (kWe) in table I and throughout this paper. User power means all system losses for generation, storage, conditioning, and distribution have been taken into account. Note that the station IOC power of 75 kWe is about an order of magnitude higher than for Skylab. Skylab, the first U.S. manned space station, was launched in 1973 and is the largest (8-kWe user power, 22-kWe array) solar power system flown in space to date. This 75-kWe requirement for the planned space station is the most challenging factor facing the power system designer.

Additional challenges arise from programmatic requirements imposed on the power system designer. These additional requirements are management and/or engineering related. They include (as do most large spacecraft projects) cost (both initial and life cycle), schedule, technical-development risk, weight, safety and contingency requirements. However, the permanent nature of space station results in some new and unique requirements such as growth capability, maintainability, and commonality of hardware and software across all station elements. Future replacement and growth of the station systems require that they be designed so that they can accept

future changes in technology (i.e., technology transparency) yet still provide the same functions. Other considerations are the station orbit altitude and decay, assembly and buildup, lifetime, load types and location, and logistics and sparing.

In the spring of 1983, the task force was expanded to include a concept development group (CDG). This group took the results from the mission analysis studies and, with the help of all the NASA centers and many aerospace companies, synthesized them into several candidate space station configurations. They also further studied and sharpened technology selection for all the station systems including the power system: PV planar, PV concentrator, microwave power transmission, solar dynamic, and nuclear systems. The power tower, or gravity gradient stabilized, and many other configurations were studied as candidate station geometries. At this time, photovoltaics appeared to be the leading candidate for the power system.

As a result of the CDG feasibility work, on January 25, 1984, President Reagan, in his State of the Union message, gave NASA approval to build the space station and have it operational by 1994. In rapid succession a new program office was formed in Washington from the core task force group and the focus of the concept development activities was enlarged and shifted to the "Skunk Works" near NASA Johnson Space Center in Houston, Texas. The skunk works expanded and refined the definition of the space station systems. They wrote a reference configuration description and a request for proposals for the next phase of the program. During this period, the importance of drag area on reboost and life-cycle cost, coupled with the very large growth power requirements (as high as 450 kWe), resulted in the adoption of solar dynamic (SD) generators with thermal energy storage and photovoltaic arrays with electrochemical energy storage for detailed study in the definition phase.

DEFINITION PHASE

The present space station configuration and the hybrid power system (fig. 3), using both PV and SD technologies, were selected in the definition, or phase B, studies which began in 1984. Nuclear and other power systems were ruled out on the basis of schedule, cost, risk, and other factors. The large size and drag area of the power system is a major consideration for selection of the overall space station geometry. This geometry must allow the station and the power system to grow. It must minimize the impact of the power system on viewing angles for experimenters and for communications. The space station and its power system must be controllable and structurally sound. The maximum degree of commonality between the station and platform power systems is necessary to reduce costs. Most important of all, the station must be passively controllable, that is, the gravity gradient must be stabilized. From these diverse and sometimes contradictory requirements, the Power Tower and later the Dual-Keel configurations were developed and studied by NASA. At the same time, the NASA Lewis Research Center and its two major phase B contractors, TRW and Rocketdyne, studied numerous power system types. These phase B definition studies are described below.

Power System Configuration Definition

Early in phase B, six cases for power system options were defined for study (fig. 4). The IOC power level of 75 kWe and the growth power level of 300 kWe were selected. The six cases were established on the basis of IOC power system type (either SD or PV) and the method of growing from 75 to 300 kWe. Case 1 was all PV. Case 6 had minimum PV (12.5) kWe) at IOC and all SD at growth. An all SD

system is not feasible because power is needed on the first launch when the accurate sun tracking required for the SD system is not possible. Cases 2 through 5 had various proportions of SD to PV. Commonality between the station and the platform solar arrays was also considered in these system studies. A solar array optimized for the platform would be smaller than one optimized for the station. As a cost saving measure, platform arrays could be used on the station so that only one development cost would be incurred. The use of SD on the platform was not feasible because of microgravity, weight, and other requirements. Also, the platform power level requirements were incompatible with a practical-sized SD unit.

The primary selection criteria for these system studies was both IOC and life-cycle cost for the station and the platforms. Development, manufacturing, verification testing, overhead, and launch costs for all the space station system hardware and software was included. An especially important life-cycle cost savings resulted from the reduced aerodynamic drag associated with the SD system. Reduced drag allowed lower orbit altitude and higher shuttle payload capacity.

As a result of these system studies, the case-5 hybrid was selected. In this case, the PV portion of the power system generates 25 kWe with four solar array wings (array power, approximately 57 kWe). The station wing is identical in design to those optimized for the platform. The station also uses nickel-hydrogen batteries identical to those designed for the platform. This commonality of hardware results in design and development cost savings for the space station program.

The SD portion of the case-5 power system generates about 50 kWe. The exact size of each SD unit will depend on the power management and distribution (PMAD) system efficiency. The SD units will use either the Brayton or Rankine system and an offset parabolic concentrator. The exact design will depend on the results of ongoing preliminary design studies. The detailed trade studies which helped define the technologies of the case-5 hybrid are described briefly in another section of this paper. These trade studies occurred at about the same time as the system level studies previously described. Overall, the technologies for the photovoltaic system are low risk and space proven, whereas the solar dynamic technologies offer reduced drag and cost.

Photovoltaic System Technology Studies

Solar array. - Several array concepts were evaluated during the phase B studies. They included planar arrays, simple flat mirror concentrators, Cassegranian concentrators, and trough concentrators. Preliminary trade studies considered all known degradation factors including optical, electrical, and mechanical effects. Packing factors, pointing and structural requirements, number of components, drag area, costs and technology readiness were also considered. On the basis of these factors, a planar array with silicon cells was selected. A Cassegranian array with gallium arsenide cells looked promising, but cell efficiencies of about 30 percent were required to compete with the planar silicon design. This cell efficiency is beyond that projected for production cells available at the start of the space station IOC array fabrication in 1988-1989.

The issue of deployable/erectable versus deployable/retractable arrays was also studied. Combinations of types of array substrate, masts, construction methods, on-orbit assembly methods, and means of integrating the substrate to the mast were devised for study. Both articulated and continuous longeron masts were considered. Evaluation factors included complexity of building and testing, cost, on-orbit (extra-vehicular activity) assembly time, array retractability, mast

stiffness, reliability, damage tolerance, repairability, atomic oxygen resistance, technology readiness, and other factors. When all these factors were considered, a planar, deployable, fold-out array with a coilable, continuous longeron mast was selected. The array wing design for the station and the platform will be the same. It will have two flexible blankets and a center mast. Each blanket will be stored in a containment box/cover assembly during launch.

This array design is similar to the NASA Office of Aeronautics and Space Technology (OAST) flight experiment, OAST-1 (fig. 5). This solar array flight experiment was performed on a space shuttle mission (STS 41D) launched in August 1984. A 13- by 105-ft array consisting of 84 hinged panels was deployed and retracted on-orbit several times. The array blanket panels were flexible. The deployment mast was a coilable longeron type. This array was built by the Lockheed Missiles & Space Company. To reduce cost, only three panels contained solar cells. If fully populated with cells, the array power output would be about 13 to 14 kWe at the wing root.

The OAST-1 flight experiment was completely successful. It showed that the array behaved well dynamically. Its performance, in general, was as predicted, and the solar cells were not damaged during the mission. This flight experiment demonstrated that this array type is technology ready and established that space station planners can have a high degree of confidence in it. A more detailed description of the array and the flight experiment results can be found in reference 3.

The OAST array has several advantages compared with other array types. It is lighter in weight and packs in a small volume for launch. It has sufficient stiffness to meet space station structural and dynamic requirements. The flexible substrate is made from Kapton, which is transparent to infrared radiation. This allows the solar cells to operate at a lower temperature and thus with higher power output per unit area.

A disadvantage of the OAST-1 array is its need for protection from the atomic oxygen present at space station altitude. The Kapton substrate and other components that contain epoxy (e.g., the mast longerons, the blanket hinge pins and containment box, and several smaller components) are attacked by atomic oxygen. These components, if unprotected, may have very limited lifetimes. The Space Station Advanced Development Program (ref. 4) is beginning a contract to demonstrate practical methods to protect the array. The primary emphasis will be on coatings that are resistant or inert to atomic oxygen attack. These coatings must also meet other array performance requirements and must be compatible with other parts of the space environment such as ultraviolet radiation and micrometeoroids. These coatings are being developed by the Space Station Advanced Development Materials community. The planned array protection contract will provide an engineering solution to the atomic oxygen problem. It will demonstrate that the protection methods are compatible with array manufacturing and that they survive that process and still protect the array. The most critical need is for the Kapton blanket.

If suitable coatings cannot be demonstrated, alternate blanket approaches are possible. These approaches include laminating Kapton sheets over an inner layer of material that is resistant to atomic oxygen or using aluminum as the substrate. These approaches might result in higher weight and/or decreased cell power output due to loss of infrared transmission through the substrate.

Solar cell. - Detailed solar cell assembly design options were studied: silicon versus gallium arsenide; base resistivity; back surface field (BSF); infrared (IR) reflector versus transparent back contacts; conventional top-bottom,

wraparound, or wrapthrough contacts; cell size and thickness; and cover glass material type and thickness. Evaluation criteria were IOC and life cycle cost, development status, and performance achieved by 1988-1989 when array fabrication will begin.

The array design features selected were N on P silicon cells with 2-Ω-cm base resistivity, 8 by 8 cm size, 8 mil thick, IR-transparent gridded back contacts, a BSF, and a wrapthrough front contact using a 6-mil cerium-doped coverglass. The wrapthrough front contact and the large cell size reduce array assembly time and cost. The gridded back allows IR transmission through the array blanket resulting in higher array power output for a fixed area.

Silicon solar cells have been used on many spacecraft in the past. They have extensive operational, assembly, and manufacturing experience. Although the selected cell is larger than those used previously, it is still a very low risk approach. The Space Station Advanced Development Program will demonstrate pilot production of these cells in early 1987. Efficiencies of 14 percent are expected.

Energy storage system. - The PV system will store energy electrochemically. This stored energy is needed during the dark portion of the orbit and for contingency purposes when the power system cannot produce and/or deliver power. The phase B studies showed that the inherent storage capability or residual energy of the electrochemical system was adequate to meet expected contigency requirements. Building in greater contingency capability would be unnecessarily expensive. Energy storage options studied included nickel-cadmium (NiCd) batteries, a regenerative fuel cell (RFC), and nickel-hydrogen (NiH_2) batteries.

NiCd batteries are established, flight-proven, low-risk devices. However, their low depth of discharge results in high storage system weight. Space cells up to 100 A-hr sizes have been produced so that development risk would be low.

The RFC uses a fuel cell and an electrolyzer to store energy in the form of hydrogen and oxygen. In the dark portion of the orbit, the hydrogen and oxygen are recombined in the fuel cell to produce water and electricity. During the lighted portion of the orbit, excess array power is used to electrolyze the water and charge the system with hydrogen and oxygen. The cycle is closed so that the fluids are not consumed. The RFC is lighter than batteries and allows storage of large amounts of contingency power with small changes in tank volume. Since the RFC is not as efficient as batteries (60 percent compared with 80 percent), the solar arrays must be larger. Also, the RFC is more complex (i.e., pumps, valves, etc.) and not as reliable as batteries. RFC's also have higher heat rejection needs. Reliability was a major consideration for the platform, where three years of operation without repair were required. However, commonality between the station and the platform to reduce development, resupply, and sparing costs was also considered.

The NiH_2 battery has been used in geosynchronous orbit (GEO) spacecraft (fig. 6) in the individual pressure vessel (IPV) type. (The bipolar NiH_2 battery has low technology maturity and was screened out by the early trade studies.) IPV, 3.5 in. diameter, 50 A-hr GEO cells are in production. Other sizes and capacities are available using scaled-up versions of existing components. The uncertainty with the NiH_2 battery stems from its charge-discharge cycle life. GEO spacecraft experience only a fraction of the cycles that LEO spacecraft experience. However the Space Station Advanced Development Program is beginning to test LEO cells with a goal of demonstrating minimum 5 year lifetimes.

As a result of the phase B trade studies, IPV NiH_2 batteries were selected for the platform. Weight, cost, reliability, development risk, and schedule requirements were the primary considerations. These batteries are about half the weight of the NiCd batteries, lower in cost than NiCd batteries, and more reliable than the RFC. An identical IPV NiH_2 battery was also selected for the station on the basis of cost and commonality with the platform. IPV NiH_2 was lower in IOC cost and only slightly higher in life-cycle cost.

Solar Dynamic Technology Studies

The solar dynamic system consists (fig. 7) of an offset parabolic concentrator mirror which focuses the suns heat into a receiver. The receiver stores the heat in a salt (e.g., LiOH) and transfers it to a working fluid (e.g., toluene or helium-xenon gas). The heated fluid drives a turbine which spins an alternator to generate electrical energy. The turbine also drives a pump which recirculates the working fluid. Excess heat is rejected to space by a radiator.

In the trade studies the two conversion cycles considered were the closed Brayton cycle (CBC) and the organic Rankine cycle (ORC). These systems have not been used in space, but a technology data base for the heat engines has resulted from terrestrial and aircraft applications. Estimating costs, schedules, and other factors during the phase B trade studies were therefore higher risk than for the PV system.

Design considerations for the SD system studied in phase B and being developed in the Advanced Development Program include low-gravity effects for two-phase (gas-liquid) flow, heat flow and distribution in the receiver, lifetime for thermal energy storage (salt) capsules, weight and optical quality of the concentrator, pointing accuracy (0.1°) for the mirror gimbals, atomic oxygen protection, launch packaging, on-orbit assembly, and other factors.

At the time of this writing both the CBC and the ORC systems were still being considered. More detailed study is required because cost and performance are nearly identical.

Power Management and Distribution Studies

The power management and distribution (PMAD) system must cope with load types and sizes that will be unknown as the station users change and increase in number. Therefore the PMAD system must be user friendly and adaptable to change and growth. The PMAD system for the space station must resemble a terrestrial utility power system rather than the PMAD system of previous spacecraft. Distribution voltages higher than the 28 V previously used are mandatory to reduce losses.

During phase B, distribution frequencies of dc, 400 Hz ac, and 20 kHz ac were studied. Component efficiency, size, and weight as well as technology readiness, availability of space components, acoustic noise, electromagnetic interference, and plasma coupling were all considerations. After much consideration, 20 kHz was selected for the PMAD distribution frequency.

The overall PMAD architecture selected is a dual-ring system with 15-kWe busses supplying power to 10 load areas on the upper and lower keels and on the transverse boom. Busses supplying the manned modules are rated at 30 kWe. The PMAD system contains numerous switching and control assemblies, as well as a control system for

sensing and commanding the loads. Isolators and power controllers will sense faults and protect the system.

SUMMARY

The present space station program traces its roots back before the dawn of the space program. The station configuration and the power system for the present program have been studied extensively in the feasibility and definition phases.

The hybrid power system selected will meet initial and future station and platform requirements. The 25-kWe PV system (57-kWe array power) will be larger than any system flown to date. The SD system will facilitate economics and growth for the power system and the station. The PMAD system enables a growable, balanced utility system approach to maximize user friendliness.

The technologies selected for PV, SD, and PMAD result in the lowest IOC cost and life cycle costs with acceptable development and schedule risk. This hybrid system also meets programmatic and technical considerations driving the power system definition. The space station power system may set the standard for future spacecraft power systems.

REFERENCES

1. Hook, W.R.: Space Stations - Historical Review and Current Plans. ASME Winter Meeting, Phoenix, AZ, Nov. 14-19, 1982.

2. Space Station Mission Synthesis Workshop. NASA Proceedings, Hampton, VA, Mar. 5-8, 1984.

3. Solar Array Flight Experiment, Final Report. Lockheed Missiles and Space Co., LMSC-F087173, Apr. 1986.

4. Forestieri, A.F.; Baraona, C.R.; and Valgora, M.E.: Space Station Power System Advanced Development. Energy for the Twenty-First Century (20th IECEC), SAE P-164, Vol. 1, SAE, 1985, pp. 1.9-1.16.

TABLE I. - SPACE STATION SYSTEM POWER REQUIREMENTS

Element	User power average, kWe		User power peak, kWe	
	Initial operational capability, (IOC)	Growth capability	Initial operational capability, (IOC)	Growth capability
Manned core	75	300	100	350
Polar platform	8	15	16	24
Co-orbiting platform	6	23	6	23

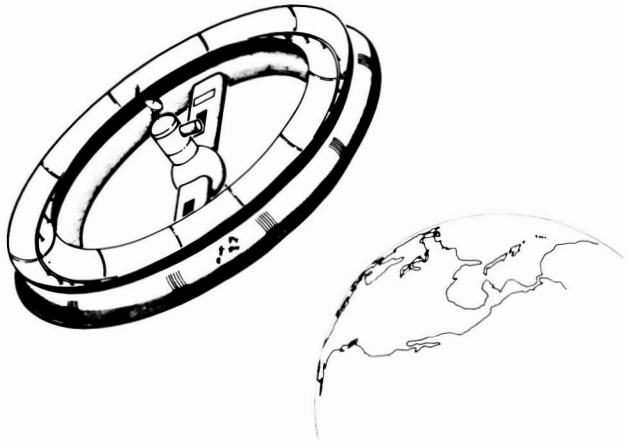

FIGURE 1. - A STATION IN SPACE; A 1952 CONCEPT.

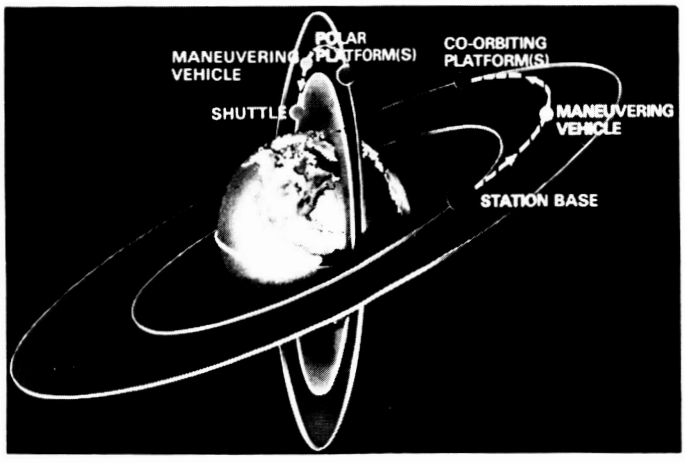

FIGURE 2. - SPACE STATION COMPLEX, EARLY 1990'S.

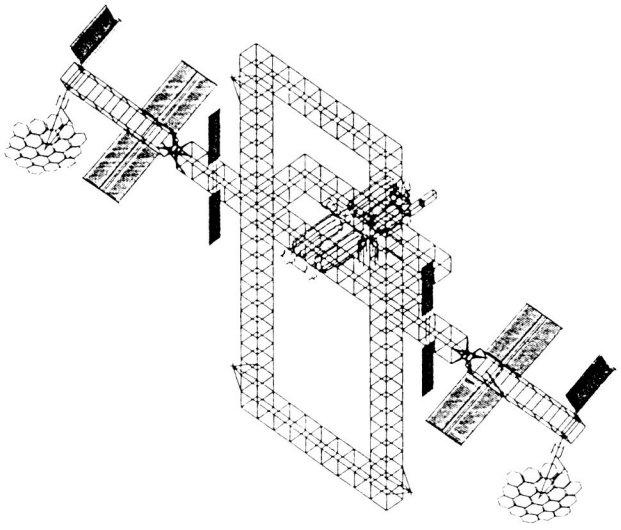

FIGURE 3. - SPACE STATION DUAL KEEL CONFIGURATION 1986.

CASE	INITIAL OPERATIONAL CAPABILITY, IOC	PHOTOVOLTAIC (PV) AND SOLAR DYNAMIC (SD) CAPABILITIES, kWE	GROWTH
1	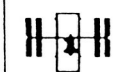	IOC PV GROWTH PV	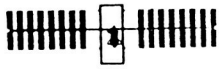
2	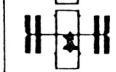	IOC PV GROWTH SD	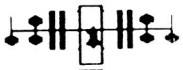
3	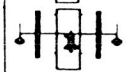	IOC 50 PV-25 SD GROWTH SD	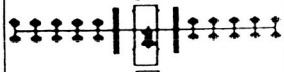
4		IOC 37.5 PV-37.5 SD GROWTH SD	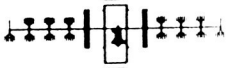
5	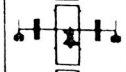	IOC 25 PV-50 SD GROWTH SD	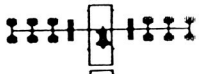
6	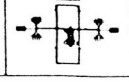	IOC 12.5 PV-75 SD GROWTH SD	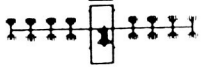

FIGURE 4. - CASES EVALUATED FOR SPACE STATION POWER SYSTEM.

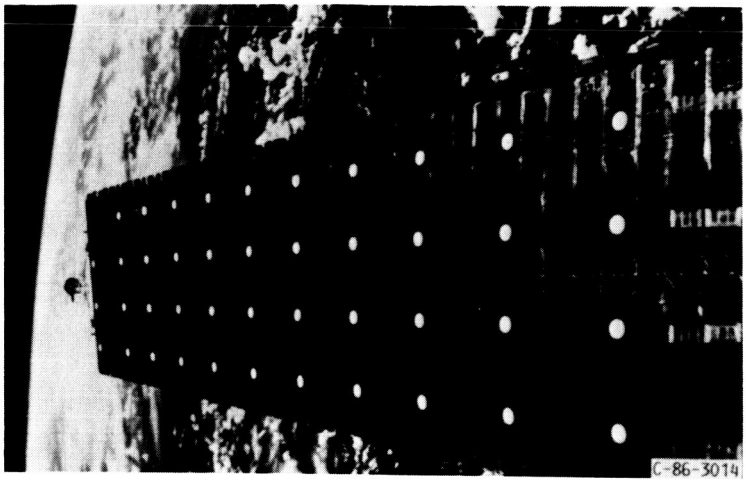

FIGURE 5. - OAST-1 SOLAR ARRAY FLIGHT EXPERIMENT, 1984.

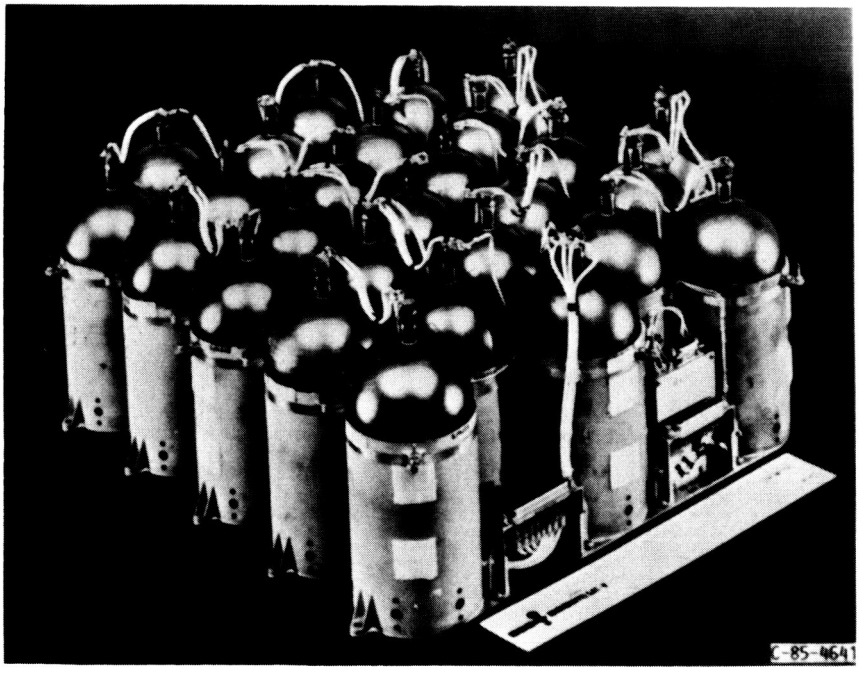

FIGURE 6. - INTELSAT V NICKEL HYDROGEN BATTERY.

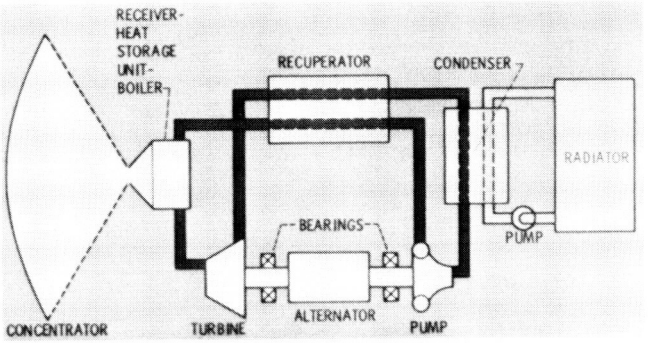

FIGURE 7. - SOLAR DYNAMIC SYSTEM SCHEMATIC, ORGANIC RANKINE CYCLE.

SPACECRAFT 2000 - THE CHALLENGE OF THE FUTURE

Henry W. Brandhorst, Jr., Karl A. Faymon, and Robert W. Bercaw
NASA Lewis Research Center
Cleveland, Ohio

Considerable opportunity exists to substantially improve the systems, subsystems, components, etc., included in the spacecraft bus, the nonpayload portion of the spacecraft. There are a broad range of technology advancements which can be brought to bear to reduce mass and cost and to increase lifetime and reliability. Over the past several years, the NASA Lewis Research Center has been working with industry, other NASA centers, and the Department of Defense (DOD) to define a new initiative that would focus on these issues, while at the same time forging new industry/government relationships that can lead to substantial benefits for both parties. The steps followed to date, the challenges being faced by industry, and the progress toward establishing a new NASA initiative which will identify the technologies required to build spacecraft of the 21st century and which will implement the technology development/validation programs necessary are described in this paper.

INTRODUCTION

Historically, the primary focus of a spacecraft designer's attention has been the payload, and this seems most reasonable. After all, the payload is the primary purpose for the existence of a satellite. However, this mode of thinking inevitably leads us into a delicate trap. The emphasis placed on increasing the sophistication of the payload (often at substantial risk) in order to accomplish the desired mission, tends to decrease the attention paid to making substantial improvements in the spacecraft bus. Figure 1 demonstrates that the payload comprises only one-fourth of the total geosynchronous (GEO) spacecraft mass and the ratios are similar for low-Earth orbiting (LEO) spacecraft. Unfortunately, spacecraft managers are less concerned with the potential benefits than the risk of making substantial changes in the bus portion of the spacecraft. It is only when the mass of the spacecraft approaches launch vehicle capacity that investment in new spacecraft bus technology becomes compelling. One example of this is the development by COMSAT Laboratories and the U.S. Air Force (USAF) of the individual pressure vessel nickel-hydrogen battery for geosynchronous applications.

In addition to being three-fourths of the spacecraft mass, the bus (defined as power, thermal management, auxiliary propulsion structure, attitude control, and telementry, tracking, and control (TT & C) incurs about one-half the satellite's cost (pretest and checkout). Cost is, of course, the major challenge to be met. In the commercial world, reduced cost means enhanced revenue or increased competitiveness. Figure 2 shows data demonstrating the sixfold reduction in INTELSAT utilization charges over the past two decades. In the competitive communications business, cost reduction is essential to profitability.

Cost reduction plays an important role in other classes of satellites - from commercial ventures in low-Earth orbit to satellites whose sole goal is scientific

knowledge. For these, cost reduction is often essential to a profitable product or the ability to fly the mission. Other major factors, such as increased performance, which enter into the arena as well will be addressed later.

In late 1984, it became apparent that a new kind of government-supported program, one that focuses on the spacecraft bus and enhanced industry-government partnership, might be in the nation's best interests. Over the past two years, we at NASA Lewis Research Center have been pursuing a path which we hope will lead to a major new initiative for NASA. It is appropriate now to review the steps that have been taken and the progress that has been made toward this goal.

PROGRAM DEVELOPMENT

The decision to pursue developing this new initiative resulted from a series of visits that the Lewis staff paid to industry in the spring of 1985. The objective was to obtain industry's view of the critical problems it was facing in its satellite business ventures. Nine organizations were visited as shown in figure 3. The range of business orientation spanned government (NASA and military), commercial communications, and communications operations. Critical concerns were identified. These included reducing spacecraft related costs and subsystem weights, increasing system lifetimes and reliability, and reducing technical risks. It is important to note that each company saw specific future technical needs somewhat differently. However, there was consensus that there was a real need to address the development of the spacecraft bus technologies.

The initial program focus was aimed at the broad range of satellites that fall generally into the classification of mass-limited missions. These include GEO satellite's and platforms, LEO polar satellites and platforms, and planetary spacecraft. This distinction, while somewhat arbitrary, is certainly helpful programmatically. It is also obvious that advances made in one class of satellites will be transferable to others.

It should be noted that mass-limited missions really reflect Earth-to-orbit booster limitations. This is most clearly shown in figure 4 which demonstrates the situation in power. For this figure, the power was computed from the known mass-to-GEO capability of the booster stage (IUS or STS/centaur), the 25 percent mass due to the power system, and the specific mass of the power system. Current technology benchmark was taken as the TDRS power system which was 7.2 W/kg for solar array, battery, cabling, and power management. With present technology a stringent limit is placed on the power available in orbit. Advanced technologies can substantially eliminate such restrictions. It is important to note that a 40 W/kg power system could be built from technologies currently under development by NASA OAST (figure 5). Similar advances are possible in all other areas of the spacecraft bus. It is entirely possible to double the payload mass fraction by focusing attention on improvements in the bus and in the design of spacecraft. This additional mass can be used to enhance reliability, add lifetime, or increase revenue.

Finally, it was also clear from these visits that international competition was becoming intense and aggressive. A cursory examination of foreign developments in power and electric propulsion showed significant activity that was promising enhanced capability. For example, figure 6 denotes the activity in European solar array development overlaying a projection by Pierce (RCA) of satellite power needs up to the next century. The European solar array developments are all available

today (they are arbitrarily distributed over time to show detail). Similar U.S. array developments have been minimal. Figure 7 demonstrates the increased voltage of European satellites in contrast to the 28 Vdc U.S. standard. Increases in voltage permit substantial reductions in cabling mass. Figure 8 shows the flights of electric propulsion systems by foreign sources, while U.S. technology has been dormant for nearly two decades.

With these examples, it is clear that there is great potential for substantial improvements in all areas of the spacecraft bus. Industry and government agree. The question is "how to proceed?"

PROGRAM APPROACH

The first step was to establish a steering committee comprised of industry, several NASA centers, and critical DOD organizations. This group reached agreement on several key points. First, they emphasized that a government/industry partnership was desirable and in the nation's best interest. The hope is that a government/industry relationship can be developed in the space arena which parallels the one that exists in the aeronautical arena. In this partnership the government supports high-risk research; industry takes the results and turns them into commercial advances. The challenge is to expand the technology-availability time horizon of industry and to bring government-sponsored research more near term.

Secondly, a total system approach at the spacecraft level should be used to define technologies for development. The technology developments should be focused and a combination of existing, modified, or new NASA and industry IRAD programs. The challenge will be to maintain proprietary rights within the company and to establish a program wherein participating organizations would develop those technologies that they view to be in their best interest. The program is not envisioned to be the traditional program in which a system is defined (e.g., a 40 W/kg power system), and a competition ensures with an organization ultimately being selected to perform the work. It is clear that many challenges must be overcome to make this approach a reality.

Next, many supporting technology issues may also have to be addressed - manufacturability, testing, servicing, supportability, etc. It will be essential to understand the operating environment of the 21st century and how it will influence satellite design. Equally important is the use of autonomy (in orbit, support, etc.) in satellite development and operation to permit a better product at a reduced cost.

Finally, the industry/government steering committee indicated the need for validating technology using terrestrial and/or in-space testbeds. This would include space act agreements covering the use of government-owned testbeds and judicious in-space testing as absolutely necessary.

The steering committee support for this new initiative has been outstanding and enthusiastic. All participants have shown a keen desire to create a new mode of operation that will enable the prompt introduction of new technologies and new ways of building and operating future spacecraft.

THE WORKSHOP

As part of developing the Spacecraft 2000 initiative, a workshop was held July 29-31, 1986 in Cleveland, Ohio. The objectives of the workshop were to identify the critical needs and technologies for spacecraft of the 21st century and to recommend technology development/validation programs and possible government/industry roles and partnerships. Forty-two organizations from both government and industry participated in the workshop. As a common base, plenary sessions delineating spacecraft needs and trends and outling the expected space infrastructure for the year 2000 were presented. Nine working group sessions covering all critical spacecraft bus technologies and systems were conducted. Each group was cochaired by industry and government representatives. In each of these working group sessions, critical technologies were identified. It was evident from the output of the groups that a bridge is required for new technologies to reach flight readiness. The need for government-sponsored terrestrial and/or in-space test beds for technology validation was also emphasized in each of the reports. During the course of the workshop, the steering committee also deliberated on government/industry relations to find common ground and a satisfactory approach for the program. Enthusiastic industry and government support for the Spacecraft 2000 program was evident. This workshop represents the first step in establishing the foundation for a new initiative to assure the broadband advocacy by all participants and to define a new partnership between government and industry that will lead to future enhancement of the spacecraft industry.

CONCLUSIONS

It is clear that the potential exists for major gains to be made in spacecraft of the 21st century. Specifically, the mass fraction of the payload could be doubled through substantial reductions in the bus mass fraction. This can be accomplished along with significant reductions in cost and increases in lifetime and reliability. Additional advances are anticipated in manufacturability, testing, servicing, and supportability. These benefits apply to all spacecraft (NASA, DOD, and commercial) and to areas such as communications, Earth observation, navigation, rescue, air traffic control, etc. The resulting cost reductions and performance improvements of this program will enable new cost-effective missions and allow enhanced competitiveness in world markets and with terrestrial alternatives.

A NASA/DOD/industry steering committee is intent on forging a new government/-industry relationship that results in benefit to both and minimizes the liabilities. The hope is to create in the space business a government/industry relationship similar to that found in the aeronautical business. The challenge (and the vision) is to construct a program that allows individual organizations to develop and validate critical technologies by judiciously using government, IRAD, and some corporate funds and to maintain their proprietary rights thus enhancing both their intraand international competitiveness. All parties can win, and the world can benefit from the successful conduct of this program.

Support for this new NASA initiative, Spacecraft 2000, is growing in industry and in government. The next year will be important, as the 1986 workshop will provide the technological foundation and the basis for government/industry relationships. The multifaceted advocacy can then be undertaken that could result in a new initiative as early as 1989.

We believe the Spacecraft 2000 initiative addresses the major needs and technological drivers for the spacecraft of the 21st century. We all must work together to bring this vision of the future into being for the national best interest.

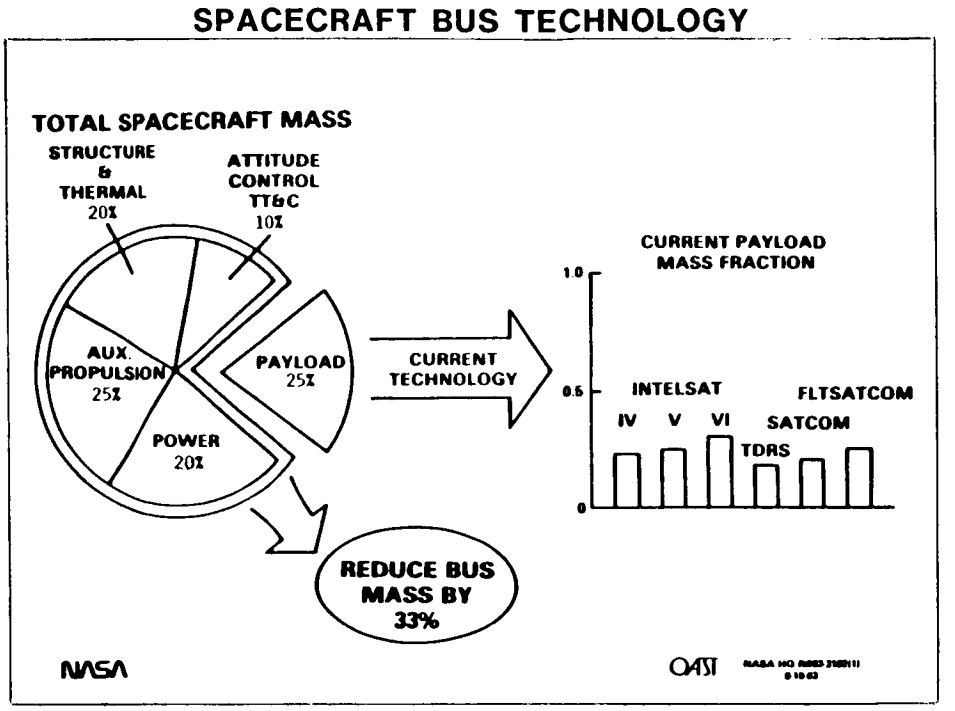

Figure 1.

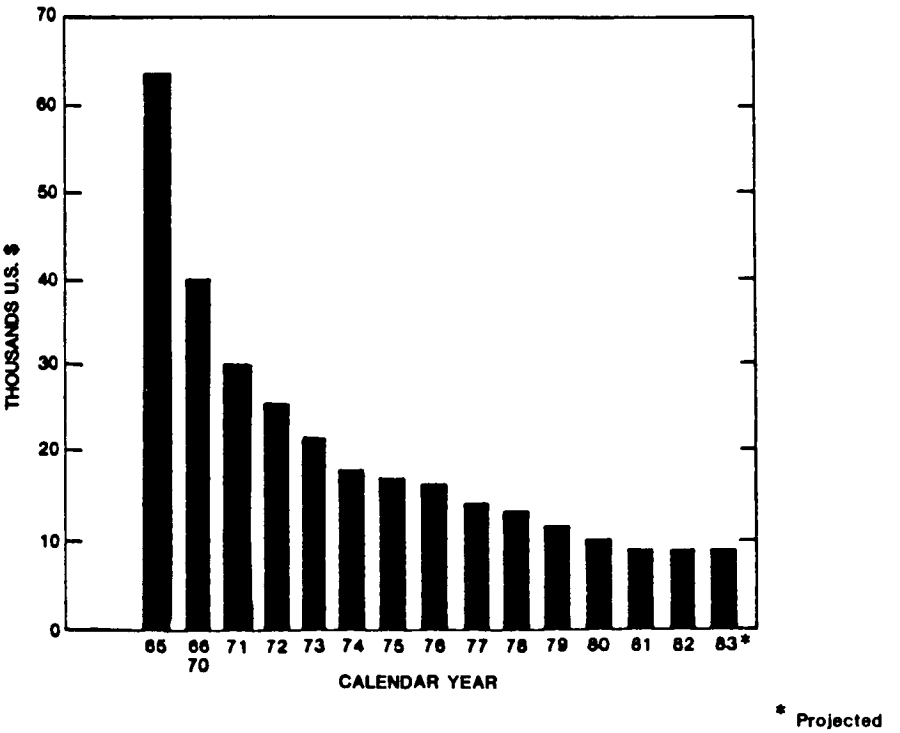

Figure 2.

SPACECRAFT 2000 INDUSTRY VISITATIONS

GENERAL ELECTRIC

FAIRCHILD CORPORATION

FORD AEROSPACE CORPORATION

LOCKHEED MISSILES AND SPACE CORPORATION

TRW INCORPORATED

ROCKWELL INCORPORATED

HUGHES AEROSPACE CORPORATION

RCA ASTRO DIVISION

COMSAT CORPORATION

Figure 3.

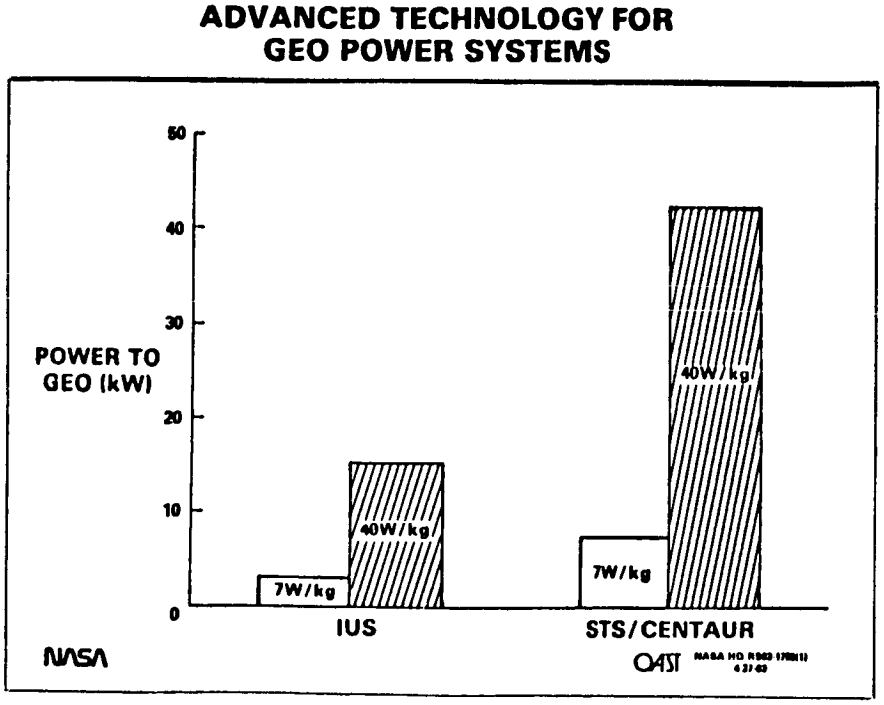

Figure 4.

ADVANCED GEO POWER SYSTEM TECHNOLOGY

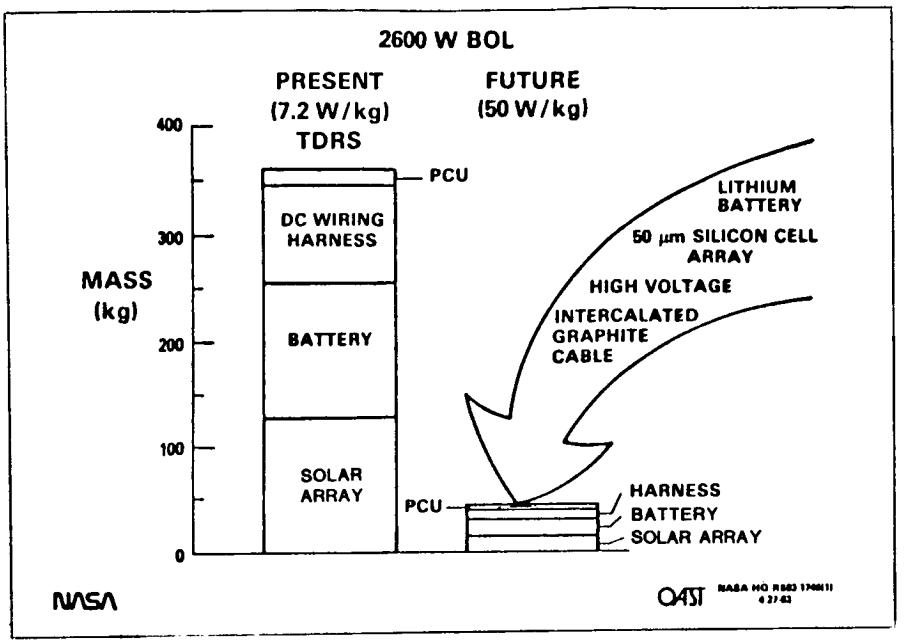

Figure 5.

EUROPEAN SOLAR ARRAY TECHNOLOGY

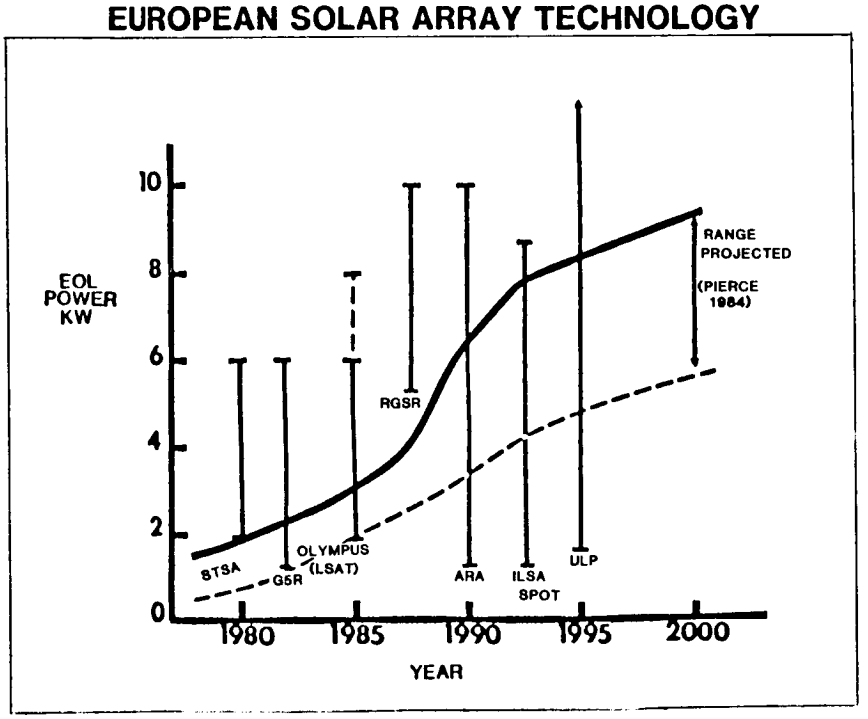

Figure 6.

SPACECRAFT BUS VOLTAGE

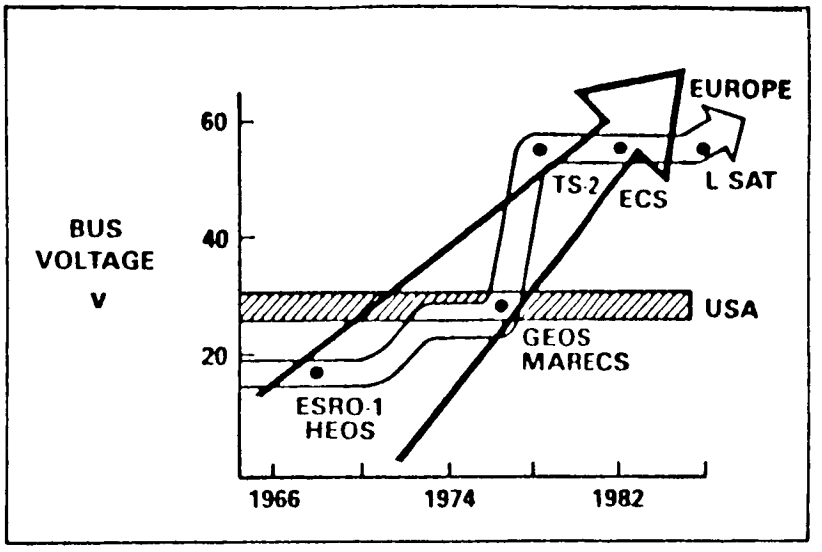

Figure 7.

ELECTRIC PROPULSION PROGRAMS

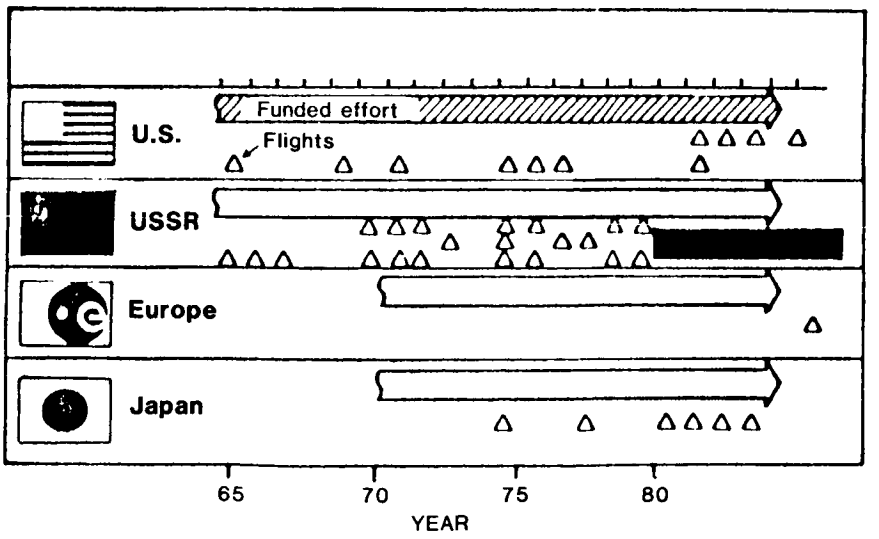

Figure 8.

ELECTRODYNAMIC TETHER

Michael Patterson
NASA Lewis Research Center
Cleveland, Ohio

An introduction to Electrodynamic Tethers and the NASA program in this area is offered via an agenda of five topics:

a. Tether Applications in Space (TAS) Program
b. Mechanical Considerations on Tethered Satellite Systems
c. What is an Electrodynamic Tether System?
d. Ground Tests and Theoretical Studies
e. Flight Demonstrations, Current and Planned

The purpose of the presentation was to introduce the program, players, and basic concepts to the noninitiated. Applications of the tether concept are rapidly growing in sophistication and complexity. An international program involving the governments of the United States and Italy is currently under way. A major experiment/demonstration, the Tethered Satellite System (TSS-1) is being built to demonstrate the following:

a. Deployment and Control Dynamics
b. Electrodynamic Power Generation

Other experiments planned, including a tethered wind tunnel to explore the more difficult to reach regions of the Earth's atmosphere.

Tethers hold promise for a variety of useful space applications. Electro-dynamic tethers depend upon the interactions between a moving insulated conductor and the Earth's magnetic field. An electric field is generated along the tether as in a conductor moving in the magnetic field of a generator. If the circuit is closed to the ambient space plasma via a plasma gun or other equivalent device, a current is enabled to flow in the tether, and electric power is generated at the expense of orbital mechanical energy. The net effect is a decrease in the altitude of the orbiting tethered system. The situation can be reversed by driving current against the electric field via an external power supply such as a photovoltaic array. In this case, the electrical energy delivered by the external supply is converted into orbital mechanical energy, the net effect being an increase in the altitude of the orbiting tethered system. Further details of this process and the means for closing the circuit to the ambient space plasma were presented.

GaAs HIGH EFFICIENCY LIMITS/GEOMETRIC ENHANCEMENTS

Mark Spitzer (Workshop Chairman)
Spire Corporation
Bedford, Massachusetts

This workshop addressed efficiency improvements that may be obtained in GaAs solar cells. The cell designs considered by the group ranged from conventional planar structures to novel devices employing superlattices or point contacts. This review will summarize the topics considered and will conclude with recommendations.

PLANAR CELLS

Planar GaAs cells have achieved AM0 efficiency of over 21% and the group consensus was that somewhat higher efficiency might be obtainable. The optical losses may be reduced by surface texture and by using low-obscuration metallization. Recombination may be reduced by improving the hetero-interface and space-charge region. It was pointed out that the Lincoln Laboratories' AlGaAs-GaAs heterojunction cell yielded a high diode ideality factor and a fill factor of 0.87. It would be interesting to determine how such fill factors can be obtained in heteroface cells.

The group discussed the manner in which the conversion efficiency of production heteroface cells might be improved. Reduction of window layer thickness was cited as a factor that would improve ones ability to form high quality antireflection coatings on LPE cells. The GaAs-on-Ge approach was cited as a way to improve the power-to-weight ratio. Simplification of the production process was also identified as a desirable goal. Such simplification might be obtained by eliminating the need for buffer layers prior to epitaxy. It was suggested that a further simplification would be obtained if the window layer could be grown directly on the substrate, which would form the base.

POINT-CONTACT AND OTHER IBC APPROACHES

Both Si and GaAs back contact designs were discussed. The radiation sensitivity is an especially important factor for such cells and it was agreed that more radiation testing and modelling are needed. It is generally assumed that concentrator systems provide enough shielding to circumvent radiation sensitivity; however, it was noted that this assumption may be invalid in many specific cases. It would therefore be useful to quantify what is meant by shielding in a concentrator system.

It was pointed out that back contact approaches are useful in III-V materials, owing to a need for co-planar, low shadow loss metallization. Structures of this type would be useful in thin-film approaches such as C.L.E.F.T. There was no consensus on the upper limit to the efficiency of point-contact GaAs cells, although

it was agreed that such cells could be at least as efficient as planar front junction cells. There was some evidence presented suggesting that point-contact and grating cells would be more efficient than planar cells.

SUPERLATTICE CELLS

The workshop considered several superlattice structures, including nipi and compositional approaches. It was agreed that a more fundamental understanding of such devices is necessary before an evaluation can be made. For the nipi approach, it is necessary to justify the assumptions of increased radiation hardness. The composition superlattice approach requires more data on optical properties. In both cases, practical problems in fabrication need to be considered.

RECOMMENDATIONS

There was a consensus that research on improved efficiency should continue. It would be desirable to have a plan for transferring laboratory results to production cells.

To better understand point contact cells, it is necessary to predict or measure performance in radiation environments. It is therefore recommended that the radiation environment within a concentrator be quantified for orbits for which concentrator systems are intended. Radiation testing and related modelling should be carried out to determine whether these cells have a role in space.

DEVICE MODELING

Richard Schwartz (Workshop Chairman)
Purdue University
West Lafayette, Indiana

This is the summary report of the activities of the device modeling workshop which was held as a part of the Space Photovoltaic Research and Technology Conference at the Lewis Research Center, October 7-9, 1986. A partial list of the participants in the workshop is attached as Appendix A.

The purpose of this workshop was to access the status of solar cell device modeling to see if it is meeting the present and future needs of the Photovoltaic Community working on the development of space solar cells.

During the course of this workshop the following questions were addressed:

1. How are present models being used?
2. What models are now available?
3. Why does one use finite difference, finite element or Monte Carlo methods? What problems are associated with each of these techniques?
4. Is the existing database adequate?
5. What additional experimental work is needed?
6. What additional theoretical work is needed?
7. How do you model superlattice devices?
8. Should dial-up access to detailed numerical models be provided?
9. Can or should detailed models be applied to radiation damaged studies?

Model Uses

Solar cell models find application throughout the cell development cycle. They are used as a design guide both for determining the factors limiting present performance of solar cells as well as providing comparison between competing solar cell designs. Models are used for performance prediction for cells which have not yet been built, operating under conditions for which they have not been tested. An example of this is the comparison of vertical junction cells, etched junction cells, conventional cells, and IBC cells, from one sun to a thousand suns, carried out for

Sandia using two dimensional silicon models. Models find extensive use in the analysis of experimental data. The more detailed and complex numerical models are frequently used to verify simpler analytic models to establish their validity and to establish the conditions under which the simplier models give valid results.

Types of Models

Analytic

In general analytic models are those for which sufficient simplifying assumptions have been applied such that closed form solutions to the equations can be found. These types of models have the advantage that they require relatively little computing time. The existence of closed form solutions allows for easy intuitive examination of the application of a model. The disadvantage is that, in many cases, the many approximations needed to reduce the complexity to the point where analytic solutions apply, has over simplified the problem to the point where significant effects have been ignored.

Numerical

Detailed numerical solutions require far fewer approximations, and hence, can deal with many physical effects simultaneously. This means that many of the interactions which occur in a solar cell can be modeled in some detail. One can expect to get excellent agreement between the model and experiments. Numerical models allow for a much more detailed physical description. On the other hand, they are usually far more complex than the analytic models, and as consequence, are less intuitive and certainly much more compute intensive.

Numerical Techniques

Finite Difference

Finite difference techniques are among the simplest way to numerically solve a set of simultaneous differential equations. However, they are, for all practical purposes, restricted to the treatment of solar cells which can be described by rectangular geometries. They are capable of computing current-voltage curves under light and dark conditions, spectral response, and can deal with a variety of spectra, under all conditions from low light intensity to one thousand sun conditions. They

provide a means of examining, in extreme detail, all of the operating mechanisms that are known to influence solar cell performance. The solutions are performed contact to contact. That is, they describe the entire operation of the solar cell without having to segment it into regions.

Finite Element

Finite element techniques are capable of handling non-rectangular geometries and would be useful for describing solar cells such as the V groove or polka dot cells. The finite element technique is one that is frequently employed in stress analysis. It is somewhat more complex than the finite difference technique, but, is capable of all the computations that a finite difference technique can handle.

Monte Carlo

The Monte Carlo formulation involves describing the operation of a solar cell at the particle level. It amounts to tracking the projectory of individual electrons and holes. It's a technique which can be employed to describe the operation of a device when hot carriers are present such as might occur when abrupt hetero structures are employed in the device design or when feature size becomes so small that classical drift and diffusion equations no longer provide an adequate description. The Monte Carlo technique is extremely compute intensive, and in general, requires very fast, very large computers or very long computer run times or perhaps both. One additional difficulty is that it involves twice the number of dimensions that either the finite difference or finite element techniques require, since one must use both real space and reciprocal space in the calculations. The technique is also not an efficient method of computing current flow through a PN junction. (It may be possible to find ways to circumvent this problem.) The Monte Carlo technique is applied only in those cases where other more conventional approaches break down. It is unlikely to be used for full contact-to-contact calculations or for the computation of current-voltage curves and spectral response as are finite difference or finite element technique.

What Are The Modeling Needs Of The Photovoltaic Community?

Two Dimensional (Three Dimensional)

There are a number of conditions under which two (or three) dimensional analysis are required. Cells which have non planar geometry such as a V groove, vertical junction, or point contact cells will require at least two dimensional and perhaps three dimensional models for an adequate description of their performance. Even conventional cells require two dimensional models when operated under high concentration.

Time Dependent Models

Time dependent models, that is those which are capable of modeling transient response, are useful for the analysis of some diagnostic experiments applied to solar cells in which a light or bias conditions are pulsed.

Other Materials

In addition to silicon and GaAs, other materials are being considerd for future application for space cells. These include a wide range of III-V materials as well as thin film materials such as amorphous silicon and $CuInSe_2$. The physics of operation of the thin film materials is significantly different from that of bulk silicon and GaAs single crystal materials. Models appropriate to thin film devices should be developed. Such models would serve as a useful aid in the design of these devices as well as in the selection of competing device designs and materials.

Database

Considerable discussion occurred as to the adequacy of the materials parameters database. Materials which were considered were silicon, III-V semiconductors, amorphous silicon-germanium and $CuInSe_2$. For the most part, an adequate database exists for silicon, and, with some noteable exceptions, for the III-V materials being considered for space applications. A possible exception is the data pertaining to InP. In the case of the amorphous silicon materials and thin film $CuInSe_2$, it was felt that the existing database should have considerable improvement. Among the materials parameters of interest are: the absorption coefficient, as a function of wave length,

composition, and doping; the bandgap is a function of composition and doping; the mobility is a function of composition and doping; and the recombination parameters. In the case of recombination centers, it's imperative to have information about density, energy level, and capture cross sections as a function of position, doping and radiation conditions. For Auger recombination, the auger coefficients need to be known. It was pointed out that a single parameter such as the surface recombination velocity is probably not adequate for very good device modeling, the surface recombination is a function of operating conditions and fabrication procedures.

Device Modeling Under Radiation Damage Conditions

Considerable insight and improvement in radiation hard solar cell designs should result from very careful detailed numerical modeling of solar cell operation in the presence of radiation damage. Some concern was expressed about whether or not enough information was known about the defect structure. Can the defects be characterized adequately with regard to energy levels, capture cross sections, and spatial distribution to be used in numerical codes? The existence of a model which could adequately handle radiation damage would be useful in the analysis of radiation damage experimental data, as well as in the design of radiation hard solar cells.

Superlattice Models

The modeling of superlattices as used in solar cells is in the very early stages. A great deal more work will need to be done before these models are useful in the design or analysis of solar cells.

Dial-Up Availability

It was felt that easy access to a detailed numerical code would be very useful, both for the solar design community, and for people tempting to verify the validity of simplier analytical models. However, some concern was expressed about having someone use these codes who was not expert in their use. Improper specification of input can lead to erroneous output.

Appendix A

Name	Company
Dean Marvin	Aerospace Corporation
Brian Good	NASA LeRC
Chris Kearney	Spire
Delores Walker	Naval Research Lab
Jerry Silver	Solarex Aerospace Division
Rosa Leon	NASA
Dick Statler	NRL
Gerald Crotty	JPL
Chandra Goradia	Cleveland State University
Tim Coutts	SERI
James R. Woodyard	Wayne State University
Allen Barnett	Univ. of Delaware
Edward Y. Wang	Arizona State University
Ralph Clark	Cleveland State University
Richard J. Schwartz	Purdue University

Executive Summary

A workshop on solar cell modeling was held at the Space Photovoltaic Research and Technology Conference on October 7, 1986. The conclusions of this workshop were as follows:

1. Solar cell models are a vital tool in the development of more efficient reliable and radiation hard solar cells, they find application throughout the entire cell development cycle.

2. While the silicon solar cell models are well developed for both one and two dimensional requirements, there is a need for further development of models which will handle non-rectangular geometries, such as those found in V groove cells and point contact cells.

3. Applications involving concentrator cells and new cell designs, such as the point contact cell, will require two and even three dimensional modeling for the efficient design of these cells.

4. The prospects for using new materials, such as InP and amorphous silicon for space applications, requires that existing models be extended to these materials. Since physics of operation of thin film amorphous cells is significantly different from that of single crystal cells, extensive model development will be required.

5. An opportunity exists in the design of radiation hard solar cells and in the prediction of their degradation due to radiation damage for the coupling of known radiation damage mechanisms with existing detailed numerical models. It is expected that development of radiation damage models using detailed numerical code would allow for comparison of competing designs and accurate prediction of the degraded properties of radiation damaged cells.

6. Modeling of superlattice solar cells is in the very early stages and will require considerable work before these models can be used reliably for solar cell design.

HIGH POWER/LARGE AREA PV SYSTEMS

Joseph Wise (Workshop Cochairman)
AF Wright Aeronautical Laboratories
Wright Patterson AFB, Ohio
and
Cosmo Baraona (Workshop Cochairman)
NASA Lewis Research Center
Cleveland, Ohio

New power requirements in the 50 to 100kW range will be needed prior to the year 2000. The photovoltaic power system option should be developed to meet these needs because of the PV System's proven record for long life, performance, and reliability with no single point of failure in a matrix of series and parallel connected solar cells and modules. In addition, the PV system has high potential for increased efficiency and survivability as well as lower weight and cost.

The workshop generated and ranked the major technology drivers for a wide variety of mission types (see Table 1). Each technology driver was ranked on a scale of high, medium, or low in terms of importance to each particular mission type. The rankings were then compiled to determine the overall importance of each driver over the entire range of space missions. In each case cost was ranked the highest. This led to the general concensus that system cost is the most important driver for high power PV systems.

Each mission also requires different critical capabilities from the solar array. Weight is of paramount importance to high altitude missions while others may be driven by the needs for survivability, radiation resistance, minimum drag, or low cost. For these reasons it is felt that two major photovoltaic solar array developments are required - lightweight planar solar arrays for minimum weight and area for low cost high orbit insertion and concentrator array technology for improved survivability and radiation resistance as enabling technology for survivable mid-altitude orbit missions as well as lower cost technology in the application of very high efficiency solar cells. These developments must be accompanied by improvements in electrical energy storage and power processing to minimize the weight of the entire power system. There are several solar cell concepts currently under consideration in research and development. Because of the long process needed to gain acceptance for a new or modified solar cell type, we must choose carefully which one or two have sufficient promise and improved performance to merit the large resources needed to reach technology readiness and producibility.

The developments needed to exploit the lightweight planar solar array potential are shown in Figure 1. This starts with the development of thin high efficiency cells and definition of solar array concepts and designs which can support these cells for high power missions. As power levels increase the need for modularity and on-orbit assembly becomes greater because the complete satellite may not be put into orbit in a single launch vehicle and on-orbit assembly is required. Also, because high power missions represent a large investment, provisions for maintenance and servicing will need to be incorporated in new system designs. As power levels increase, the voltage at which power is generated, transmitted, and utilized must also be increased. This increases the probability of interaction with the

space environment such as leakage to the plasma, arcing due to charge buildup, and contamination of array surfaces. Also, new cell types such as GaAs and InP have demonstrated the ability to recover performance degraded by particulate radiation through relatively low temperature annealing. This capability should be further investigated and exploited in solar array design for operation in high radiation orbits.

Development of concentrator photovoltaic arrays requires more design and testing since it is a new development without prior flight experience, and the performance required from them is greater. The developments and tests needed are shown in Figure 2. The pointing requirements are in the neighborhood of ±1 degree which is certainly within the state of the art of pointing and tracking systems. Difficulty may arise, however, in keeping a very large area array (5-10 sq. meter/kW) oriented to this accuracy when warping or thermal effects cause bending or distortion of the panels. Also, the concentrators are expected to provide shielding to increase survivability from natural and threat irradiation exposure. These effects need to be modeled and tested. The resultant hardware designs need extensive ground testing such as thermal cycling. They also need space flight testing to determine interactions with the orbital environment, especially plasma and contamination from debris associated with large space vehicles - dust, effluents from altitude control and propulsion thrusters. One of the techniques needed for survivability is autonomy - independence from ground station control. This is a new technology that is just now being investigated. It is more likely to be incorporated into second generation concentrator array technology. One of the more important attributes of concentrator arrays is their potential for high efficiency at low cost because the cell area is only about 1% of the collector area of the array. Thus the cell costs associated with the greater number of processing steps needed for high efficiency multibandgap solar cells are minimized. Each of these new cell types may require customized interconnect, mounting and cooling assemblies to operate for extended periods in space. This also may be second generation technology.

It is apparent that all of the effort outlined in the previous two figures cannot be accomplished instantly and not necessarily in single programs. They are, therefore, divided into three major thrusts as shown in Figure 3. The design concept development is the R&D needed to implement a high power array for a specific vehicle configuration and should be undertaken when the orbit, mission, and potential vehicle characteristics can be specified.

The operational issues cited are for the development and testing needed to intelligently design a high voltage, high power solar array. Defining them involves close work with environmental specialists in modeling of environmental interactions with various hardware configurations and flight testing to both measure the environmental species present and their interaction with the experimental array hardware.

The cell module design and development is that work needed to demonstrate that a particular cell type can be applied to a solar array concept, planar or concentrator. This includes determining the radiation resistance, thermal characteristics, and performance parameters of the cells and fabrication and testing of modules utilizing these cells. Under this thrust we need to choose which concepts should be developed for thin large area, high efficiency cells for planar applications and which are suitable for concentrator applications. These module developments need to be compatible with the large array design concepts but are not necessarily a part of the large concept developments.

TABLE 1

Importance of Technology for High Power Missions

Mission Type

Technology Driver	Electric Propulsion	Planetary	GEO	LEO	Surveillance	Total Pts.
Cost	1	1	1	1	1	5
Conversion Efficiency	2	2	1.5	1	1	7.5
Weight	1	1	1	3	2	8
Environmental Interactions	1	2	2	1	2	8
Heat Rejection	2	2	2	2	1	9
Life (reliability 5-10 yr/maintenance in LEO)	2-3	1	1	3	2	9.5
Military Survivability	3	3	2	1	1	10
Array High Voltage	1	2.5	1	3	2-3	10
Robust	2	2	3	1	3	11
Radiation Resistance	1	3	3	3	1.5	11.5

Technology Ready by year 2000

Importance Scale:
1. High
2. Medium
3. Low

Ranking:
1. Cost
2. Efficiency
3. Weight & Environmental Interactions

DEVELOPMENT NEEDED FOR LIGHTWEIGHT PLANAR ARRAYS

- THIN HIGH EFFICIENCY CELLS
- DEPLOYMENT, STOWAGE CONFIGURATION (DESIGN CONCEPTS)
- ASSEMBLY APPROACHES
- MODULARITY
- 300 W/KG
- LOW COST CELL TECHNOLOGY
- $300/WATT ARRAY LEVEL
- ON ORBIT MAINTENANCE ROBOTICS
- 200 W/M^2
- ENVIRONMENT CONTROL EFFECTS
- HIGH VOLTAGE
- THIN CELL COVERS
- ANNEALING GaAs, InP

FIGURE 1

DEVELOPMENTS NEEDED FOR CONCENTRATOR ARRAYS

- SURFACE POINTING
- ENVIRONMENTAL SURVIVAL TEST PROGRAM
- UNDERSTAND ENVIRONMENTAL EFFECTS
- STOWAGE, DEPLOYMENT 5-50 KW
- DESIGN FOR ORBIT/FLIGHT PATH
- HIGH EFFICIENCY CELLS, OPTICS
- THERMAL ENVIRONMENT
- EXPERIMENTAL FLIGHT
- DESIGN FOR HIGH VOLTAGE
- ELECTROSTATIC EFFECTS
- THREAT ENVIRONMENTS
- MINIMUM WT. & END OF LIFE
- POWER SYSTEM INTERFACE
- AUTONOMOUS CONTROL
- ELECTRIC ENGINE STORAGE

FIGURE 2

TECHNOLOGY THRUSTS - THREE MAIN THRUSTS

- 0 DESIGN CONCEPT DEVELOPMENT
  - LAUNCH SCENARIO
  - STOWAGE, ASSEMBLY, DEPLOYMENT, ORIENTATION, POWER THRUST, AUTONOMOUS CONTROL, VEHICLE INTERACTIONS, STRUCTURE, MATERIALS, TECHNOLOGY
- 0 OPERATIONAL/ISSUES
  - LIFE, RADIATION, ENVIRONMENTAL DEBRIS, O_2, CONTAMINATION, THERMAL CYCLING, MISSION CONSTRAINTS
- 0 CELL MODULE DESIGN AND DEVELOPMENT
  - EFFICIENT EOL WEIGHT, RADIATION RESISTANCE
  - COST, THERMAL EFFECTS
  - GROUND/FLIGHT TESTS
  - LARGER CELL/MODULE SIZE
  - NEW APPROACHES OF DESIGNS
  - THIN SYSTEMS, THIN MBG A-SI, GAAS ON GE, CLEFT

FIGURE 3

OPPORTUNITIES FOR PV APPLICATIONS

John A. Scott-Monck (Workshop Cochairman)
Jet Propulsion Laboratory
Pasadena, California

and

W. Patrick Rahilly (Workshop Cochairman)
The Aerospace Corporation
Los Angeles, California

Rather than dwell on the obvious future applications that could be satisfied by photovoltaics (PV), the workshop members devoted the majority of the time to discussing future prospects for technology support. PV has provided power for almost every spacecraft launched in the free world during the past 25 years. Over this time, PV has demonstrated impressive growth in power level, operating lifetime and specific power (W/kg and W/m^2). Yet, the current attitude toward this reliable form of space power generation is likely to preclude further dramatic performance gains in PV.

CURRENT STATUS

This paradoxical situation has been largely brought about by the success that PV has enjoyed. The tremendous increase in spacecraft traffic and their very high unit cost has occurred in part because a reliable power generation approach, PV, has been demonstrated and proven in space. However, in order to reduce the risk involved in operating a high cost spacecraft, decisions on the subject of new PV technology are mostly resolved in favor of heritage rather than performance. This management approach has acted as a brake on PV progress at the spacecraft level, thus leading to the current unfavorable perception of PV.

The perception of PV at the organizational levels where technology support decisions are made seems to be that it is a mature technology with limited growth potential. In turn, this has caused attention to be given to unproven space technology competitors such as nuclear reactors and solar thermal dynamic systems. This perception has led to a severe decline in funding support for PV with no clear indications that the trend will be reversed in the immediate future, a self-fulfilling prophecy.

Because these competing power generation approaches have not yet operated in space, it is relatively easy for their proponents to forecast performance characteristics that are significantly superior to the state-of-the-art PV systems now powering operational spacecraft. Here, too, the success of PV acts to prevent its proponents from optimistically projecting performance characteristics that meet the forecasts of the competing systems because there is an existing base of sound information available for PV performance forecasting. Unfortunately, the decision maker has no way to factor in the inherently conservative attitude of the users of space PV which has acted to significantly reduce the rate of progress that PV has demonstrated in space.

Another trend that acts to further handicap progress involves the DOD, a major supporter of PV technology. DOD PV requirements, which in the past closely matched those of NASA, have diverged significantly as the result of survivability concerns. Thus, space PV research has lost most of the benefits that common NASA and DOD objectives provided.

Future DOD requirements, driven by the SDI, are for operational power levels orders of magnitude greater than today's PV systems. This unquestionably justifies the pursuit of non-PV power generation options. It does not, however, justify the opinion that solutions to ultra-high space power needs can be automatically translated to significantly lower power levels. Unfortunately, this attitude seems to be gaining some degree of acceptance, further reducing advocacy for a viable PV program.

SURVIVING THE NEXT DECADE

Although the current situation is distressing, the workshop members agreed that PV has a future for providing the power for such ambitious objectives as geosynchronous platforms, electric propulsion, growth Space Station and a lunar base. Thus, the issue becomes one of sustaining the PV infrastructure which includes the space solar cell suppliers, NASA and DOD organizations that provide funding for the development of advanced PV and the cadre of dedicated researchers who develop the technology.

There is no doubt that at this time PV technology contains more options, with respect to solar cell materials, for significantly enhancing space power performance than have existed since the demonstration of the solar cell. This is due in part to the substantial commitment of resources made by the DOE in the area of PV. The technical momentum generated by the recent emphasis of terrestrial research on high efficiency has provided a major infusion of ideas and technical talent into space PV. It is essential that this be encouraged.

Unfortunately, current resources devoted to space PV research and technology development cannot provide the proper level of support necessary to bring all the emerging cell technologies such as GaAs, cascade, InP and amorphous silicon to technical readiness. Priorities must be established to maximize the impact of the relatively limited funding likely to be available for space PV in the next five to ten years.

There are a number of ways this might be accomplished. NASA and DOD could agree that each would only fund one cell technology to avoid redundant support. There could be cooperative ventures between DOE and NASA or DOD to accelerate a particularly promising cell technology. Space PV support agencies could leave PV cell development to the DOE and concentrate on testing and evaluation of DOE developed technology. All solar array and systems associated development could be eliminated and all resources devoted to advanced solar cell technology.

Assuring that the cell suppliers survive this bleak period is a more challenging problem. Its solution involves the realization by NASA and DOD that their present research and development policies will lead to either a virtual monopoly or no U.S. supplier of space-qualified solar cells. The current situation with respect to GaAs solar cells is a classic example of what can occur when a particular organization is funded externally in order to supply an advanced solar cell. Solar cell suppliers

cannot be expected to bear the burden of transferring new technology since the nature of the space PV market does not allow for a high, constant profit margin. Unless serious attention is given to this situation, it is very possible that foreign suppliers of space-qualified solar cells will be the only option available when PV once more is required to demonstrate its ability to grow in response to space power needs.

A major objective that should be strongly supported by the PV community is developing a realistic strategy that does three things. In proper sequence, it is necessary to: (1) develop and implement an approach to rapidly translate technology from the laboratory to the supplier, (2) provide regular opportunities to verify the reliability of new PV technology in space, and (3) spread out the risk or responsibility for employing new PV technology in flight programs.

The responsibility for developing this strategy should be shouldered by those NASA and DOD organizations involved in supporting PV research and technology development. If this challenge is met, then PV will be properly postured to exploit the opportunities that can exist in the 1990s.

AN OPTIMISTIC SCENARIO FOR THE 1990s

For at least the next five years, power generation options such as nuclear reactor and solar thermal dynamic systems will continue to receive the attention and funding support warranted by their potential. If they succeed in demonstrating their projected performance levels, then the deemphasis of PV technology will have been a correct decision. However, if they show signs of failing to fulfill their promise, attention will once more be directed to PV.

PV will become the only means to support most of the mission commitments now being made on the assumption that alternate, high performance power systems will become a reality. Among these commitments will likely be geosynchronous platforms requiring perhaps 50 kW_e for periods up to ten years, a growth Space Station that needs 300 kW_e for an indeterminant length of time, electric propulsion which could require 100 to 500 kW_e of power that can survive years in the extremely high radiation environment located between LEO and GEO orbits and a lunar base dependent on a central power station that can deliver a magawatt.

What aspects of technology should be emphasized now in order for PV to be in a position to justify the level of support required in the 1990s to sustain the ambitious plans described previously? The workshop members concluded that the ultimate driver is cost.

Cost advantages can be manifested in many ways when considering the PV option. High efficiency translates to a cost advantage in the case of the growth Space Station where orbital induced drag is of paramount importance. Radiation resistance and low weight translate to a cost benefit in the case of long lived geosynchronous platforms and electric propoulsion vehicles used to transfer payloads out of LEO orbit. Weight and operational lifetime mean cost advantages for a lunar central power station. Reliability is perhaps the ultimate cost advantage. Here PV has no competition and can argue its case on flight history and, hopefully, information obtained from flight experiments.

Thus, it is the opinion of the workshop members that no one particular PV technology should be emphasized at this time. However, the fact that a number of

viable options exist to meet the various cost associated PV criteria, such as efficiency, weight and radiation resistance, supports the view that PV has a good chance to retain its role as the primary source of power for space missions well into the 21st century.

C-5

InP MATERIALS/CELL FABRICATION

T.J. Coutts (Workshop Chairman)
Solar Energy Research Institute
Golden, Colorado

This report describes the main points of discussion, conclusions, and recommendations of the Workshop on InP held at the NASA SPRAT conference. An unusual level of interest in this workshop was shown with 37 delegates being in attendance. The names, affiliations and telephone numbers of these persons are shown in Appendix I.

The meeting commenced with a presentation by the chairman (T.J. Coutts), of issues he believed are central to the development of InP as a solar cell absorber. The object of this was to stimulate subsequent discussion in the anticipation that the topic may be relatively unfamiliar to most of the attendees. A copy of all slides used in the chairman's presentation is given in Appendix II. The key points emerging from the workshop were summarized on the final morning of the conference. The viewgraphs used for this presentation are also appended.

I. Chairman's Presentation

It is considered that it will become important to assess the quality of p-InP crytals supplied by different vendors, whether they are to be used as an active part of the device or as a substrate for the growth of epi-layers. At present very few manufacturers will deliver moderately doped (10^{15}-10^{17} cm^{-3}) p-type material. Only five have been found so far (slide 4). At SERI, the analyses shown in slide 5 can now be routinely performed and the capabilities are being extended systematically. Examples of photoluminescence (PL) measurement of minority carrier lifetime and its variation with impurity concentration are shown in (slides 6 and 7). PL has also been used to assess

the effect of low power rf plasma exposure of substrates and typical spectra are shown in slide 8. Cathodoluminescence (CL) has also been used to examine the surfaces of freshly prepared substrates. Slide 9 shows the presence of many non-radiative defects. In future, attempts will be made to profile the depth distribution of the defects and to minimize their density using different preparation/conditions. It is also planned to use high resolution cross-sectional transmission electron microscopy using a newly acquired ion-milling machine.

The issue of back contacts to solar cells is one frequently ignored by researchers, but in reality it is of great importance. In slide 10 the obvious parameters influencing the contact resistance are shown and in slide 11 the areas which, it is considered, should be studied. Such investigations are now well underway at SERI and initial results are beginning to clarify the changes shown in slide 12. The nature of the junction formation was then discussed and a review of substrate cleaning techniques was presented; see slides 13, 14, 15. Generally, the effectiveness of cleaning techniques is not quantified, but the group at SERI (under NASA support) is currently using monochromatic ellipsometry (in-house) and spectroscopic ellipsometry (in conjunction with D. Aspnes of Bell Labs) to investigate native oxides and surface roughness. An example of native oxide growth after cleaning is shown in slide 16. Using techniques developed more recently, residual oxide thicknesses have been reduced below 10 A. Slide 17 shows the Raman spectrum (performed by F. Pollack's group at Brooklyn College) of a freshly polished substrate. The line width indicates minimal surface damage and residual strain. Hence, is seems possible that substrate preparation techniques are adequate to produce reasonable devices, but the CL study shows that there is room for improvement in substrate quality.

Techniques for junction formation were then discussed and it was pointed out that the largest values of V_{oc} had been achieved by the group at Arizona State University, using a p- on n-substrate; slides 18, 19. A photoreflectance spectrum of an ITO/InP junction prepared by (ion-beam) sputtering is shown in slide 20 (obtained at Brooklyn College), and the sharpness of the features again indicates that reasonable quality devices are being made.

Techniques like this should be applied by other workers using different fabrication methods.

An estimate of the maximum probable AM1.5, 100 mW cm^{-2} efficiency was then made (slide 21). This was 23%; i.e., approximately equal to that of GaAs devices. It was pointed out that further improvements will probably depend on the development of cells grown by OMCVD. SERI and several other groups are now investigating this possibility. Technological aspects of optimized gridding and AR coatings were then discussed (slides 23, 24, 25, 26). SERI has put considerable effort into these topics over the duration of the NASA contract and it is expected that this ground work will be very valuable when good quality junctions are being produced. Slide 28 shows a summary of the highest efficiencies reported in the literature for InP based cells.

Finally, in slide 29 other issues were raised. Not least of these is the question of reporting efficiencies accurately. It was emphasized that there is a great need to report AM0 data for cells of realistic area and under well defined experimental conditions; and to report only total area efficiencies. Issues were also raised on the reliability of radiation resistance data; on the cost of InP (this is falling, but needs to fall much further), and on the chemical stability of significant interfaces. Under the category "Others", issues related to increasing the power/mass ratio, utilizing concentrator systems, the use of non-InP substrates for epi-films etc were raised. Discussion of these will be left until the end of the report on the main points emerging from the workshop conversations, subsequent to these opening remarks by the chairman.

II. Workshop Discussions

2.1 Need to Increase Efficiency of InP Based Cells

At present, the highest efficiency reported for an InP based cell is around 15% (AM0). This is based on a calculation performed by I. Weinberg of NASA Lewis Research Center on a result reported by the Japanese group at N.T.T. Although 15% is very encouraging, the device cannot really be taken seriously until substantial improvements have been made; despite its excellent radiation resistance. There is scope for improvement in J_{sc}, V_{oc} and fill-

factor, but particularly in the first two of these. The largest value of AM1.5, 100 mW cm^{-2} reported is 27.7 mA cm^{-2} (ITO/InP discussed by Coutts at this meeting). From the spectral response of this cell it was calculated that J_{sc} at AM0 would be 33.5 mA cm^{-2} which for an 8% grid coverage, translates to 36.5 mA cm^{-2} active area. With improved gridding and AR coating, an upper limit of 37 mA cm^{-2} would seem realistic, for the total area. This is equivalent to 90% x the maximum theoretical value which is comparable to that achieved for more mature technologies.

There was extensive discussion about the maximum achievable V_{oc}. Finally a value of 0.7 x E_g = 945 mV was agreed upon, again by comparison with GaAs. The highest V_{oc} reported to date is 845 mV (by Shen et al, at this meeting) so, as with J_{sc}, there is an estimated improvement of about 10-12% to be made.

If such an improvement in V_{oc} were made there would also be a significant gain in FF, and an estimate of 85% was made for the practicable maximum. Hence, the participants of the workshop believed that a well-funded program on InP cells could ultimately lead to an AM0 efficiency of 21.7%. This rather startling figure caused a reconsideration, based on intuition, and one or two participants felt that 20.5% was perhaps a more realistic target. Earlier in the meeting, Goradia had made a similar prediction.

2.2 Means of Improving Efficiency

Although InP is usually believed to have a low surface recombination velocity, it was suggested that passivation would nevertheless, lead to further significant gains in V_{oc}. A lattice matched ternary window layer to InP, analogous to AlGaAs/GaAs, is a possibility, and one which may be appropriate is AlAsSb. The disadvantage of this material is that it may be difficult to grow an abrupt AlAsSb/InP interface. Assuming that the devices are ultimately based on epitaxially grown InP, the transition to AlAsSb will of necessity be more demanding than that from GaAs to AlGaAs. Considerable effort has been made to passivate the surface of InP with various insulators for MISFET's. Varying degrees of success have been achieved and this is another area worth studying in the present context. It may, for example, be possible to fabricate devices based on the PESC design used for Si cells.

Advances could also be made using deeper junctions but this would necessitate a substantial improvement in the materials properties and, in particular, in the minority carrier lifetime. Improvements in material quality of substrates were also believed to be important and the need to characterize crystals supplied by different vendors was emphasized.

Finally, there are substantial improvements to be made in efficiency merely through better gridding and A.R. coatings. The internal quantum efficiency of many devices is already high, but substantial losses result from lack of attention to processing aspects.

2.3 Efficiency Measurements

At present, efficiencies quoted in the literature tend to lack any standardized form. Worse, it is not always clear whether a particular measurement refers to AM0, AM1, AM1.5 or some other air mass number, what simulator was used, whether total or active area was used, and what the measurement temperature was. Hence, workers in the field are encouraged, at least, to specify their measurement conditions accurately. A further preference was expressed that measurements should all refer to AM0, since these cells are more likely to be used for space, rather than terrestrial applications.

Finally, the view was expressed that data would be much more significant if larger area devices were made. Clearly, much greater inaccuracies result for small area cells. An acceptable area was, however, not defined, but areas greater than 0.3 cm^2 are to be preferred.

2.4 Radiation Testing

The present high level of interest in InP based cells results from their excellent radiation resistance. It is necessary, therefore, that these results (mainly of the Japanese group) be confirmed. It is also necessary to perform the radiation tests on devices of as high efficiency as are available. This is particularly relevant since there are indications that radiation resistance may be a function of impurity concentration, which in turn influences efficiency. Hence, it may be that high efficiency and high radiation resistance are mutually exclusive.

In this context, radiation damage models should be developed to identify the defects leading to degradation, and to account for the apparently high radiation resistance.

This has also raised the issue that there may be materials with even greater radiation resistance than InP. Might it be possible to predict these in advance rather than devoting years of study to a less than optimum material?

2.5 Future Developments

At some point it will be necessary to increase the power/mass ratio of these cells. To date, only cursory studies have been made and it may be advisable to initiate more thorough systems studies at an early date.

Since cost is of pre-eminent importance (as stressed by J. Scott-Monck in the final workshop presentation of this conference) a reduction in the cost of InP is necessary. Early consultations with substrate suppliers could therefore be advantageous and could lead to forecasts of cost/supply. Alternatively, studies of InP growth on other low cost substrates would seem to be a promising area, even if technically complicated. CLEFT studies could also lead to cost reductions and, funding permitting, should be pursued.

Finally, concentrator studies should be initiated with a view to determinign cost and system design considerations. This could include determining the optimum concentration ratio, the reduction in radiation damage by the concentrator optics etc.

Appendix I — Attendees at InP Workshop

Attendees	Affiliation	Phone No.
Tim Coutts +*	SERI	(303) 231-1261
Kou-I Chang	ASEC	
Paul R. Aron	LeRC	
Ruth A. Narayanan	Hughes	(213) 317-5076
James B. McNeely	Astropower	(302) 366-0400
Gerry Negley	Astropower	(302) 366-0400
John Stupica	Cleveland State Univ.	
Mircea Faur	Cleveland State Univ.	(216) 687-3537
George Mazaris	NASA Lewis	(216) 433-2227
Ralph Thomas	NASA Lewis	(216) 433-2293
Hans Rauschenbach	TRW	(213) 535-7790
James Geier	Cleveland State Univ.	
Roger Gillette	Boeing	(206) 773-9802
Russell E. Hart Jr.	NASA Lewis	(216) 433-2233
Lan Hsu	Rockwell	(213) 594-3687
Kwan-Yiu Choi*	Arizona State Univ.	(602) 965-2924
Clifford Swartz	NASA Lewis	(216) 433-2232
E.Y. Wang	Arizona State Univ.	(602) 965-3749
R.W. Hoffman Jr.	Svendrup/LeRC	(216) 433-2235
Gerald Cootty	Jet Propulsion Lab	(818) 354-6500
Dave Lillington	Spectrolab Inc.	(818) 365-4611
Allen Barnett	Univ. of Delaware	(302) 451-8784
C.C. Shen	Arizona State Univ.	(602) 965-4456
Robert Y. Loo	Hughes Research Lab	(213) 317-5593
Ram Kachare	Jet Propulsion Lab	(818) 354-4790
Mark Spitzer*	SPIRE	(617) 275-6000
Irv Weinberg*	NASA Lewis	(216) 433-2229
Stan Vernon	SPIRE	(617) 275-6000
Wayne Anderson	SUNY-Buffalo	(716) 636-3109
Jose M. Borrego*	Rensselaer Polytechnic Institute	(518) 266-6684

Tim Gessert	SERI	(303) 231-1870
Anne Arrison	NASA Lewis	(216) 433-2238
Mark Wanlass	SERI	(303) 231-7632
Frank Junga	Lockheed R&D	(415) 424-2227
Chris Keaney	SPIRE	(617) 275-6000
Delores Walker	Naval Research Lab	(202) 767-2446
Richard Statler	Naval Research Lab	(202) 767-2446

37 Attendees

+Chairman

*Paper presented on InP (paper on InP also presented by Chandra Goradia of Cleveland State University).

RELATIVE RADIATION RESISTANCES OF Si, GaAs, and InP HOMOJUNCTION CELLS

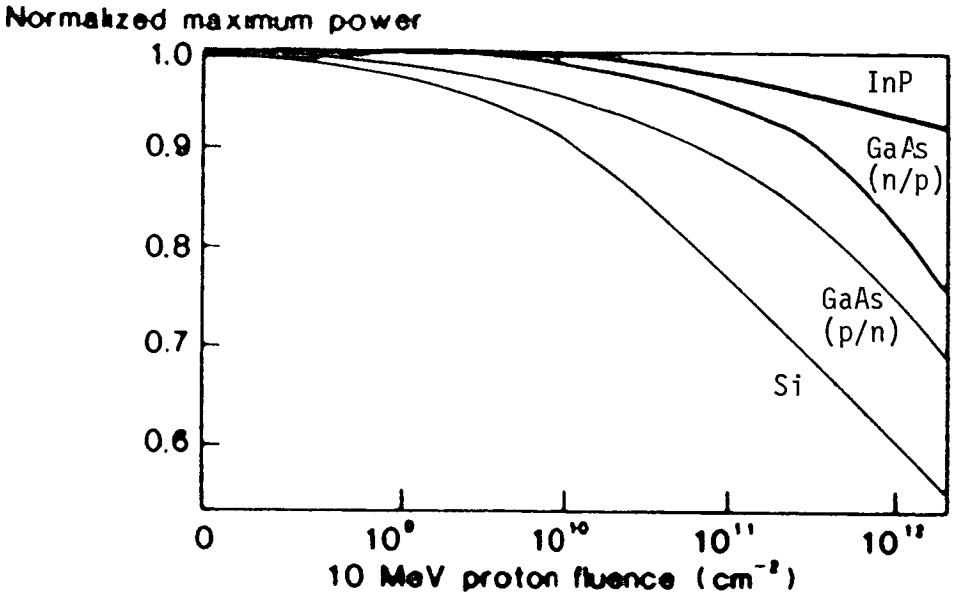

Source: Weinberg et al, IEEE Photovoltaic Specialist Conf., Las Vegas, 1985

Slide 1.

Objectives

- To assess existing knowledge
- To identify areas of limited knowledge
- To recommend key research directions

Slide 2.

SUBSTRATES

Q1: What do we know about the optimum impurity concentration?

Obvious parameters affected are:

- Space charge width
- Minority carrier lifetime
- Minority carrier diffusion length
- Contact resistance
- Radiation resistance
- Others?

Slide 3.

Q2: What is known about relative quality of substrates from different suppliers? e.g.,

- MCP (Crystal Specialties)
- Cambridge Instruments
- Crysta-Comm
- Scientific International
- Sumitomo

See also, Solid State Technology 1986, Process and Production Buyers Guide

Slide 4.

Substrate Quality (cont.):

Probably no comparative studies exist. At SERI We are starting to examine:

- Diffusion length - electrolyte SPV
- Lifetime - photoluminescence decay
- Impurity states - low-temperature photoluminescence
- Nonradiative defects - cathodoluminescence
- Defects - high-resolution cross-sectional TEM

Slide 5.

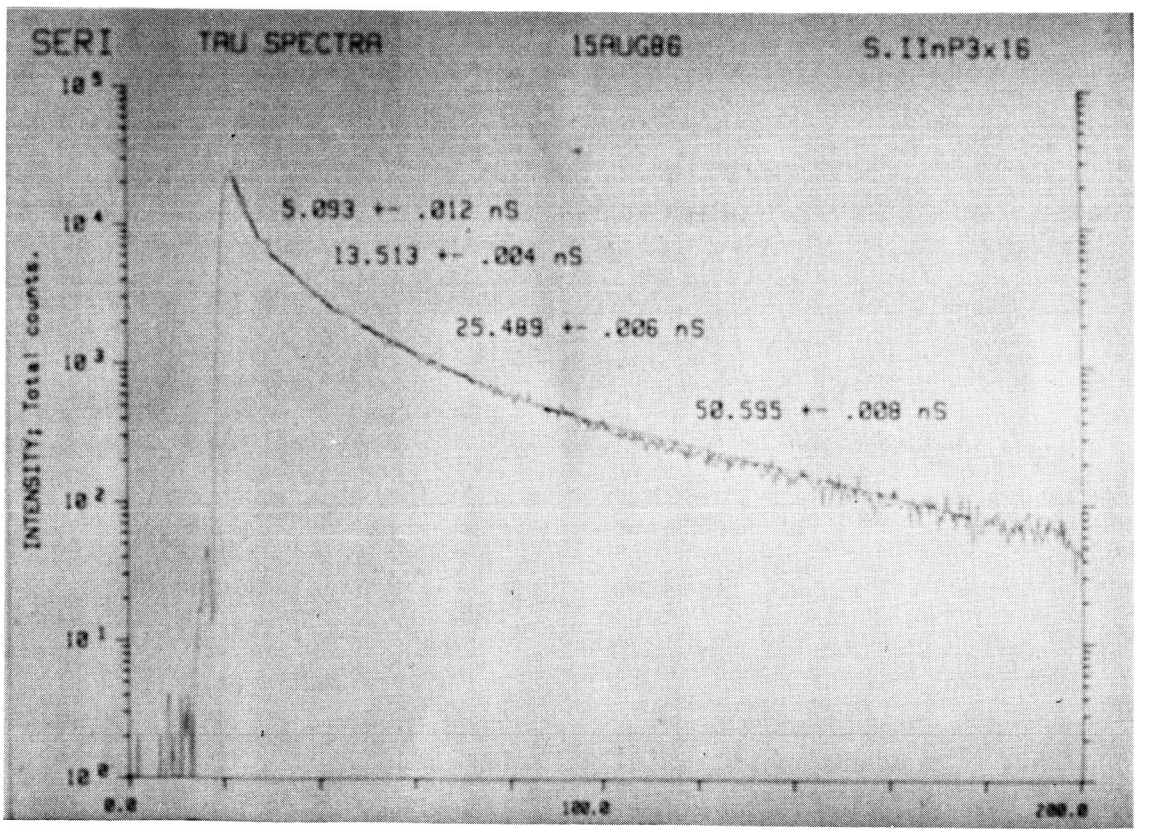

Slide 6.

VARIATION OF MINORITY CARRIER LIFETIME WITH
IMPURITY CONCENTRATION MCP MATERIALS

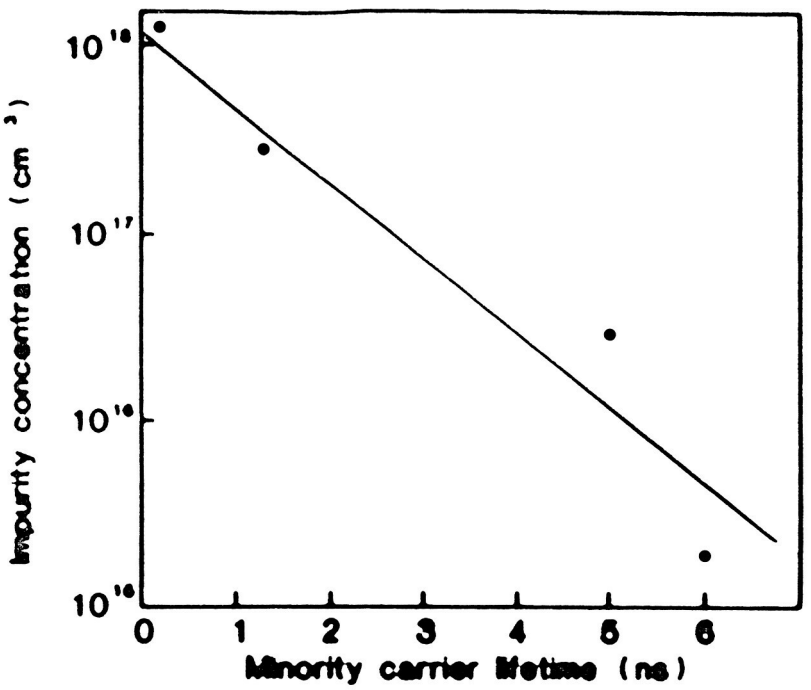

Slide 7.

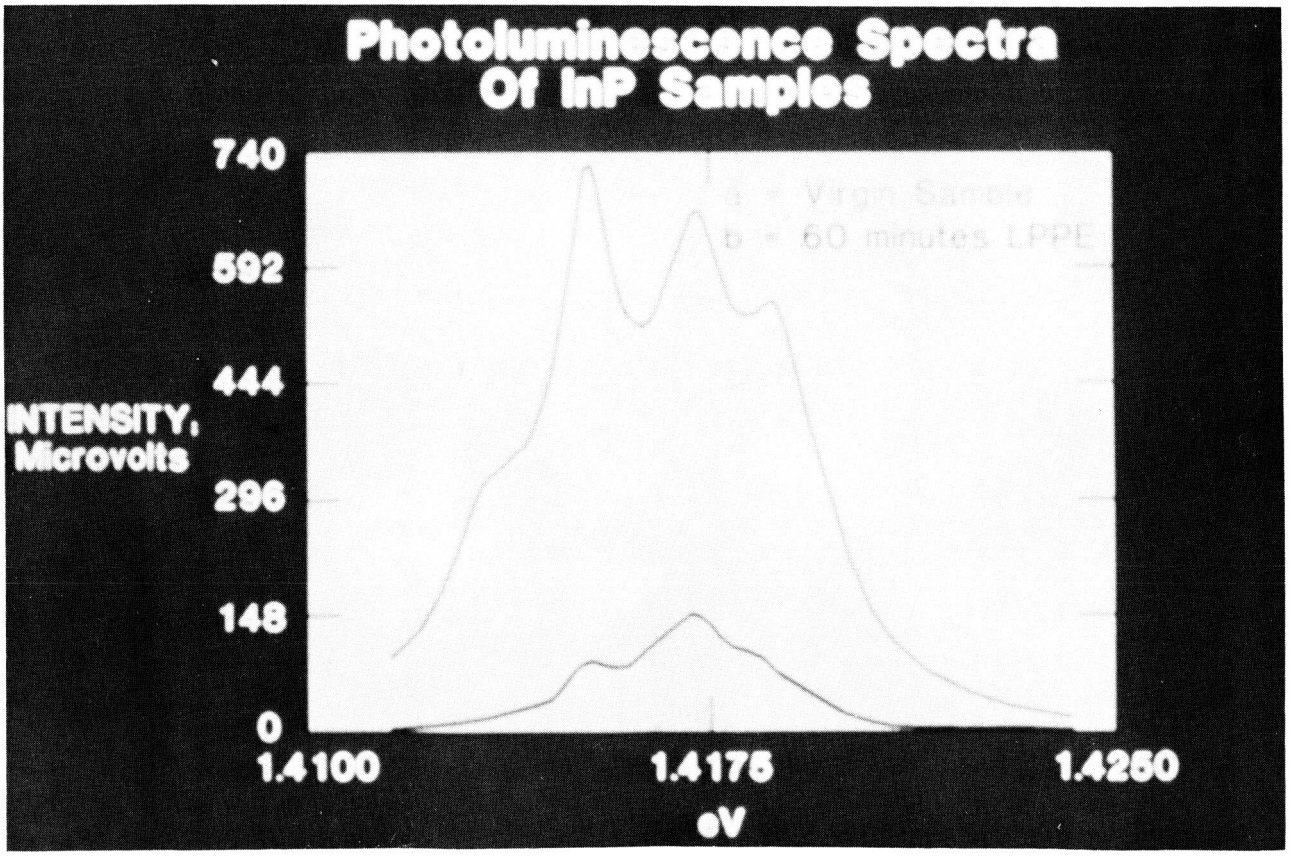

Slide 8.

Cathodo-luminescence from 100 InP

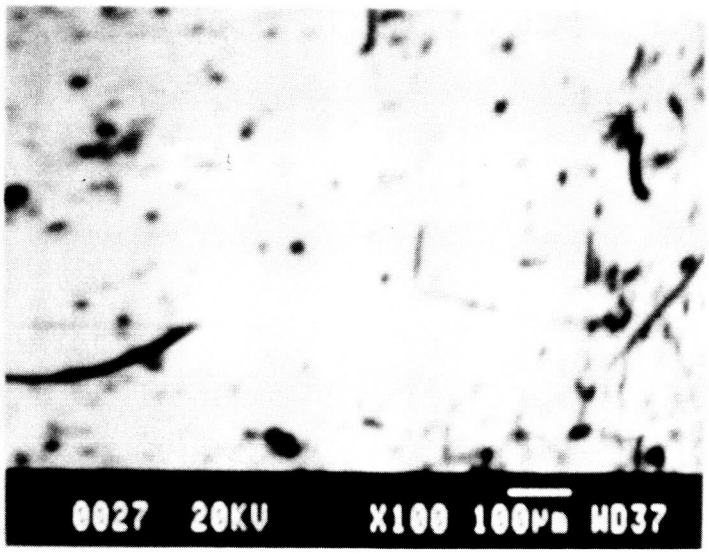

Slide 9.

Q3: What do we know about back-contacts?

Very little work done on contact resistance to p-InP. Usually Au/Zn, Au/Mg, Au/Be used.

Identifiable variables are:

- Alloying temperature and duration
- Gaseous environment
- Ratio of group II/Au
- Method of deposition
- Substrate preparation

Slide 10.

Contacts (cont.):

Very little known about:

- Lower limit of r_e
- Nature of reactions at interface
- What establishes ohmicity
- Long-term reliability

Slide 11.

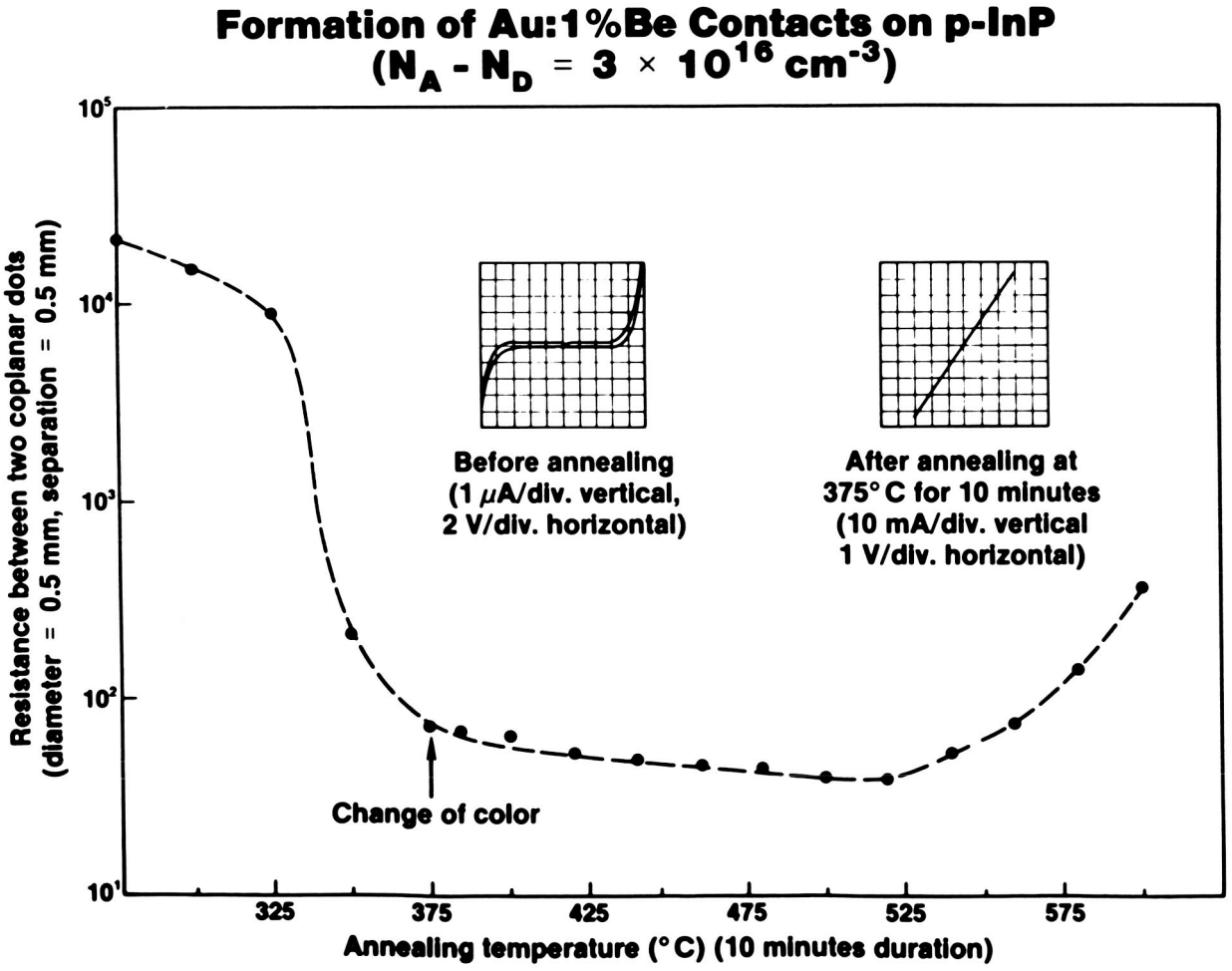

Slide 12.

JUNCTION FORMATION

Q1: What do we know about cleaning techniques prior to junction formation?

- Various cleaning techniques recommended
- Nothing readily quantifiable
- Can examine surface ellipsometrically to determine thickness of native oxides
- Can use spectroscopic ellipsometry to obtain $\epsilon_1(\lambda)$ and $\epsilon_2(\lambda)$

Slide 13.

Cleaning Techniques:

Both wet chemical and gas phase used, typically after degreasing in organic solvent.

Wet chemical etches include:

- Br/methanol (0.2 - 3.0 v/o)
- $Br/HBr/H_2O$ (1:12:68)
- $H_2SO_4/H_2O_2/H_2O$ (4-20:1:1)
- HCl/H_2O (2:1)
- Lactic acid/HNO_3/HF (50:8:2)
- Additional solutions including H_3PO_4, NaOCl, NH_4OH

Slide 14.

Cleaning Techniques (cont.):

Vapor phase before VPE growth

- HCl gas
- Ethylene dibromide vapor

Substrates often held at elevated temperature in phosphorus rich environment to volatilize and drive off native oxides.

Techniques generally successful but not quantified. Small differences may have major influence on interface and device properties.

Slide 15.

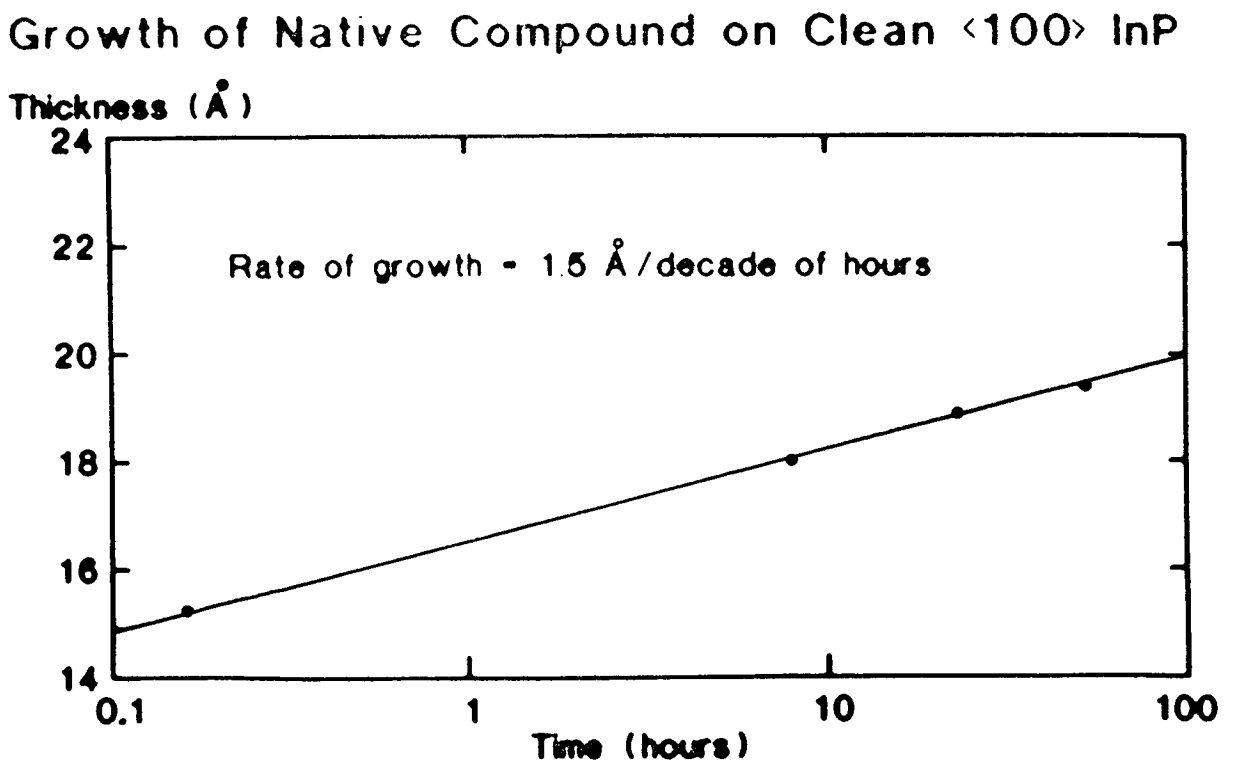

Slide 16.

Raman Spectrum of Polished InP Substrate

($N_A - N_D \cdot 3 \times 10^{16} cm^{-3}$)

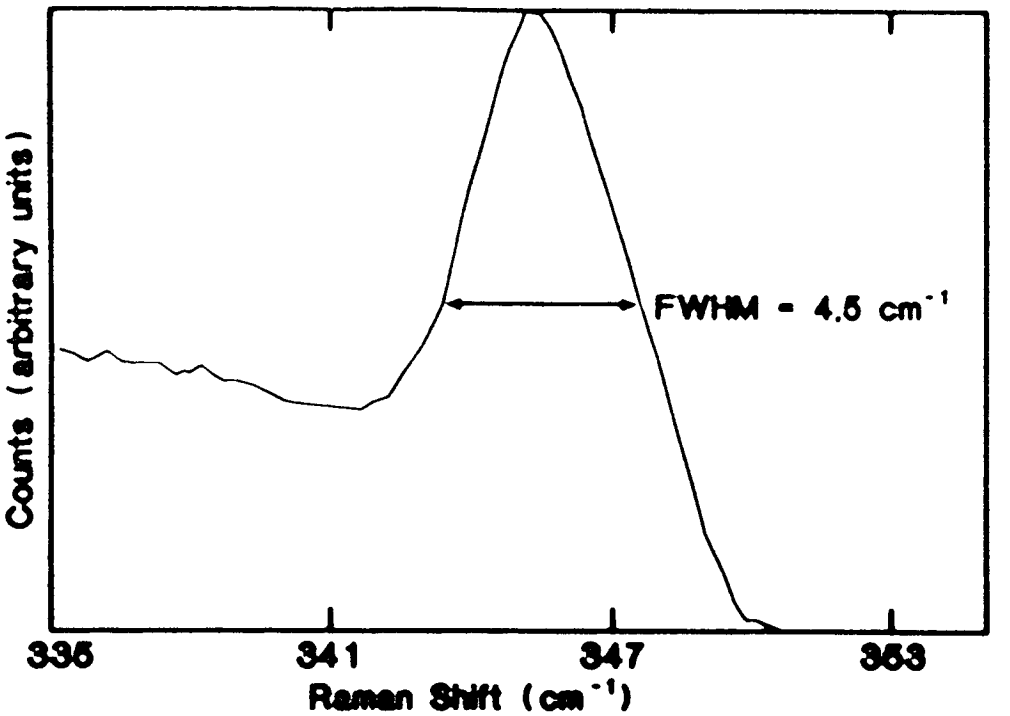

Slide 17.

Q2 What do we know about junction formation?

Three techniques reported in literature:

- RF sputtered ITO (SERI/Newcastle)*
- Ion-beam sputtered ITO (SERI)**
- Diffused junction (NTT, Oklahoma, Rutgers)*

---

*Probably homojunctions

**Probably a true heterojunction

Slide 18.

Junction Formation (cont.):

Limitations of these devices are:

- Homojunctions have nonoptimal blue response
- Damage causes excessive J_o, reduced V_{oc}, and FF
- With diffused junctions the problem is not so severe and V_{oc} = 845 mV

Slide 19.

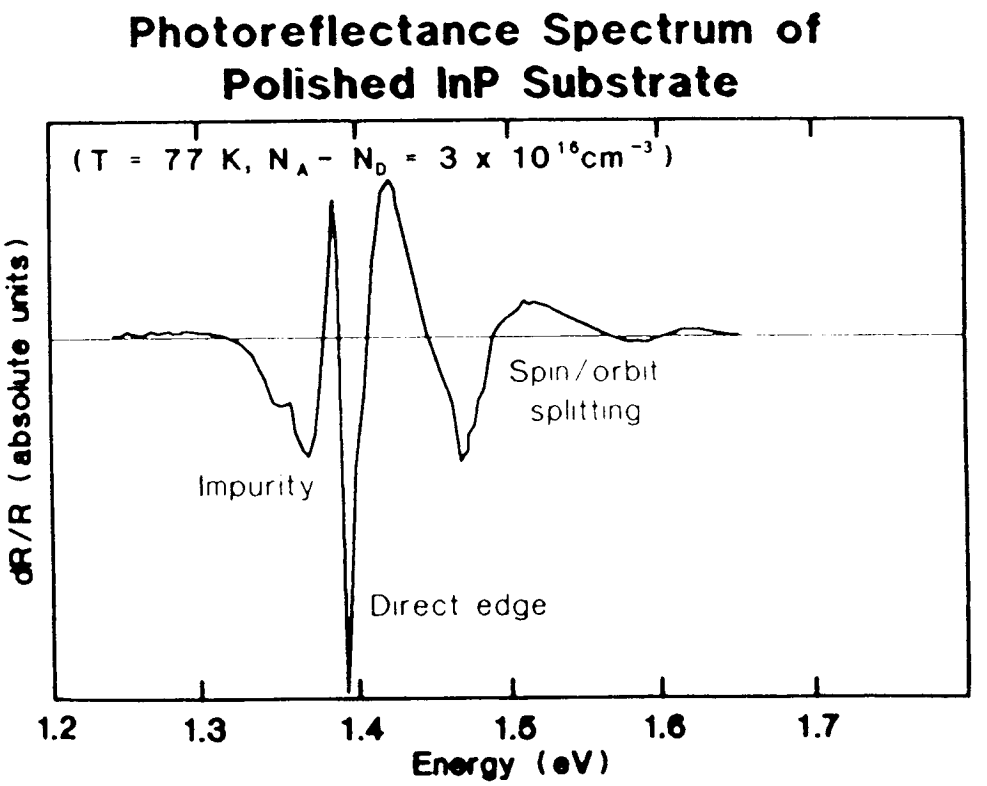

Slide 20.

Optimized Junction:

Should be possible to achieve:

- V_{oc} = 900 mV
- J_{sc} = 31 mA cm^{-2} (maximum possible = 36 mA cm^{-2})
- FF = 82 %

Therefore, η (AM1.5) = 23% should be achievable.

Slide 21.

Optimized Junction (cont.):

Major area for development is reduction of J_o. SERI is studying various methods of junction growth and in particular will very soon have an OMCVED apparatus commissioned. Related activities include:

- Device modelling
- Growth of "special" structures
- Development of in-situ ellipsometry to study nucleation and growth

Slide 22.

Technological Aspects:

- Grid optimization - straightforward, but often ignored. Routines available at SERI to optimize simple grids, provided relevant electrical parameters (resistivity, contact resistance, etc.). Device Modeling Group offers this as a service.

Slide 23.

Technological Aspects (cont.):

- AR coating design

Once again, usually neglected.

We now have data on $n(\lambda)$ and $k(\lambda)$ for:

- InP (spectroscopic ellipsometry)
- ITO (spectrophotometry)
- MgF_2 (spectrophotometry)

We have not yet examined texturing.

Slide 24.

Power Loss in Cell Associated with the Grid

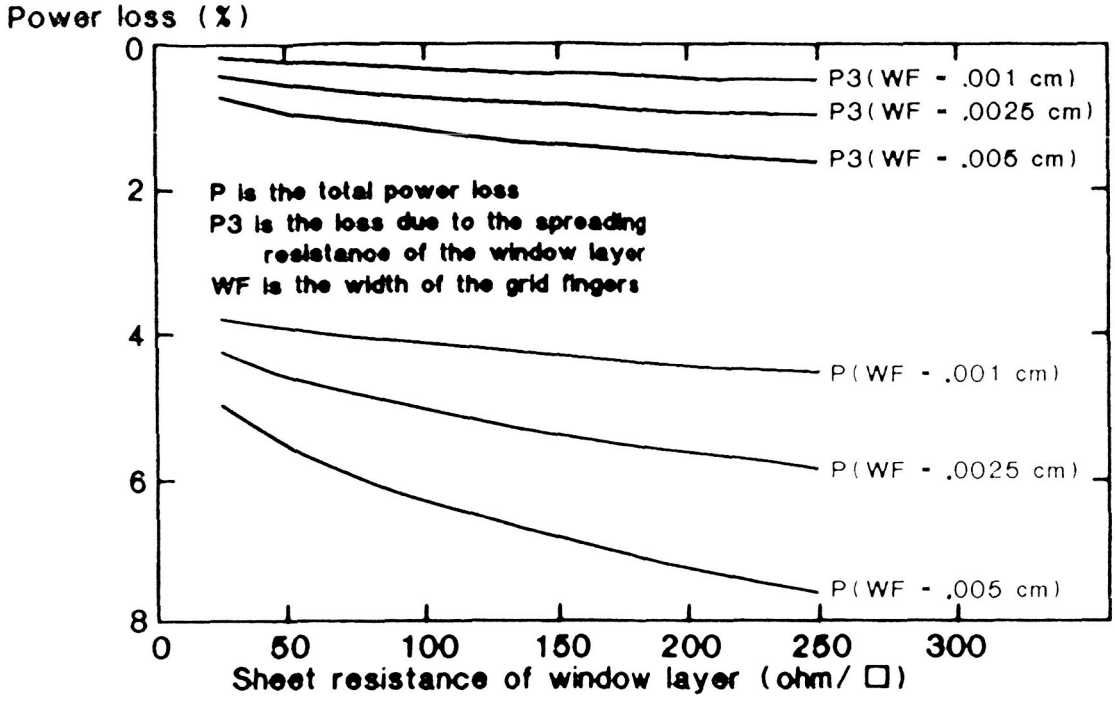

Slide 25.

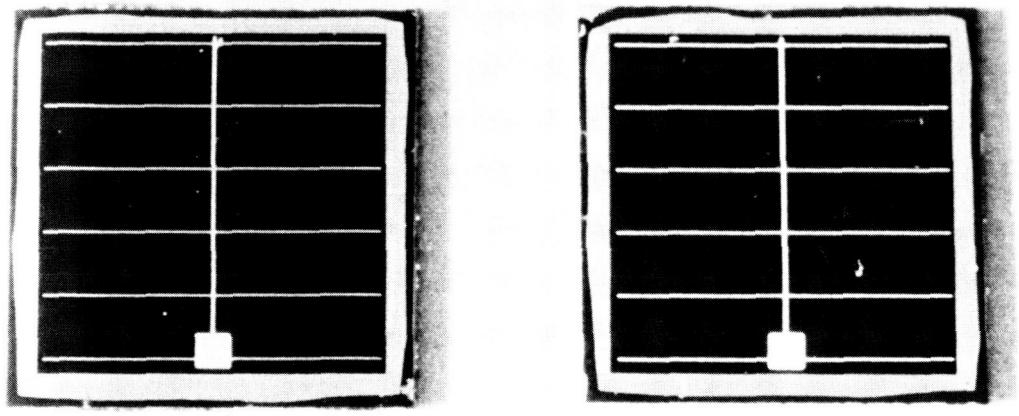

Slide 26.

REFLECTANCE FROM ITO/InP

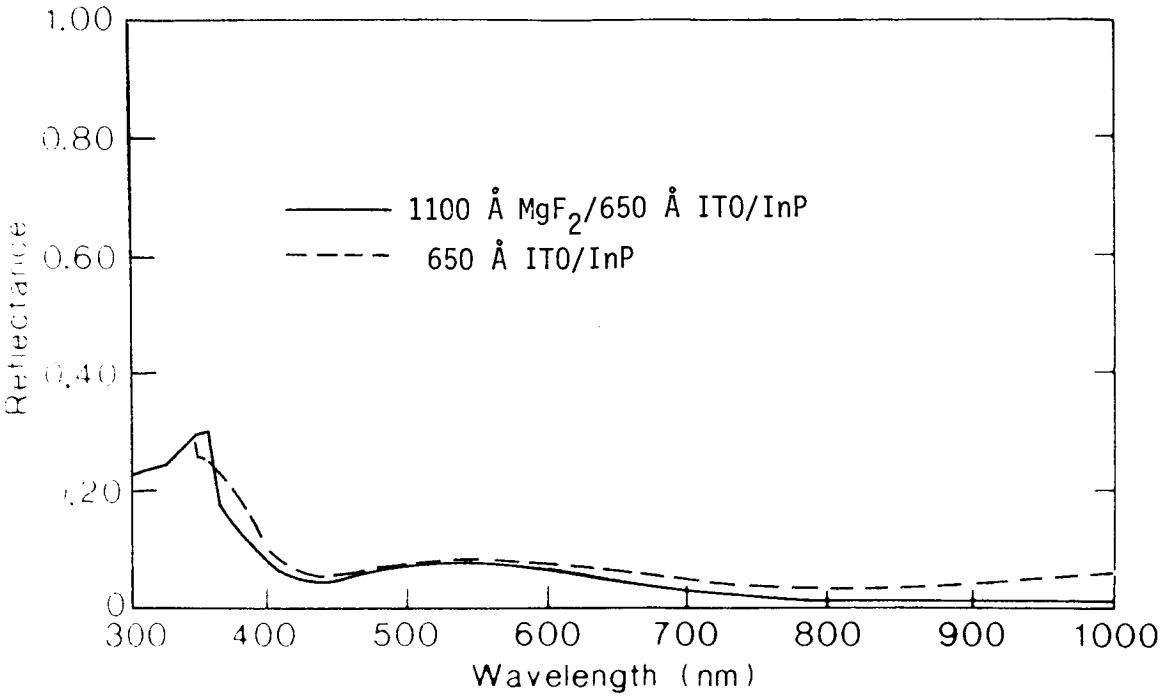

Slide 27.

Summary of Performance of Various InP Based Solar Cells

Group	Structure	η (%)	J_{sc} (mA cm^{-2})	V_{oc} (mV)	FF	Area (cm^2)	Air Mass
Newcastle (Coutts et al)	ITO/InP	16.2	26.9	768	76.7	≃ 1.0	1.5
Newcastle	ITO/InP	≃ 12.3*	?	?	?	≃ 4.0	0
Rensselaer (Parat et al)	n^+–p	16.3	24.7	800	81.5	0.313	1
Rensselaer	n^+–p	14.2	30.5	814	78.5	0.313	0
N.T.T. (Yamaguchi et al)	n^+–p	21.4	31.1	832	82.8	0.250	1.5
N.T.T.	n^+–p–p^+	20.0	30.0	830	80.0	0.250	1.5
N.T.T.	p^+–n	18.1	28.2	835	78.8	0.250	1.5
N.T.T.	p^+–i–n	22.0	35.8	811	76.0	0.250	1.5
Newcastle (Himrane)	CdS/InP	15.3	23.6	813	80.0	≃0.65	1.5

Slide 28.

Other Issues

- Efficiencies claimed by NTT overstated?
- Is the radiation resistance a lasting phenomenon?
- Is the cost of InP problematic?
- What do we know about interface stability, disregarding radiation?
- Others.

Slide 29.

InP WORKSHOP SUMMARY

BEGAN WITH A SHORT PRESENTATION TO SUGGEST TOPICS POSSIBLY SUITABLE FOR DISCUSSION. SET AS OBJECTIVES:

- IDENTIFY AREAS OF LIMITED KNOWLEDGE
- RECOMMEND KEY RESEARCH ACTIONS.

STRESSED THE NEED TO ASSESS THE QUALITY OF SUBSTRATES AND TO CHARACTERIZE THEIR ELECTRO-OPTICAL PROPERTIES. POSSIBLY COMPARE MATERIAL FROM DIFFERENT VENDORS.

ALSO FEEL SUBSTRATE PREPARATION PRIOR TO JUNCTION FORMATION MAY BE IMPORTANT.

CONTACT FORMATION IS NOT MUCH STUDIED AND COULD ALSO BE RELEVANT.

DIFFERENT JUNCTION FORMATION TECHNIQUES, SPUTTERING OF ITO, DIFFUSION, OMCVD - ALL GIVING ENCOURAGING RESULTS.

WHAT IS ULTIMATE REALISABLE EFFICIENCY? MY GUESS, FOR AM .5 WAS

V_{oc} = 900 mV

J_{sc} = 31 mA cm^{-2}

F.F. = 82%

$\therefore \eta = 23\%$

DISCUSSED THE NEED FOR PROPERLY ENGINEERED CELLS, I.E., OPTIMISED GRIDS AND AR COATINGS.

KEY POINTS FROM DISCUSSION

0 NEED TO INCREASE EFFICIENCY SIGNIFICANTLY

- ALL CELL PARAMETERS, NOT JUST Voc

- TARGETS COULD BE

  Jsc = 0.9 x Jsc (THEORY) = 37 mA cm^{-2} (AMO 37.2 mW cm^{-2})

  Voc = 0.7 x .35 = 945 mV (+ ?)

  F.F. = 85%

  $\therefore \eta_{MAX} = 21.7\%$

  STILL SEEMS RATHER HIGH (INTUITIVELY)

  cf BEST JAPANESE RESULT 15%

0 HOW DO WE IMPROVE EFFICIENCY?

- SURFACE PASSIVATION INCLUDING LATTICE MATCHED WINDOW LAYERS OR DIELECTRICS

- DEEPER JUNCTIONS

- NOVEL STRUCTURES

- BETTER UNDERSTANDING OF MATERIALS QUALITY. WHAT DO DEFECTS IN THE SUBSTRATES DO? NEED FOR BETTER SUBSTRATES CHARACTERIZATION.

- BETTER TECHNOLOGY, I.E., GRIDDING AND AR COATING, I.E., HIGHER EXTERNAL QUANTUM EFFICIENCY.

- EFFICIENCY MEASUREMENTS
  - NEED TO STANDARDISE ON AMO
  - AT LEAST SPECIFY ACCURATELY MEASUREMENT CONDITIONS USED.
  - STRESS 'LARGE' AREAS TO LEND MORE MEANING TO DATA.

- RADIATION TESTING
  - NEED TO CONFIRM DATA FROM NTT
  - ENSURE HIGH EFFICIENCY CELLS TESTED
  - CAN WE ATTAIN HIGH EFFICIENCY AND STILL MAINTAIN GOOD RADIATION RESISTANCE?
  - CAN RADIATION DAMAGE MODELS BE DEVELOPED?
  - ARE THERE STILL BETTER MATERIALS THAN InP?
  - NEED TO KNOW MORE ABOUT DAMAGE MECHANISMS

- FUTURE DEVELOPMENTS
  - HIGH POWER/MASS RATIO
  - REDUCE MATERIALS COST
  - CONCENTRATOR STUDIES
  - ALTERNATIVE SUBSTRATES
  - CLEFT POSSIBILITIES

NASA
National Aeronautics and Space Administration

Report Documentation Page

1. Report No.	2. Government Accession No.	3. Recipient's Catalog No.
NASA CP-2475		

4. Title and Subtitle	5. Report Date
SPACE PHOTOVOLTAIC RESEARCH AND TECHNOLOGY—1986 High Efficiency, Space Environment, and Array Technology	June 1987
	6. Performing Organization Code 506-41-11
7. Author(s)	8. Performing Organization Report No. E-3450
	10. Work Unit No.
9. Performing Organization Name and Address National Aeronautics and Space Administration Lewis Research Center Cleveland, Ohio 44135	11. Contract or Grant No.
	13. Type of Report and Period Covered Conference Publication
12. Sponsoring Agency Name and Address National Aeronautics and Space Administration Washington, D.C. 20546	14. Sponsoring Agency Code

15. Supplementary Notes

16. Abstract

This three-day conference, eighth in a series that began in 1974, was held at the NASA Lewis Research Center on October 7–9, 1986. The conference provided a forum to assess the progress made, the problems remaining, and the strategy for the future of space photovoltaic research. Papers were presented in a variety of technical areas, including cell research and technology, space environmental effects, and array technology and applications. Five workshops were held based on the following topics:

High Power/Large Area Systems
Opportunities for PV Applications
GaAs High Efficiency Limits
Device Modeling
InP Materials/Cell Fabrication

All presented papers, as well as summaries of the five workshops, are included in this proceedings.

17. Key Words (Suggested by Author(s))	18. Distribution Statement
Space power Photovoltaic cells Solar cells Solar arrays	Unclassified – unlimited STAR Category 44

19. Security Classif. (of this report)	20. Security Classif. (of this page)	21. No of pages	22. Price*
Unclassified	Unclassified	400	A17

NASA FORM 1626 OCT 86

*For sale by the National Technical Information Service, Springfield, Virginia 22161